ATTACHMENT 13

METOCEAN SOLUTIONS

MORPHODYNAMIC EVOLUTION MODELLING FOR THE NORTHPORT ENVIRONMENT

Numerical modeling of the
Sediment dynamics at Northport

Report prepared for
Northport

Northport

Specialists in
Oceanography

MetOcean Solutions Ltd: Report P0367 – 01

February 2018

Report status

Version	Date	Status	Approved by
RevA	15/02/2018	Draft for internal review	Monetti
RevB	05/03/2018	Draft for internal review	Beamsley

It is the responsibility of the reader to verify the currency of the version number of this report.

TABLE OF CONTENTS

LIST OF FIGURES

LIST OF TABLES

1. INTRODUCTION

Northport is a deep-water commercial port strategically situated at Marsden Point near Whangarei in Northland, New Zealand. Northport is New Zealand's newest port, designed and built as a flexible, multi-purpose facility to cater for a wide range of cargoes and their associated vessel types.

Northport's current footprint totals 48.46 hectares, made up of 570 linear metres of berthage consisting of three berths, 33.615 hectares of reclamation and 14.845 metres of berth with a depth at Chart Datum (CD) of 14.5 m and 2.3 hectares of reclamation providing for a total consented footprint of 840 linear meters (4 berths) and 50.76 hectares. Historical hydrographic surveys of the swinging basin have highlighted the fact that infilling is occurring over time, and there is a requirement to understand future infilling rates from a maintenance and operability perspective.

Further, Ports strategic planning has identified potential for the facilities to expand up to 250 metres and include a 13.0-hectare reclamation westward, with the entire berth length cut to 14.5 m CD, with 700 metres capable of a depth up to 16 m CD (Figure 1.2).

To protect and ensure the port's ability to expand as the market or NZ port strategy demands, the opportunity to undertake the consent application for the remaining potential reclamation footprint is currently being considered. While at the early stages, Northport feel that the timing is right to start to undertake the first steps towards securing the required port growth.

Northport recognise that there is scope to reclaim areas to both the east and west of the current reclaimed facility (Areas 5 and 6, Figure 1.2). To undertake these capital works, there are a suite resource consents that will be required, including dredging (see Figure 1.3), earthworks, discharges to the harbour as well as ongoing land use type consents and discharge consents. Dredging areas and estimated volume to be dredged are given in Figure 1.2 (Areas 1-3), with a total of approximately 973,000 m^3 expected to be dredged (Capital Dredging). This sediment is intended to be used to provide clean fill to the areas being reclaimed (Figure 1.2); mitigating the need to dispose of sediment at an offshore site.

It is likely that Capital dredging will also be undertaken using a TSHD given the sediment, however a Backhoe Dredger (BHD) or Cutter Suction Dredge (CSD) may be used.

From an operational and consenting perspective, Northport require an understanding of the effects of longer term sedimentation within the swinging basin and potential morphological responses to the proposed capital dredging and reclamations – this is achieved through the application of a calibrated and validated morphological model (i.e. Delft3d). Qualitative and quantitative calibration is achieved through the comparison of morphological model outputs against hydrographic survey data; specifically between 2016 and 2017. Once calibrated, the morphological model can be used to assess future morphological response for both the existing port and proposed port alterations (i.e. capital dredging and reclamations).

This report represents a technical reference document that details:

- The establishment of the hydro-morphological numerical model used to capture the morphological changes observed between 2016 and 2017 within the swinging basin and the surroundings.

- The methodology and the outcomes of the numerical model performance assessment.

The report is structured as follows; the complete methodology applied in this study is detailed in Section 2, including a description of the model settings and the methodology applied to assess the model skills. Results of the validation process and predictions of the infilling process are given and discussed in Section 3. A brief summary is presented in Section 4 while the references cited in this document are listed in Section 5. Additional figures are provided in Appendix A and B for completeness

Figure 1.1 Location of Northport within Whangarei Harbour.

Figure 1.2 Draft plan of area to be expanded.

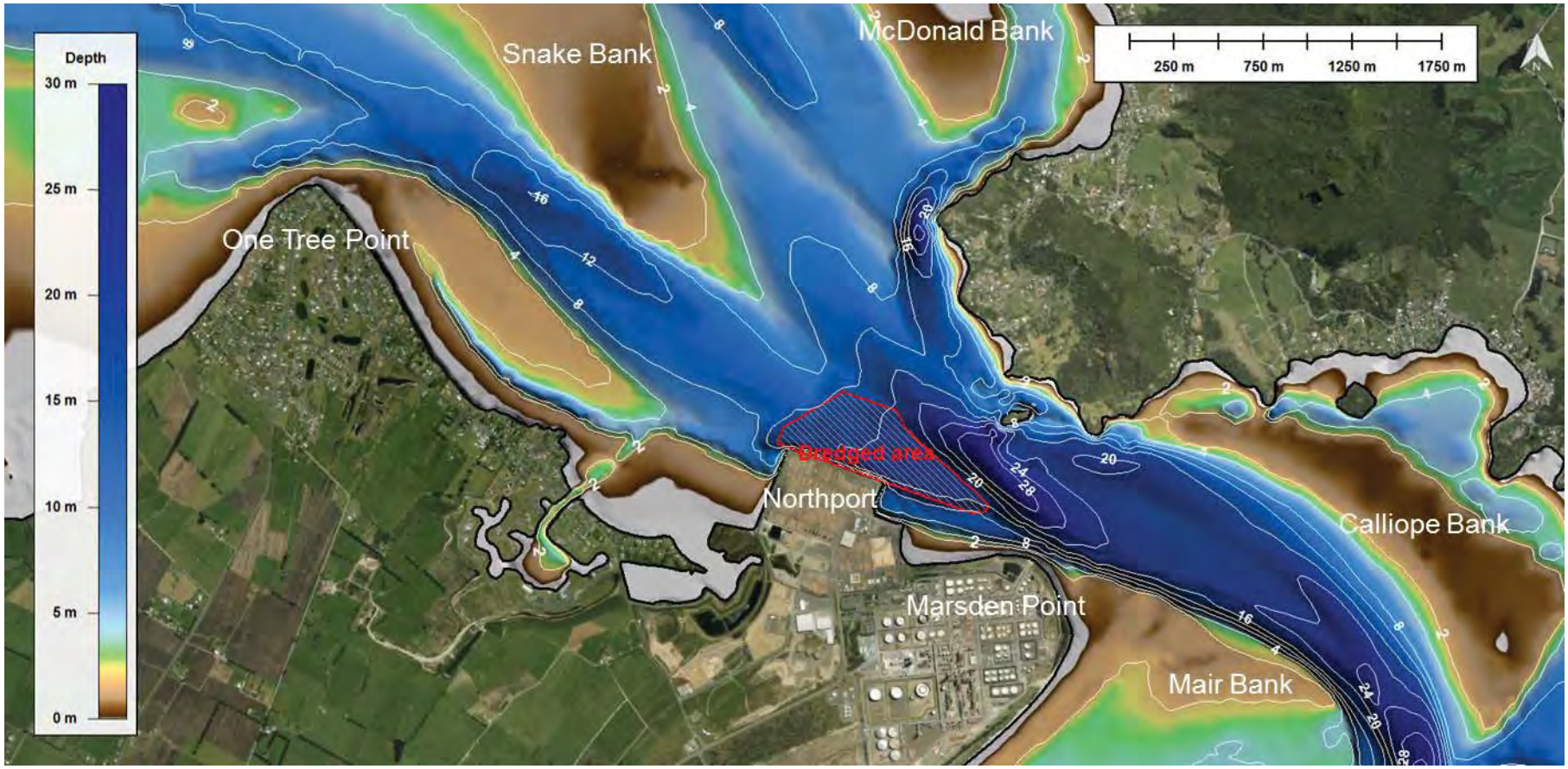

Figure 1.3 Location of Northport near the entrance to Whangarei Harbour. The colour scale details the bathymetry (MSL) derived from multiple data sources. Key locations and the dredged area corresponding to the swinging basin are also indicated on the map.

2. METHODS

The primary objective of the study was to capture the existing sediment dynamics and morphological response within the swinging basin at Northport with the use of a numerical model. To meet this objective, the focus was first on establishing a suitable modelling approach to accurately predict the annual infilling rates measured from consecutive hydrographic surveys between 2016 and 2017. The present section details the methods applied for the implementation and the validation of the morphological numerical modelling.

2.1. Bathymetry

Northport has undertaken an extensive monitoring program of the access channel, swinging basing and berths over the last decade to assess the naturally occurring morphological response, including sedimentation, of the environs. Hydrographic surveys using single and multi-beam echo-sounders have been conducted annually, with data available for the period 2006-2017.

In the present work, an analysis of the measured depth from 2007 to 2017 was carried out to improve the understanding of the infilling processes occurring within the swinging basin. Estimations of the annual volumetric infilling rates were estimated over three areas adjacent to Northport, which are proposed to be dredged in the near future.

In the context of coastal numerical modelling, bathymetry is an essential requirement. MetOcean Solutions has compiled an extensive national and regional bathymetric dataset derived from Electronic Navigation Charts (ENC), which are used as the foundation for creating the required model domains. These datasets were supplemented with recent hydrographic survey datasets (Figure 2.1) in order to develop suitable model domain bathymetry (Figure 2.2). The measured depth changes observed over subsequent years were used to calibrate the morphological numerical model.

We determined that the accuracy of measurements varies depending on the instrument, the frequency of soundings and the surveyed area was approximately ± 0.15 m based on inter-annual comparisons of the measured depth changes. This margin of error has been taken into accounts when comparing the model and against measurements morphological response.

Results of the measured data analysis are presented in Section 3.2.

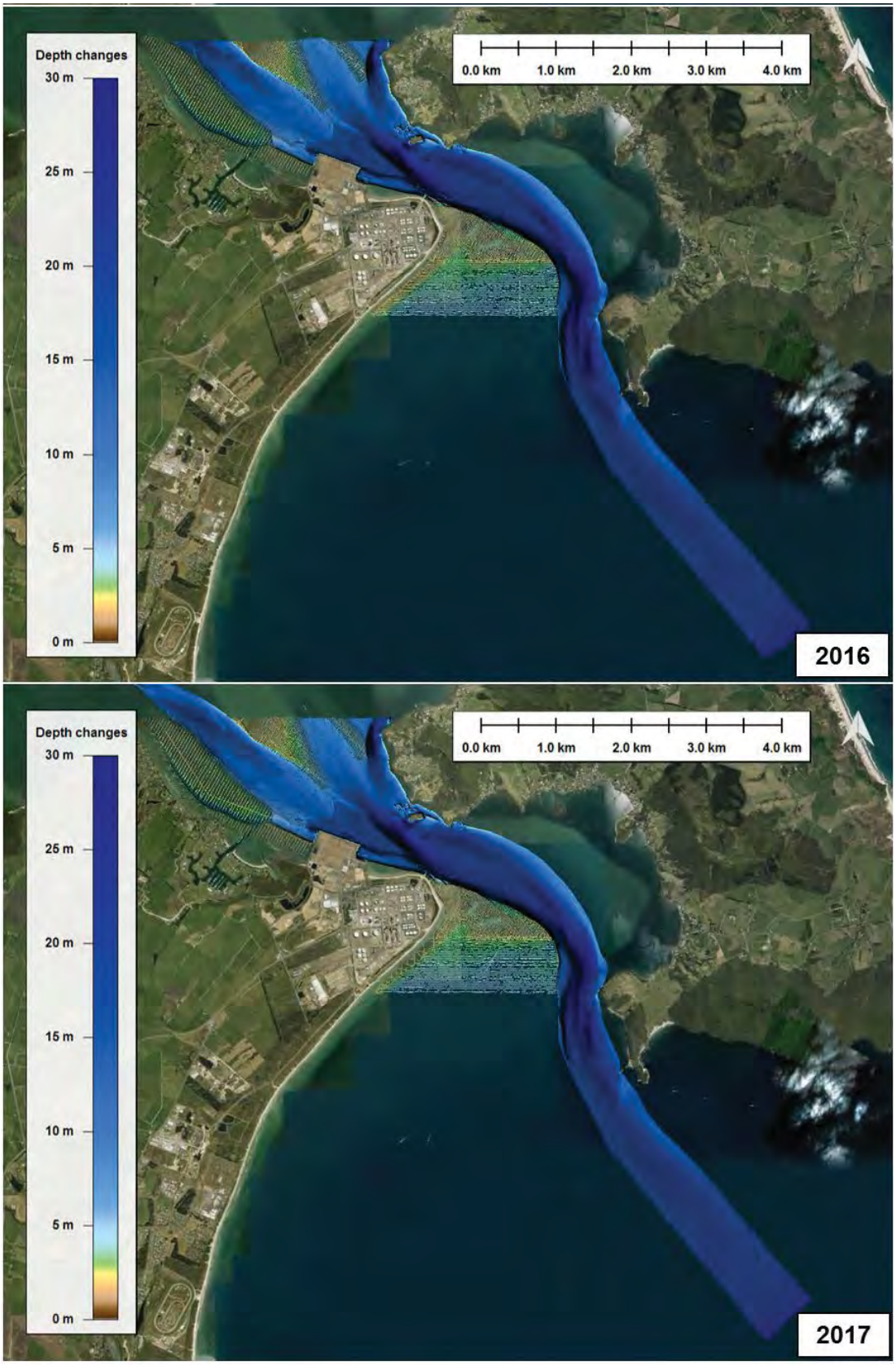

Figure 2.1 Bathymetric multi-beam survey data for 2016 and 2017 used to update the model bathymetry in the channel and at Northport for the setup and the calibration of the morphological model.

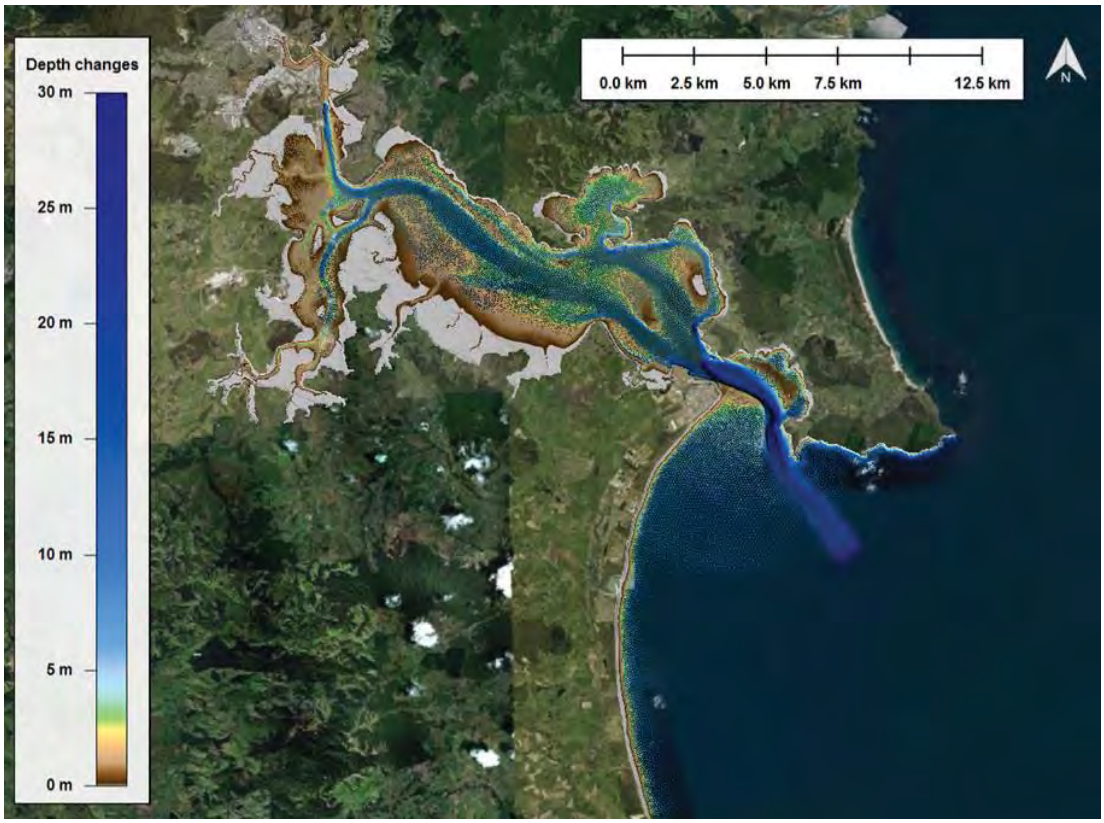

Figure 2.2 Mesh-gridded bathymetry data used to set up the model domain. Note that recent bathymetric survey data were used to update depths in the channel and near Northport.

2.2. Model description

The modelling system Delft3D (Lesser et al., 2004) was used to set up and run high-resolution process-based morphodynamic models. The software is based on interlinking three separate components (Delft3D – WAVE, Delft3D – FLOW and Delft3D – MOR) that together simulate flows, waves and sediment transport. The three components are fully coupled to simulate morphodynamic feedbacks.

Delft3D has been specifically developed to simulate the dynamics of complex coastal regions controlled by a wide range of physical and morphological process interactions. Its multi-disciplinary approach makes this tool applicable for predicting morphological developments as a response to both naturally occurring processes and anthropogenic activities such as land reclamation, channel maintenance, disposal activities or coastal protection.

Delft3D has been successfully applied worldwide for a large range of coastal studies, including within the New Zealand context, i.e. Port Otago (Weppe et al., 2015), Tauranga Harbour (Ramli et al., 2015) and Rees River (Williams et al., 2016).

The present sub-section gives a brief description of the different Delft3D modules used to replicate the coastal dynamics from northern Bream Bay to One Tree Point within Whangarei Harbour.

2.2.1. Delft3D – FLOW

The hydrodynamic module Delft3D – FLOW is a multi-dimensional (2 or 3-dimensional) hydrodynamic model which calculates non-steady flows and transport processes.

Delft3D – FLOW solves the Navier – Stokes equations on a staggered mode grid for an uncompressible fluid under the shallow water and Boussinesq assumptions. The system solves the horizontal equations of motion, the continuity equation, the transport equations for conservative constituents and a turbulence closure scheme. The details of equations and associated sub-modules are fully described in Lesser et al. (2004) and Deltares (2017b).

2.2.2. Delft3D – WAVE

The third-generation SWAN model (Simulating WAves Nearshore) was used as the wave module (Booij et al., 1999; Ris et al., 1999). SWAN computes the evolution of random, short-crested waves in coastal regions with deep, intermediate and shallow water depths. The SWAN model accounts for (refractive) propagation due to depth and current and can represent the processes of wave generation by wind, dissipation due to while-capping, bottom friction and depth-induced wave breaking and non-linear wave-wave interactions explicitly with state-of-the-art formulations (Deltares, 2017b). Wave forces computed by the wave model on the basis of the radiation shear stress gradients can be used as a driving force to compute the wave-induced currents and set-up in the flow module. More details on the coupling between SWAN and Delft3D – FLOW are given in Deltares (2014).

2.2.3. Delft3D – MOR

The Delft3D – MOR module integrates the effects of waves, currents and sediment transport on the morphological development. At each computational time step the model computes both bed-load and suspended-load sediment transport components within the model domain. The bed level is then updated as a result of the sediment sink and sources terms and computed transport gradients. DelfT3D – MOR is designed to simulate wave propagation, currents, sediment transport and morphological developments in coastal, river and estuarine areas (Deltares, 2014). The model is able to simulate the sediment dynamics associated with both non-cohesive (sandy) and cohesive (silt/mud) sediment mixed layers or layered bed stratigraphy.

The transfer of sediment between the bed and the flow is modelled using sink and source terms acting on the near-bottom layer. Bed-load and equilibrium suspended-load transport resulting from the combined effect of waves and currents can be modelled by a range of formulations, among which are Engelund-Hansen, Meyer-Peter-Muller, Bijker, Bailard and Van Rijn. The streamwise and transverse bed slope effects on the magnitude and direction of transport are also included in the model.

The modelling and transport of cohesive sediment requires an approach that is fundamentally different to mobile sand transport. For very fine sediment size (i.e. silt or clay-sized), the inter-particles forces due to ionic charges becomes significant relative to the gravitational forces which strongly dominate the sand transport processes. As a result, processes including flocculation, hindered settling, and bed consolidation have important roles in the movement of cohesive particles. An extensive description of the associated sub-models in Delft3D is given in Deltares (2017b).

In Delft3D – MOR the cohesive sediment transport is calculated by solving the advection-diffusion equation for the suspended sediment (Eq. 2.1). Note that no bed load transport is considered for cohesive sediments.

$$\frac{\partial C}{\partial t}+\frac{\partial uC}{\partial x}+\frac{\partial vC}{\partial y}+\frac{\partial (w-w_s)C}{\partial z}=\ \frac{\partial}{\partial x}\left(\varepsilon_{s,x}\frac{\partial C}{\partial x}\right)+\frac{\partial}{\partial y}\left(\varepsilon_{s,y}\frac{\partial C}{\partial y}\right)+\frac{\partial}{\partial z}\left(\varepsilon_{s,z}\frac{\partial C}{\partial z}\right)$$

(Eq. 2.1)

where,

E	Mass concentration [kg.m^{-3}]
u, v, w	Velocity components [m.s^{-1}],
$\varepsilon_{s-x,y,z}$	Eddy diffusivities in the x,y,z directions [m^2.s^{-1}],
w_s	Sediment settling velocity [m. s^{-1}].

Sediment fluxes between the water phase and the bed are calculated using the Partheniades-Krone formulations (Partheniades,1965).

$$E = M.S(\tau_{cw}, \tau_{cr,erosion}) \quad \text{(Eq. 2.2)}$$

$$D = w_s.c_b.S(\tau_{cw}, \tau_{cr,deposition}) \quad \text{(Eq. 2.3)}$$

$$c_b = c(z = \frac{\Delta z_b}{2}, 2) \quad \text{(Eq. 2.4)}$$

where,

E	Erosion flux [kg/m^{-2}.s^{-1}]
M	User-defined erosion parameter [kg/m^{-2}.s^{-1}]
$S(\tau_{cw}, \tau_{cr,erosion})$	Erosion step function:

$$S(\tau_{cw}, \tau_{cr,erosion}) = \begin{cases} \left(\frac{\tau_{cw}}{\tau_{cr,erosion}} - 1\right), & when\ \tau_{cw} > \tau_{cr,erosion} \\ 0 & , when\ \tau_{cw} > \tau_{cr,erosion} \end{cases}$$

(Eq. 2.5)

D	Deposition flux [kg/m^{-2}.s^{-1}]
M	User-defined erosion parameter [kg/m^{-2}.s^{-1}]
w_s	Sediment settling velocity [m. s^{-1}].
c_b	Average sediment concentration near bottom [kg.m^{-3}]

$$S(\tau_{cw}, \tau_{cr,deposition}) = \begin{cases} \left(\frac{\tau_{cw}}{\tau_{cr,deposition}} - 1\right), & when\ \tau_{cw} > \tau_{cr,erosion} \\ 0 & , when\ \tau_{cw} > \tau_{cr,erosion} \end{cases}$$

(Eq. 2.6)

τ_{cw}	Maximum bed shear stress due to current and waves.
$\tau_{cr,erosion}$	User defined critical erosion shear stress [N. m^{-2}]
$\tau_{cr,deposition}$	User defined critical deposition shear stress [N. m^{-2}]

Erosion and deposition terms are finally used as bed boundary conditions;

$$-w_s.C - \varepsilon_{s,z}\ \frac{\partial C}{\partial z} = D - E\ ,\ at\ z = z_b \quad \text{(Eq. 2.7)}$$

The formulation requires the specification of erosion and deposition shear stresses.

2.3. Model settings

2.3.1. Hydrodynamic model

The base hydrodynamics were computed in the Delft3D – FLOW module, which can be used in a full 3-dimensional or depth-averaged (2D) mode. Ranasinghe and Pattiaratchi (1999) have shown that return flows caused by breaking waves in nearshore areas were not fully replicated in 2D hydrodynamic models. While this limitation is susceptible to reduce the morphological model performance in a mixed-energy tidal inlet or at a tidal inlet entrance, the use of the depth-averaged mode was considered appropriate within the context of the Northport environs. This choice aimed to economise computational resources allocated to the morphological module for a better representation of the infilling process within the swinging basin.

The model curvilinear grid (Figure 2.3) covered the tidal inlet entrance from northern Bream Bay to One Tree Point. The grid resolution varied from 10 m to 100 m focusing on Northport and the adjacent swinging basin. The grid consisted of 219 by 449 cells.

Figure 2.3 Map showing the Delft3D – FLOW and MOR grids used to replicate the hydro- and morpho-dynamics over the entrance to Whangarei Harbour. The resolution of the grid varies from 10 m to 100 m.

Bed shear stresses were computed in the model using a quadratic friction law. The non-linear enhancement of the bed shear stresses in the presence of waves was taken into account by means of the wave-current interaction model of Fredsøe (1984). Standard viscosity parameters in Delft3D were kept at default settings

The bottom roughness distribution was defined following the depth-dependant Manning's formulation. The Manning's coefficients of roughness for the longitudinal and transverse components typically range from 0.01 for a clean and smooth bed to 0.06 for a rocky bed with debris and/or vegetation. Here, deepest areas of the channel are typically characterised by gravelly shell lag while shelly sand is found on tidal flats

(Figure 2.4). Therefore, space-varying Manning's coefficients ranging from 0.018 to 0.034 were applied over the shallowest and deepest regions of the domain, respectively (see Figure 2.5).

Weakly reflective Riemann boundary conditions (Engquist and Majda, 1977, 1979; Verboom and Slob, 1984; Verboom and Segal, 1987) were applied rather than water elevation or current conditions at boundaries. The Riemann boundaries typically improve the model stability when feeding the hydrodynamic model with the wave forces computed by SWAN, and limit the propagation of artificial disturbances over the model domain. The formulation of the Riemann boundaries are detailed in Deltares (2017a).

Boundary conditions were prescribed from a 2D tidal high-resolution hindcast implemented by MetOcean Solutions over the entire Whangarei Harbour.

Spatially-constant wind fields were prescribed at the ocean – atmosphere interface. Wind conditions were derived from a 12 km Weather Research and Forecast (WRF) model atmospheric hindcast produced by MOS. Validation of the wind velocities at Marsden Point is provided in Appendix B for completeness.

The numerical time step was set to 3 seconds based on a stability criterion defined for a Courant Number lower than 10 in Delft3D (Deltares, 2017a). A smoothing time of 15 minutes was used to prevent introduction of short wave disturbances into the model during the spin-up phase.

A summary of the Delft3D settings applied for this study is provided in Section 2.3.4.

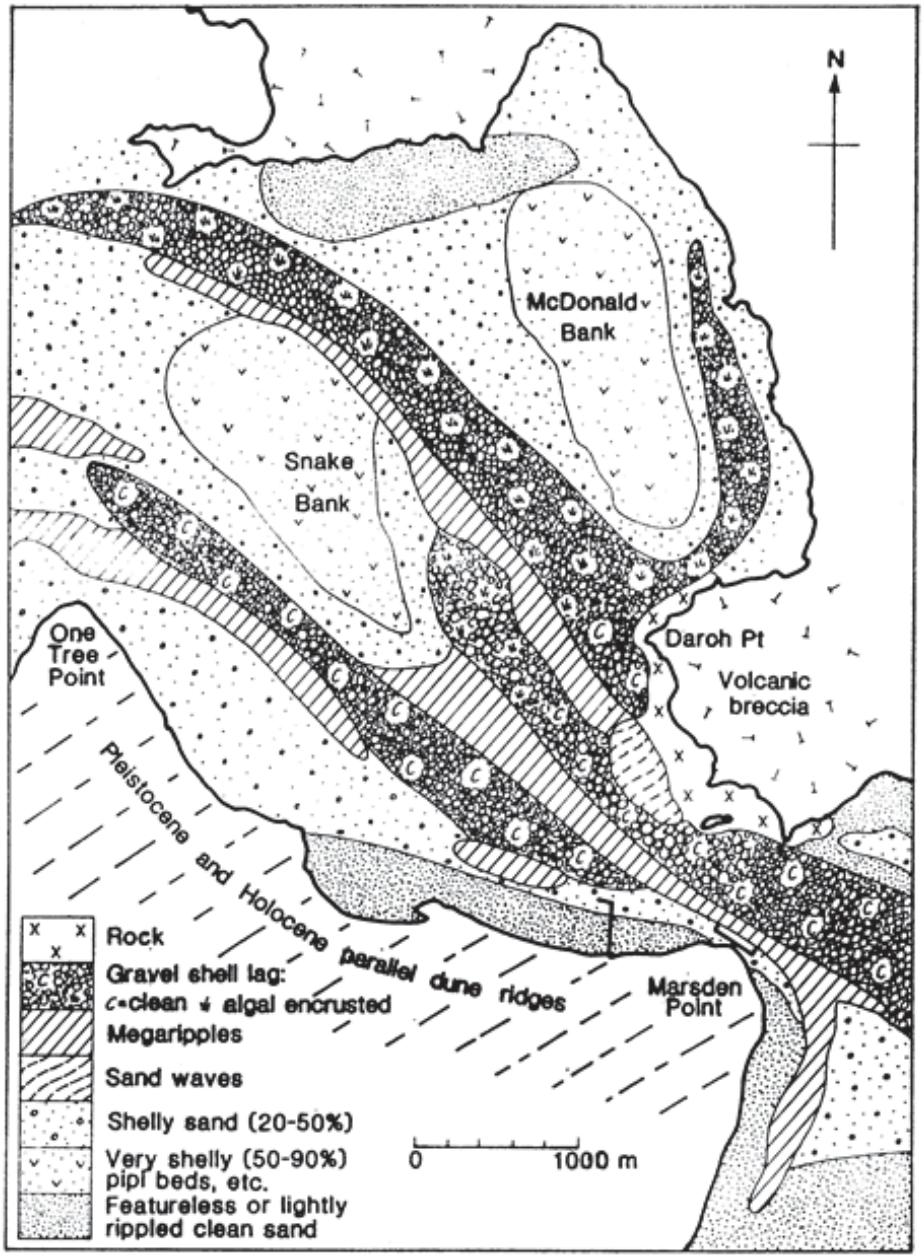

Figure 2.4 Simplified bottom sediment facies for Whangarei Harbour based on integration of side-scan sonar survey, underwater photographic and underwater video surveys, SCUBA diver observations, and bottom sediment analysis. The boundaries between facies are schematized (Source: Black et al., 1989).

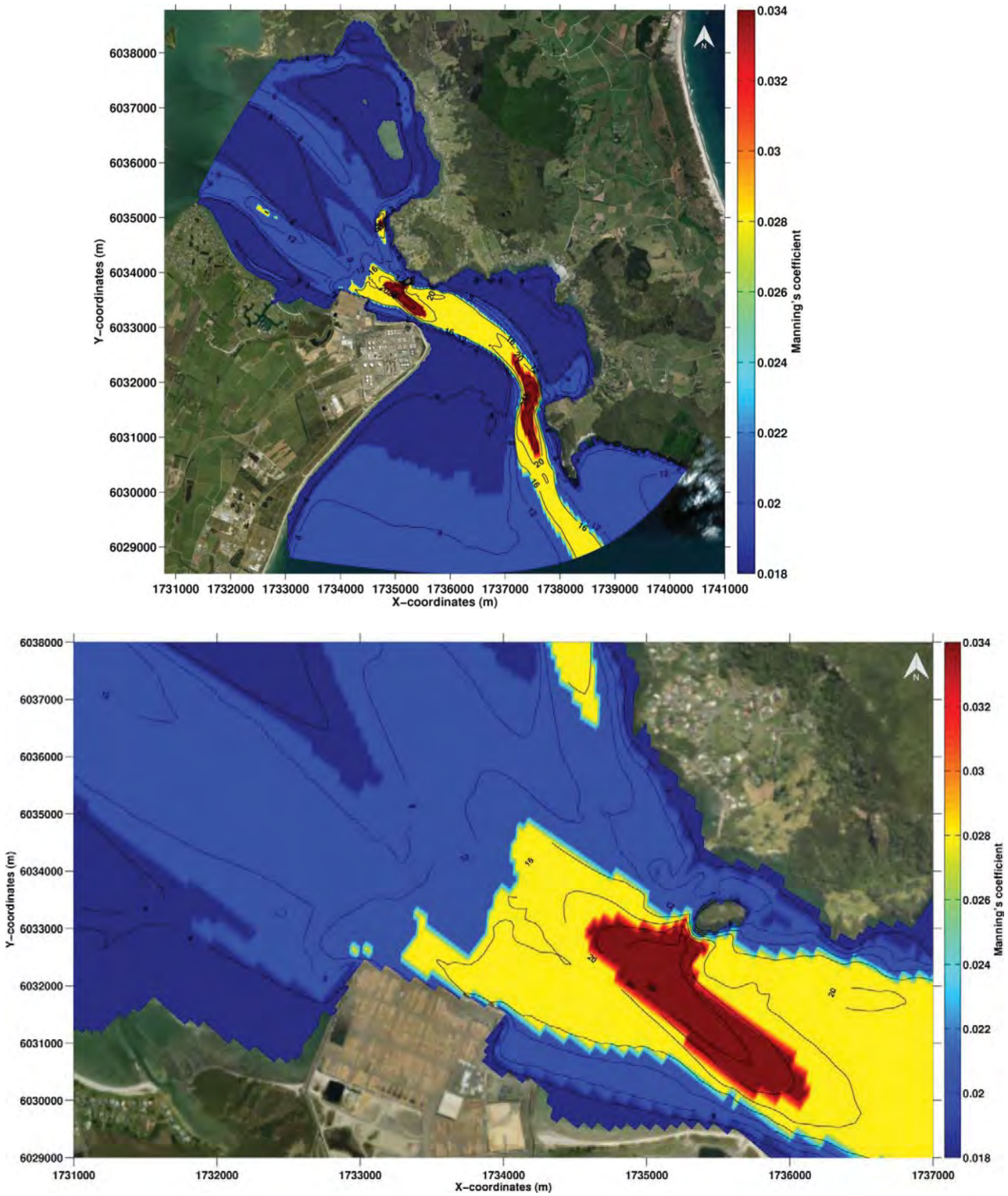

Figure 2.5 Map showing the space-varying Manning's coefficients used in Delft3D – FLOW to simulate the effect of bed roughness on hydrodynamics.

2.3.2. Spectral wave model

The spectral wave modelling consisted in a two-level nesting approach in Delft3D – WAVE allowing the retention of spatial variability in the incident wave field due to large scale regional refraction and sheltering effects. Open-boundary conditions were prescribed using constant wave parameters (significant wave height, peak period, peak direction and directional spreading) associated with each simulated scenario. The regional wave grid extended approximately 120 km offshore Whangarei Head with resolutions ranging from 490 m to 3300 m (Figure 2.6).

The interval of the sequential two-way coupling between SWAN and Delft3D – FLOW was of 60 min allowing the exchange of relevant parameters onto the curvilinear model grids via a communication file. Wave parameters and forcing terms associated with the wave radiation stresses computed by SWAN were read by the Deflt3D – FLOW module to model the hydrodynamic conditions. At the end of each assigned 60 minutes runtime, bottom elevation, water level and current fields were used as input to the SWAN model. The model looped through these sequential module applications until the end of the complete simulation. Morphodynamic modelling was performed through the implementation of a fully coupled wave – hydrodynamic system based on wave and current interactions.

Spatially-constant wind fields were prescribe using 12 km WRF atmospheric hindcast data produced by MetOcean Solutions and validated at Marsden Point (Appendix B). This inclusion of wind fields allowed capturing the wave growth effect in the generation and propagation of waves over the domains.

Bottom friction was modelled using the formulation of Collins (1972) with a coefficient of 0.015. The model also computed wave dissipation by whitecapping based on the formulation of Van der Westhuysen et al. (2007).

The depth induced breaking followed the formulation of Battjes and Janssen (1978) with the coefficients *Alfa* = 1 and *Gamma* = 0.73 (default values). Diffraction processes were not included in the SWAN modelling due to instabilities for very fine resolutions (Enet et al., 2006). As such, the wave field behind obstacles where diffraction is likely to be important is expected to be relatively poorly resolved, however morphological responses with Whangarei Harbour and in the vicinity of Northport, where diffraction may occur, are expected to be tidally dominated.

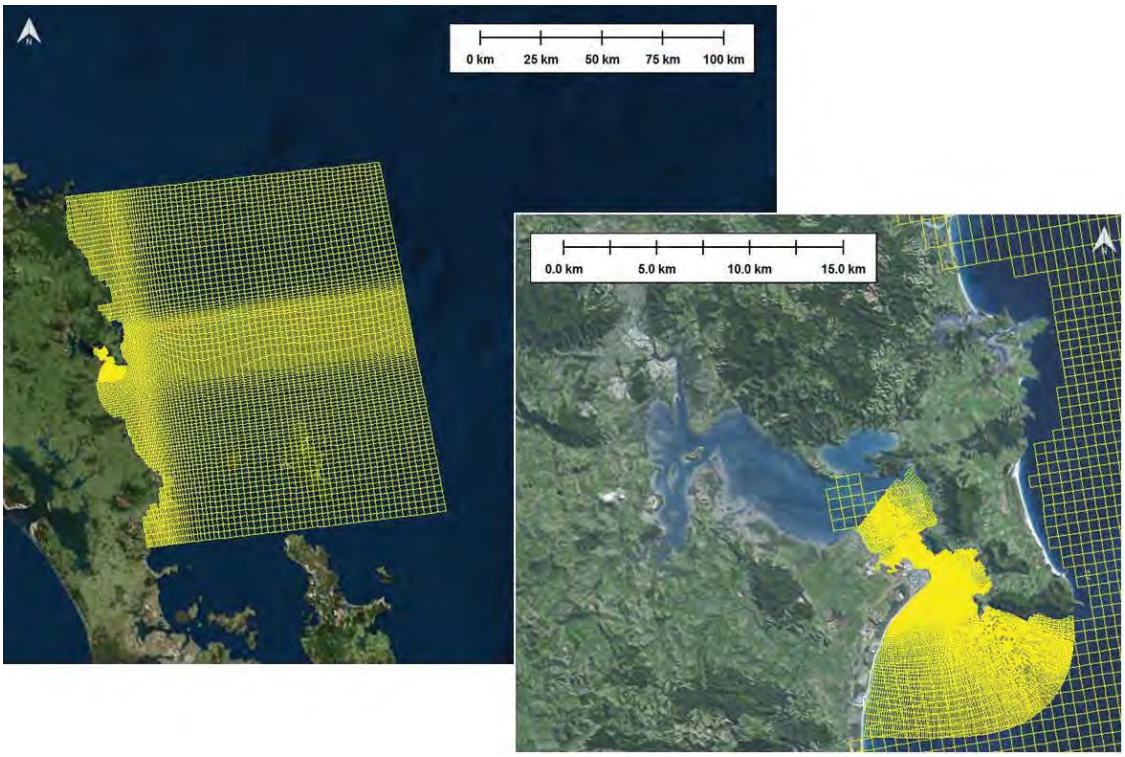

Figure 2.6 Map showing the two-level nesting strategy applied in SWAN (Delft3D – WAVE) to replicate the wave dynamics from northern Hauraki Gulf to Whangarei Harbour. The resolution of the finest grid ranges between 11 m and 260 m focusing on Northport and the adjacent swinging basin. The coarse grid resolution varies from 490 m to 3400 m.

2.3.3. Morphological model

Two strategies are generally considered when applying process-based morphodynamic models in coastal regions.

The first approach is based on dynamic equilibrium and consists in initialising the sediment availability and bed composition imposed by hydrodynamics. A bed stratigraphy scheme is used to redistribute a range of grain size fractions vertically between layers (e.g. Van der Wegen et al., 2011). This strategy is generally used for long-term process studies (decades to centuries) to limit unrealistic divergence that can occur due to uncorrected non-linear feedbacks between waves, currents and morphology.

For the second approach the sediment availability and characteristics are “manually” define over the domain using *in situ* data. This approach may lead to unrealistic divergences between the hydrodynamic conditions and the sea bed composition. The erosion rate becomes therefore the limiting factor regarding the overall sediment dynamics, particularly for fine-sized particles. To ensure realistic erosion rates of material in shallow waters, a careful process of calibration is required to limit the formation of unrealistic morphological patterns over time, particularly when using thick surficial sediment layers.

Previous work has shown that the morphology of sand banks and channels within Whangarei Harbour was linked to the presence of a significant biomass of shellfish (Morgan et al., 2011). The shell material produced by these populations maintaining stability by armouring the underlying sandy sediments from erosion (e.g. Mair Bank)

While most of the sandy material is predicted to be eroded under strong tidal current and breaking wave actions, the bio-stabilisation provided by live shellfish and their

residual shell fragments played a dominant role maintaining Mair Bank stable. Given the impossibility of simulating the bio-stabilisation effect in the model, the first approach described above based on dynamic equilibrium was preferred here.

A bed composition generation (BCG) run or “sedimentological spin-up” was therefore performed to initialise the bed composition imposed by hydrodynamics. Further details about the BCG run are provided in Section 2.4.

Core sampling carried out by NIWA (NIWA, 2012) at 109 sites within Whangarei Harbour showed surficial sediment was comprised of predominantly fine- to medium-grained size sand particles. Low to moderate concentrations of gravel, coarse sand and fine sand were also identified. The percentage of mud in the surficial sediment cores over eastern Whangarei Harbour was negligible. To ensure good model performances in replicating channel and sand bank dynamics, eight non-cohesive sediment classes were defined in Delft3D – MOR with grain sizes ranging from 100 µm to 2000 µm (Table 2.1). The spatial distribution of sediments in the morphological model obtained from the BCG run outputs are presented and discussed in Section 3.

Table 2.1 Non-cohesive sediment classes defined in the morphological Delft3D – MOR module.

Sediment class	Aggregate type	Grain size (µm)	Dry bed density ($kg.m^{-3}$)
Class 1	Very fine gravel	2000	1600
Class 2	Very coarse sand	1200	
Class 3	Coarse sand	800	
Class 4	Coarse sand	500	
Class 5	Medium sand	350	
Class 6	Medium/fine sand	250	
Class 7	Fine sand	180	
Class 8	Very fine sand	100	

2.3.4. Summary of Delft3D settings

The input parameters used in Delft3D – FLOW, WAVE and MOR (version 6.02.13.7545, 13 6.02.13.7545, 13 September 2017) to predict the sediment dynamics and morphology in in Whangarei Harbour are summarised in

Table 2.2 and Table 2.3. The calibration of the model has been essentially performed comparing the measured changes with the morphological response predicted by the model. Note that many parameters existing in the Delft3D system are not explicitly defined in these tables. For these parameters, no calibration process has been undertaken as they do not significantly influence the model results. Where not stipulated, default values were applied.

Table 2.2 Delft3D – FLOW and WAVE parameters used for the morphological modelling in Whangarei Harbour.

Parameter	Description	Value
Wave		
BedFriction	Seabed friction formulation	Collins (1972)
BedFricCoef	Collins's frictions coefficient	0.015
Breaking	Depth induced breaking model	TRUE (Battjes and Janssen, 1978)
BreakAlpha	Rate of dissipation	1
BreakGamma	Breaker parameter Hmax/h	0.73
WaveSetup	Wave-induced setup model	TRUE
Whitecapping	Dissipation by whitecapping	TRUE (Van der Westhuysen et al., 2007)
Hydrodynamics		
Dt	Computational time step [s]	3.0
DryFlc	Minimum depth for drying/flooding [m]	0.1
Vicouv	Horizontal background eddy viscosity [$m^2.s^{-1}$]	1
Dicouv	Horizontal background eddy diffusivity [$m^2.s^{-1}$]	0.1
Rouwav	Model for bottom stress formulation due to combined wave and current action	#FR84# (Fredsoe, 1984)
Roumet Ccofu,Ccofv	Manning Coefficient [-]	#M# 0.018 – 0.034
Thick	Depth-averaged mode	100

Table 2.3 Delft3D – MOR parameters used for the morphological modelling in Whangarei Harbour.

Parameter	Description	Value
Sediment transport		
Non – Cohesive Sediment (Sand)		
RhoSol	Sediment density [kg/m3]	2650
SedTyp	Sediment type	Sand
SedDia	Median sediment diameter (D50) [m]	2.0E-03 1.2E-03 8.0E-04 5.0E-04 3.5E-04 2.5E-04 1.8E-04 1.0E-04
CDryB	Dry bed density [kg.m^{-3}]	1600
IFORM	Sediment transport formulation	(TR2004, Van Rijn et al., 2004)
Morphology		
AlfaBs	Streamwise bed gradient factor for bed load transport [-]	1
AlfaBn	Transverse bed gradient factor for bed load transport [-]	1.5
Sus	Multiplication factor for suspended sediment reference concentration [-]	0.15
Bed	Multiplication factor for bed-load transport vector magnitude [-]	0.45
SusW	Wave-related suspended sediment transport factor [-]	0.1
BedW	Wave-related bed-load sediment transport factor [-]	0.1
SedThr	Minimum water depth for sediment computations [m]	0.1
ThetSD	Factor for erosion of adjacent dry cells [-]	0.5

2.4. Sedimentological spin-up

The initialisation of spatially varying seabed grain distribution in a process-based model is often constrained by a lack of appropriate field data for the entire model domain. As the seabed composition is partially dependent on the bed shear stress imposed by the local hydrodynamics and wave environments, using grain-size observations as initial conditions typically lead to unrealistic erosion or accretion patterns. Indeed, Camenen and Larroudé (2003) and Pinto et al. (2006) have shown that the physical parameter responsible for the greatest errors in the sediment characteristics is the spatial heterogeneity of grain size distributions of the surface sediment in the area of interest.

As such, an initial model run was initiated by applying a 2-layer bed composition approach. The thickness of the active layer was set to 40 cm to allow a rapid coarsening of the system to reduce the spin-up period. The second layer, which supplies sediments to the active layer when erosion occurs, was defined as 8 m thick.

The eight sediment fractions were initially defined in the active layer according to the general distribution obtained through the sediment sampling study (see Table 2.4 and Figure 2.7). To ensure a correct convergence between bed composition and hydrodynamics, these fractions were defined equally in the second layer (i.e. 12.5% per sediment class).

During the simulation, sediment grain size fractions were redistributed vertically between layers and spatially within the domain by the salient hydrodynamics. At the end of the simulation, the bed composition converged to a more realistic sedimentological setting corresponding to the initial bathymetry, removing errors due to the initial model setup. Information about sediment mixtures and bed stratigraphy features in Delft3D is available in Jagers (2012).

The sedimentological spin-up was undertaken over twenty days characterised by fair-weather conditions. Morphological acceleration was applied using a factor (MORFAC) of 12 to simulate the equivalent of eight months of sediment transport. The choice of this period was motivated by the relative quick convergence of the net transport over the whole domain. No update of the model bathymetry was allowed over the simulated period.

Table 2.4 Mass percentage specific to each sediment class in both the active and the under-layer within the BCG simulation.

Sediment class	Grain size (µm)	Mass percentage in active layer	Mass percentage in under-layer
Class 1	2000	5%	~11%
Class 2	1200	3%	~11%
Class 3	800	4%	~11%
Class 4	500	5%	~11%
Class 5	350	20%	~11%
Class 6	250	23%	~11%
Class 7	180	35%	~11%
Class 8	100	5%	~11%

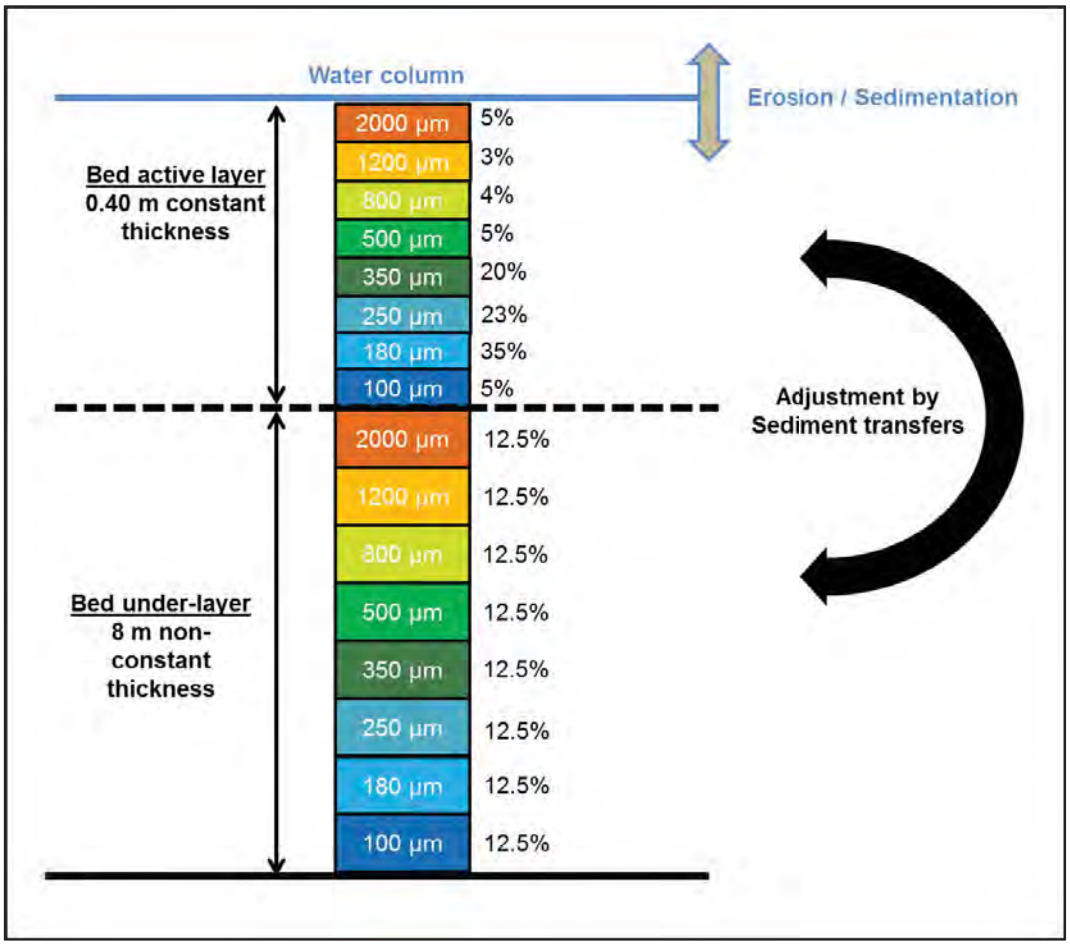

Figure 2.7 Bed stratigraphy approach implemented in Delft3D to initialise the bed composition over the domain.

2.5. Medium-term modelling approach

The main challenge when applying process-based models to predict coastal and estuarine dynamics is that the morphology of these systems generally develops over time scales several orders of magnitude larger than the time scale of the hydrodynamic fluctuations driving the sediment transport (i.e. hours to days versus years to decades and more). This means that a model system that is able to predict the time series of instantaneous hydrodynamics and sediment transport will require a considerable computation runtime. Luijendijk et al. (2017) followed this approach simulating historical morphological changes over 1 year with Delft3D set up in depth-averaged mode (2D).

Several strategies are commonly used to simplify and accelerate the modelling of medium to long term morphological evolution (i.e. De Vriend et al., 1993; Roelvink, 2006). The approach employed here combines the reduction of the input forcing with the use of morphological acceleration factors; which is one of the most commonly applied methods and an industry standard technique.

The medium-term morphological modelling was performed based on the reduction of waves and tides over 365 days from 2016 to 2017. Input reduction essentially means selecting a limited number of representative forcing conditions that will reproduce the medium-term residual sediment transport patterns and associated morphological evolution (De Vriend et al., 1993). The morphological factor is a technique to improve computational efficiency by accelerating computed morphological evolution.

2.5.1. Tidal input reduction

Astronomical tides are deterministic and can therefore be accurately predicted for any period of time. However tidal oscillations exhibits significant long-term modulations (e.g. spring/neap, yearly and nodal cycles), which make chronological simulations of such cycles computationally demanding.

The basis for tidal input reduction is to find a representative tide that most closely reproduce the net and gross sediment transport as the naturally varying tides over the region of interest and for the time period considered. In the present study, the 'representative' tide was determined following the approach of Latteux (1995), which is commonly applied (e.g. Grunnet et al., 2004; Brown and Davies, 2009; Dastgheib, 2012).

Given the duration of the simulations (i.e. 1 year), the main concern was to capture the residual effects of the spring-neap oscillations, so a time period of 12 cycles (~1 year) or longer was considered necessary.

Tidal signals at a reference point located near the Northland Port swinging basin were generated from a high resolution tidal constituents grid extracted from a SCHISM model implementation and a time series of sediment transport were estimated using a simple power law $Q=A.u^{b}$ (where Q is the transport flux, A is a constant factor, u is current velocity, b=5 following Engelund and Hansen (1967)). The single tide best reproducing the net and gross transport magnitude was identified and used in the accelerated simulations. The representative tide is compared to M2 tidal signals in Figure 2.8. A four hour spin-up at flood stage with no morphological update was applied to initialise the hydrodynamic model.

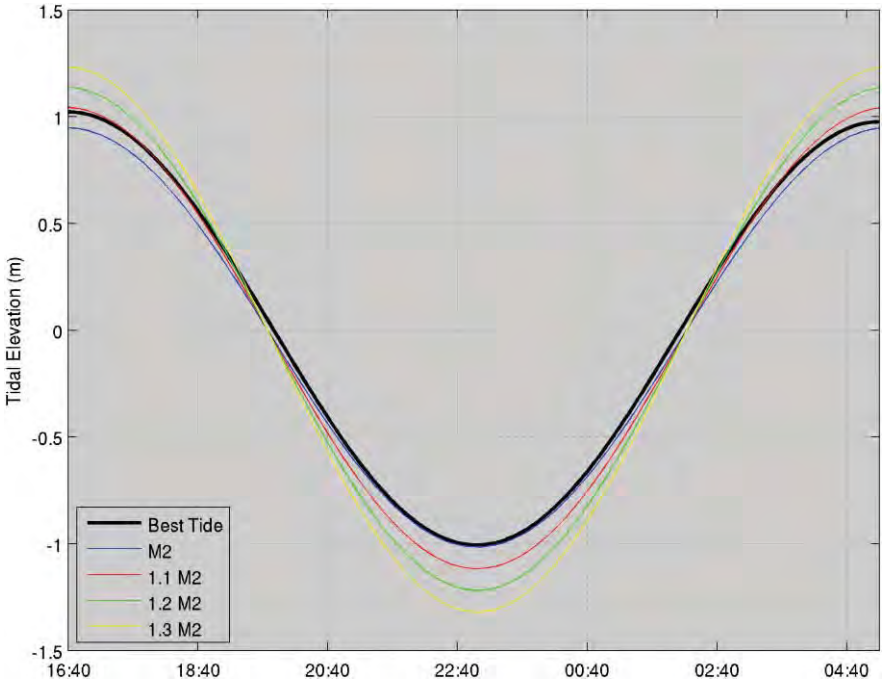

Figure 2.8 Comparison between the best representative tide, pure M2 tide, 1.1 M2, 1.2 M2 and 1.3 M2 tide curves at the control site located within the NorthPort swinging basin.

2.5.2. Wave input reduction

The objective of the wave input reduction is to define a set of offshore wave boundary conditions which reproduce the same residual sediment transport patterns and

morphological evolution as the real time forcing over a given time period. The approach employed here followed the input reduction methodology of Lesser (2009) and Walstra et al. (2013).

The first step is the selection of a reduction period, which is the length of real-time wave time series that is used to define the representative conditions. This is typically governed by the time scale of the morphological evolution of interest (e.g. monthly, seasonal, annual behaviour). In the present study, the reduction was undertaken based on a 365 day hindcast wave climate obtained from SWAN simulations to define an average annual wave climate. The wave conditions time-series was extracted at the middle of the eastern boundary of the coarse wave model domain.

In a second step, a set of representative wave classes was defined by distributing the discrete wave data points into a finite number of height and direction bins, and computing a representative value for each bin. The basic method to determine a representative value within a bin is to use a weighted average of the data points by their frequency of occurrence:

$$F_{rep,j} = \frac{\sum_{i=1}^{n} f_i . F}{\sum_{i=1}^{n} f_i} \quad \text{(Eq. 2.9)}$$

where *F* represents the wave height, period or direction, *f* is the frequency of occurrence of the wave condition *i* and *n* is the number of data points within a bin.

To account for the non-linear dependence of sediment transport on wave height, an additional weighting can be applied for the computation of the representative height:

$$H_{s,rep,j} = \left(\frac{\sum_{i=1}^{n} f_i . H_{s,i}^{p}}{\sum_{i=1}^{n} f_i} \right)^{1/p} \quad \text{(Eq. 2.10)}$$

where *p* is the power to which the sediment transports are assumed to be related to the wave height. Typically *p* is set to 2 to 3. The exponent ensures that larger waves will have a relatively greater contribution in the computation of the representative wave height.

Here Eq. 2.10 was solved with a value of p = 2.5 which corresponds to the CERC formula for longshore transport (CERC, 1984) and is frequently used to estimate the morphological impact of waves. Associated representative periods and directions were determined using the same weighting as the wave height.

The initial wave data binning is relatively arbitrary and can be equidistant or non-equidistant (i.e. varying bin size). In the non-equidistant case, bins can be defined following either (subjective) scientific judgment or more objective approaches. Here, the height and direction bins were defined so that the relative “morphological impact of waves” was similar in each bin (e.g. Lesser, 2009; Dastgheib, 2012).

The morphological impact of waves of a given wave class was estimated according to:

$$M_j = p_j . H_{s,rep,j}^{2.5} \quad \text{(Eq 2.11)}$$

where p_j is the probability of occurrence of the bin *j*, and $H_{s,rep,j}$ the representative wave height of that bin (Lesser, 2009). Note that this is equivalent to “potential sediment transport” indicator used in Dastgheib (2012).

To automate the determination of bin limits, this indicator was initially computed for a joint probability of wave height and direction with very fine equidistant bins (ΔH = 0.1 m, ΔDir = 2 deg.). Based on the number of directional and wave height bins to be used for the classification, the directional bin limits were determined first, in a way that the sum of the morphological impact of waves M_j within each bin was approximately equal. The same principle was then used within each of these directional bins to define the wave height bin limits. This way, the "morphological impact of waves" was similar in each bin.

The wave climate classification used in the following morphological simulation from 2016 to 2017 was defined using 4 directional bins and 4 wave height bins (Figure 2.9 and Figure 2.10). The general classification obtained for the average annual wave climate at the reference site did reproduce the directional variability of the levels of wave energy observed in the hindcast data. A summary of the wave classes used for the medium-term modelling from 2016 to 2017 is provided in Table 2.5. Model significant wave height fields associated with each class are presented in Appendix B.

Table 2.5 Wave classification based on an average annual wave climate defined from hindcast data over 2016.

	Representative	Representative	Representative	Probability of	MORFAC
class	Hs (m)	Tp (sec)	Dp (deg.)	occurrence	
1	1.615	9.335	34.4	15.10%	106.5
2	2.395	10.57	35.33	4.75%	33.48
3	2.921	9.38	35.49	2.66%	18.79
4	4.121	10.57	31.18	1.37%	9.634
5	1.346	9.23	82.25	21.58%	152.2
6	1.994	9.232	83.42	7.92%	55.87
7	2.818	11.53	80.41	2.94%	20.71
8	4.307	11.88	91.19	1.40%	9.874
9	1.588	7.14	198.1	15.27%	107.7
10	2.5	8.194	185.1	4.85%	34.2
11	3.679	9.099	143.7	1.71%	12.04
12	6.644	12.09	119.9	0.48%	3.372
13	1.695	8.448	333.1	13.15%	92.72
14	2.703	8.48	328.4	3.72%	26.25
15	3.42	8.685	323.4	2.02%	14.21
16	4.503	9.402	319.4	1.06%	7.466

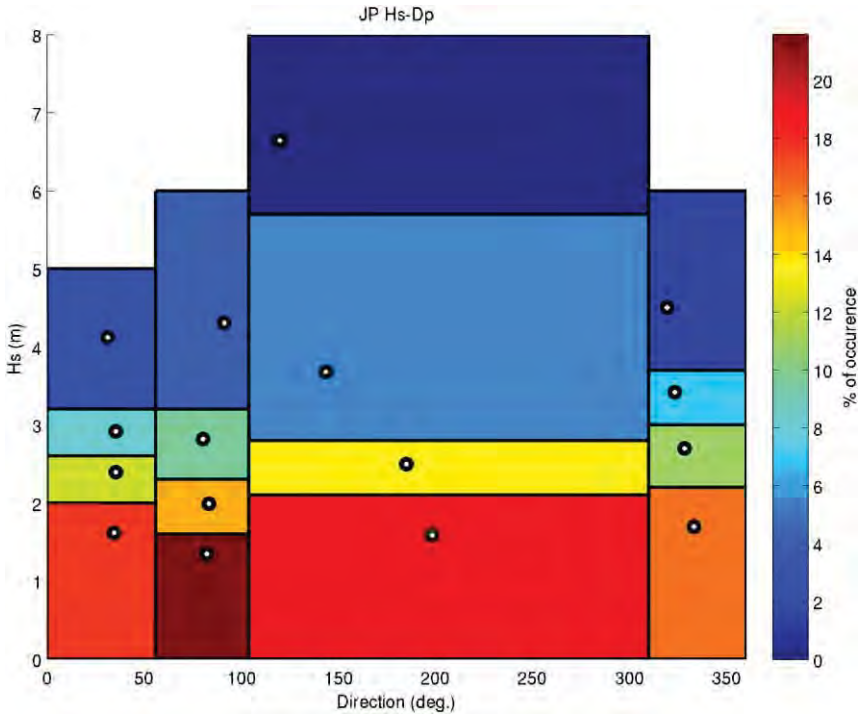

Figure 2.9 Reduced average annual wave climate based on the 2016 wave hindcast. Colours indicate the probability of occurrence of a given class. The white dots are the representative wave condition of each wave class.

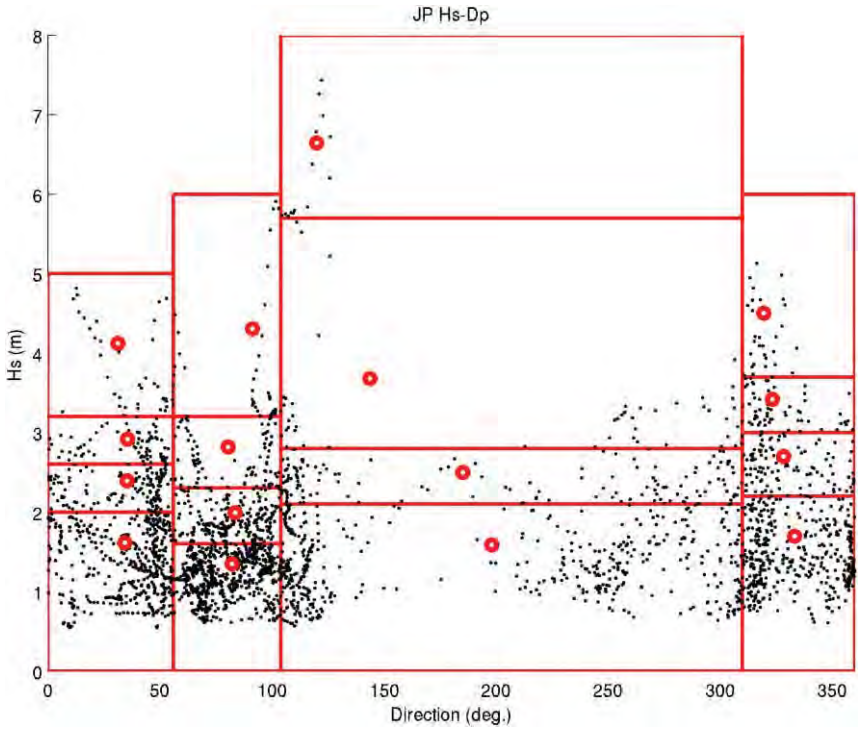

Figure 2.10 Reduced average annual wave climate based on the 2016 wave hindcast. The black dots correspond to the hindcast significant wave height and peak direction. The white dots are the representative wave condition of each wave class.

2.5.3. Wind input reduction

The reduction of the wind climate was performed averaging both zonal and meridional components of the wind velocity at 10 m associated with the wave events of each bin.

Wind data were extracted from a 12 km WRF atmospheric hindcast data produced by MOS and validated at Marsden Point (Appendix C).

In the absence of guidance on the inclusion of additional forcing in the input reduction approach (e.g. Lesser et al., 2004), the choice of the wind reduction was motivated by the partial correlation that exists between wave heights and wind speeds. It is, however assumed here that such approach is relatively simplistic as the swell component of the wave dynamics is independent of the local wind dynamics. Irrespective, wind forcings are likely to represent a very minor component of the overall sediment transport regime, and hence morphological response.

Table 2.6 Wind classification based on an annual wind climate defined from hindcast data at the delta entrance over 2016.

class	Wind Speed ($m.s^{-1}$)	Wind direction (coming from)
1	1.09	358.11
2	0.21	153.86
3	2.86	241.21
4	3.32	289.84
5	2.36	27.67
6	0.97	79.09
7	5.48	223.59
8	6.18	293.94
9	3.81	21.86
10	0.81	68.33
11	6.11	220.03
12	7.73	303.60
13	8.63	49.04
14	3.20	99.76
15	11.24	150.82
16	10.99	293.99

3. RESULTS

The key aim of the present work is to calibrate and validate the morphological model so that it can be reliably used to predict morphological evolution of the existing and modified environment (i.e. post dredging and reclamation) at NorthPort. This is achieved by qualitatively and quantitatively comparing measured changes in the morphological evolution to those predicted by the morphological model..

3.1. Sedimentological spin-up

A sedimentological spin-up simulation has been carried out to initiate the bed composition over the domain based on the existing hydrodynamics.

The rate of sediment relocation over the domain throughout the sedimentological spin-up simulation decreased considerably after 9 days (Figure 3.1). At the end of the 20 day simulation, the bed composition in the top layer was stable. The fraction specific to each sediment class into the transport layer was therefore used to initialise the space-varying bed composition in the annual morphological simulation. For this simulation, a sediment mixture approach has been chosen to reduce the computational cost. Because this approach aimed to reproduce the stable behaviour of the seabed rather than the bed composition measured in the sediment samplings, no analysis of the outputted *d50* grain size values is shown here.

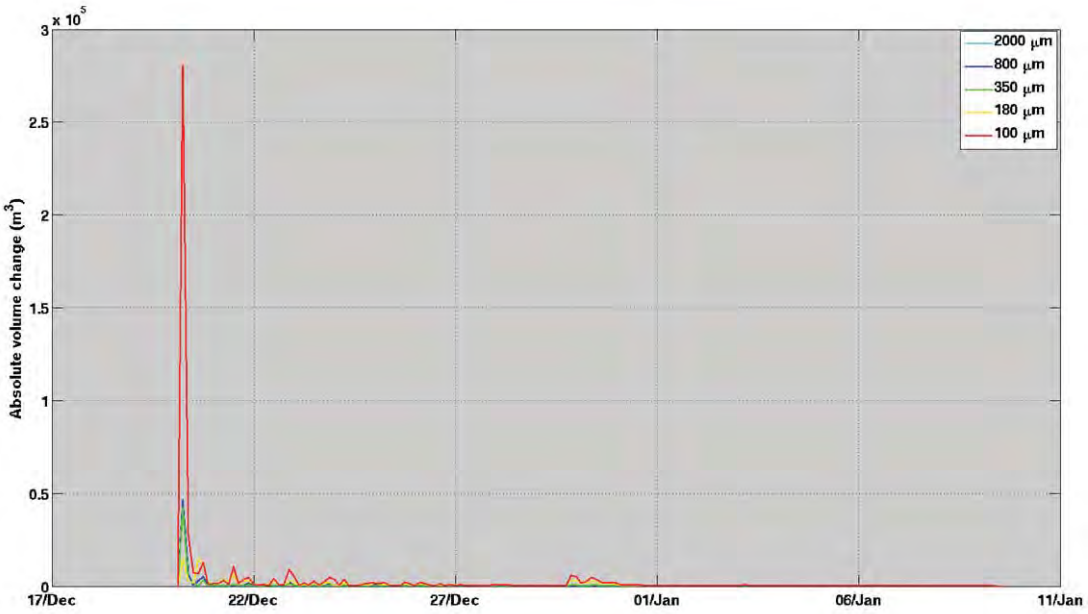

Figure 3.1 Absolute volume change for five sediment classes in the transport layer. Calculations were performed every three hours over the entire domain.

3.2. Medium-term measured morphological change

Single beam survey data from 2007 to 2014 were examined to better understand the infilling process occurring within the swinging basin at Northport.

Some survey error is apparent in the soundings, as shown by the rhythmic alternating accretion and erosion zones (Figure 3.2, bottom), however in general surveys show a

gradual eastward migration of the toe of Snake Bank at a rate of approximately 10 $m.yr^{-1}$ (Figure 3.2 and Figure 3.3); consistent with the observations of Cryer and Parkinson (2001) and Cryer et al. (2003)

Sand bank morphological changes are often part of a decadal-scale cycle which may be significantly influenced by anthropogenic activities, such as land reclamation or dredging projects. The prediction of the morphological response to anthropogenic activities remains a complex exercise in such dynamic environment. The numerical modelling undertaken in the present study aimed to calibrate the morphological model on the basis of the scale at which morphological changes are observed to have developed between 2016 and 2017.

Analysis of the morphological changes over Area 1 and 2 (see Figure 1.2) revealed annual volumetric variations of approximately +16,497 $m^3.yr^{-1}$ and -24,397 $m^3.yr^{-1}$, respectively. Area 3 which is proposed to be dredged in the near future was characterised by a sediment accretion of approximately 28,315 $m^3.yr^{-1}$. By contrast, the gradual north-eastern face of Snake Bank was eroded of up to 1.5 m. The southern inter-tidal area of Snake Bank also experienced erosion of the order 0.2 m to 0.5 m. It is likely that the erosion of the inter-tidal area and bed-load transports supplies sediment to the steepest face of Snake Bank. Over the south-western margin of Snake Bank, significant patches of sand accretion up to 0.6 m were identified in measurements.

Table 3.1 Volumetric change from 2007 to 2014 estimated using mono-beam bathymetry survey data.

Area	Volumetric change from 2007 to 2010	Volumetric change from 2010 to 2014	Volumetric change from 2007 to 2014
	[m^3]	[m^3]	[m^3]
Area 1	-2,315	18,641	16,497
Area 2	-17,622	-6,789	-24,397
Area 3	8,371	19,934	28,315

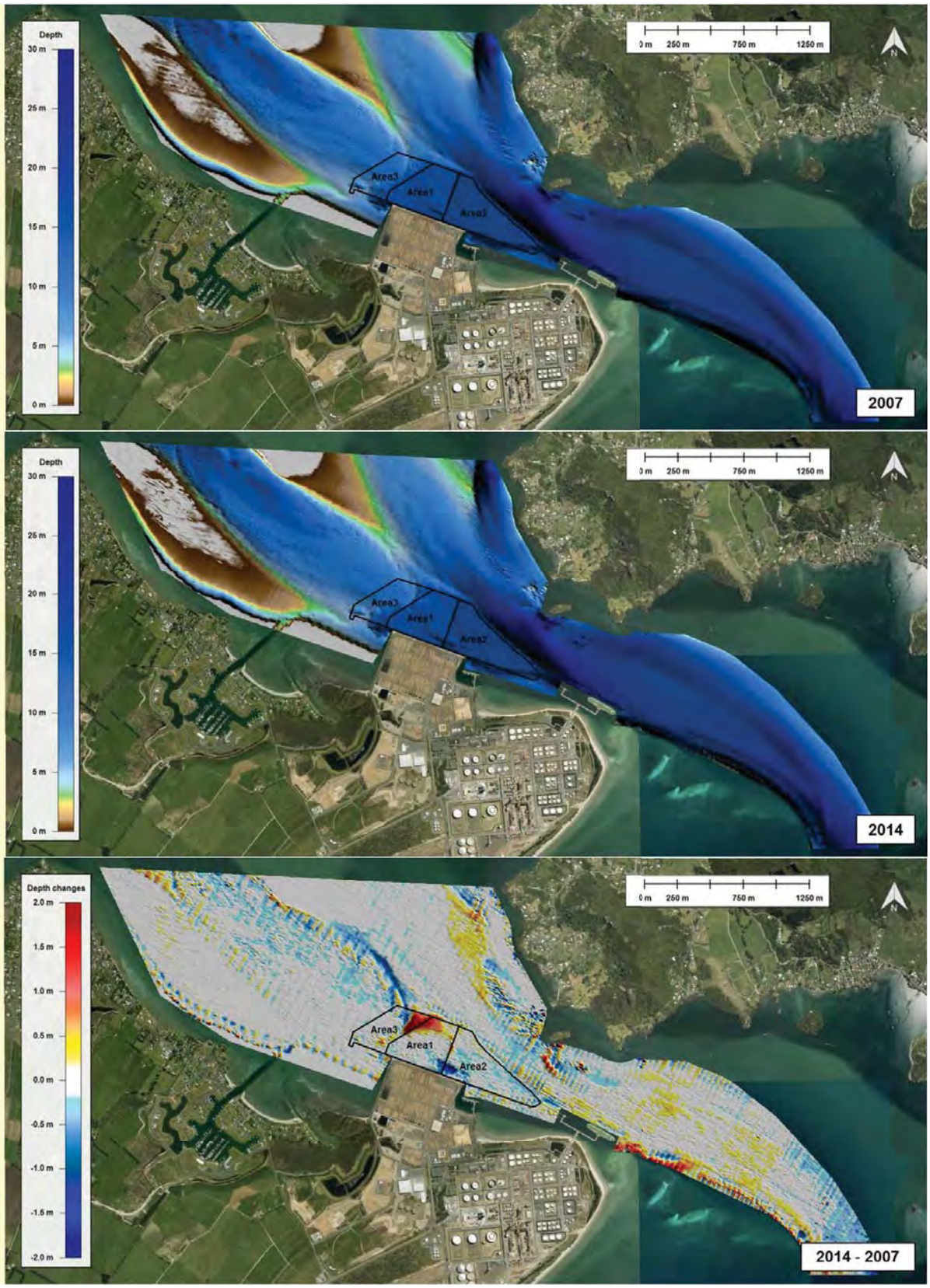

Figure 3.2 Bathymetry maps for 2007 and 2014 obtained from the interpolation of mono-beam survey data over the entrance to Whangarei Harbour. A comparison between both bathymetries is also provided at the bottom.

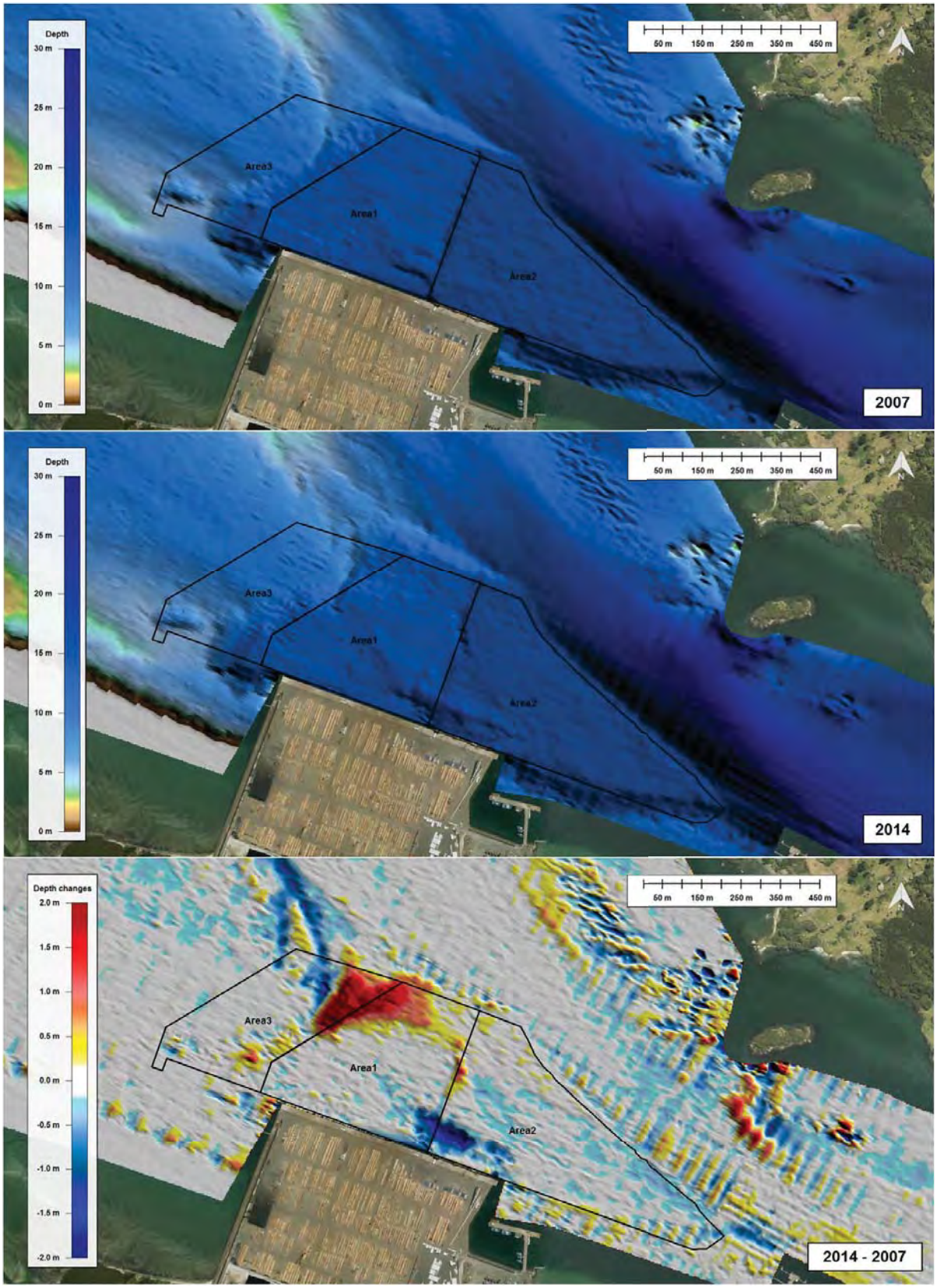

Figure 3.3 Bathymetry maps for 2007 and 2014 obtained from the interpolation of mono-beam survey data at Northport. A comparison between both bathymetries is also provided at the bottom.

3.3. Recent measured morphological change from 2015 to 2017

As with the period 2007-2014, survey data between 2015 and 2017 shows an eastward migration of the toe of Snake Bank into the Northport Swinging basin (Figure 3.4 - Figure 3.5), with a similar rate of change (i.e. ~10 $m.yr^{-1}$).

Volumetric depth changes from 2015 to 2017 for Areas 1-3 (see Figure 1.2) are provided in Table 3.2. Annual infilling rates are highest in Area 1 adjacent to the Berth 1 and 2, with a total of approximately 10,000 m^3 deposited within the area between 2015-2017. Infilling of approximately 5,000 m^3 is observed to have occurred in Area 3, and this is attributed to material advected into the Area from Snake Bank. Limited infilling is observed in Area 2 (adjacent Berth 3), with approximately 1,300 m^3 deposited over the two year period 2015-2016.

Within Areas 1 and 3 more infilling is observed to have occurred between 2016-2017 than during the previous year, while conversely ~1,500 m3 of sediment is expected to have eroded out of Area 2 during the 2016-2017 period. The difference between the two periods is attributed to incident wind and wave climate being more energetic for 2016 than 2015 (see Figure 3.6 and Figure 3.7)

Table 3.2 Volumetric change from 2015 to 2017 estimated using multi-beam bathymetric survey data.

Area	Volumetric change from 2015 to 2016	Volumetric change from 2016 to 2017	Volumetric change from 2015 to 2017 (Total)
	[m^3]	[m^3]	[m^3]
Area 1	+3,985	+6,260	+10,245
Area 2	+2,917	-1,597	+1,320
Area 3	+831	+3,973	+4,804

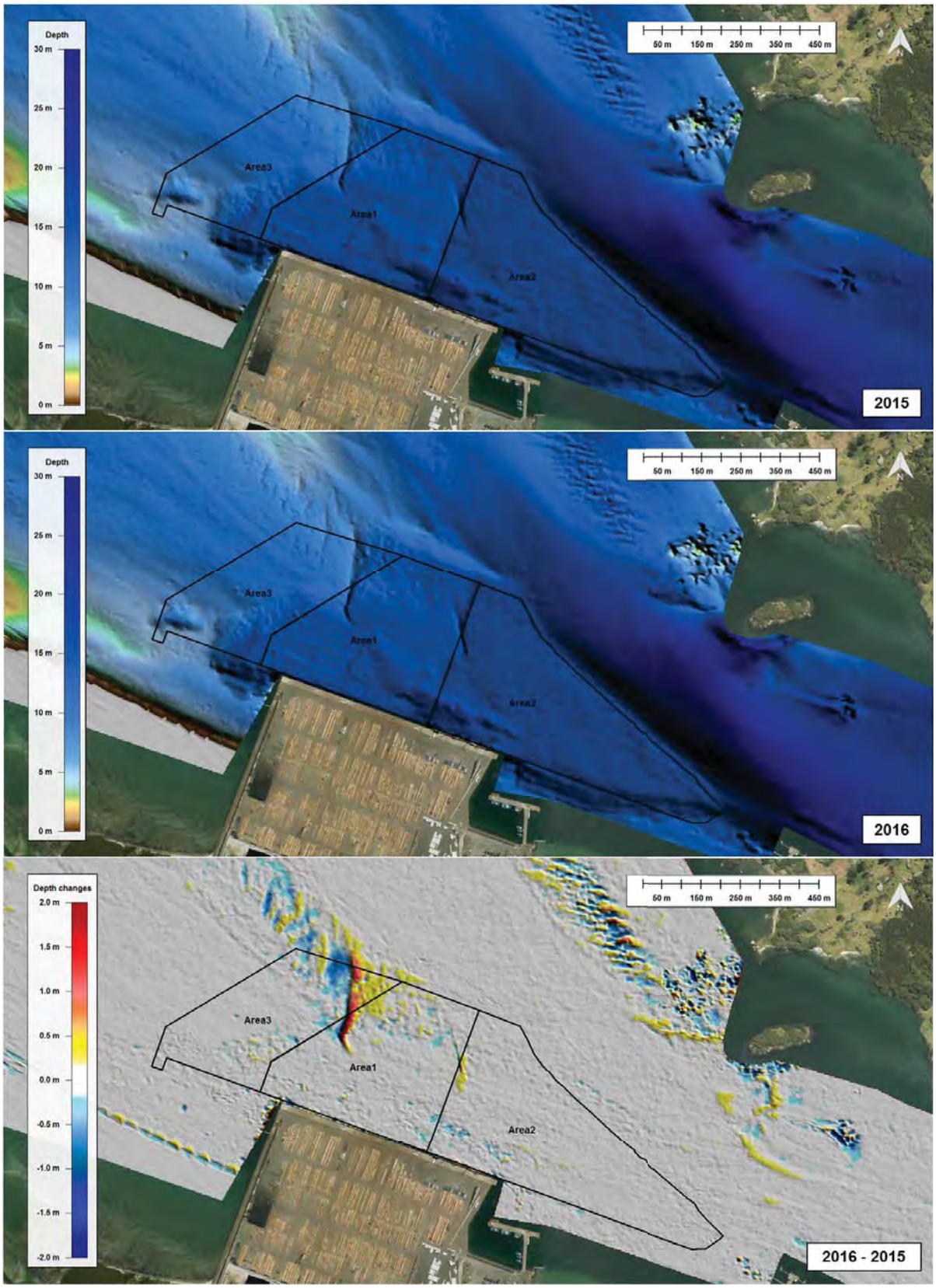

Figure 3.4 Bathymetry maps for 2015 and 2016 obtained from the interpolation of single-beam survey data at Northport. A comparison between both bathymetries is also provided at the bottom.

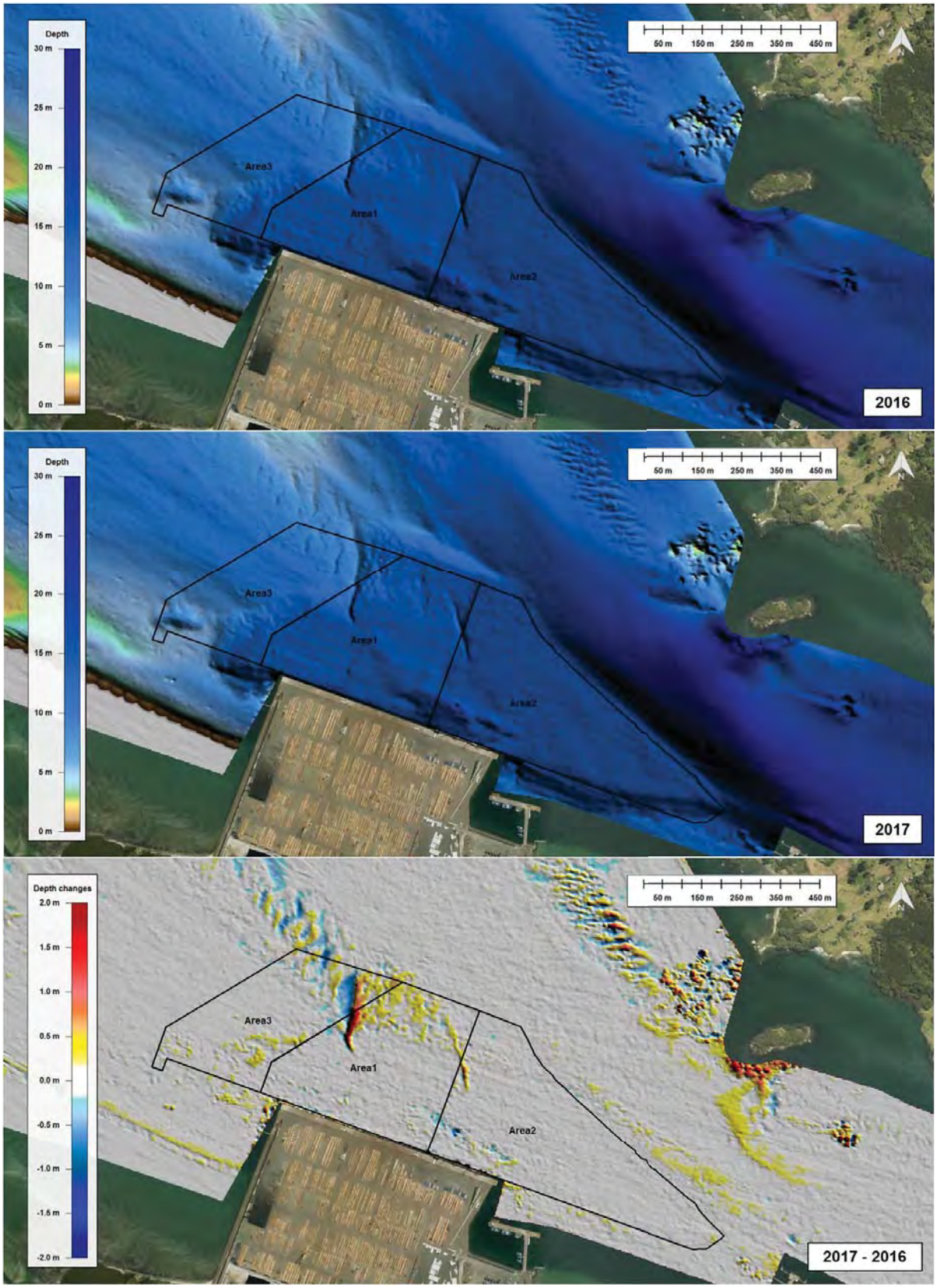

Figure 3.5 Bathymetry maps for 2016 and 2017 obtained from the interpolation of single-beam survey data at Northport. A comparison between both bathymetries is also provided at the bottom.

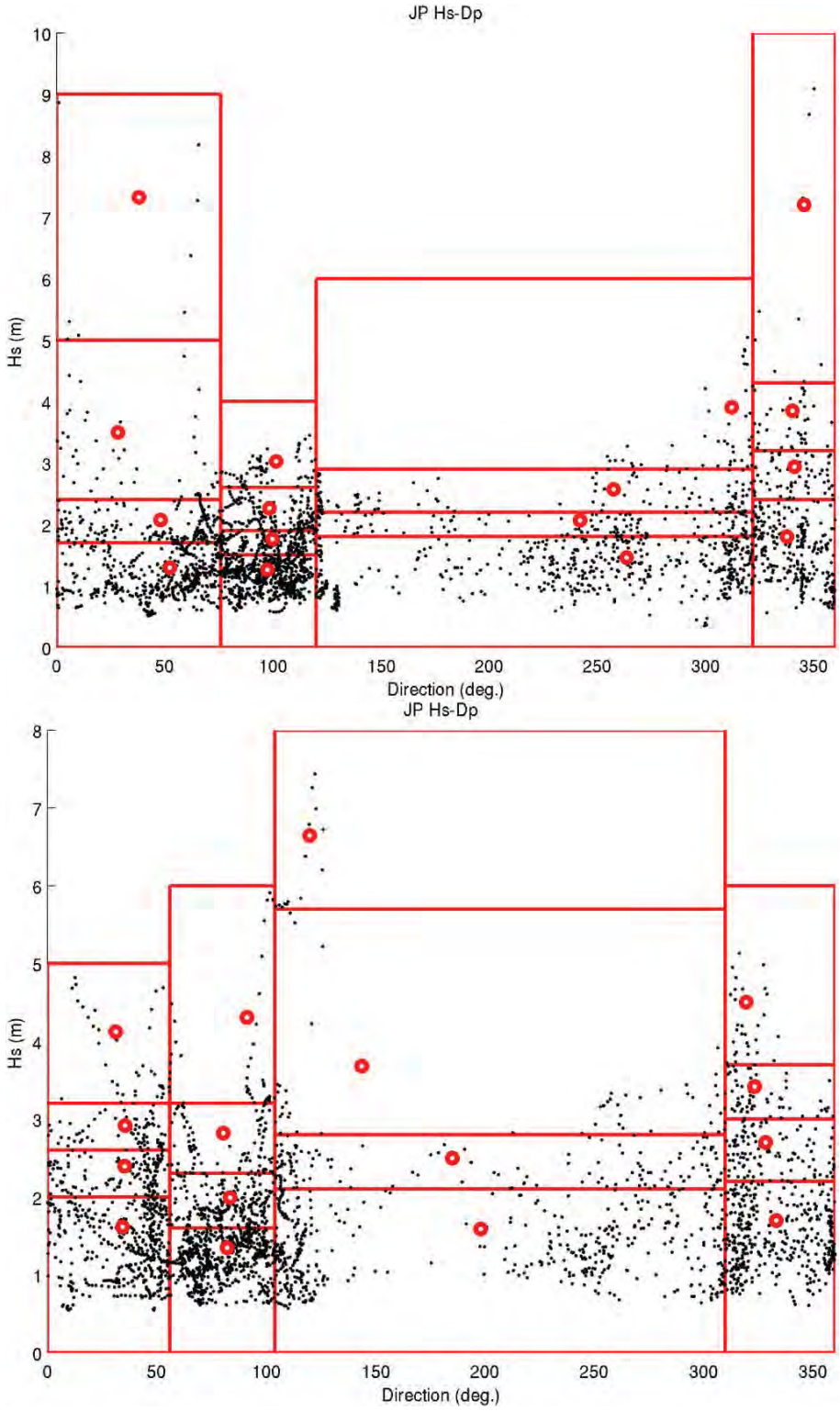

Figure 3.6 Reduced average annual wave climate based on the 2015 (top) and 2016 (2016) wave hindcast. The black dots correspond to the hindcast significant wave height and peak direction. The red circles are the representative wave condition of each wave class.

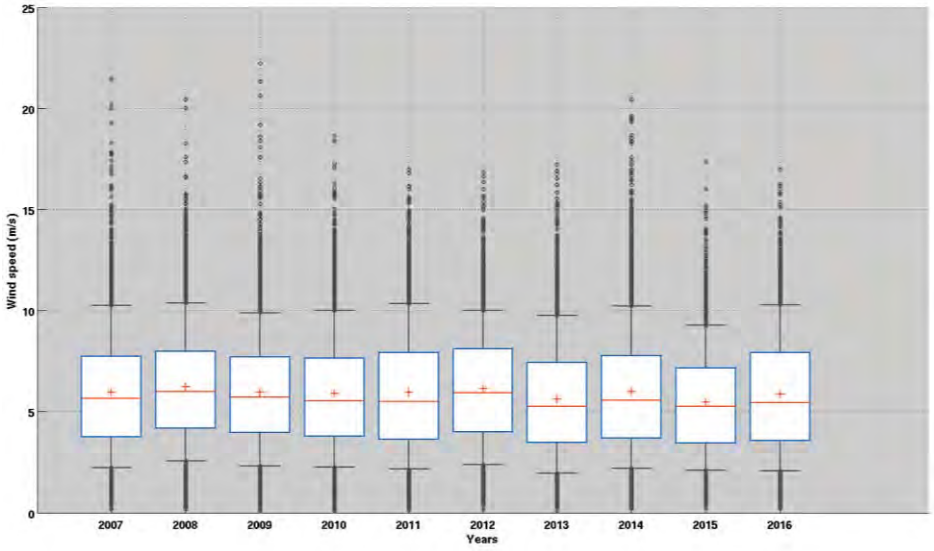

Figure 3.7 Wind climate statistics from the WRF atmospheric hindcast for years 2007-2016. The blue rectangle corresponds to the 25th and 75th percentiles of the annual distribution. Red crosses and red lines indicate the annual median and mean respectively.

3.4. Characterising the tidal dynamics

Model spring ebb and flood tidal current patterns are shown in Figure 3.8 and Figure 3.9 respectively.

Flood flows gradually accelerate through the inlet with velocities ranging from 0.8 m.s^{-1} adjacent Home Point/Busby Head to ~1.3 m.s^{-1} near Motukaroro Island. At peak ebb, current velocities adjacent to Motukaroro Island are of the order 0.3-0.8 m.s^{-1}, accelerating up to ~1.3 m.s^{-1} in the channel adjacent to Mair Bank and Home Point.

Increased water depth within the Northport swinging basin results in a decrease in the tidal velocities, with velocities of the order 0.8 m.s^{-1} peak for both ebb and flood tidal stages expected. In contrast, flow acceleration is predicted over the shallow areas of Snake Bank (up to 1 m.s^{-1}, see Figure 3.9). The inter-relationship between the bathymetry and tidal velocities influences the spatial distribution of the mean bed shear-stress fields within the Northport environs (Figure 3.10). The gradient in bed shear-stress at the tip of Shake Bank suggests that this area is likely to experience active bedload transport, with infilling of the swinging basing likely to be exacerbated with deepening by dredging.

Within the marginal channel between One Tree Point and Snake Bank, segregation of the flows tends to reduce the current velocities for both flood and neap tides leading to current speed of approximately 0.6 – 0.7 m.s^{-1} . However, slight changes in the channel geometry cause localised accelerations of the tidal flows up to 1 m.s^{-1} along the channel margin (Figure 3.9), with the south-western flank of Snake Bank subjected to an increase of the bed shear stress due to increasing ebb and flood tidal flow velocities (Figure 3.10).

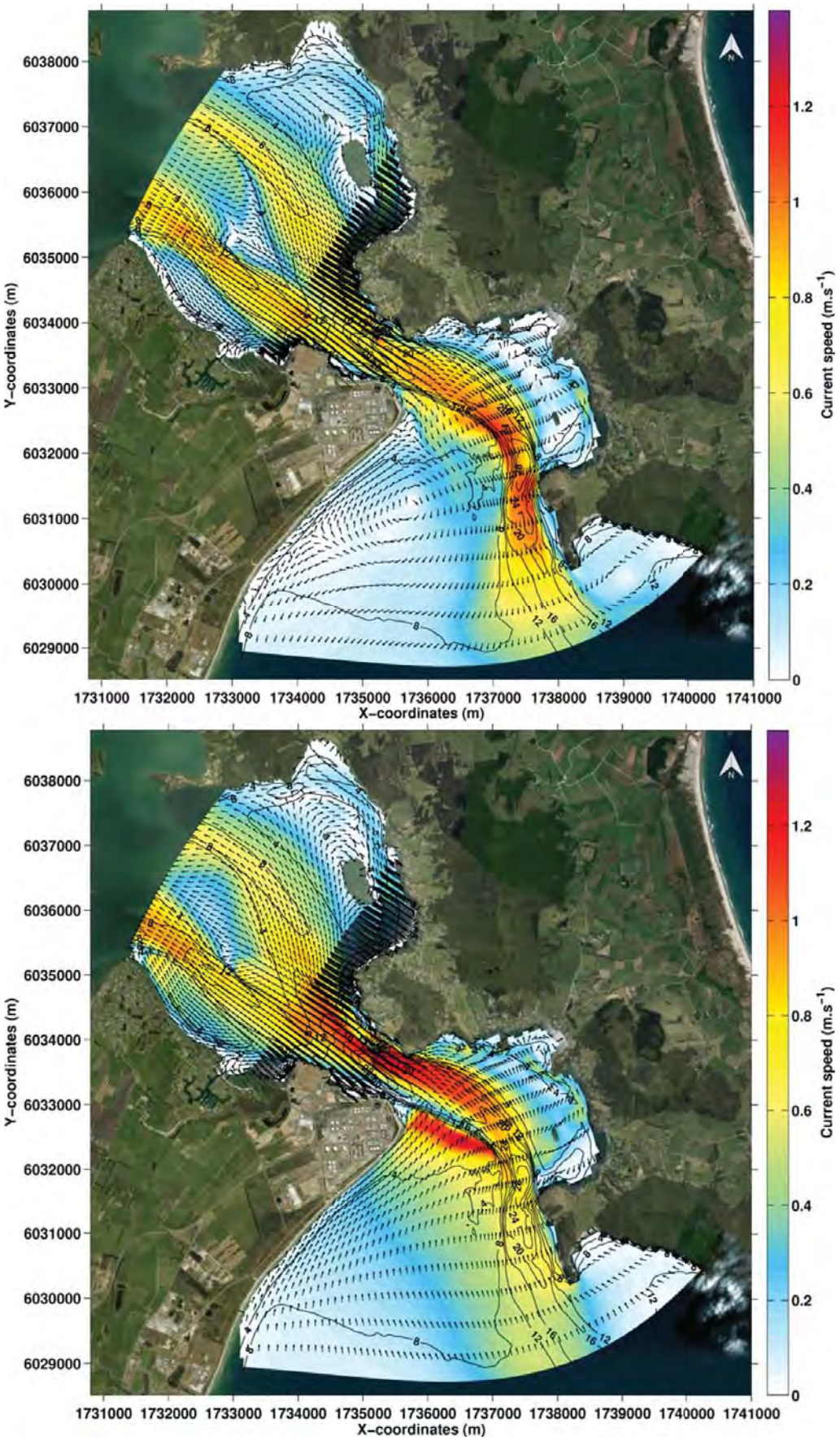

Figure 3.8 Model depth-averaged tidal currents at the entrance to Whangarei Harbour during ebb (top) and flood (bottom) stages.

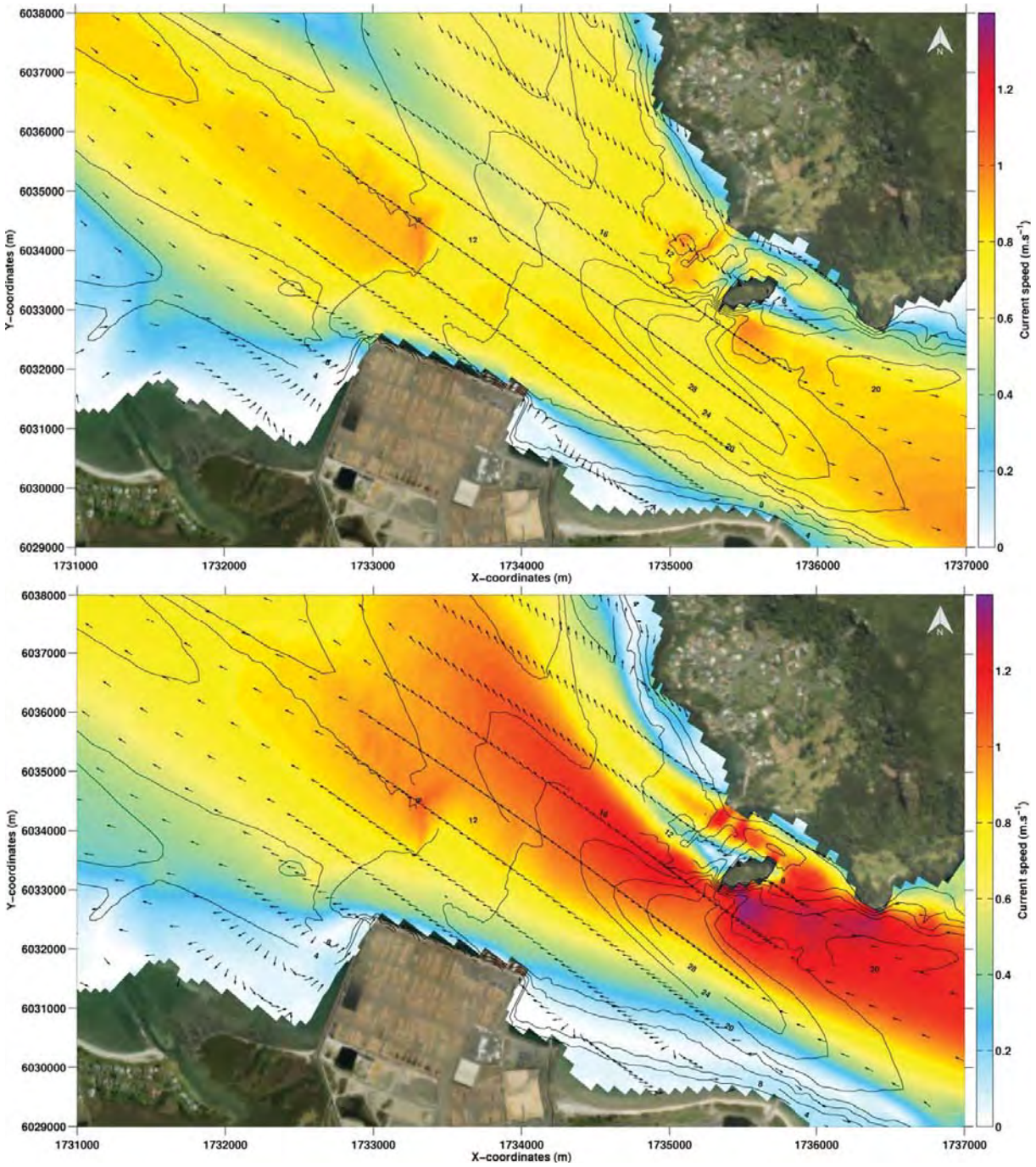

Figure 3.9 Model depth-averaged tidal currents at Northport during ebb (top) and flood (bottom) stages.

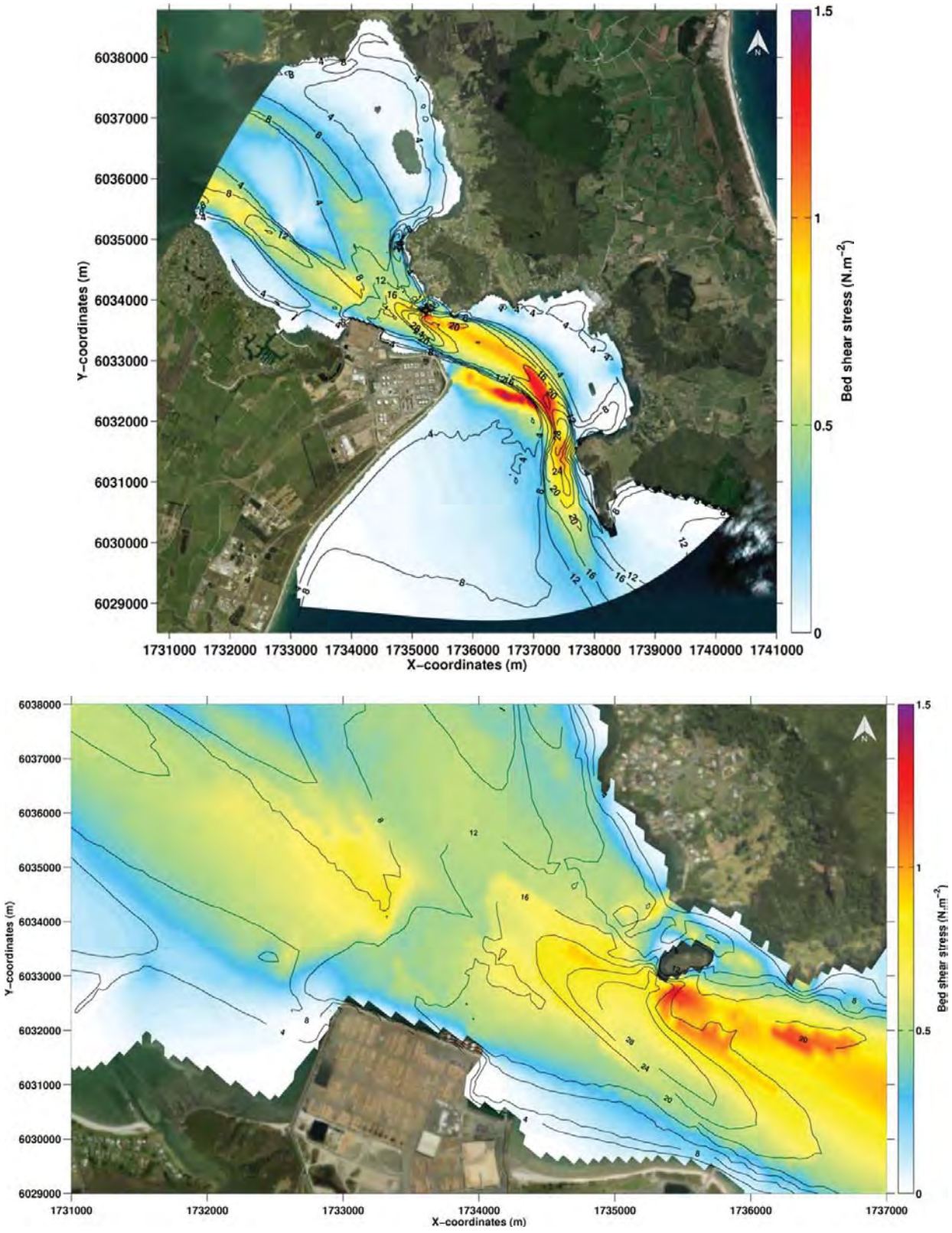

Figure 3.10 Model mean bed shear stress field over 28 days at the entrance to Whangarei Harbour (top) and Northport (bottom). No wave forcing was prescribed.

3.5. Predicted sediment dynamics

Calibration of the Delft3D morphological model for the period 2016-2017 was undertaken by comparing model predicted annual morphological changes to those observed (see Figure 3.11).

Qualitatively, model results show a good agreement spatially with the measured morphological changes, with the model capturing the migration of Snake Bank into the swinging basin and the succession of erosion and accretion along the southern margin of bank (see Figure 3.11). The high degree of stability observed elsewhere in the channel was relatively well reproduced in the predictions, as is the strong activity over the deep area adjacent to Motukaroro Island

Quantitatively, the accretion of sand from the tip of Snake Bank into the swinging basin by bedload transport is somewhat under-estimated. It is likely that a lack of resolution in the model grid resulted in decreasing bed slope gradients which influenced greatly the bedload component of the sediment transport. Irrespective, within the order of magnitude errors expected for hydrographic surveys, the model showed a good capability in predicting realistic volumetric infilling rates within Areas 1 to 3; +8,128 m^3 and +3,658 m^3 respectively (Table 3.3). Within Area 2, the morphological model predicted a similar order of magnitude in the total bed erosion to that observed (i.e. 2500 m^3 and 1,600 m^3 respectively, Table 3.3).

The successful validation of the morphological model indicates that the modelling approach is applicable for examining both the existing morphological evolution and the response of the system to the proposed dredging and reclamations.

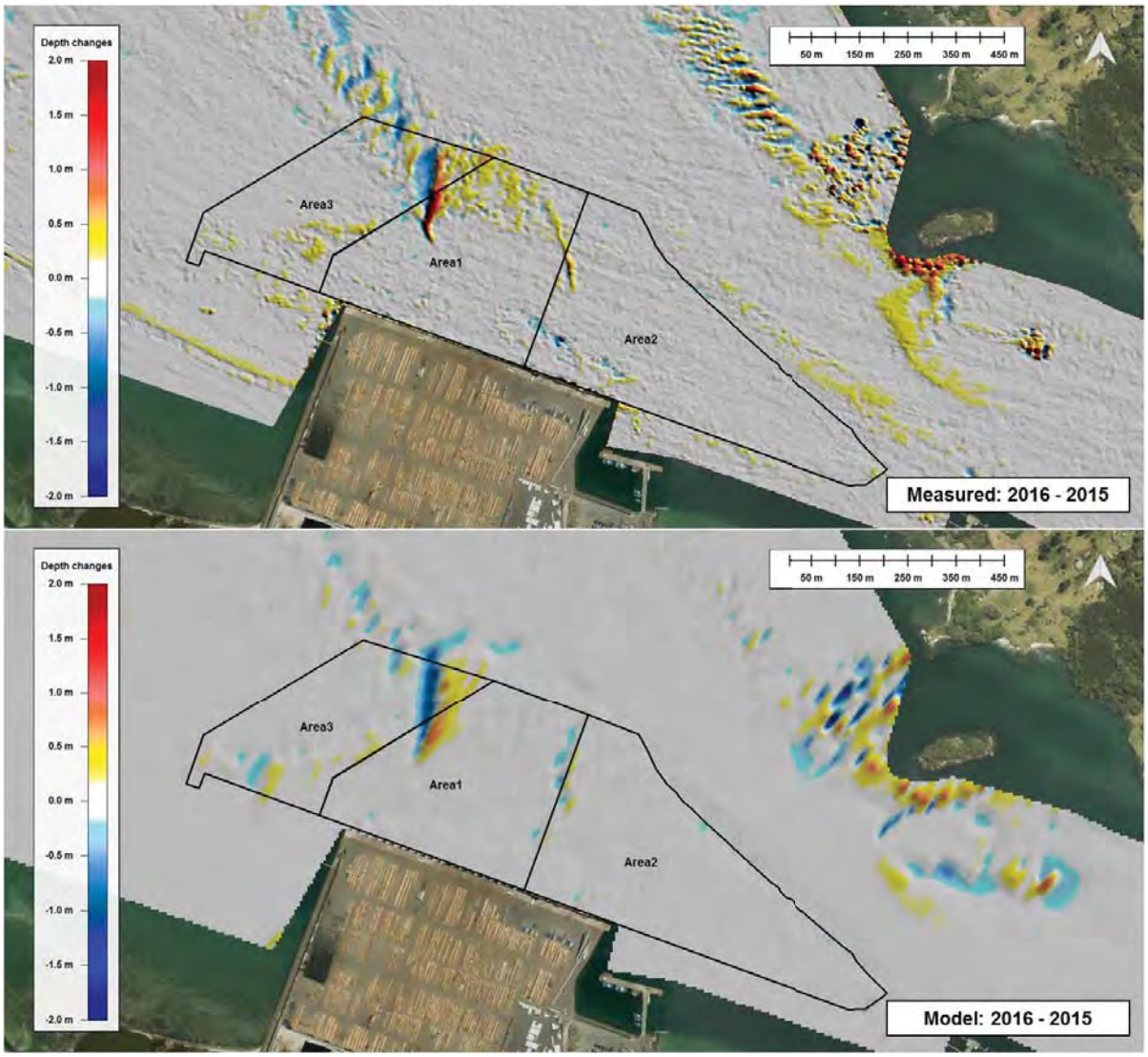

Figure 3.11 Measured (top) and model (bottom) depth change after one year from 2016 to 2017.

Table 3.3 Volumetric change from 2016 to 2017 estimated using model outputs and bathymetric survey data.

Area	Volumetric change between 2016 and 2017 [$m^3.yr^{-1}$]	
	Measurements	Model
Area 1	+6,260	+8,128
Area 2	-1,597	-2,489
Area 3	+3,973	+3,658

4. SUMMARY

The open-source Delft3D system was used to run high-resolution process-based morphodynamic simulations at Whangarei Harbour, focused on Northport. The numerical modelling involved fully-coupled wave, current and seabed interactions.

The modelling approach consisted in replicating the sediment dynamics over a one year period by applying an input reduction technique and morphological acceleration factors. The morphological model was validated against bathymetric survey data.

It has been demonstrated that the numerical model replicated relatively well the dominant morphological processes at Northport. The model showed good skills in reproducing the gradual migration of Snake Bank toward the swinging basin.

The successful validation of the morphological model indicates that the modelling approach is applicable for examining both the existing morphological evolution and the response of the system to the proposed dredging and reclamations.

REFERENCES

Battjes, J.A., Janssen, J., 1978. Energy loss and set-up due to breaking of random waves, in: Coastal Engineering 1978. pp. 569–587.

Bert Jagers, 2012. Sediment mixtures and bed stratigraphy - Deltares library.

Black, K.P., Healy, T.R., Hunter, M.G., 1989. Sediment dynamics in the lower section of a mixed sand and shell-lagged tidal estuary, New Zealand. J. Coast. Res. 503–521.

Booij, N., Ris, R.C., Holthuijsen, L.H., 1999. A third-generation wave model for coastal regions: 1. Model description and validation. J. Geophys. Res. Oceans 104, 7649–7666.

Brown, J.M., Davies, A.G., 2009. Methods for medium-term prediction of the net sediment transport by waves and currents in complex coastal regions. Cont. Shelf Res. 29, 1502–1514.

Camenen, B., Larroudé, P., 2003. Comparison of sediment transport formulae for the coastal environment. Coast. Eng. 48, 111–132.

CERC, U.A., 1984. Shore protection manual. US Army Corps Eng. Wash.

Collins, J.I., 1972. Prediction of shallow-water spectra. J. Geophys. Res. 77, 2693–2707.

Cryer, M., McKenzie, J.R., Breen, P.A., Kim, S., Parkinson, D.M., Smith, M.D., MacKay, G., Tasker, R., 2003. Biomass surveys and stock assessment of cockles in Whangarei Harbour, including Snake Bank, 2002. Draft New Zealand Fisheries Assessment Report for Ministry of Fisheries project 2001/01. 40 p. Unpubl. Rep. Held Minist. Fish. Wellingt.

Cryer, M., Parkinson, D.M., 2001. Biomass surveys and preliminary stock assessment of cockles, Snake Bank, Whangarei Harbour, 2001. Final Research Report for Ministry of Fisheries Research Project COC2000/01, Objectives 1 & 3. 15 p.(Unpublished report held by Ministry of Fisheries, Wellington.).

Dastgheib, A., 2012. Long-term process-based morphological modeling of large tidal basins. UNESCO-IHE, Institute for Water Education.

De Vriend, H.J., Capobianco, M., Chesher, T., De Swart, H. de, Latteux, B., Stive, M.J.F., 1993. Approaches to long-term modelling of coastal morphology: a review. Coast. Eng. 21, 225–269.

Deltares, 2017a. User Manual Delft3D-FLOW. draft version 3.15. Deltares.

Deltares, 2017b. User Manual Delft3D-WAVE. draft version 3.05. Deltares.

Deltares, 2014. User Manual Delft3D-Functional Specifications. draft version 2.20. Deltares.

Enet, F., Nahon, A., Van Vledder, G., Hurdle, D., 2006. Evaluation of diffraction behind a semi-infinite breakwater in the SWAN Wave Model, in: Proceedings of Ninth International Symposium on Ocean Wave Measurement and Analysis-WAVES06.[Links].

Engelund, F., Hansen, E., 1967. A monograph on sediment transport in alluvial streams. Tech. Univ. Den. 0stervoldgade 10 Cph. K.

Engquist, B., Majda, A., 1979. Radiation boundary conditions for acoustic and elastic wave calculations. Commun. Pure Appl. Math. 32, 313–357.

Engquist, B., Majda, A., 1977. Absorbing boundary conditions for numerical simulation of waves. Proc. Natl. Acad. Sci. 74, 1765–1766.

Fredsøe, J., 1984. Turbulent boundary layer in wave-current motion. J. Hydraul. Eng. 110, 1103–1120.

Grunnet, N.M., Walstra, D.-J.R., Ruessink, B.G., 2004. Process-based modelling of a shoreface nourishment. Coast. Eng. 51, 581–607.

Latteux, B., 1995. Techniques for long-term morphological simulation under tidal action. Mar. Geol. 126, 129–141.

Lesser, G.R., 2009. An approach to medium-term coastal morphological modelling. UNESCO-IHE, Institute for Water Education.

Lesser, G.R., Roelvink, J. v, Van Kester, J., Stelling, G.S., 2004. Development and validation of a three-dimensional morphological model. Coast. Eng. 51, 883–915.

Luijendijk, A.P., Ranasinghe, R., de Schipper, M.A., Huisman, B.A., Swinkels, C.M., Walstra, D.J., Stive, M.J., 2017. The initial morphological response of the Sand Engine: A process-based modelling study. Coast. Eng. 119, 1–14.

Morgan, K.M., Kench, P.S., Ford, R.B., 2011. Geomorphic change of an ebb-tidal delta: Mair Bank, Whangarei Harbour, New Zealand. N. Z. J. Mar. Freshw. Res. 45, 15–28.

NIWA, 2012. Predicting suitable shellfish restoration sites in Whangarei Harbour - Larval dispersal modelling and verification. Report prepared for Ministry of Science and Innovation Envirolink Fund to Northland Regional Council.

Pinto, L., Fortunato, A.B., Freire, P., 2006. Sensitivity analysis of non-cohesive sediment transport formulae. Cont. Shelf Res. 26, 1826–1839.

Ramli, A.Y., de Lange, W., Bryan, K., Mullarney, J., 2015. Coupled flow-wave numerical model in assessing the impact of dredging on the morphology of Matakana Banks, in: Australasian Coasts & Ports Conference 2015: 22nd Australasian Coastal and Ocean Engineering Conference and the 15th Australasian Port and Harbour Conference. Engineers Australia and IPENZ, p. 758.

Ranasinghe, R., Pattiaratchi, C., 1999. The seasonal closure of tidal inlets: Wilson Inlet—a case study. Coast. Eng. 37, 37–56.

Ris, R.C., Holthuijsen, L.H., Booij, N., 1999. A third-generation wave model for coastal regions: 2. Verification. J. Geophys. Res. Oceans 104, 7667–7681.

Roelvink, J.A., 2006. Coastal morphodynamic evolution techniques. Coast. Eng. 53, 277–287.

Van der Wegen, M., Jaffe, B.E., Roelvink, J.A., 2011. Process-based, morphodynamic hindcast of decadal deposition patterns in San Pablo Bay, California, 1856–1887. J. Geophys. Res. Earth Surf. 116.

van der Westhuysen, A.J., Zijlema, M., Battjes, J.A., 2007. Nonlinear saturation-based whitecapping dissipation in SWAN for deep and shallow water. Coast. Eng. 54, 151–170.

Van Rijn, L.C., Walstra, D.J.R., Ormondt, M. van, 2004. Description of TRANSPOR2004 and Implementation in Delft3D-ONLINE. Z3748.

Verboom, G.K., Segal, A., 1987. Weakly-Reflective Boundary Conditions for Shallow Water Equations, in: Research in Numerical Fluid Mechanics. Springer, pp. 115–129.

Verboom, G.K., Slob, A., 1984. Weakly-reflective boundary conditions for two-dimensional shallow water flow problems, in: Finite Elements in Water Resources. Springer, pp. 621–633.

Walstra, D.J.R., Hoekstra, R., Tonnon, P.K., Ruessink, B.G., 2013. Input reduction for long-term morphodynamic simulations in wave-dominated coastal settings. Coast. Eng. 77, 57–70.

Weppe, S., McComb, P., Coe, L., 2015. Numerical Model Studies to Support the Sustainable Management of Dredge Spoil Deposition in a Complex Nearshore Environment, in: The Proceedings of the Coastal Sediments 2015.

Williams, R.D., Measures, R., Hicks, D.M., Brasington, J., 2016. Assessment of a numerical model to reproduce event-scale erosion and deposition distributions in a braided river. Water Resour. Res. 52, 6621–6642.

APPENDIX A. ADDITIONAL MEASURED DEPTH

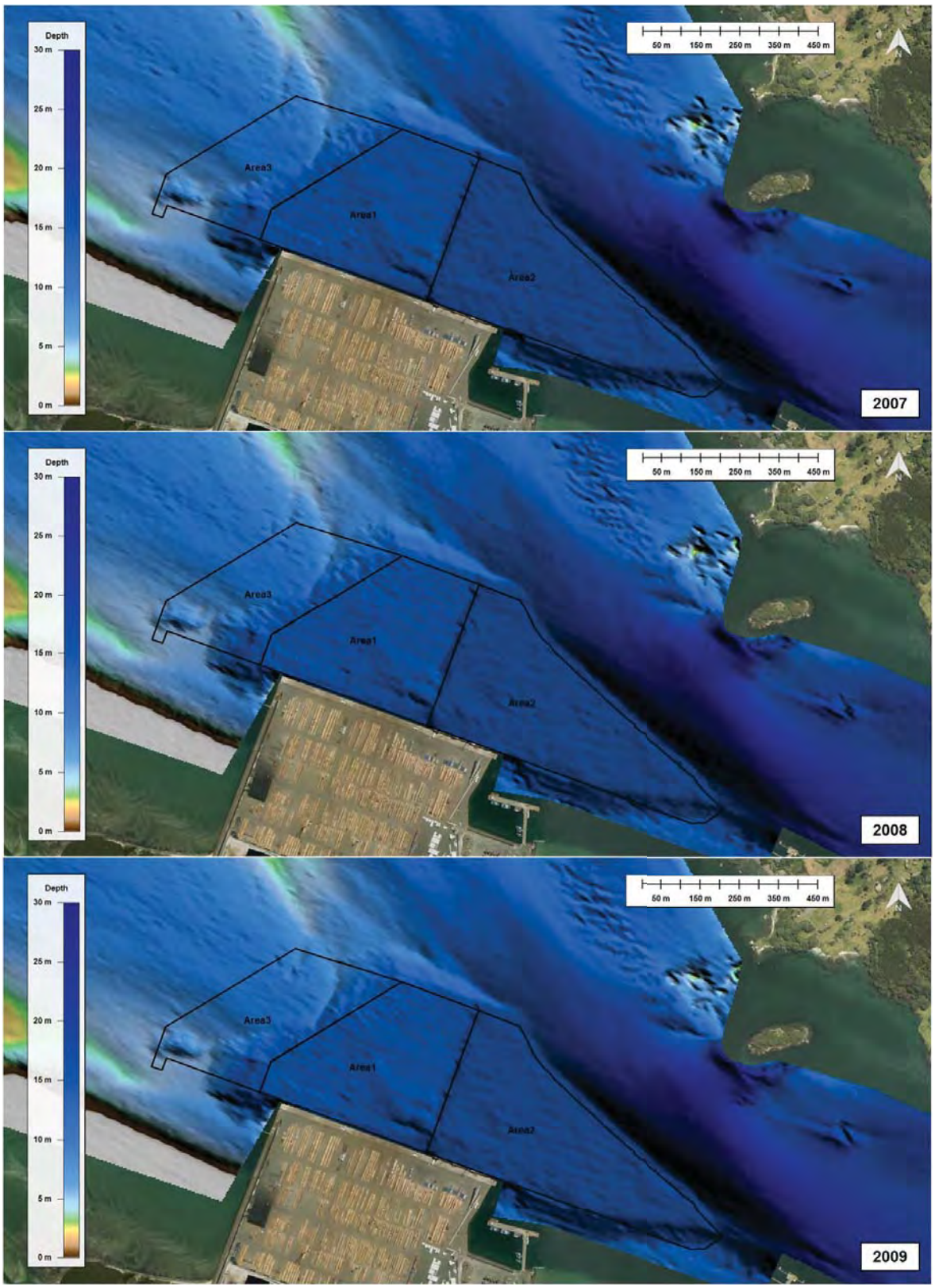

Figure A.1 Bathymetry maps for 2007, 2008 and 2009 obtained from the interpolation of single beam survey data over the entrance to Whangarei Harbour.

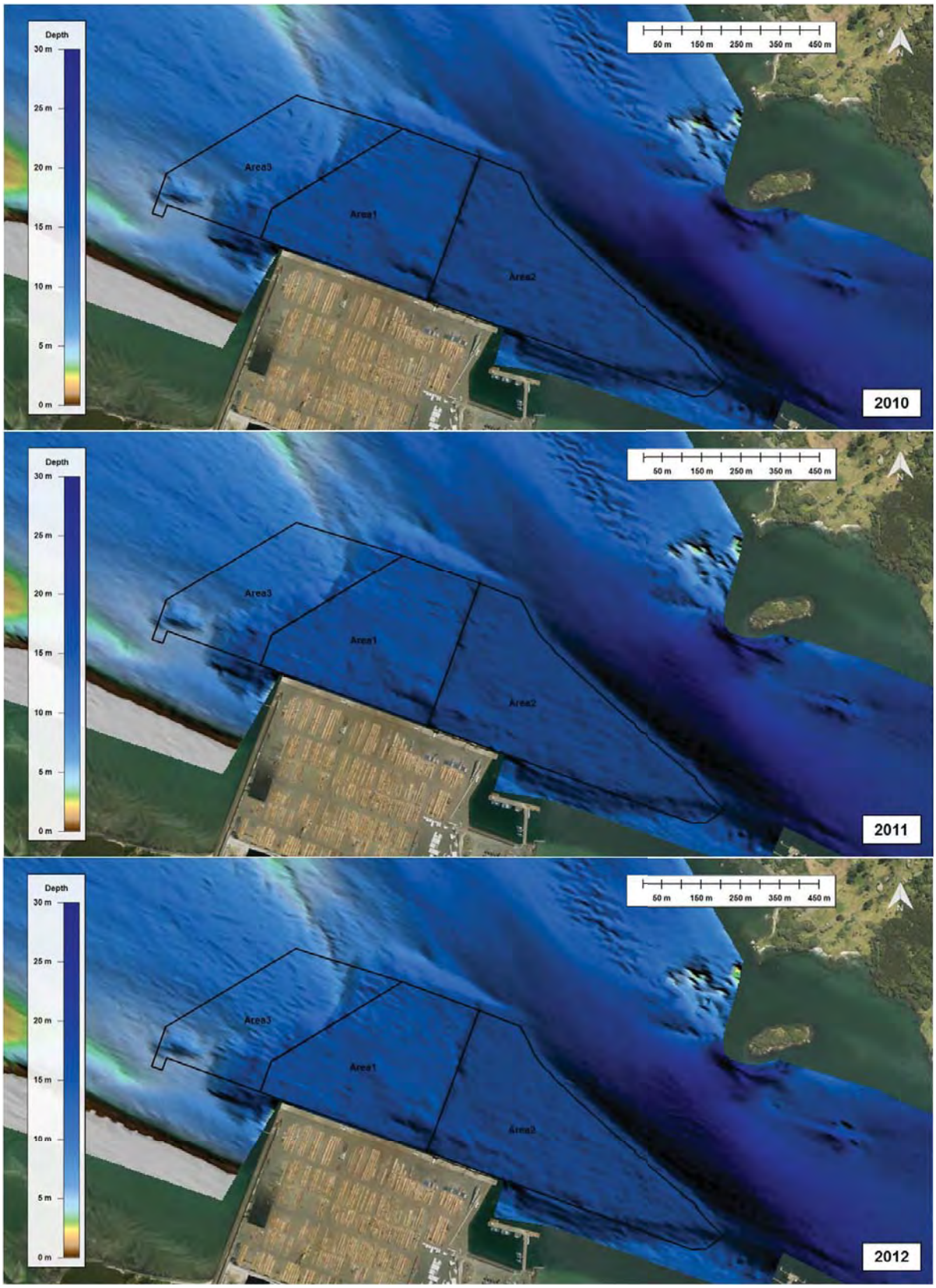

Figure A.2 Bathymetry maps for 2010, 2011 and 2012 obtained from the interpolation of single-beam survey data over the entrance to Whangarei Harbour.

APPENDIX B. MOEL SIGNICIANT WAVE HEIGHT ASSOCIATED WITH EACH SCENARIOS

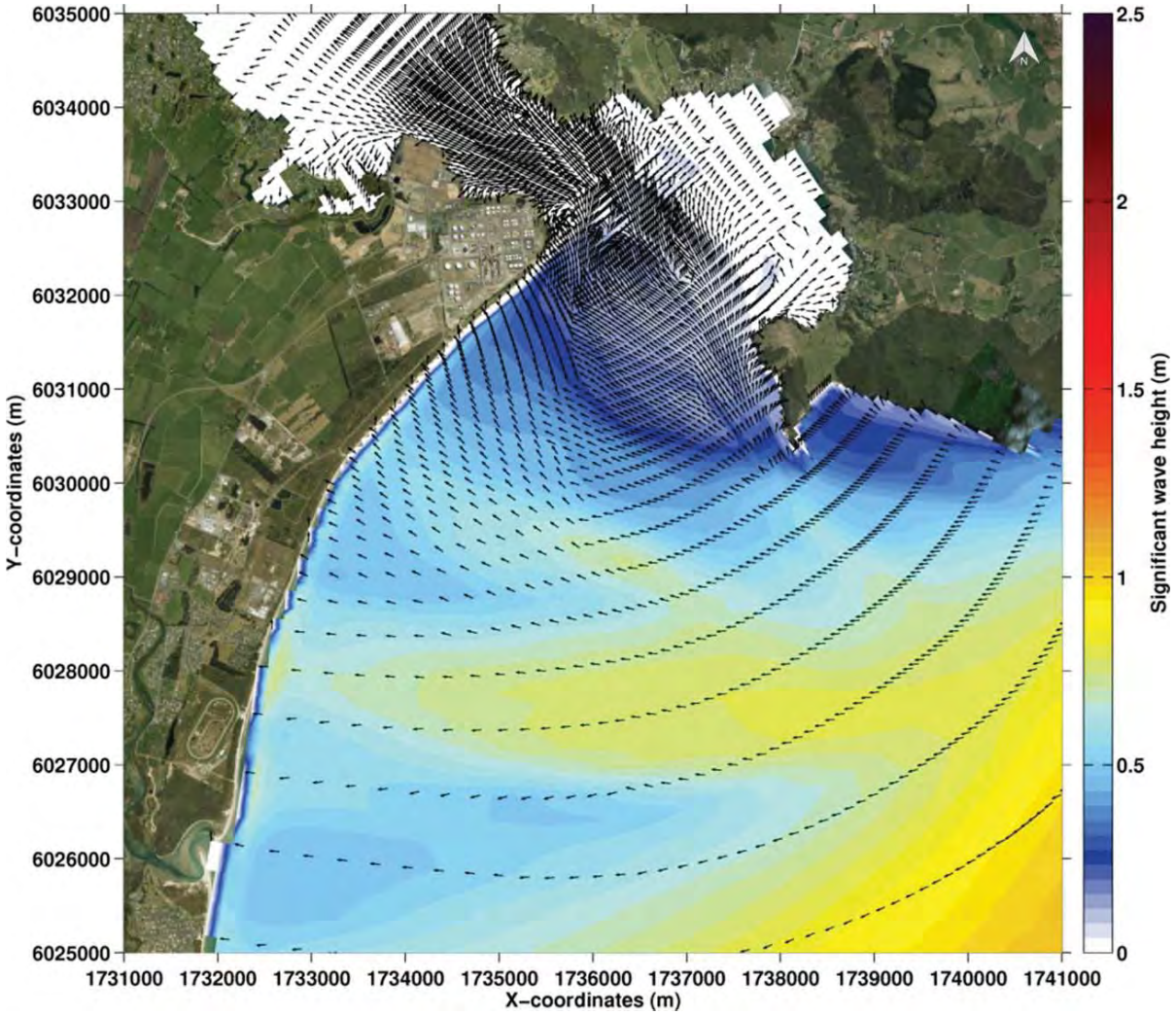

Figure B.1 Significant wave height field associated with Class 1 of the input reduction.

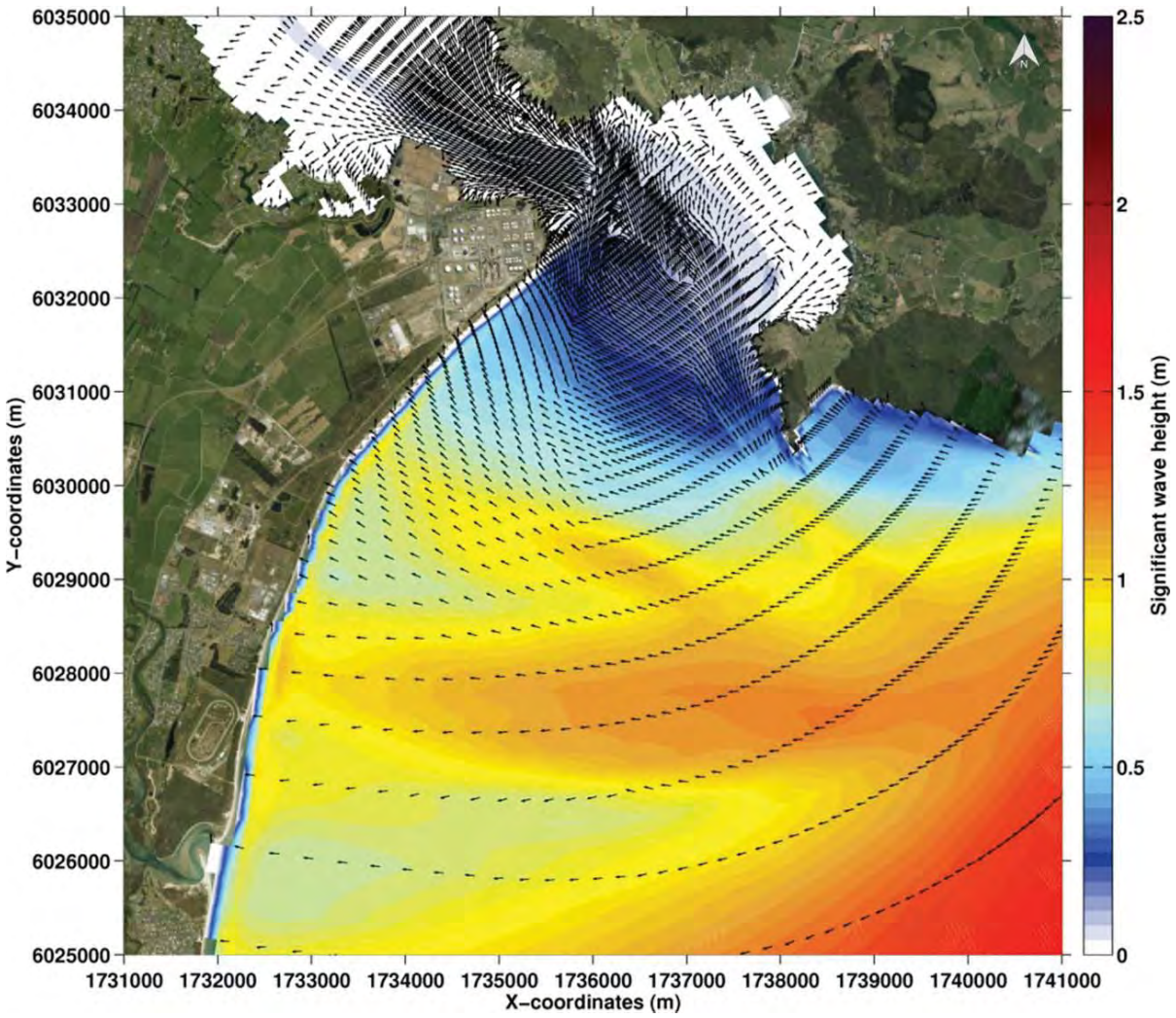

Figure B.2 Significant wave height field associated with Class 2 of the input reduction.

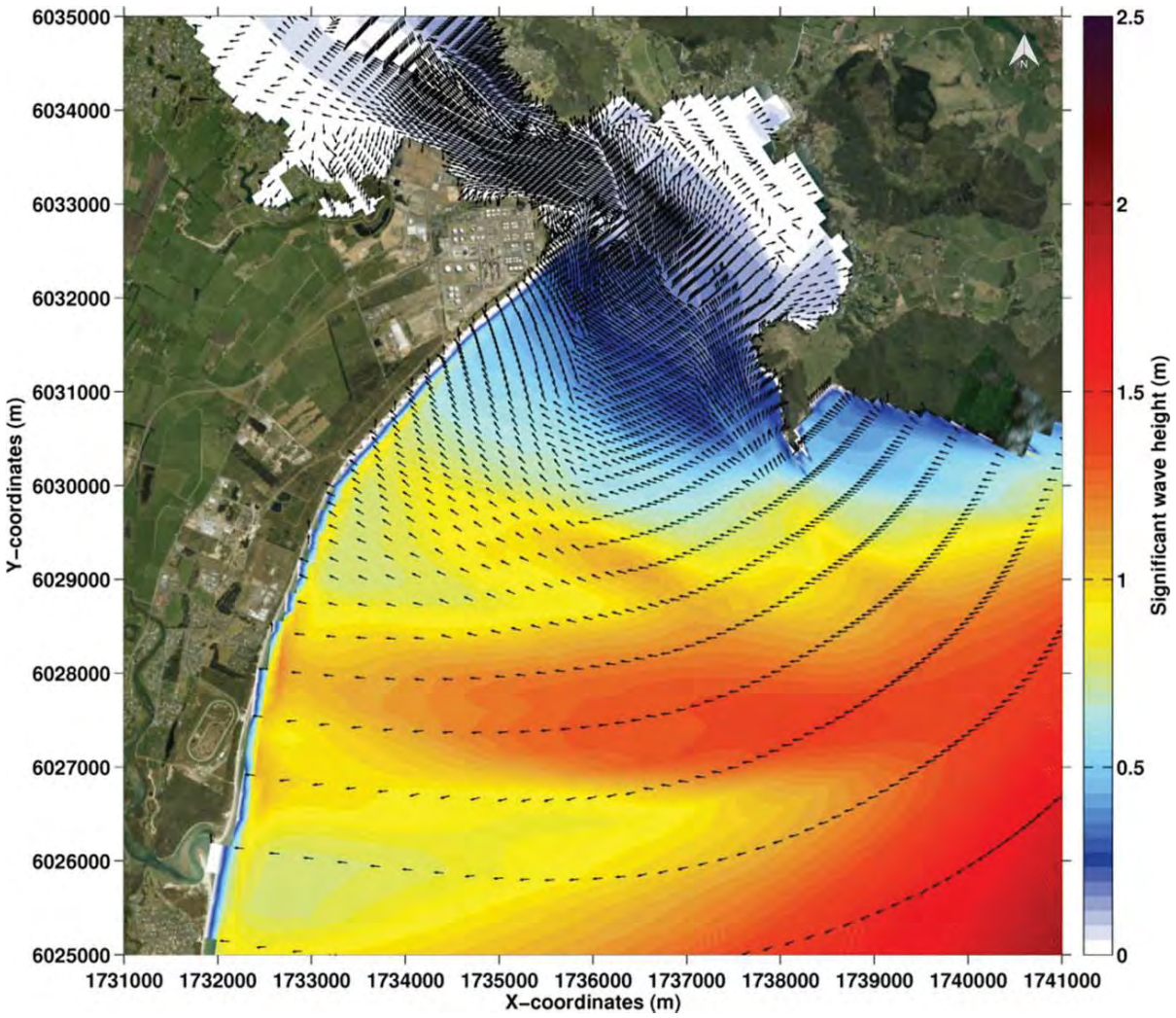

Figure B.3 Significant wave height field associated with Class 3 of the input reduction.

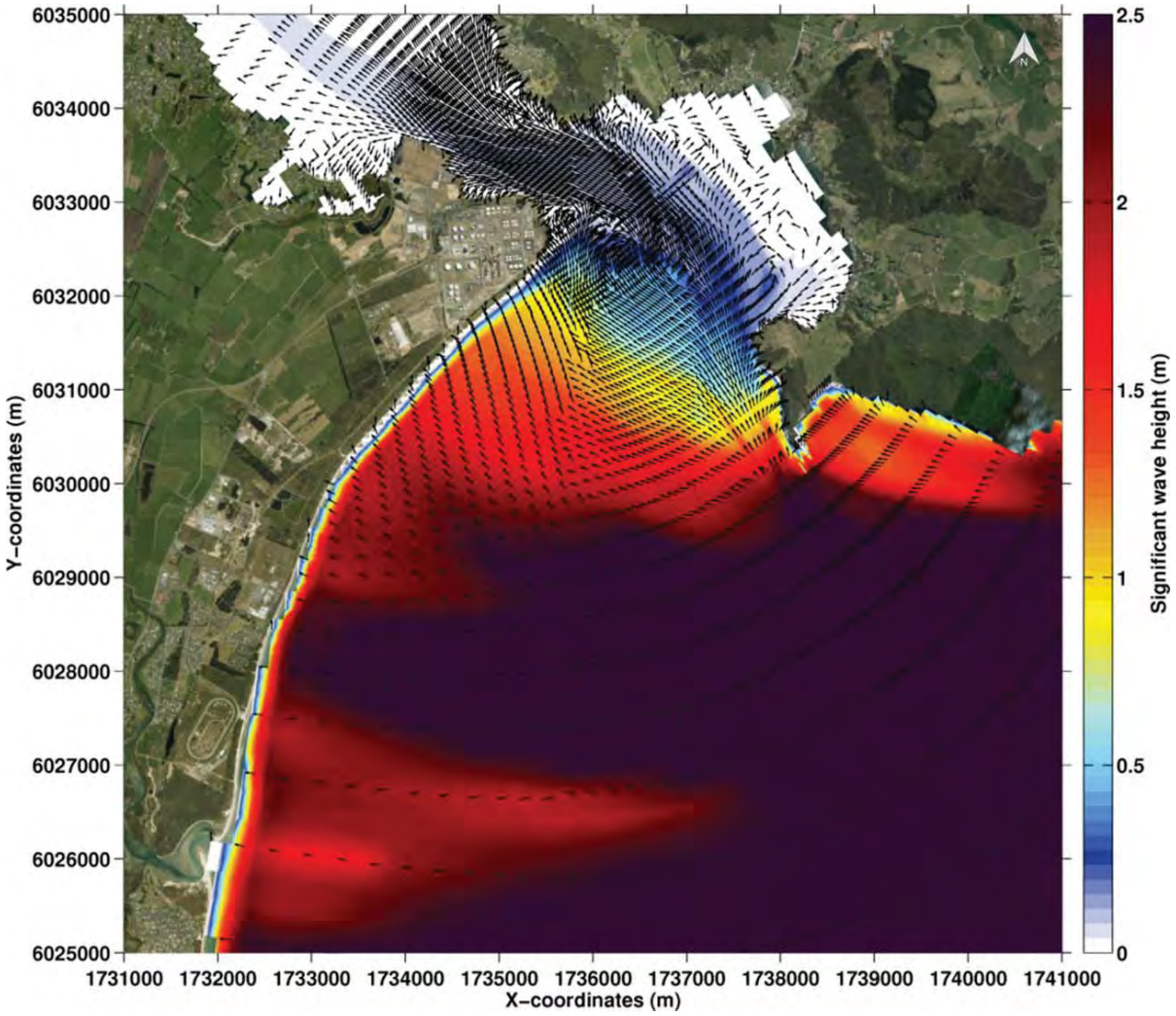

Figure B.4 Significant wave height field associated with Class 4 of the input reduction.

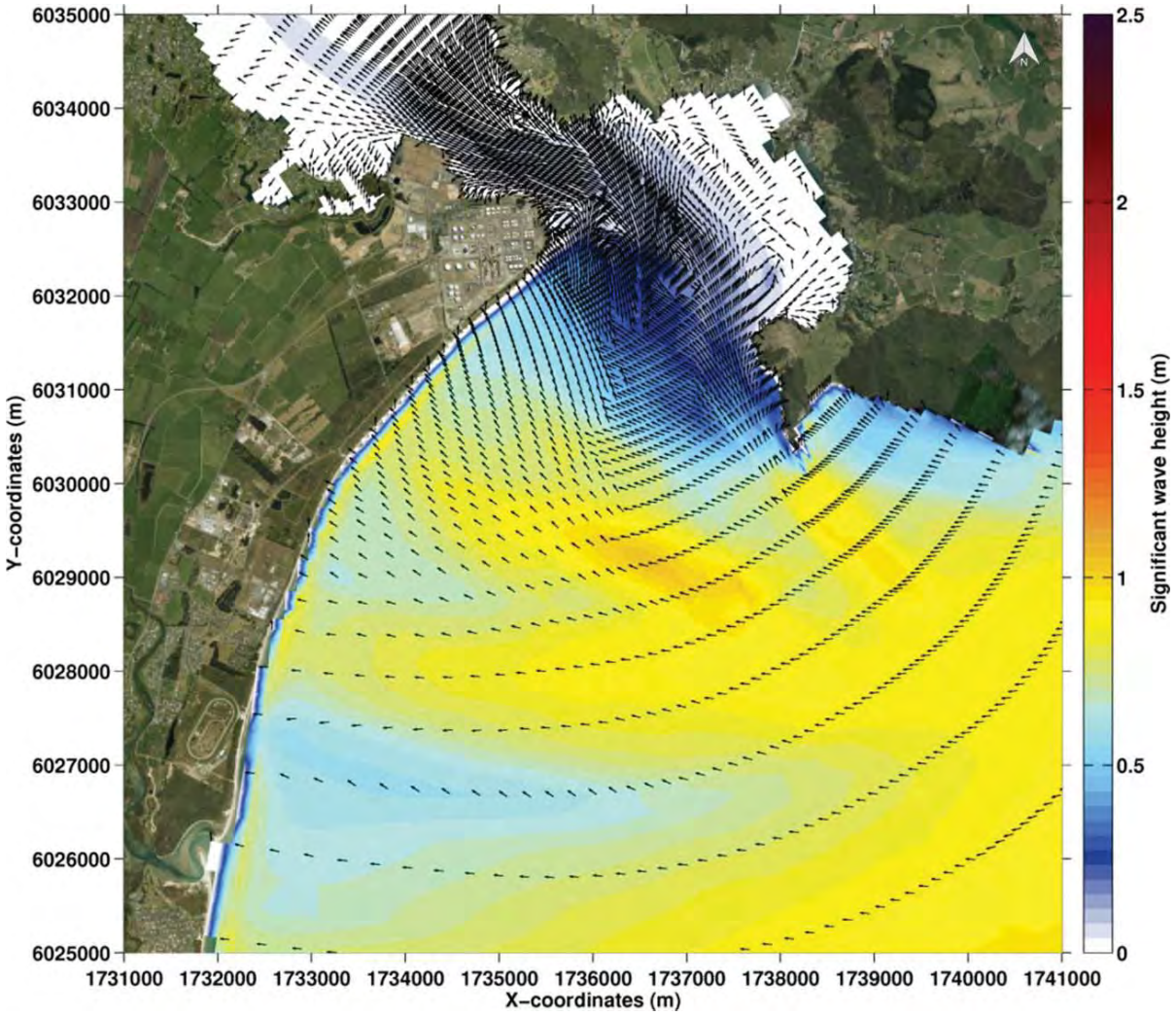

Figure B.5 Significant wave height field associated with Class 5 of the input reduction.

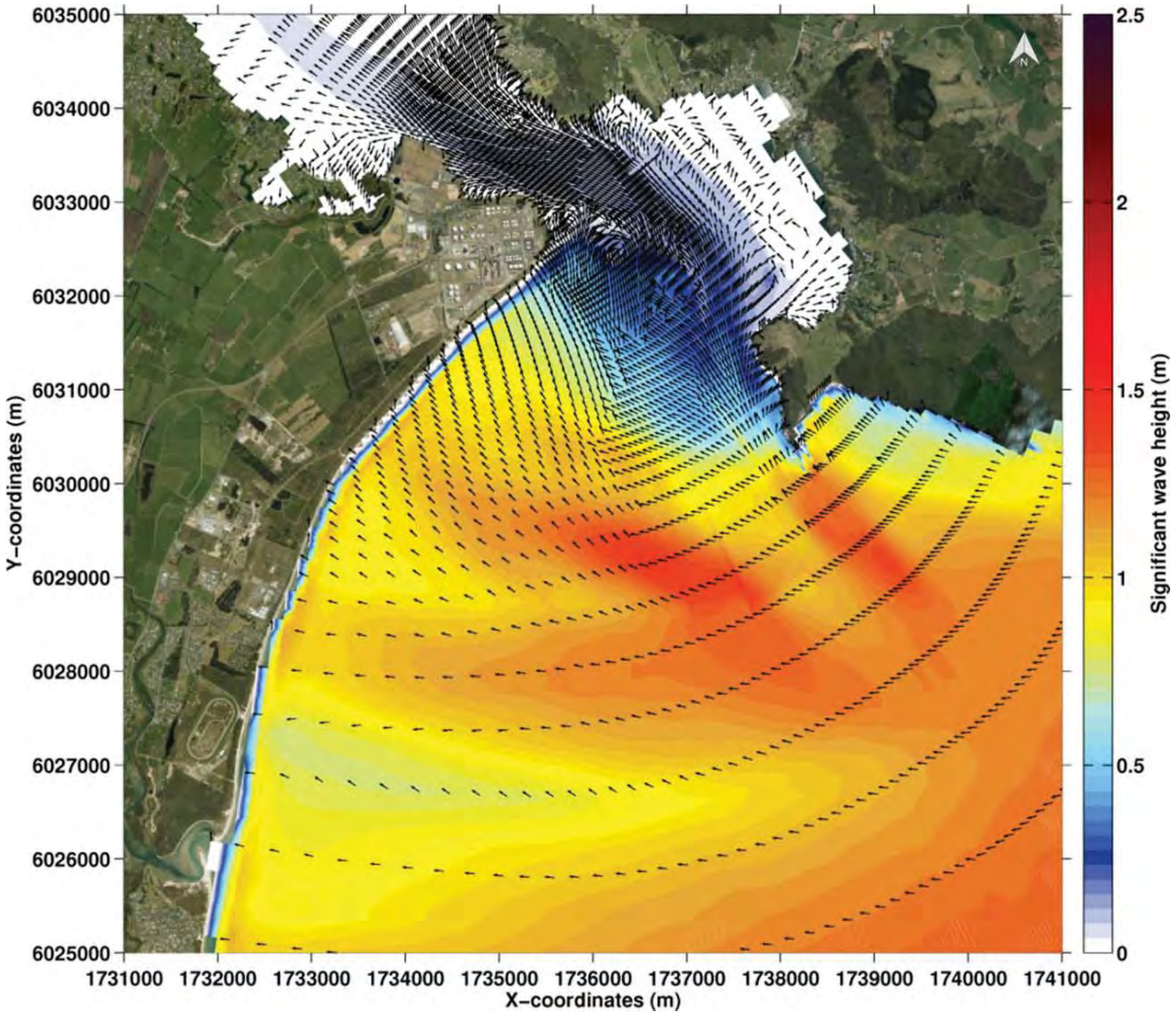

Figure B.6 Significant wave height field associated with Class 6 of the input reduction.

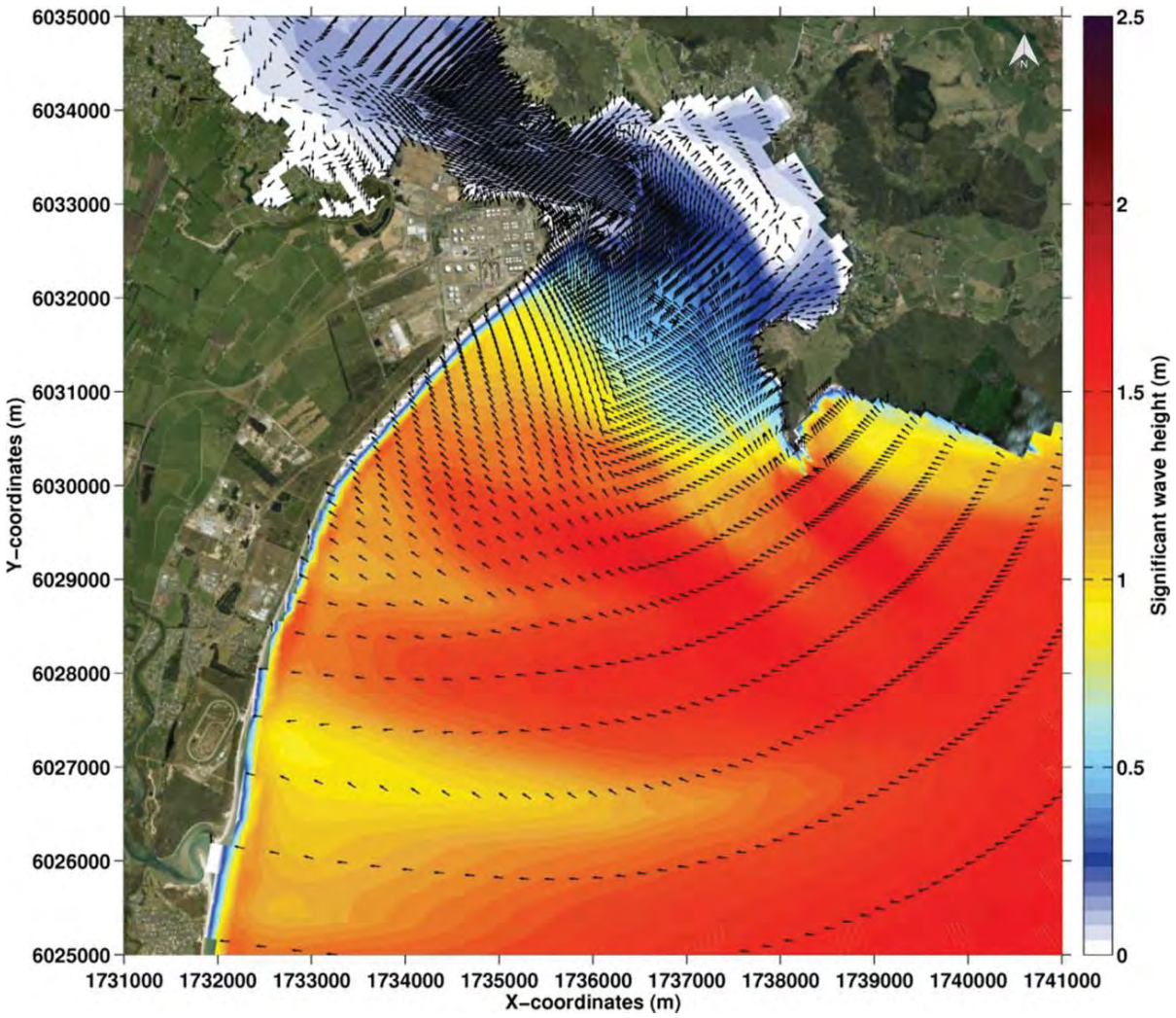

Figure B.7 Significant wave height field associated with Class 7 of the input reduction.

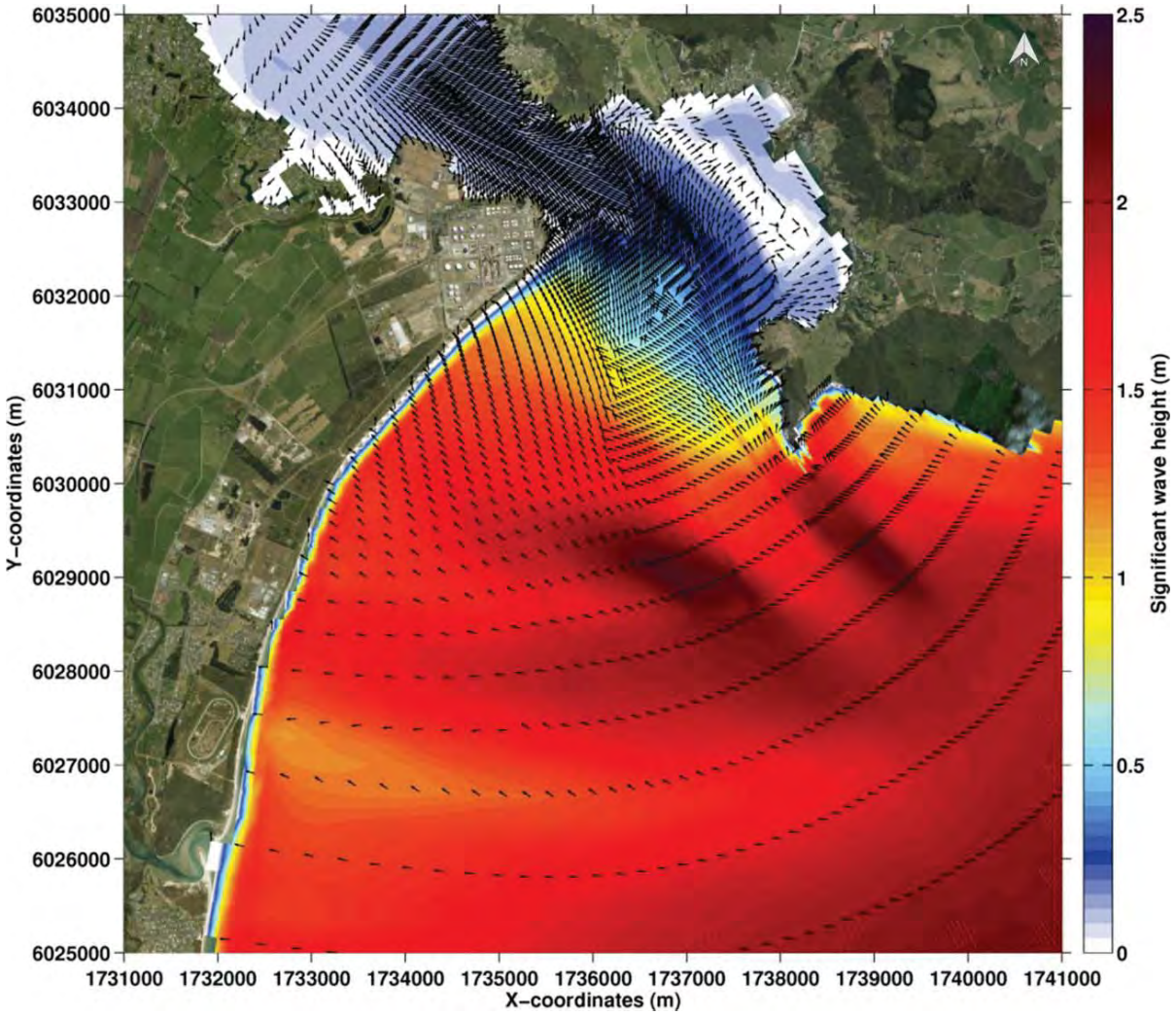

Figure B.8 Significant wave height field associated with Class 8 of the input reduction.

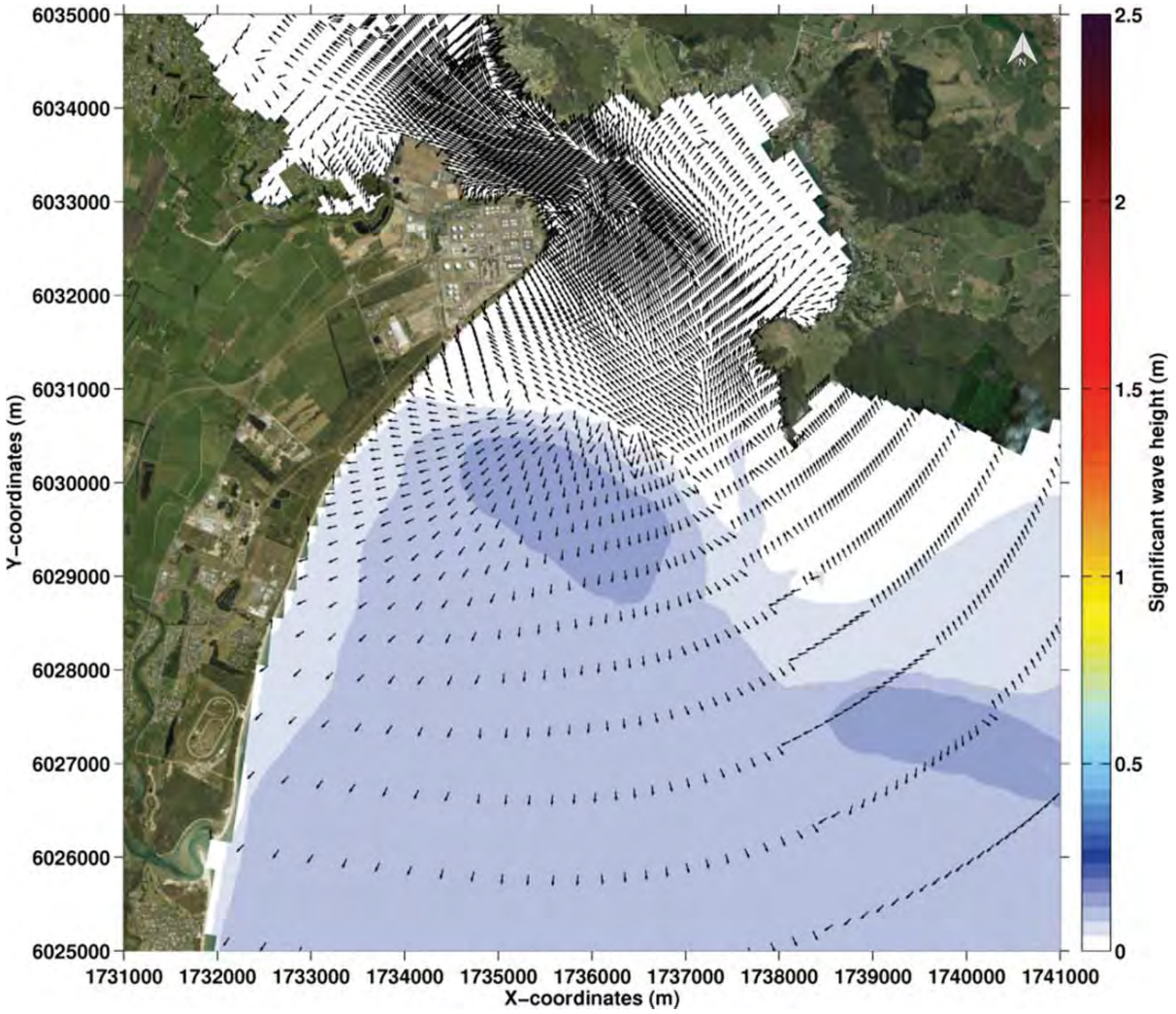

Figure B.9 Significant wave height field associated with Class 9 of the input reduction.

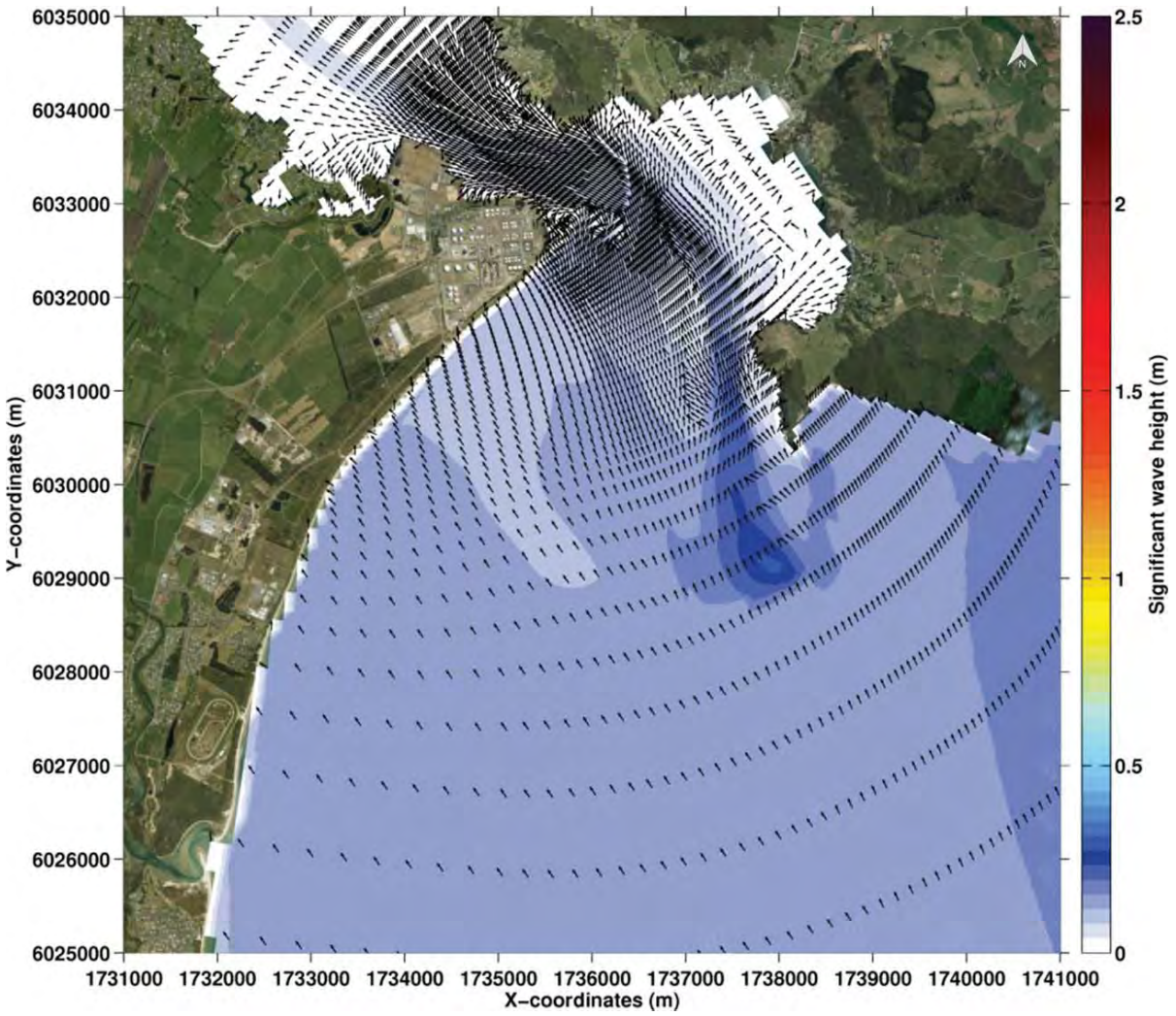

Figure B.10 Significant wave height field associated with Class 10 of the input reduction.

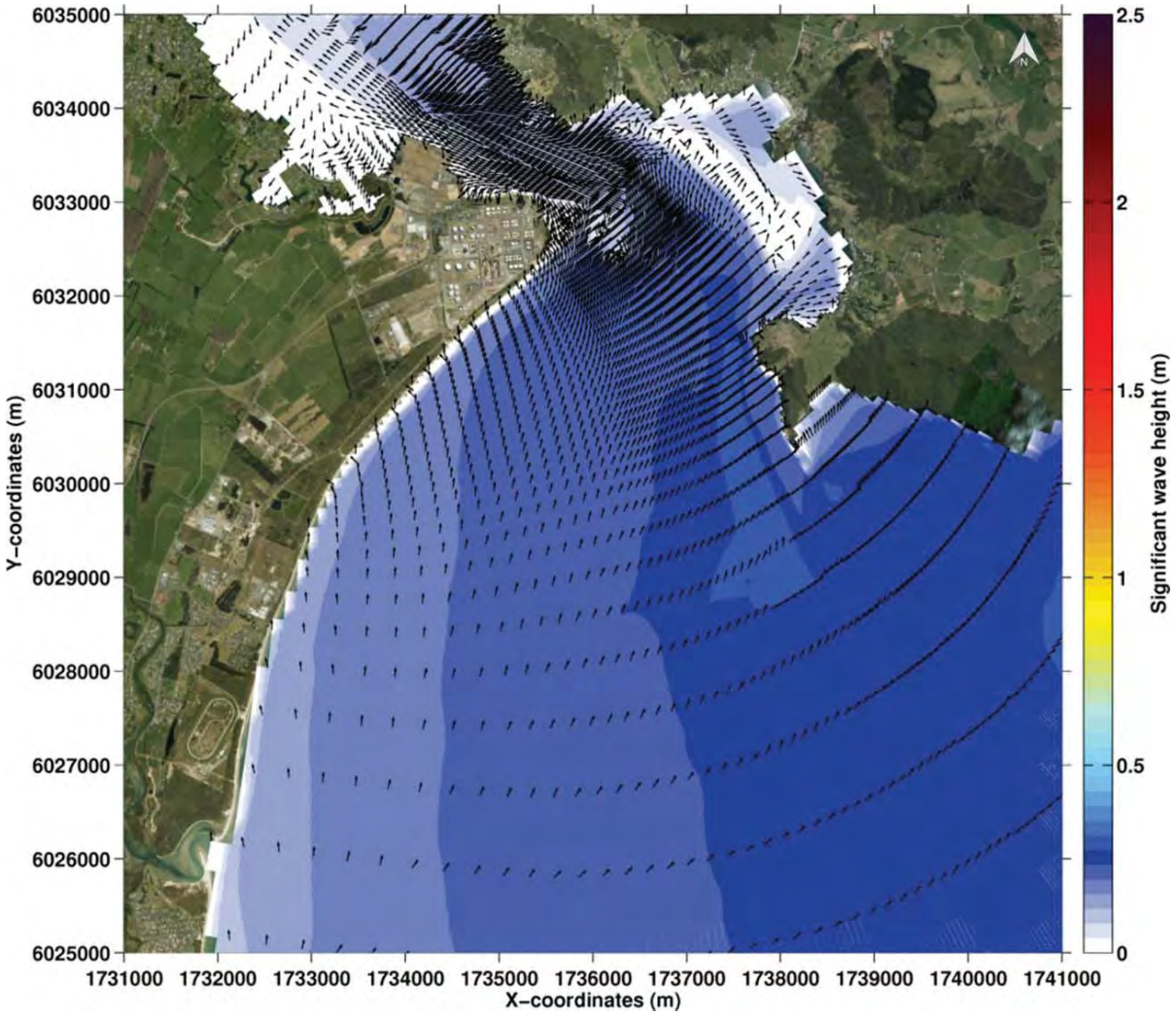

Figure B.11 Significant wave height field associated with Class 11 of the input reduction.

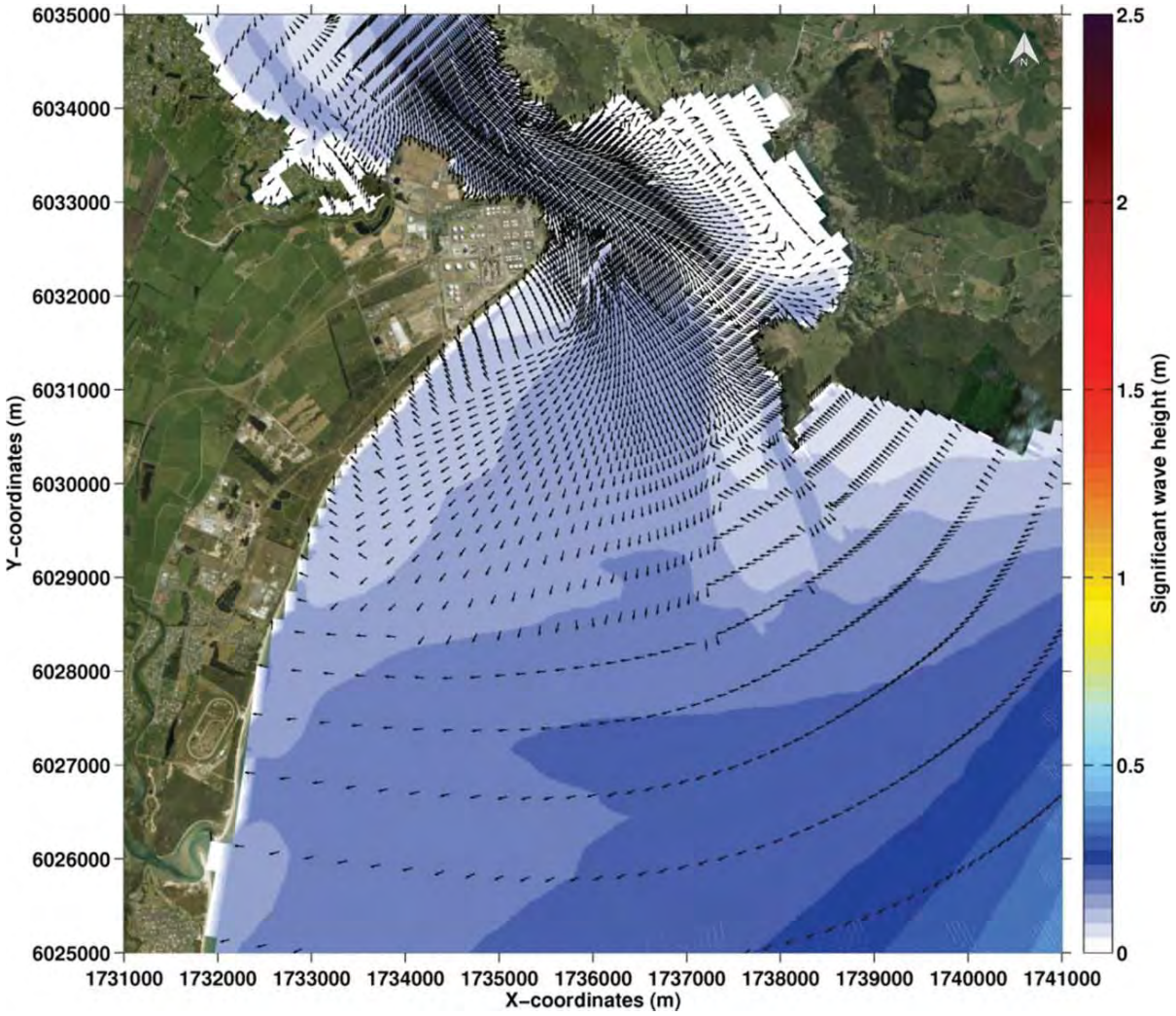

Figure B.12 Significant wave height field associated with Class 12 of the input reduction.

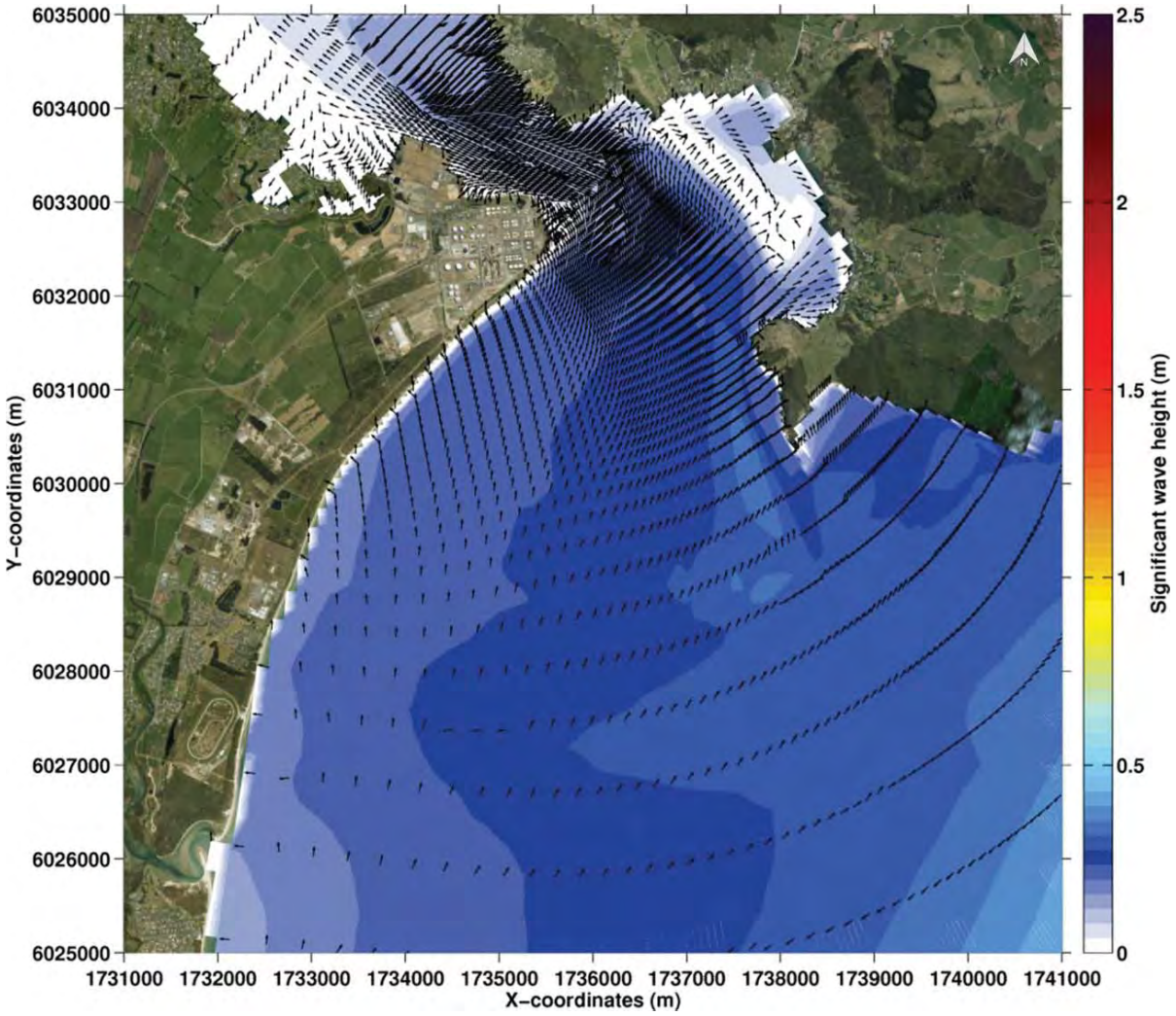

Figure B.13 Significant wave height field associated with Class 13 of the input reduction.

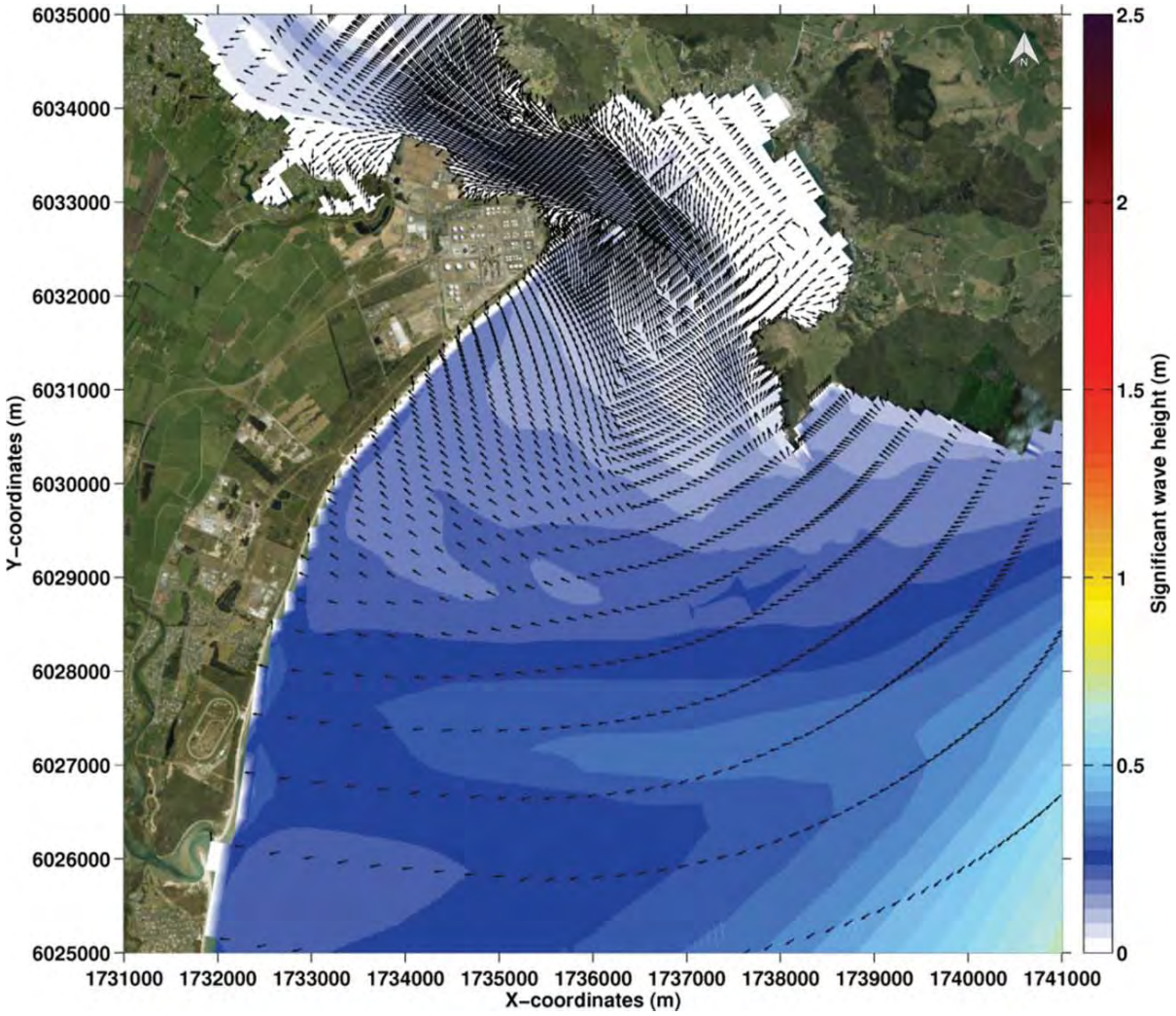

Figure B.14 Significant wave height field associated with Class 14 of the input reduction.

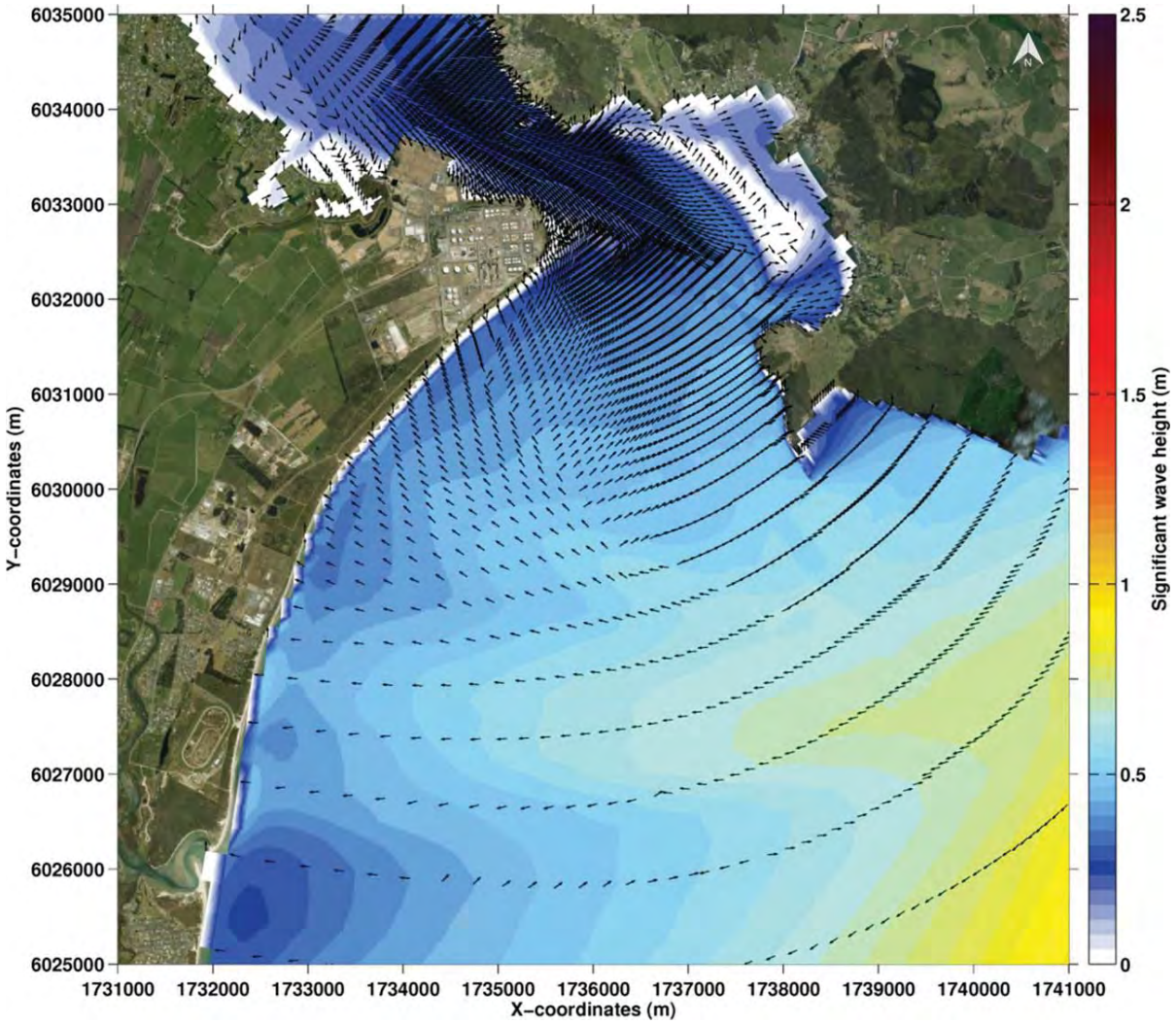

Figure B.15 Significant wave height field associated with Class 15 of the input reduction.

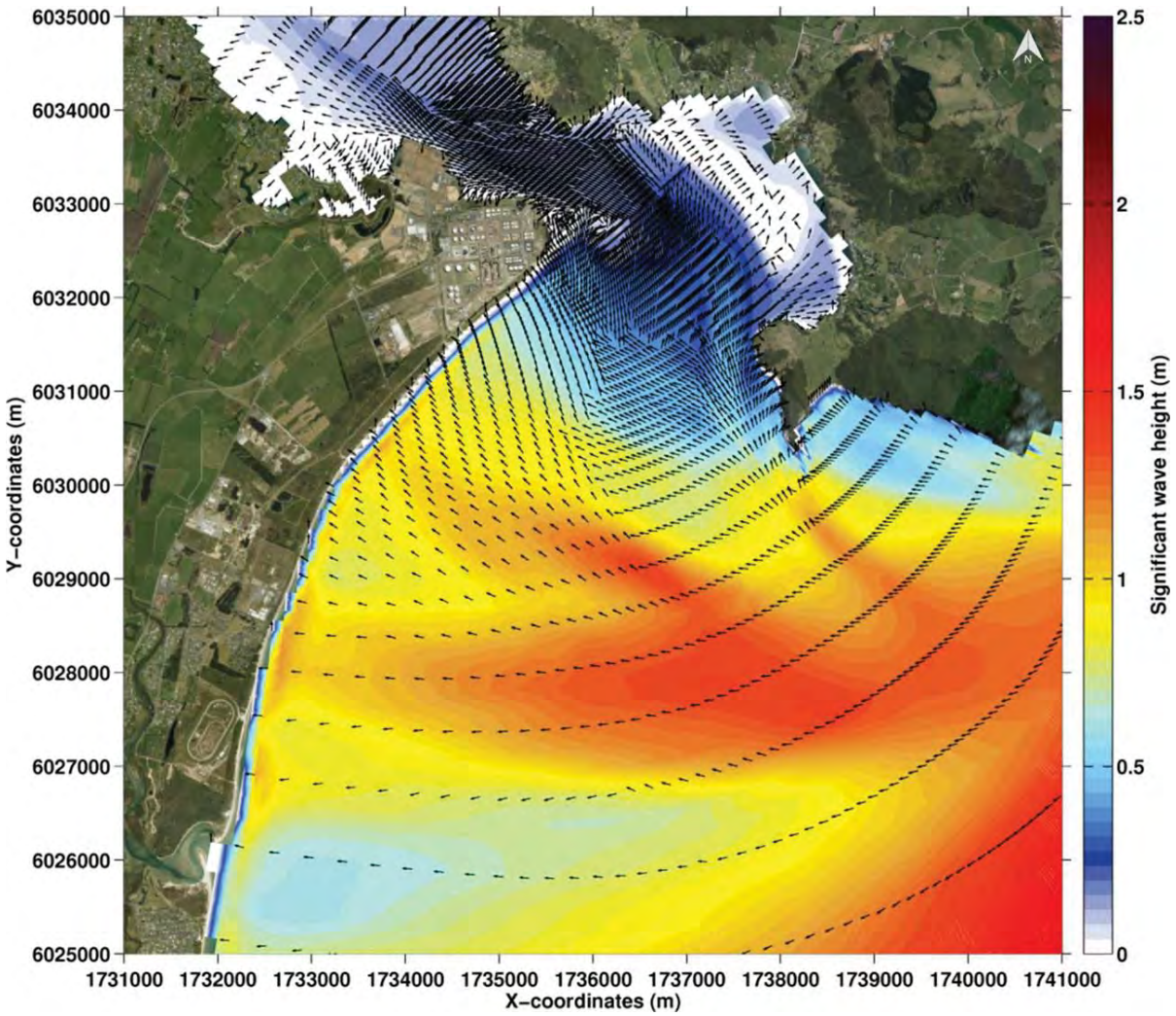

Figure B.16 Significant wave height field associated with Class 16 of the input reduction.

APPENDIX C. WIND VALIDATION

Figure C.1 Location of the wind station (red circle) at Mardsen Point.

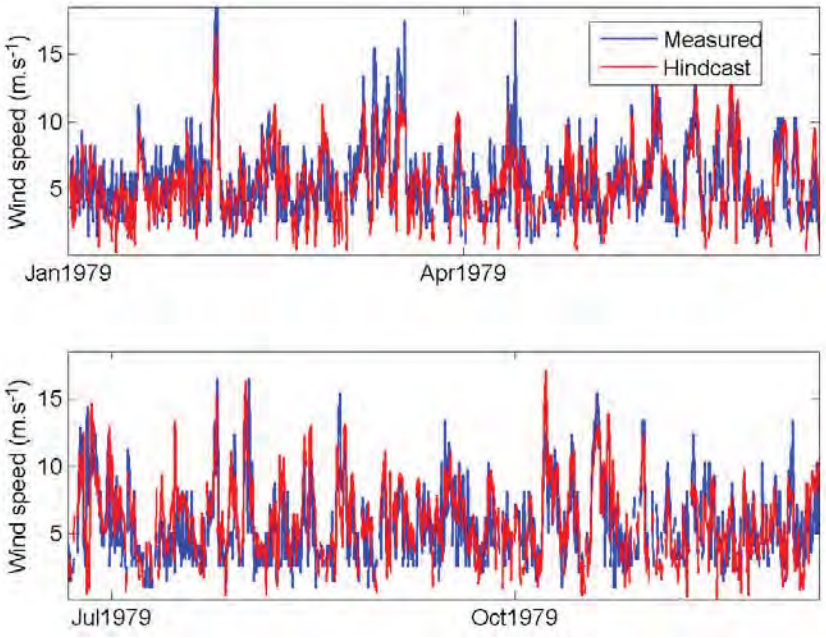

Figure C.2 Time series plot of the measured and hindcast wind speed and wind direction at Marsden Point (year 1979). Note only a portion of the 12 years of data used for validation is shown here for better visualisation.

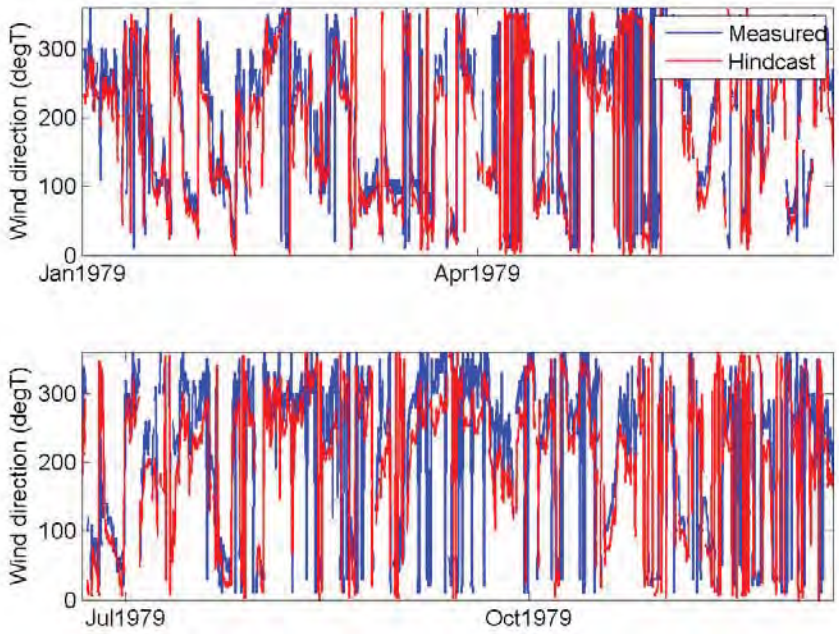

Figure C.3 Time series plot of the measured and hindcast wind direction at Marsden Point (year 1979). Note only a portion of the 12 years of data used for validation is shown here for better visualisation.

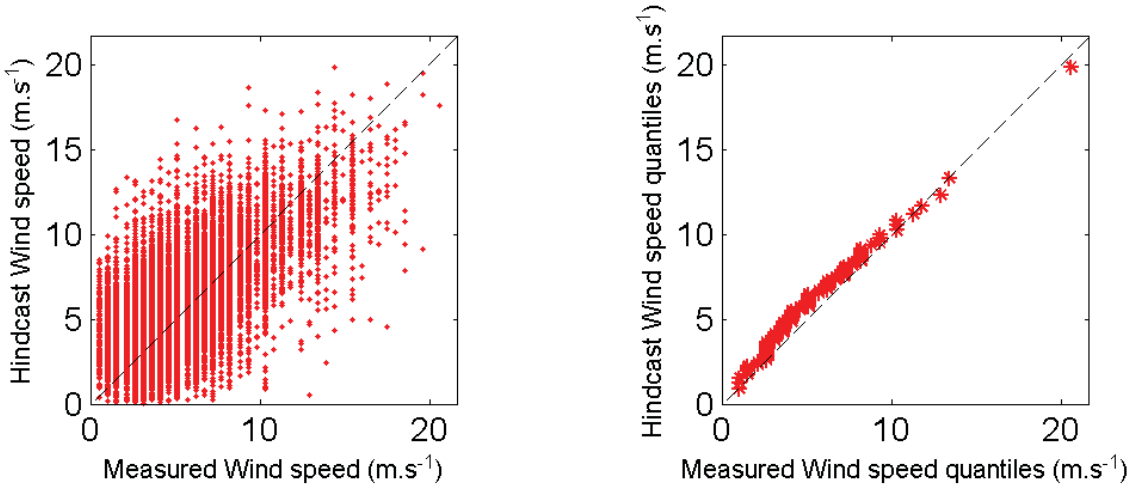

Figure C.4 Scatter and Quantile-Quantile plots of the measured and hindcast wind speed at Marsden Point (1979-1990). Also shown are the lines of equivalence.

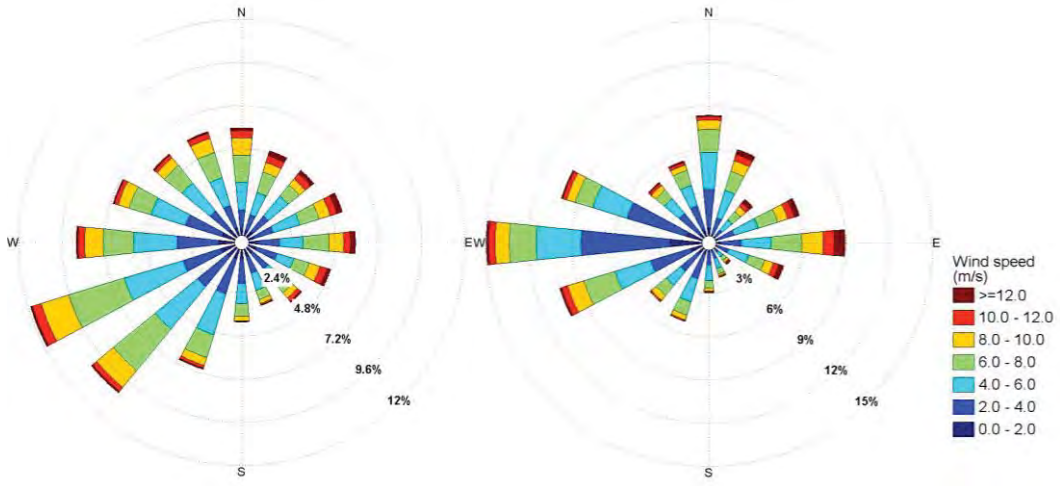

Figure C.5 Modelled (left) and measured (right) annual wind rose at position WS.

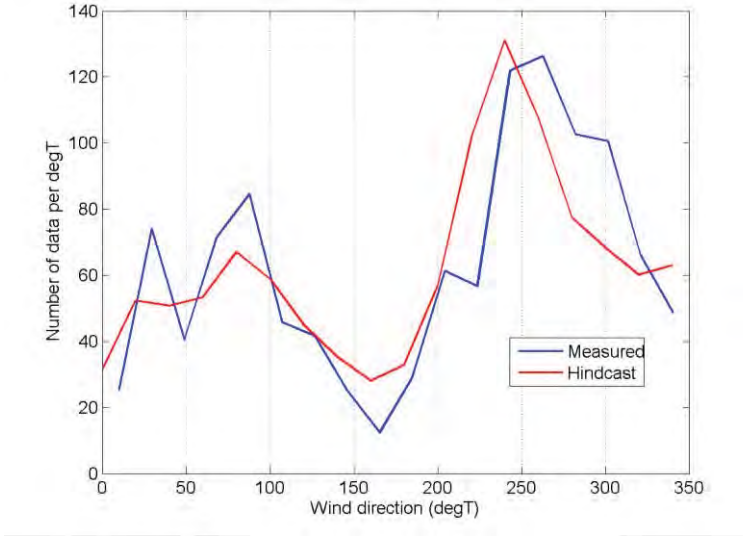

Figure C.6 Histograms of measured and hindcast wind directions at Marsden Point (1979-1990).

METOCEAN SOLUTIONS

HYDRODYNAMIC MODELLING

Methodology, validation and simulations

Report prepared for
Northport

Northport

Specialists in
Oceanography

MetOcean Solutions Ltd: Report P0367 – 02

April 2018

Report status

Version	Date	Status	Approved by
RevA	04/04/2018	Draft for internal review	Beamsley
RevB	05/04/2018	Draft for internal review	Berthot
RevC	10/04/2018	Draft for client review	Beamsley

It is the responsibility of the reader to verify the currency of the version number of this report.

TABLE OF CONTENTS

LIST OF FIGURES

1. INTRODUCTION

Northport is a deep-water commercial port strategically situated at Marsden Point near Whangarei in Northland, New Zealand. Northport is New Zealand's newest port, designed and built as a flexible, multi-purpose facility to cater for a wide range of cargoes and their associated vessel types.

Northport's current footprint totals 48.46 hectares, made up of 570 linear metres of berthage consisting of three berths, 33.615 hectares of reclamation and 14.845 metres of berth with a depth at Chart Datum (CD) of 14.5 m and 2.3 hectares of reclamation providing for a total consented footprint of 840 linear meters (4 berths) and 50.76 hectares. Historical hydrographic surveys of the swinging basin have highlighted the fact that infilling is occurring over time, and there is a requirement to understand future infilling rates from a maintenance and operability perspective.

Further, Ports strategic planning has identified potential for the facilities to expand up to 250 metres and include a 13.0-hectare reclamation westward, with the entire berth length cut to 14.5 m CD, with 700 metres capable of a depth up to 16 m CD (Figure 1.2).

To protect and ensure the port's ability to expand as the market or NZ port strategy demands, the opportunity to undertake the consent application for the remaining potential reclamation footprint is currently being considered. While at the early stages, Northport feel that the timing is right to start to undertake the first steps towards securing the required port growth.

Northport recognise that there is scope to reclaim areas to both the east and west of the current reclaimed facility (Areas 5 and 6, Figure 1.2). To undertake these capital works, there are a suite of resource consents that will be required, including dredging (see Figure 1.3), earthworks, discharges to the harbour as well as ongoing land use type consents and discharge consents. Dredging areas and estimated volume to be dredged are given in Figure 1.2 (Areas 1-3), with a total of approximately 973,000 m^3 expected to be dredged (Capital Dredging). This sediment is intended to be used to provide clean fill to the areas being reclaimed (Figure 1.2); mitigating the need to dispose the sediment at an offshore site. The proposed port development has been broken into 3 stages (Stage 1-3), consisting of;

1. Area 6 (less 50m along northern edge) to be reclaimed (Stage 1)

2. Area 6 including northern edge constructed, plus Area 3 dredged (Stage 2)

3. Balance of Areas 4 & 5 constructed, as well as Areas 1 & 2 dredged to 14.5m below CD (Stage 3).

It is likely that Capital dredging will also be undertaken using a Trailer Suction Hopper Dredge (TSHD) given the sediment, however a Backhoe Dredge (BHD) or Cutter Suction Dredge (CSD) may be used.

From an operational and consenting perspective, Northport require an understanding of the effects of the proposed modifications on the hydrodynamics of the harbour in responses to the proposed capital dredging and reclamations – this is achieved through the application of a calibrated and validated hydrodynamic model (i.e. SELFE). Qualitative and quantitative calibration is achieved through the comparison of hydrodynamic model outputs against measured current velocities.

Once calibrated, the hydrodynamic model can be used to assess the hydrodynamic response for both the existing port and proposed port alterations (i.e. capital dredging and reclamations).

This report represents a technical reference document that details:

- The methodology and the outcomes of the numerical model performance assessment.

- The predicted hydrodynamic changes within the swinging basin and the surroundings in response to the proposed reclamations and capital dredging.

The report is structured as follows; the complete methodology applied in this study is detailed in Section 2, including a description of the model settings and the methodology applied to assess the model skills and model validation. Results of hydrodynamic modelling are presented in Section 3. A brief summary is presented in Section 4 while the references cited in this document are listed in Section 5.

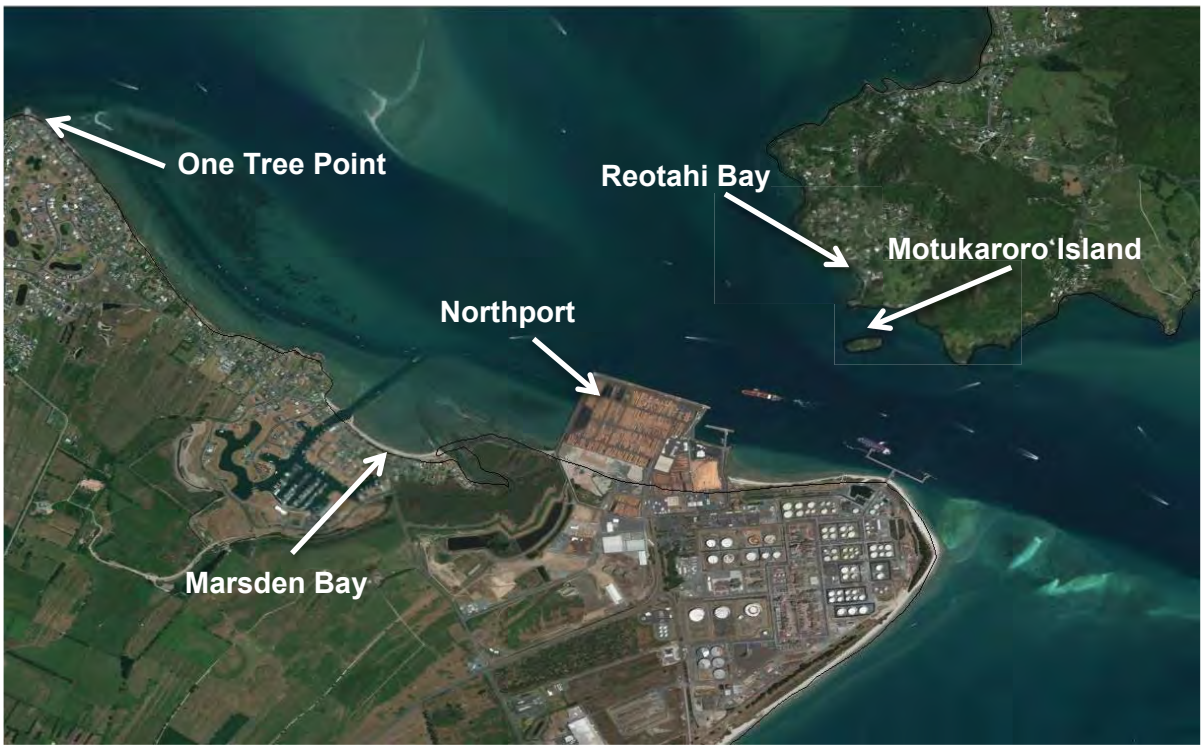

Figure 1.1 Location of Northport within Whangarei Harbour.

Figure 1.2 Draft plan of area to be expanded.

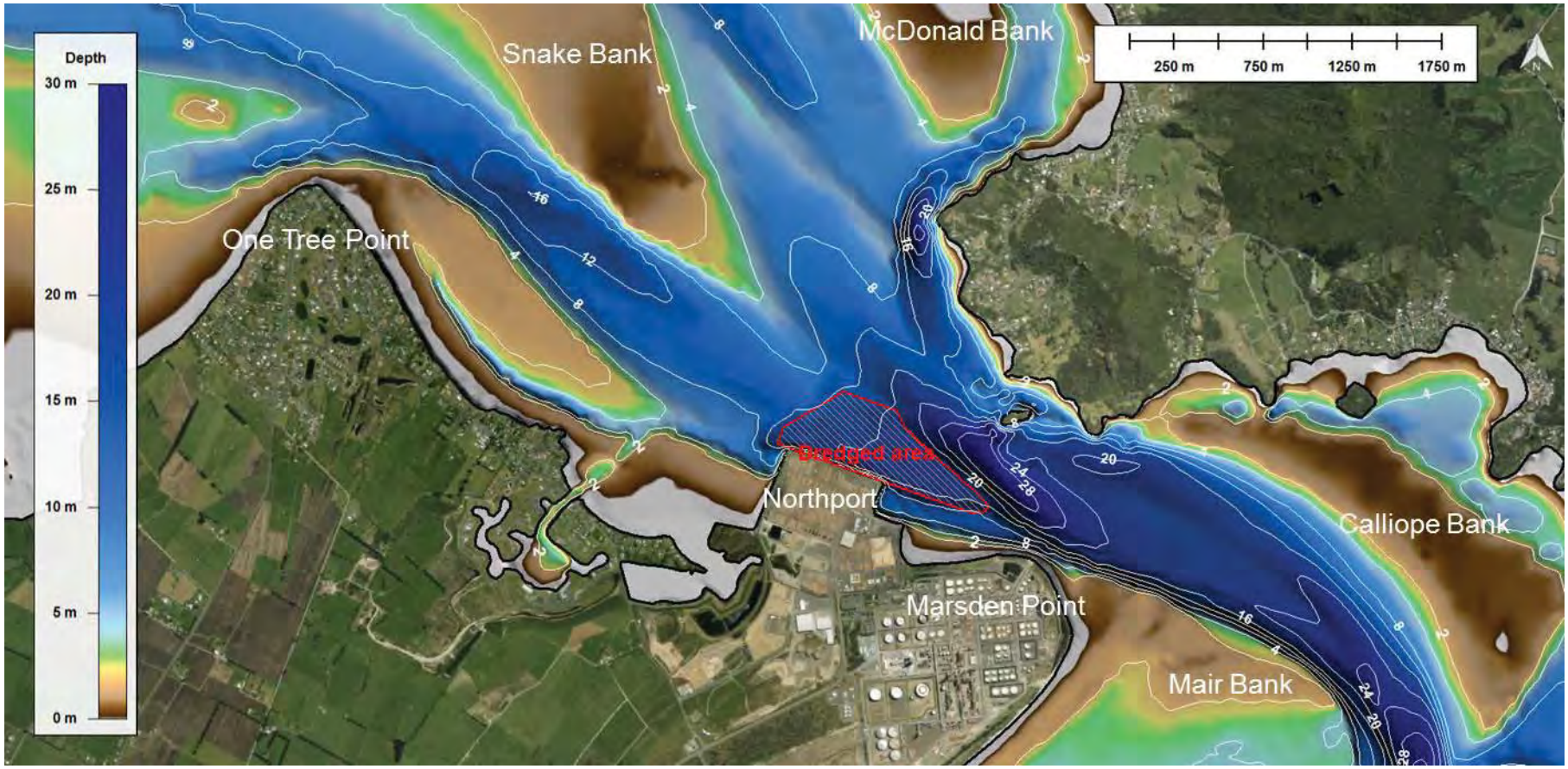

Figure 1.3 Location of Northport near the entrance to Whangarei Harbour. The colour scale details the bathymetry (MSL) derived from multiple data sources. Key locations and the dredged area corresponding to the swinging basin are also indicated on the map.

2. METHODS

The primary objective of the study is to present the calibration and validation of the hydrodynamic model, and results from the application of the calibrated model to examine the effects of the proposed capital dredging and reclamations.

The present section details the methods applied for the implementation and the validation of the hydrodynamic numerical model. The hydrodynamic model extends on the calibration and validation of the Whangarei Harbour model produced as part of the Refining New Zealand study (MetOcean Solutions Ltd, 2017).

2.1. Model description

SELFE is a prognostic finite-element unstructured-grid model designed to simulate 3D baroclinic, 3D barotropic or 2D barotropic circulation. The barotropic mode equations employ a semi-implicit finite-element Eulerian-Lagrangian algorithm to solve the shallow-water equations, forced by relevant physical processes (atmospheric, oceanic and fluvial forcing). SELFE uses either pure terrain-following sigma, or S-layer coordinates in the vertical, or a hybrid system using both S and Z-layers as required and uses sophisticated vertical turbulent closure models. A detailed description of the SELFE model formulation, governing equations and numerics can be found in Zhang and Baptista (2008).

The SELFE model is physically realistic, in that well understood laws of motion and mass conservation are implemented. Therefore water mass is generally conserved within the model although it can be added or removed at open boundaries (e.g. through tidal motion at the ocean boundaries, or river discharges) and water is redistributed by incorporating aspects of the real-world systems (e.g. bathymetric information, forcing by tides and wind). The model transports water and other constituents (e.g. salt, temperature, turbulence) through the use of triangular volumes (connected 3-D polyhedrons) of varying size, and is described as an unstructured finite element model. The unstructured grid approach allows for the accurate delineation of the shoreline, key morphological features that control hydrodynamics (i.e. channels, sand banks etc.) and increased grid resolution in areas of interest, such as within the port environs.

The SELFE model has been extensively applied to study circulation in coastal margins (bays, estuaries, tidal inlets and rivers) around the world (www.strccmop.org), including within wave-dominated tidal inlets (e.g. Dodet, 2013).

2.2. Model domain and bathymetry

Bathymetry is an essential requirement for numerical model studies, and as such MetOcean Solutions (MOS) has compiled an extensive national and regional bathymetric dataset derived from Electronic Navigation Charts (ENC), which are used as the foundation for creating the required model domains. These datasets were supplemented with recent hydrographic survey datasets (Figure 2.1) and LIDAR data in order to develop suitable model domain bathymetry of the existing harbour configuration. The model domain extents and existing bathymetry are shown in Figure 2.2. The domain was developed to ensure that appropriate offshore tidal boundaries (elevations and velocities) could be applied. The mesh resolution varies from approximately 300 m offshore, to ~5 m nearshore and around salient features (i.e. harbour reclamations/dredging areas).

This existing harbour model domain has been modified to account for the proposed reclamation and dredging developments (see Figure 1.2). Three stages of development are proposed, with Figure 2.3 illustrating the proposed harbour configurations at each stage.

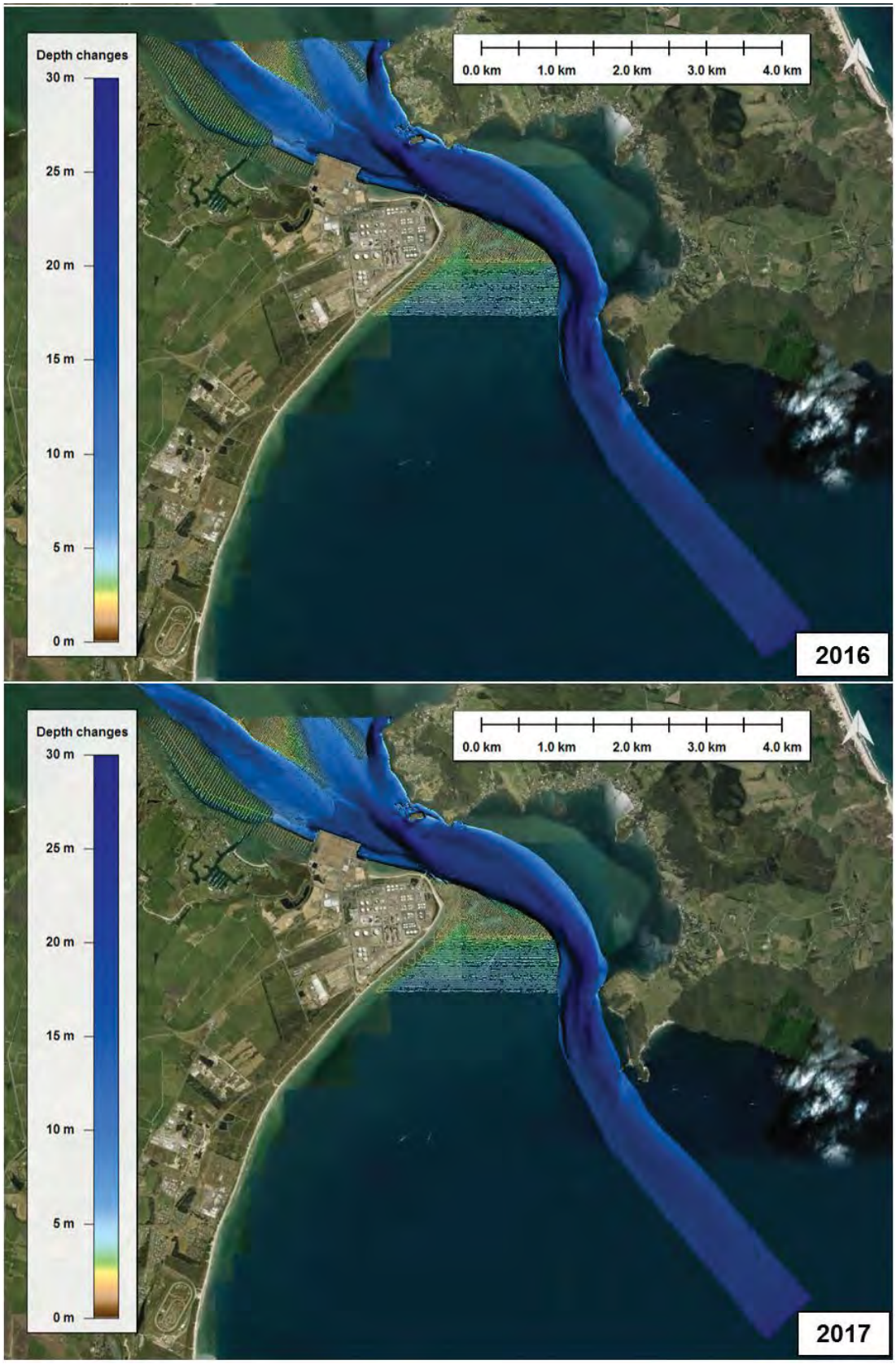

Figure 2.1 Bathymetric multi-beam survey data for 2016 and 2017 used to update the model bathymetry in the channel and at Northport for the setup and the calibration of the morphological model.

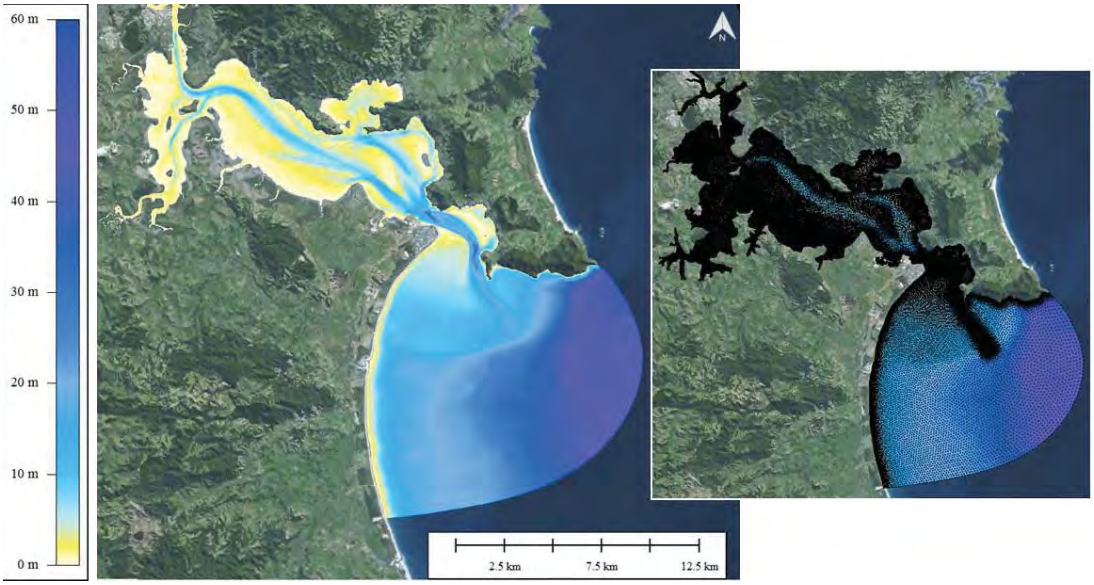

Figure 2.2 Model depth and mesh of the Whangarei Harbour and surrounds. Depths are given in metres below Mean Sea Level (MSL). The mesh covers the offshore region, including the ebb tidal delta, while salient bathymetric features are represented inside the harbour.

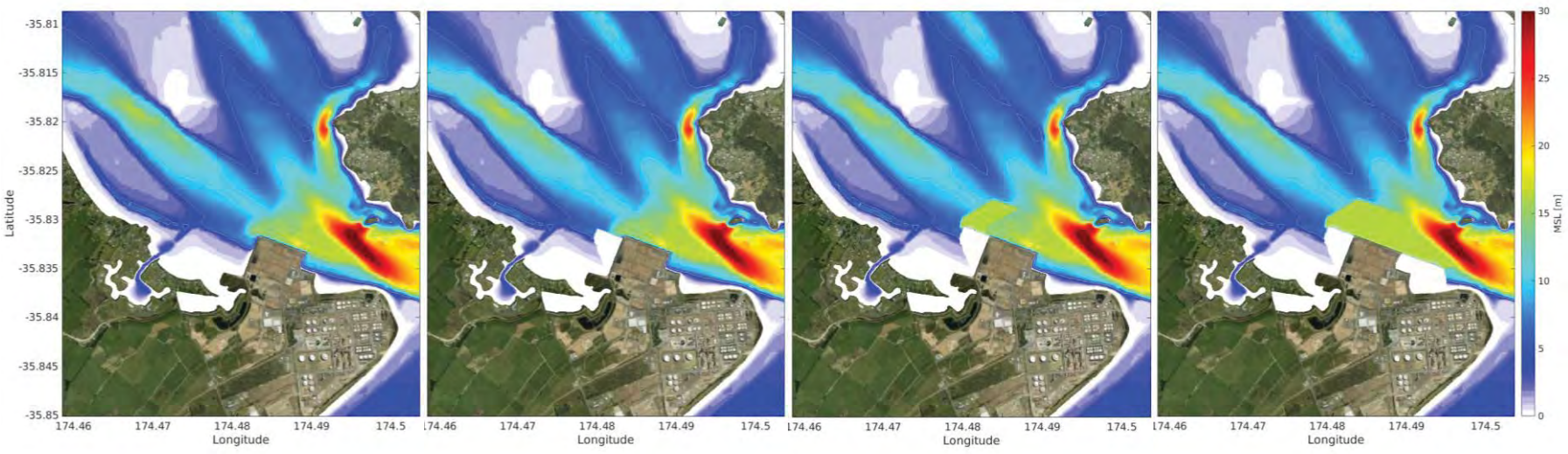

Figure 2.3 Bathymetry considering the Existing, Stage 1, Stage 2 and Stage 3 (from left to right) Northport harbour configuration. Reclaimed areas are depicted as white.

2.3. Open boundary conditions

A national New Zealand tidal solution derived from an implementation of the Princeton Ocean Model (POM) nested within the TPXO7.2 Pacific inverse tidal dataset (Egbert and Erofeeva, 2002) was used to prescribe the tidal elevation and current velocity at the boundaries of the grid. Depth dependant velocities along the offshore boundaries were defined using a standard logarithmic velocity profile. Using equation 2.2.13 in (Van Rijn, 1993), shown in equation 2.2 for the *u* component:

$$\tilde{u}(x,y,z,t) = \left[\frac{\bar{u}(x,y,t)}{z_0 / h - 1 + \ln(h / z_0)} \right] \ln\left(\frac{z}{z_0} \right) \tag{2.2}$$

where z is the particle elevation above the seabed, z_0 is the zero-velocity elevation (set here at 1 mm), h is the water-column height boundary node location (x,y), and $\bar{u}(x,y,t)$ is the depth-averaged horizontal current velocity at the boundary node location.

2.4. Model validation

Model calibration and validation was originally undertaken as part of the Whangarei Harbour study for Refining New Zealand, as detailed in MetOcean Solutions Ltd, (2017). The SELFE model was calibrated and validated against both measured current velocities (sampled using a vessel mounted ADCP) and water level measurements at 4 locations within the harbour.

Comparisons between the measured and predicted water levels (Figure 2.5 to Figure 2.8) indicate that the model reproduces the tidal water elevation variability within Whangarei Harbour well. The magnitude and timing of the tidal propagation throughout the harbour confirms both the suitability of the tidal boundary conditions as well as the ability of the model to replicate the hydrodynamics, which include the prescription of the bathymetry and the frictional parameterisation.

The validation of the depth-averaged flows indicates the model is able to replicate the complex tidal hydrodynamics within the Whangarei Harbour environs. Snapshots of the measured and modelled flows are presented in Figure 2.9 to Figure 2.11 for the peak tidal ebb and flood situation, and show good agreement, including in zones of high-flow. Quantile-Quantile plots of measured and modelled current velocities show a good correlation (Figure 2.12).

Additional validation of the hydrodynamic model has been undertaken against LINZ published tidal elevations at two locations within Whangarei Harbour (Figure 2.13). For both locations, the model is shown to capture the timing and elevation of the tidal stages (see Figure 2.14 and Figure 2.15).

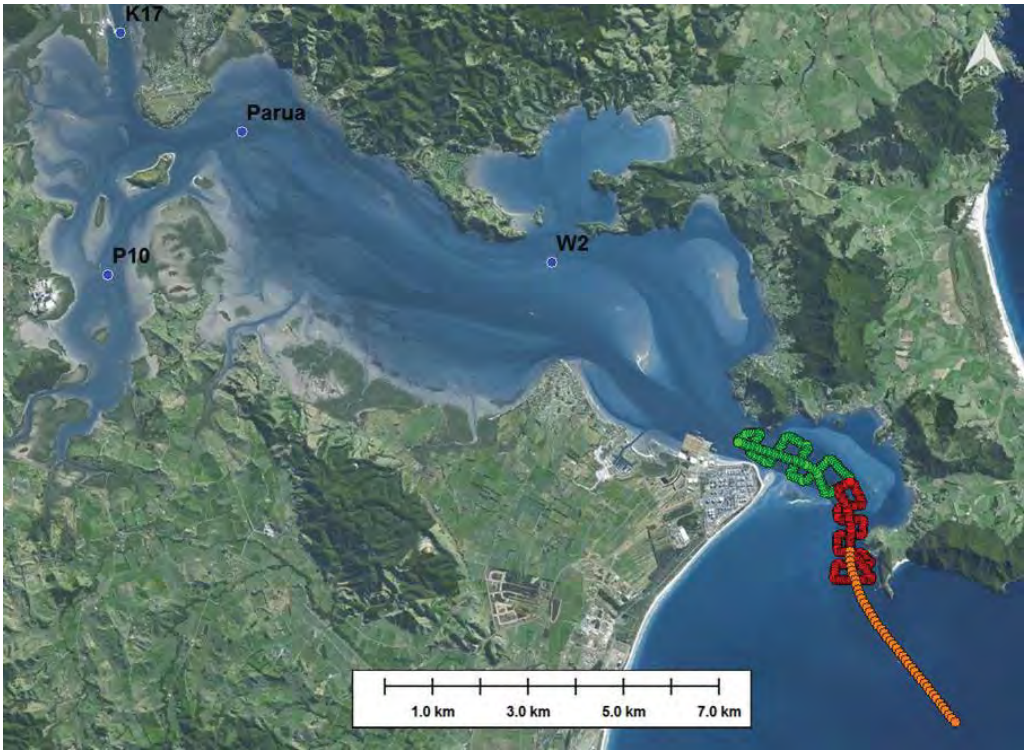

Figure 2.4 Locations of current velocity measurements (Zone A in green, B, in red and C in orange) and water level measurements (K17, P10, W2 and Parua) used to calibrate and validate the SELFE tidal model within Whangarei Harbour and Bream Bay.

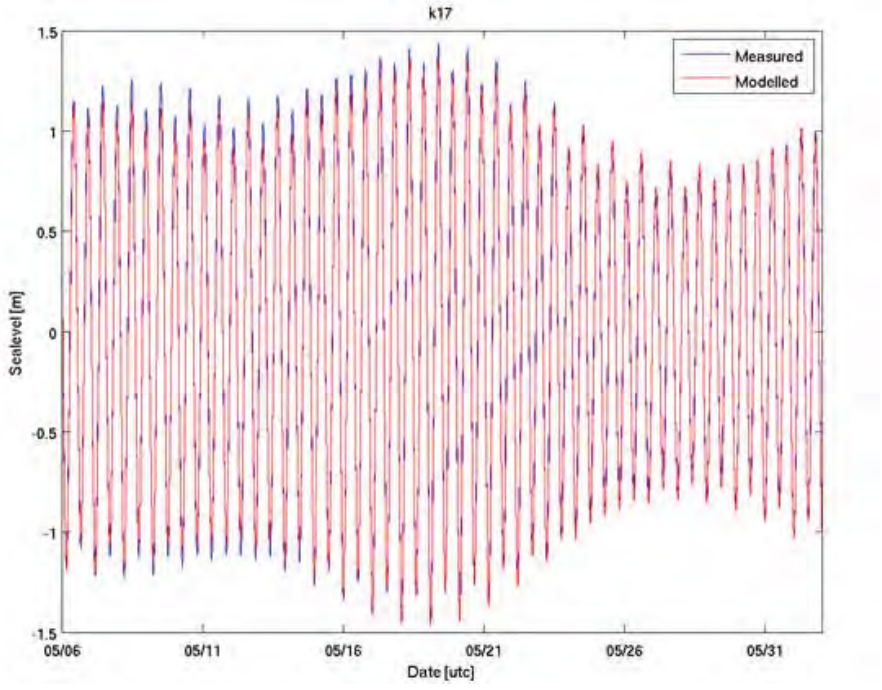

Figure 2.5 Measured and modelled water level comparisons at site k17.

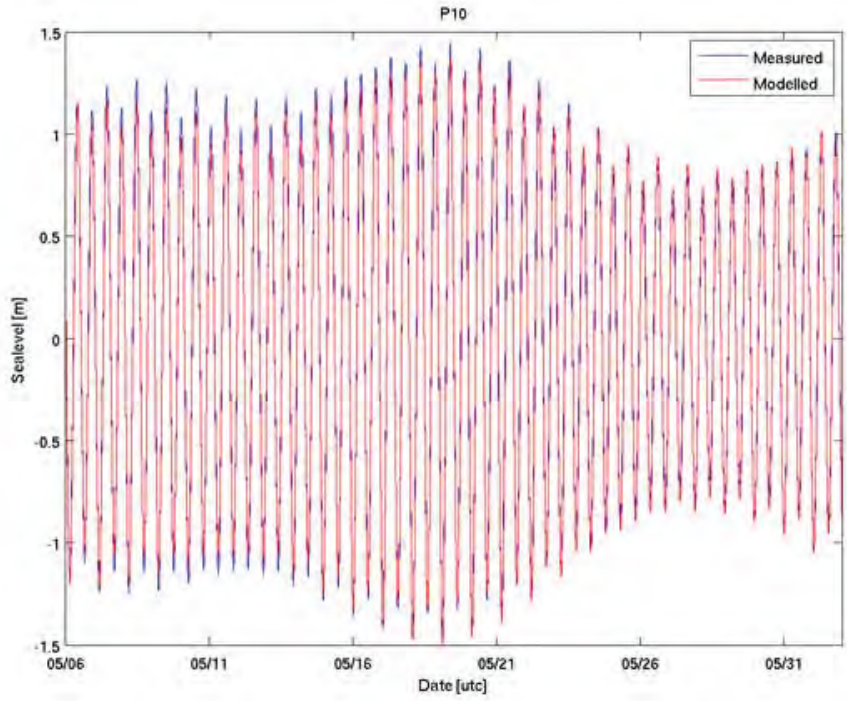

Figure 2.6 Measured and modelled water level comparisons at site p10.

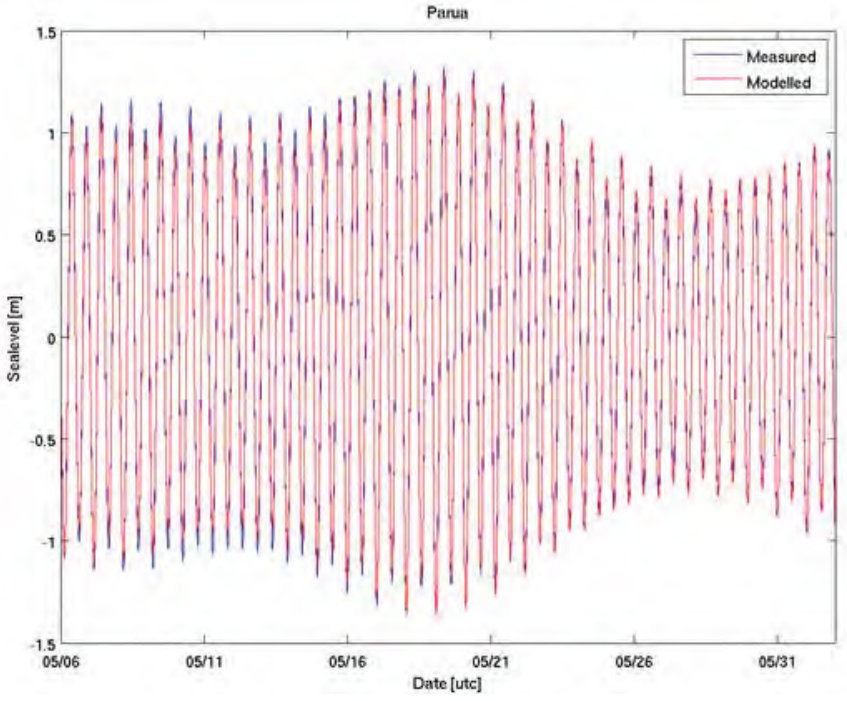

Figure 2.7 Measured and modelled water level comparisons at site Parua.

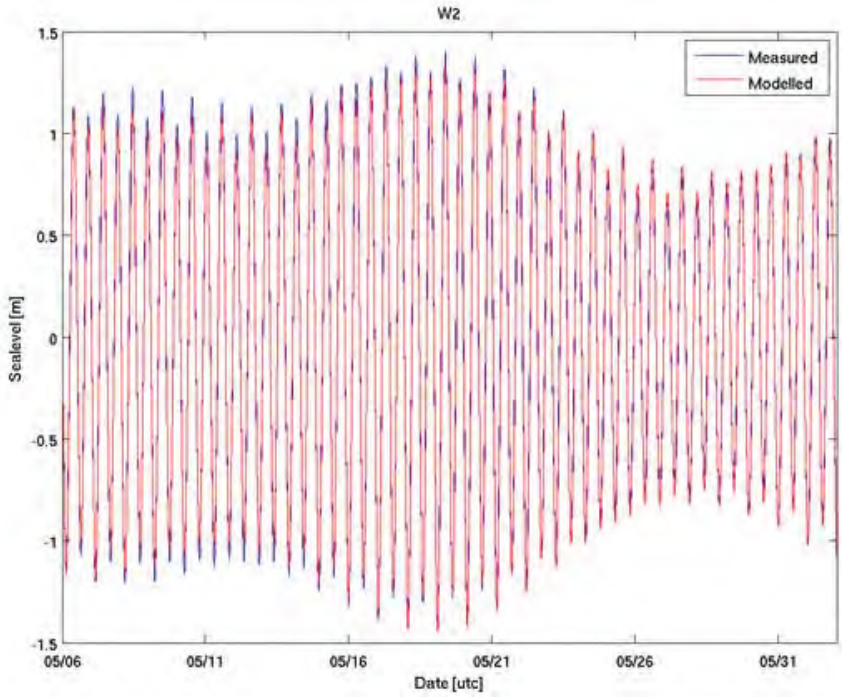

Figure 2.8 Measured and modelled water level comparisons at site W2.

Figure 2.9 Modelled (SELFE) and measured velocity comparisons within Zone A (Figure 2.4) for the peak ebb (upper) and flood (lower) tidal stages.

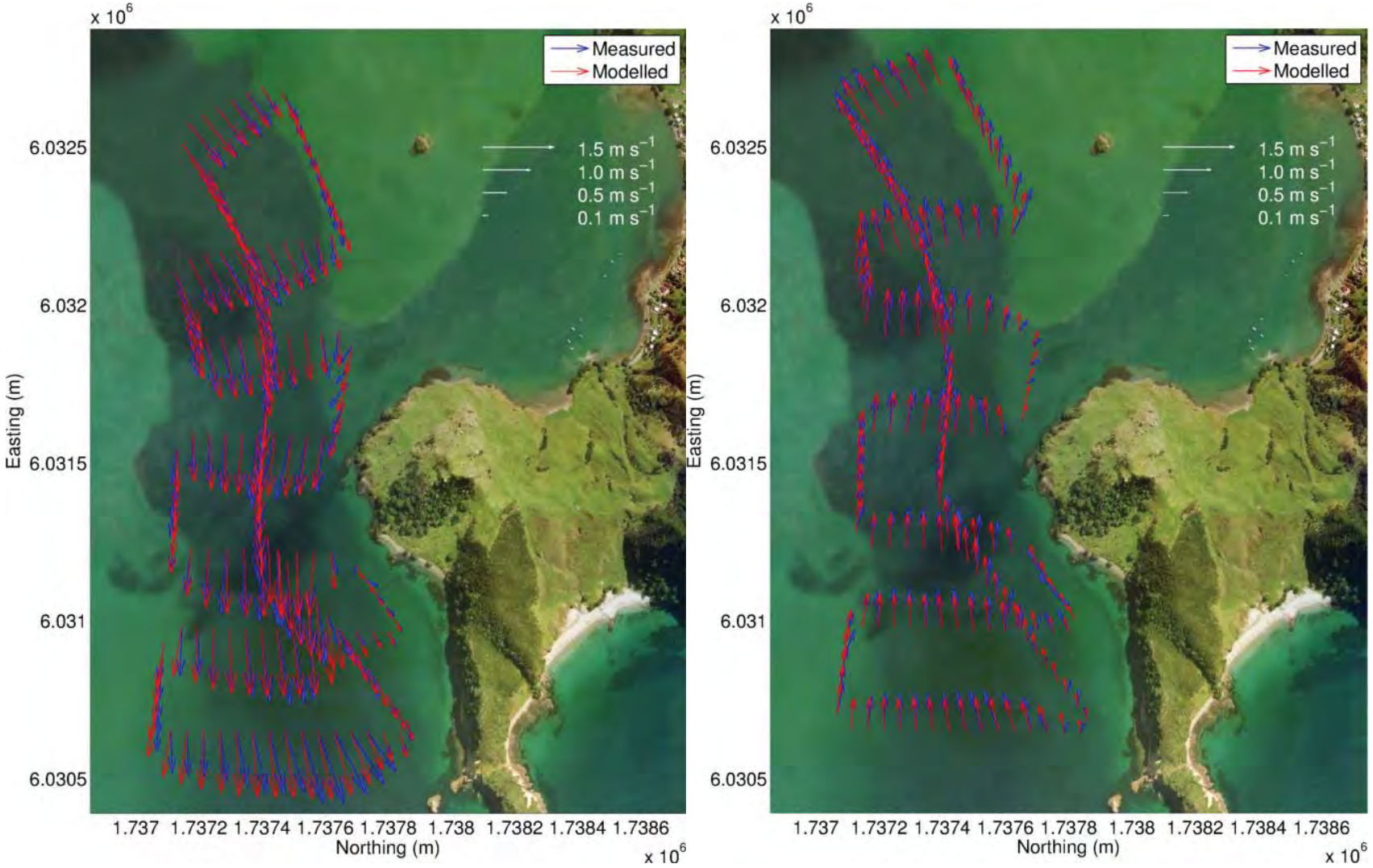

Figure 2.10 Modelled (SELFE) and measured velocity comparisons within Zone B (Figure 2.4) for the peak ebb (left) and flood (right) tidal stages.

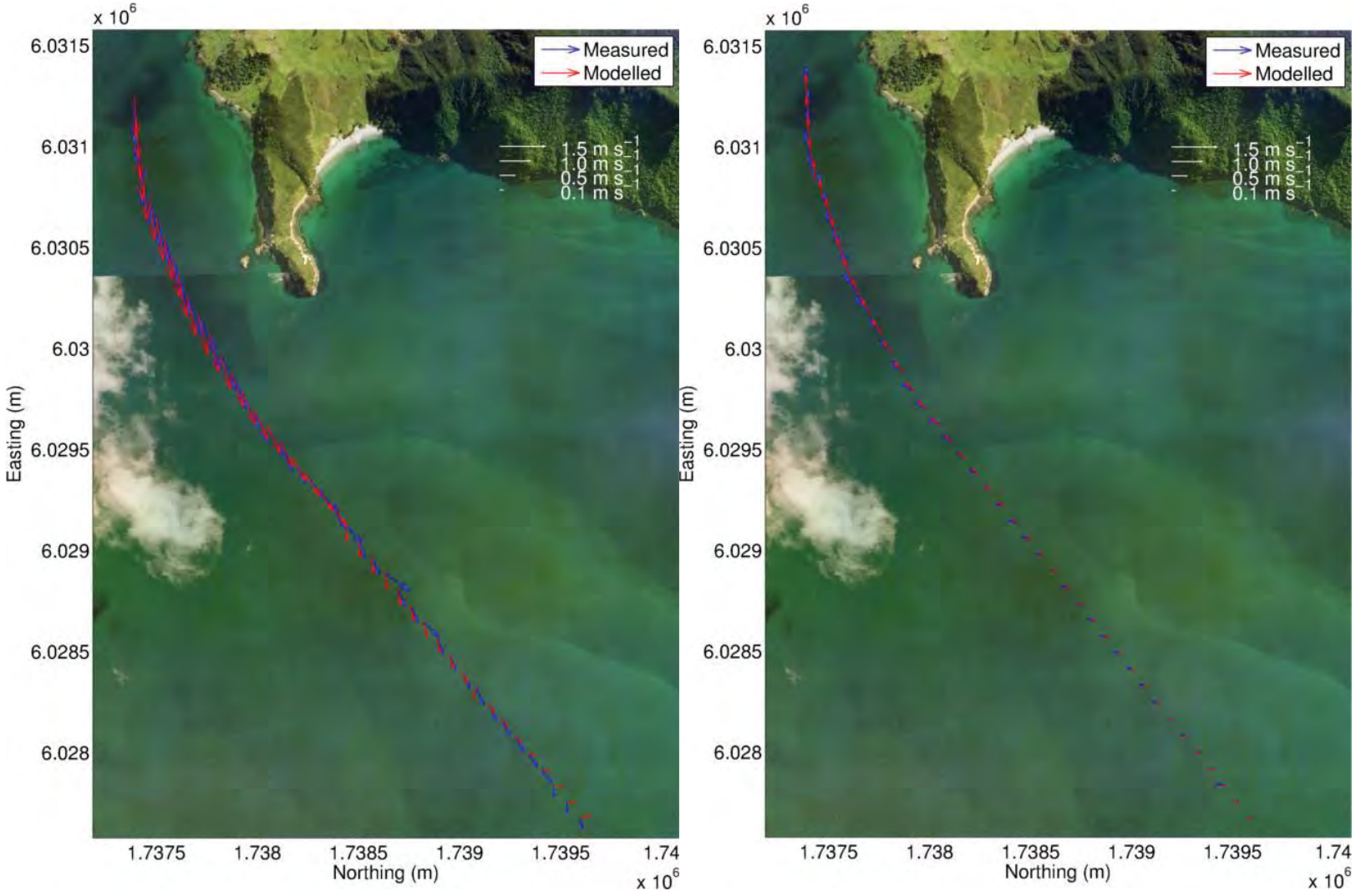

Figure 2.11 Modelled (SELFE) and measured velocity comparisons within Zone C (Figure 2.4) for the peak ebb (left) and flood (right) tidal stages.

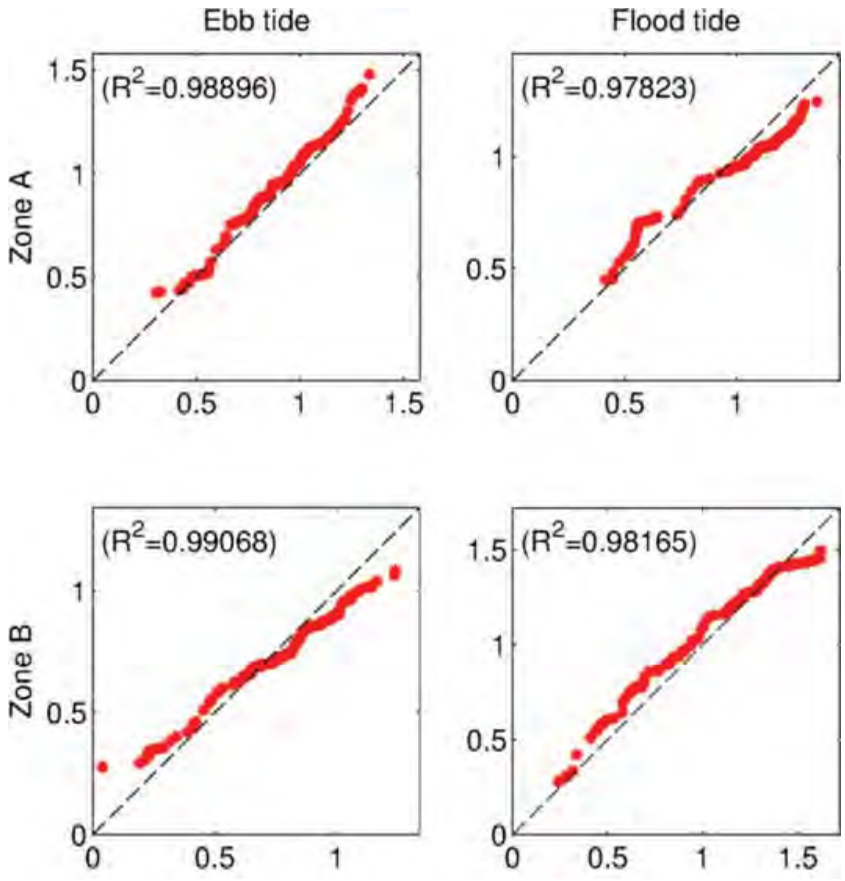

Figure 2.12 Quantile – Quantile plots of the measured and modelled (SELFE) peak tidal ebb and flood current speed (m/s) along the vessel tracks within zones A and B for both peak ebb and flood stages. The root mean squared errors corresponding to the different distributions are presented in the top-left corner of each plot.

Figure 2.13. Positions of LINZ sites used for model validation.

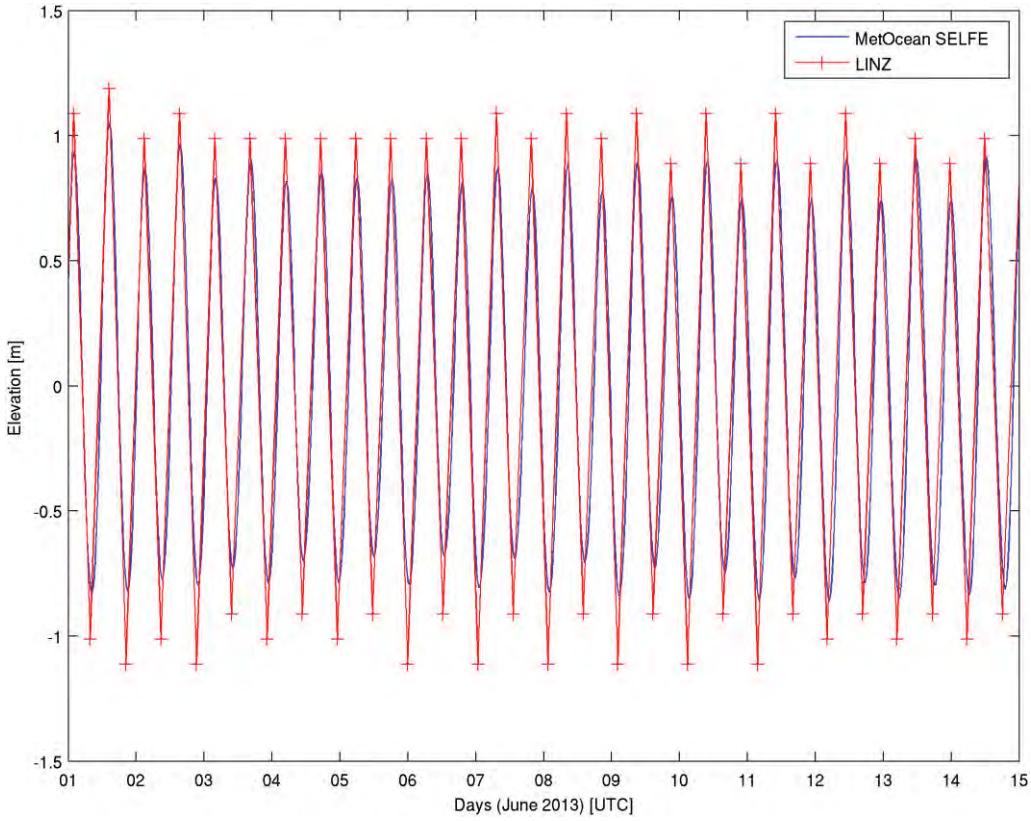

Figure 2.14. Comparison between modelled LINZ and MetOcean Solutions SELFE tidal elevation at Whangarei Harbour.

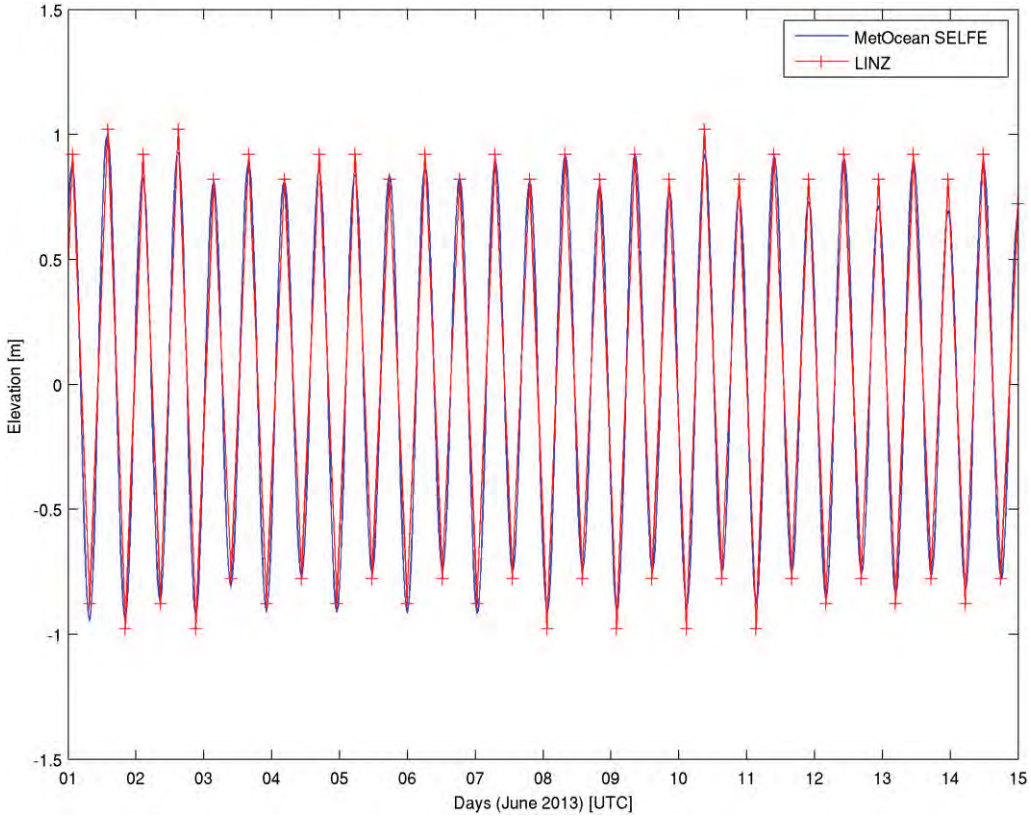

Figure 2.15. Comparison between modelled LINZ and MetOcean Solutions SELFE tidal elevation at Marsden point.

3. RESULTS

3.1. Existing hydrodynamics

Hydrodynamics of the existing harbour configuration are used to quantify the scale of expected changes to the hydrodynamics associated with the proposed reclamations and dredging.

Hydrodynamic conditions for the existing harbour configuration and the existing harbour configuration assuming the granting of the Refining New Zealand channel deepening are presented in Figure 3.1-Figure 3.4 for peak ebb and flood tidal stages under both spring and neap tidal ranges. Current velocities immediately around the port environment are provided in Figure 3.5 for both peak spring ebb and flood conditions, and illustrate the formation of eddies in both up and down stream of the port structures. Depth averaged velocity profiles across the harbour along the transect shown in Figure 3.6 for both ebb and flood tidal stages and under neap and spring tidal ranges are provided in Figure 3.7-Figure 3.8.

Only very slight differences are predicted between current velocities for the existing harbour configuration and the existing harbour configuration assuming the granting of the Refining New Zealand channel deepening. This is consistent with the findings of MetOcean Solutions Ltd, (2017).

The aspect of Whangarei Harbour channels results in the cross-channel characteristics of the current velocities in the vicinity of NorthPort varying between ebbing and flooding tidal stages.

During spring ebbing tidal stages, current velocities tend to be stronger adjacent to the port berths and within the swinging basin as the harbour drains through the main channel linking the harbour entrance to the inner Whangarei harbour. Conversely, during flooding tidal stages the fastest current velocities are situated on the north side of the harbour cross-section and aligned with the main entrance channel (Figure 3.1, Figure 3.3 and Figure 3.8).

Adjacent to the port berths current velocities are expected to peak ~1.0 $m.s^{-1}$ during spring ebbing tides and ~0.8 $m.s^{-1}$ during spring flooding tides (Figure 3.1 and Figure 3.3 respectively). Current velocities during neap flood and ebb tidal conditions are of the order 0.5 $m.s^{-1}$ adjacent to the port berths, compared to approximately 0.6 $m.s^{-1}$ on the north side of the harbour adjacent to Motukaroro Island (Figure 1.1) during flooding neap tides (Figure 3.2, Figure 3.4 and Figure 3.7).

Mean residual spring tide current velocities for the existing harbour configuration are given in Figure 3.9. Areas of low or diverging residual current velocities highlight areas of potential sediment accretion.

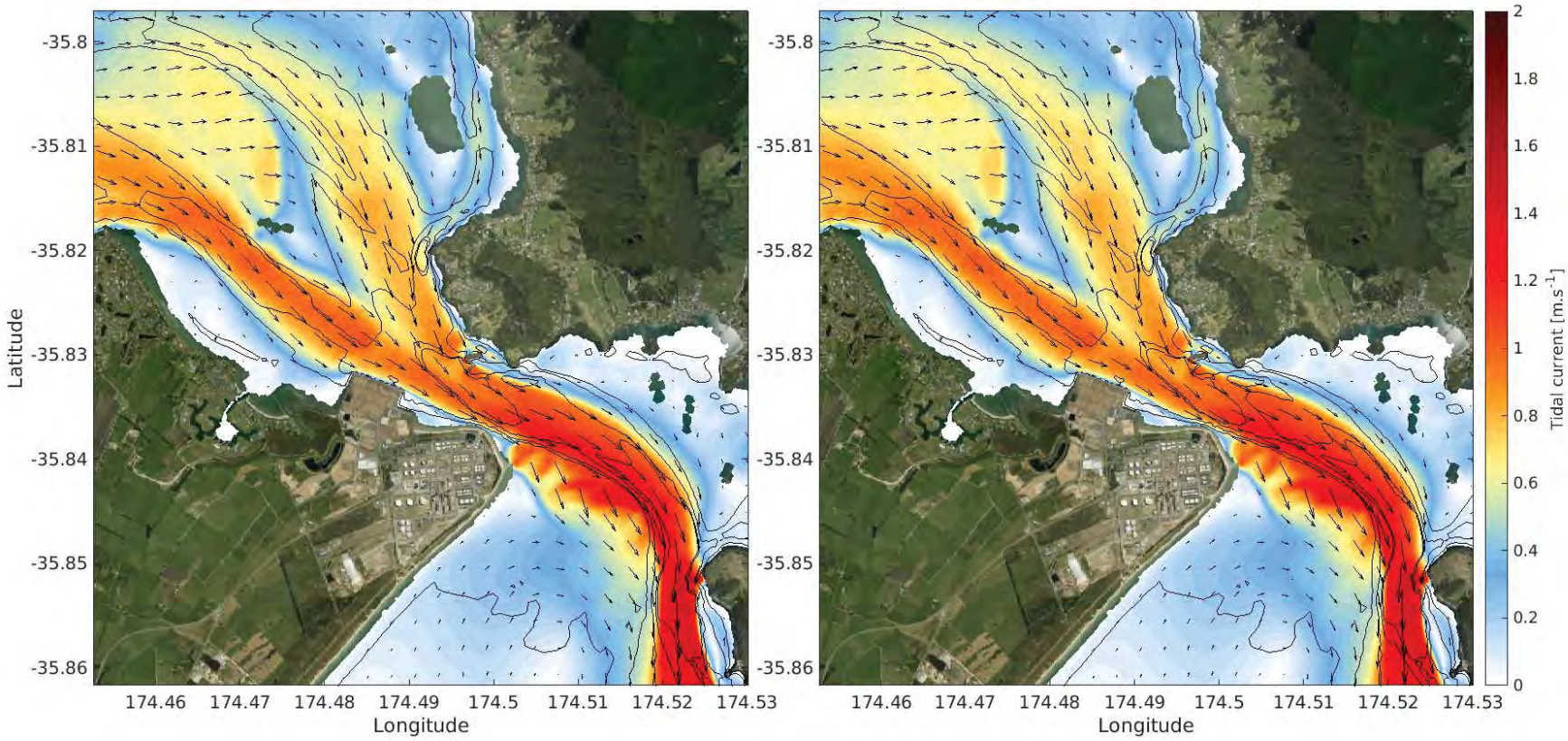

Figure 3.1 Modelled peak ebb flows during spring tide in the vicinity of Northport and Whangarei Harbour entrance for the existing harbour configuration (right) and the existing harbour configuration assuming channel deepening as per the RNZ consent (left).

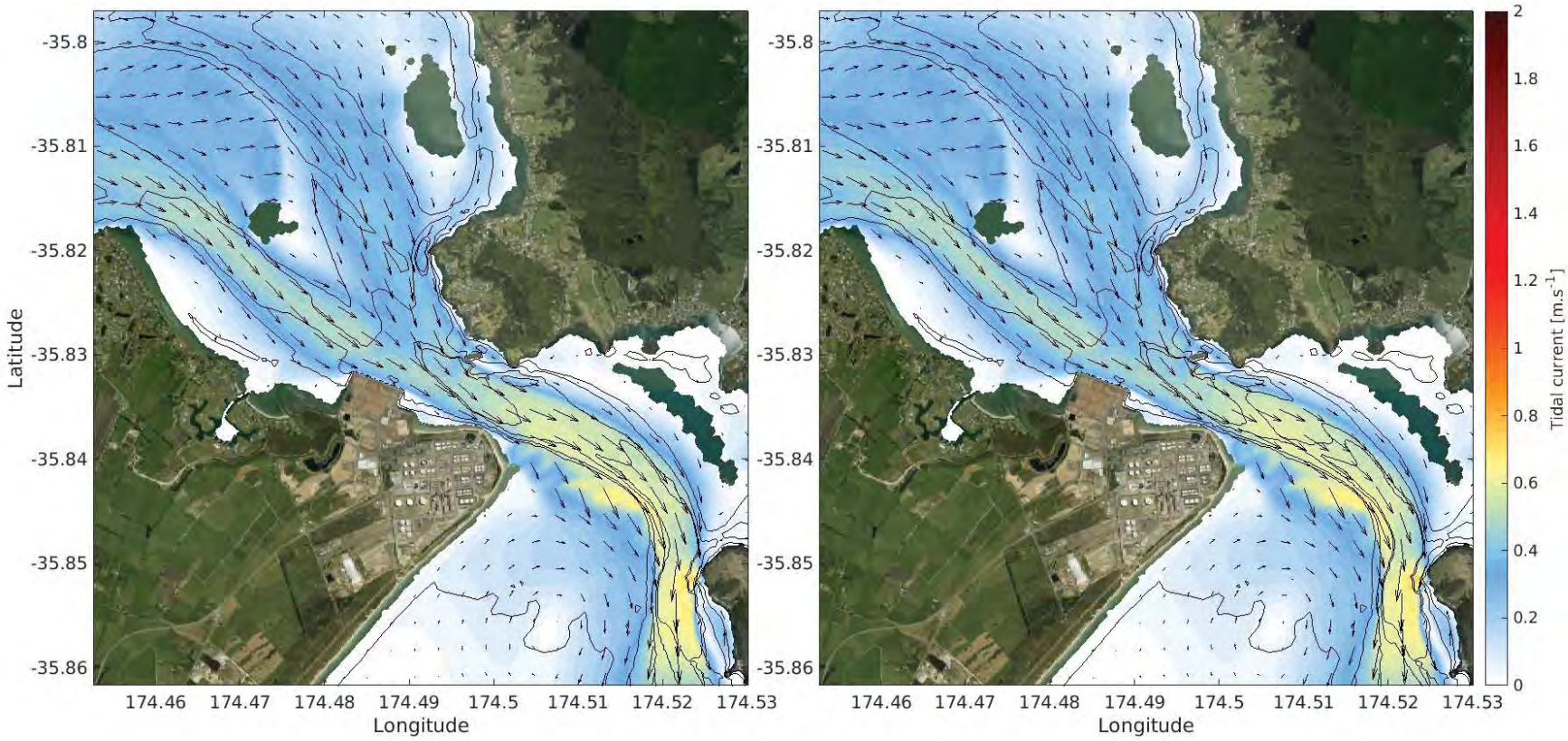

Figure 3.2 Modelled peak ebb flows during neap tide in the vicinity of Northport and Whangarei Harbour entrance for the existing harbour configuration (right) and the existing harbour configuration assuming channel deepening as per the RNZ consent (left).

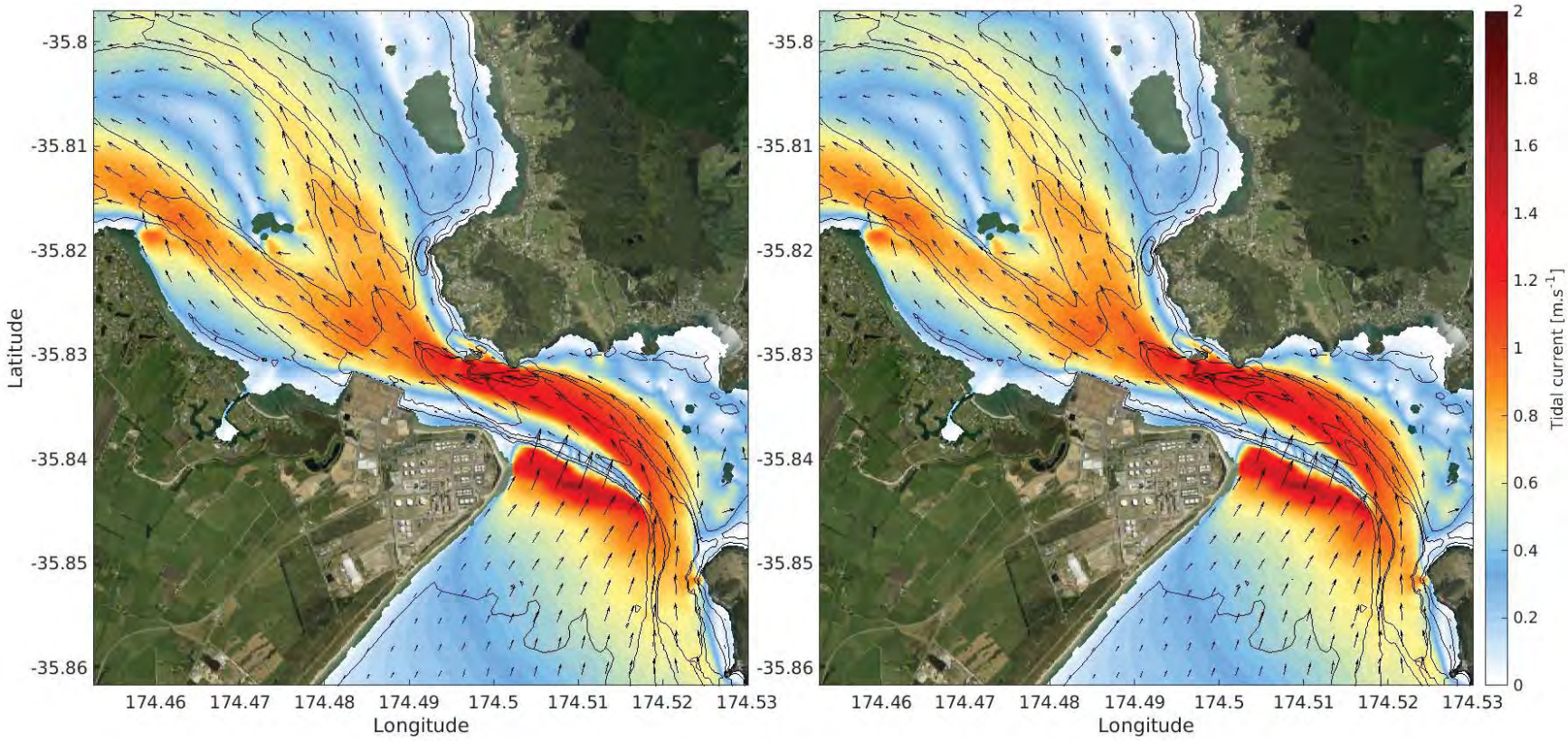

Figure 3.3 Modelled peak flood flows during spring tide in the vicinity of Northport and Whangarei Harbour entrance for the existing harbour configuration (right) and the existing harbour configuration assuming channel deepening as per the RNZ consent (left).

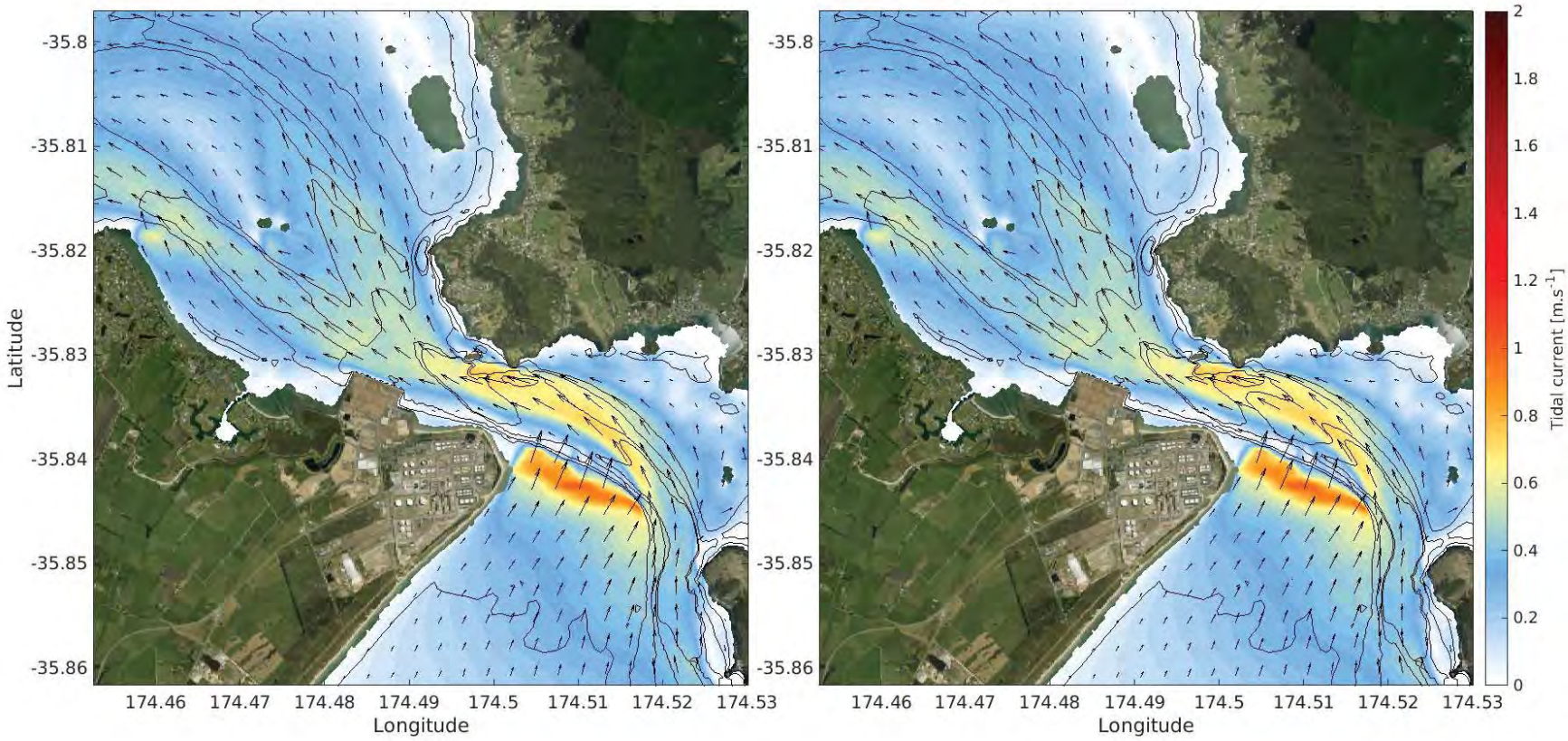

Figure 3.4 Modelled peak flood flows during neap tide in the vicinity of Northport and Whangarei Harbour entrance for the existing harbour configuration (right) and the existing harbour configuration assuming channel deepening as per the RNZ consent (left).

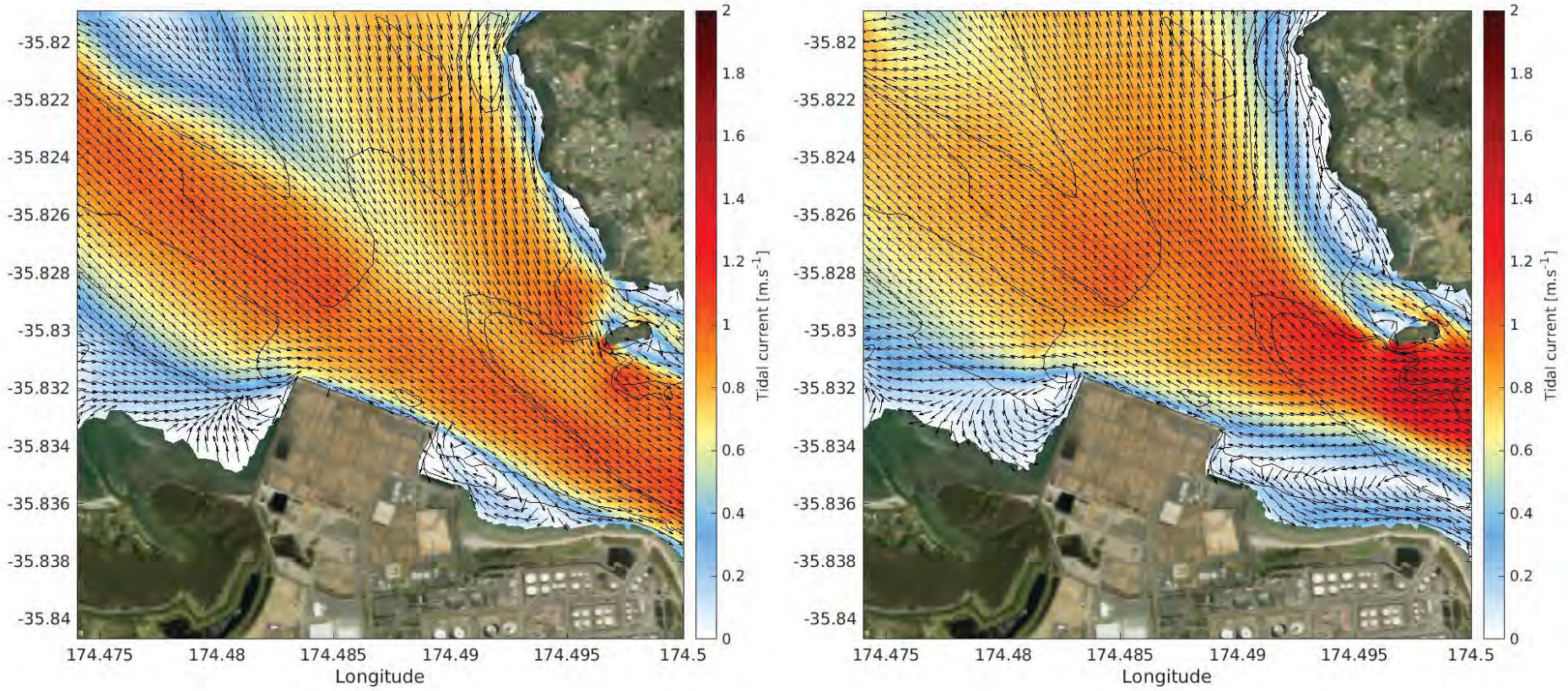

Figure 3.5 Modelled peak ebb (left) and flood (right) flows in the port environs showing formation of back eddies in the lee of the port structures both up and down stream.

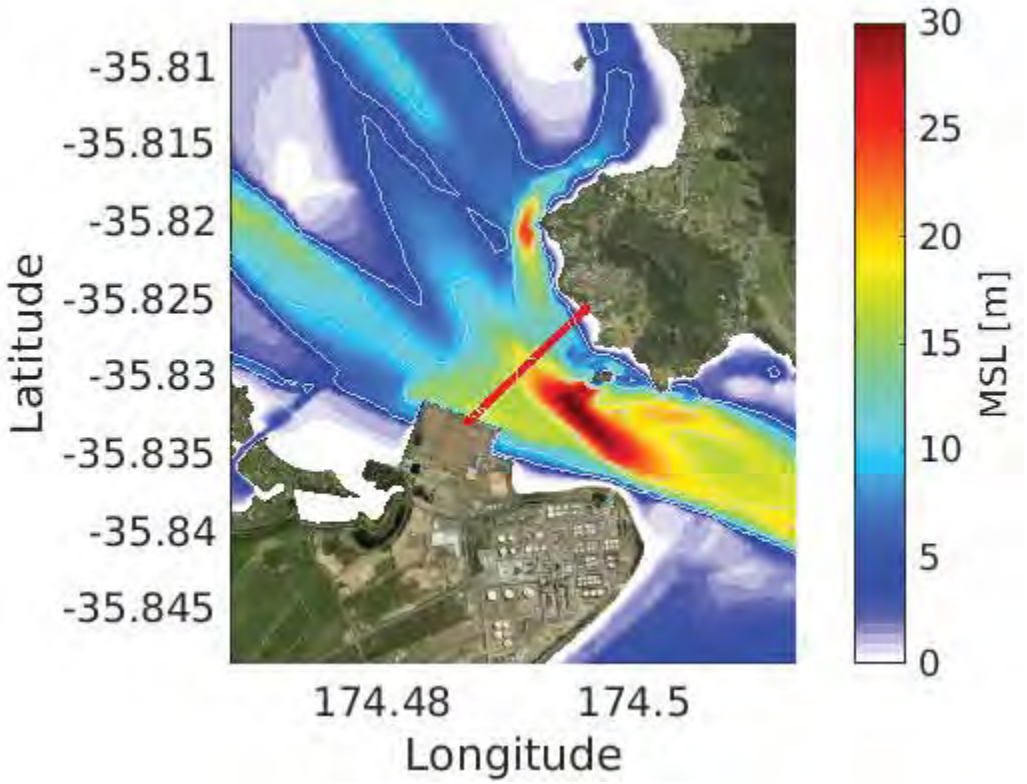

Figure 3.6 Model bathymetry in the vicinity of NorthPort, showing the transect location from which velocity transect data has been extracted.

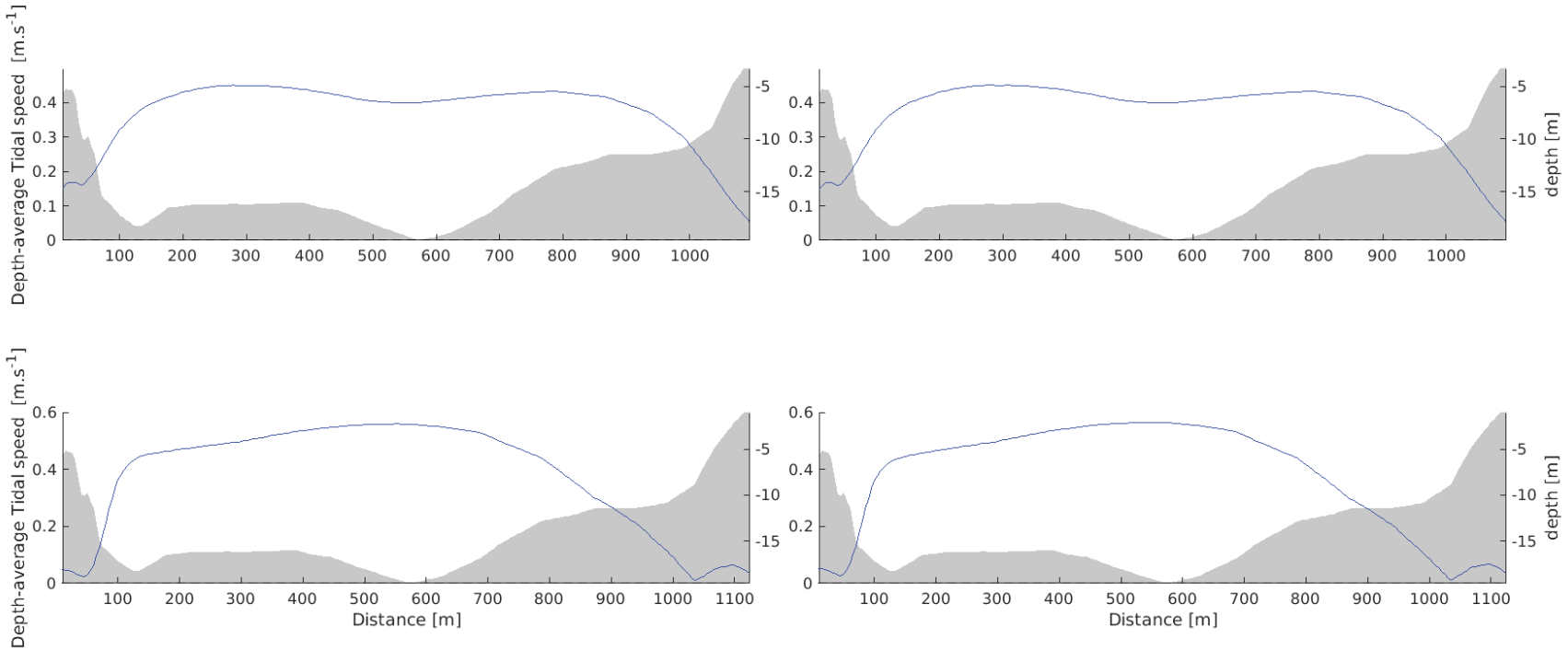

Figure 3.7 Depth averaged current velocity (blue) transects for neap ebb (top) and flood (bottom) tides for the existing bathymetry (left) and the existing bathymetry inclusive of the proposed Refining New Zealand channel deepening (right)

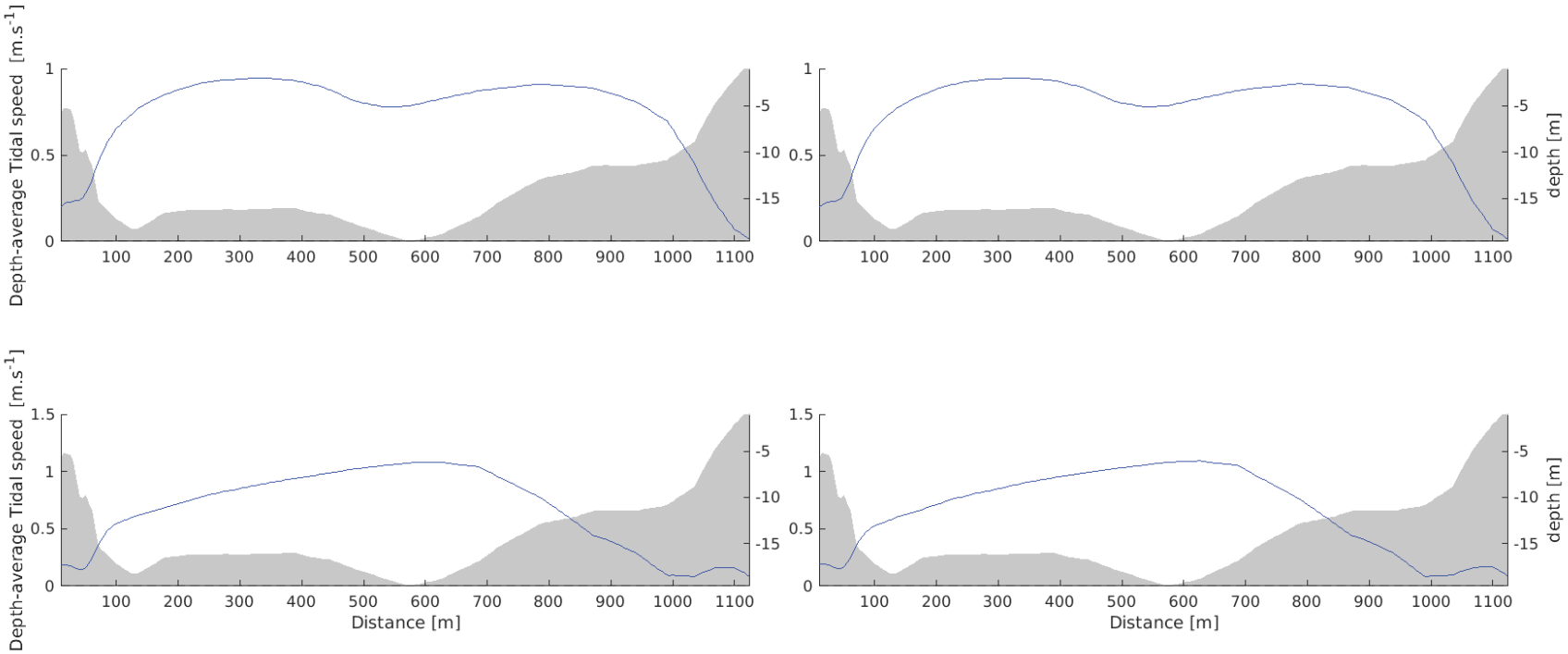

Figure 3.8 Depth averaged current velocity (blue) transects for spring ebb (top) and flood (bottom) tides for the existing bathymetry (left) and the existing bathymetry inclusive of the proposed Refining New Zealand channel deepening (right)

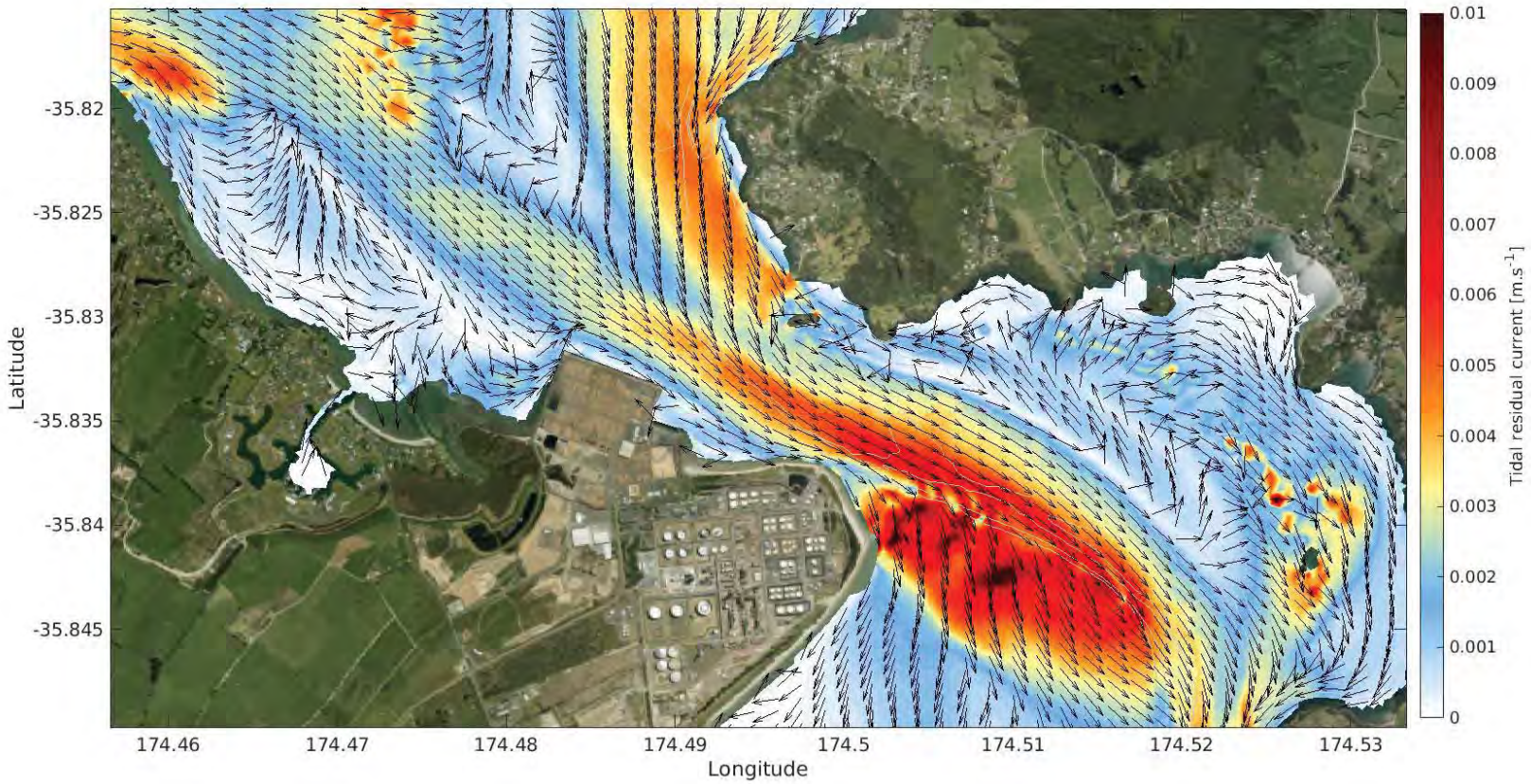

Figure 3.9 Spring tide mean residual tidal current velocity determined over one complete tidal cycle for the existing harbour configuration.

3.2. Stage 1 hydrodynamics

Stage 1 of the proposed port development consists of reclaiming Area 6, less 50m along northern edge as shown in Figure 1.2 and Figure 2.3.

Hydrodynamic conditions for the Stage 1 harbour configuration and the Stage 1 harbour configuration assuming the granting of the Refining New Zealand channel deepening are presented in Figure 3.10-Figure 3.13 for peak ebb and flood tidal stages under both spring and neap tidal ranges. Current velocities immediately around the port environment are provided in Figure 3.14 for both peak spring ebb and flood conditions, and illustrate the formation of eddies in both up and down stream of the port structures, including the Stage 1 proposed reclamation area. Depth averaged velocity profiles across the harbour along the transect shown in Figure 3.6 for both ebb and flood tidal stages and under neap and spring tidal ranges are provided in Figure 3.15-Figure 3.16.

Only very slight differences are predicted between current velocities for the Stage 1 harbour configuration and the Stage 1 harbour configuration assuming the granting of the Refining New Zealand channel deepening.

As with the existing harbour configuration, the aspect of Whangarei Harbour results in the cross-channel characteristics of the current velocities in the vicinity of NorthPort varying between ebbing and flooding tidal stages.

During spring ebbing tidal stages, current velocities tend to be stronger adjacent to the port berths and within the swinging basin as the harbour drains through the main channel linking the harbour entrance to the inner Whangarei harbour. Conversely, during flooding tidal stages the fastest current velocities are situated on the north side of the harbour cross-section and aligned with the main entrance channel (Figure 3.10, Figure 3.12 and Figure 3.16).

Adjacent to the port berths current velocities are expected to peak ~1.0 $m.s^{-1}$ during spring ebbing tides and ~0.8 $m.s^{-1}$ during spring flooding tides (Figure 3.10 and Figure 3.12 respectively). Current velocities during neap flood and ebb tidal conditions are of the order 0.5 $m.s^{-1}$ adjacent to the port berths, compared to approximately 0.6 $m.s^{-1}$ on the north side of the harbour adjacent to Motukaroro Island (Figure 1.1) during flooding neap tides (Figure 3.11, Figure 3.13 and Figure 3.15).

Mean residual spring tide current velocities for the existing and Stage 1 harbour configurations are given in Figure 3.17. Areas of low or diverging residual current velocities highlight areas of potential sediment accretion. Mean residual current velocities directed towards the port are expected to increase to the east of the reclamation within the main channel, while slightly stronger SE directed residual currents are also expected along Marsden Bay. Reduced tidal residuals are expected within the lee of the proposed reclamation.

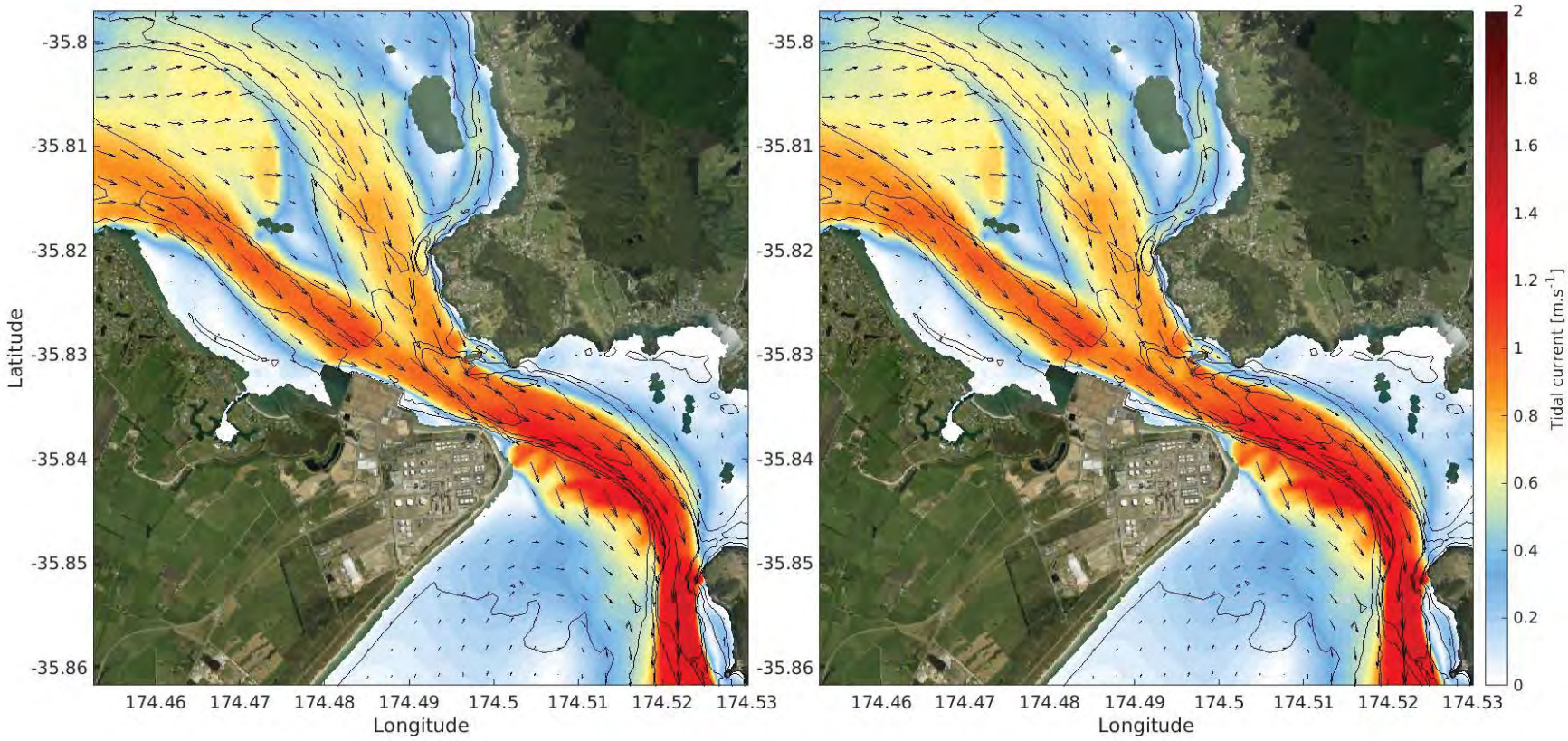

Figure 3.10 Modelled peak ebb flows during spring tide in the vicinity of Northport and Whangarei Harbour entrance for the Stage 1 harbour configuration (right) and the Stage 1 configuration assuming channel deepening as per the RNZ consent (left).

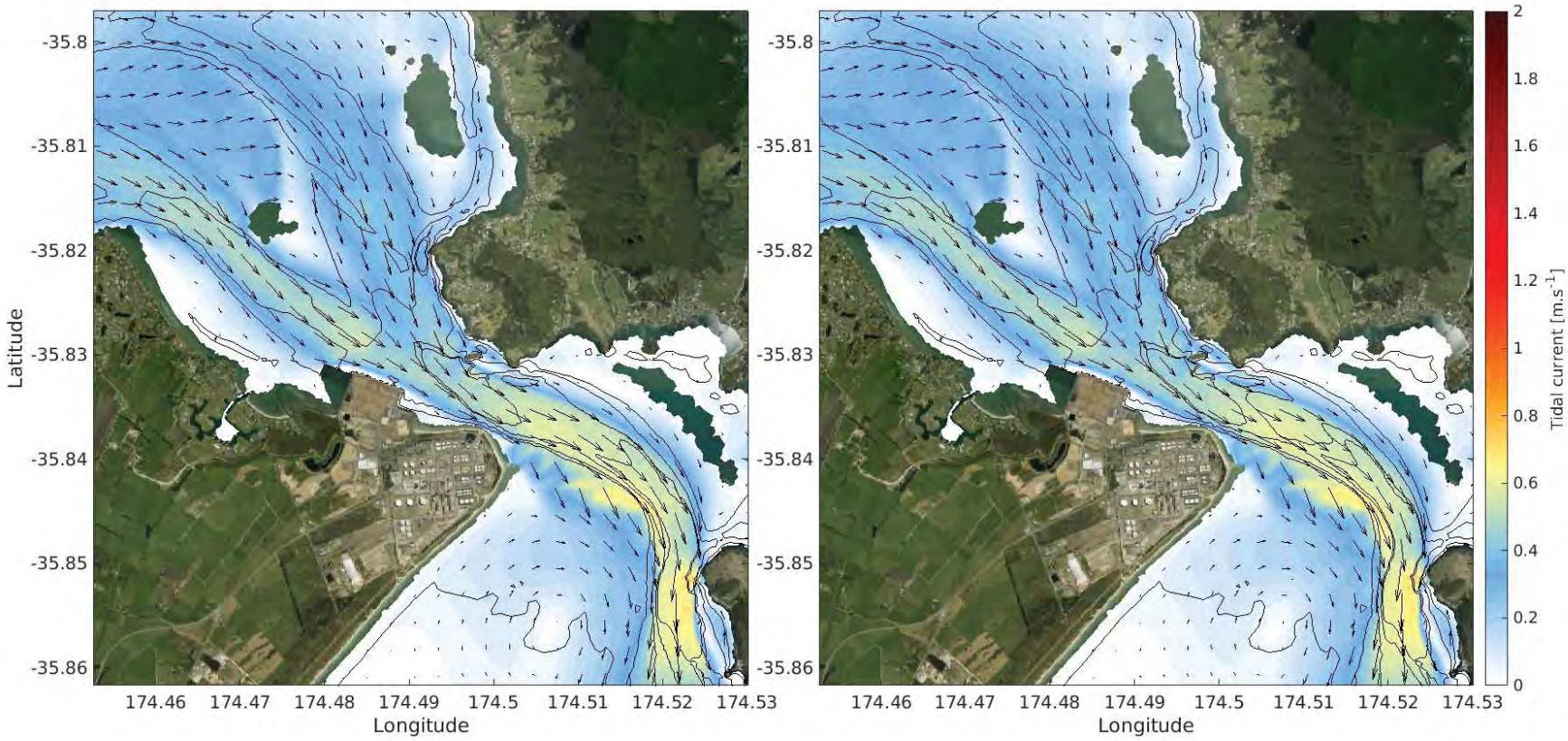

Figure 3.11 Modelled peak ebb flows during neap tide in the vicinity of Northport and Whangarei Harbour entrance for the Stage 1 harbour configuration (right) and the Stage 1 configuration assuming channel deepening as per the RNZ consent (left).

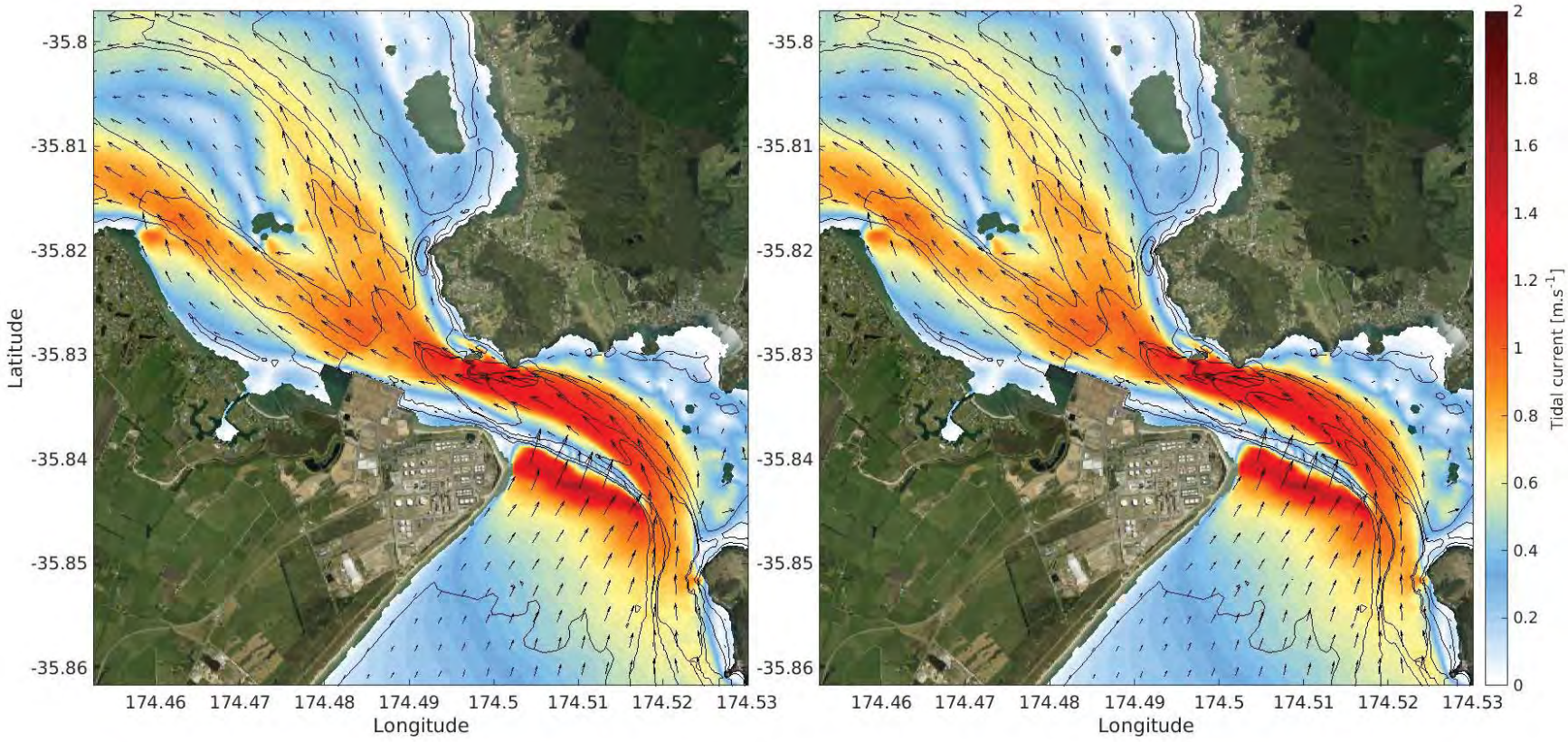

Figure 3.12 Modelled peak flood flows during spring tide in the vicinity of Northport and Whangarei Harbour entrance for the Stage 1 harbour configuration (right) and the Stage 1 configuration assuming channel deepening as per the RNZ consent (left).

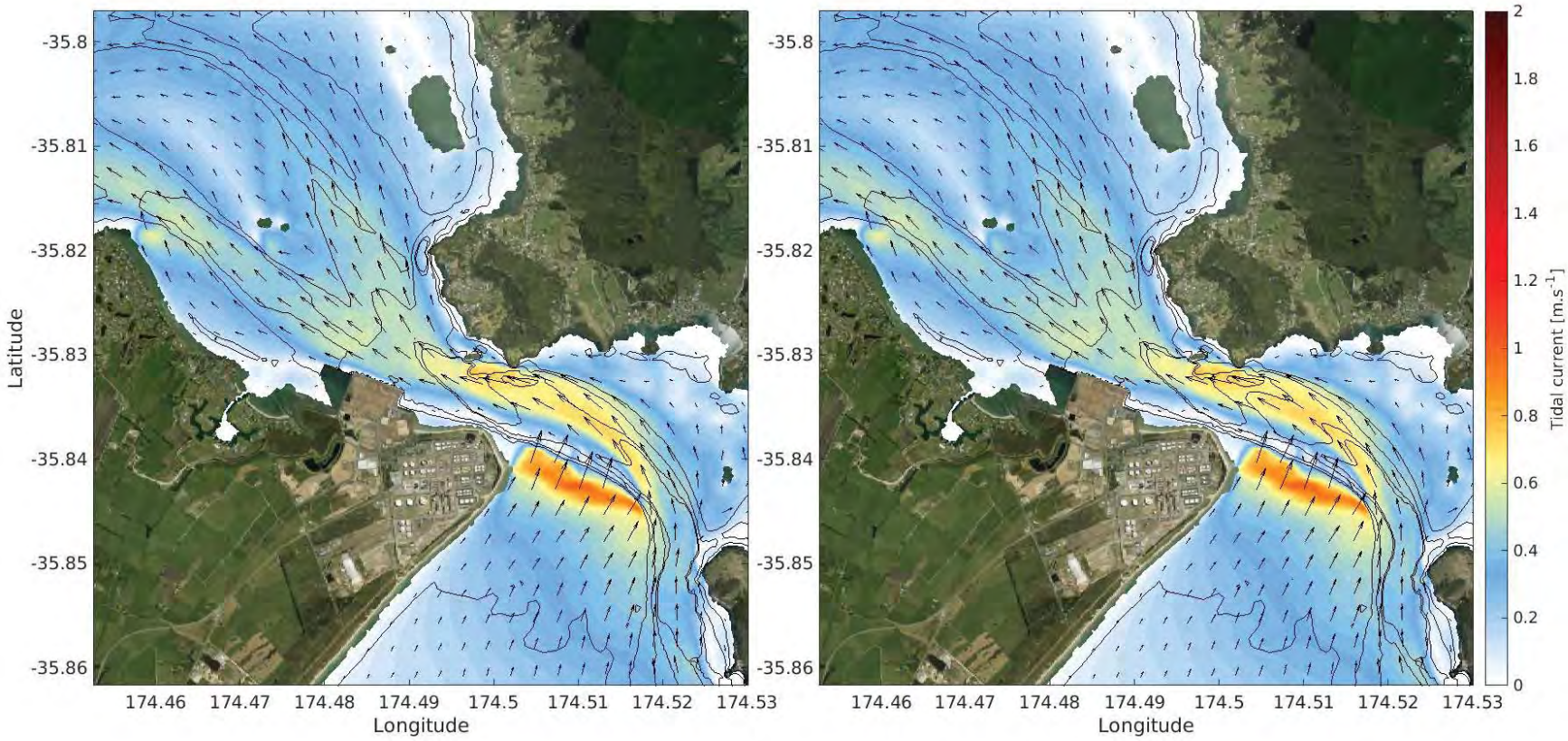

Figure 3.13 Modelled peak flood flows during neap tide in the vicinity of Northport and Whangarei Harbour entrance for the Stage 1 harbour configuration (right) and the Stage 1 configuration assuming channel deepening as per the RNZ consent (left).

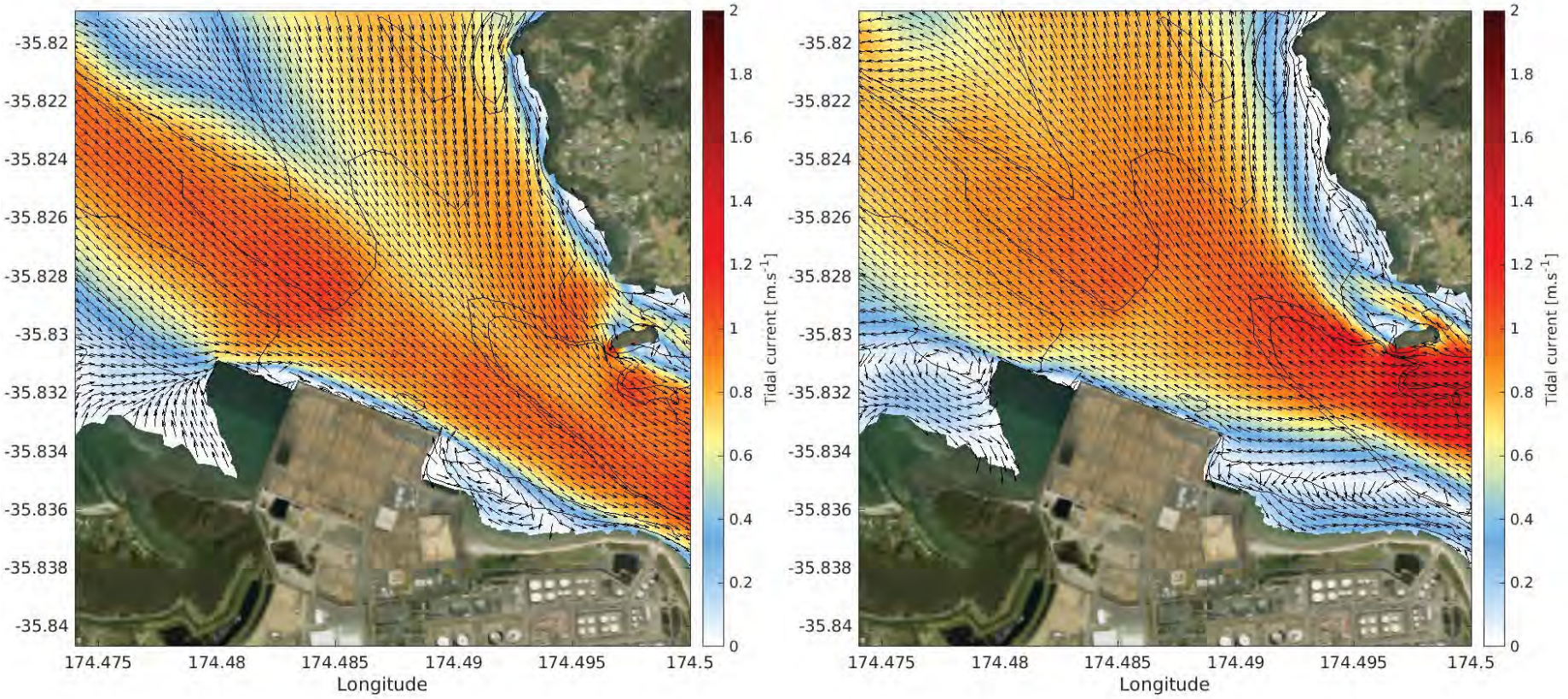

Figure 3.14 Modelled peak ebb (left) and flood (right) flows in the port environs showing formation of back eddies in the lee of the port structures both up and down stream for the Stage 1 bathymetry.

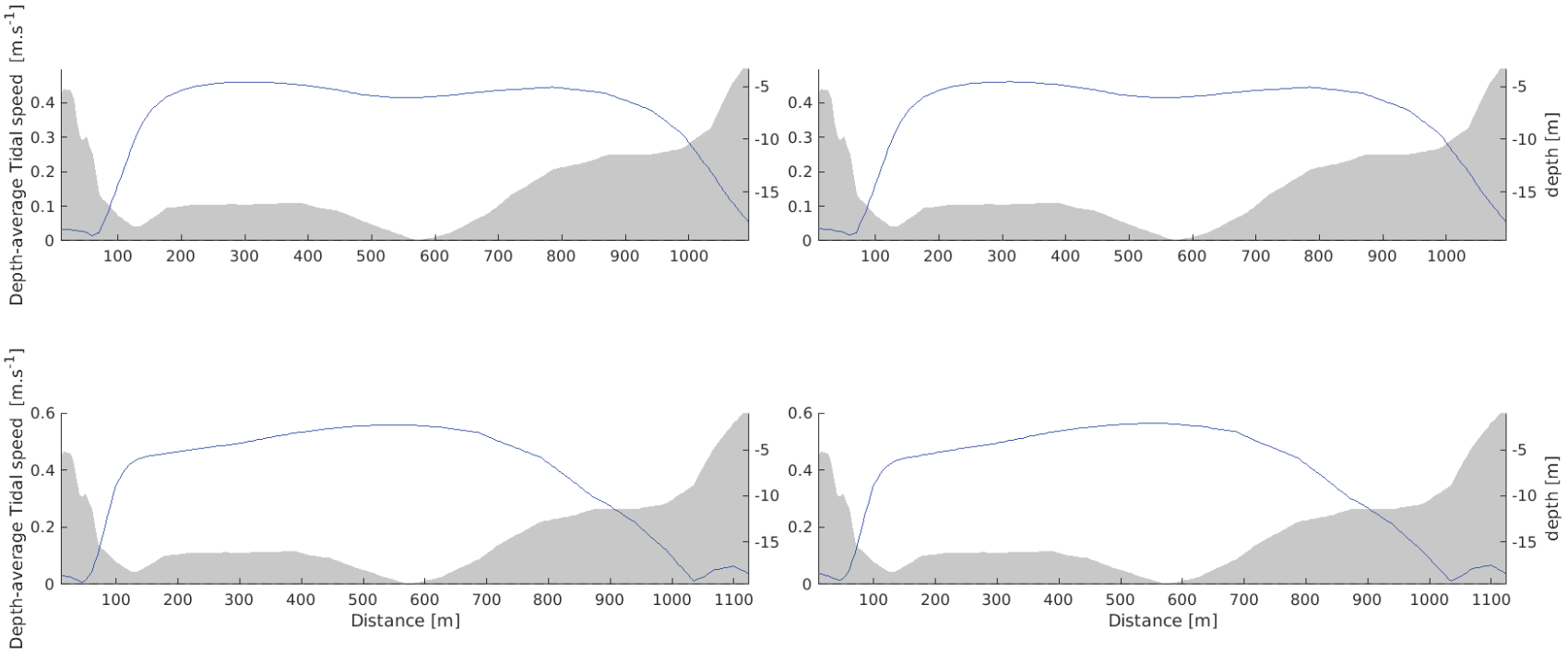

Figure 3.15 Depth averaged current velocity (blue) transects for neap ebb (top) and flood (bottom) tides for the Stage 1 bathymetry (left) and the Stage 1bathymetry inclusive of the proposed Refining New Zealand channel deepening (right)

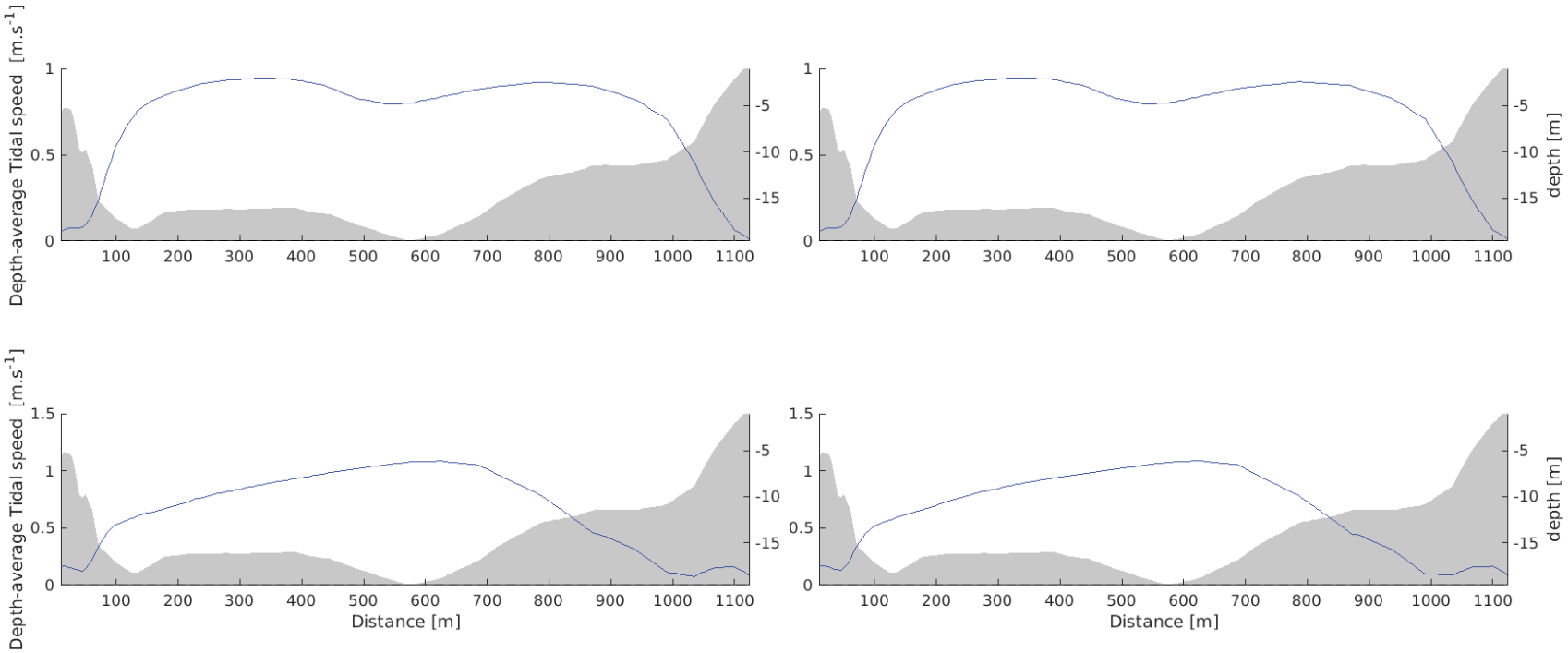

Figure 3.16 Depth averaged current velocity (blue) transects for spring ebb (top) and flood (bottom) tides for the Stage 1 bathymetry (left) and the Stage 1 bathymetry inclusive of the proposed Refining New Zealand channel deepening (right)

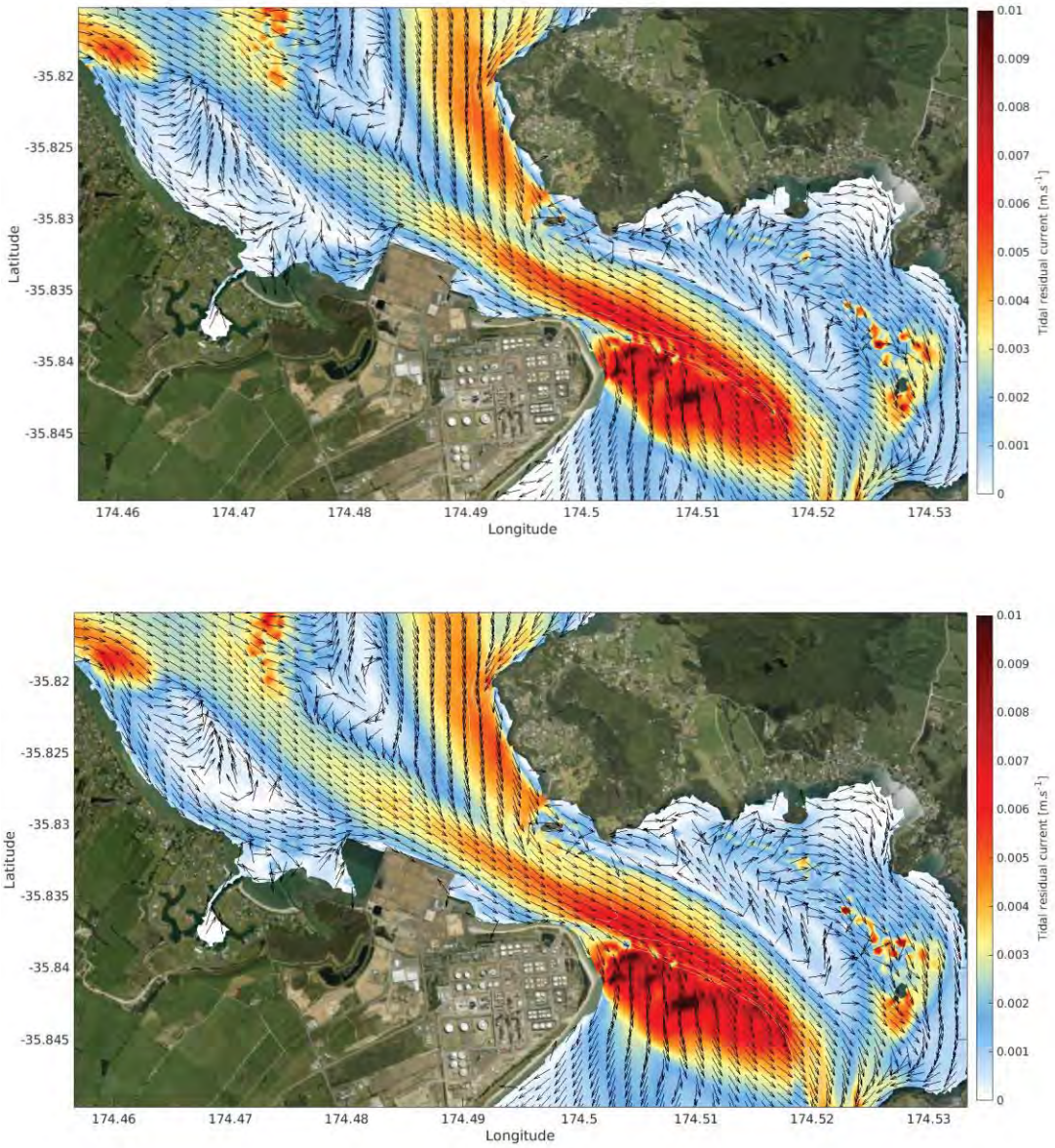

Figure 3.17 Spring tide mean residual tidal current velocity determined over one complete tidal cycle for the existing harbour configuration (top) and Stage 1 bathymetry (bottom).

3.2.1. Stage 1 effect on tidal hydrodynamics

The absolute and relative (i.e. percentage difference) between the existing and Stage 1 hydrodynamics under ebbing and flooding tidal stages for a worst-case spring tidal range are provided in Figure 3.18-Figure 3.19. Absolute and relative differences during neap tidal stages are comparatively smaller than during spring tides. Comparisons are made between the existing harbour configuration and the Stage 1 harbour configuration, and between the existing harbour and the Stage 1 harbour configuration assuming the granting of the Refining New Zealand channel deepening. Depth averaged velocity profiles across the harbour along the transect shown in Figure 3.6 for both ebb and flood tidal stages and under neap and spring tidal ranges are provided in Figure 3.20-Figure 3.21.

Only very slight differences are predicted between current velocities for the Stage 1 harbour configuration and the Stage 1 harbour configuration assuming the granting of the Refining New Zealand channel deepening. Further, similar spatial extents, but greater relative effects are observed during spring tidal conditions as opposed to neap tidal conditions (Figure 3.18-Figure 3.19 and Figure 3.20-Figure 3.21), and as such are discussed below.

During peak ebb spring tidal conditions current velocities immediately adjacent to the port berths are expected to decrease by as much as ~0.15 $m.s^{-1}$, while current velocities further north within the main channel and adjacent to Reotahi Bay (Figure 1.1) are expected to slightly increase (of the order 0.01 $m.s^{-1}$, Figure 3.20). Slightly increased current velocities of the order 0.01 $m.s^{-1}$ are expected along the eastern side of One Tree Point and around the western headland of Marsden Bay, while decreased current velocities are predicted within Marsden Bay (Figure 3.18).

During peak flood spring tidal conditions current velocities adjacent to the port berths and out to ~500-600 m from the berth are expected to decrease by ~0.01-0.02 $m.s^{-1}$, while current velocities further north within the main channel and adjacent to Reotahi Bay (Figure 1.1) are expected to slightly increase by a similar order of magnitude (Figure 3.21). Slightly decreased current velocities of the order 0.02-0.05 $m.s^{-1}$ are expected along the eastern side of One Tree Point and around the western headland of Marsden Bay, while increased current velocities are predicted within Marsden Bay (Figure 3.19) due to the formation of an eddy upstream of the proposed reclamation (Figure 3.14).

Percentage changes in bed shear stress for both ebb and flood tidal stages under a spring tidal range are given in Figure 3.22. Bed shear stress is a direct measure of the energy that can be transferred from the flowing water to the seabed, and is a useful analogy for potential sediment transport, but needs to be considered in conjunction with the critical shear stress for erosion (i.e. Figure 3.23 and Figure 3.25). Results show that changes of the order ~10% in the bed shear stress levels are expected over Snake Bank during ebbing tides and over both Snake Bank and the main channel to the west of NorthPort during flooding tides. A reduction in the bottom bed shear stress is predicted in the lee of the proposed reclamation and also along the eastern side of One Tree Point and within Marsden Bay. With respect the critical shear stress for erosion of the surficial sediment, overall patterns are similar between the existing port configuration, Stage 1 and Stage 1 inclusive of the Refining New Zealand dredged channel (Figure 3.23 and Figure 3.24), which suggests that while the percentage change in shear stress is relatively large, the absolute changes to the shear stress are not significant enough to fundamentally change the sediment transport patterns and hence morphology of the harbour, though localised morphological changes in the vicinity of the reclamation may occur.

The expected changes in current velocities associated with the Stage 1 reclamation (Figure 3.18-Figure 3.19) results in changes to the percentage of time the bed shear stress exceeds the critical threshold for entrainment of 200 μm sand (Figure 3.25), with increases predicted to the east of the proposed reclamation along the channel, while decreases are expected in the immediate lee of the reclamation during both ebbing and flooding tidal stages. During ebb tidal stages, increases in the percent of time the critical shear stress threshold for 200 μm sand are predicted within the main channel heading NW past Reotahi Bay (Figure 3.25). Minor perturbations are expected at other locations. Similar outcomes are expected for both the Stage 1 bathymetry and Stage 1 assuming the granting of the Refining New Zealand channel deepening consents.

The effects on harbour morphology of the expected changes to the hydrodynamics are addressed in MetOcean Solutions Ltd, (2018).

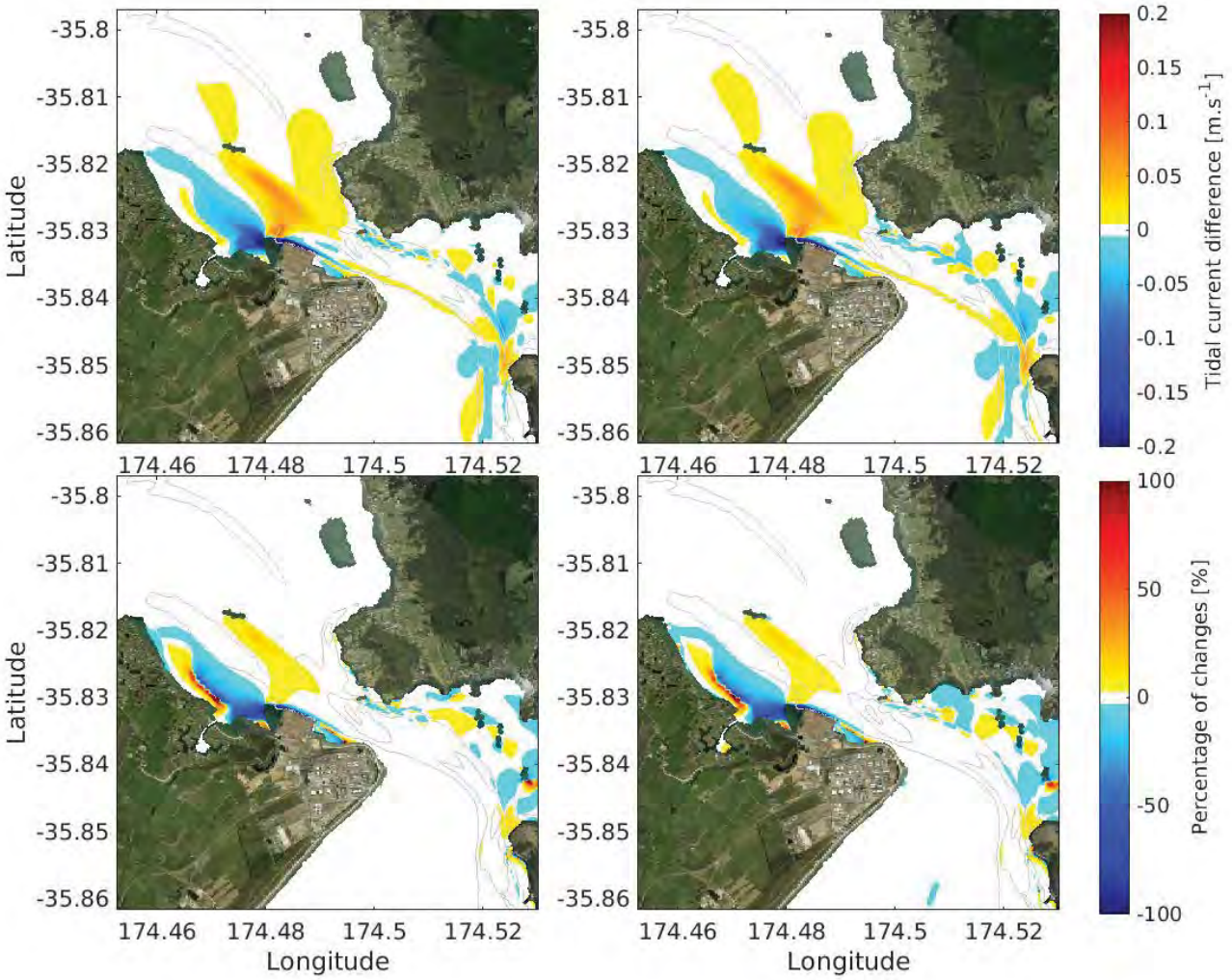

Figure 3.18 Absolute (top) and relative (bottom) difference in peak ebb tidal flows for the Stage 1 harbour configuration (right) and the Stage 1 configuration assuming channel deepening as per the RNZ consent (left). Positive values indicate a predicted increase in flow (red scale), while the negative values indicate a decrease (blue scale).

.

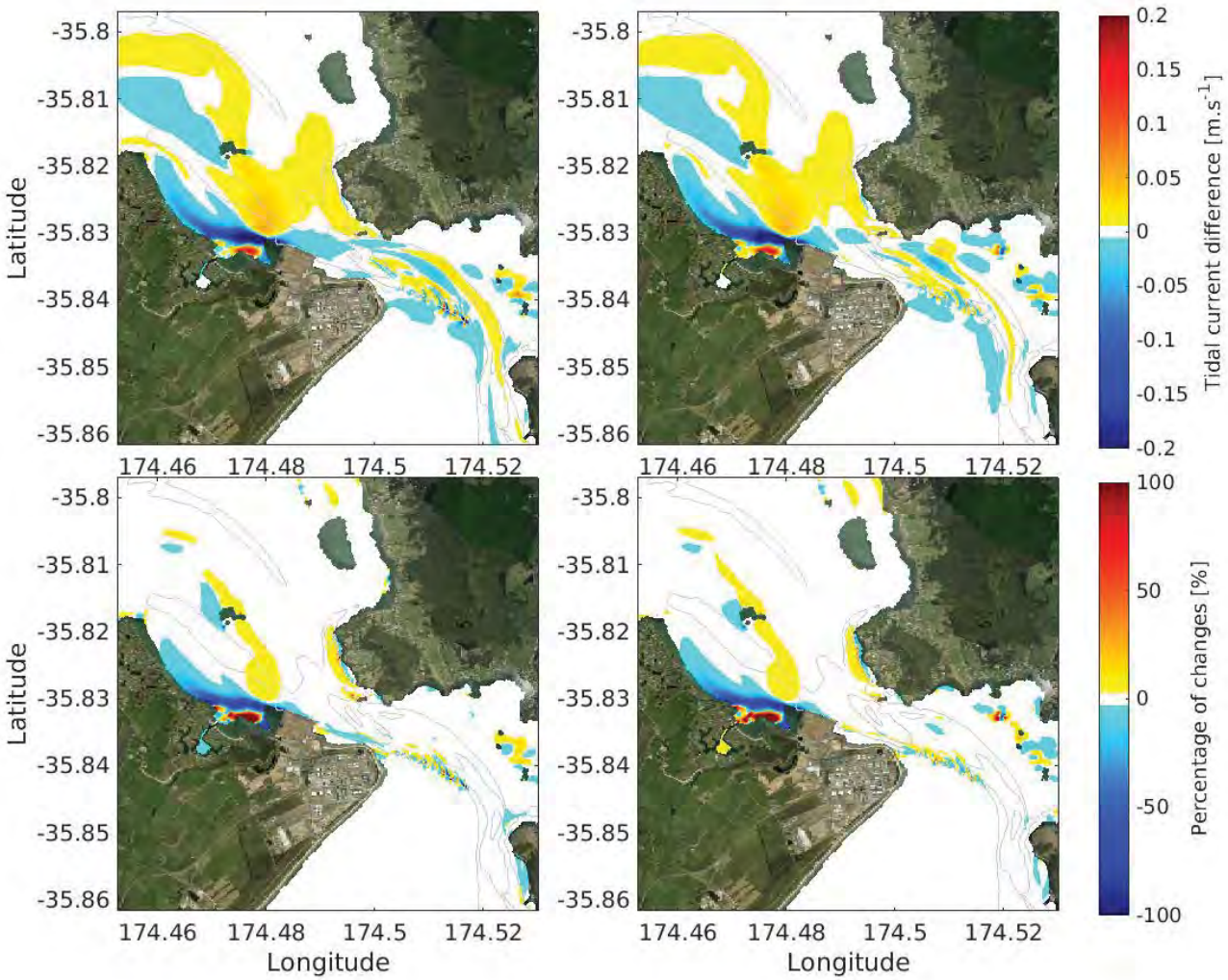

Figure 3.19 Absolute (top) and relative (bottom) difference in peak flood tidal flows for the Stage 1 harbour configuration (right) and Stage 1 configuration assuming channel deepening as per the RNZ consent (left). Positive values indicate a predicted increase in flow (red scale), while the negative values indicate a decrease (blue scale).

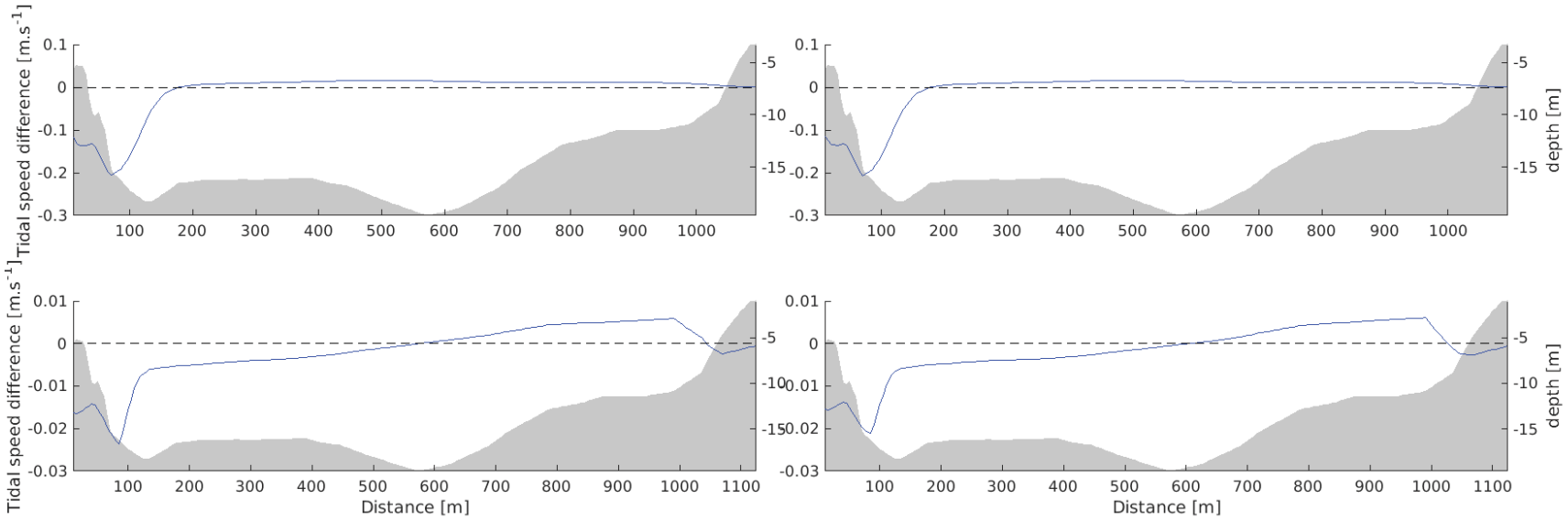

Figure 3.20 Depth averaged current difference (blue) transects for neap ebb (top) and flood (bottom) tides for the Stage 1 bathymetry (left) and Stage 1 bathymetry inclusive of the proposed Refining New Zealand channel deepening (right)

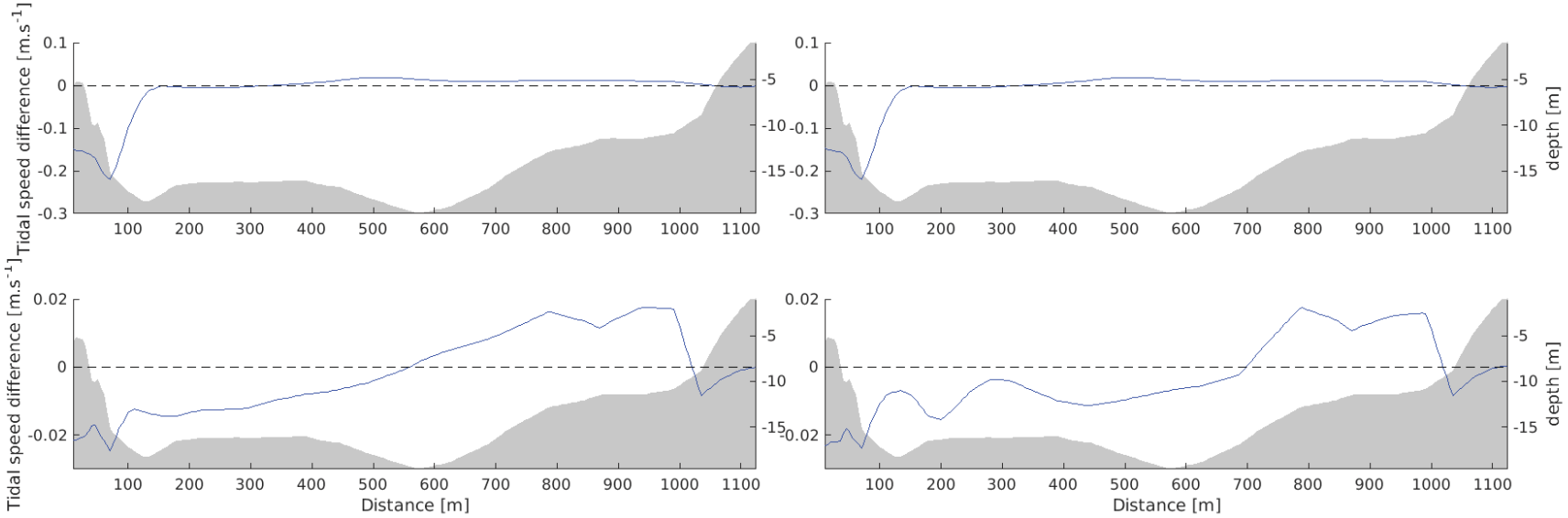

Figure 3.21 Depth averaged current difference (blue) transects for spring ebb (top) and flood (bottom) tides for the Stage 1 bathymetry (left) and Stage 1 bathymetry inclusive of the proposed Refining New Zealand channel deepening (right)

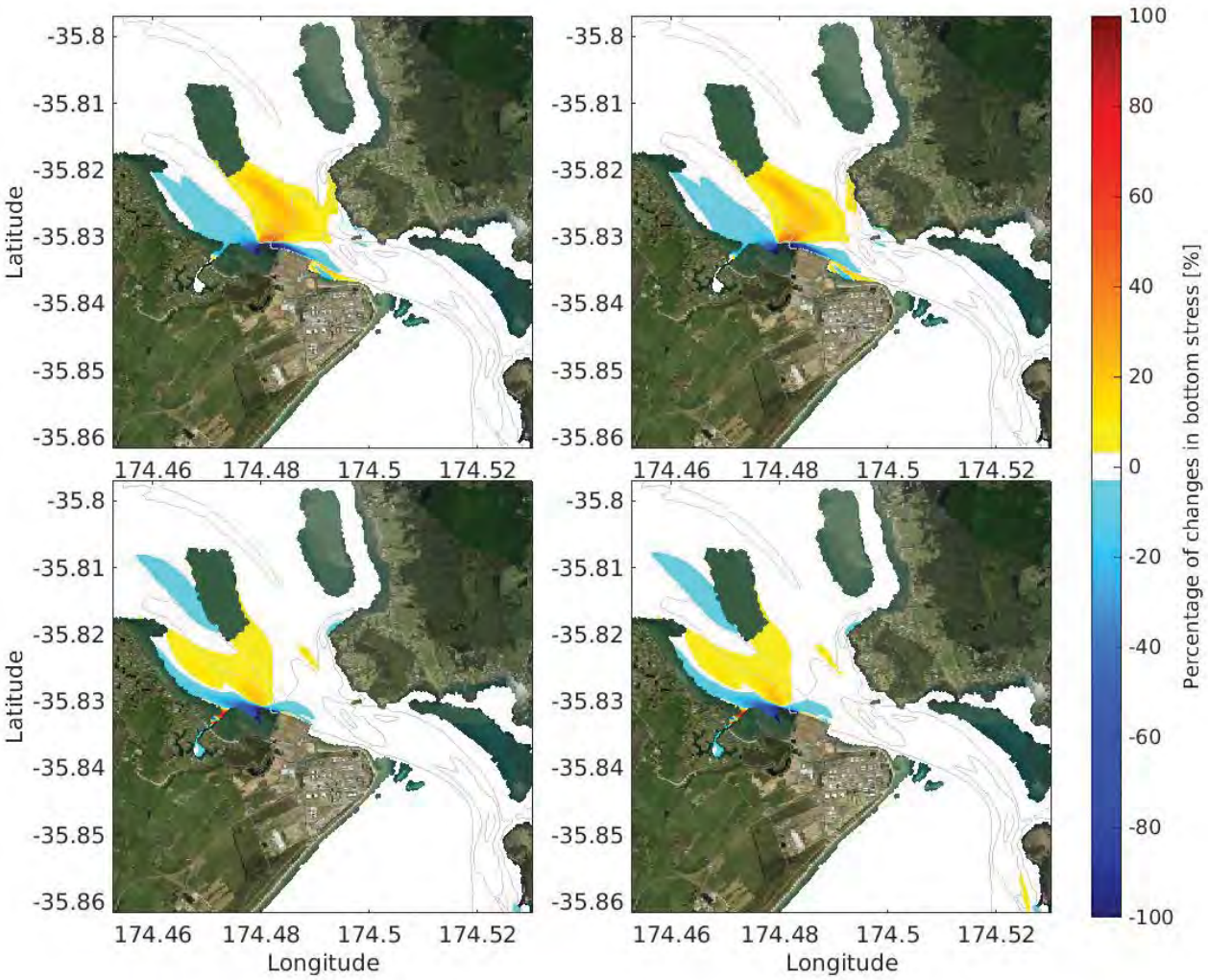

Figure 3.22 Percentage of change in the bed shear stress fields during peak ebb (top) and flood stages (bottom) between the existing and Stage 1 harbour configuration (right), and between the existing and Stage 1 assuming channel deepening as per the RNZ consent (left).

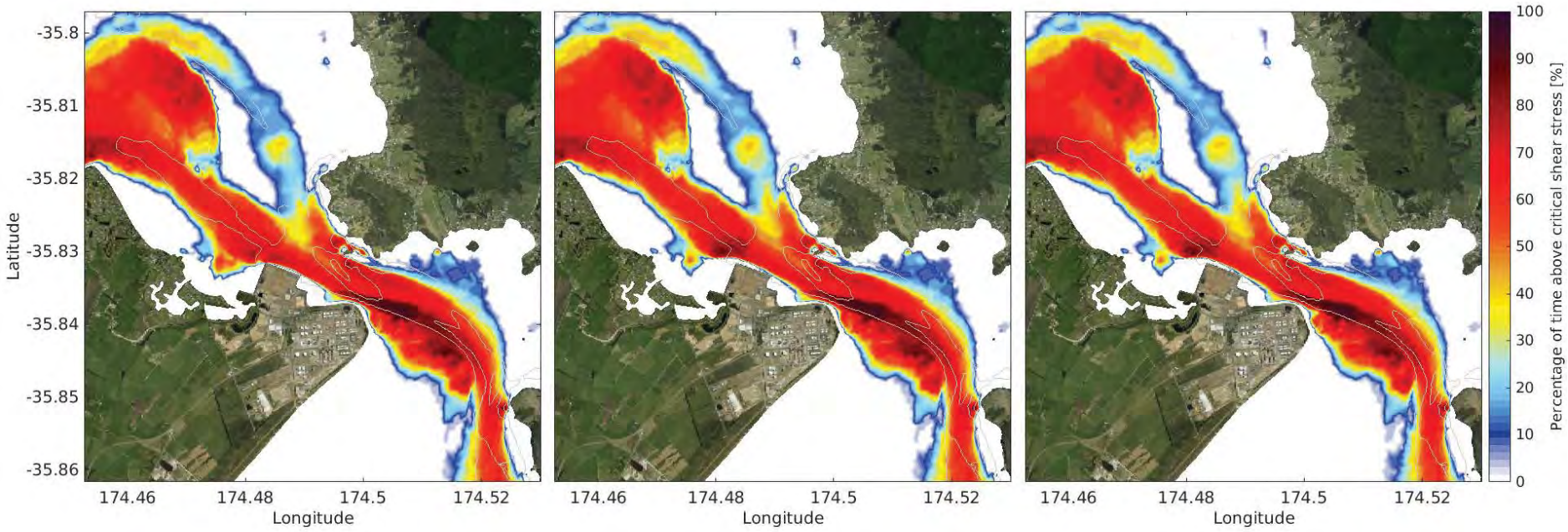

Figure 3.23 Percentage of time the bed shear stress exceeds the critical shear stress threshold for 200 µm sand at ebb tide. Calculated from a 28-day simulation of the existing harbour (left), the Stage 1 harbour configuration (centre) and Stage 1 assuming channel deepening as per the RNZ consent (right).

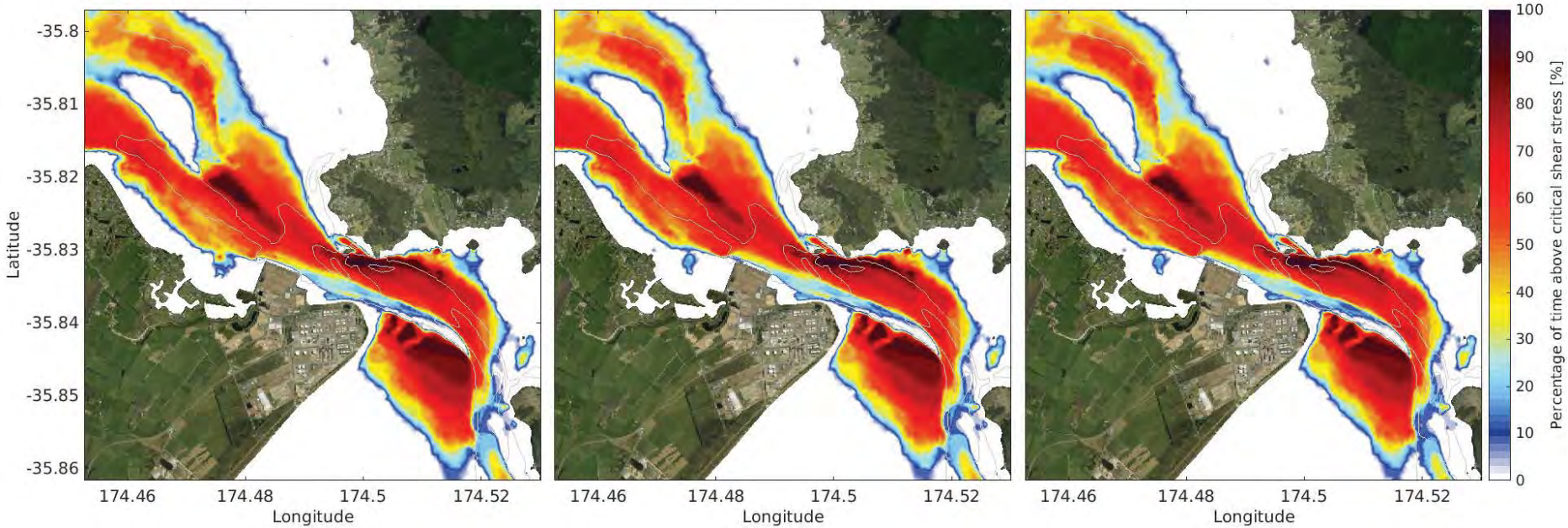

Figure 3.24 Percentage of time the bed shear stress exceeds the critical shear stress threshold for 200 µm sand at flood tide. Calculated from a 28-day simulation of the existing harbour (left), the Stage 1 harbour configuration (centre) and Stage 1 assuming channel deepening as per the RNZ consent (right).

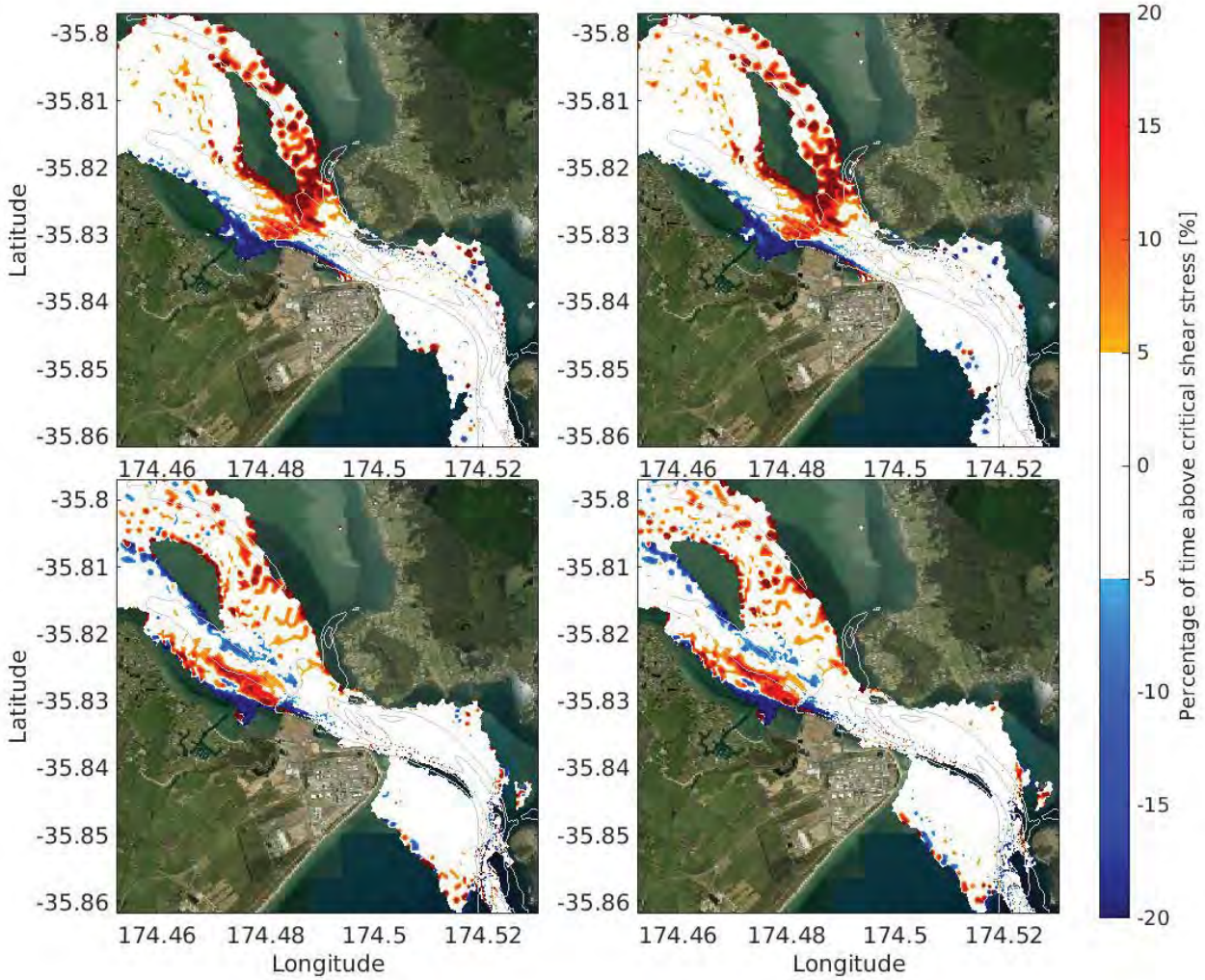

Figure 3.25 Difference of percentage of time the bed shear stress exceeds the critical shear stress threshold for 200 µm sand at ebb (top) and flood (bottom) tidal stages, from a 28-day simulation of the Stage 1 assuming channel deepening as per the RNZ consent (left) and the existing harbour configuration (right).

3.3. Stage 2 hydrodynamics

Stage 2 of the proposed port development consists of reclaiming Area 6 and dredging Area 3 as shown in Figure 1.2 and Figure 2.3.

Hydrodynamic conditions for the Stage 2 harbour configuration and the Stage 2 harbour configuration assuming the granting of the Refining New Zealand channel deepening are presented in Figure 3.26-Figure 3.29 for peak ebb and flood tidal stages under both spring and neap tidal ranges. Current velocities immediately around the port environment are provided in Figure 3.30 for both peak spring ebb and flood conditions, and illustrate the formation of eddies to the west of the port under both ebb and flood conditions. The eddy to the west of the port observed in the Stage 1 bathymetry is no longer present (see Section 3.2). Depth averaged velocity profiles across the harbour along the transect shown in Figure 3.6 for both ebb and flood tidal stages and under neap and spring tidal ranges are provided in Figure 3.31-Figure 3.32.

Only very slight differences are predicted between current velocities for the Stage 2 harbour configuration and the Stage 2 harbour configuration assuming the granting of the Refining New Zealand channel deepening.

As with the existing harbour configuration, the aspect of Whangarei Harbour results in the cross-channel characteristics of the current velocities in the vicinity of NorthPort varying between ebbing and flooding tidal stages.

During spring ebbing tidal stages, current velocities tend to be stronger adjacent to the port berths and within the swinging basin as the harbour drains through the main channel linking the harbour entrance to the inner Whangarei harbour. Conversely, during flooding tidal stages the fastest current velocities are situated on the north side of the harbour cross-section and aligned with the main entrance channel (Figure 3.26, Figure 3.28 and Figure 3.32).

Adjacent to the port berths current velocities are expected to peak ~1.0 $m.s^{-1}$ during spring ebbing tides and ~0.8 $m.s^{-1}$ during spring flooding tides (Figure 3.26 and Figure 3.28 respectively). Current velocities during neap flood and ebb tidal conditions are of the order 0.5 $m.s^{-1}$ adjacent to the port berths, compared to approximately 0.6 $m.s^{-1}$ on the north side of the harbour adjacent to Motukaroro Island (Figure 1.1) during flooding neap tides (Figure 3.27, Figure 3.29 and Figure 3.31).

Mean residual spring tide current velocities for the existing and Stage 2 harbour configurations are given in Figure 3.33. Areas of low or diverging residual current velocities highlight areas of potential sediment accretion. Mean residual current velocities directed towards the port are expected to increase to the east of the reclamation within the main channel, while slightly stronger SE directed residual currents are also expected along Marsden Bay. Reduced tidal residuals are expected within the lee of the proposed reclamation.

In general, the effects of completing the reclamation of Area 6 and dredging Area 3 (i.e. Stage 2) are to reduce the overall effects of Stage 1 on the harbour hydrodynamics. This is due to the fact that the acceleration of the current velocities due to the confining of the harbour cross-section by the proposed reclamation is balanced by the reduction in velocities through the deeper, dredged areas (i.e. Area 3, Figure 1.2).

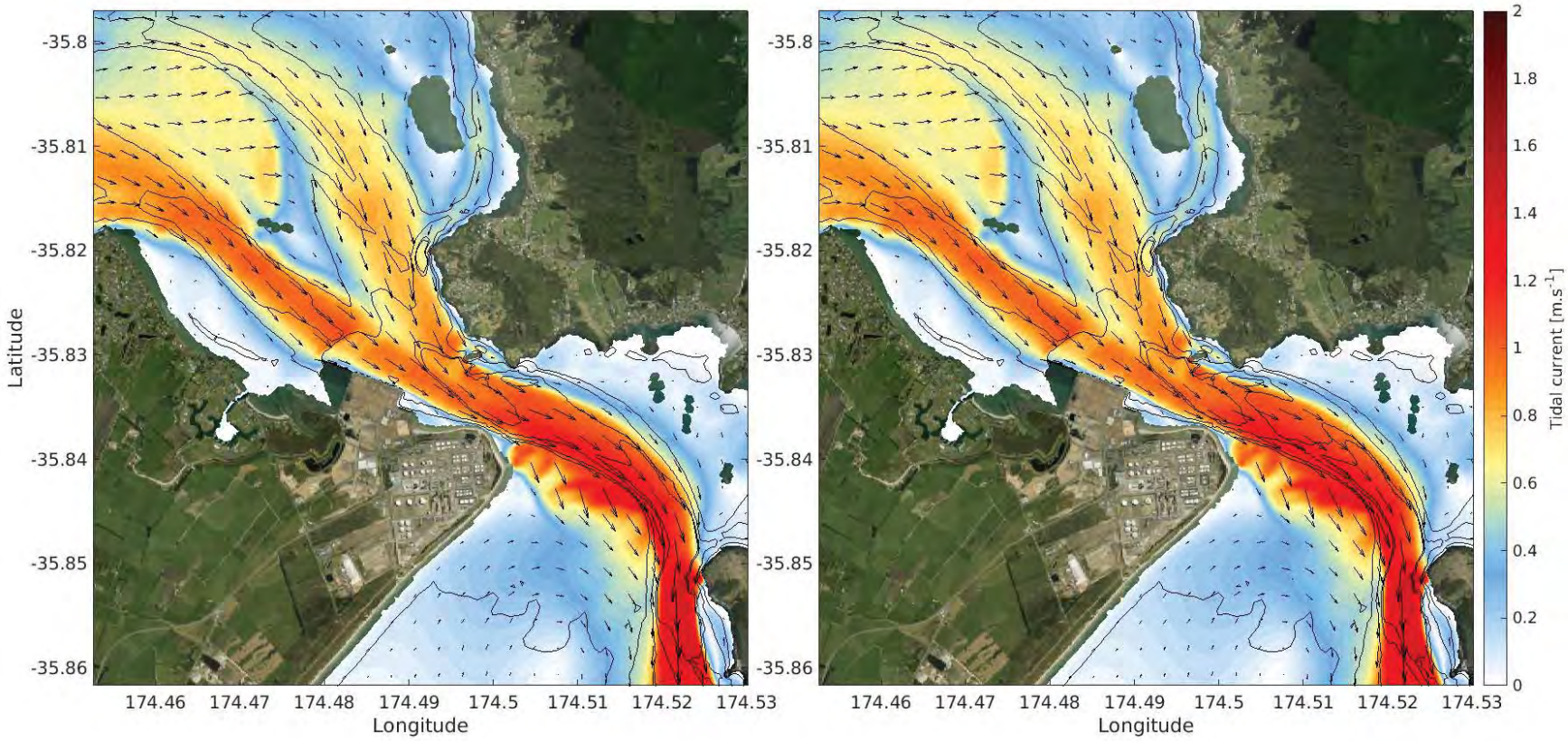

Figure 3.26 Modelled peak ebb flows during spring tide in the vicinity of Northport and Whangarei Harbour entrance for the Stage 2 harbour configuration (right) and Stage 2 assuming channel deepening as per the RNZ consent (left).

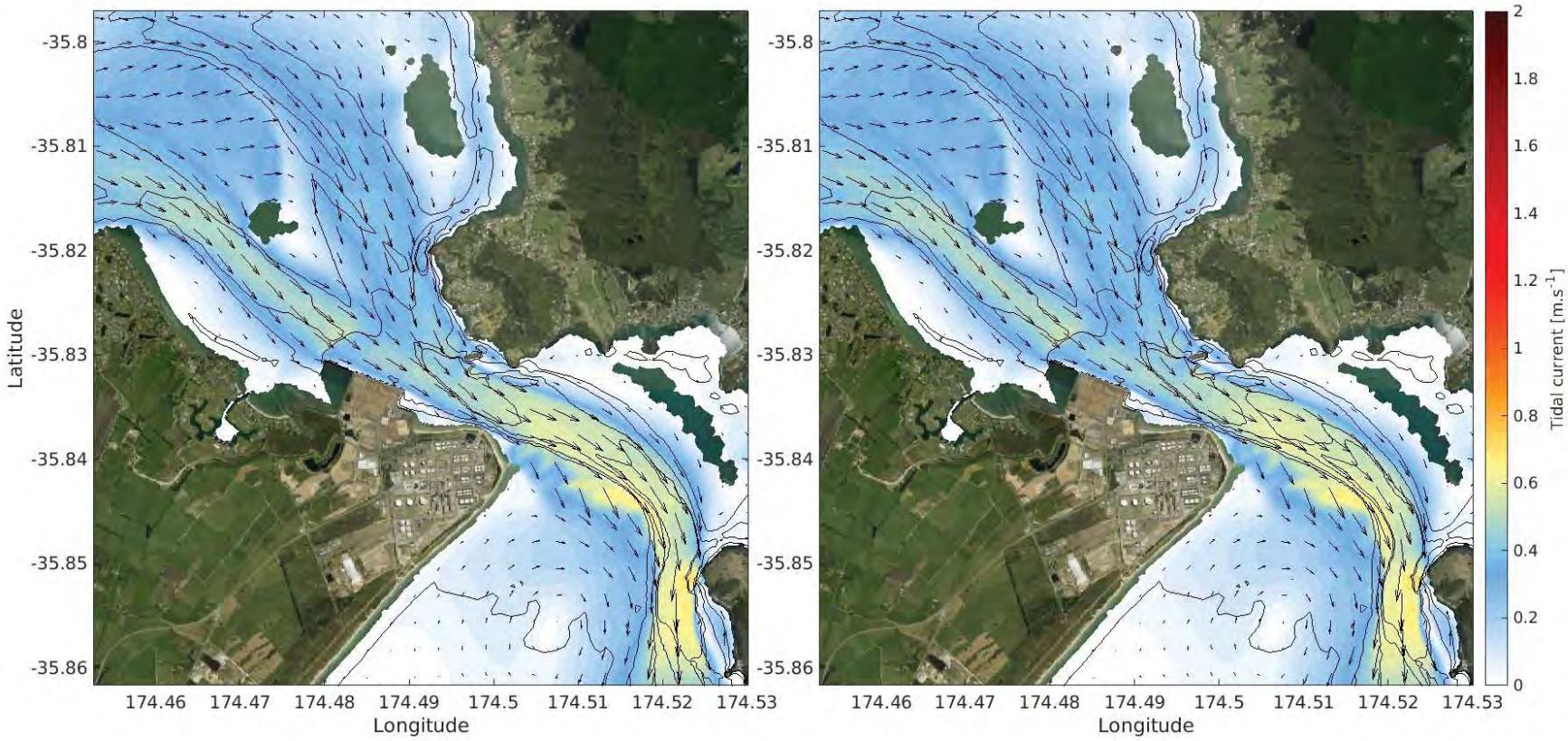

Figure 3.27 Modelled peak ebb flows during neap tide in the vicinity of Northport and Whangarei Harbour entrance for the Stage 2 harbour configuration (right) and Stage 2 assuming channel deepening as per the RNZ consent (left).

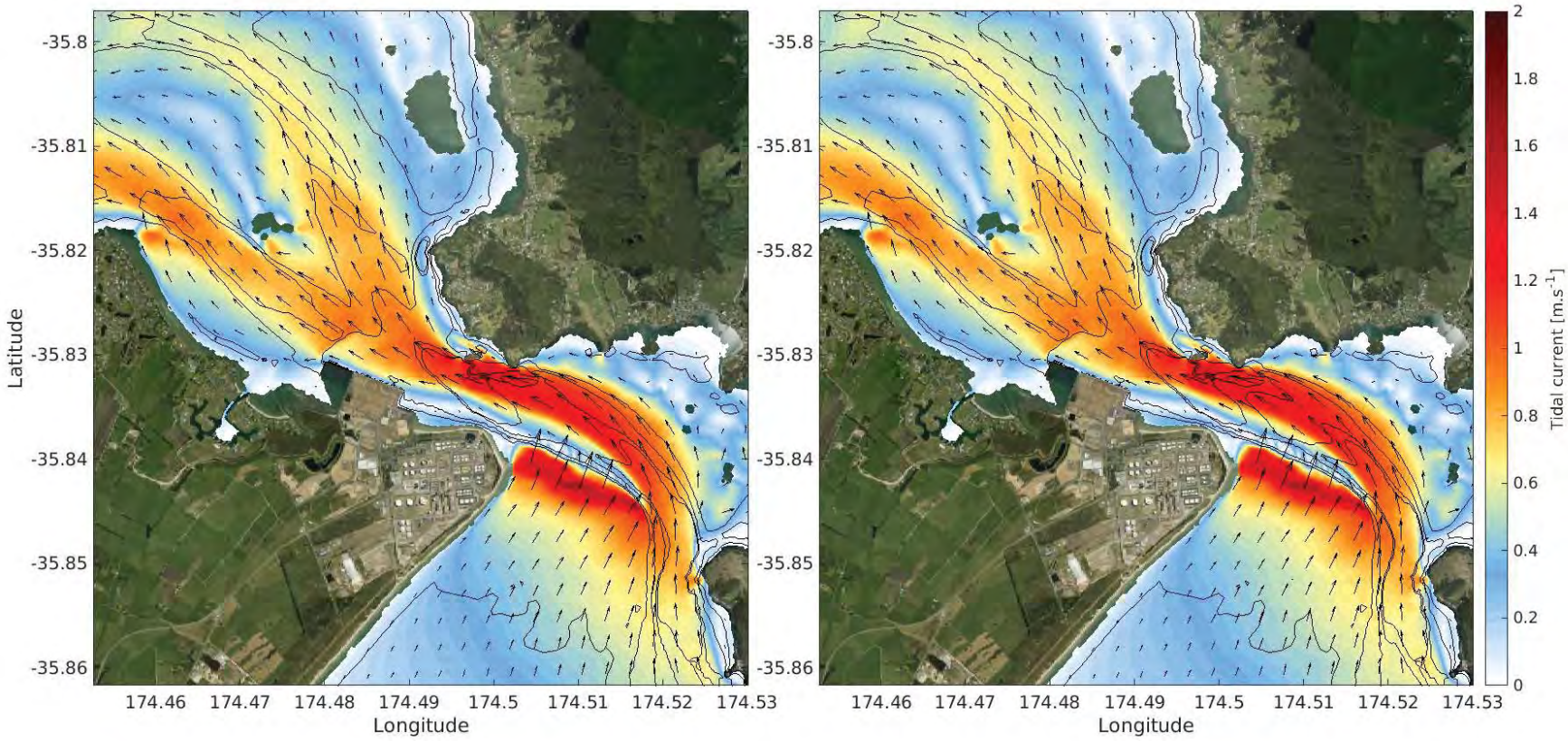

Figure 3.28 Modelled peak flood flows during spring tide in the vicinity of Northport and Whangarei Harbour entrance for the Stage 2 harbour configuration (right) and Stage 2 assuming channel deepening as per the RNZ consent (left).

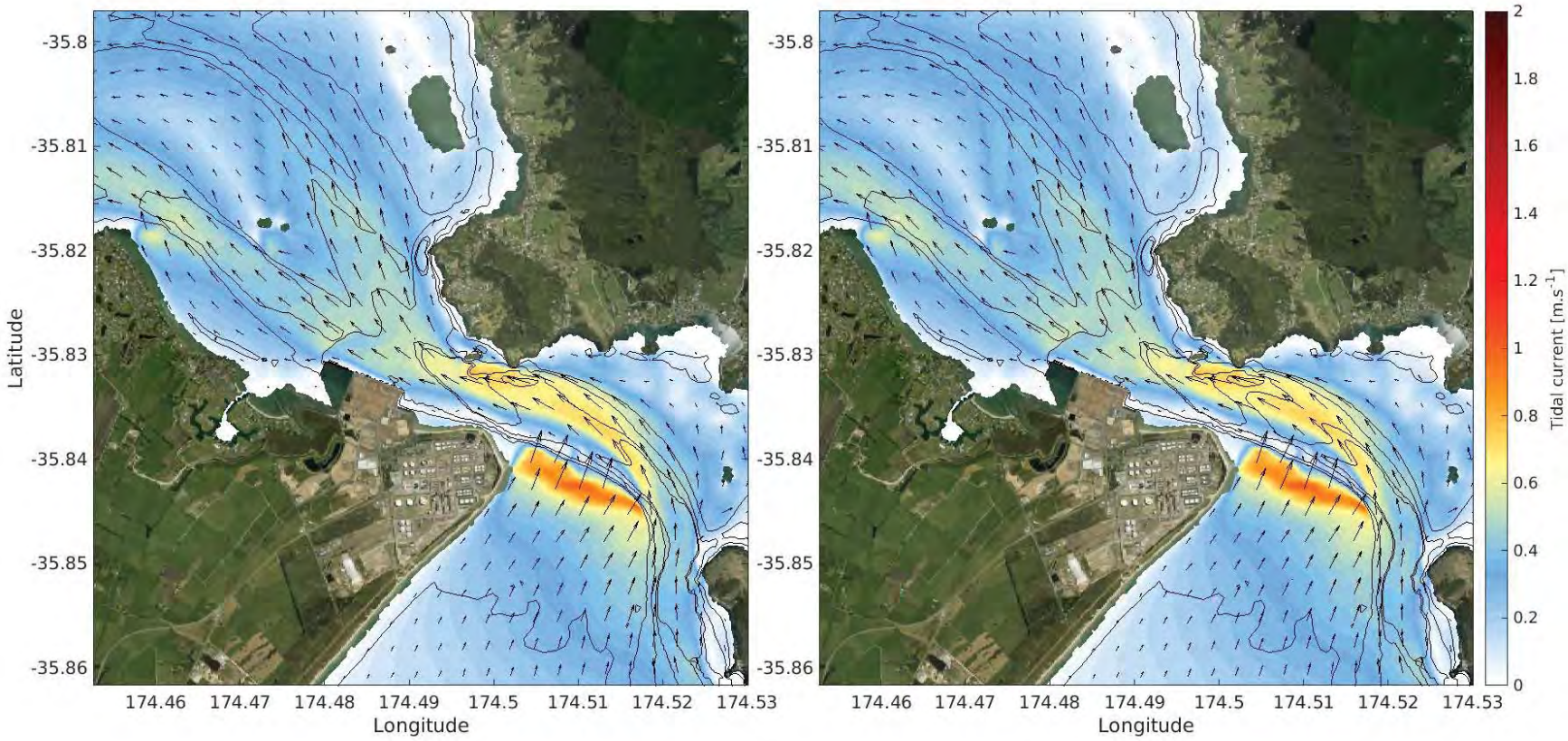

Figure 3.29 Modelled peak flood flows during neap tide in the vicinity of Northport and Whangarei Harbour entrance for the Stage 2 harbour configuration (right) and Stage 2 assuming channel deepening as per the RNZ consent (left).

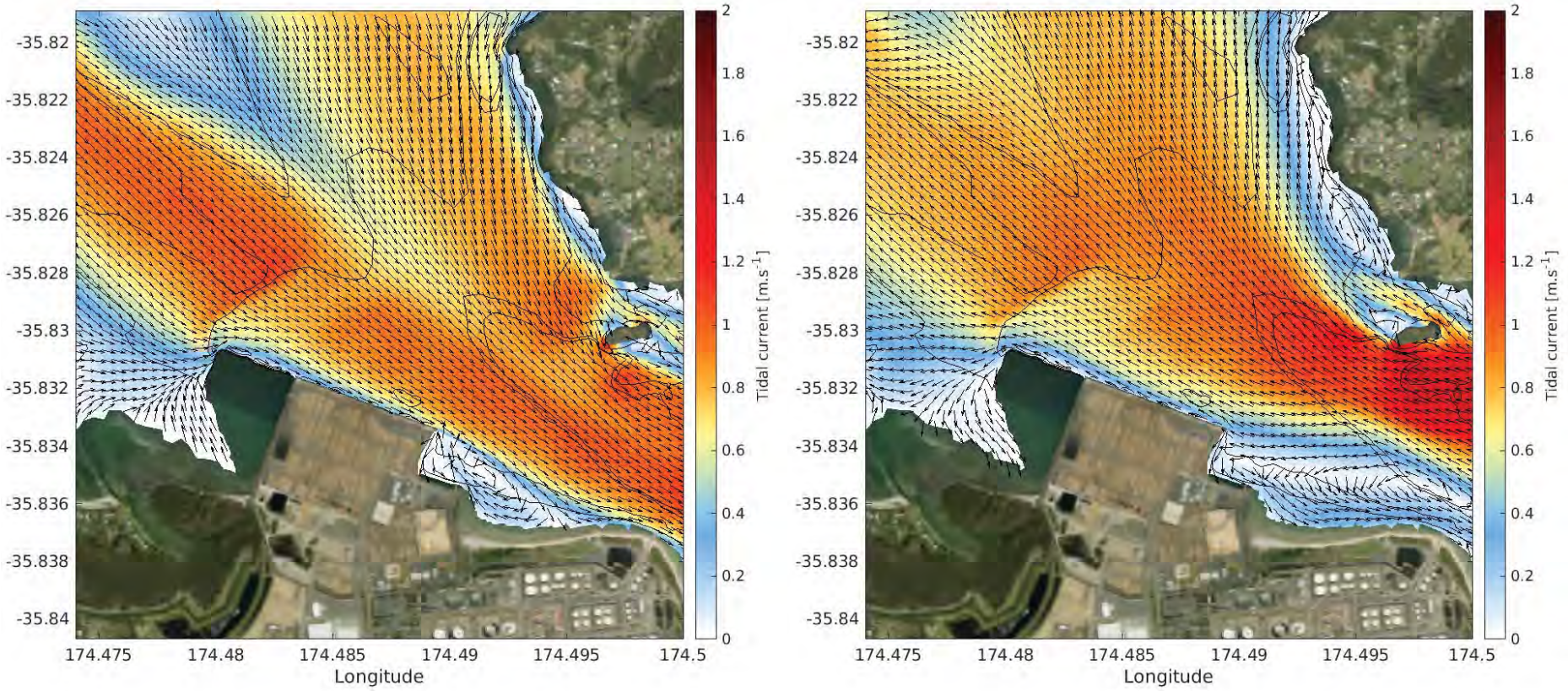

Figure 3.30 Modelled peak ebb (left) and flood (right) flows in the port environs showing formation of back eddies in the lee of the port structures both up and down stream for the Stage 2 bathymetry.

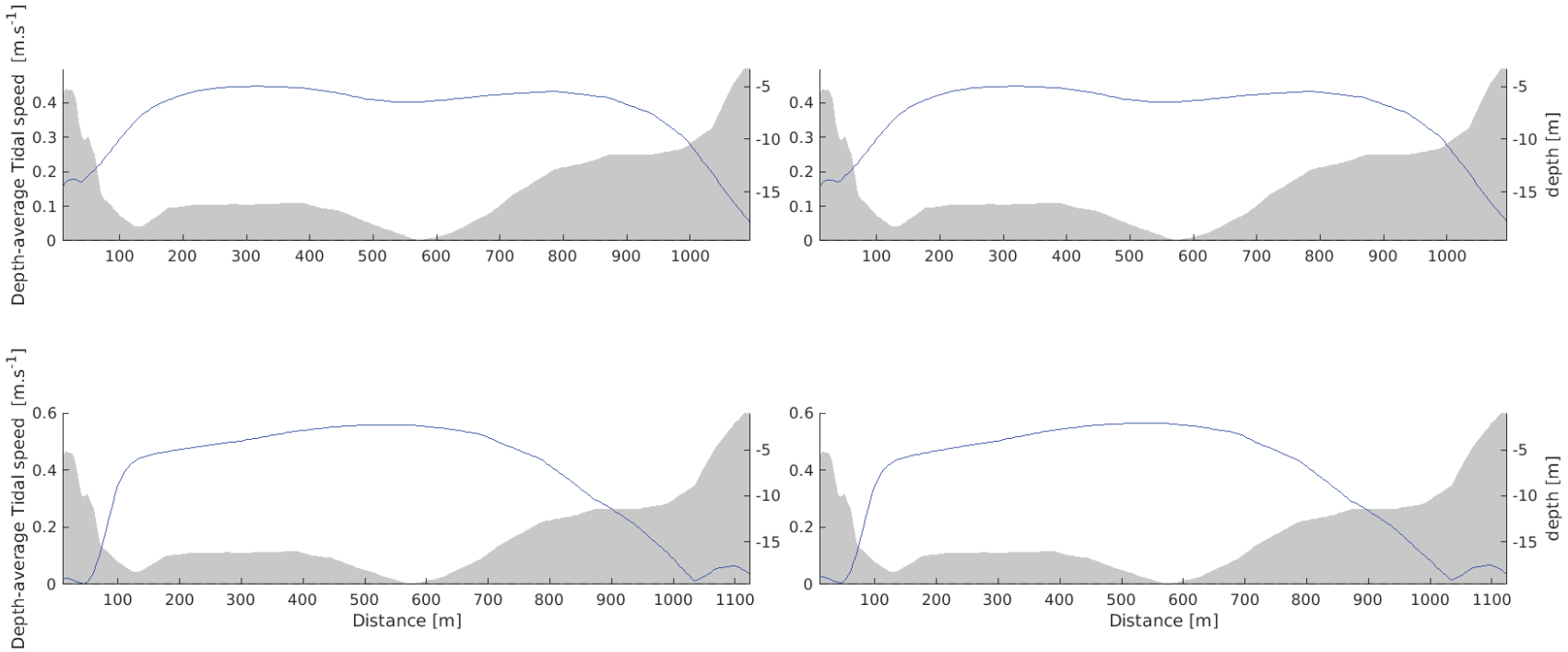

Figure 3.31 Depth averaged current velocity (blue) transects for neap ebb (top) and flood (bottom) tides for the Stage 2 bathymetry (left) and the Stage 2 bathymetry inclusive of the proposed Refining New Zealand channel deepening (right)

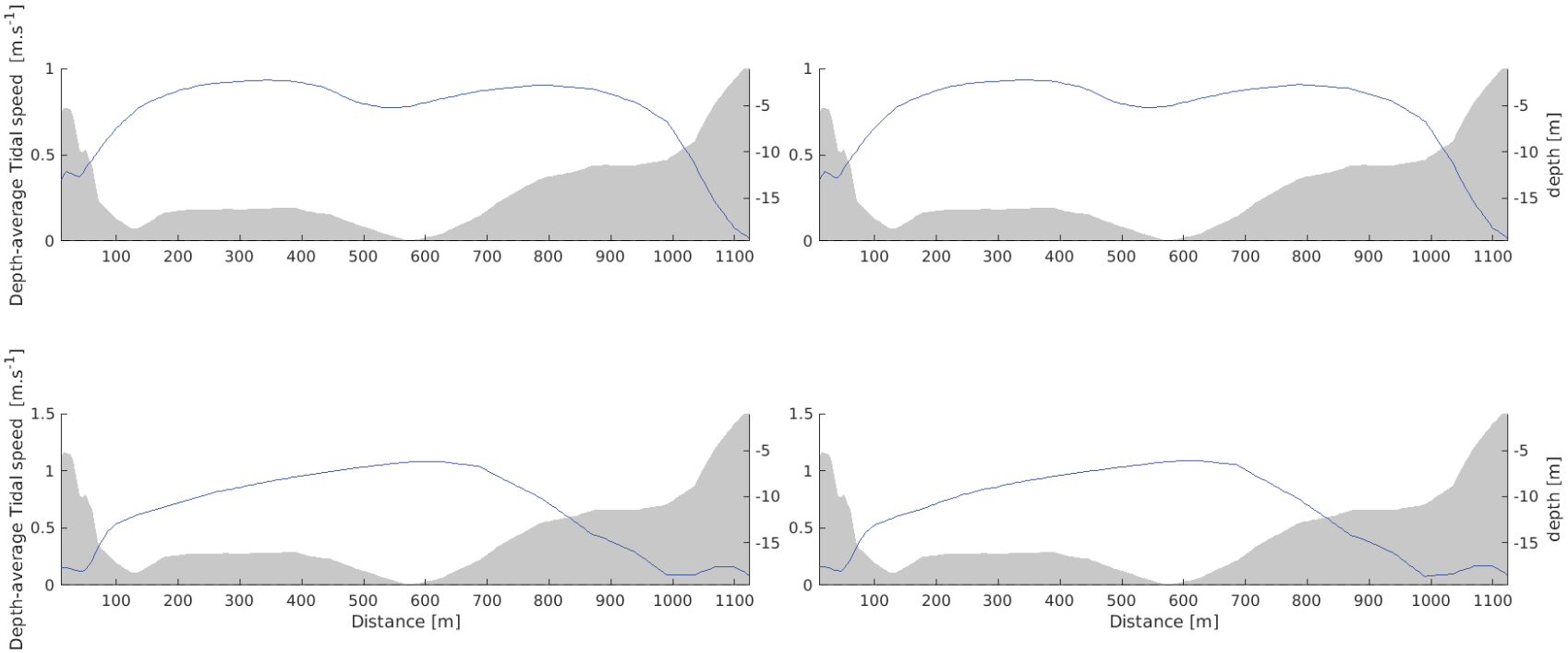

Figure 3.32 Depth averaged current velocity (blue) transects for spring ebb (top) and flood (bottom) tides for the Stage 2 bathymetry (left) and the Stage 2 bathymetry inclusive of the proposed Refining New Zealand channel deepening (right)

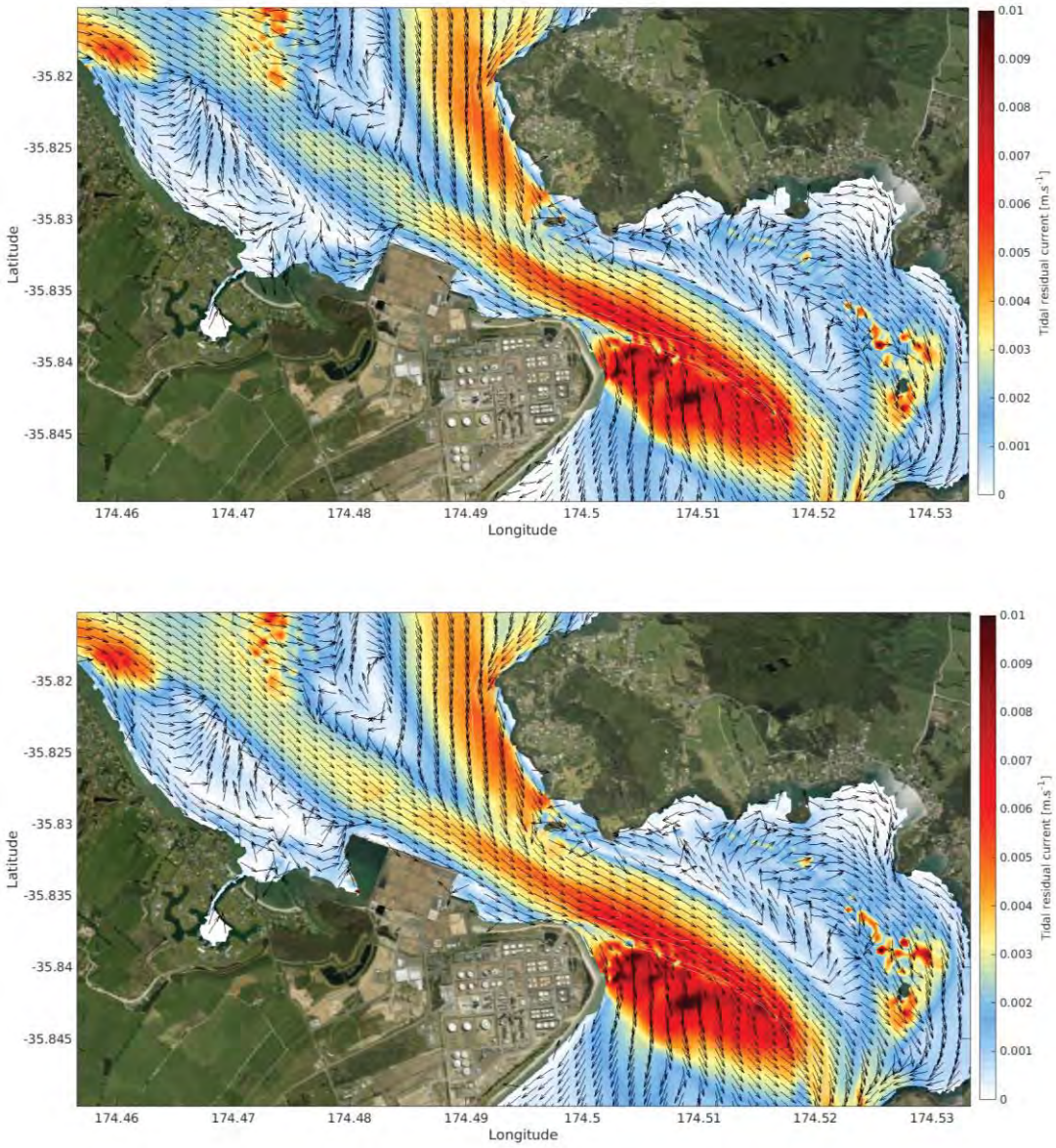

Figure 3.33 Spring tide mean residual tidal current velocity determined over one complete tidal cycle for the existing harbour configuration (top) and Stage 2 bathymetry (bottom).

3.3.1. Stage 2 effect on tidal hydrodynamics

The absolute and relative (i.e. percentage difference) between the existing and Stage 2 hydrodynamics under ebbing and flooding tidal stages for a worst-case spring tidal range are provided in Figure 3.34-Figure 3.35. Absolute and relative differences during neap tidal stages are comparatively smaller than during spring tides. Comparisons are made between the existing harbour configuration and the Stage 2 harbour configuration and between the existing harbour configuration and the Stage 2 harbour configuration assuming the granting of the Refining New Zealand channel deepening. Depth averaged velocity profiles across the harbour along the transect shown in Figure 3.6 for both ebb and flood tidal stages and under neap and spring tidal ranges are provided in Figure 3.36-Figure 3.37.

Only very slight differences are predicted between current velocities for the Stage 2 harbour configuration and the Stage 2 harbour configuration assuming the granting of the Refining New Zealand channel deepening. Further, similar spatial extents, but greater relative effects are observed during spring tidal conditions as opposed to neap tidal conditions (Figure 3.34-Figure 3.35 and Figure 3.36-Figure 3.37), and as such are discussed below.

During peak ebb spring tidal conditions current velocities immediately adjacent to the port berths and out to ~100 m are expected to increase by as much as ~0.15 $m.s^{-1}$ along the transect, while current velocities further north within the main channel and adjacent to Reotahi Bay (Figure 1.1) are expected to remain essentially the same as for the existing harbour configuration (Figure 3.37). Largest predicted current velocity changes are expected immediately within the area to be dredged, with the increased depth resulting in a predicted current velocity decrease of the order 0.15-0.2 $m.s^{-1}$, and a corresponding increase of the order 0.05 $m.s^{-1}$ immediately to the east of the dredged area (Figure 3.34)

During peak flood spring tidal conditions current velocities adjacent to the port berths and out to ~100 m from the berth are expected to decrease by ~0.01-0.02 $m.s^{-1}$. Current velocities further north within the main channel and adjacent to Reotahi Bay (Figure 1.1) are expected to be a similar order of magnitude to those of the existing harbour configuration, while closer to Reotahi Bay a slight reduction in current velocities is expected (Figure 3.37). Largest predicted current velocity changes are expected immediately within the area to be dredged, with the increased depth resulting in a predicted current velocity decrease of the order 0.15-0.2 $m.s^{-1}$, and a corresponding increase of the order 0.05 $m.s^{-1}$ immediately to the east of the dredged area (Figure 3.35).

Percentage changes in bed shear stress for both ebb and flood tidal stages under a spring tidal range are given in Figure 3.38. Bed shear stress is a direct measure of the energy that can be transferred from the flowing water to the seabed, and is a useful analogy for potential sediment transport, but needs to be considered in conjunction with the critical shear stress for erosion (i.e. Figure 3.39 and Figure 3.40).

Results show that changes of the order ~20% reduction in the bed shear stress levels are expected within the dredged Area 3, while a ~10% increase is expected immediately outside the dredged areas to both the east and west during ebbing tides. A reduction in the bottom bed shear stress is predicted in the lee of the proposed reclamation and also along the eastern side of One Tree Point and within Marsden Bay during flood tides (Figure 3.38)

With respect the critical shear stress for erosion of the surficial sediment, overall patterns are similar between the existing port configuration, Stage 2 and Stage 2 inclusive of the Refining New Zealand dredged channel (i.e. Figure 3.39 and Figure 3.40), which suggests that while the percentage change in shear stress is relatively large, the absolute changes to the shear stress are not significant enough to fundamentally change the sediment transport patterns and hence morphology of the harbour, though localised morphological changes in the vicinity of the reclamation and dredged areas can be expected.

The expected changes in current velocities associated with the Stage 2 reclamation (Figure 3.34-Figure 3.35) results in changes to the percentage of time the bed shear stress exceeds the critical threshold for entrainment of 200 μm sand (Figure 3.41), with a decrease predicted within the area to be dredged and along Marsden Bay to the east of the proposed reclamation under both ebbing and flooding tidal stages. Minor perturbations are expected at other locations. Similar outcomes are expected for both the Stage 2 bathymetry and Stage 2 assuming the granting of the Refining New Zealand channel deepening consents.

The effects on harbour morphology of the expected changes to the hydrodynamics are addressed in MetOcean Solutions Ltd, (2018).

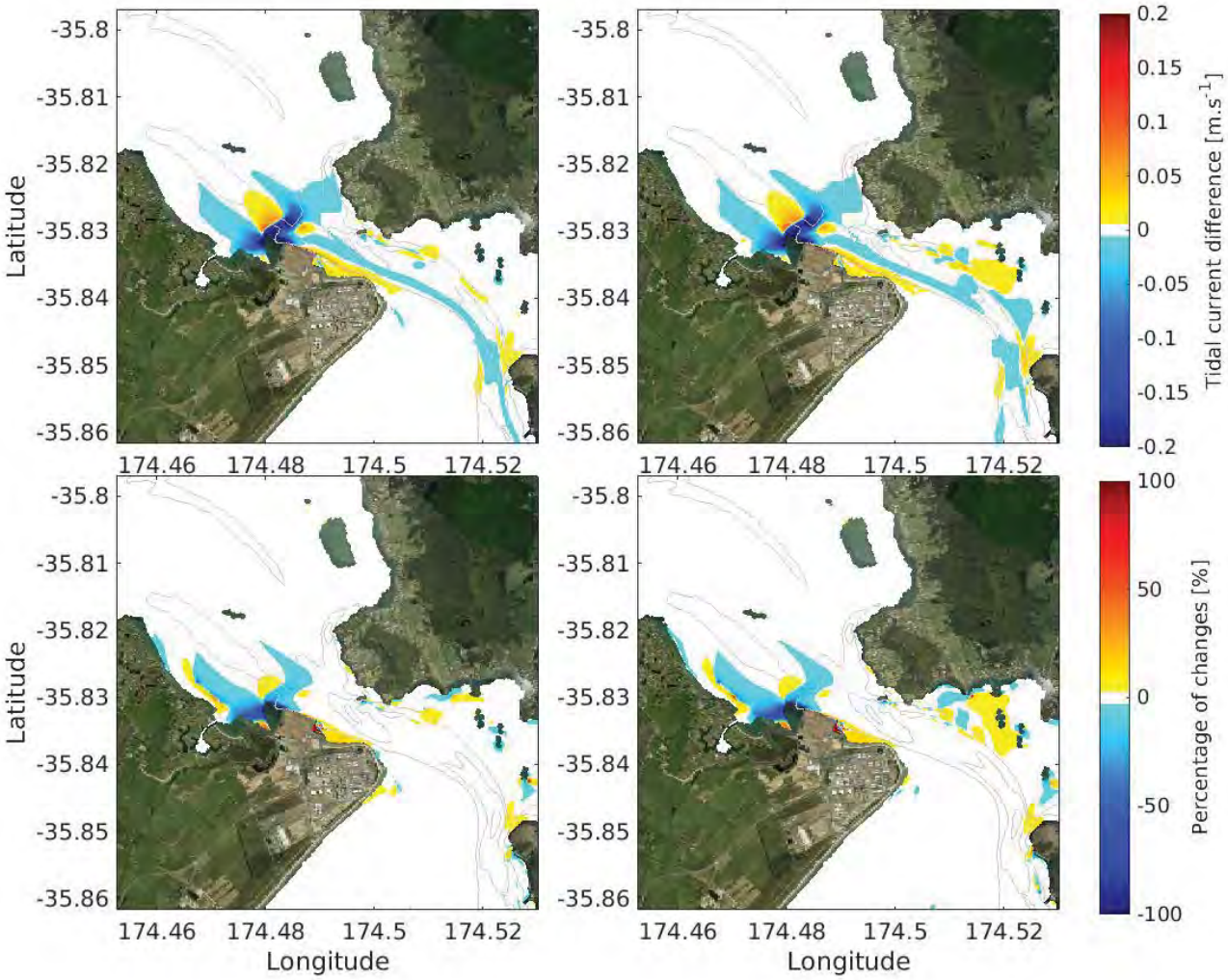

Figure 3.34 Absolute (top) and relative (bottom) difference in peak ebb tidal flows for the Stage 2 harbour configuration (right) and the Stage 2 configuration assuming channel deepening as per the RNZ consent (left). Positive values indicate a predicted increase in flow (red scale), while the negative values indicate a decrease (blue scale).

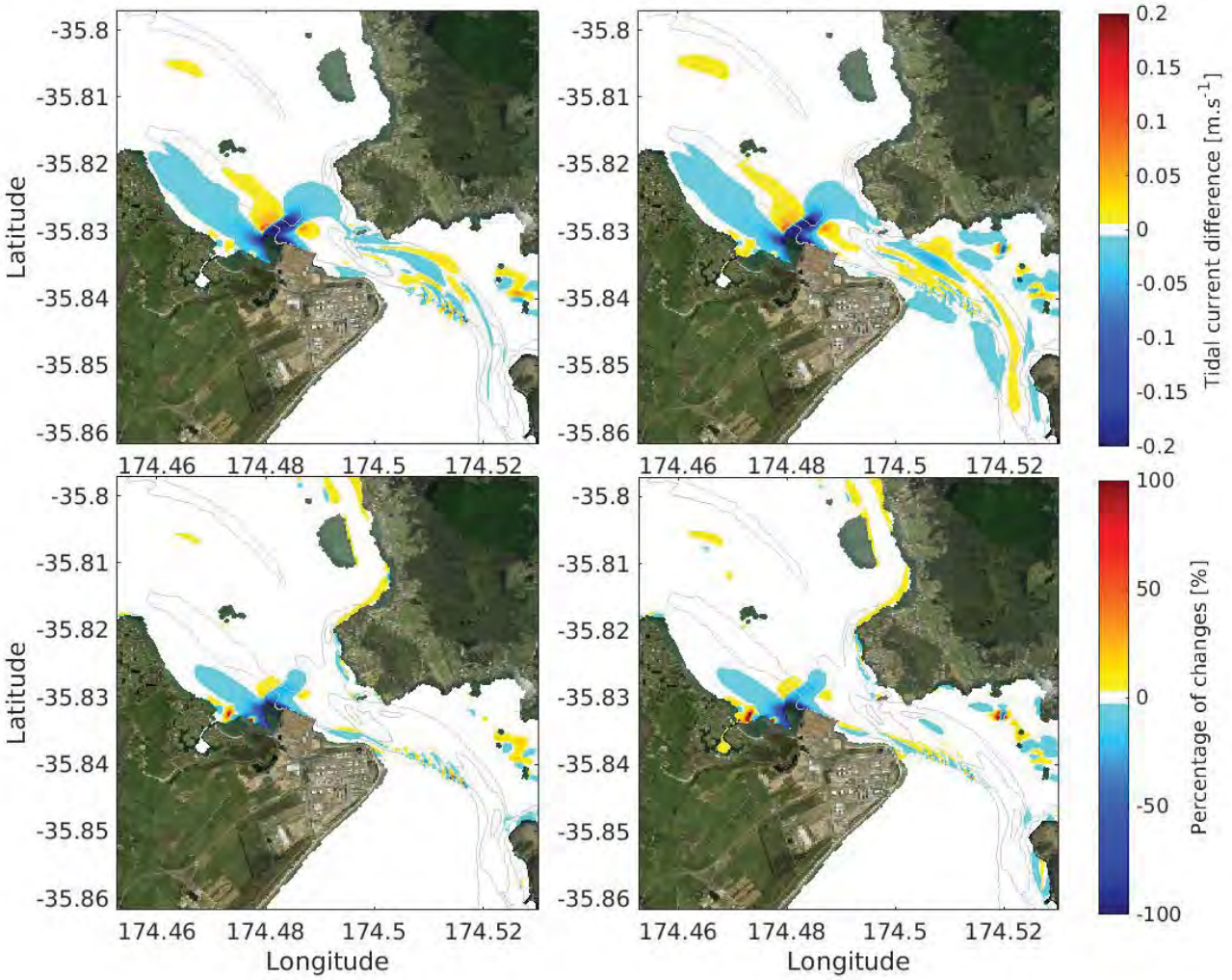

Figure 3.35 Absolute (top) and relative (bottom) difference in peak flood tidal flows for the Stage 2 harbour configuration (right) and Stage 2 configuration assuming channel deepening as per the RNZ consent (left). Positive values indicate a predicted increase in flow (red scale), while the negative values indicate a decrease (blue scale).

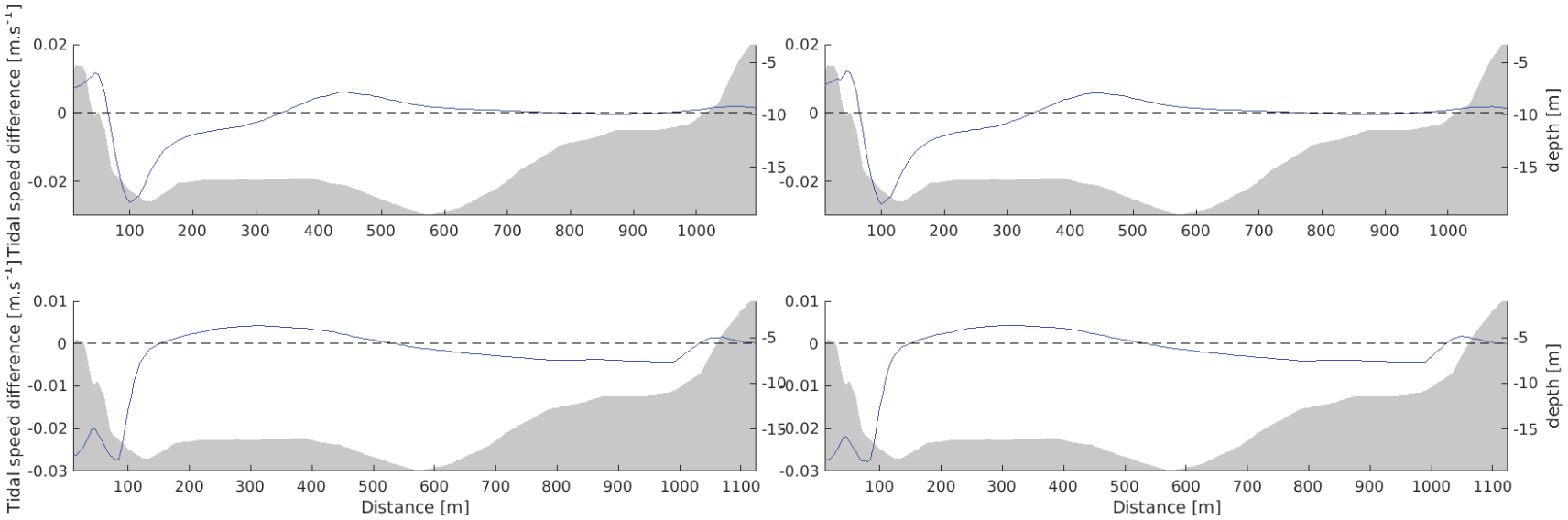

Figure 3.36 Depth averaged current difference (blue) transects for neap ebb (top) and flood (bottom) tides for the Stage 2 bathymetry (left) and Stage 2 bathymetry inclusive of the proposed Refining New Zealand channel deepening (right)

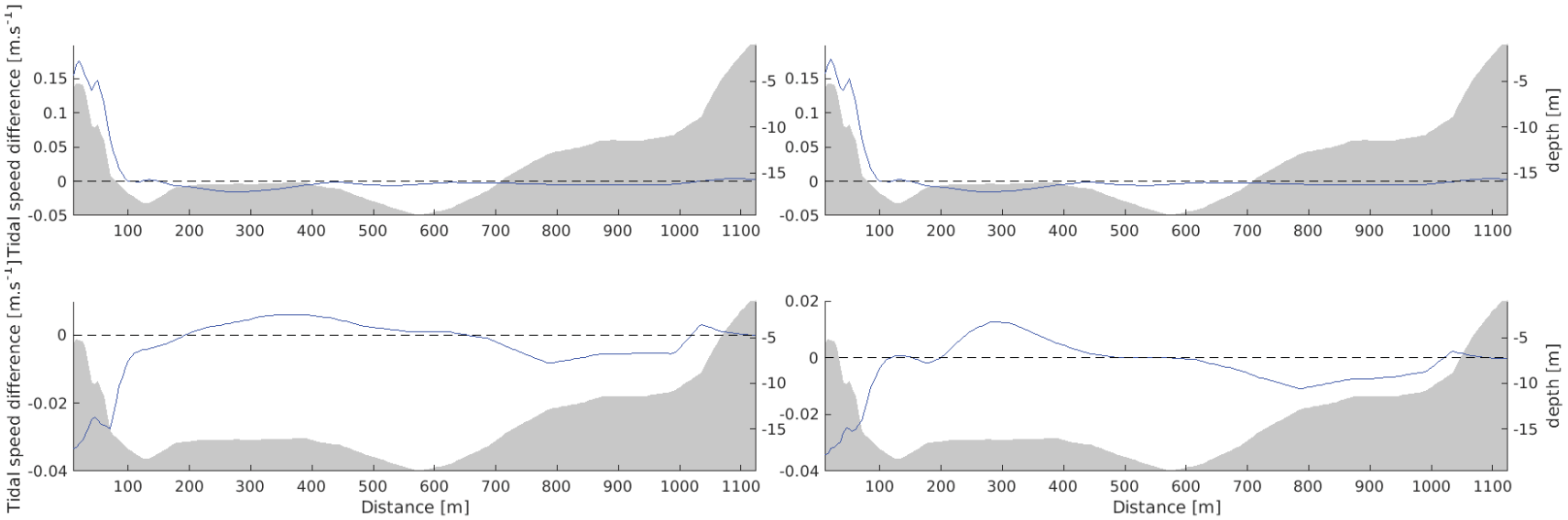

Figure 3.37 Depth averaged current difference (blue) transects for spring ebb (top) and flood (bottom) tides for the Stage 2 bathymetry (left) and Stage 2 bathymetry inclusive of the proposed Refining New Zealand channel deepening (right)

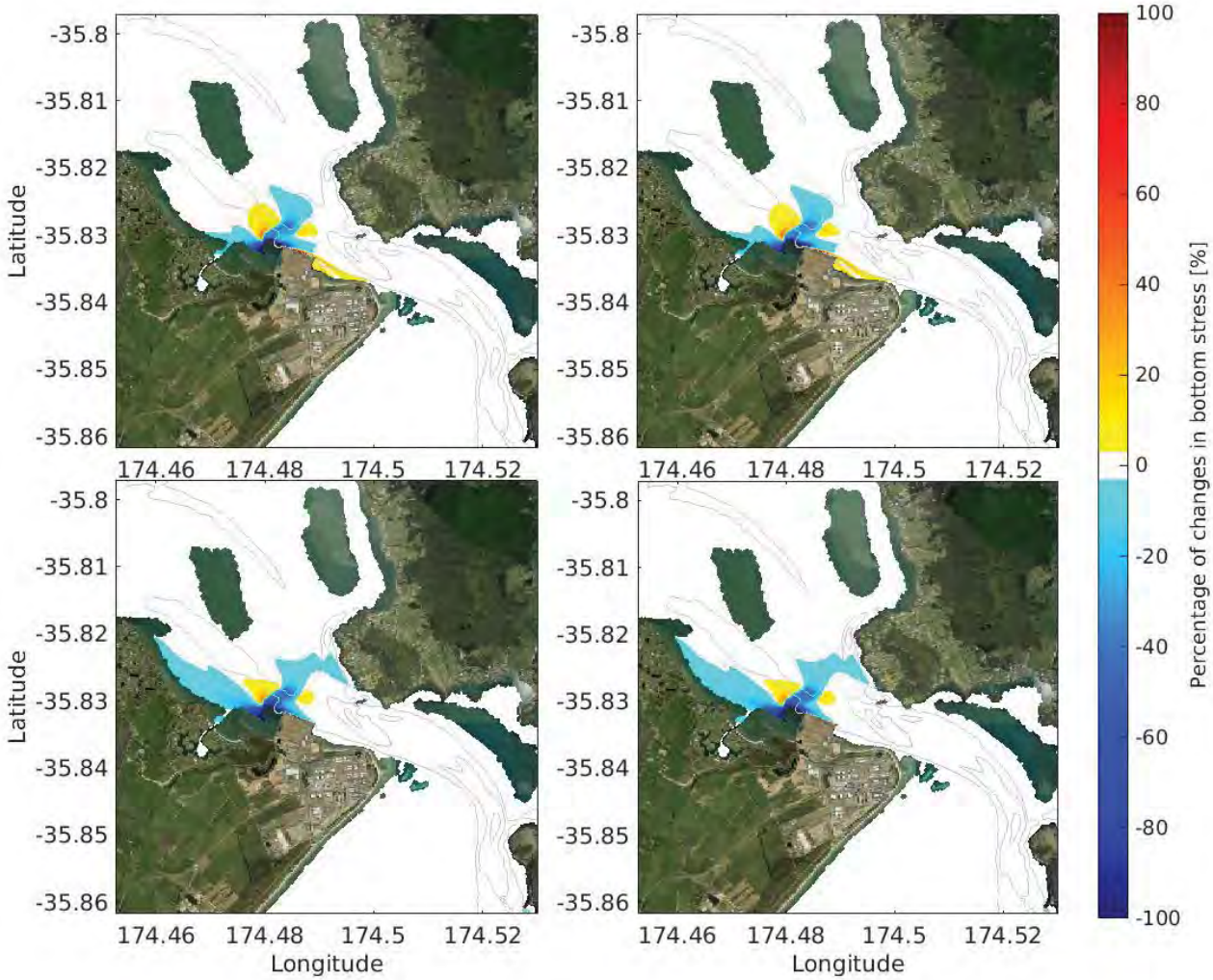

Figure 3.38 Percentage of change in the bed shear stress fields during peak ebb (top) and flood stages (bottom) between the existing Stage 2 harbour configuration (right) and Stage 2 assuming channel deepening as per the RNZ consent (left).

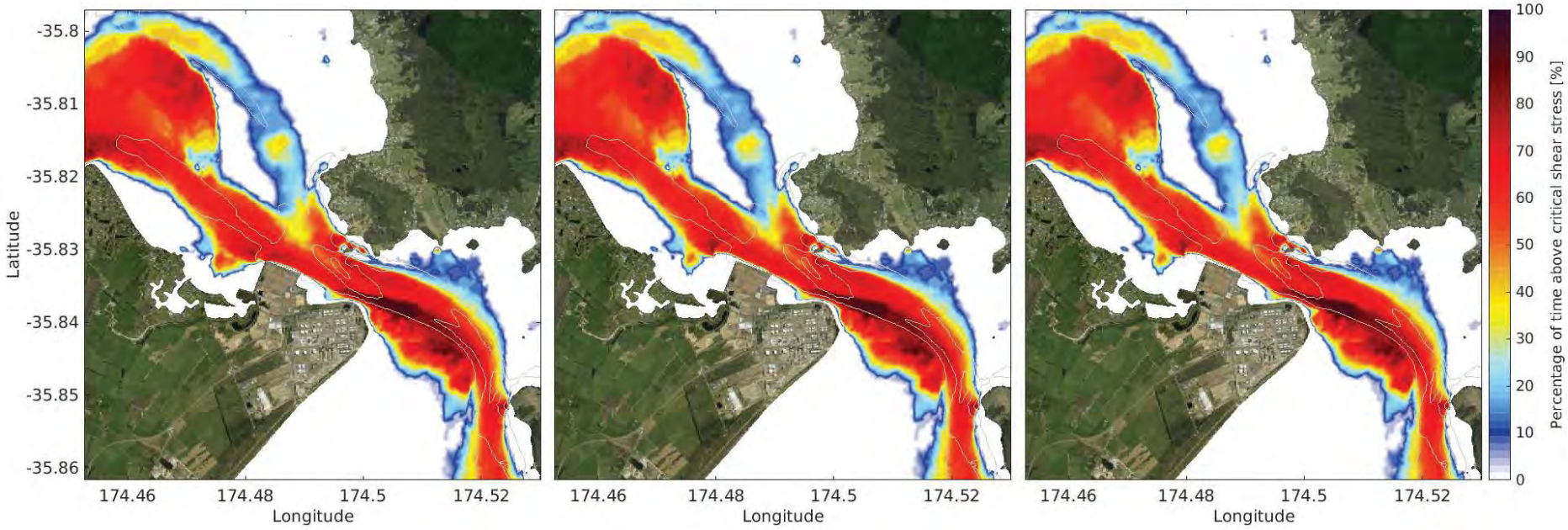

Figure 3.39 Percentage of time the bed shear stress exceeds the critical shear stress threshold for 200 µm sand at ebb tide. Calculated from a 28-day simulation of the existing harbour (left), the Stage 2 harbour configuration (centre) and Stage 2 assuming channel deepening as per the RNZ consent (right).

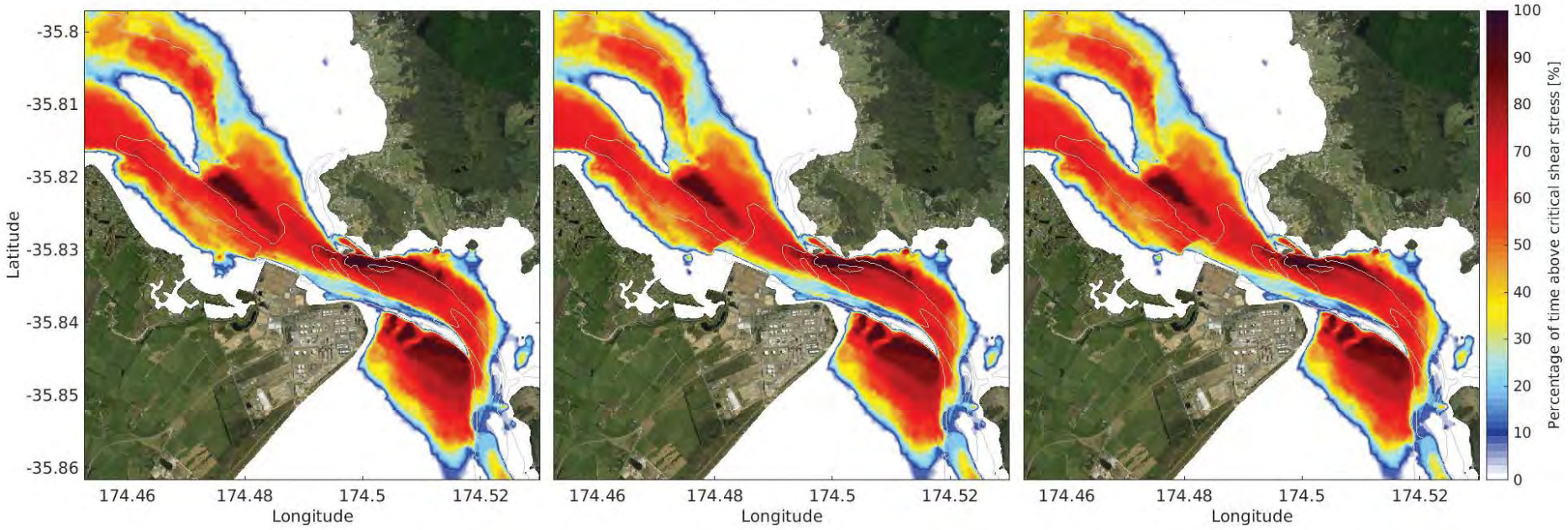

Figure 3.40 Percentage of time the bed shear stress exceeds the critical shear stress threshold for 200 µm sand at flood tide. Calculated from a 28-day simulation of the existing harbour (left), the Stage 2 harbour configuration (centre) and Stage 2 assuming channel deepening as per the RNZ consent (right).

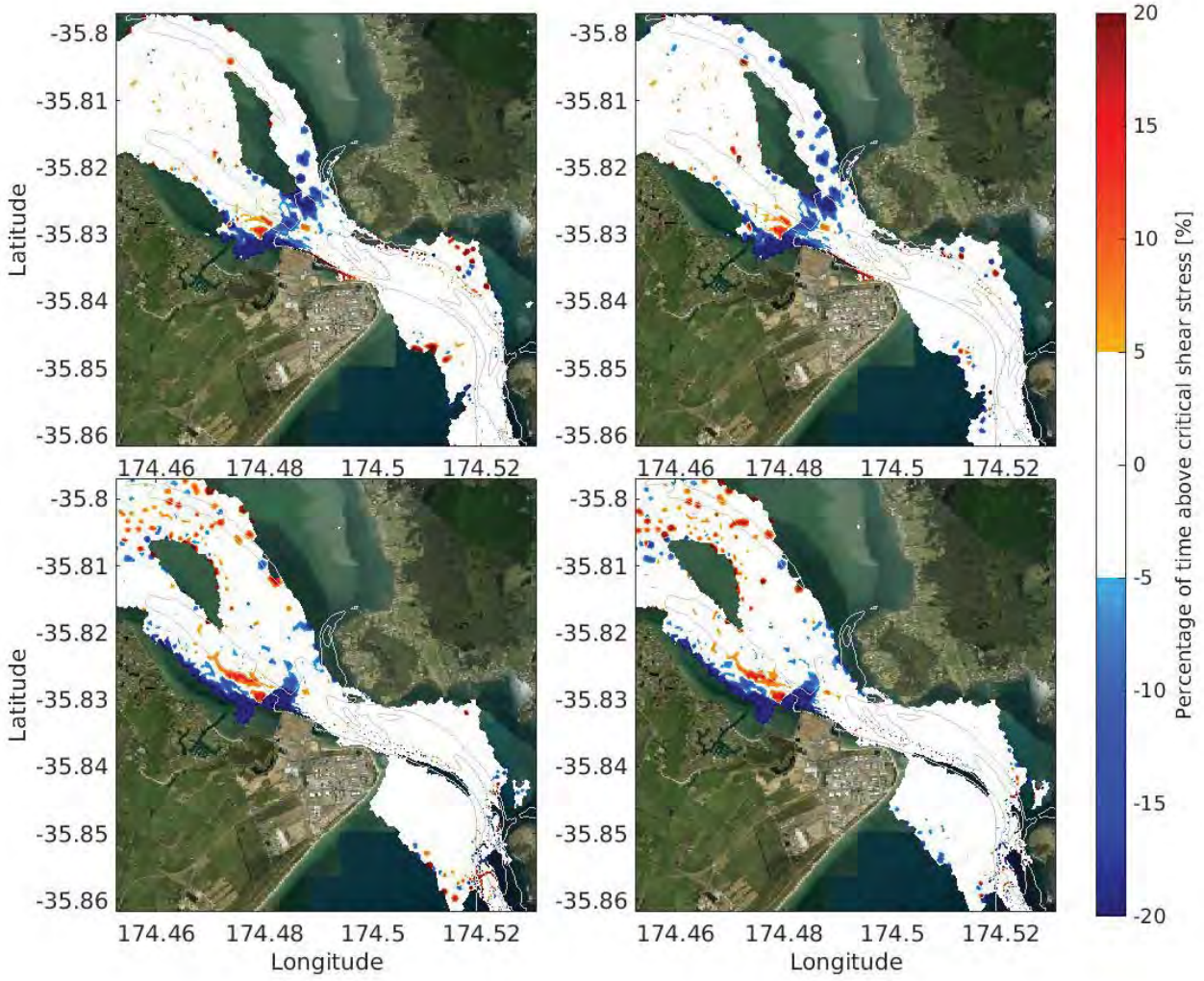

Figure 3.41 Difference of percentage of time the bed shear stress exceeds the critical shear stress threshold for 200 µm sand at ebb (top) and flood (bottom) tidal stages, from a 28-day simulation of the Stage 2 assuming channel deepening as per the RNZ consent (left) and the existing harbour configuration (right).

3.4. Stage 3 hydrodynamics

Stage 3 of the proposed port development consists of reclaiming Areas 4 and 5 as well as dredging Areas 1 and 2 as shown in Figure 1.2 and Figure 2.3.

Hydrodynamic conditions for the Stage 3 harbour configuration and the Stage 3 harbour configuration assuming the granting of the Refining New Zealand channel deepening are presented in Figure 3.42-Figure 3.45 for peak ebb and flood tidal stages under both spring and neap tidal ranges. Current velocities immediately around the port environment are provided in Figure 3.46 for both peak spring ebb and flood conditions, and illustrate the formation of eddies to the east of the port under both ebb and flood conditions. The eddy to the west of the port observed in the Stage 1 bathymetry is no longer present (see Section 3.2). Depth averaged velocity profiles across the harbour along the transect shown in Figure 3.6 for both ebb and flood tidal stages and under neap and spring tidal ranges are provided in Figure 3.47-Figure 3.48.

Only very slight differences are predicted between current velocities for the Stage 3 harbour configuration and the Stage 3 harbour configuration assuming the granting of the Refining New Zealand channel deepening.

As with the existing harbour configuration, the aspect of Whangarei Harbour results in the cross-channel characteristics of the current velocities in the vicinity of NorthPort varying between ebbing and flooding tidal stages.

During spring ebbing tidal stages, current velocities tend to be stronger adjacent to the port berths and within the swinging basin as the harbour drains through the main channel linking the harbour entrance to the inner Whangarei harbour. Conversely, during flooding tidal stages the fastest current velocities are situated on the north side of the harbour cross-section and aligned with the main entrance channel (Figure 3.42, Figure 3.44 and Figure 3.32).

Adjacent to the port berths and within the swinging basin current velocities are expected to peak ~1.0 $m.s^{-1}$ during spring ebbing tides and ~0.8 $m.s^{-1}$ during spring flooding tides (Figure 3.42, and Figure 3.48 respectively). Current velocities during neap flood and ebb tidal conditions are of the order 0.5 $m.s^{-1}$ adjacent to the port berths and within the swinging basin, compared to approximately 0.6 $m.s^{-1}$ on the north side of the harbour adjacent to Motukaroro Island (Figure 1.1) during flooding neap tides (Figure 3.43, Figure 3.45 and Figure 3.47).

Mean residual spring tide current velocities for the existing and Stage 3 harbour configurations are given in Figure 3.49. Areas of low or diverging residual current velocities highlight areas of potential sediment accretion. In general, the effects of completing Stage 3 of the proposal is to align the hydrodynamics more to the existing harbour configuration that either Stage 1 or 2. This is due to the fact that the acceleration of the current velocities due to the confining of the harbour cross-section by the proposed reclamation is balanced by the reduction in velocities through the deeper, dredged areas (i.e. Area 1,2, and 3, Figure 1.2).

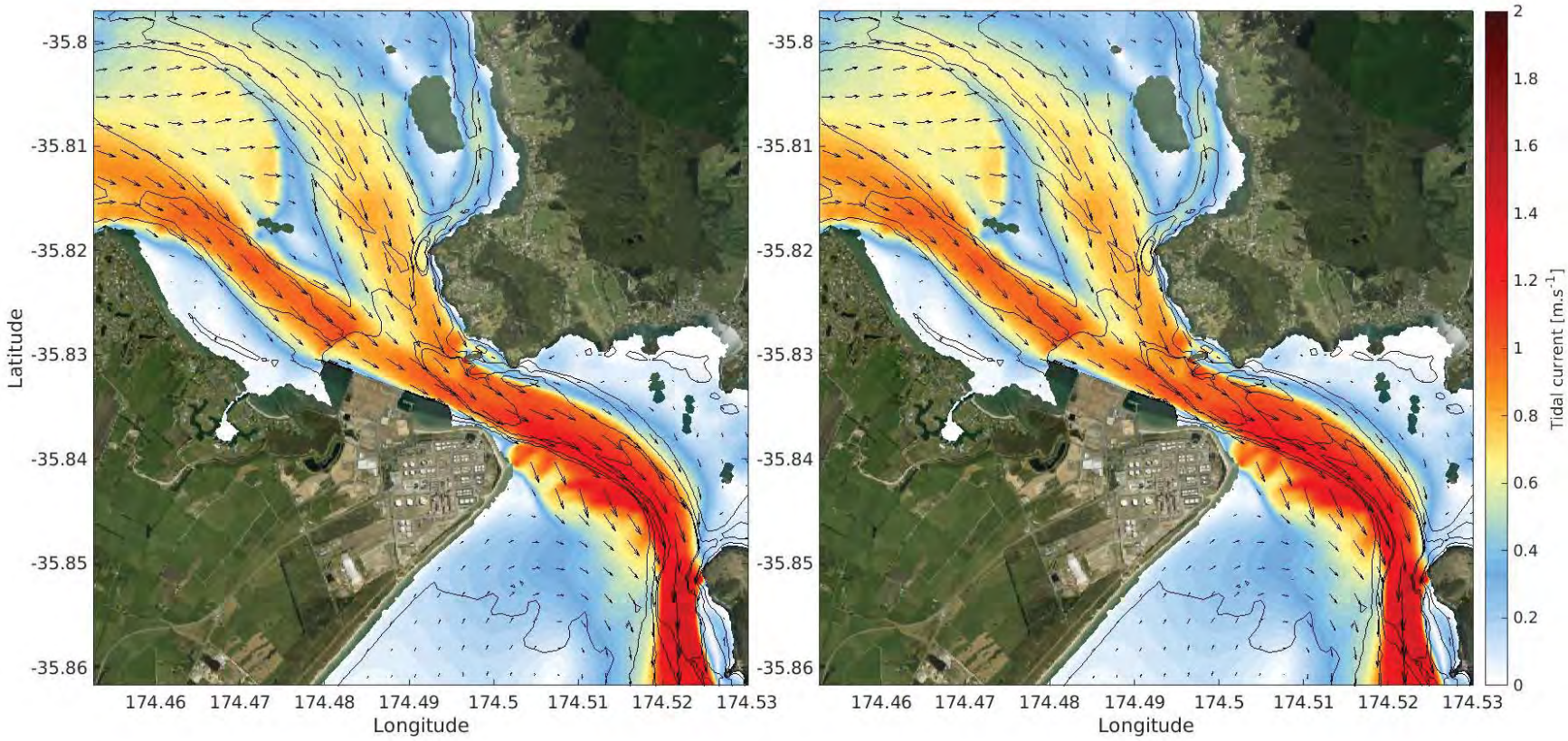

Figure 3.42 Modelled peak ebb flows during spring tide in the vicinity of Northport and Whangarei Harbour entrance for the Stage 3 harbour configuration (right) and Stage 3 assuming channel deepening as per the RNZ consent (left).

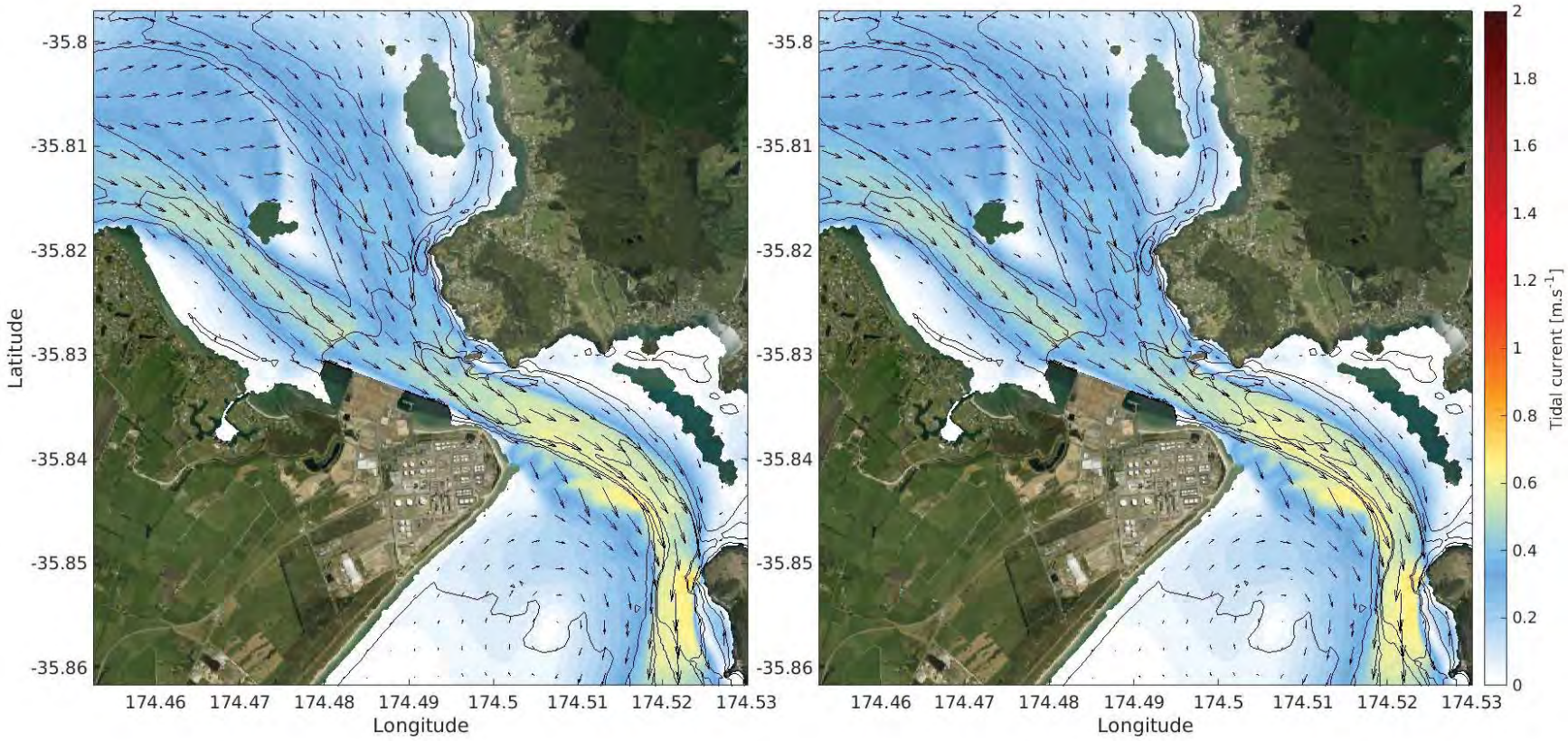

Figure 3.43 Modelled peak ebb flows during neap tide in the vicinity of Northport and Whangarei Harbour entrance for the Stage 3 harbour configuration (right) and Stage 3 configuration assuming channel deepening as per the RNZ consent (left).

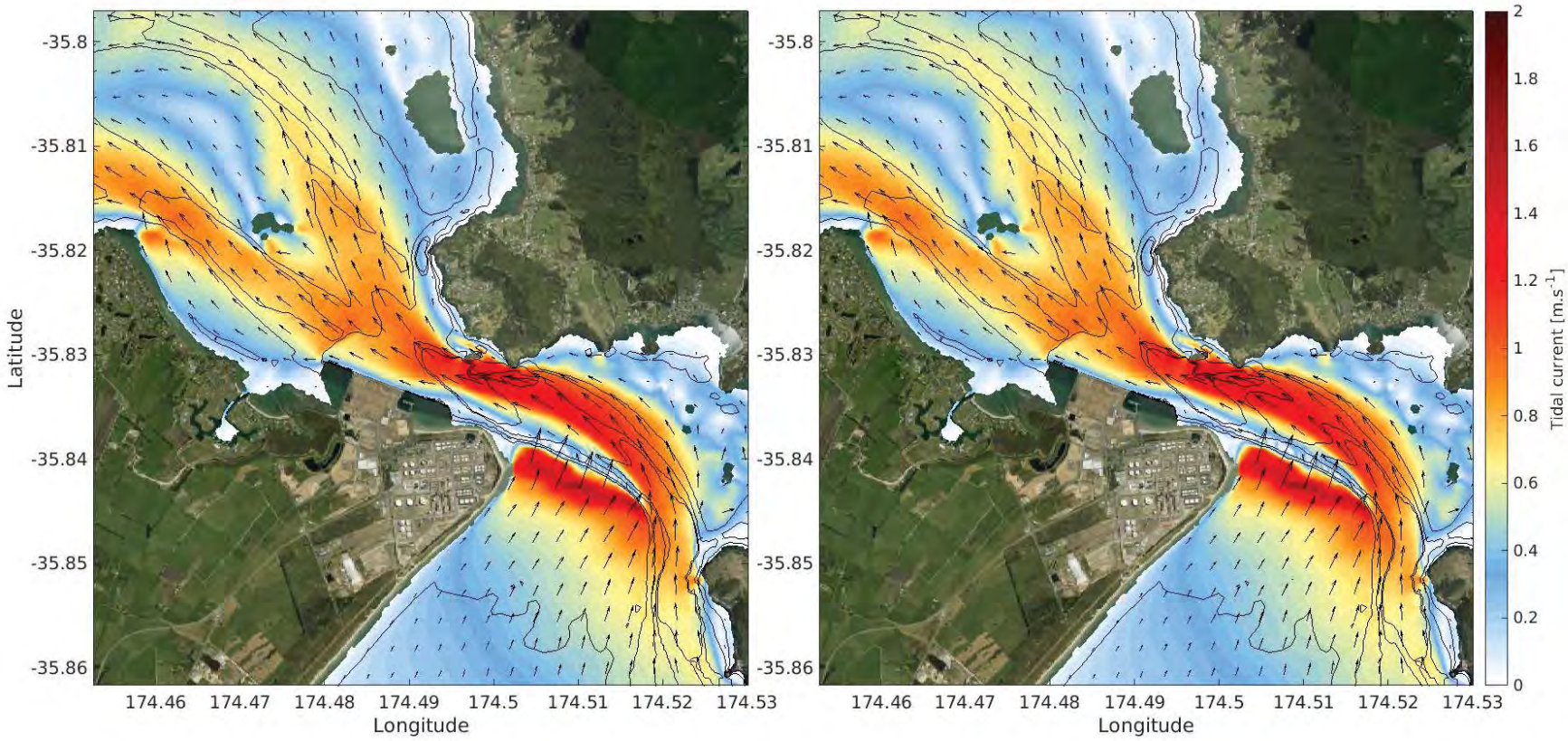

Figure 3.44 Modelled peak flood flows during spring tide in the vicinity of Northport and Whangarei Harbour entrance for the Stage 3 harbour configuration (right) and Stage 3 configuration assuming channel deepening as per the RNZ consent (left).

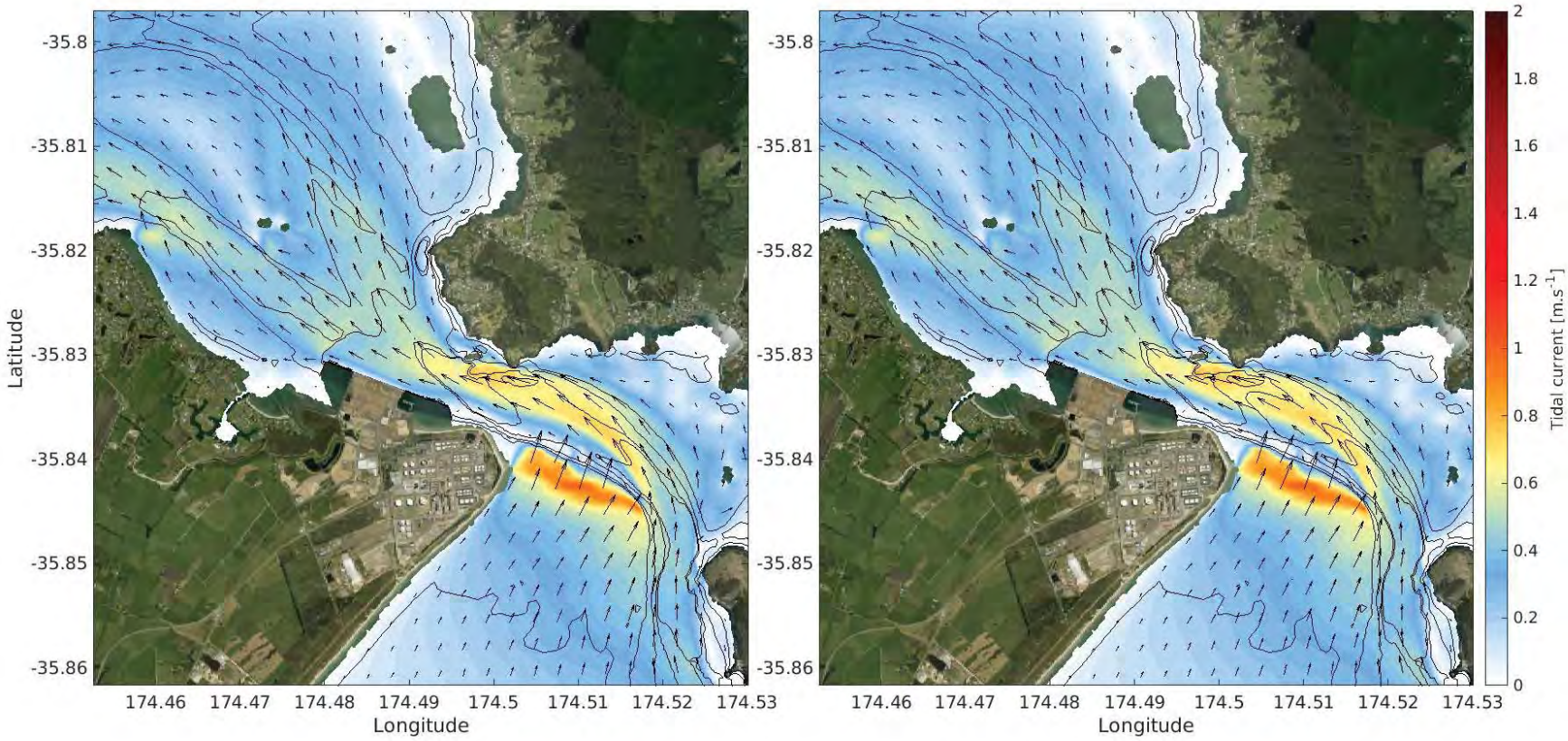

Figure 3.45 Modelled peak flood flows during neap tide in the vicinity of Northport and Whangarei Harbour entrance for the Stage 3 harbour configuration (right) and Stage 3 configuration assuming channel deepening as per the RNZ consent (left).

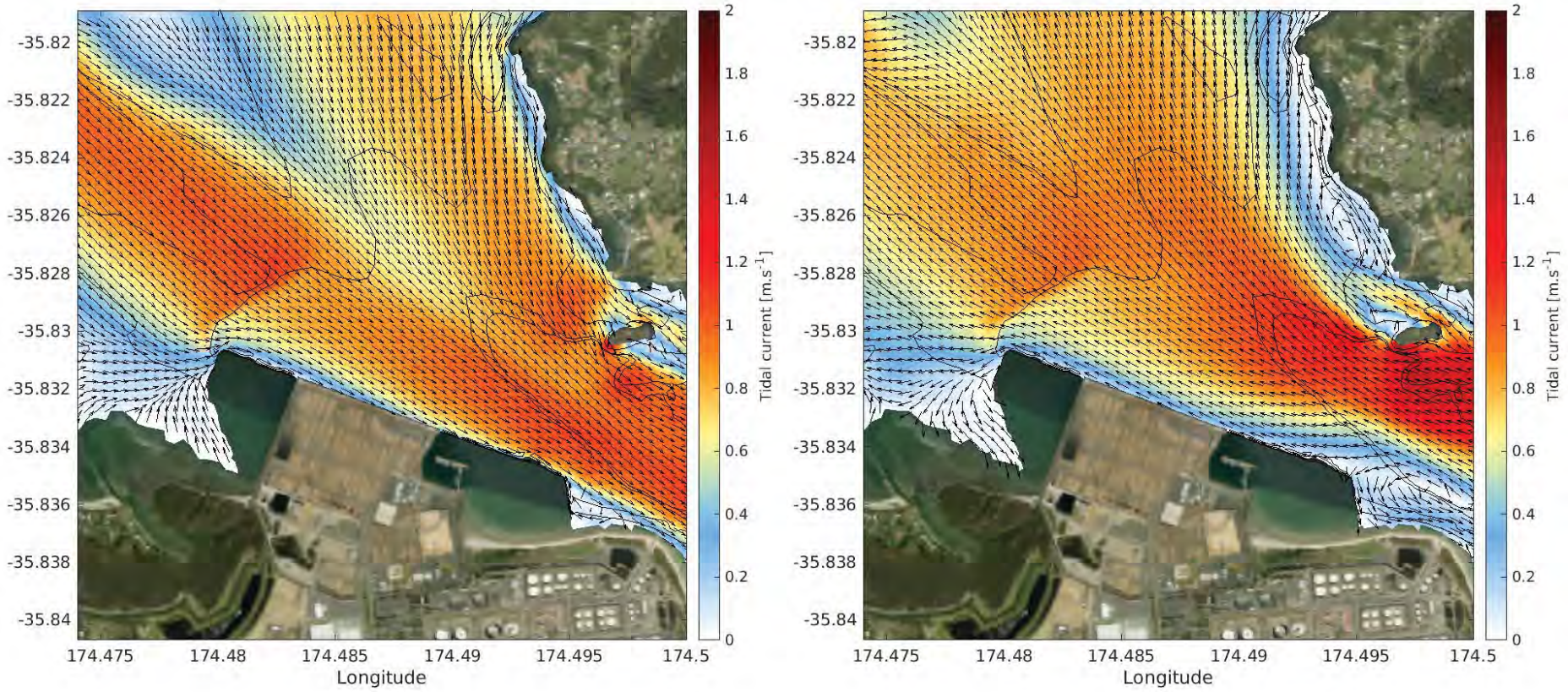

Figure 3.46 Modelled peak ebb (left) and flood (right) flows in the port environs showing formation of back eddies in the lee of the port structures both up and down stream for the Stage 3 bathymetry.

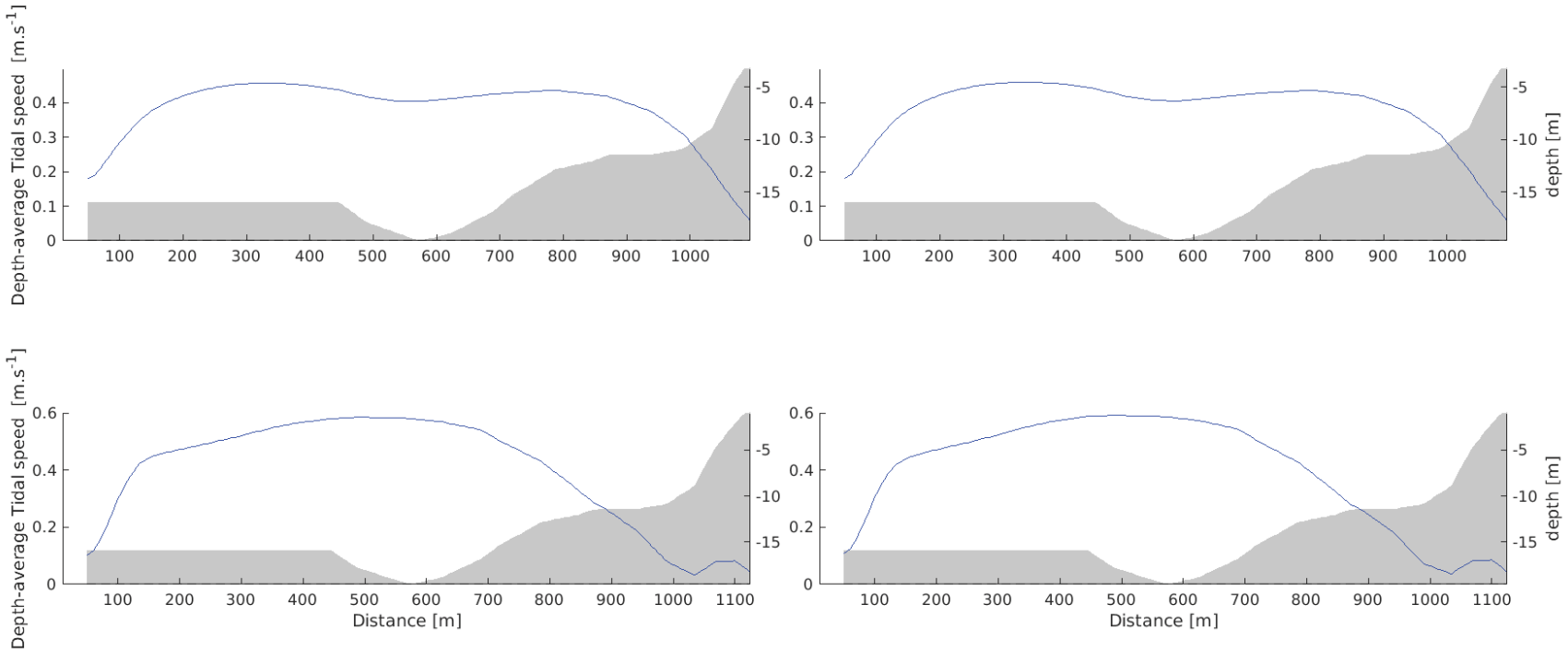

Figure 3.47 Depth averaged current velocity (blue) transects for neap ebb (top) and flood (bottom) tides for the Stage 3 bathymetry (left) and the Stage 3 bathymetry inclusive of the proposed Refining New Zealand channel deepening (right)

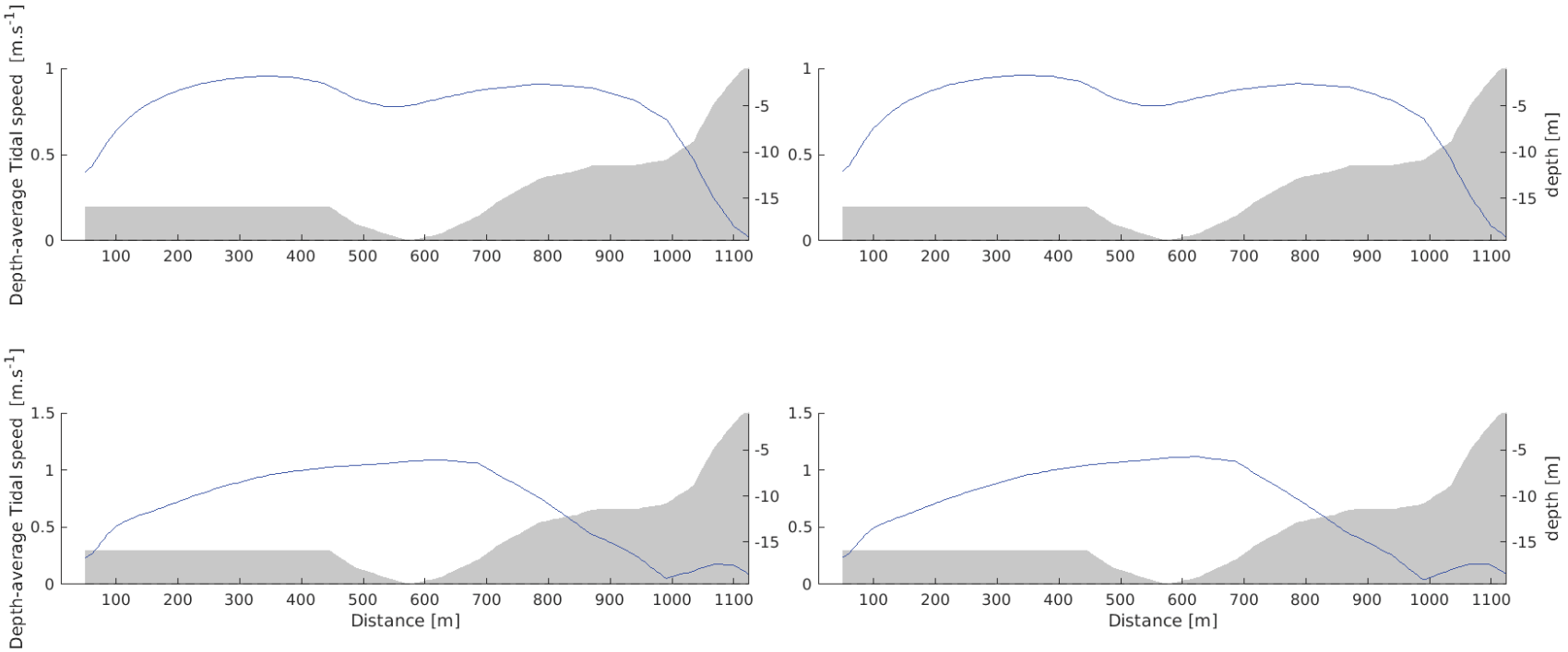

Figure 3.48 Depth averaged current velocity (blue) transects for spring ebb (top) and flood (bottom) tides for the Stage 3 bathymetry (left) and the Stage 3 bathymetry inclusive of the proposed Refining New Zealand channel deepening (right)

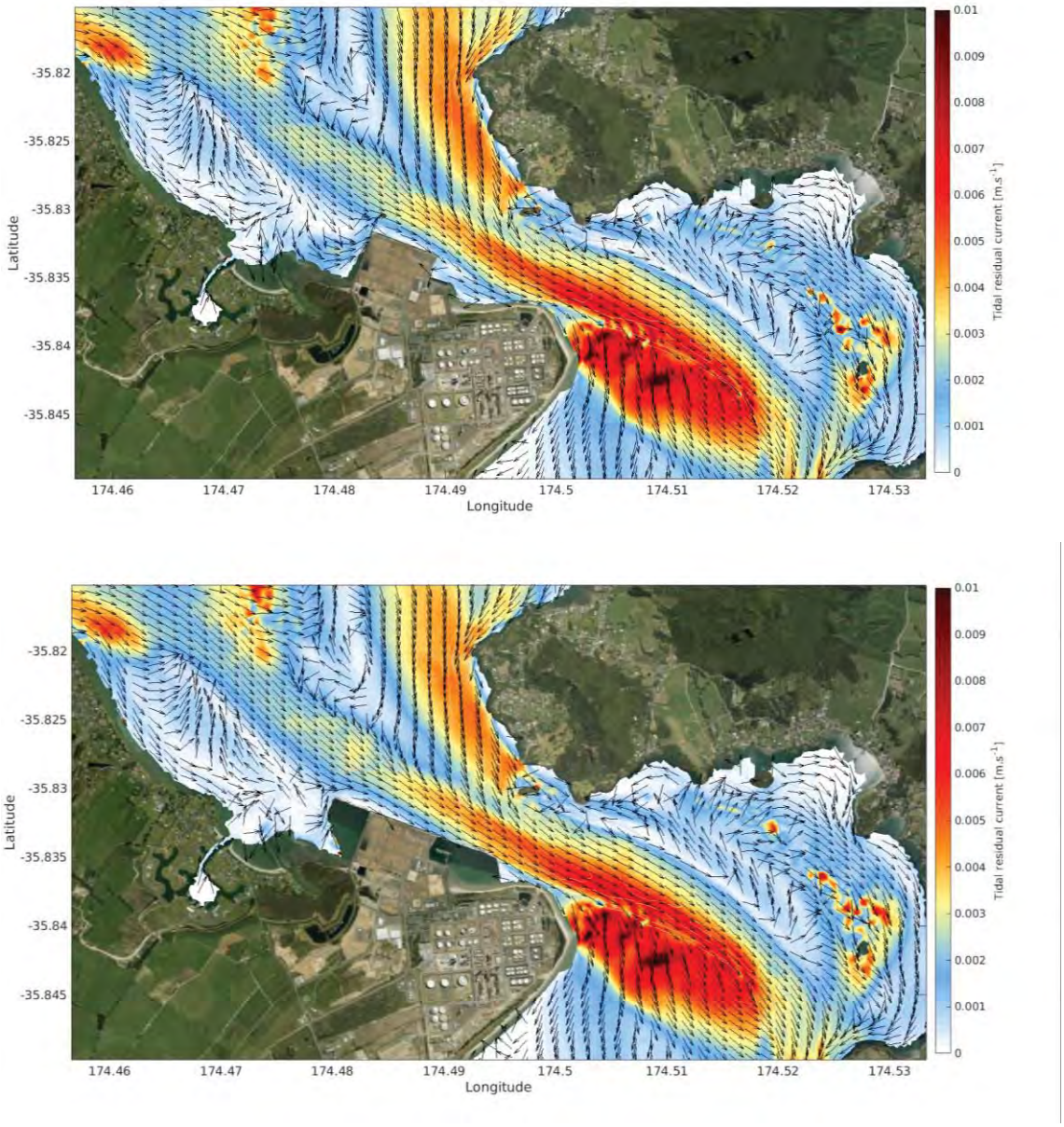

Figure 3.49 Spring tide mean residual tidal current velocity determined over one complete tidal cycle for the existing harbour configuration (top) and Stage 3 bathymetry (bottom).

3.4.1. Stage 3 effect on tidal hydrodynamics

The absolute and relative (i.e. percentage difference) between the existing and Stage 2 hydrodynamics under ebbing and flooding tidal stages for a worst-case spring tidal range are provided in Figure 3.50-Figure 3.51. Absolute and relative differences during neap tidal stages are comparatively smaller than during spring tides. Comparisons are made between the existing harbour configuration and the Stage 3 harbour configuration and between the existing harbour configuration and the Stage 3 harbour configuration assuming the granting of the Refining New Zealand channel deepening. Depth averaged velocity profiles across the harbour along the transect shown in Figure 3.6 for both ebb and flood tidal stages and under neap and spring tidal ranges are provided in Figure 3.52-Figure 3.53.

Only very slight differences are predicted between current velocities for the Stage 3 harbour configuration and the Stage 3 harbour configuration assuming the granting of the Refining New Zealand channel deepening. Further, similar spatial extents, but greater relative effects are observed during spring tidal conditions as opposed to neap tidal conditions (Figure 3.50-Figure 3.51 and Figure 3.52-Figure 3.53), and as such are discussed below.

During peak ebb spring tidal conditions current velocities immediately adjacent to the port berths and out to ~50 m are expected to increase by as much as ~0.10 $m.s^{-1}$ along the transect, while current velocities further north within the main channel and adjacent to Reotahi Bay (Figure 1.1) are expected to remain essentially the same as for the existing harbour configuration (Figure 3.53). Largest predicted current velocity changes are expected immediately within the area to be dredged, with the increased depth resulting in a predicted current velocity decrease of the order 0.15-0.2 $m.s^{-1}$, and a corresponding increase of the order ~0.05 $m.s^{-1}$ immediately to the east of the dredged area (Figure 3.50). Increased current velocities of the order 0.02-0.05 $m.s^{-1}$ are predicted to the west of the port within the main channel south of Motukeroro Island, extending past Refining New Zealand (Figure 3.50); however current velocities in the lee of the reclamations, including at the RNZ berths are predicted to decrease.

During peak flood spring tidal conditions current velocities adjacent to the port berths along the transect (Figure 3.6) are expected to increase by ~0.07 $m.s^{-1}$, but decrease between 20-100 m off the berth by ~0.02-0.05 $m.s^{-1}$. Current velocities in the outer swing basing are expected to increase by a similar order of magnitude (Figure 3.53). Further north adjacent to Reotahi Bay current velocities decrease by ~0.02-0.05 $m.s^{-1}$ due the main flow shifting slightly south to the deeper area. Largest predicted current velocity changes are expected immediately within Area 3 (Figure 1.2), with the increased depth resulting in a predicted current velocity decrease of the order 0.15-0.2 $m.s^{-1}$. Conversely, in dredged Areas 1 and 2 current velocities can be expected to increase by approximately 0.02-0.05 $m.s^{-1}$. Current velocities in the lee of the reclamations, including at the RNZ berths are predicted to decrease (Figure 3.51).

Percentage changes in bed shear stress for both ebb and flood tidal stages under a spring tidal range are given in Figure 3.54. Bed shear stress is a direct measure of the energy that can be transferred from the flowing water to the seabed, and is a useful analogy for potential sediment transport, but needs to be considered in conjunction with the critical shear stress for erosion (i.e. Figure 3.55 and Figure 3.56).

Results show that changes of the order ~20% reduction in the bed shear stress levels are expected within the dredged Areas 1, 2 and 3, while a ~10% increase is

expected immediately outside the dredged areas to both the east and west during ebbing tides. A reduction in the bottom bed shear stress is predicted in the lee of the proposed reclamation and also along the eastern side of One Tree Point and within Marsden Bay during flood tides (Figure 3.54).

With respect the critical shear stress for erosion of the surficial sediment, overall patterns are similar between the existing port configuration, Stage 3 and Stage 3 inclusive of the Refining New Zealand dredged channel (i.e. Figure 3.55 and Figure 3.56), which suggests that while the percentage change in shear stress is relatively large, the absolute changes to the shear stress are not significant enough to fundamentally change the sediment transport patterns and hence morphology of the harbour, though localised morphological changes in the vicinity of the reclamation and dredged areas can be expected.

The expected changes in current velocities associated with the Stage 3 reclamation (Figure 3.50-Figure 3.51) results in changes to the percentage of time the bed shear stress exceeds the critical threshold for entrainment of 200 μm sand (Figure 3.57), with a decrease predicted within Area 3 and parts of Area 1 and 2 (Figure 1.2) and along Marsden Bay to the east of the proposed reclamation under both ebbing and flooding tidal stages. A small increase is also predicted to occur immediately north of Area 2. Minor perturbations are expected at other locations. Similar outcomes are expected for both the Stage 3 bathymetry and Stage 3 assuming the granting of the Refining New Zealand channel deepening consents.

The effects on harbour morphology of the expected changes to the hydrodynamics are addressed in MetOcean Solutions Ltd, (2018).

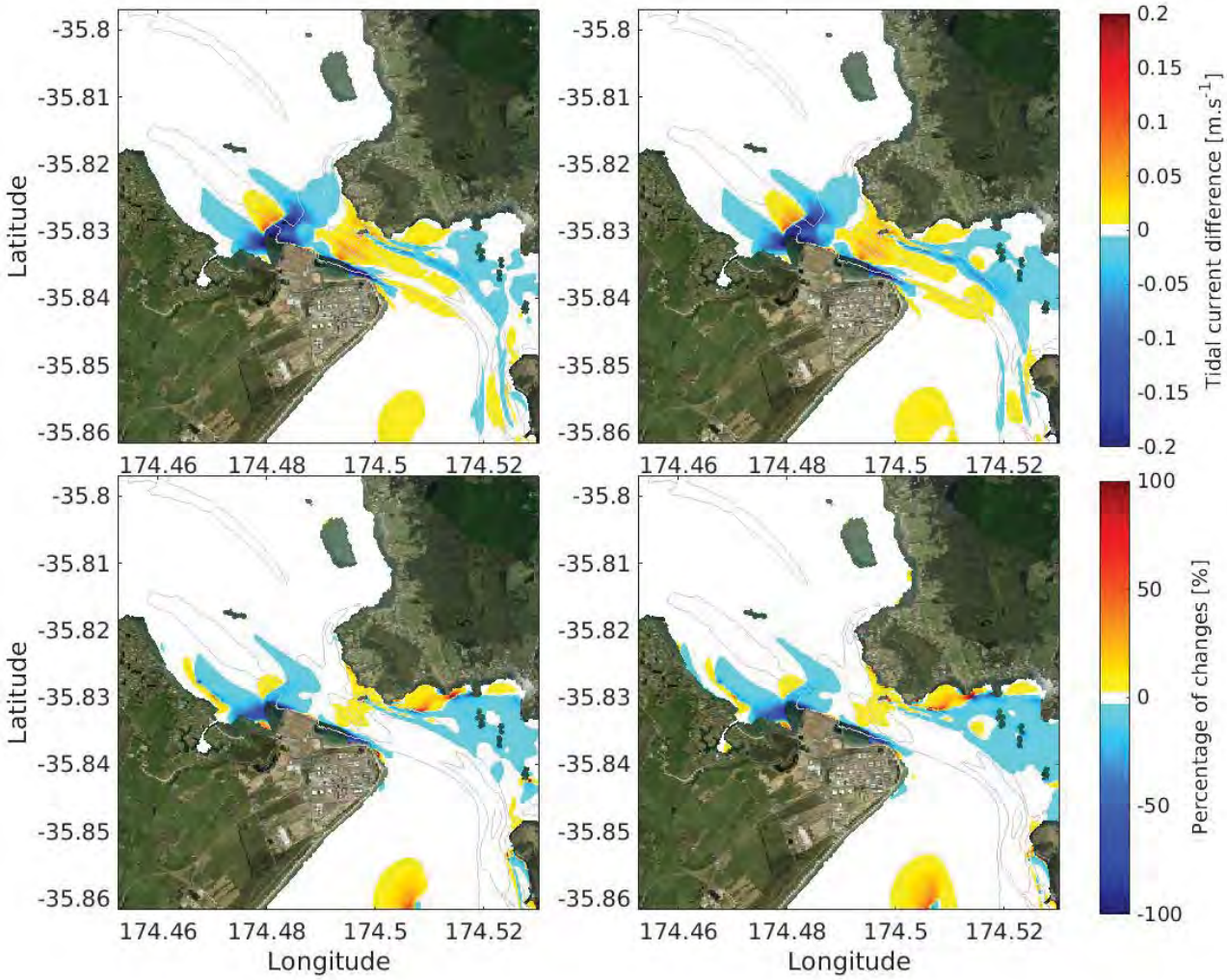

Figure 3.50 Absolute (top) and relative (bottom) difference in peak ebb tidal flows for the Stage 3 harbour configuration (right) and the Stage 3 configuration assuming channel deepening as per the RNZ consent (left). Positive values indicate a predicted increase in flow (red scale), while the negative values indicate a decrease (blue scale).

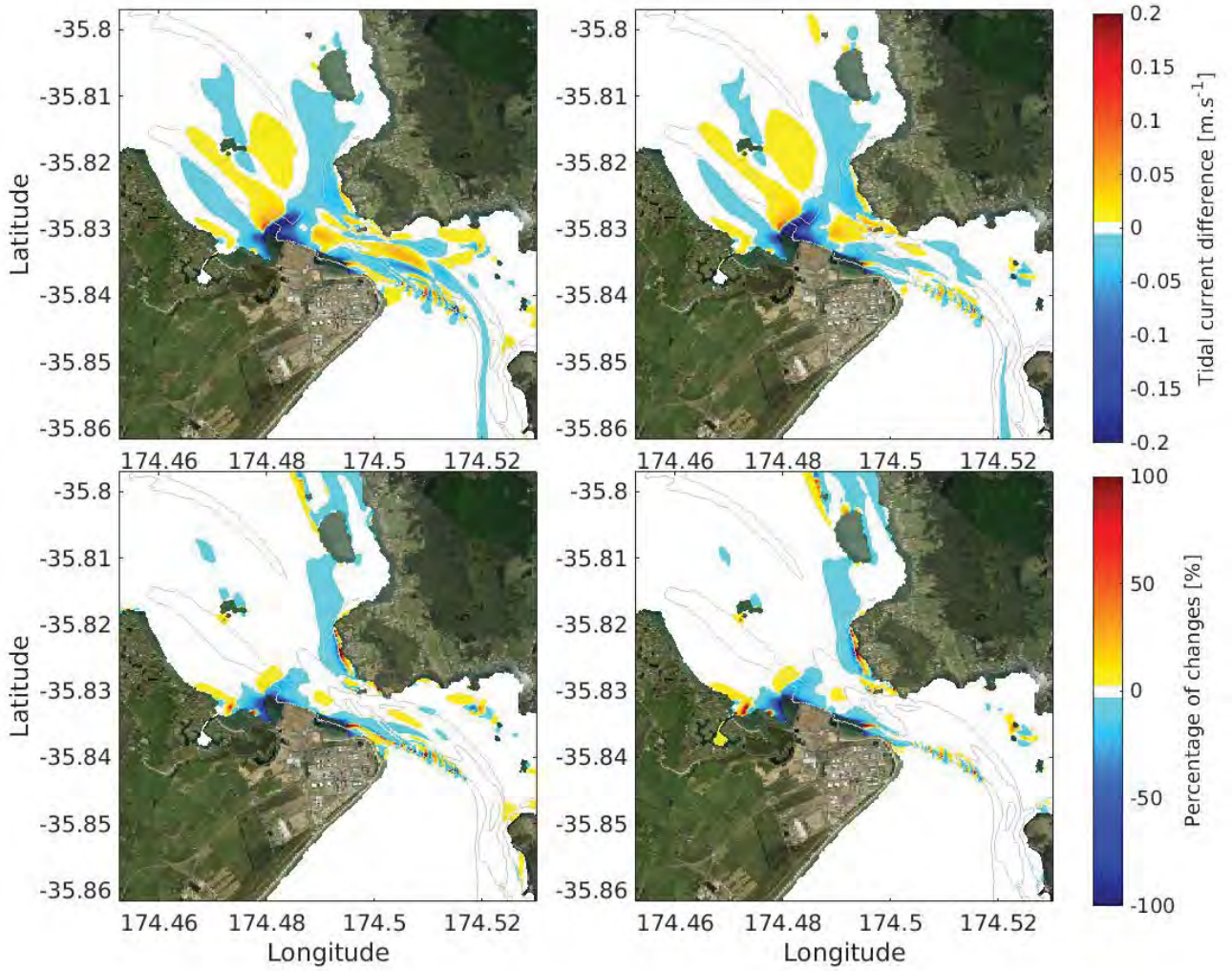

Figure 3.51 Absolute (top) and relative (bottom) difference in peak flood tidal flows for the Stage 3 harbour configuration (right) and Stage 3 configuration assuming channel deepening as per the RNZ consent (left). Positive values indicate a predicted increase in flow (red scale), while the negative values indicate a decrease (blue scale).

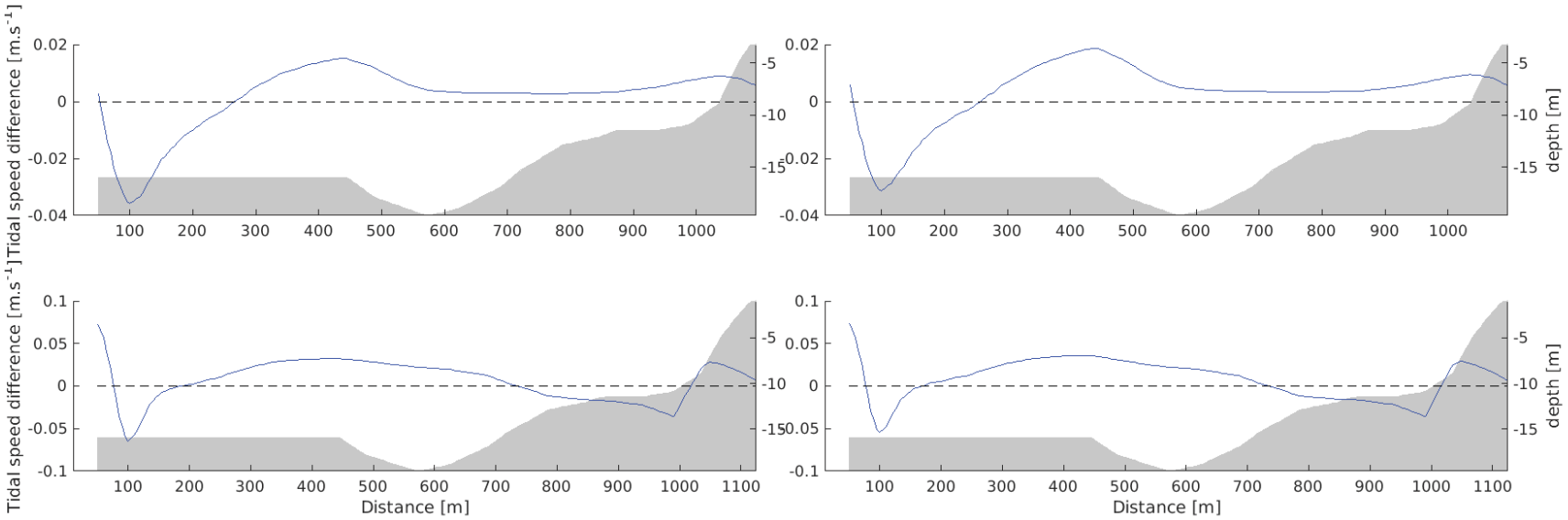

Figure 3.52 Depth averaged current difference (blue) transects for neap ebb (top) and flood (bottom) tides for the Stage 3 bathymetry (left) and Stage 3 bathymetry inclusive of the proposed Refining New Zealand channel deepening (right)

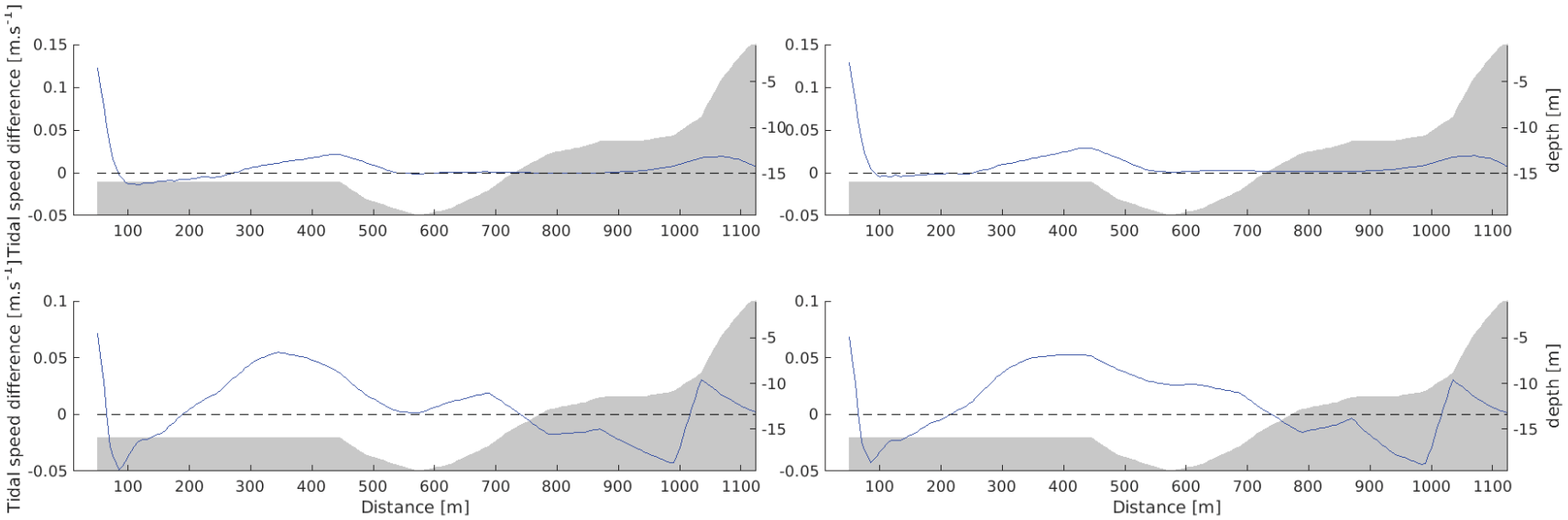

Figure 3.53 Depth averaged current difference (blue) transects for spring ebb (top) and flood (bottom) tides for the Stage 3 bathymetry (left) and Stage 3 bathymetry inclusive of the proposed Refining New Zealand channel deepening (right)

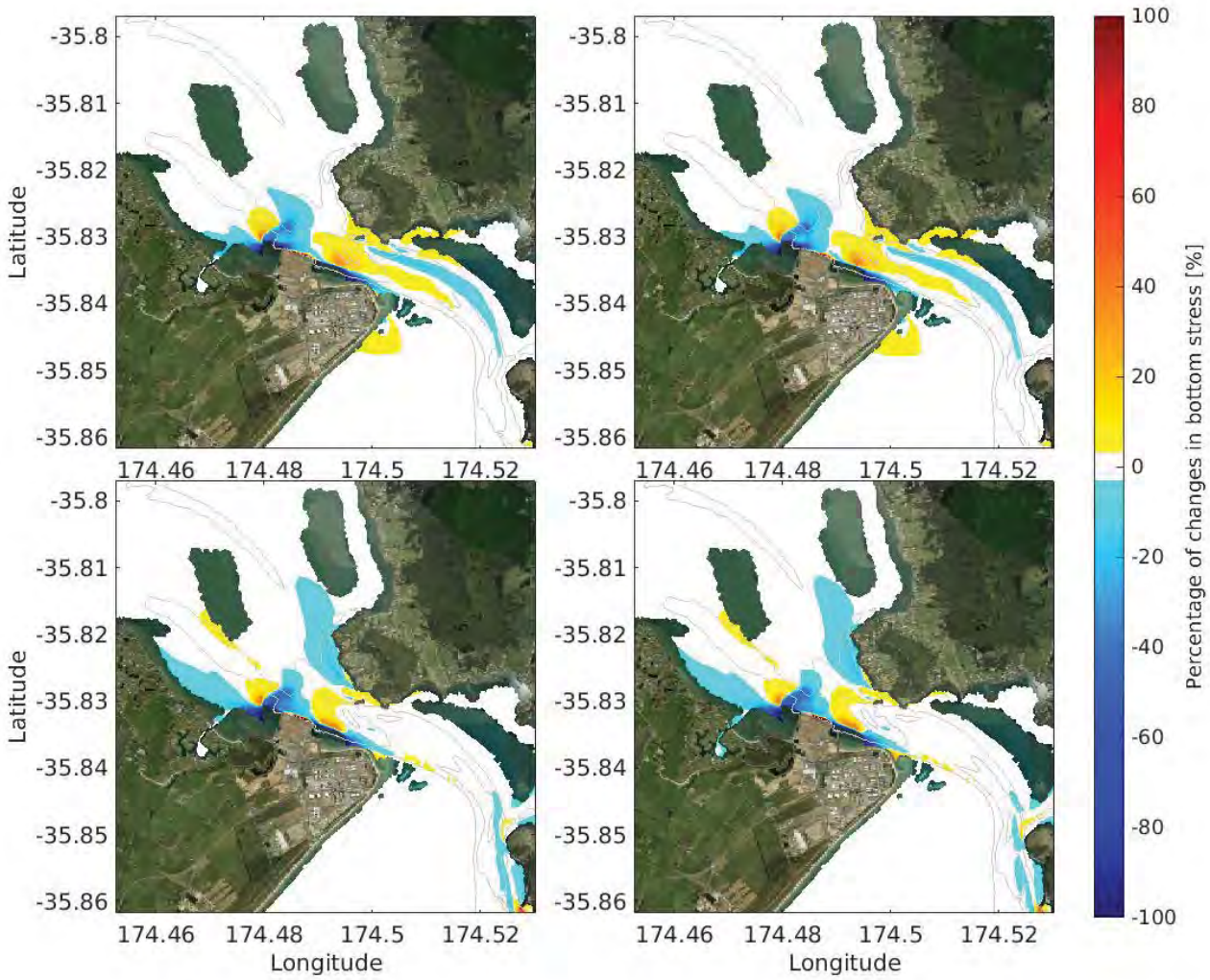

Figure 3.54 Percentage of change in the bed shear stress fields during peak ebb (top) and flood stages (bottom) between the existing Stage 3 harbour configuration (right) and Stage 3 assuming channel deepening as per the RNZ consent (left).

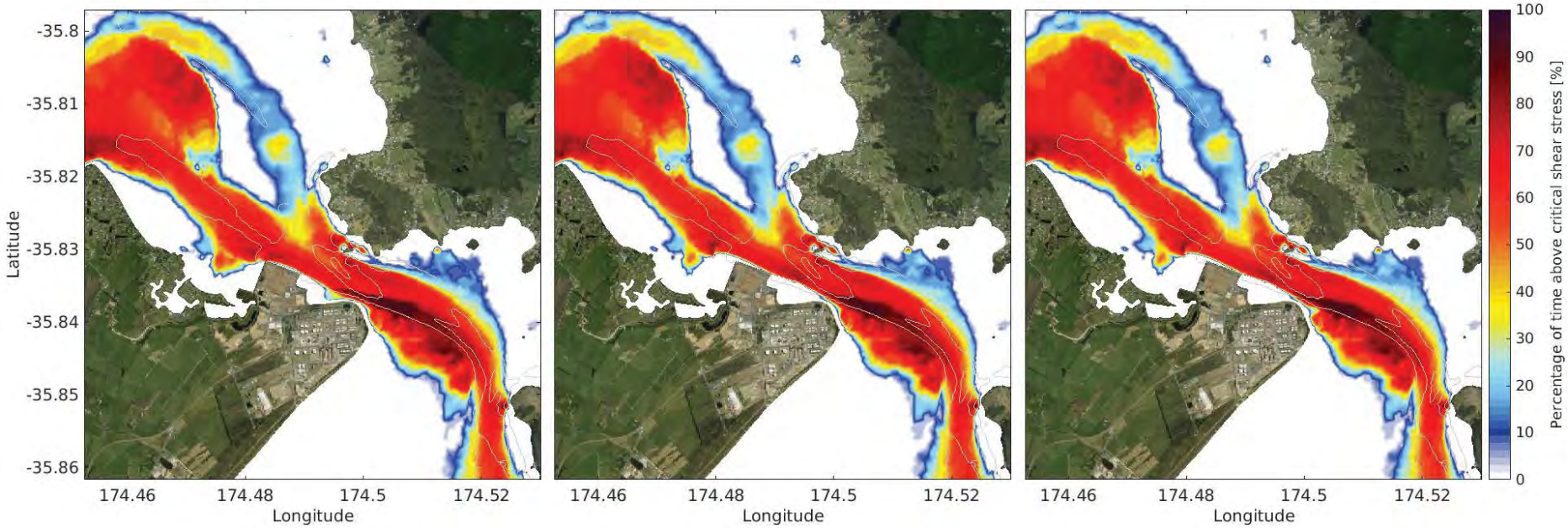

Figure 3.55 Percentage of time the bed shear stress exceeds the critical shear stress threshold for 200 µm sand at ebb tide. Calculated from a 28-day simulation of the existing harbour (left), the existing Stage 3 harbour configuration (centre) and Stage 3 assuming channel deepening as per the RNZ consent (right).

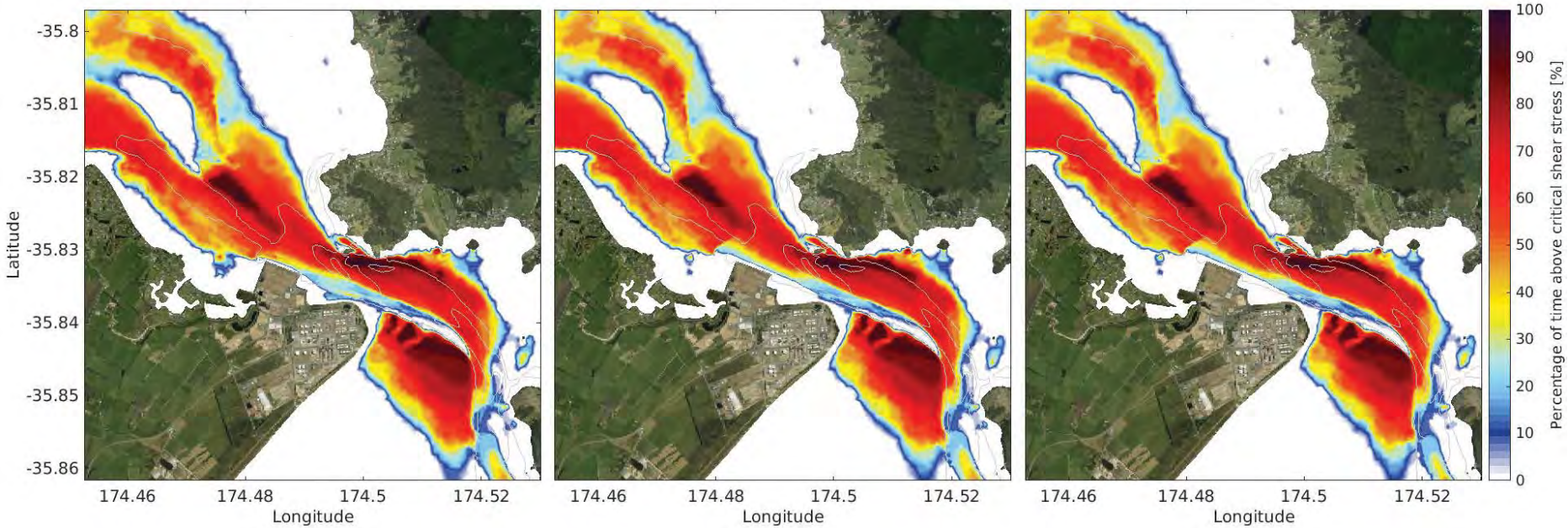

Figure 3.56 Percentage of time the bed shear stress exceeds the critical shear stress threshold for 200 µm sand at flood tide. Calculated from a 28-day simulation of the existing harbour (left), the existing Stage 3 harbour configuration (centre) and Stage 3 assuming channel deepening as per the RNZ consent (right).

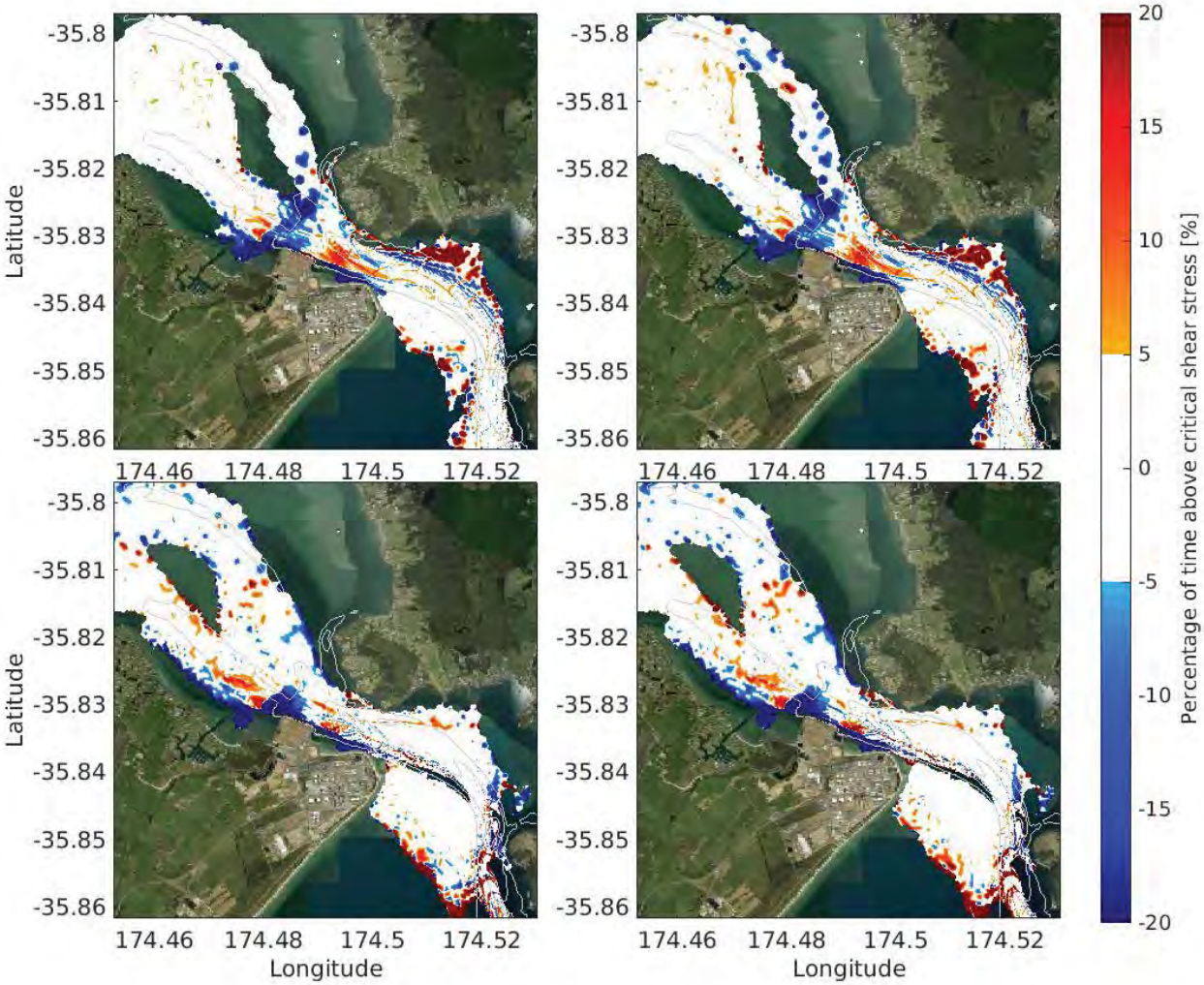

Figure 3.57 Difference of percentage of time the bed shear stress exceeds the critical shear stress threshold for 200 µm sand at ebb (top) and flood (bottom) tidal stages, from a 28-day simulation of the Stage 3 assuming channel deepening as per the RNZ consent (left) and the existing harbour configuration (right).

4. SUMMARY

Hydrodynamic models of the existing, Stage 1, 2 and 3 harbour configurations have been undertaken in order to determine the effects of the proposed capital dredging and reclamation on the Whangarei Harbour. The relative effects of the three stages proposed by NorthPort (Stage 1, 2 and 3) have been compared with both the existing bathymetry and the bathymetry of the harbour assuming the proposed Refining New Zealand channel deepening Resource Consent is granted.

The three stages being considered include;

1. Area 6 (less 50m along northern edge) to be reclaimed (Stage 1)

2. Area 6 including northern edge constructed, plus Area 3 dredged (Stage 2)

3. Balance of Areas 4 & 5 constructed, as well as Ares 1 & 2 dredged to 14.5m below CD (Stage 3).

The spatial coverage of the different areas are provided in in Figure 1.2.

Only very slight differences are predicted between current velocities for the different Stages and for the different Stages assuming the granting of the Refining New Zealand channel deepening consent.

In general, modifications to the current velocities are localised to the area where the capital works are proposed, and interestingly the scale of effects of the proposed capital works on the harbour hydrodynamics reduces from Stage 1 through to Stage 3 (e.g. Figure 3.18, Figure 3.34 and Figure 3.50 for Stage 1, 2 and 3 respectively). This is due the reclamations acting to confine the water between a longer, narrower throat in the harbour, which acts to increase the current velocities, being balanced by the increased depth due to dredging causing a reduction in current velocity.

Summary details in bullet point of the effect of each stage on the harbour hydrodynamics are provided in the following sections.

The effects on harbour morphology of the expected changes to the hydrodynamics for each of the proposed stages is addressed in MetOcean Solutions Ltd, (2018).

4.1. Stage 1

- During peak spring ebb tidal conditions, current velocities are expected to decrease by as much as ~0.15 $m.s^{-1}$ adjacent to the port berths.

- During ebb tidal conditions, slightly increased current velocities of the order 0.01 $m.s^{-1}$ are expected along the eastern side of One Tree Point and around the western headland of Marsden Bay

- During peak spring flood tidal conditions, current velocities are expected to decrease by as much as ~0.01 $m.s^{-1}$ within ~500-600 of the port berths

- During peak spring flood tidal conditions, slightly decreased current velocities of the order 0.02-0.05 $m.s^{-1}$ are expected along the eastern side of One Tree Point and around the western headland of Marsden Bay.

- During peak spring flood tidal conditions, the formation of an eddy upstream of the proposed reclamation results in increased current velocities within Marsden Bay (of the order 0.05-0.1 $m.s^{-1}$).

- Changes of the order ~10% in the bed shear stress levels are expected over Snake Bank during ebbing tides and over both Snake Bank and the main channel to the west of NorthPort during flooding tides

- A reduction in the bottom bed shear stress is predicted in the lee of the proposed reclamation and also along the eastern side of One Tree Point and within Marsden Bay

- The absolute changes to the shear stress between the existing harbour configuration and the Stage 1 configuration are not significant enough to fundamentally change the sediment transport patterns and hence morphology of the harbour, though localised morphological changes in the vicinity of the reclamation may occur.

- Increases in the percent of time the critical threshold for entrainment of 200 μm sand is exceeded are predicted to the east of the proposed reclamation along the channel, while decreases are expected in the immediate lee of the reclamation during both ebbing and flooding tidal stages.

4.2. Stage 2

- During peak spring ebb tidal conditions, current velocities immediately adjacent to the port berths and out to ~100 m are expected to increase by as much as ~0.15 $m.s^{-1}$.

- During peak spring ebb tidal conditions, the increased dredged depth within Area 3 results in a predicted current velocity decrease of the order 0.15-0.2 $m.s^{-1}$ within the area to be dredged.

- During peak spring ebb tidal conditions, increases of the order 0.05 $m.s^{-1}$ in current velocities are expected immediately to the east of the dredged area.

- During peak spring flood tidal conditions, velocities adjacent to the port berths and out to ~100 m from the berth are expected to decrease by ~0.01-0.02 $m.s^{-1}$.

- During peak spring flood tidal conditions, largest predicted current velocity changes are expected immediately within the area to be dredged, with the increased depth resulting in a predicted current velocity decrease of the order 0.15-0.2 $m.s^{-1}$.

- During peak spring flood tidal conditions, current velocities to the east of the dredged area are expected to increase by ~0.05 $m.s^{-1}$.

- Changes of the order ~20% reduction in the bed shear stress levels are expected within the dredged Area 3, while a ~10% increase is expected immediately outside the dredged areas to both the east and west during ebbing tides.

- A reduction in the bottom bed shear stress is predicted in the lee of the proposed reclamation and also along the eastern side of One Tree Point and within Marsden Bay during flood tides.

- The absolute changes to the shear stress between the existing harbour configuration and the Stage 2 configuration are not significant enough to fundamentally change the sediment transport patterns and hence morphology of the harbour, though localised morphological changes in the vicinity of the reclamation are expected.

- Decreased in the percent of time the critical threshold for entrainment of 200 μm sand is exceeded are predicted within the area to be dredged and along Marsden Bay to the east of the proposed reclamation under both ebbing and flooding tidal stages.

4.3. Stage 3

- During peak spring ebb tidal conditions, current velocities immediately adjacent to the port berths and out to ~50 m are expected to increase by as much as ~0.10 $m.s^{-1}$.

- During peak spring ebb tidal conditions, the increased dredged depth within Areas 1, 2 and 3 results in a predicted current velocity decrease of the order 0.15-0.2 $m.s^{-1}$ within the area to be dredged

- During peak spring ebb tidal conditions, increases of the order 0.05 $m.s^{-1}$ in current velocities are expected immediately to the east of the dredged area.

- During peak spring ebb tidal conditions, increases of the order 0.02-0.05 $m.s^{-1}$ in current velocities are expected to the west of the port within the main channel south of Motukeroro Island, extending past Refining New Zealand.

- During peak spring ebb tidal conditions, current velocities in the lee of the reclamations, including at the RNZ berths are predicted to decrease.

- During peak flood spring tidal conditions, current velocities immediately adjacent to the port berths are expected to increase by ~0.07 $m.s^{-1}$, but decrease between 20-100 m off the berth by ~0.02-0.05 $m.s^{-1}$.

- During peak flood spring tidal conditions, the increased dredged depth within Areas 3 results in a current velocity decrease of the order 0.15-0.2 $m.s^{-1}$. Conversely, in dredged Areas 1 and 2 current velocities can be expected to increase by approximately 0.02-0.05 $m.s^{-1}$.

- During peak flood spring tidal conditions, current velocities in the lee of the reclamations, including at the RNZ berths are predicted to decrease slightly (~0.05 $m.s^{-1}$).

- Changes of the order ~20% reduction in the bed shear stress levels are expected within the dredged Area 1, 2 and 3, while a ~10% increase is expected immediately outside the dredged areas to both the east and west during ebbing tides.

- A reduction in the bottom bed shear stress is predicted in the lee of the proposed reclamation and also along the eastern side of One Tree Point and within Marsden Bay during flood tides

- The absolute changes to the shear stress between the existing harbour configuration and the Stage 3 configuration are not significant enough to fundamentally change the sediment transport patterns and hence morphology of the harbour, though localised morphological changes in the vicinity of the reclamation are expected.

- Decreased in the percent of time the critical threshold for entrainment of 200 μm sand is exceeded are predicted within Area 3 and parts of Area 1 and 2 and along Marsden Bay to the east of the proposed reclamation under both ebbing and flooding tidal stages.

REFERENCES

Dodet, G., 2013. Morphodynamic modelling of a wave-dominated tidal inlet: the Albufeira lagoon. La Rochelle.

Egbert, G.D., Erofeeva, S.Y., 2002. Efficient inverse modeling of barotropic ocean tides. J. Atmospheric Ocean. Technol. 19, 183–204.

MetOcean Solutions Ltd, 2018. Predicted morphological response to proposed capital dredging and reclamation - Wharangai Harbour. A report prepared for NorthPort (No. P0367- 03).

MetOcean Solutions Ltd, 2017. Crude Shipping Project, Whangarei Harbour. Establishment of numerical models of wind, wave, current and sediment dynamics. (Technical report P0297-01 prepared for Chancery Green for Refining NZ, published on February 2017.).

Van Rijn, L.J., 1993. Principles of sediment transport in rivers, estuaries and coastal seas. Aqua Publications, Amsterdam, Netherlands.

Zhang, Y.L., Baptista, A.M., 2008. A semi-implicit Eulerian-Lagrangian finite element model for cross-scale ocean circulation. Ocean Model. 21, 71–96.

MetOcean Solutions

MORPHODYNAMIC EVOLUTION MODELLING FOR THE NORTHPORT ENVIRONMENT

Predicted morphological response to proposed capital dredging and land reclamation

Report prepared for Northport

Northport

Specialists in Oceanography

MetOcean Solutions Ltd: Report P0367 – 03

April 2018

Report status

Version	Date	Status	Approved by
RevA	10/04/2018	Draft for internal review	Monetti
RevB	13/04/2018	Draft for internal review	Beamsley
RevC	13/04/2018	Draft for client review	Monetti

It is the responsibility of the reader to verify the currency of the version number of this report.

TABLE OF CONTENTS

LIST OF FIGURES

LIST OF TABLES

1. INTRODUCTION

Northport is a deep-water commercial port strategically situated at Marsden Point near Whangarei in Northland, New Zealand. Northport is New Zealand's newest port, designed and built as a flexible, multi-purpose facility to cater for a wide range of cargoes and their associated vessel types.

Northport's current footprint totals 48.46 hectares, made up of 570 linear metres of berthage consisting of three berths, 33.615 hectares of reclamation and 14.845 metres of berth with a depth at Chart Datum (CD) of 14.5 m and 2.3 hectares of reclamation providing for a total consented footprint of 840 linear meters (4 berths) and 50.76 hectares. Historical hydrographic surveys of the swinging basin have highlighted the fact that infilling is occurring over time, and there is a requirement to understand future infilling rates from a maintenance and operability perspective.

Further, Ports strategic planning has identified potential for the facilities to expand up to 250 metres and include a 13.0-hectare reclamation westward, with the entire berth length cut to 14.5 m CD, with 700 metres capable of a depth up to 16 m CD (Figure 1.2).

To protect and ensure the port's ability to expand as the market or NZ port strategy demands, the opportunity to undertake the consent application for the remaining potential reclamation footprint is currently being considered. While at the early stages, Northport feel that the timing is right to start to undertake the first steps towards securing the required port growth.

Northport recognise that there is scope to reclaim areas to both the east and west of the current reclaimed facility (Areas 5 and 6, Figure 1.2). To undertake these capital works, there are a suite resource consents that will be required, including dredging (see Figure 1.3), earthworks, discharges to the harbour as well as ongoing land use type consents and discharge consents. Dredging areas and estimated volume to be dredged are given in Figure 1.2 (Areas 1-3), with a total of approximately 973,000 m^3 expected to be dredged (Capital Dredging). This sediment is intended to be used to provide clean fill to the areas being reclaimed (Figure 1.2); mitigating the need to dispose of sediment at an offshore site. The proposed port development has been broken into 3 stages (Stage 1-3), consisting of;

1. Area 6 (less 50m along northern edge) to be reclaimed (Stage 1)

2. Area 6 including northern edge constructed, plus Area 3 dredged (Stage 2)

3. Balance of Areas 4 & 5 constructed, as well as Areas 1 & 2 dredged to 14.5m below CD (Stage 3).

It is likely that Capital dredging will also be undertaken using a TSHD given the sediment, however a Backhoe Dredger (BHD) or Cutter Suction Dredge (CSD) may be used.

From an operational and consenting perspective, Northport require an understanding of the effects of longer term sedimentation within the swinging basin and potential wider morphological responses to the proposed capital dredging and reclamations – this is achieved through the application of a calibrated and validated morphological model (i.e. Delft3D). Qualitative and quantitative calibration of Delft3D has been previously undertaken for the NorthPort region through the

comparison of morphological model outputs against hydrographic survey data (MetOcean Solutions Ltd., 2018a).

In the present study, the calibrated numerical model is used to assess the likely morphological response to the proposed dredging and land reclamation programs at Northport. The present report is a technical reference that characterises the existing environment and investigates the likely morphological effects of the different stages of the project. Details of the modelling configuration and application are provided in MetOcean Solutions Ltd., (2018a).

The report is structured as follows; the methodology applied in this study is detailed in Section 2, including a description of the different scenarios simulated. Results are discussed in Section 3, while a brief summary is presented in Section 4. References cited in this document are listed in Section 5.

Figure 1.1 Location of Northport within Whangarei Harbour.

Figure 1.2 Draft plan of areas proposed to be reclaimed (greed) and dredged (light blue).

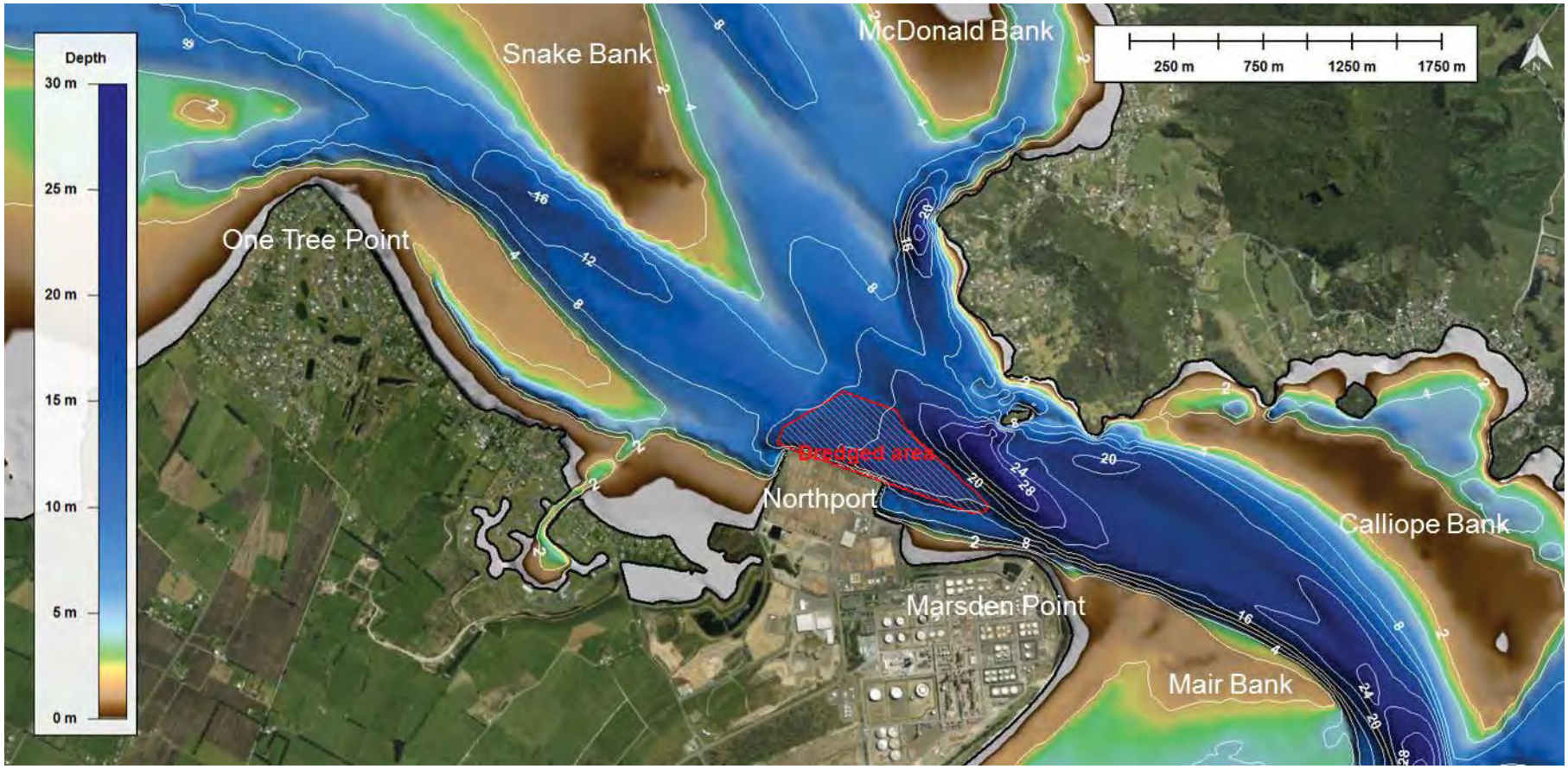

Figure 1.3 Location of Northport near the entrance to Whangarei Harbour. The colour scale details the bathymetry (MSL) derived from multiple data sources. Key locations and the dredged area corresponding to the swinging basin are also indicated on the map.

2. METHODS

The primary objective of the study was to understand the likely morphological response of the existing environment to the proposed capital dredging and land reclamation programs. To achieve this objective, morphological modelling of each of the proposed development stages was undertaken using a calibrated and validated Delft3D configuration (see MetOcean Solutions Ltd., 2018a). The model methodology applied an input reduction technique combined with morphological acceleration factors to examine medium-term sediment dynamics and morphological response within the Whangarei Harbour.

The following sections details the methodology used to undertake the morphological response assessment of the proposed development stages.

2.1. Numerical modelling strategy

2.1.1. Initial bathymetry

Northport has undertaken an extensive hydrographic monitoring program of the access channel, swinging basing and berths over the last decade to assess the naturally occurring morphological response, including sedimentation, of the environs. Hydrographic surveys using single and multi-beam echo-sounders have been conducted annually, with data available for the period 2006 – 2017.

In MetOcean Solutions Ltd. (2018a), we used both the 2016 and the 2017 multi-beam hydrographic survey datasets to setup, calibrate and validate the morphological numerical model. This calibrated and validated numerical model is used to examine the predicted morphological effects of the different proposed development stages by modifying the underlying bathymetry. The predicted morphological effects assuming the granting of the Refining New Zealand (RNZ) channel deepening Resource Consent (Royal HaskoningDHV, 2016) are also considered.

The morphological response of 8 different scenarios has been examined (Table 2.1, Figure 2.1 and Figure 2.2). For simplicity, each of the different scenarios has been assigned specific reference code within this report, as provided in Table 2.1.

Table 2.1 Classification of the scenarios tested with the calibrated morphological model for the period 2016 – 2017.

Code	Description of scenarios
Existing	Existing
Existing$_a$	Existing **+** Dredging of access channel
Stage1	Reclamation of Area 6
Stage1$_a$	Reclamation of Area 6 **+** Dredging of access channel
Stage2	Reclamation of Area 6 **+** Dredging of Area 3
Stage2$_a$	Reclamation of Area 6 **+** Dredging of Area 3 **+** Dredging of access channel
Stage3	Reclamation of Areas 4, 5 and 6 **+** Dredging of Areas 1, 2 and 3
Stage3$_a$	Reclamation of Areas 4, 5 and 6 **+** Dredging of Areas 1, 2 and 3 **+** Dredging of access channel

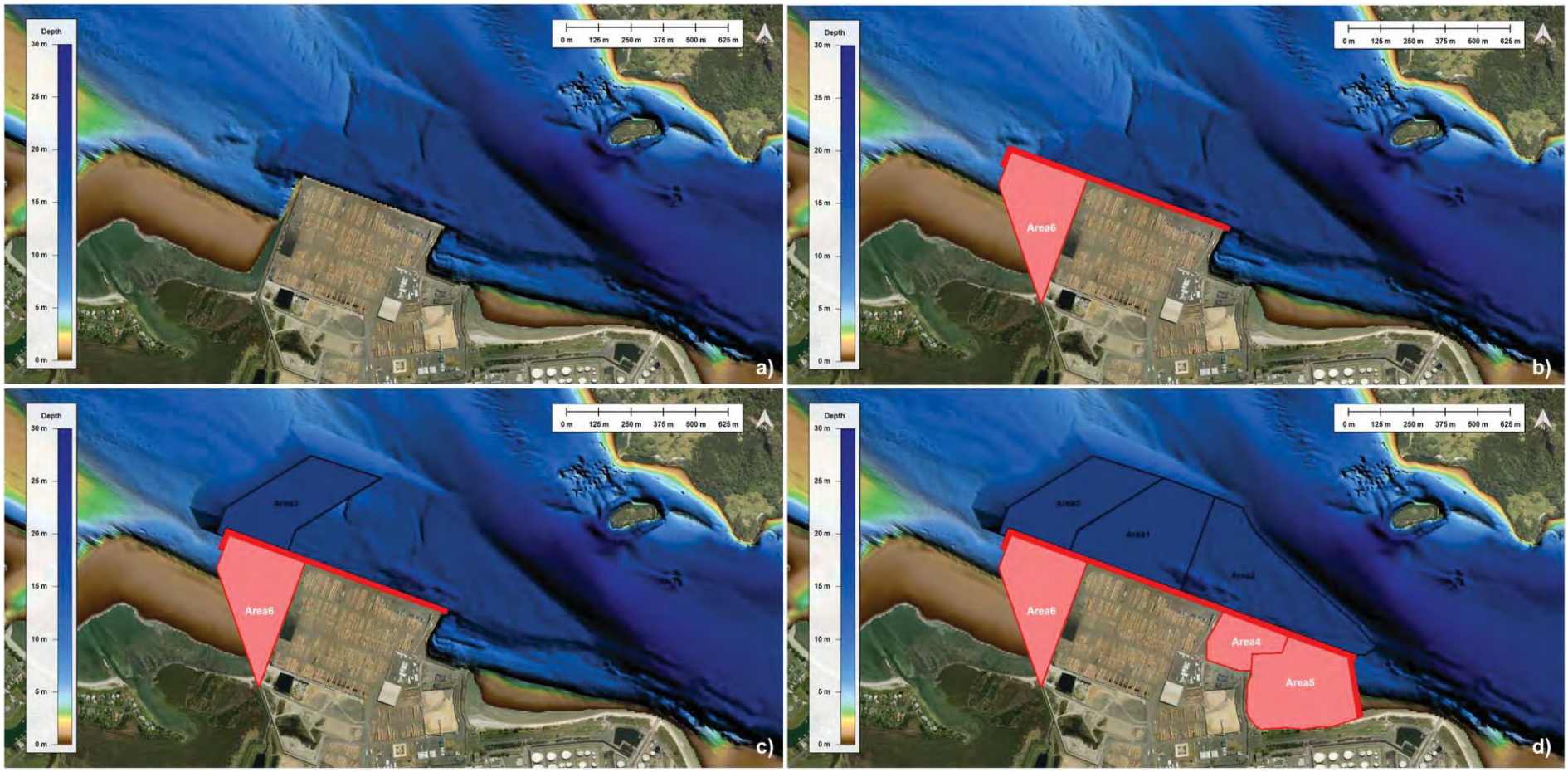

Figure 2.1 Bathymetric maps (MSL datum) of Northport extracted from the 2016 hydrographic survey dataset including the different proposed development stages.

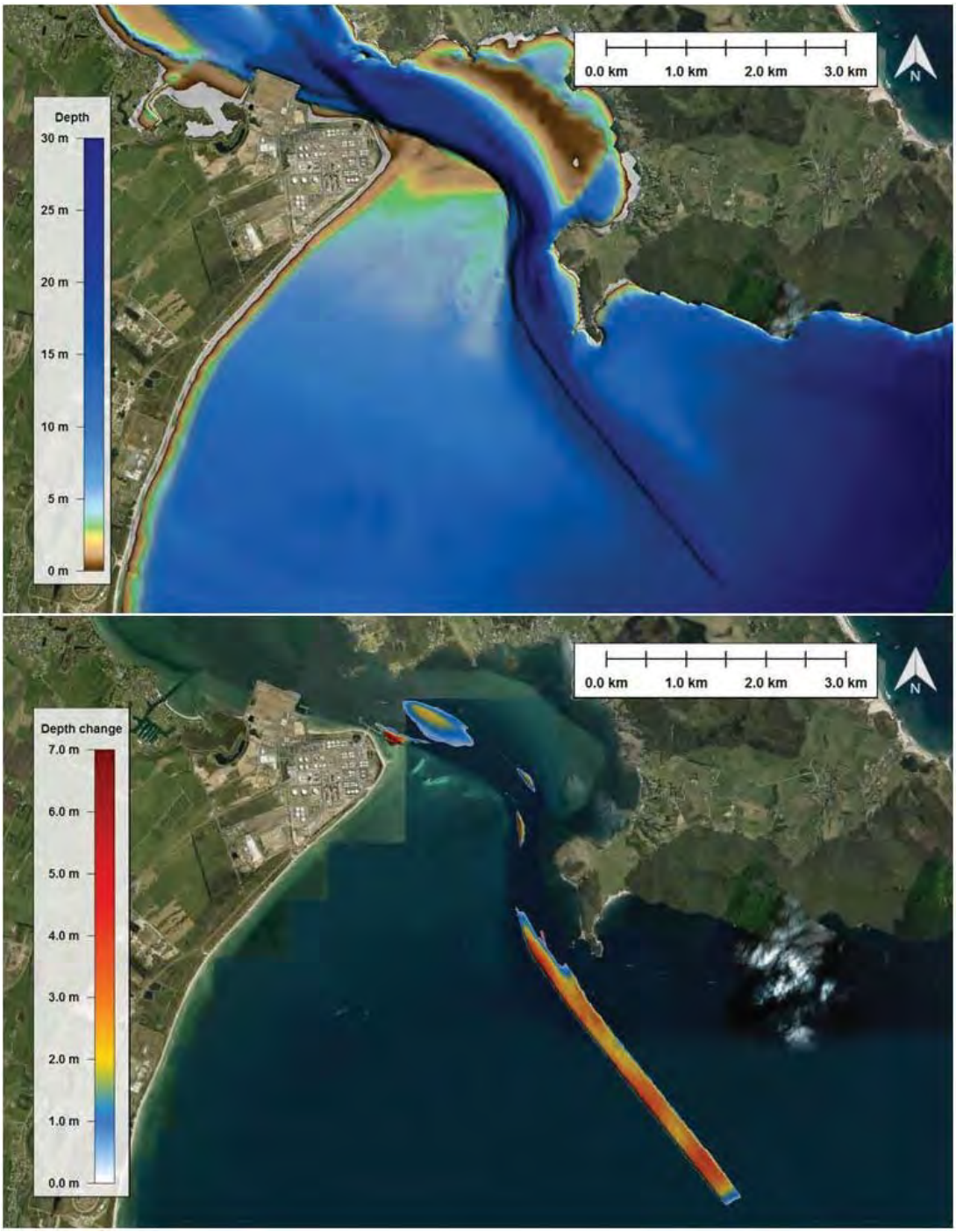

Figure 2.2 Bathymetry map (top; MSL datum) of the entrance to Whangarei Harbour including the RNZ Resource Consent dredged channel, which is in application stage (April, 2018). The bottom map shows the depth change resulting from the consented capital dredging program.

2.1.2. Initial bed composition

An accurate definition of the surficial sediment grain size distribution in the area of interest plays an important role in correctly determining sediment dynamics and morphological response. As such, a sedimentological spin-up following a bed stratigraphy approach was carried out in MetOcean Solutions Ltd. (2018a), whereby the spatial surficial sediment distribution was allow to adjust to the *in-situ* bed shear-stresses associated with both hydrodynamics and wave forcing. The

derived surficial sediment grain size distributions were applied to the bathymetry defining the proposed staged developments.

2.1.3. Forcing

Winds, waves and tidal currents were defined as in MetOcean Solutions Ltd. (2018a) to allow comparing the effect of the proposed dredging and land reclamation program on the existing sediment dynamics and morphological response.

Because the southern extension of the Delft3D–FLOW domain did not include the entire delta entrance, model derived tidal constituents associated with each of the proposed stages, and inclusive of the proposed RNZ channel deepening consent, were used to define the Delft3D–FLOW boundary tidal currents as appropriate (see MetOcean Solutions Ltd., 2018b).

2.2. Model settings

The same model configuration derived from the calibration and validation process was used to initiate the modelling. An overview of the parameters and settings used within Delft3D is provided MetOcean Solutions Ltd. (2018a).

3. RESULTS

The morphological response of the proposed development stages (both capital dredging and reclamation) are assessed for the period 2016 – 2017.

The morphological response of each of the proposed stages (i.e. Stage 1, 2 and 3) are compared with both the existing harbour bathymetry (scenarios A0-D0, Table 2.1) and the existing harbour bathymetry assuming the granting of the RNZ channel deepening Resource Consent (scenarios A1-D1, Table 2.1).

In order to isolate the effects of just the different proposed stages on the morphological response of the system, the predicted changes have been assessed by taking into account both the stage response and the existing harbour response, such that

$$Response\_areas = (Stage_{end} - Stage_{start}) - (Exist_{end} - Exist_{start}) \qquad \text{eqn. 3.1}$$

Where $Stage_{end}$ and $Stage_{start}$ are the staged model bathymetry at the end and start of the 1-year model simulation respectively, $Exist_{end}$ and $Exist_{start}$ are the existing harbour configuration at the start and end of the 1-year model simulation respectively, and *Response areas* is the morphological response at the end of the simulation period due to the staged development only. It is important to note that the *Response areas* results do not represent the actual morphological response of the system; rather they identify areas that are morphologically responding to the staged development only.

3.1. Existing harbour configuration

The morphological response of the existing harbour configuration in the vicinity of NorthPort with and without the channel deepening associated with the RNZ Resource Consent are given in Figure 3.1, while the predicted difference between the two model outcomes is presented in Figure 3.2. The proposed channel deepening is not expected to have any significant effect on the overall morphology within the vicinity of NorthPort.

These morphological results are used to place the morphological response of the staged development into context in the following sections.

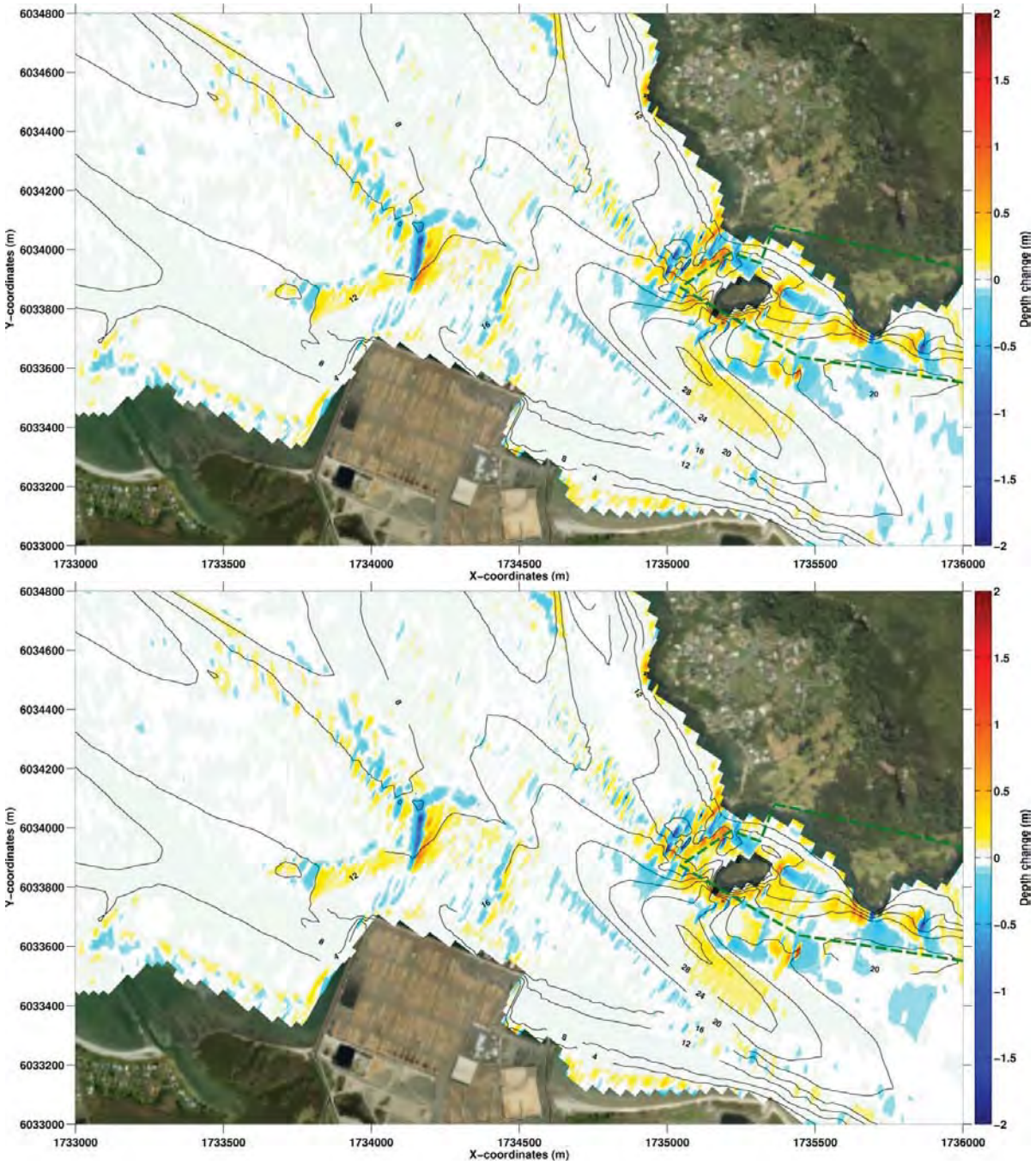

Figure 3.1 Predicted morphological response for the Existing harbour bathymetry (top) and Existing bathymetry assuming the granting of the RNZ channel deepening Resource Consent (bottom).

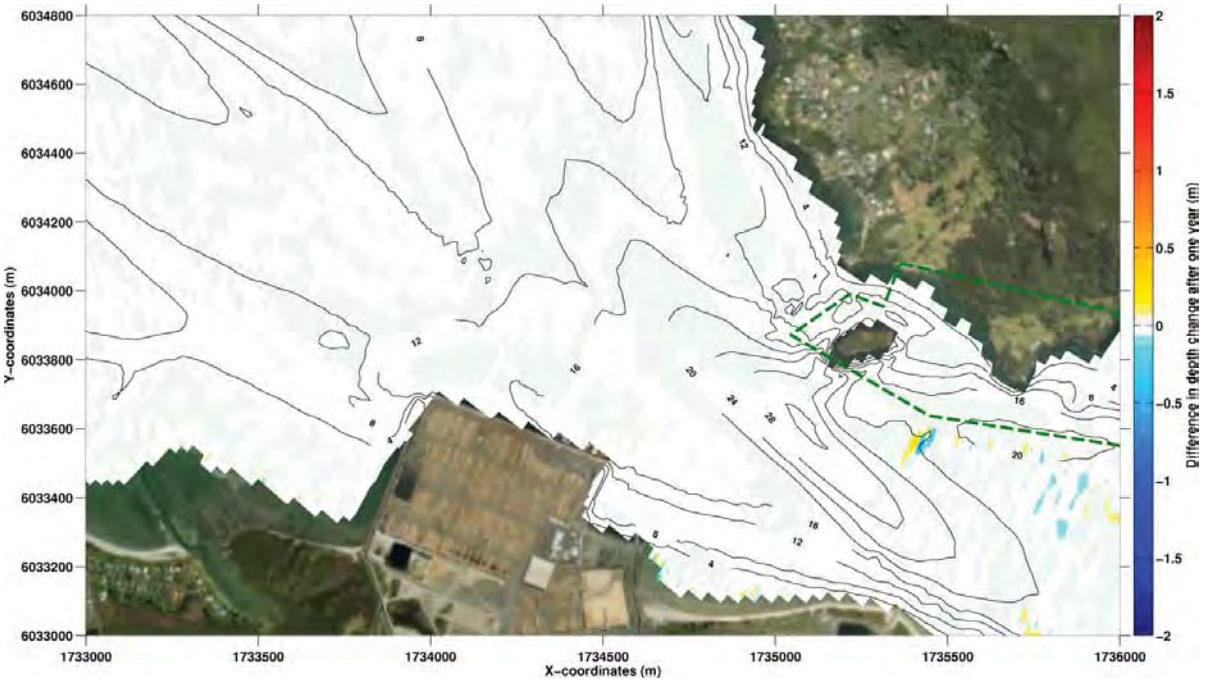

Figure 3.2 Model predicted morphological response difference between the Existing harbour bathymetry and Existing bathymetry assuming the granting of the RNZ channel deepening Resource Consent.

3.2. Stage 1 morphological response

Stage 1 of the proposed port development consists of reclaiming Area 6, less 50m along northern edge as shown in Figure 1.2.

Predicted net sediment transport rates for the Existing and Stage 1 development averaged over one tidal cycle and the percentage difference in the net transport rates are presented in Figure 3.3.

To understand the effect of these percentage differences on the morphological response of the system it is important to consider them in the context of the total net transport. While large changes in the percentage transport rates are expected within Marsden Bay and in the lee of the reclamation (see Figure 3.3), the net transport rates in these areas is low, so it is unlikely morphological changes will occur. Largest percentage differences in net transport rate are expected along the southern side of Snake Bank, adjacent to the proposed reclamation and within Marsden Bay (Figure 3.3). Results are consistent with the expected changes in hydrodynamics as described in MetOcean Solutions Ltd. (2018b).

The predicted annual morphological changes for the Existing and the Stage 1 bathymetry (not including the RNZ Resource Consent) are provided in Figure 3.4. Also shown in Figure 3.4 is the area of morphological response associated with the Stage 1 development only (i.e. eqn. 3.1). The morphological effect of the Stage 1 development is expected to be limited to the immediate port environs, consistent with the changes to the underlying hydrodynamic process predicted in MetOcean Solutions Ltd. (2018b); with only very subtle modifications to the overall sediment dynamics within the broader region (Figure 3.4).

The largest morphological changes are predicted to occur near the tip of Snake Bank and within the swinging basin immediately adjacent to the reclaimed area (Figure 3.4).

Within the north-western area immediately adjacent to the Stage 1 reclamation, accelerated current velocities (see MetOcean Solutions Ltd., 2018b) and increased net transport rates (Figure 3.3) are expected to result in erosion of the seabed by ~0.20–0.40 $m.yr^{-1}$ (Figure 3.4), while accretion of the order 0.10–0.30 $m.yr^{-1}$ can be expected within the existing swinging basin (Figure 3.4). This morphological response to the modified tidal dynamic is expected to decrease over time as a new equilibrium between the surficial sediment characteristics, controlled by the critical bed shear stress, and the tidal hydrodynamics is reached.

The predicted morphological changes at the tip of Snake Bank are associated with the propagation of the large sand-waves or mega-ripples within this area. Historical bathymetric survey analysis between 2007-2016 (MetOcean Solutions Ltd., 2018a) indicates an ~10 $m.yr^{-1}$ eastward migration of these morphological features. The rate of propagation of these features has been shown by Besio et al. (2004) and Tonnon et al. (2007) to be dependent on the tidal asymmetry and maximum current velocities. The increased current velocities adjacent to the reclamation (see MetOcean Solutions Ltd., 2018a) are expected to increase in the eastward migration of these features to ~12 $m.yr^{-1}$.

Within Marsden Bay, the localised increase of the net sediment transport (Figure 3.3) is not expected to change the morphology of the bay, with very small localised adjustments of the water depth in the order $\pm$0–0.10 m (Figure 3.4).

Comparisons between the predicted morphological response for Stage 1 with and without the granting of the RNZ channel deepening Resource Consent are provided in Figure 3.5. The proposed channel deepening is not expected to have any significant effect on the overall morphology within the vicinity of NorthPort at Stage 1, nor does the combined effect of Stage 1 and channel deepening exacerbated the expected morphological response.

No significant changes to the existing sediment transport rates or morphology is expected within the Motukaroro Marine Reserve for either the Stage 1 or Stage 1 assuming the granting of the RNZ channel deepening Resource Consent (see **Error! Reference source not found.** and Figure 3.5).

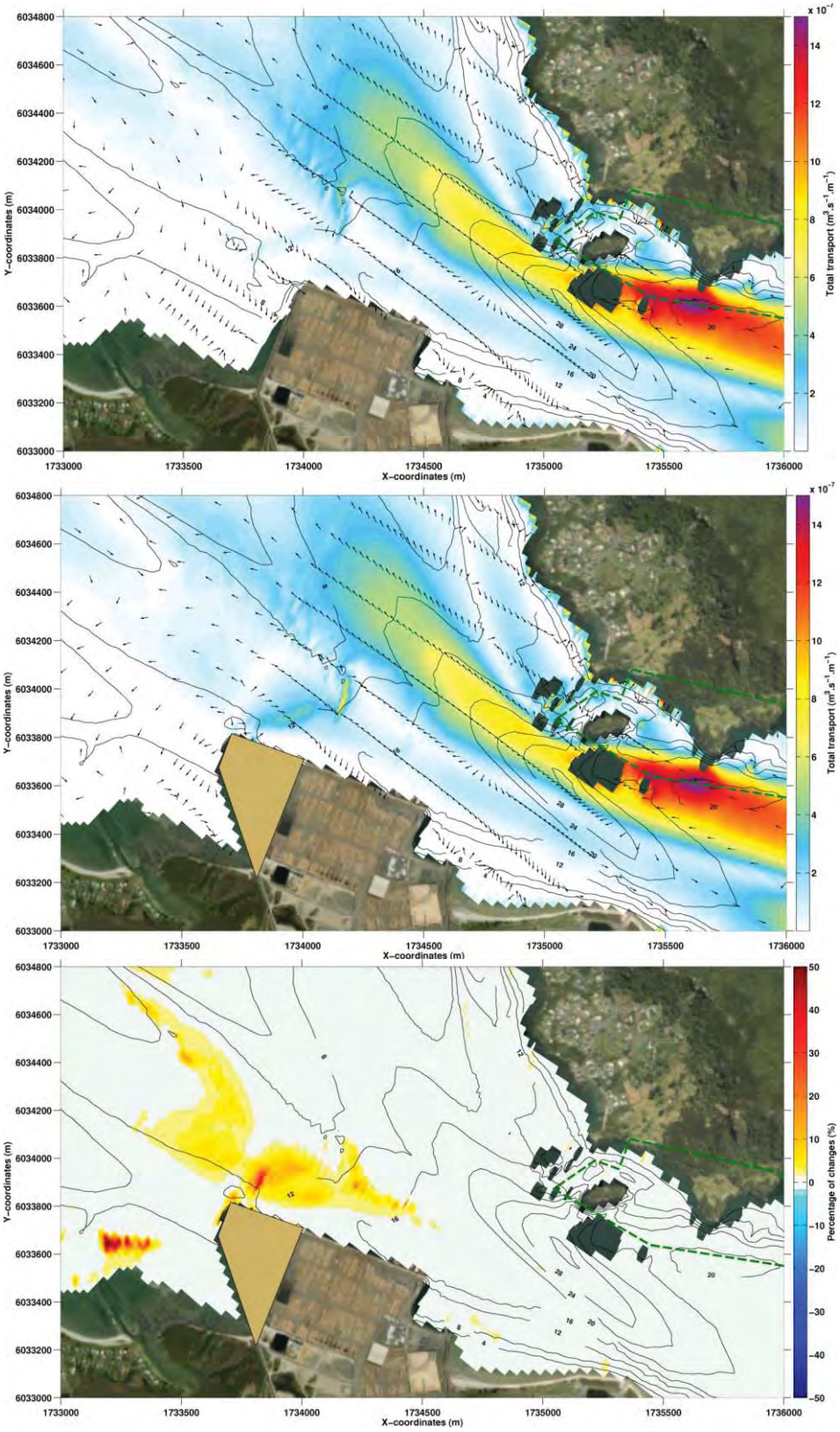

Figure 3.3 Predicted net transport at Northport averaged over one tidal cycle (~12.25 hours) for the Existing and Stage 1 development for the Wave Class 11 (see MetOcean Solutions Ltd., 2018a). The percentage difference in net transport rates are provided in the bottom panel. The green dashed line delimits the Motukaroro Marine Reserve.

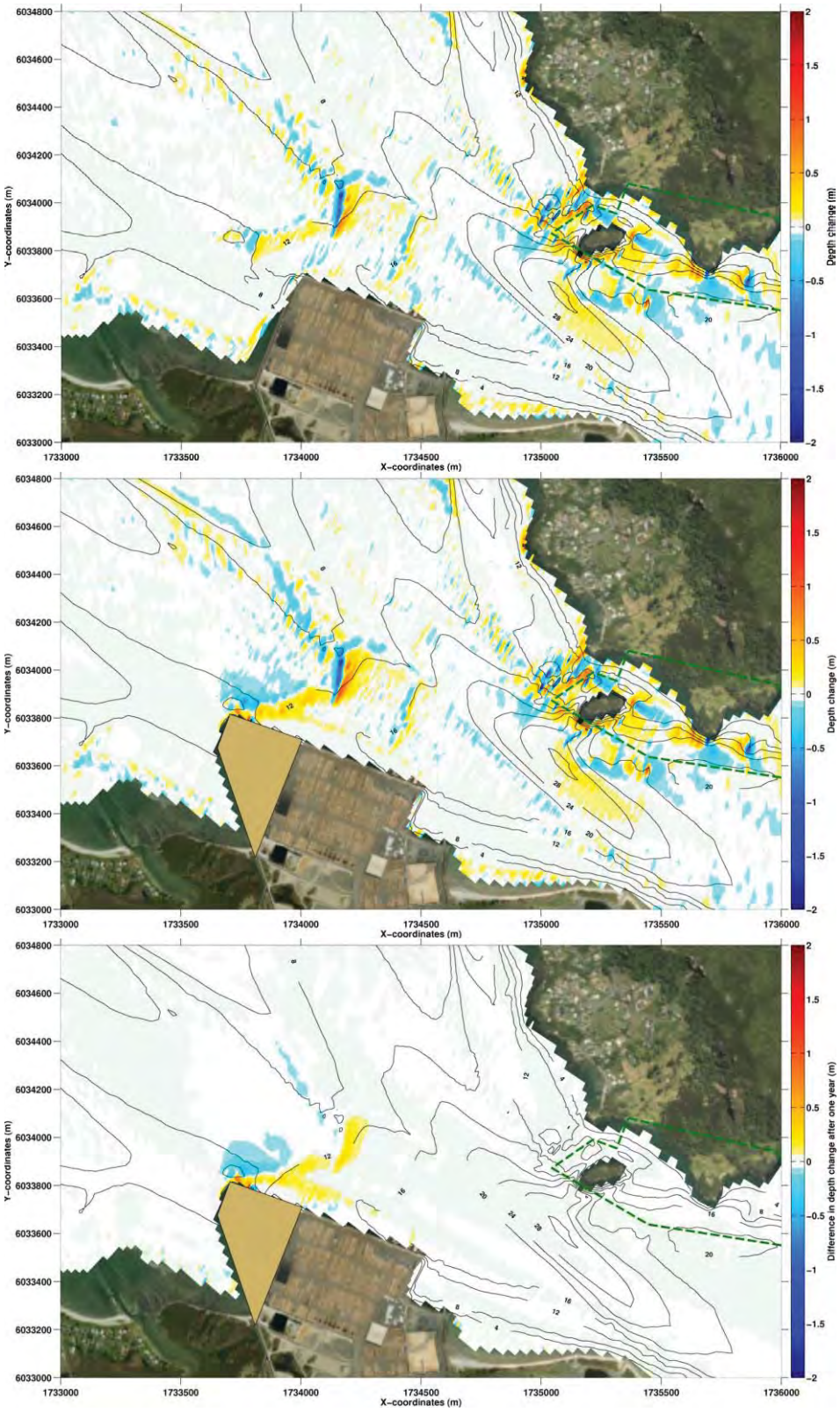

Figure 3.4 Depth change predicted at Northport for the period 2016 – 2017 considering the Existing (Top) and Stage 1 harbour bathymetry (Middle), while areas of morphological response associated with the Stage 1 development only is presented in the Bottom panel. This does not represent the actual morphological response of the system (which is present in the middle panel); rather it identifies areas that are morphologically responding to the staged development only. The Motukaroro Marine Reserve is shown by the green dashed line.

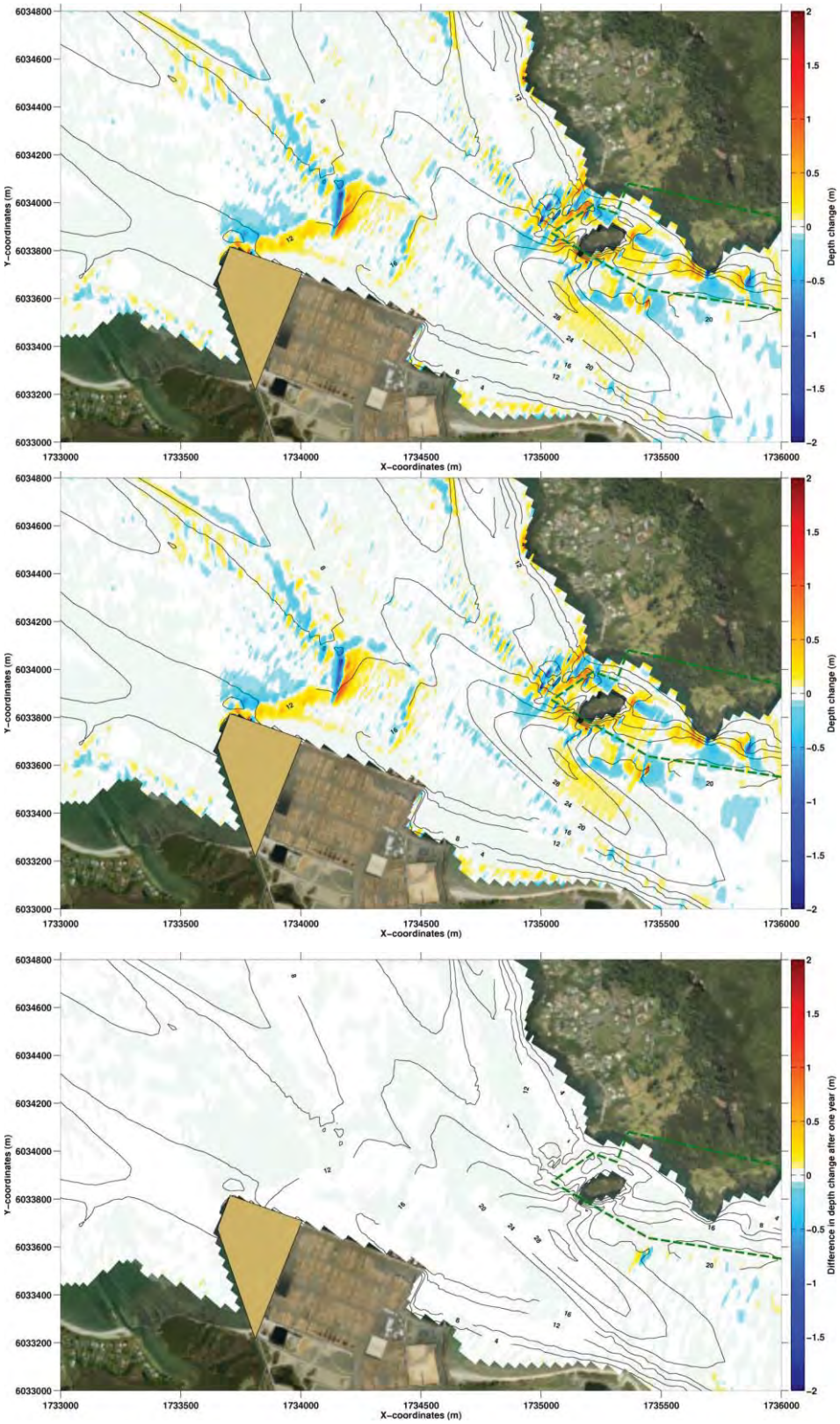

Figure 3.5 Model predicted depth changes predicted over the period 2016-2017 for the Stage 1 (top) and Stage 1 considering the channel deepening RNZ Resource Consent (middle) in the vicinity of NorthPort. The bottom panel illustrates the model predicted differences in morphological response for the Stage 1 and Stage 1 considering the channel deepening RNZ Resource Consent.

3.3. Stage 2 morphological response

Stage 2 of the proposed port development consists of reclaiming Area 6 and dredging Area 3 as shown in Figure 1.2.

Predicted net sediment transport rates for the Existing and Stage 2 development averaged over one tidal cycle and the percentage difference in the net transport rate are presented in Figure 3.6. Dredging Area 3 acts to largely mitigate the effect of the proposed Stage 1 reclamation on the net transport (i.e. see Figure 3.3) by reducing the current velocities in the vicinity of the reclamation. To understand the effect of these percentage differences on the morphological response of the system it is important to consider them in the context of the total net transport. While large changes in the percentage transport rates are expected in the lee of the reclamation (see Figure 3.6), the net transport rates in these areas is low, so it is unlikely morphological changes will occur. Relatively large predicted differences in the net transport rate are expected along the southern side of Snake Bank to the west of the dredged area, consistent with the expected changes in hydrodynamics as described in MetOcean Solutions Ltd. (2018b).

The predicted annual morphological changes for the Existing and the Stage 2 bathymetry (not including the RNZ Resource Consent) are provided in Figure 3.7 Also shown in Figure 3.7 is the area of morphological response associated with the Stage 2 development only (i.e. eqn. 3.1). The morphological effect of the Stage 2 development is expected to be limited to the immediate port environs, consistent with the changes to the underlying hydrodynamic process predicted in MetOcean Solutions Ltd. (2018b); with only very subtle modifications to the overall sediment dynamics within the broader region (Figure 3.7).

The largest morphological changes associated with the Stage 2 development are predicted to occur within the battered area to the west of the dredged area, while an area infilling is also predicted in the north-east corner of the dredged area (Figure 3.7). Large differences between the Stage 2 development and the existing harbour configuration are likewise observed in the north-east corner of the dredged area (Figure 3.7, bottom panel), however this represents the removal of a sand-wave or mega-ripple feature from the existing bathymetry during the dredging of the swinging basin rather than and expected morphological response; which is shown in the central panel of Figure 3.7.

Within Marsden Bay, the localised increase of the net sediment transport (Figure 3.6) is not expected to change the morphology of the bay, with very small localised adjustments of the water depth in the order $\pm$0–0.10 m (Figure 3.7).

The morphological response along four depth transects through the batter to the west of the dredged (see Figure 3.8) are presented in Figure 3.9 and Figure 3.10, and show a pattern of erosion along the crest of the batter, with deposition on the flank and at the toe of the batter, consistent with the batter moving towards an equilibrium profile shape.

Approximate infilling and erosion rates, as well as the total change in volume within different areas of the proposed development are provided in Table 3.1. Infilling of ~2,706 m^3 is expected within the dredged Area 3, while erosion of a similar magnitude is expected in Areas 1 and 2 (~2,640 m^3). Sedimentation of ~2,814 m^3 is expected with the batter area. The total sedimentation within the swinging basing (Areas 1-3) and batter area after 1-year is expected to be of the order 2,880 m^3 (Table 3.1).

In general, the morphological response to the modified tidal dynamic is expected to decrease over time as a new equilibrium between the surficial sediment characteristics, controlled by the critical bed shear stress, and the tidal hydrodynamics are reached.

Comparisons between the predicted morphological response for Stage 2 with and without the granting of the RNZ channel deepening Resource Consent are provided in **Error! Reference source not found.**. The proposed channel deepening is not expected to have any significant effect on the overall morphology within the vicinity of NorthPort at Stage 2, nor does the combined effect of Stage 2 and channel deepening exacerbated the expected morphological response. Alternating patterns of positive and negative depth change to the east of the port (**Error! Reference source not found.**, bottom panel) are representative of changing propagation speeds of sand-wave/mega-ripple bed-forms rather than significant morphological adjustments.

No significant changes to the existing sediment transport rates or morphology is expected within the Motukaroro Marine Reserve for either the Stage 2 or Stage 2 assuming the granting of the RNZ channel deepening Resource Consent (see Figure 3.7 and **Error! Reference source not found.**).

Table 3.1 Predicted annual volumes change within Areas 1 to 3 and the batter area for Stage 2.

		Volumetric changes (m^3)				
		Areas 1 and 2	**Area 3**	**Areas 1, 2 and 3**	**Batter**	**Total**
Stage 2	**Infilling**	6,134	3,031	9,165	5,242	14,407
	Erosion	-8,774	-324	-9,098	-2,428	-11,526
	Total	-2,640	2,706	66	2,814	2,880

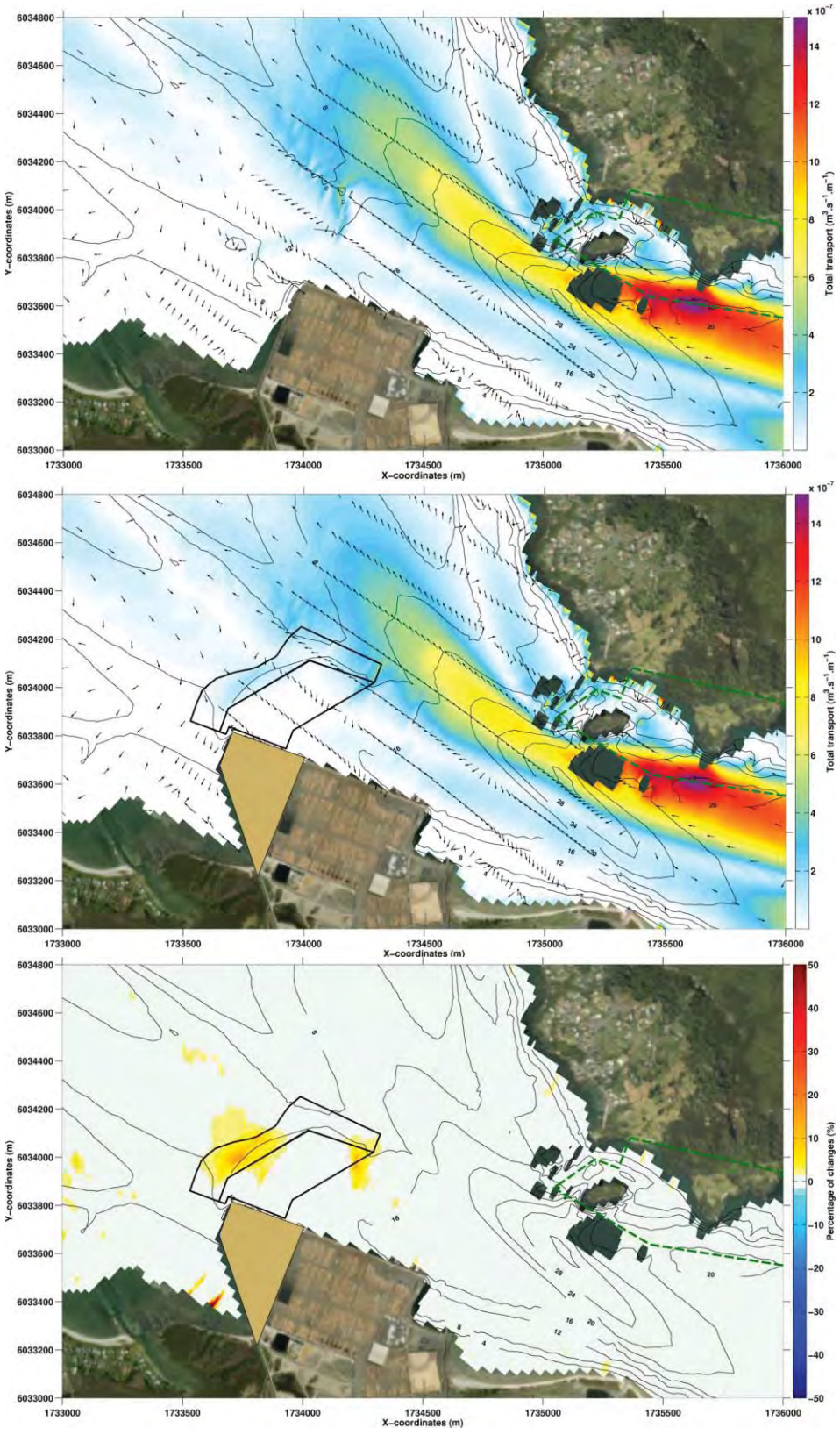

Figure 3.6 Predicted net transport at Northport averaged over one tidal cycle (~12.25 hours) for the Existing and Stage 2 development for the Wave Class 11 (see MetOcean Solutions Ltd., 2018a). The percentage difference in net transport rates are provided in the bottom panel. The green dashed line delimits the Motukaroro Marine Reserve.

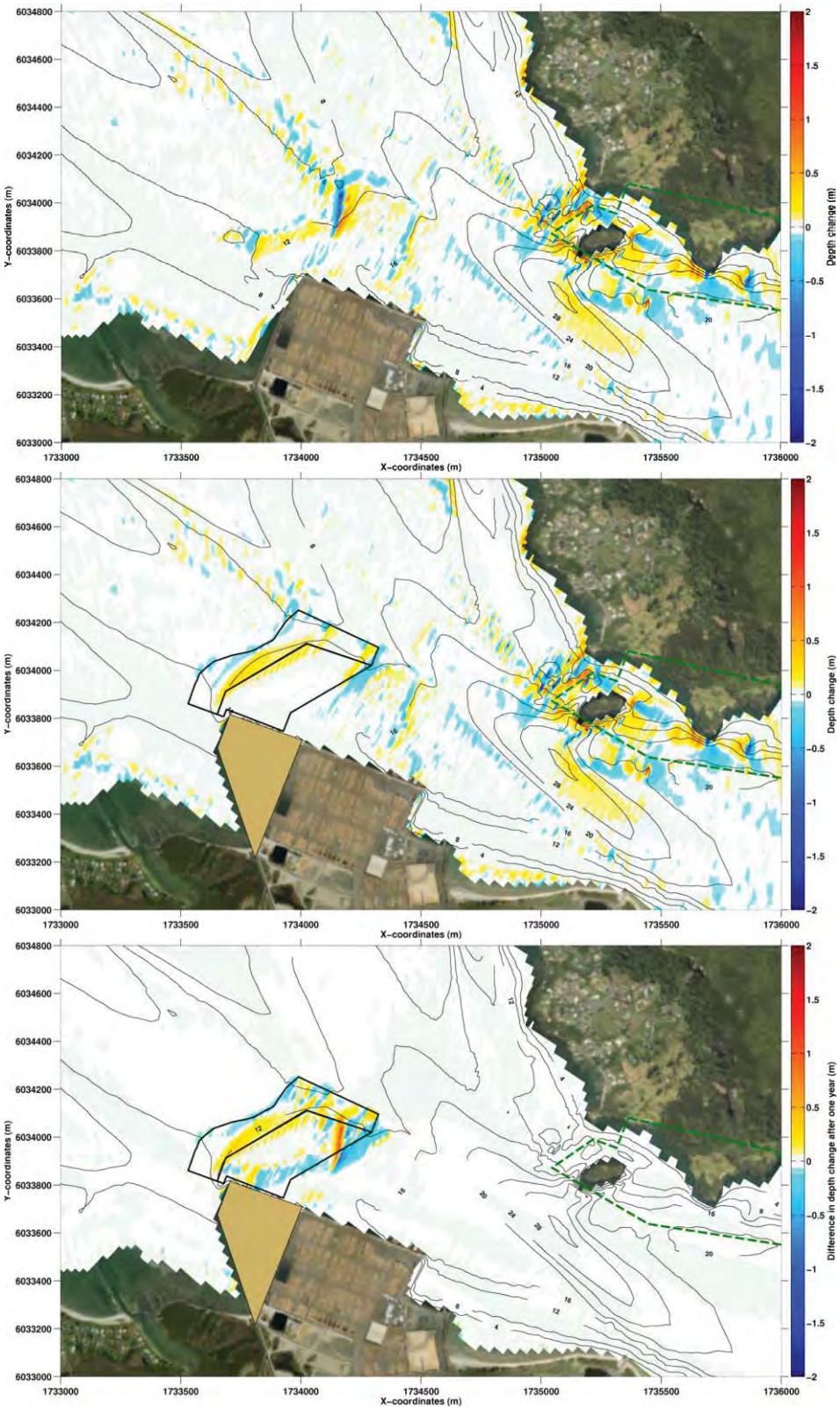

Figure 3.7 Depth change predicted at Northport for the period 2016 – 2017 considering the Existing (Top) and Stage 2 harbour bathymetry (Middle), while areas of morphological response associated with the Stage 2 development only is presented in the Bottom panel. This does not represent the actual morphological response of the system (which is present in the middle panel); rather it identifies areas that are morphologically responding to the staged development only. The Motukaroro Marine Reserve is shown by the green dashed line.

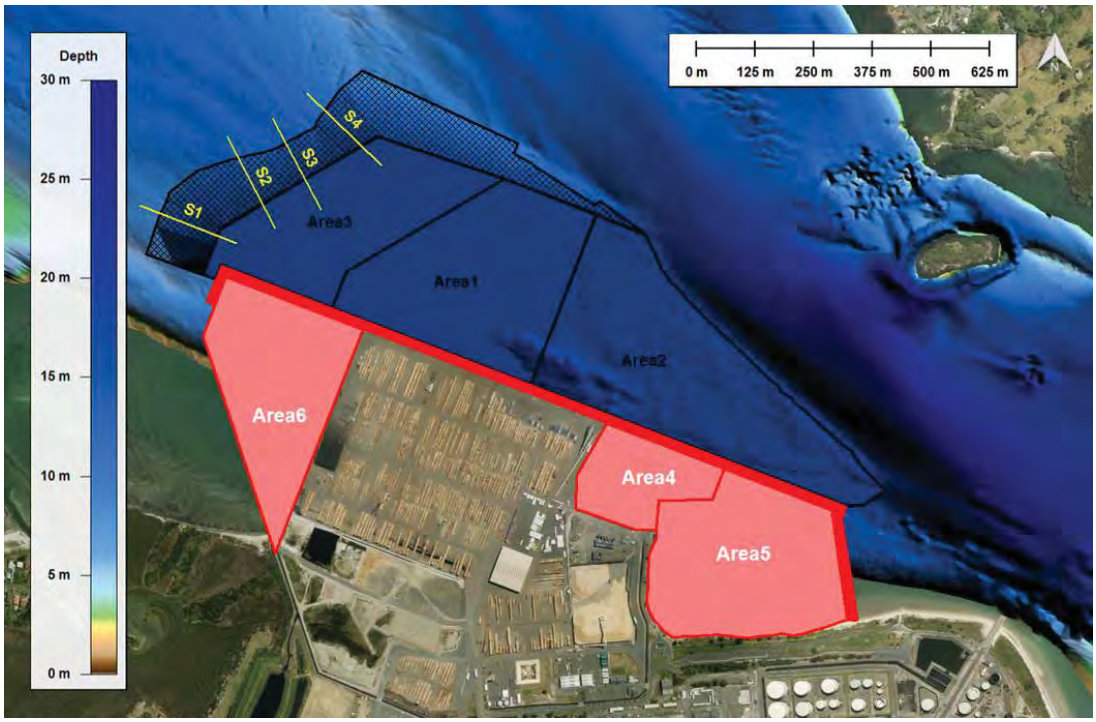

Figure 3.8 Transect locations from which the morphological response of the batter are assessed

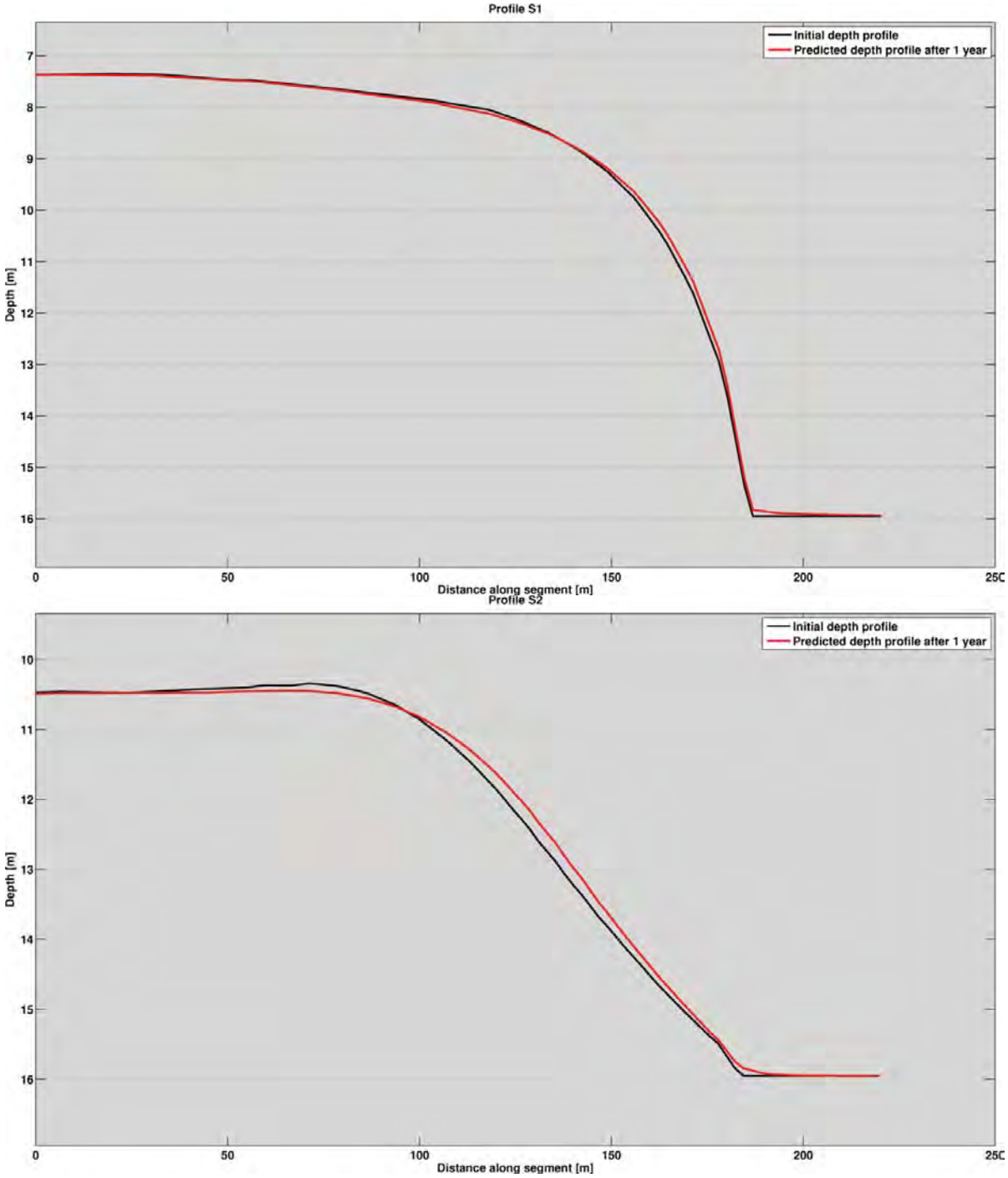

Figure 3.9 Depth profiles extracted from the initial (Black) and the predicted (Red) Stage 2 bathymetries along segments S1 (top) and S2 (bottom) showing the expected morphological response of the batter after 1-year. Location of transects is given in Figure 3.8.

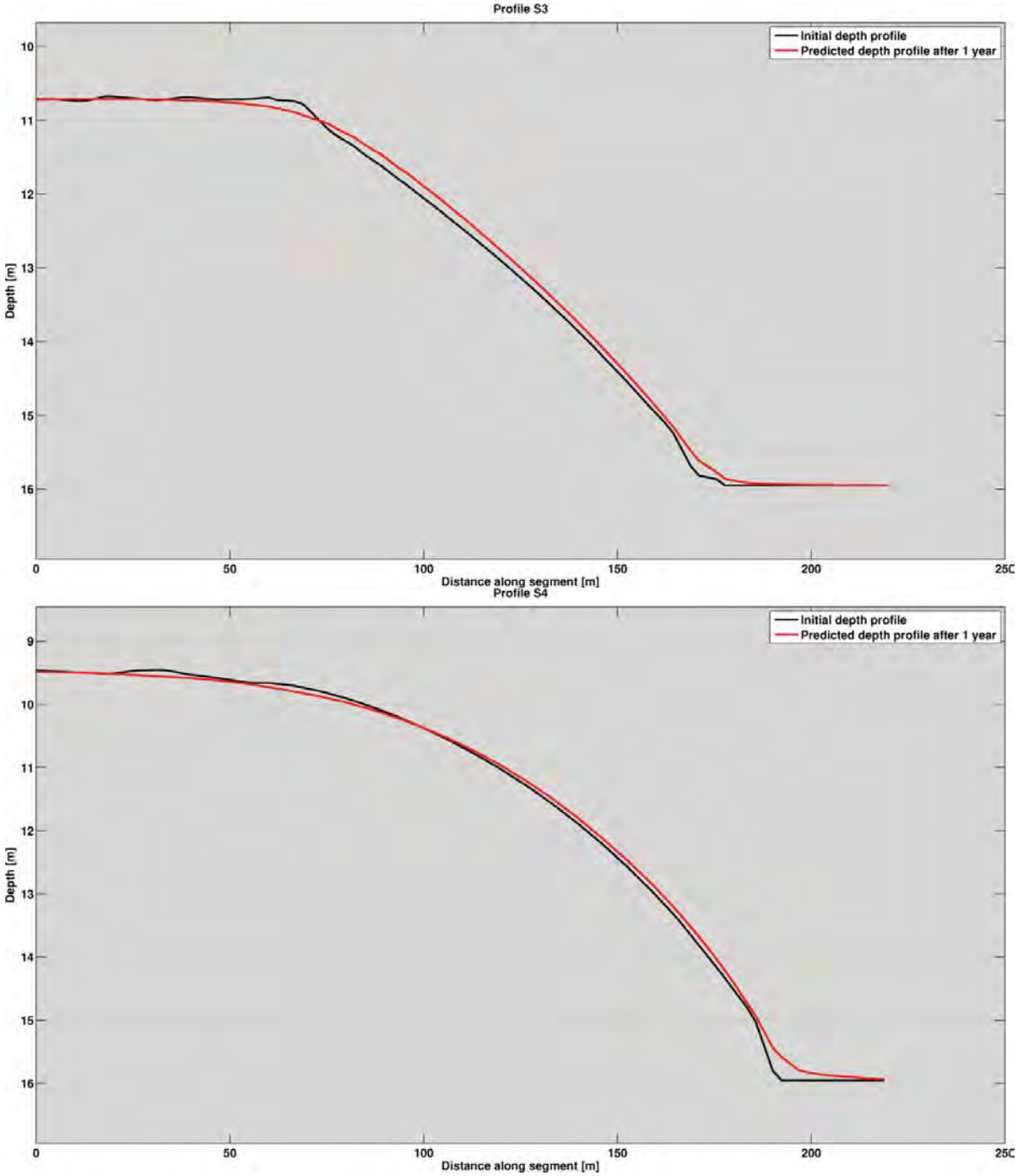

Figure 3.10 Depth profiles extracted from the initial (Black) and the predicted (Red) Stage 2 bathymetries along segments S3 (top) and S4 (bottom) showing the expected morphological response of the batter after 1-year. Location of transects is given in Figure 3.8.

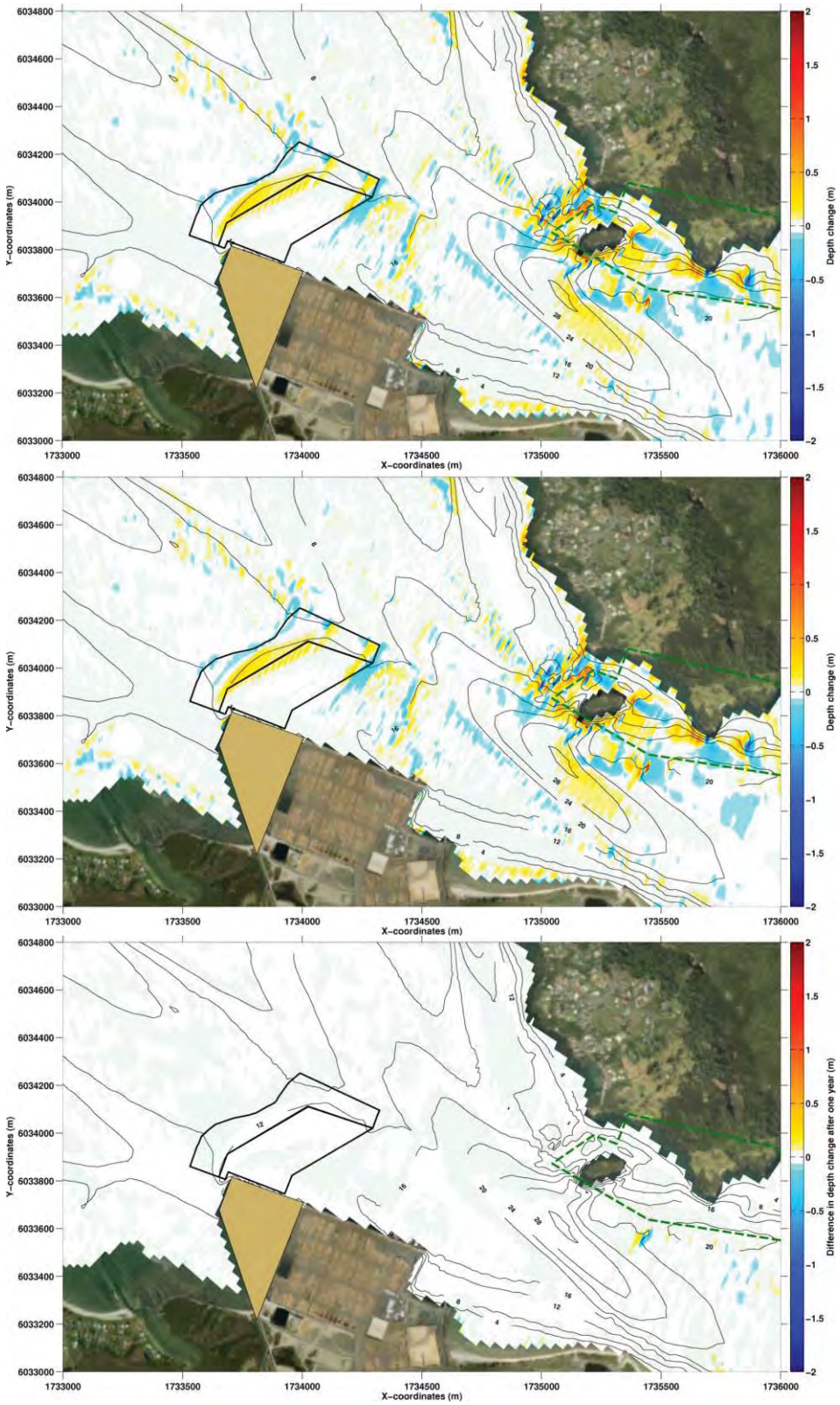

Figure 3.11 Model predicted depth changes predicted over the period 2016-2017 for the Stage 2 (top) and Stage 2 considering the channel deepening RNZ Resource Consent (middle). The bottom pane illustrates the model predicted differences in morphological response for the Stage 2 and Stage 2 considering the channel deepening RNZ Resource Consent.

3.4. Stage 3 morphological response

Stage 3 of the proposed port development consists of reclaiming Areas 4, 5 and 6 as well as dredging Areas 1, 2 and 3 as shown in Figure 1.2.

Predicted net sediment transport rates for the Existing and Stage 3 development averaged over one tidal cycle and the percentage difference in the net transport rate are presented in Figure 3.12. As with the Stage 2 development, the combination of Stage 2, dredging Areas 1 and 2 and reclaiming Areas 4 and 5 acts to largely mitigate the effect of the proposed Stage 1 reclamation on the net transport (i.e. see Figure 3.3) by reducing the current velocities in the vicinity of the reclamation. To understand the effect of these percentage differences on the morphological response of the system it is important to consider them in the context of the total net transport. While large changes in the percentage transport rates are expected to the west of the Stage 2 reclamation (see Figure 3.12), the net transport rates in these areas is low, so it is unlikely morphological changes will occur. Relatively large predicted differences in the net transport rate are expected along the southern side of Snake Bank to the west of the dredged area, consistent with the expected changes in hydrodynamics as described in MetOcean Solutions Ltd. (2018b).

The predicted annual morphological changes for the Existing and the Stage 3 bathymetry (not including the RNZ Resource Consent) are provided in Figure 3.13 Also shown in Figure 3.13 is the area of morphological response associated with the Stage 3 development only (i.e. eqn. 3.1). The morphological effect of the Stage 3 development is expected to be predominantly limited to the immediate port environs, consistent with the changes to the underlying hydrodynamic process predicted in MetOcean Solutions Ltd. (2018b); with only very subtle modifications to the overall sediment dynamics within the broader region (Figure 3.13).

The largest morphological changes associated with the Stage 3 development are predicted to occur within the battered area to the west of Area 3 (Figure 1.2). The morphological model predicts erosion to occur along the north-east edge of the dredged Area 2 (Figure 3.13), and this is attributed to the net transport rate within this region (as shown in Figure 3.12). Large differences between the Stage 3 development and the existing harbour configuration are likewise observed in the north-east corner of the dredged area (Figure 3.13, bottom panel), however this represents the removal of a sand-wave or mega-ripple feature from the existing bathymetry during the dredging of the swinging basin rather than an expected morphological response; which is shown in the central panel of Figure 3.13.

Within Marsden Bay, the localised increase of the net sediment transport (Figure 3.12) is not expected to change the morphology of the bay, with very small highly localised adjustments of the water depth in the order $\pm$0–0.10 m (Figure 3.13).

The morphological response along four depth transects through the batter to the west of the dredged (see Figure 3.8) are presented in Figure 3.14 and Figure 3.15, and show a pattern of erosion along the crest of the batter, with deposition on the flank and at the toe of the batter, consistent with the batter moving towards an equilibrium profile shape.

Approximate infilling and erosion rates, as well as the total change in volume within different areas of the proposed development are provided in Table 3.2. Infilling of ~2,474 m^3 is expected within the dredged Area 3, while erosion of a similar magnitude is expected in Areas 1 and 2 (~2,210 m^3). Sedimentation of ~2,225 m^3 is

expected within the batter area. The total sedimentation within the swinging basin (Areas 1-3) and batter area after 1-year is predicted to be of the order 2489 m^3 (Table 3.2) following the Stage 3 development.

In general, the morphological response to the modified tidal dynamic is expected to decrease over time as a new equilibrium between the surficial sediment characteristics, controlled by the critical bed shear stress, and the tidal hydrodynamics are reached.

Comparisons between the predicted morphological response for Stage 3 with and without the granting of the RNZ channel deepening Resource Consent are provided in Figure 3.16. The proposed channel deepening is not expected to have any significant effect on the overall morphology within the vicinity of NorthPort at Stage 3, nor does the combined effect of Stage 3 and channel deepening exacerbated the expected morphological response. Alternating patterns of positive and negative depth change to the east of the port (Figure 3.16, bottom panel) are representative of changing propagation speeds of sand-wave/mega-ripple bed-forms rather than significant morphological adjustments.

No significant changes to the existing sediment transport rates or morphology is expected within the Motukaroro Marine Reserve for either the Stage 2 or Stage 2 assuming the granting of the RNZ channel deepening Resource Consent (see Figure 3.13 and Figure 3.16). Areas of alternating erosion and accretion along the northern edge of the reserve represent the movement of bed-forms rather than a significant morphological response.

Table 3.2 Predicted annual volumes change within Areas 1 to 3 and the batter area for Stage 3. Note the batter area is larger for Stage 3 than for Stage 2.

		Volumetric changes (m^3)				
		Areas 1 and 2	**Area 3**	**Areas 1, 2 and 3**	**Batter**	**Total**
Stage 2	**Infilling**	4,946	2,997	7,943	5,370	13,313
	Erosion	-7,157	-523	-7,680	-3,145	-10,825
	Total	-2,210	2,474	264	2,225	2,489

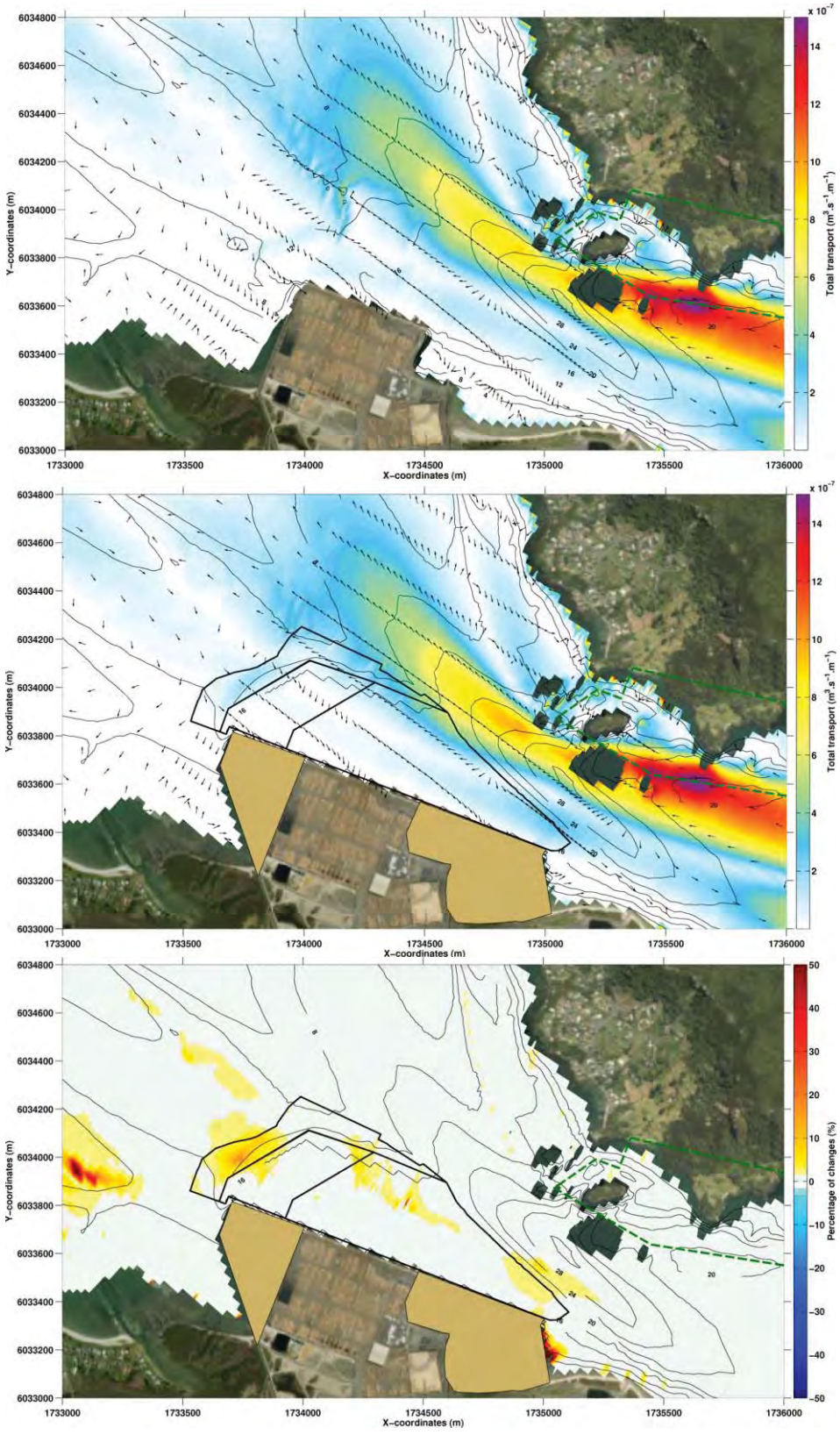

Figure 3.12 Predicted net transport at Northport averaged over one tidal cycle (~12.25 hours) for the Existing and Stage 3 development for the Wave Class 11 (see MetOcean Solutions Ltd., 2018a). The percentage difference in net transport rates are provided in the bottom panel. The green dashed line delimits the Motukaroro Marine Reserve.

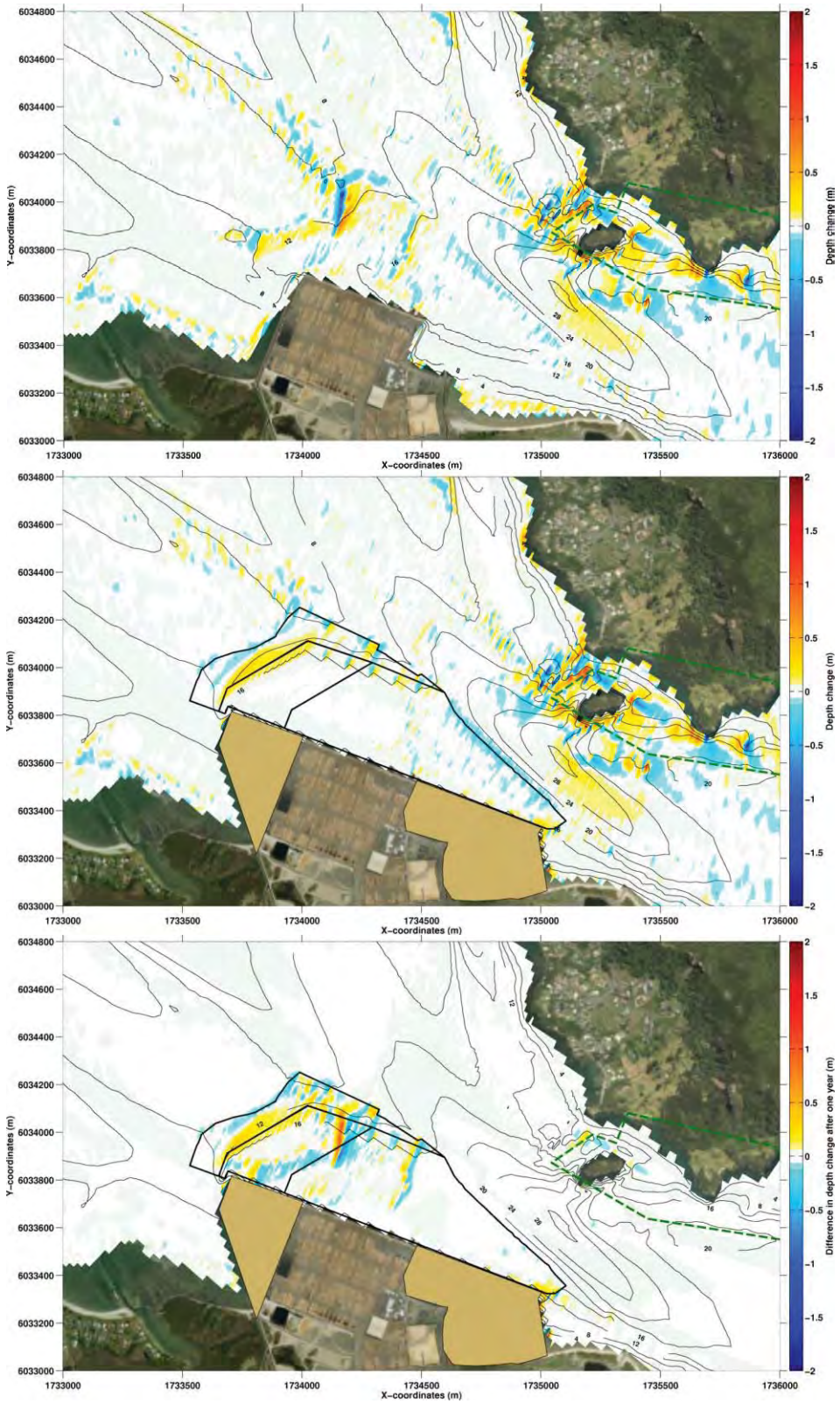

Figure 3.13 Depth change predicted at Northport for the period 2016 – 2017 considering the Existing (Top) and Stage 3 harbour bathymetry (Middle), while areas of morphological response associated with the Stage 3 development only is presented in the Bottom panel. This does not represent the actual morphological response of the system (which is present in the middle panel); rather it identifies areas that are morphologically responding to the staged development only. The Motukaroro Marine Reserve is shown by the green dashed line.

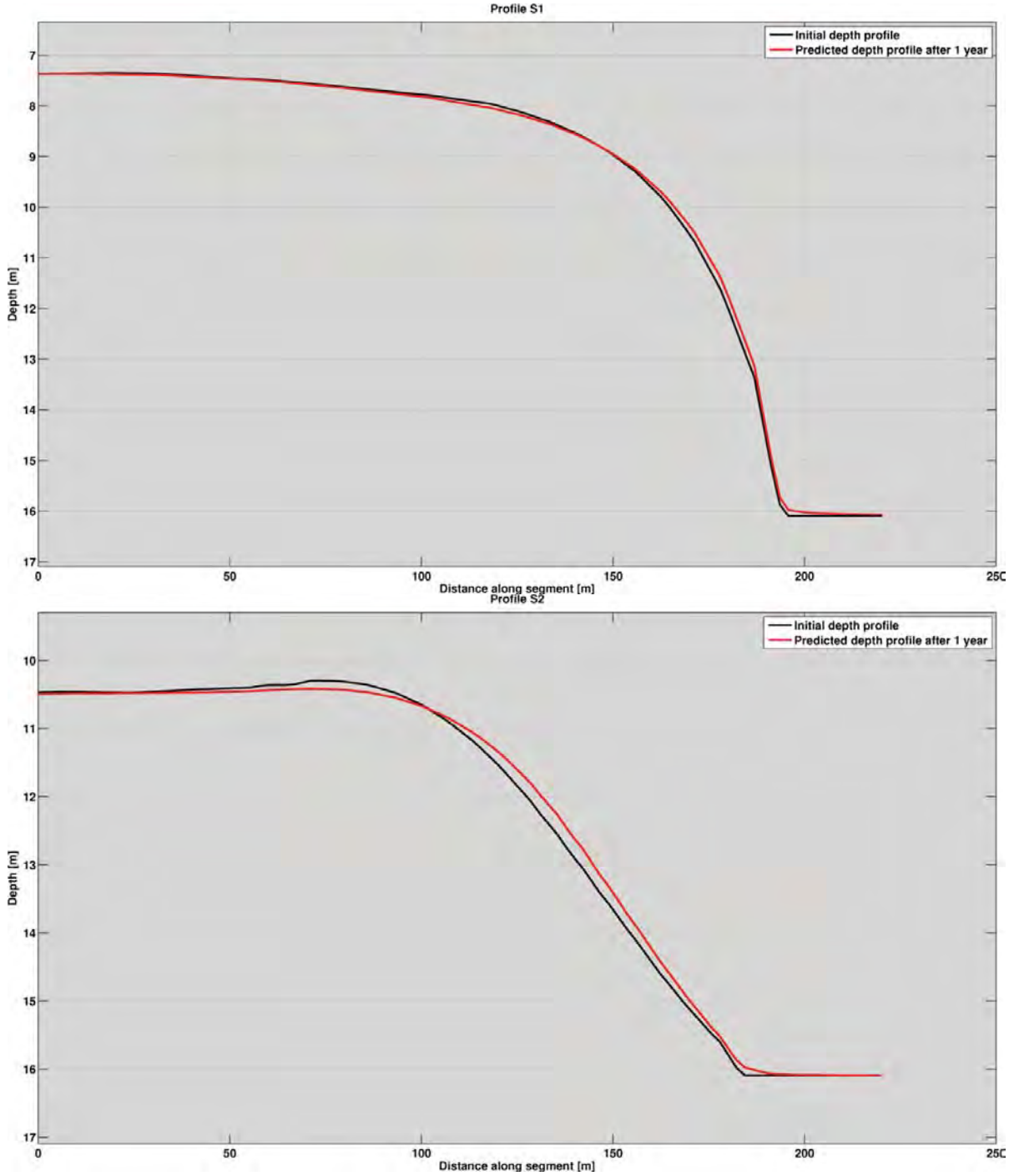

Figure 3.14 Depth profiles extracted from the initial (Black) and the predicted (Red) Stage 2 bathymetries along segments S1 (top) and S2 (bottom) showing the expected morphological response of the batter after 1-year. Location of transects is given in Figure 3.8.

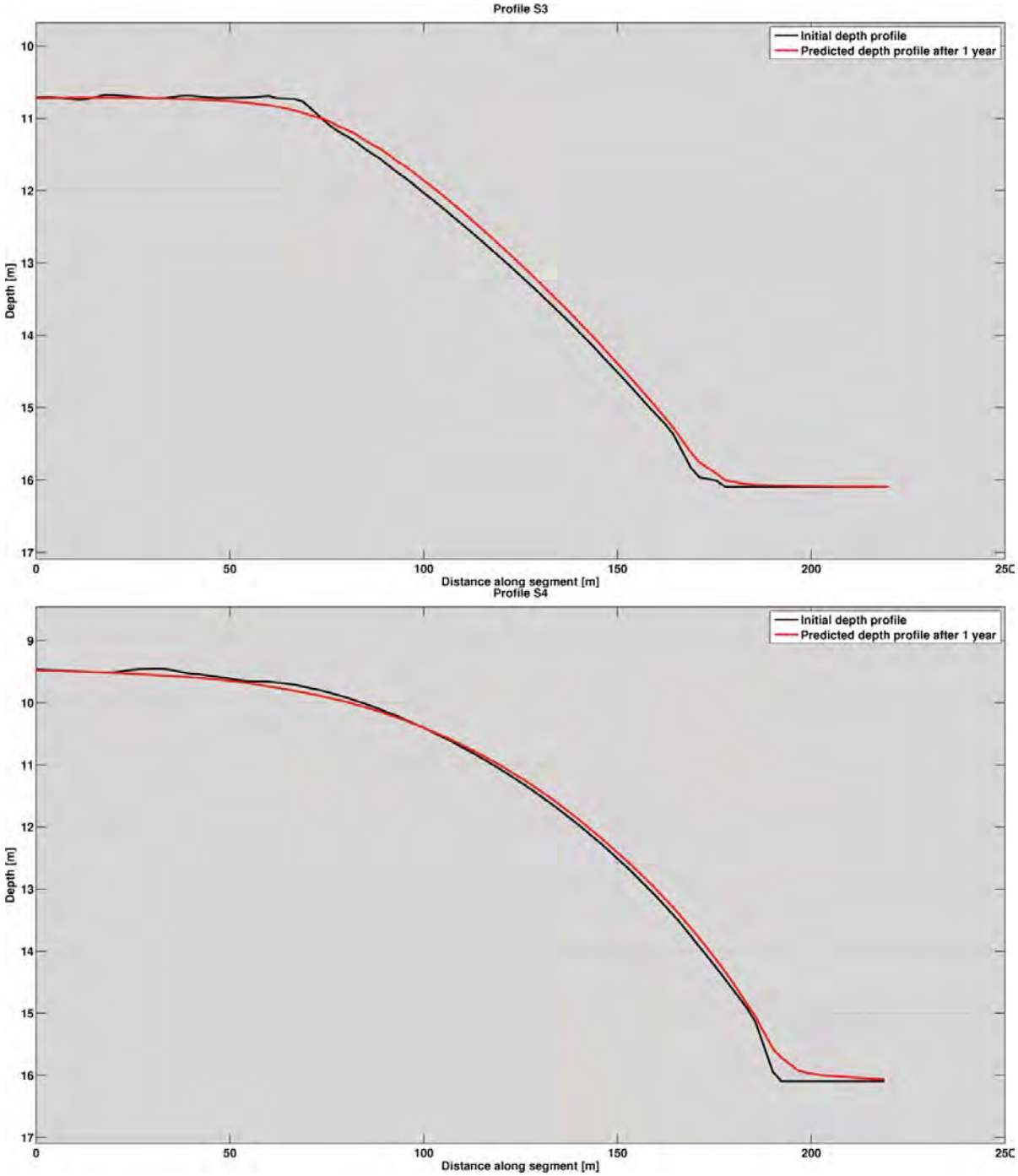

Figure 3.15 Depth profiles extracted from the initial (Black) and the predicted (Red) Stage 2 bathymetries along segments S3 (top) and S4 (bottom) showing the expected morphological response of the batter after 1-year. Location of transects is given in Figure 3.8.

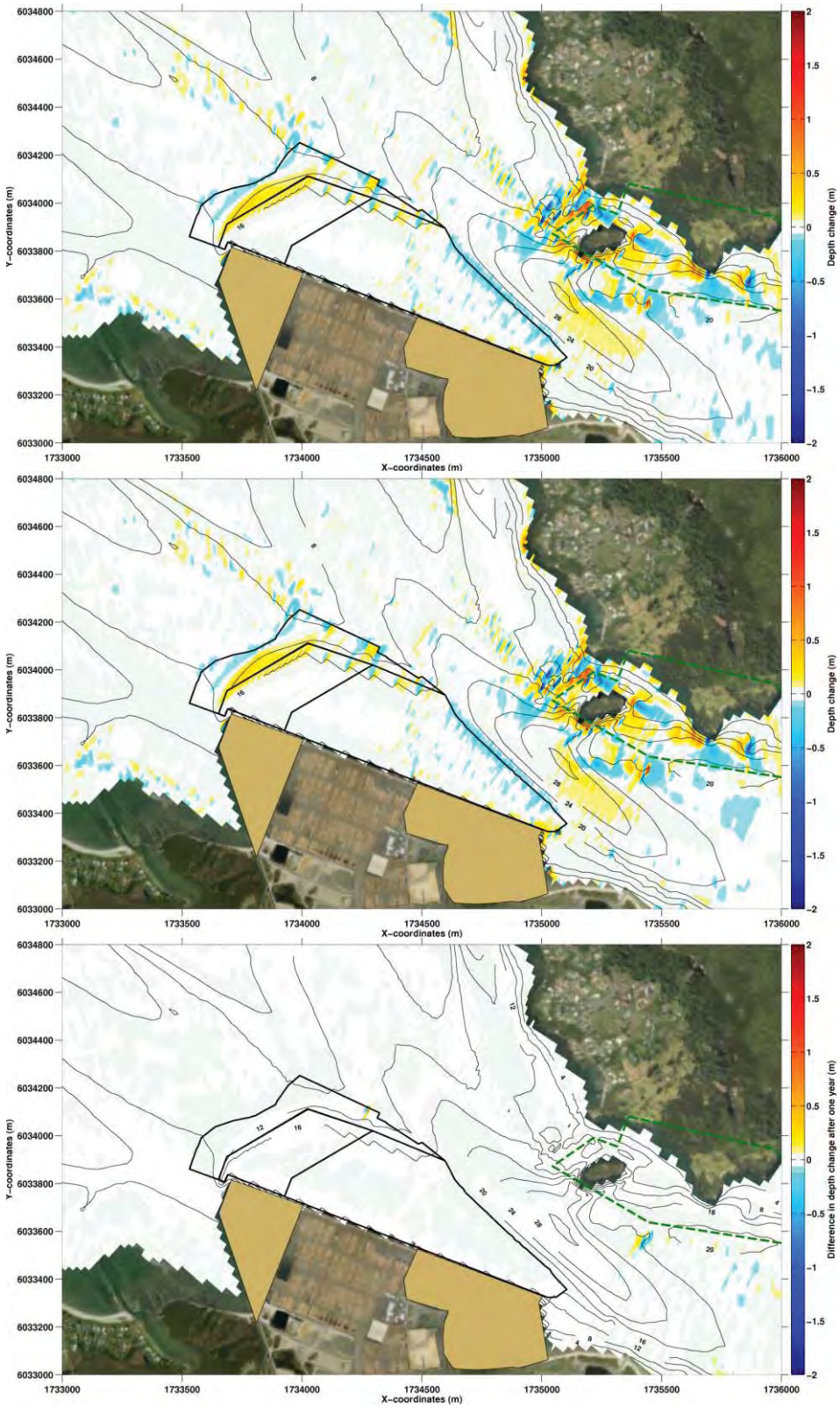

Figure 3.16 Model predicted depth changes predicted over the period 2016-2017 for the Stage 3 (top) and Stage 3 considering the channel deepening RNZ Resource Consent (middle). The bottom pane illustrates the model predicted differences in morphological response for the Stage 3 and Stage 3 considering the channel deepening RNZ Resource Consent.

4. SUMMARY

The calibrated and validated open-source Delft3D system (see MetOcean Solutions Ltd., 2018a) has been used to run high-resolution process based morphodynamic simulations of the Whangarei Harbour in the vicinity of NorthPort in order to understand the likely morphological response of the existing environment to the proposed capital dredging and land reclamation programs. The numerical modelling involved fully-coupled wave, current and seabed interactions.

The modelling approach consisted in simulating the sediment dynamics over the period 2016 – 2017 by applying an input reduction technique and morphological acceleration factors. Details of the applied approach can be found in MetOcean Solutions Ltd., (2018a).

A summary of the main conclusions are as follows;

- Land reclamation associated with Stage 1 development are expected to result in morphological changes near the tip of Snake Bank, due to the propagation of large sand-waves / mega-ripples, and within the swinging basin immediately adjacent to the reclaimed area (Figure 3.4). North-west of the reclamation area erosion of the order ~0.20–0.40 $m.yr^{-1}$ is expected, while accretion of the order 0.10–0.30 $m.yr^{-1}$ can be expected within the existing swinging basin (Figure 3.4).

- While increases in the percentage changes to the sediment transport rate are predicted within Marsden Bay for Stage 1 development, morphological modelling suggests these will not alter the bays morphology.

- No significant changes to the existing sediment transport rates or morphology is expected within the Motukaroro Marine Reserve for either the Stage 1 or Stage 1 assuming the granting of the RNZ channel deepening Resource Consent.

- The morphological response associated with the combination of land reclamation and dredging of Area 3 (Figure 1.2) associated with the Stage 2 development is expected to be limited to the immediate port environs expected.

- Dredging Area 3 associated with the Stage 2 development acts to largely mitigate the effect of the proposed Stage 1 reclamation on the net transport.

- The largest morphological response associated with the Stage 2 development is expected to occur within the battered area to the west of the dredged area, where accretion is expected. An area of accretion is also predicted in the north-east corner of the dredged area (Figure 3.7).

- While increases in the percentage changes to the sediment transport rate are predicted within Marsden Bay for Stage 2 development, morphological modelling suggests these will not alter the bays morphology.

- At Stage 2, the total sedimentation within the swinging basing (Areas 1-3) and batter area after 1-year associated with the development of Stage 2 is expected to be of the order 2,880 m^3 (Table 3.1), with the majority of the

sedimentation occurring with Area 3 and the battered area. Gross infilling (i.e. excluding erosional areas) is expected to be of the order 13,313 m^3

- No significant changes to the existing sediment transport rates or morphology is expected within the Motukaroro Marine Reserve for either the Stage 2 or Stage 2 assuming the granting of the RNZ channel deepening Resource Consent.

- For the Stage 3 development, the effect of land reclamation to accelerate current velocities past NorthPort is largely mitigated by deepening the swinging basin.

- The Stage 3 development morphological response is expected to be limited to the immediate port environs expected, with the largest morphological changes associated predicted to occur within the battered area to the west of Area 3. Erosion is predicted to occur along the north-east edge of the dredged Area 2 (Figure 3.13), and this is attributed to the net transport rate within this region (as shown in Figure 3.12).

- While increases in the percentage changes to the sediment transport rate are predicted within Marsden Bay for Stage 3 development, morphological modelling suggests these will not alter the bays morphology.

- At Stage 3, the total sedimentation within the swinging basing (Areas 1-3) and batter area after 1-year associated with the development of Stage 3 is expected to be of the order 2,489 m^3 (Table 3.1), with the majority of the sedimentation occurring with Area 3 and the battered area. Gross infilling (i.e. excluding erosional areas) is expected to be of the order 14,407 m^3

- No significant changes to the existing sediment transport rates or morphology is expected within the Motukaroro Marine Reserve for either the Stage 3 or Stage 3 assuming the granting of the RNZ channel deepening Resource Consent.

REFERENCES

Besio, G., Blondeaux, P., Brocchini, M., Vittori, G., 2004. On the modeling of sand wave migration. J. Geophys. Res. Oceans 109.

MetOcean Solutions Ltd., 2018a. Morphodynamic evolution modelling for the Northport environment. Numerical modelling of the sediment dynamics at North. Report prepared for Northport.

MetOcean Solutions Ltd., 2018b. Hydrodynamic modelling. Methodology, validation and simulations. Report prepared for Northport.

Royal HaskoningDHV, 2016. Refining NZ Crude Shipping Project - Shiiping Channel - Concept Design Report prepared for Refining NZ.

Tonnon, P.K., Van Rijn, L.C., Walstra, D.J.R., 2007. The morphodynamic modelling of tidal sand waves on the shoreface. Coast. Eng. 54, 279–296.

CRUDE FREIGHT SHIPPING PROJECT, WHANGAREI HARBOUR

Characterisation of the physical environment at the Whangarei Harbour entrance and establishment of numerical models of wave, current and sediment dynamics

Prepared for Chancery Green for Refining New Zealand

MET OCEAN SOLUTIONS LTD
www.metocean.co.nz

PO Box 441, New Plymouth, New Zealand
T: 64-6-7585035 E: enquiries@metocean.co.nz

MetOcean Solutions Ltd: P0236-02

April 2016

Report status

Version	Date	Status	Approved by
RevA	26/04/2016	Draft for internal review	Gardiner
RevB	28/04/2016	Draft for internal review	Felsing
RevC	07/05/2016	Draft for client review	McComb

It is the responsibility of the reader to verify the currency of the version number of this report.

TABLE OF CONTENTS

LIST OF FIGURES

LIST OF TABLES

1. INTRODUCTION

Refining New Zealand (RNZ) is investigating options for the deepening of the shipping channel leading to the Marsden Point Refinery at the entrance to the Whangarei Harbour. Increasing the navigable depth is necessary to allow vessels with increased draft to safely transit to the refinery. MetOcean Solutions Ltd (MSL) have been contracted to provide coastal oceanographic expertise and investigate the potential effects of channel deepening on the physical environment. The scope of work includes i) a comprehensive evaluation of the wave, hydrodynamic and sediment dynamic regime throughout the Whangarei Harbour entrance region, ii) consideration of the effects of capital dredging on this environment, iii) potential effects on the coastal sediment budgets, iv) the stability of the adjacent beaches and the sub-tidal delta, and v) the effects of dredging and disposal on water quality in the receiving environment.

The study investigations are presented in three reports. The present report (MSL Report P0236-02) is a technical reference document that characterises the existing environment and provides details on the establishment numerical models of wave, current and sediment dynamics. The predicted effects of the channel deepening and dredge spoil disposal are presented in a separate technical reference document (MSL Report P0236-03). The results from these two technical reports are summarised in a high level report, MSL Report P0236-04, which is intended for both technical and non-technical readers. A flow diagram of the overall project process is shown in Figure 1.1.

This report is structured as follows. A review of previous studies is provided in Section 2, while an analysis of historic seabed and bathymetry changes in the harbour entrance are presented in Section 3. The wind and wave climate is described in Sections 4 and 5 and the regional hydrodynamic regime is described in Section 6. The nearshore hydrodynamic regime is detailed in Section 7, and the dominant sediment transport processes are described in Section 8. A summary of the report is provided in Section 9.

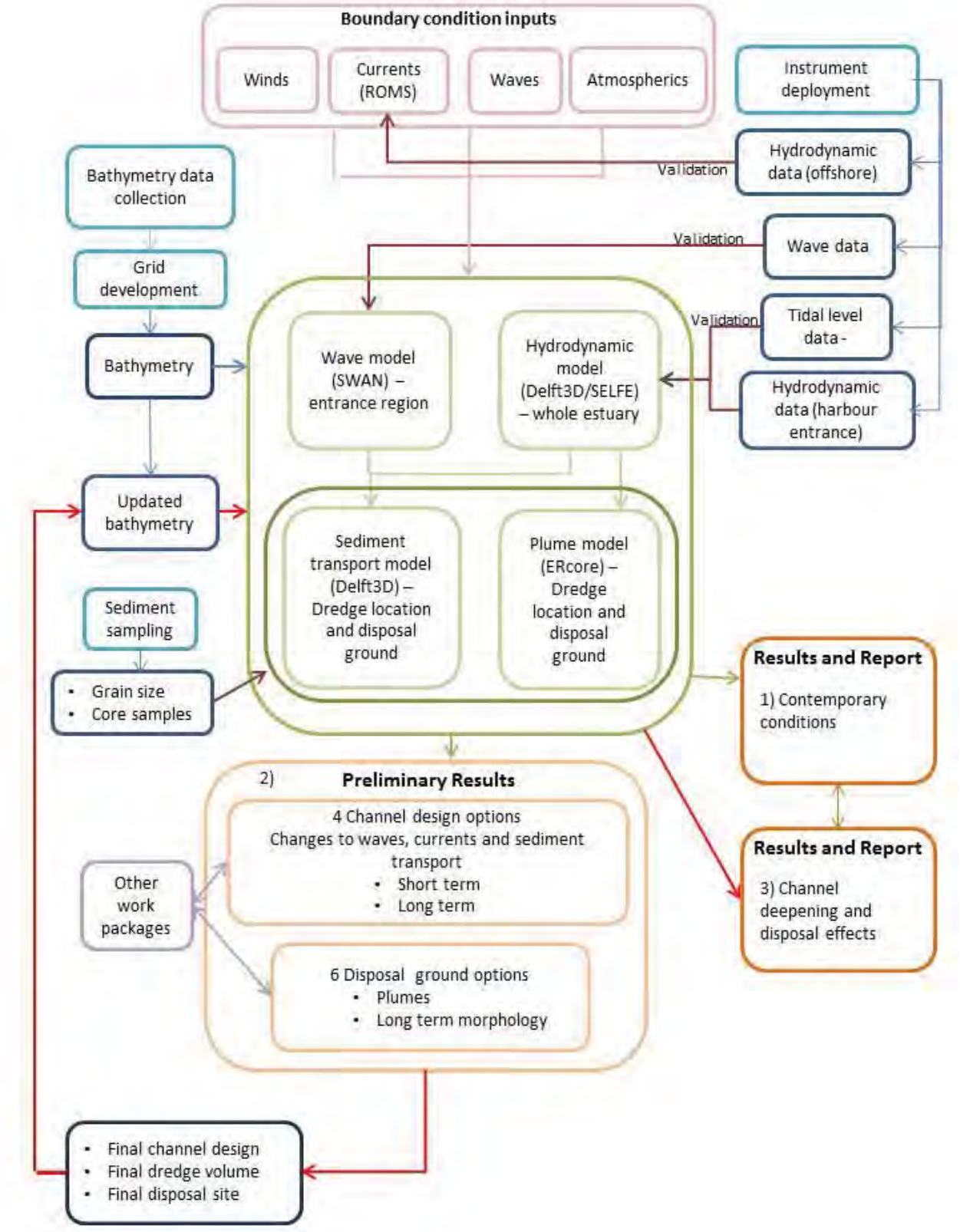

Figure 1.1 Flow chart showing the numerical modelling process for the study.

2. REVIEW OF PREVIOUS STUDIES

This section summarises the findings of relevant previous studies carried out in Whangarei Harbour and the wider Hauraki Gulf. The purpose of the section is to provide regional context as well as summarise the important historical data and findings for considered in the present study.

2.1. Studies of the Whangarei Harbour

2.1.1. Harbour setting

Whangarei Harbour (Figure 2.1) is a mesotidal barrier-enclosed lagoon (lower harbour) and drowned-valley (upper harbour) estuarine system (Longdill and Healy, 2007; Swales et al., 2013) that extends for a distance of ~24 km in length and ~100 km^2 in area (Inglis et al., 2006). The estuary sits at the northern end of the coastal embayment Bream Bay (Lundquist et al., 2009), in the Hauraki Gulf, and includes a diverse range of habitats; including 54 km^2 of intertidal flats, 14 km^2 of mangroves and 2 km^2 of saltmarsh. The harbour has a high-tide surface area of ~104 km^2 and is relatively shallow (mean high-tide depth 4.4 m) due to extensive intertidal flats, particularly in the lower harbour which account for 58% of the high-tide area (Swales et al., 2013).

The harbour is extensively used by the shipping industry, with relatively high traffic of large vessels and cargoes on a national basis. There are three ports within the confines of the harbour: Marsden Point (southeast lower harbour), Portland Cement Terminal (west inner harbour) and Port Whangarei (northwest inner harbour). Port Whangarei was largely developed during the 1920s to 1940s, while construction on the Marsden Point facility first commenced in 2000. These facilities are the most northern multi-purpose ports in New Zealand and the closest ports to the many of New Zealand's international markets.

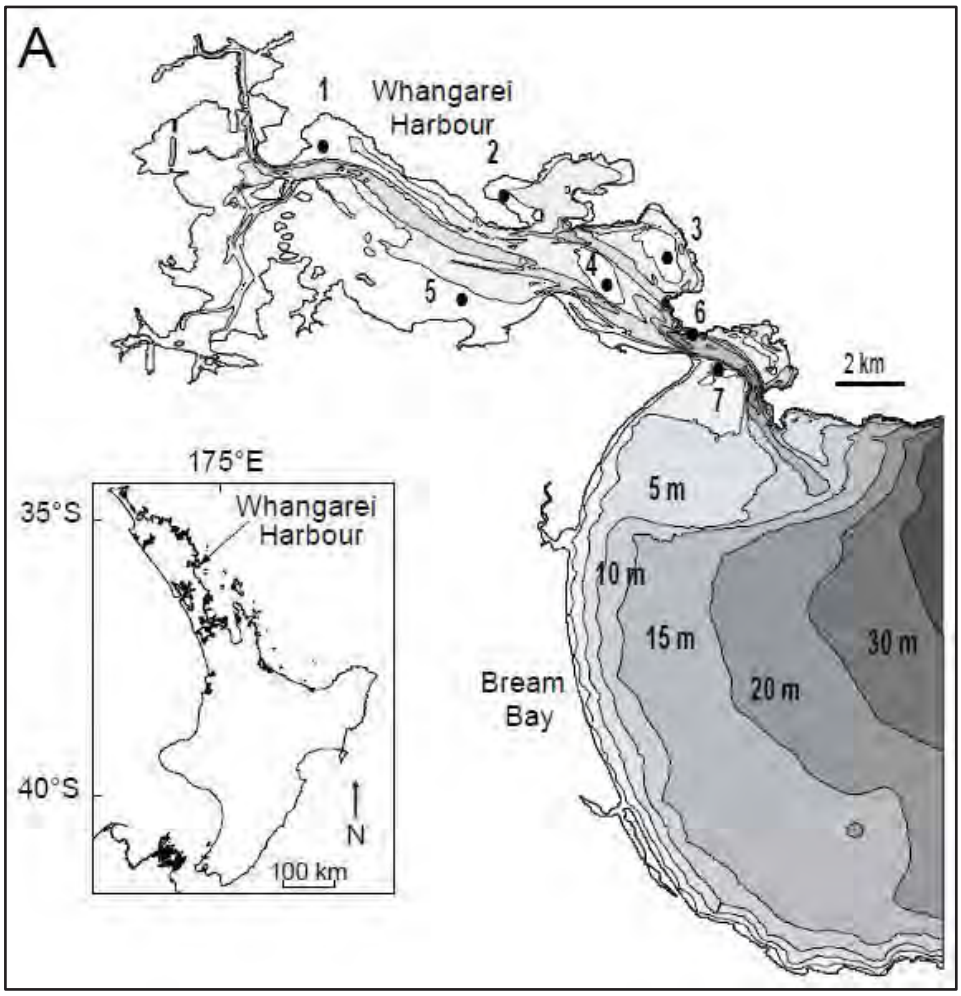

Figure 2.1 Whangarei Harbour situated at the northern side of Bream Bay, northeast New Zealand (rom Lundquist et al., 2009).

2.1.2. Studies of the sediment patterns

The mean grain size of sediments in the Whangarei Harbour decrease with distance up-harbour and away from the main channels, reflecting a decrease in dispersal energy and current velocities (Inglis et al., 2006). The sediment grain size ranges from fine and very fine sands (63 to 250 μm) at the entrance to mud (<63 μm) in the upper tidal creeks (Lundquist et al., 2009).

The upper harbour is dominated by the sheltered tidal arms of the Mangapai and Hātea Rivers (Figure 2.2), which have substantially infilled with sediment (Swales et al., 2013). From the 1920s to the 1970s a major source of mud into the upper harbour was waste material from the Portland cement works, which were directly discharged into the Portland arm of the upper harbour (Inglis et al., 2006).The channel divides near Onerahi, with one arm going north along the Hātea River channel, and the other going southeast into the Portland arm.

The Onerahi Peninsula and Limestone Island (Figure 2.2) form a natural constriction through which sediments transported by river plumes and ebb-tidal currents are exported to the middle and lower reaches of the harbour (Swales et al, 2013). The middle harbour is 45 km wide, with the main channel located at the northern side, and extensive intertidal flats to the south (Inglis et al., 2006). It is predominantly covered by mud and fine sand.

The lower harbour is 2.4 km wide at the mouth, with water depths of 15–31 m (Inglis et al., 2006). The entrance is bounded by Tertiary volcanic rocks on the northern side (Lort Point) and a Holocene prograded sandy barrier spit on the southern side, which forms Marsden Point (Longdill and Healy, 2007). Several bays indent the northern shoreline of the lower harbour, the largest of which is Parua Bay (Figure 2.2). The seafloor in this entrance region is dominated by coarse and fine sands, with extensive regions of shell lag. Also part of the lower harbour, the southeast end region is wider and has small areas of intertidal flats. Sediments in this area of the harbour are mainly fine to medium sands that have been deposited via the harbour entrance (Inglis et al., 2006).

The bathymetry of the lower harbour is relatively stable. Although tidal currents are strong enough to entrain sand on the delta, they do not entrain the shell-lagged channel beds (Black et al., 1989). There is a relatively narrow inlet gorge ~730 m wide which is naturally deep, reaching ~32 m. The inlet throat is dominated by fine sands and shell lag areas (Figure 2.3; Longdill and Healey, 2007). Past dredging has removed some of the shell lag from the area neighbouring the reclamation and exposed medium-sized sandy sediments. Snake Bank and McDonald Bank are the two main flood-tidal deltas located within the harbour inlet embayment (Figure 2.4). Mair Bank and Calliope Bank are two ebb-tidal deltas positioned on the ocean side of the entrance (Morgan et al., 2011).

Mair Bank (**Error! Reference source not found.**) is an intertidal sand and shell ebb tidal delta, and much of the surficial bank sediment is discarded shell, approximately 5-30 cm deep, produced by prolific populations of pipi (*Paphies australis*) that inhabit the elevated southern edge (Morgan et al., 2011). The bank is fully submerged at high tide, but at low tide has a subaerial component of tightly packed shell that extends approximately 1.1 km along its southern edge (Morgan et al., 2011). The bank extends offshore from Marsden Point and is separated from the Bream Bay coast by a narrow channel that expands westward into the harbour. Sandy drifts composed primarily of quartz and feldspar from the Hauraki Gulf facies are located along the northern harbour margin of the delta and along the marginal flood channel (Morgan et al., 2011).

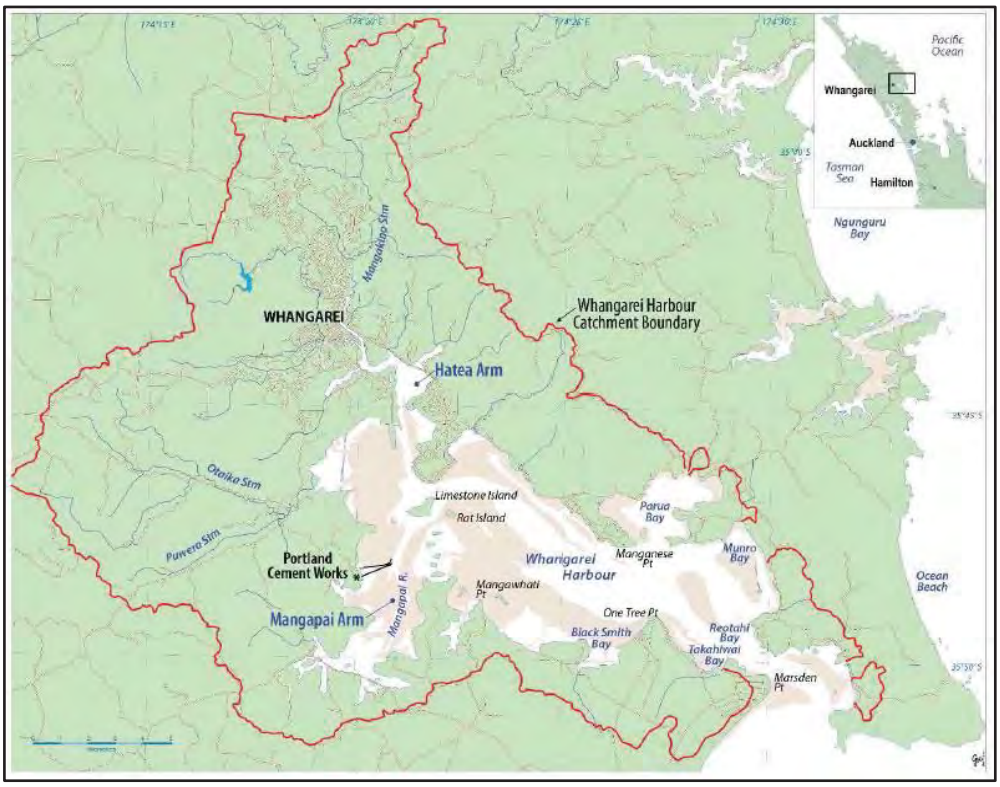

Figure 2.2 Whangarei Harbour and catchment boundary. The lower harbour comprises the region between Marsden Point and Parua Bay/One Tree Point. The middle harbour extends up to Limestone Island, from where the harbour splits and forms two arms (Hātea and Mangapai), which characterise the upper harbour. The city of Whangarei and Port Whangarei are at the upper region of the estuary, along Hātea River. From Swales et al. (2013).

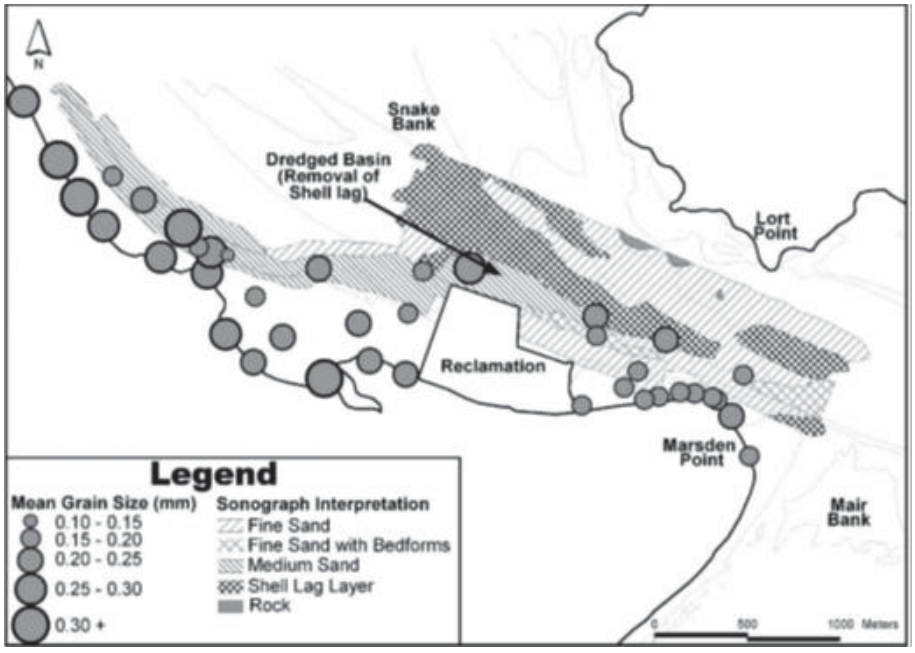

Figure 2.3 Mean grain sizes (sampled 2002), shell lag distributions, and sediments inferred from side scan sonar record (surveyed 2003) at lower Whangarei Harbour. From Longdill and Healy (2007).

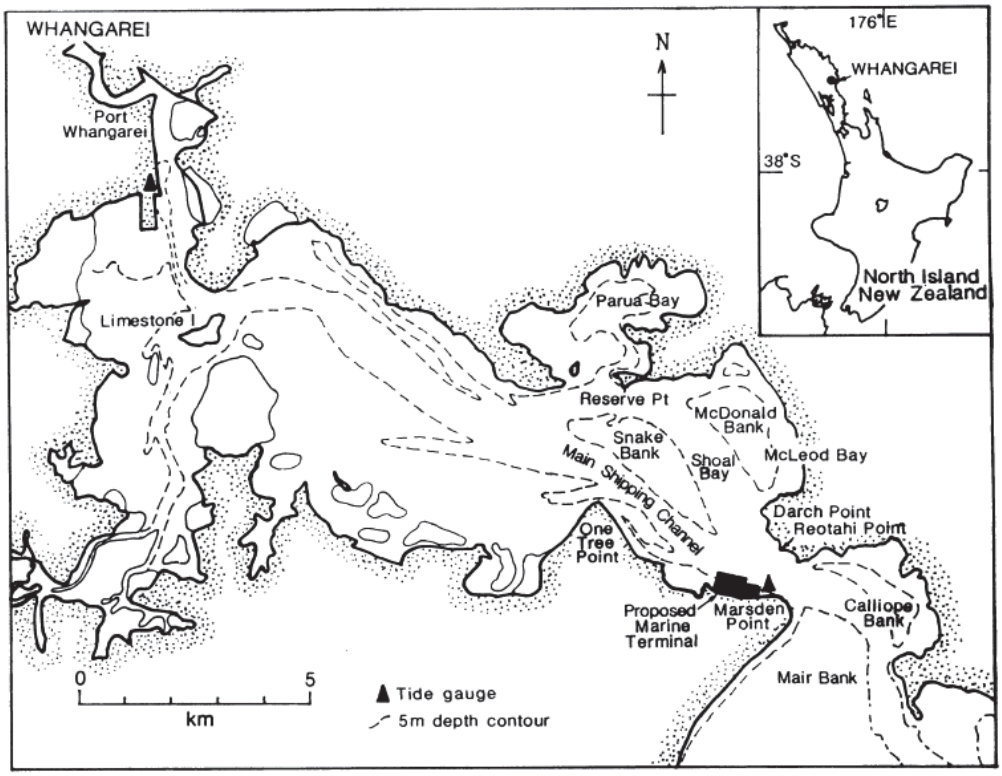

Figure 2.4 Whangarei Harbour, the position of major associated sand bodies and other relevant locations. From Black et al.(1989).

2.1.3. Studies of the sediment transport processes

The Whangarei Harbour has been classified as a stable tidal inlet system. Flushing of accumulated sands from the channel seaward by ebb-currents prevents the inlet channel from infilling, whilst a residual shell lag armours the inlet gorge preventing lateral and vertical erosion of the throat (Morgan et al., 2011).

The lower harbour sediment dynamics are consistent with established patterns for tide-dominated inlets, with separation of the channel into areas of ebb and flood dominance, and typical transport patterns over the flood tidal delta. Broad-scale inlet geomorphology has been maintained, which is consistent with other dredged tide dominated inlets (Longdill and Healy, 2007). Concentrations of shell gravel lag were found to play an important stabilising role in determining the overall characteristics of the inlet stability and sediment dynamics. In the Mair Bank ebb delta, the shell was not only effective locally, but it also reduced sediment transport overall by limiting the availability of sand that could go into suspension in the strong flood and ebb-tidal currents (Black et al., 1989). The detrital shell material armours underlying finer-grained sediments reducing actual sediment transport rates well below the potential rates of transport. Live pipi also appear to be an integral part in maintaining overall stability by increasing the shear resistance of Mair Bank to tidal currents and reducing overall transport. The planform position of Mair Bank has been shown to be relatively stable at decadal time scales; however, extensive changes in surface morphology has occurred in response to local energy conditions (Morgan et al., 2011). Significant declines in pipi populations have been documented to increase the ‘erodibility’ of Mair Bank under storm conditions (Morgan et al., 2011; Pawley, 2014). Morgan et al. (2011) showed that the morphological footprint of Mair Bank has remained relatively static at multi-decadal time scales, but showed significant variation in surface morphology inter-annually.

The shell swashbar on the southern margin of the delta demonstrated the most movement. Net movement of the swashbar was northward (landward), with significant variability in the rate of movement occurring along its extent. The northern margin of Mair Bank (southern edge of the Whangarei Harbour channel) showed complete stability at long-term time scales.

Comparisons of bathymetric surveys revealed that the lower harbour is very stable with essentially no change to bathymetry in many areas over a 20-year interval. Recorded tidal flows were found to be faster than the threshold speed for typical sandy sediments, but insufficient to disturb lagged shell beds (Black et al., 1989). Previous studies suggest that suspended sediment transport in the lower harbour is low and that the majority of sediment transport in the channels and channel margins occurs as bed load (Longdill and Healey 2007).

Residual distance vectors computed by Longdill and Healy (2007) in the lower harbour indicate that since 2002 (i.e. post NorthPort developments), the large-scale pattern of sediment transport dynamics remained consistent. Minor and localised modification of transport potentials were observed immediately adjacent to the NorthPort developments. These modifications included a slight realignment of current flows near the reclamation wall and some leakage from a previously identified transport loop near the dredged basin. The potential for scour was identified along the eastern margin of the dredged basin, and it was suggested this could remove material moving downslope into the basin from its western edge. These observations were considered to be consistent with the numerical model results that predicted minimal consequences resulting from the developments.

Sediment transport pathways were inferred by Black et al. (1989) from observations and numerical modelling (Figure 2.5). According to their results, there is a net ebb imbalance in the lower harbour southern end and they suggested that deposition as a result of the NorthPort developments should be minimal.

2.1.4. Studies of the tides, currents and waves

The harbour has a spring tidal prism of 186 x 10^6 m^3, with approximately 28% of the estuary volume flushed each tide (Black et al., 1989; Inglis et al., 2006). The mean tidal range is 1.7 m during neap tides and 2.3 m during spring tides (Swales et al., 2013). On the basis of several different morphologic classification schemes, the Whangarei Harbour inlet entrance is considered tidally dominated (Longdill and Healey, 2007) and characterised by a deep main ebb channel extending offshore. Within the tide-dominated framework, the harbour has both well-developed flood tidal delta (Snake and McDonald Banks) and ebb tidal delta (Mair and Calliope Banks) systems (Figure 2.3; Longdill and Healey, 2007).

Tidal current velocities gradually decrease up-harbour, from around 1 m s^{-1} at Marsden Point to 0.8 m s^{-1} at Limestone Island (Inglis et al., 2006). Tidal streams are strongest in the area adjacent to Home Point southeast of Marsden Point, where rates up to 3 knots may be experienced (Inglis et al., 2006). The constricted tidal inlet results in currents reaching peak depth-averaged velocities of 1.1-1.3 m s^{-1} during spring tides (Black et al., 1989; Longdill and Healy, 2007).

The estuary is typically unstratified (Lundquist et al., 2009) and has minimal inputs of fresh water (Inglis et al., 2006). The Hātea River is the main source of fresh water to the harbour, with a mean annual flow of 1 m^3 s^{-1}. The Waiarohia and Raumahanga streams have mean annual flows of 0.35 m^3 s^{-1} and 0.34 m^3 s^{-1}, respectively (Reeve et al., 2010). During summer, most of the harbour is well

mixed, while in winter the lower harbour is well mixed and the upper harbour is partially mixed. High freshwater inputs cause a salt-wedge structure in the Port Whangarei area and causes the lower harbour to become partially mixed.

The residence times calculated for water masses in Whangarei Harbour range from 24 days in winter to 120 days in summer (Inglis et al., 2006). Residence times typically decrease with increasing freshwater input into the harbour, although freshwater input is generally low due to the small size of the surrounding catchment (Inglis et al., 2006).

Wave refraction patterns in Bream Bay show that the Whangarei Harbour inlet entrance emerges in a zone of low energy that provides natural stability to the inlet (Morgan et al., 2011). Wave activity inside the harbour is mostly locally generated (fetch ~5km near Marsden Point) although some ocean swell refracts and diffracts to reach the port vicinity (Black and Healy, 1982). Mair Bank is protected from ocean wave activity by Busby Head to the east, with generally only E-SE storm waves reaching it with any significant intensity (Black and Healy, 1982).

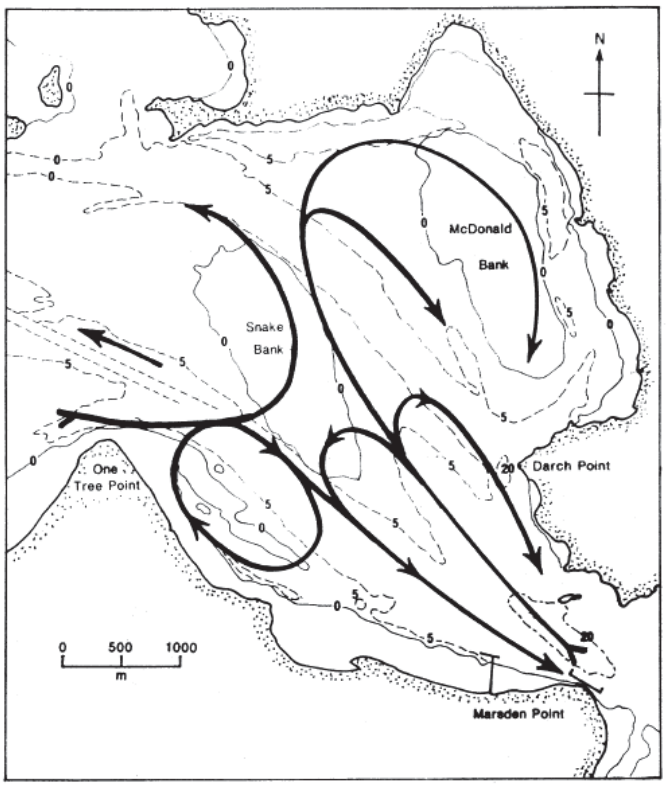

Figure 2.5 Schematic diagram showing sediment transport loops and pathways revealed by the residual velocities and distances from a 2 dimensional model taken in conjunction with field observations and measurements. From Black et al. (1989).

2.2. Studies of the regional circulation and wave patterns

Bream Bay is a coastal embayment located at the north end of the Hauraki Gulf (northeast coast of New Zealand) which receives the estuarine waters from Whangarei Harbour (Figure 2.1). It is generally aligned to the north east and is approximately 23 km long (Tonkin and Taylor, 2010). The region experiences a low to moderate energy wave climate, in the New Zealand context. The maximum recorded wave height for Bream Bay is 9 m (H_{max}), which occurred during a July 1978 storm event (Swales et al., 2013). This record appears consistent with other more recent observed maximum wave heights in the area. The mean significant wave height for Bream Bay was recorded at 0.7 m for the period March 1995 to June 1997 (Nichol, 2002). The principal direction of swell incidence to the Bream Bay coast is from the north east to east sector. The Bream Bay coast is partially sheltered from this direction by the promontory of Bream Head (Figure 2.6). Bream Head forces waves from the north east direction to refract fully before reaching the shoreline.

Based on hydrographic charts the 10 m depth contour is approximately 830 m offshore along the majority of the bay (slope of 0.012). The offshore bathymetry changes north of the Ruakaka River mouth, where the Whangarei Harbour ebb tide delta reduces the offshore slope to 0.0045. The wide, low gradient nearshore zone associated with the ebb tide delta has a dissipative effect on incident waves in this area (Swales et al., 2013).

The Hauraki Gulf is a shallow, funnel-shaped semi-enclosed sea on the northeast coast of New Zealand's North Island (Black et al., 2000). The Gulf is adjacent to a narrow continental shelf which quickly broadens from only 11 km wide at Cape Brett (out to the 200 m contour) to 120 km wide off Great Barrier Island, before narrowing again off Coromandel Peninsula. It has semi-estuarine characteristics in the inner embayments and spatially variable tidal and residual currents. With maximum water depths of up to 30-60 m, the Hauraki Gulf is prone to thermal stratification from austral spring through to autumn. The outer Gulf is directly exposed to ocean waves from the eastern quadrant and is essentially open shelf, but somewhat sheltered by the headlands and islands to the southeast and northeast, and behaves like a large-scale coastal embayment (Black et al., 2000).

The large scale oceanography of northern New Zealand is dominated by a general west to east movement of oceanic water from the Tasman Sea (Tomczak and Godfrey, 1994). Part of this flow temporarily attaches to the northeastern New Zealand continental shelf as it flows toward the Eastern Pacific, forming a southeastward-flowing current of warm (16 - 22^{o}C), saline (>35.4 psu) subtropical water, the East Auckland Current (EAUC) (Stanton et al., 1997; Zeldis et al., 2004). Due to the narrow continental shelf in the gulf region, the proximity of EAUC slope waters has significant implications for the inner shelf and coastal zone physics and nutrient supply (Zeldis et al., 2004).

The salinity ranges between 34.5 and 35.7 psu in open waters and is not greatly influenced by land runoff because of relatively small catchments, except in the shallow southern sector (Firth of Thames and Waitemata Harbour), where salinities can be lowered to 33-34 psu in winter after heavy rain (Black et al., 2000). The long sea surface temperature record off Leigh (Cape Rodney) show a 20-year annual mean of 17.1 ± 3.3^{o}C, peaking in late summer (February) and lowest in August (Bell and Goring, 1998).

In the analysis of current meter data from 5 locations inside the Gulf, Greig (1990) observed that the strongest signal in the time series were associated with tidal forcing. The major constituents for the area were M_2, S_2 and N_2, where the first was the dominant signal and flows were virtually rectilinear (ellipticity small) being aligned with the local bathymetry. The phases were consistent with the essentially standing-wave nature typical of gulf tides and found in the M_2 numerical model of Greig and Proctor, (1988). Maximum recorded flows are of the order of 0.25-0.4 m s^{-1} throughout the Gulf except near Cape Colville where 0.8 m s^{-1} was recorded. Greig and Proctor (1988) modelled the response of the gulf to M_2 tidal forcing and they found that tidal residual circulation is weak. Using current meter observations, Sharples and Greig (1998) inferred that seasonal and weather-band variability in the strength of vertical stratification has a marked effect on the observed tidal currents through the addition of a baroclinic tide, which is highly non-linear. They also found that surface mean flows observed throughout all deployments were generally along the shelf edge, and towards the southeast at speeds of 0.2-0.3 m s^{-1} and reaching 0.6 m s^{-1} at times near Cape Brett.

Circulation in the Hauraki Gulf is strongly 3-dimensional, with a primary dynamical balance between surface wind stress and the associated pressure gradients against the land (Black et al., 2000). This leads to persistent up/downwelling and surface manifestations in sea surface temperature patterns which are shown to vary systematically and markedly with wind direction and stratification intensity. (Sharples and Greig, 1998; Zeldis et al., 2004) showed that the non-tidal residual shelf circulation is highly responsive to the seasonal wind field, with dominant upwelling in winter and spring, and a change to downwelling in summer, when intrusions of low-nutrient surface waters of the EAUC cross the shelf break.

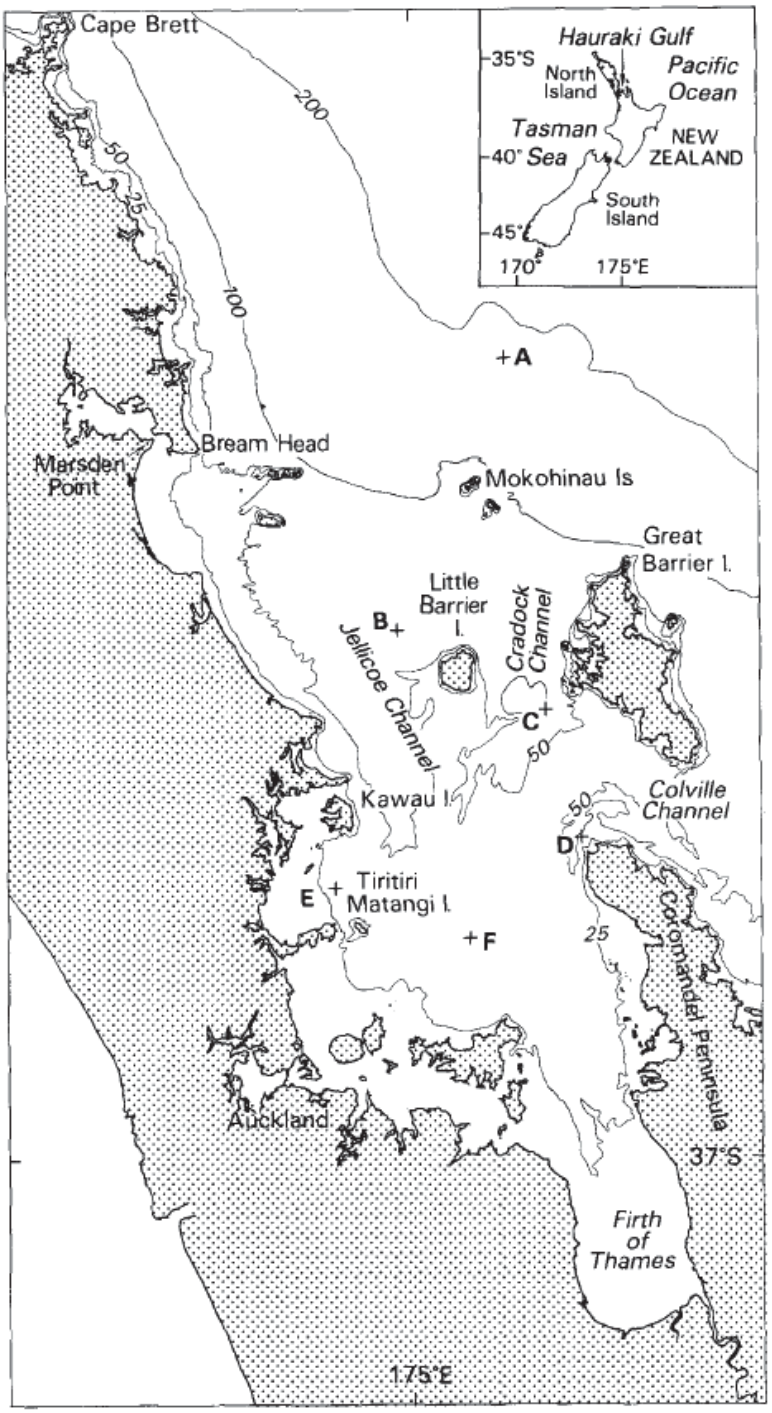

Figure 2.6 Map of Hauraki Gulf, which is limited by the Firth of Thames (at the south end) and Coromandel Peninsula and Great Barrier Island (at the east side). The Gulf's northern limit is at Cape Brett. Bathymetric contours of 25 m, 50 m, 100 and 200 m are indicated. From Greig (1990).

The shelf system was also modelled by Proctor and Greig (1989) and Black et al. (2000), who simulated the wind responses of the shelf circulation. They found that the residual circulation owing to the tides is weak with the main feature a north-westerly flow of 0.01-0.02 m s^{-1} over much of the mid and western parts of the Gulf. Considerable variability was evident close to shore, caused by the numerous irregular coastal features. In the Gulf, a greater response is seen to winds orientated NW/SE than to winds from NE or SW. Thus, the wind-forcing causing

the largest changes to the residual circulation in the Gulf will be that from the NW, as SE winds are relatively weak in this area (Figure 2.7). Black et al. (2000) suggested that observed spatial patterns could be largely explained by the interaction of the wind and tidal circulation with the unique morphology of the Gulf.

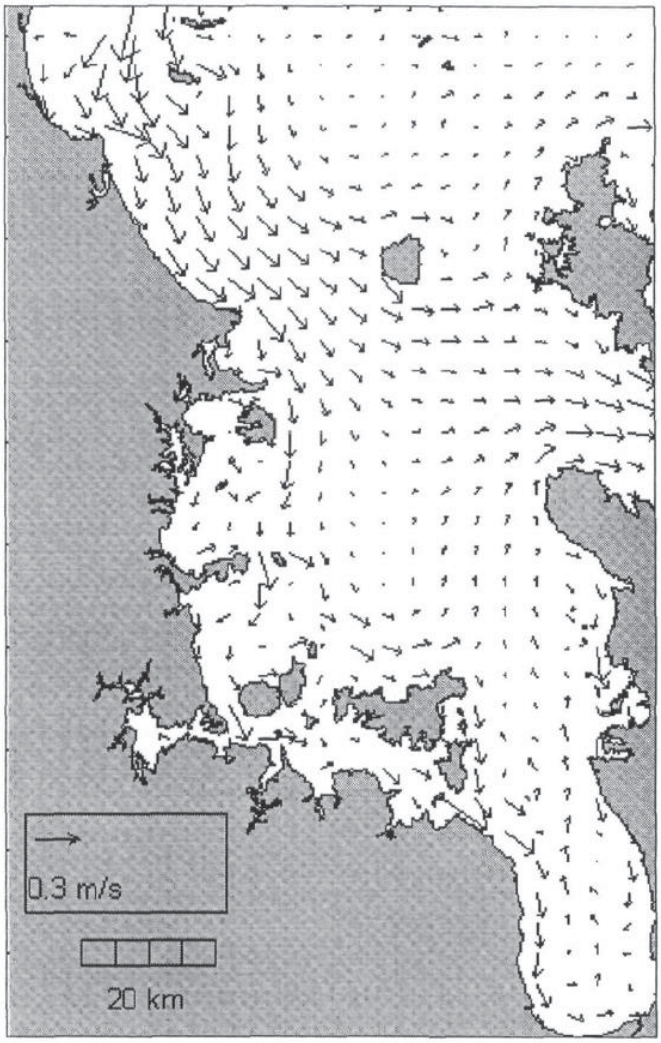

Figure 2.7 Predicted depth-averaged, near-steady-state velocities for the Hauraki Gulf, New Zealand, for a northwest wind of 15 m s^{-1}. From Black et al. (2000).

3. BATHYMETRY AND SEABED CHARACTER

This section presents seabed bathymetry and the changes that can be inferred from a detailed analysis of the historical measurements. A summary of the nature of the surficial sediments in the channel and the offshore harbour delta is also provided.

3.1. Historic bathymetry

The morphology of Mair Bank has been studied by several authors including Black (1983); Morgan (2008) and Morgan et al. (2011) as outlined in Section 2. Here, a new analysis of the historic changes of the seabed morphology in the entrance region up until present day (2015) has been undertaken. The purpose is to understand the natural variability of the seabed shape within the harbour entrance region. Such observations provide important evidence of the historical variability that can assist with the interpretation of the numerical prediction of future changes associated with a deepened channel. The data sets used in this study include fare sheets and the contemporary surveys of the ebb tidal shoal, the Mair Bank and the inner shoal regions. All data has been reduced to Chart datum (CD), which corresponds to the lowest astronomical tide and so is the approximate division between the subtidal and intertidal regions.

Faresheet data from 1939, 1959 and 1981 and a multibeam survey from 2015 were compared to assess the historic morphological change of the wider tidal shoal (Figure 3.1 and Figure 3.2); illustrating that very little broad-scale change has occurred across the wider shoal region since at least 1939. In contrast, a close examination of shallow regions of Mair Bank reveals significant variation in morphology (Figure 3.3). However, the sides of the main channel adjacent to Mair Bank show very little morphological variation up to the 2 m depth contour.

Multibeam surveys over the Mair Bank and main channel region have been regularly made since 2001. The sequence of morphological changes isshown in Figure 3.4 to Figure 3.6, with the cross sectional profiles indicated on these images shown in Figure 3.7. A gradual northwards migration of Mair Bank and the shell ridges has also been observed (Figure 3.8 to Figure 3.10). Cross section profiles across multiple locations on the bank show the migration of these ridges northwards through time, extending the bank into the channel in some locations. These observations support the previous findings (Morgan et al., 2011) that sediment reworking is an important process on the Mair Bank and governs its local scale morphology. However as a large scale delta-feature, it has maintained relative spatial stability.

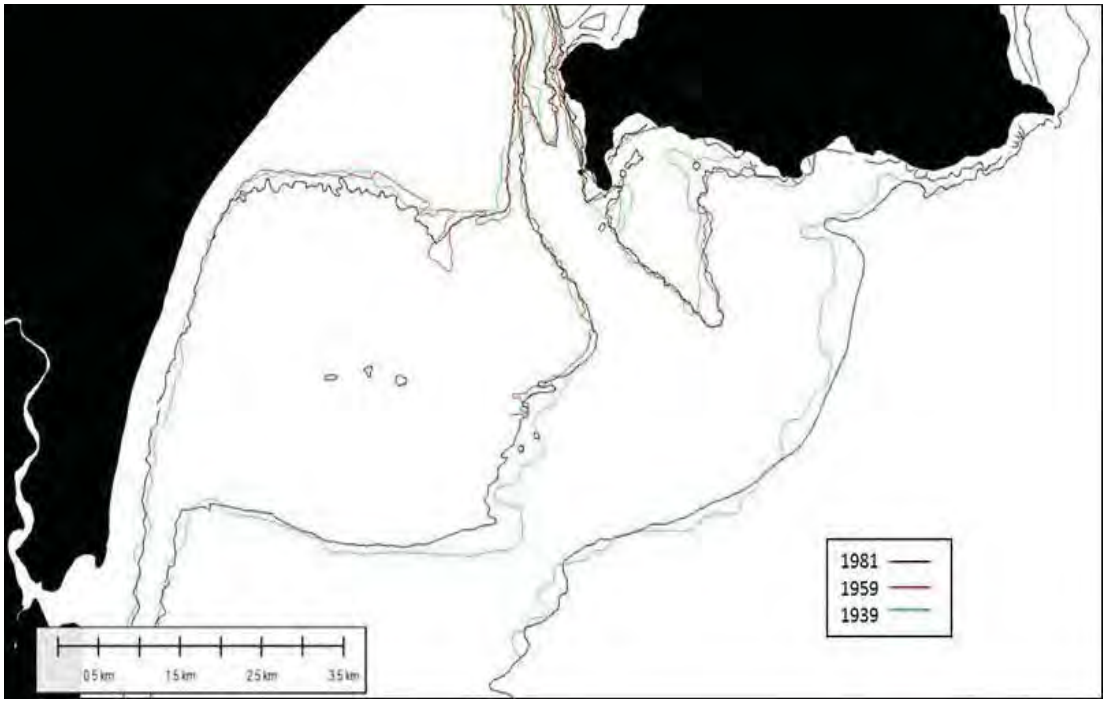

Figure 3.1 Depth contours derived from historic digitised fare sheet data for 1981,1959 and 1939.

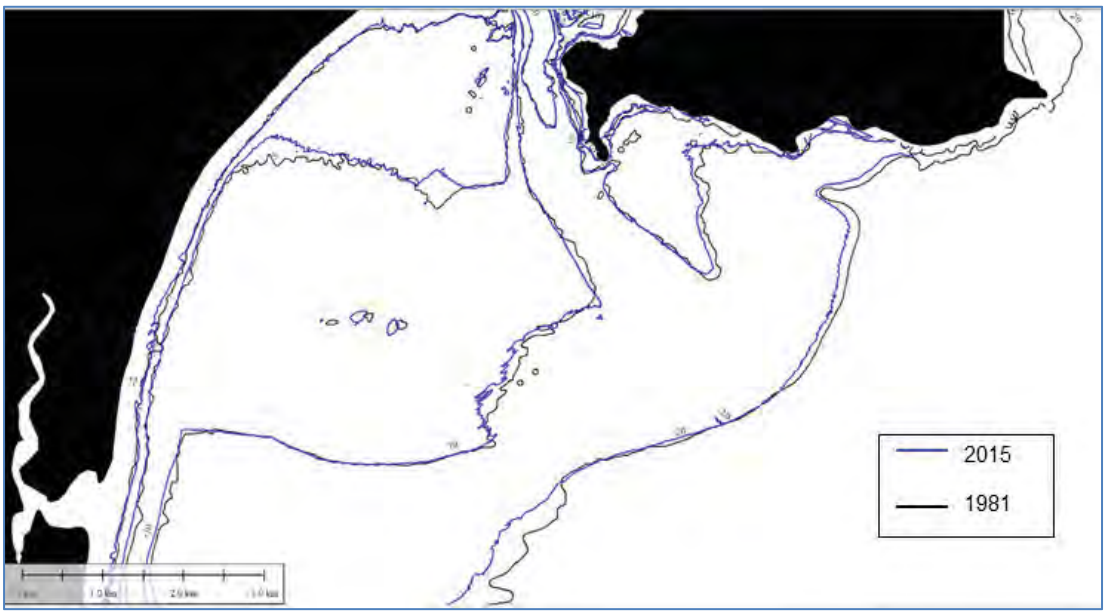

Figure 3.2 Depth contours derived from historic fare sheet data from 1981, alongside contours derived from a 2015 multibeam survey.

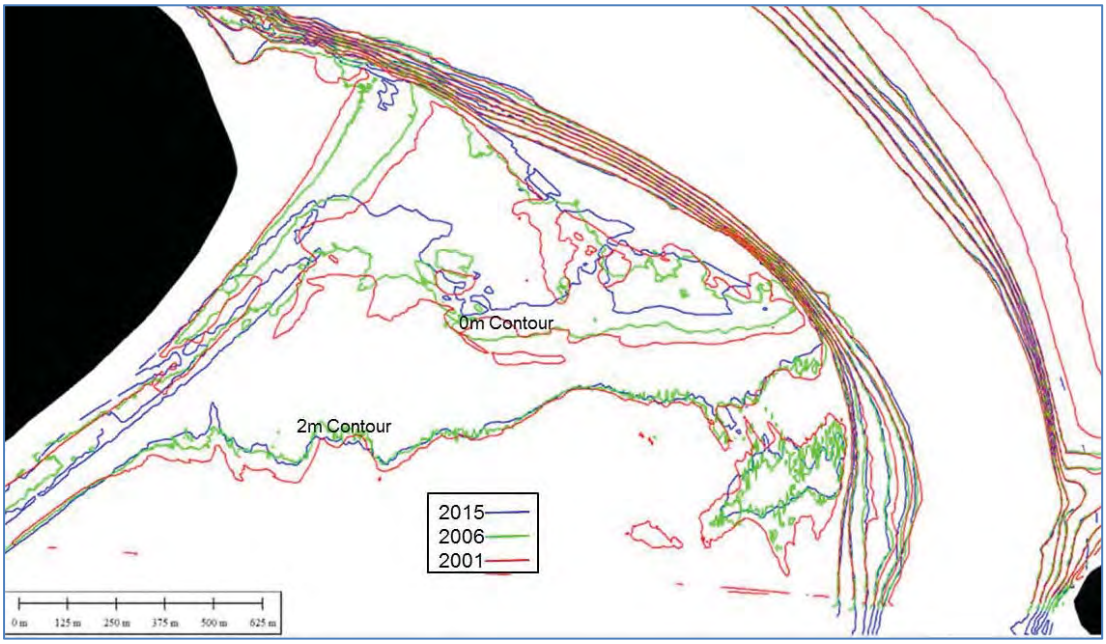

Figure 3.3 Depth contours for Mair bank derived from multibeam surveys.

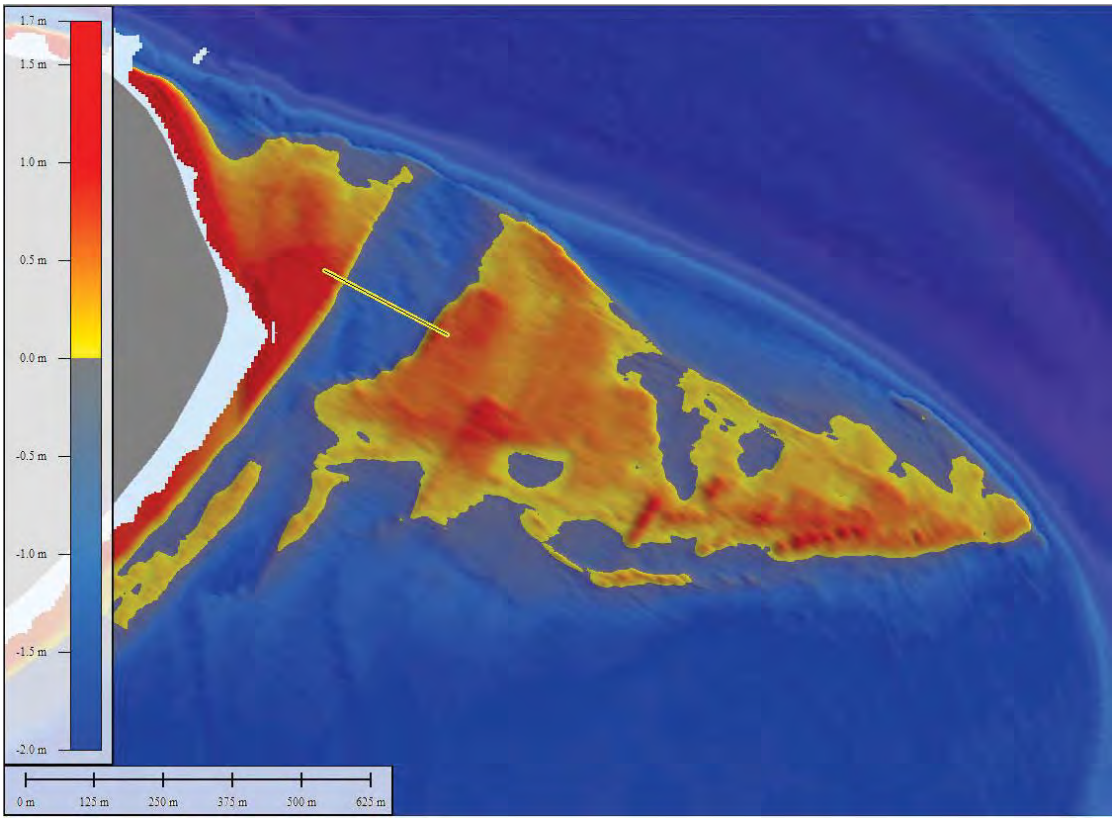

Figure 3.4 Multibeam survey from 2001 and cross sectional profile (yellow, shown in Figure 3.7)

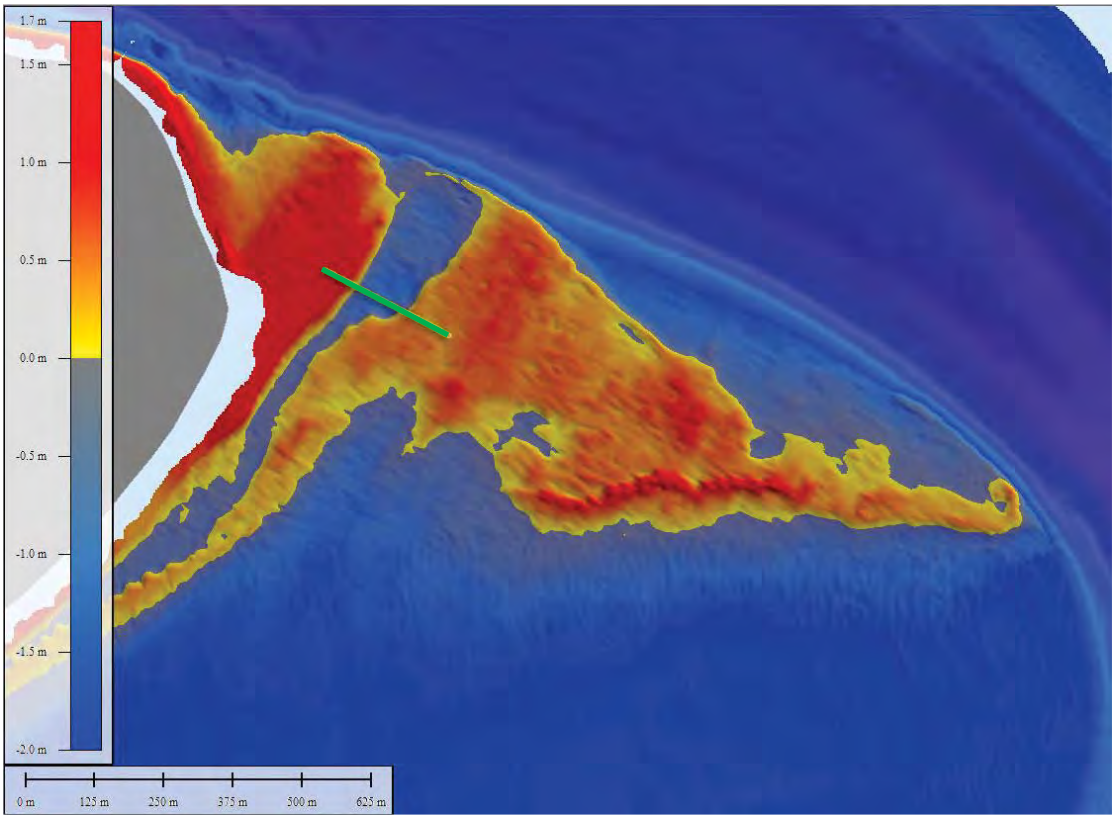

Figure 3.5 Multibeam survey from 2009 and cross sectional profile (green, shown in Figure 3.7)

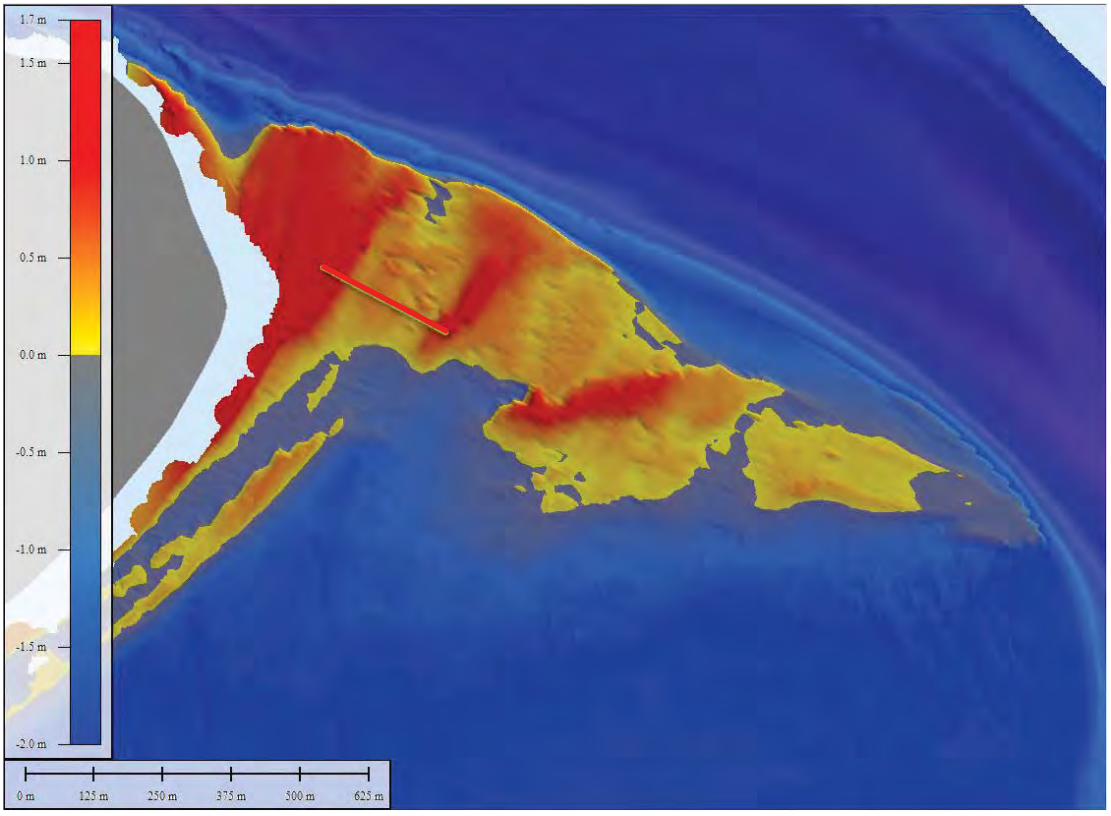

Figure 3.6 Multibeam survey from 2015 and cross sectional profile (red, shown in Figure 3.7)

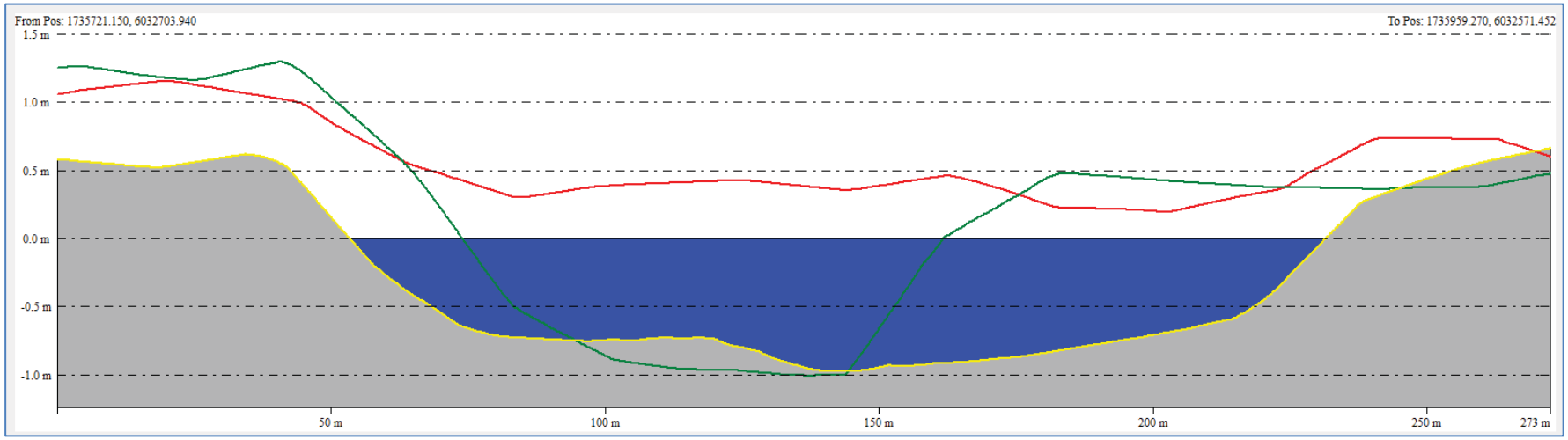

Figure 3.7 Cross section profile (west to east) across historic channel (location shown in Figure 3.4 to Figure 3.6)

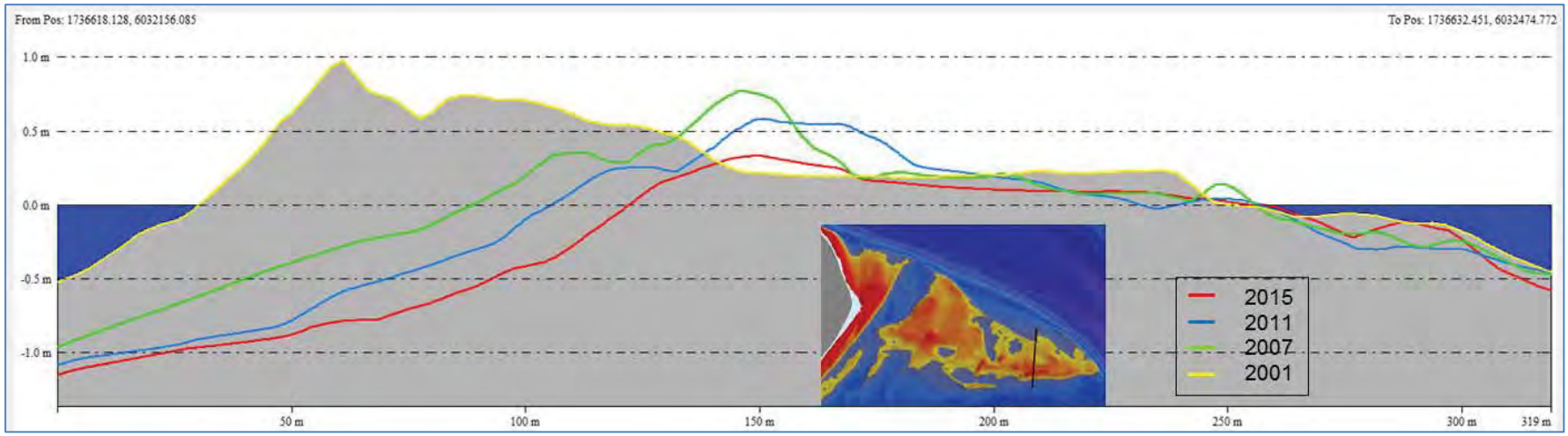

Figure 3.8 Cross section profiles (south to north) across Mair Bank at eastern end of the bank (location indicated), for four different years.

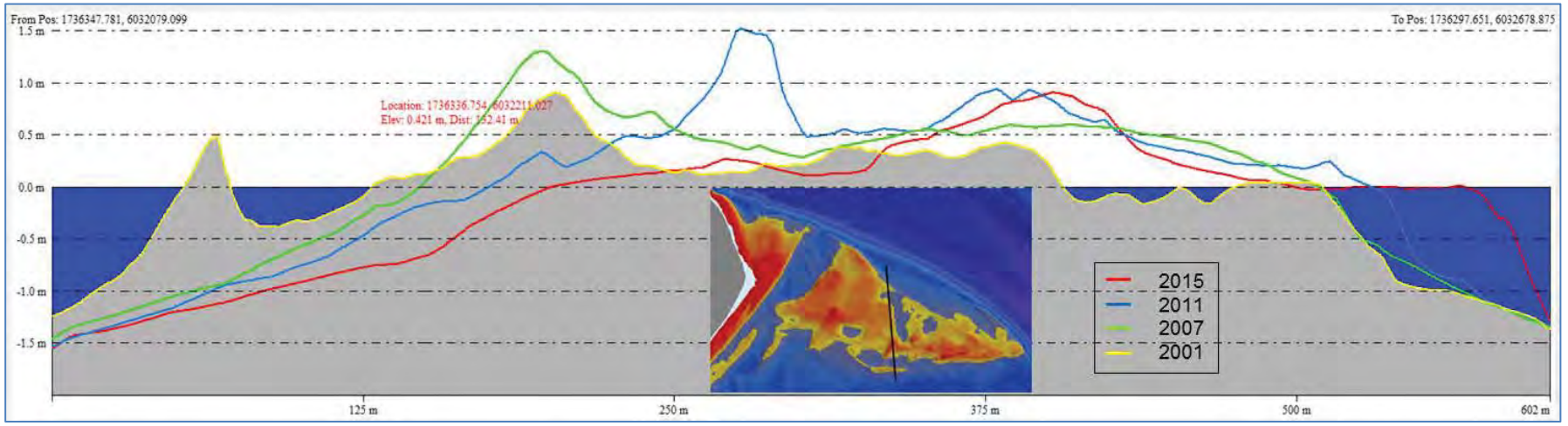

Figure 3.9 Cross section profiles (south to north) across Mair Bank across the centre of the bank (location indicated), for four different years.

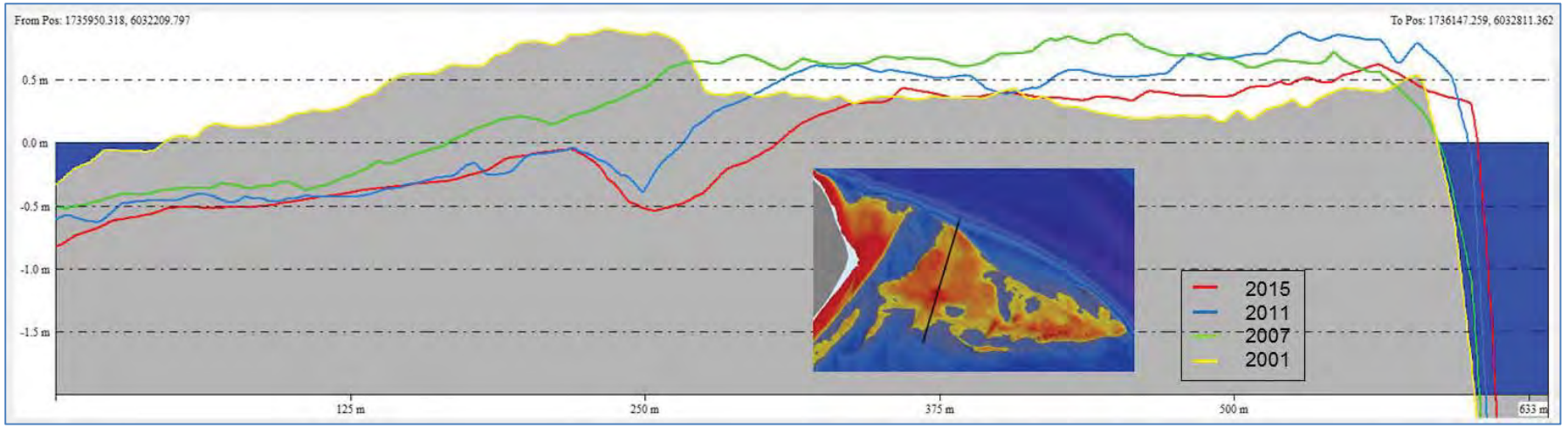

Figure 3.10 Cross section profiles (south to north) across Mair Bank at the western end of the bank (location indicated), for four different years.

3.2. Contemporary bathymetry

Bathymetry is an essential component of the numerical modelling process. Extensive national and regional bathymetric datasets have been compiled from various sources and used and validated in previous hydrodynamic studies. These datasets have been updated with the latest Whangarei Harbour, main channel and offshore surveys. Specialist data manipulation tools have been used to merge, interpolate and quality check e of raw bathymetric data when establishing numerical model domains. Bathymetry data and sources are shown in Figure 3.11.

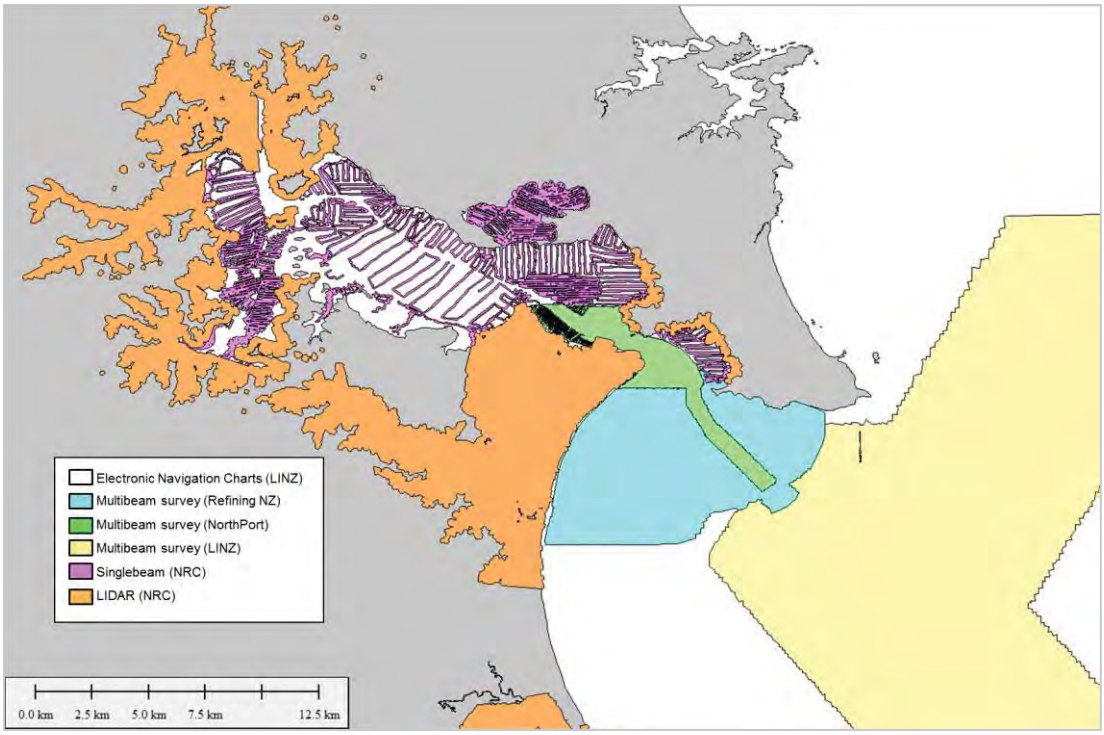

Figure 3.11 Sources of bathymetry data used in the numerical model studies.

3.3. Surficial sediments

xx

xx

4. WIND CLIMATE

This section summarises the wind conditions in the Whangarei Harbour vicinity. These data are used, along with outputs from the ROMS hydrodynamic model (described in Section 6) to provide boundary conditions for the local wave and hydrodynamic modelling carried out for the study.

The near-surface wind field was prescribed by a 36-year (1979-2014) regional atmospheric hindcast carried out by MSL. The WRF (Weather Research and Forecasting) model was established over all of New Zealand at hourly intervals and approximately 12 km resolution. The hindcast was specifically tuned to provide highly accurate marine wind fields for metocean studies around New Zealand. The WRF model boundaries were sourced from the CFSR (Climate Forecast System Reanalysis) dataset distributed by NOAA (Saha et al., 2010), which was available at hourly intervals and 0.31° spatial resolution. While the WRF hindcast produced atmospheric parameters at hourly intervals over the 36 years, only the near surface wind field (i.e. 10 minute mean at 10 m elevation) will be used in the study. Validation of the WRF reanalysis has been undertaken at various locations around New Zealand.

A summary of the wind speed statistics for the 10-minute mean at 10 m elevation at the wave rider buoy (WRB) site (WGS84: 174.548294°E, 35.883099°S) is provided in Table 4.1. The annual mean wind speed is 6.10 m s^{-1}, while the windiest month is July (mean 6.69 m s^{-1}) and the least windy month is February (mean 5.58 m s^{-1}).

The monthly and annual wind speed exceedance probabilities are provided in Table 4.2, and indicate that wind speeds exceeding 16 m s^{-1} can occur throughout the year, with July having the highest occurrence of strong wind events.

Joint probability distributions of the wind speed and direction are presented in Table 4.3 for the annual conditions. The same data are presented in the wind rose plots in Figure 4.1 and Figure 4.2Figure 4.1 Annual wind rose plot at WRB. Sectors indicate the direction from which wind is coming. showing the annual predominance of winds coming from the SW quadrant.

Table 4.1 Annual and monthly wind speed statistics at WRB.

Wind speed (m/s))	Parameter					
	Mean ($m\ s^{-1}$)	Median ($m\ s^{-1}$)	P90 ($m\ s^{-1}$)	P95 ($m\ s^{-1}$)	P99 ($m\ s^{-1}$)	Max ($m\ s^{-1}$)
Jan	5.71	5.45	9.28	10.52	13.22	19.24
Feb	5.58	5.35	9.09	10.33	13.33	17.32
Mar	5.75	5.54	9.34	10.71	13.61	23.74
Apr	5.64	5.36	9.25	10.61	13.14	20.01
May	6.10	5.84	10.04	11.21	13.59	19.54
Jun	6.50	6.23	10.60	12.18	14.99	20.09
Jul	6.69	6.26	11.22	13.02	16.14	22.76
Aug	6.46	6.14	10.75	12.09	14.79	20.02
Sep	6.48	6.25	10.44	11.92	14.87	19.88
Oct	6.43	6.24	10.32	11.52	13.65	18.91
Nov	6.17	5.99	9.82	10.95	13.77	20.05
Dec	5.70	5.47	9.31	10.46	13.06	18.56
1979	5.82	5.46	9.60	10.96	13.72	18.91
1980	6.25	6.06	10.26	11.61	14.62	20.08
1981	6.19	5.81	10.37	11.60	13.78	18.11
1982	5.87	5.57	9.62	11.14	13.51	20.39
1983	6.16	5.89	9.76	11.21	14.15	21.08
1984	5.83	5.53	10.03	11.39	14.06	18.49
1985	6.23	6.01	10.35	11.46	14.41	19.63
1986	5.64	5.35	9.39	10.84	13.91	19.24
1987	5.95	5.69	9.86	11.09	13.41	17.13
1988	6.35	6.09	10.34	11.86	15.01	23.74
1989	6.34	5.92	10.59	12.36	15.30	20.02
1990	5.71	5.45	9.34	10.55	13.27	18.49
1991	6.13	6.00	9.65	10.71	12.82	16.61
1992	6.35	6.20	10.10	11.22	14.15	19.20
1993	5.89	5.66	9.71	10.89	13.91	20.07
1994	6.42	6.25	10.20	11.37	13.81	18.30
1995	6.09	5.94	9.64	10.87	13.20	19.88
1996	6.52	6.31	10.33	11.82	14.35	20.09
1997	6.11	5.74	10.05	11.66	14.74	19.21
1998	6.34	5.90	10.70	12.36	15.67	20.05
1999	6.02	5.79	9.87	11.00	13.61	16.56
2000	6.14	5.74	10.09	12.20	14.95	18.20
2001	6.27	6.10	9.92	11.22	14.34	18.08
2002	6.45	6.29	10.16	11.22	13.70	19.58
2003	6.14	5.77	10.03	11.55	14.09	18.51
2004	6.21	6.01	10.07	11.51	13.81	17.13
2005	5.78	5.48	9.65	10.82	14.21	17.98
2006	5.93	5.68	9.66	10.81	14.09	19.58
2007	6.07	5.78	10.12	11.69	14.74	21.62
2008	6.36	6.10	10.19	11.90	14.65	20.83
2009	6.08	5.84	9.87	11.22	14.51	22.76
2010	6.00	5.63	9.94	11.70	14.08	18.89
2011	6.05	5.61	10.27	11.79	14.20	17.27
2012	6.25	6.06	9.99	11.34	13.75	17.29
2013	5.72	5.38	9.63	11.08	13.83	17.39
2014	6.09	5.68	10.15	11.97	15.53	20.85
Annual	6.10	5.83	9.99	11.36	14.27	23.74

Table 4.2 Monthly and annual wind speed exceedance probabilities at WRB.

Wind speed (m/s)	Exceedance (%)												
	January	**February**	**March**	**April**	**May**	**June**	**July**	**August**	**September**	**October**	**November**	**December**	**Year**
>2	92.95	92.33	92.53	92.19	93.22	94.07	94.37	94.33	94.21	94.69	94.46	93.18	93.55
>4	70.93	69.37	71.42	70.12	74.10	77.45	78.45	77.18	78.00	78.02	76.81	71.38	74.46
>6	42.44	40.78	43.49	41.48	48.07	52.86	53.24	51.59	53.15	53.42	49.92	42.11	47.75
>8	19.37	17.88	19.44	18.92	24.94	29.84	30.19	29.00	28.91	28.67	24.29	19.05	24.24
>10	6.72	5.94	7.34	6.76	10.22	13.11	15.47	13.65	12.33	12.12	8.85	6.65	9.96
>12	2.51	2.09	2.58	2.23	2.99	5.38	7.43	5.34	4.77	3.77	2.60	2.03	3.65
>14	0.59	0.66	0.72	0.54	0.80	1.86	3.24	1.76	1.66	0.74	0.88	0.50	1.17
>16	0.16	0.14	0.24	0.15	0.15	0.58	1.10	0.43	0.42	0.16	0.24	0.11	0.32
>18	0.04	0.00	0.11	0.03	0.03	0.17	0.38	0.10	0.08	0.04	0.06	0.03	0.09
>20	0.00	0.00	0.07	0.01	0.00	0.02	0.13	0.01	0.00	0.00	0.01	0.00	0.02
>22	0.00	0.00	0.03	0.00	0.00	0.00	0.01	0.00	0.00	0.00	0.00	0.00	0.00

Table 4.3 Annual joint probability distribution (parts per thousand) of the wind speed and wind direction at WRB.

Wind speed (m/s)	Wind direction (degT, from)								
	337.5 -22.5	22.5 -67.5	67.5 -112.5	112.5 -157.5	157.5 -202.5	202.5 -247.5	247.5 -292.5	292.5 -337.5	Total
0 - 2	6.3	6.2	7.0	7.0	8.1	10.5	11.0	8.3	64.4
2 - 4	17.0	19.3	21.9	18.6	22.5	33.0	35.2	23.4	190.9
4 - 6	25.5	26.1	26.3	20.1	26.1	56.1	49.9	37.1	267.2
6 - 8	25.9	20.2	25.8	14.3	16.2	59.9	43.9	28.9	235.1
8 - 10	19.9	12.4	17.3	9.6	7.8	31.1	29.6	15.2	142.9
10 - 12	10.3	8.0	9.6	5.6	2.8	9.8	11.5	5.5	63.1
12 - 14	4.2	4.6	4.7	3.3	1.0	2.5	3.0	1.6	24.9
14 - 16	1.3	1.9	2.4	1.0	0.4	0.5	0.6	0.3	8.4
16 - 18	0.3	0.5	0.7	0.4	0.1	0.1	0.1	0.0	2.2
18 - 20	0.1	0.2	0.3	0.1	0.0	0.0	0.0	0.0	0.7
20 - 22	0.0	0.0	0.1	0.0	0.0	0.0	0.0	0.0	0.1
Total	110.8	99.4	116.1	80.0	85.0	203.5	184.8	120.3	1000.0

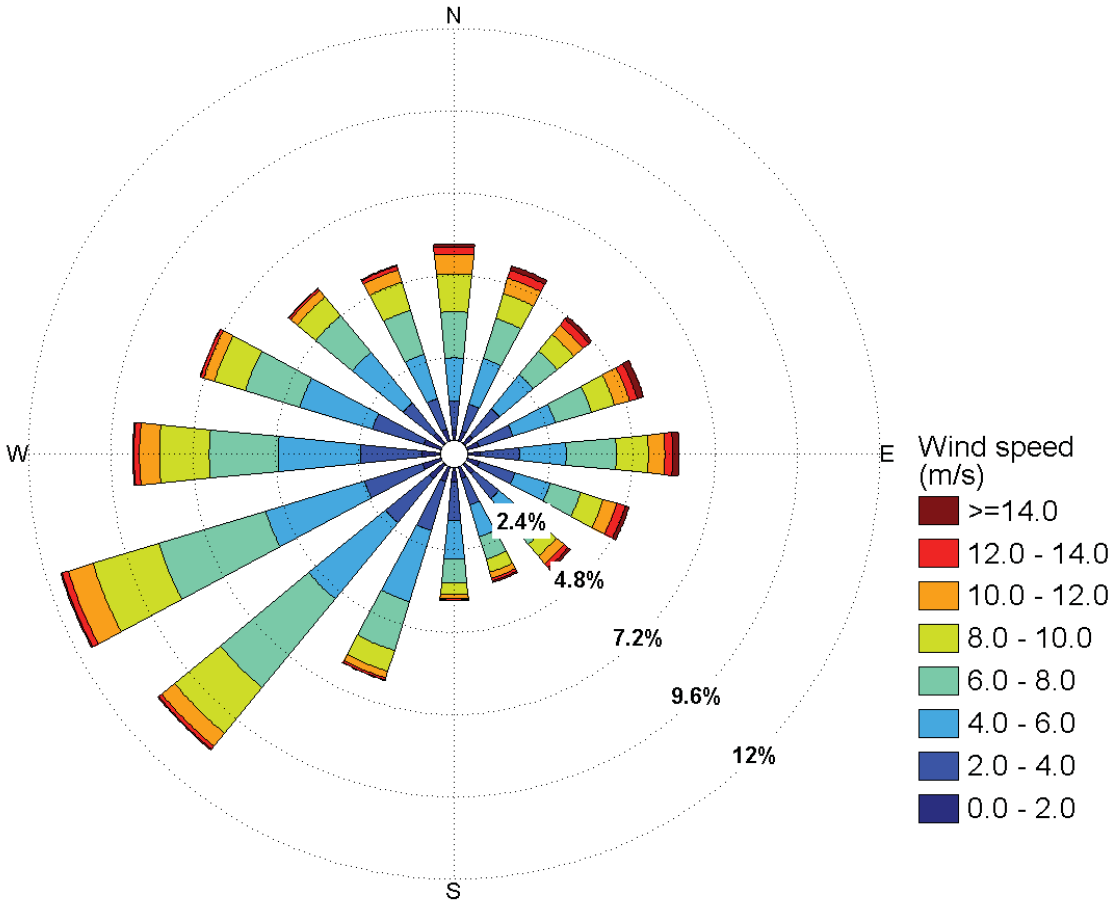

Figure 4.1 Annual wind rose plot at WRB. Sectors indicate the direction from which wind is coming.

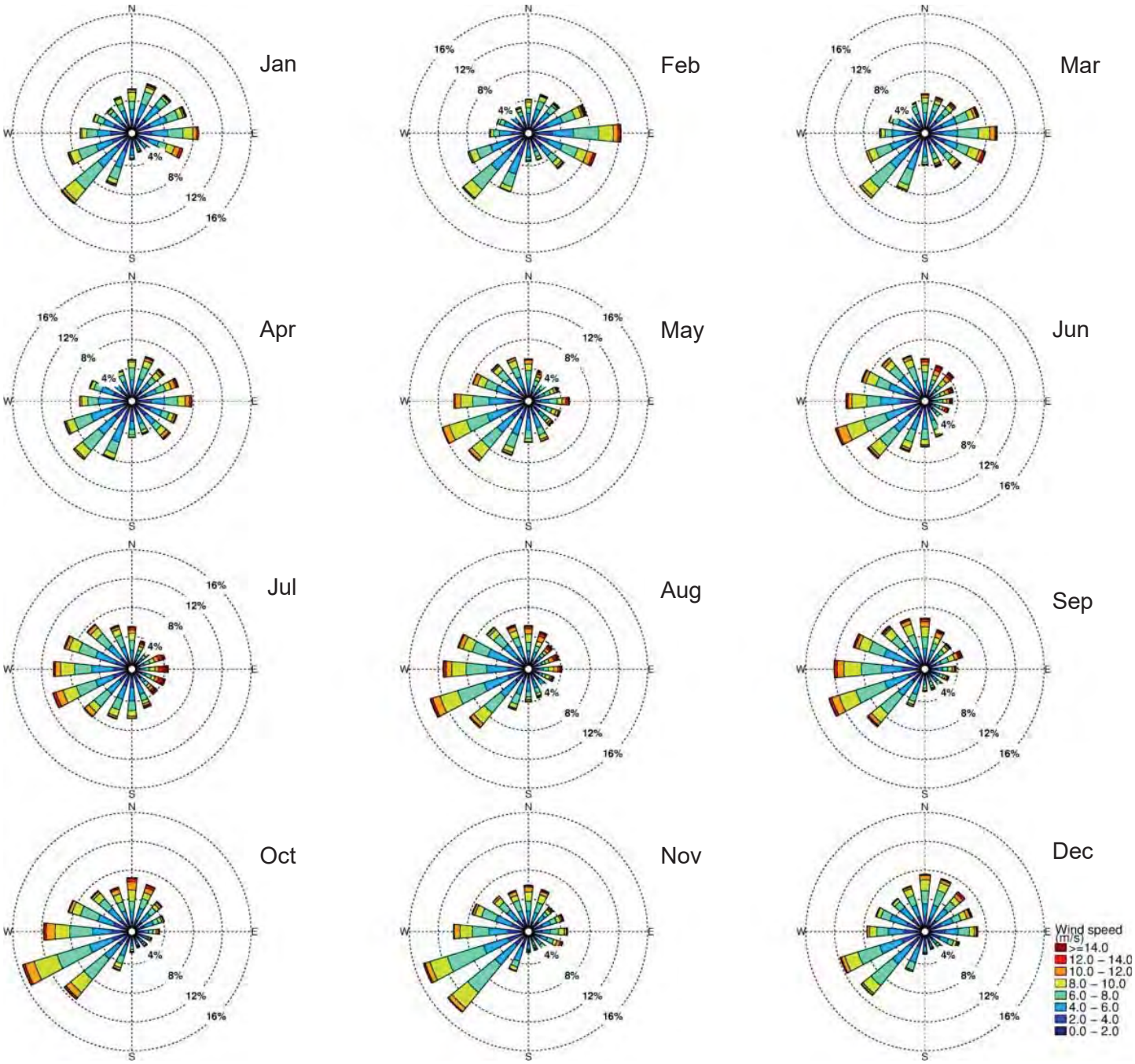

Figure 4.2 Monthly wind rose plots at WRB. Sectors indicate the direction from which the wind is coming.

5. WAVE CLIMATE

This section details the numerical wave hindcast modelling used to characterise the regional wave climate as well as the nearshore wave transformation to the harbour entrance.

5.1. Model methodology

5.1.1. Model description

A modified version of SWAN[1] (Simulating Waves Nearshore) was used for the hindcast wave modelling. The hindcast extended over a 36-year period between years 1979 and 2014.

SWAN is a third generation ocean wave propagation model, which solves the spectral action density balance equation for wavenumber-direction spectra. This means that the growth, refraction, and decay of each component of the complete sea state, each with a specific frequency and direction, is solved, giving a complete and realistic description of the wave field as it changes in time and space. A detailed description of the model equations, parameterisations and numerical schemes can be found in Holthuijsen (2007) or the SWAN documentation[2].

Physical processes that are simulated include the generation of waves by surface wind, dissipation by white-capping, resonant nonlinear interaction between the wave components, bottom friction and depth limited breaking. All 3rd generation physics are included. The BYDRZ physics package developed for WW3 model, which accounts for the effects of full air flow separation and therefore relative reduction of the input at strong wind forcing, was implemented in SWAN and used for the hindcast. The Collins (1972) friction scheme was used for wave dissipation by bottom friction.

The solution of the wave field is found for the non-stationary (time-stepping) mode. Boundary conditions, wind forcing and resulting solutions are all time dependent, allowing the model to capture the growth, development and decay of the wave field.

5.1.2. Model domain and boundary conditions

The wave hindcast involved three-level SWAN downscaling to model the nearshore region at about 50 m resolution. Full spectral boundaries for the parent domain were prescribed from MSL implementation of WAVEWATCH3 global wave model (Tolman, 1991) with the Tolman and Chalikov (1996) physics.

The limits and resolutions for each SWAN nest are shown in Table 5.1. The parent domain was forced with full spectral boundaries from WW3 and provided boundaries to run a first SWAN child at 0.0015 degree. A second child nest with about 50 m resolution was defined to resolve the complex bathymetric features near the shore. All nests were configured with 24 frequency bins (logarithmic scale from 0.04 to 0.66 Hz) and 36 directional bins. Model depth and snapshots of significant wave height (Hs) are shown for the three SWAN nests in Figure 5.1 - Figure 5.3. SWAN was run with wind fields specified from the MSL New Zealand Reanalysis.

[1] Modified from SWAN version of the 40.91 release (publicly available code)

[2] http://swanmodel.sourceforge.net/online_doc/online_doc.htm

Table 5.1 Boundary, resolution and limits defined for each SWAN nest.

Domain	Boundary	Longitude (degree)			Latitude (degree)		
		x1	x2	dx	y1	y2	dy
Parent	WW3	174.45	174.45	0.009	-37.23	-35.23	0.009
Child 1	Parent	174.451	174.8	0.0015	-36.04	-35.8	0.0015
Child 2	Child 1	174.458	174.558	0.0005	-35.925	-35.825	0.0005

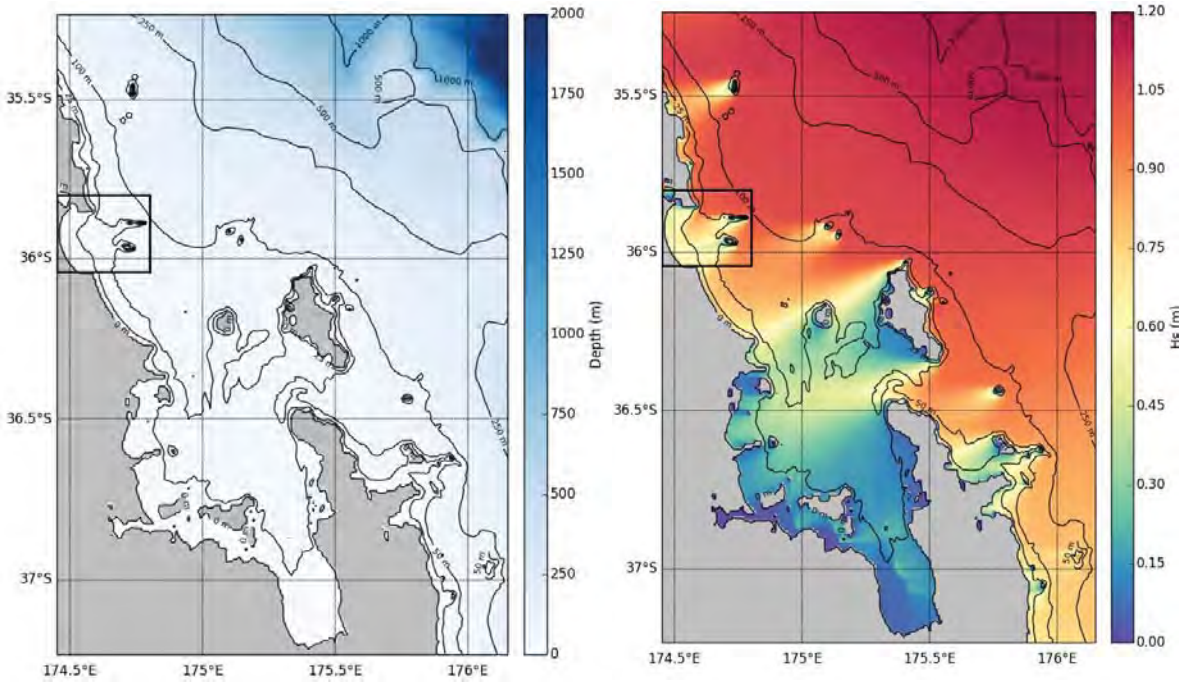

Figure 5.1 Model depths (top) and snapshot of modelled significant wave height (bottom) for the 0.009 degree SWAN parent domain. Extension of the first child nest is shown by the black rectangle.

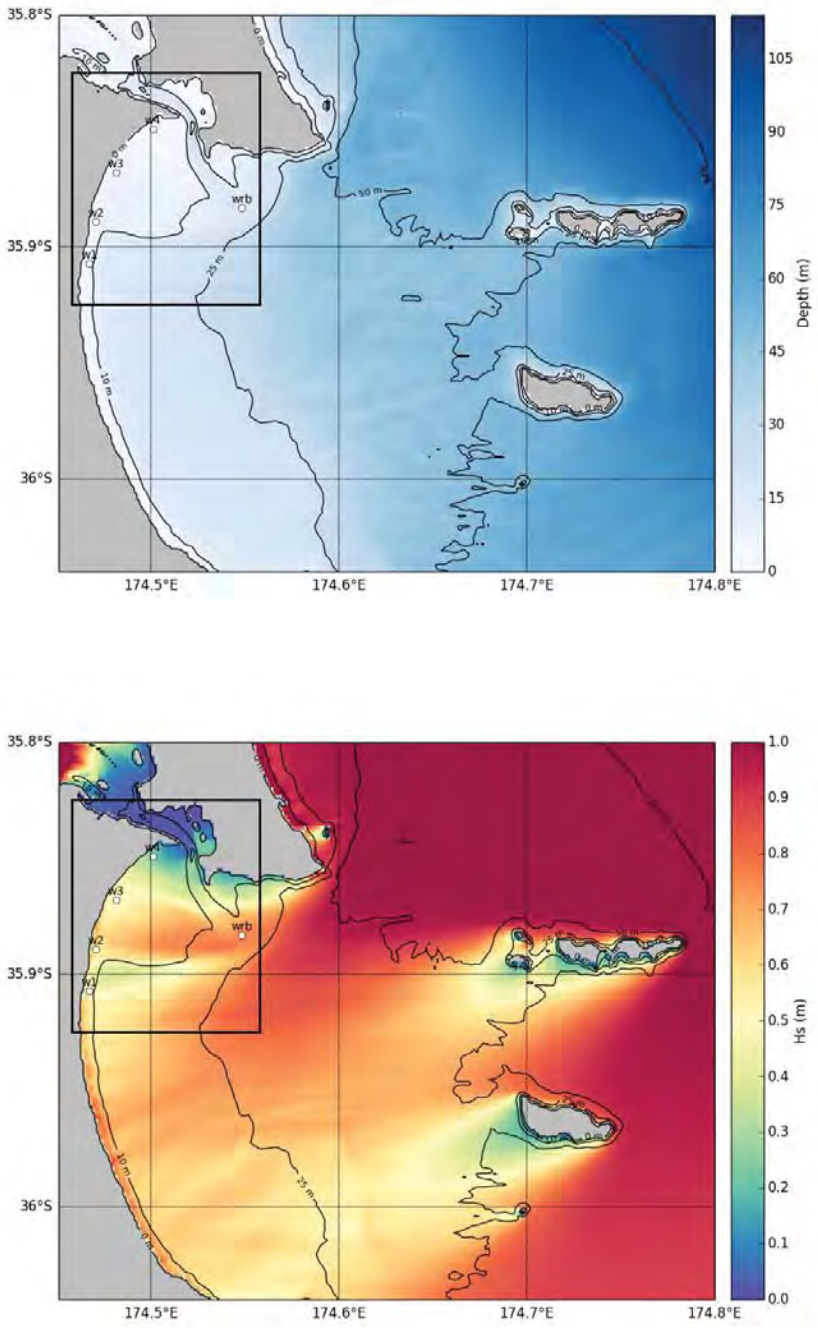

Figure 5.2 Model depths (top) and snapshot of modelled significant wave height (bottom) for the 0.0015 degree SWAN child domain. Extension of the second child nest is shown by the black rectangle. White circles show locations of the wave gauges.

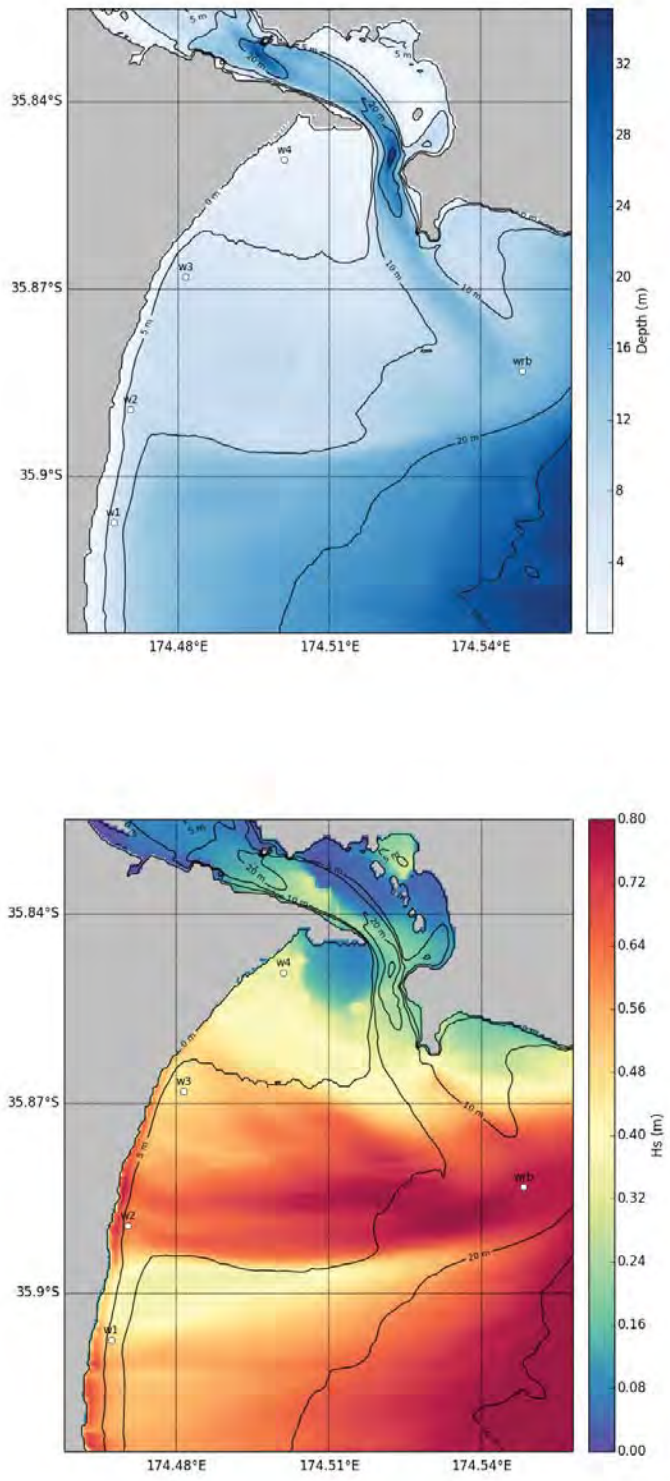

Figure 5.3 Model depths (top) and snapshot of modelled significant wave height (bottom) for the 0.0005 degree SWAN child nest. White circles show locations of the wave gauges. Notice the strong gradient in wave energy along the coast.

5.1.3. Post-processing

Two-dimensional frequency-direction wave spectra were output at hourly intervals from the highest resolution SWAN domain at the locations of the wave gauges (Figure 5.3). The coordinates and depths of the output sites are shown in Table 5.2. The spectra were post-processed to calculate wave statistics for the total wave field, as well as for sea and swell components.

Table 5.2 Measured wave data sources used for the hindcast validation.

Site name	Longitude (deg)	Latitude (deg)	Water depth (m)	Data coverage
WRB	174.5483	-35.8831	15.0	continuous
W1	174.4672	-35.9074	6.9	10/07 to 08/08 2015
W2	174.4705	-35.8893	7.0	10/07 to 08/08 2015
W3	174.4814	-35.8680	6.9	10/07 to 08/08 2015
W4	174.5011	-35.8493	2.8	10/07 to 08/08 2015

One-dimensional frequency spectra were defined by integrating over all directions:

$$S_n(f) = \int_{-\pi}^{\pi} E_n(f,\theta)d\theta \tag{5.1}$$

Spectral moments were calculated as:

$$m_x = \int \int f^x E(f,\theta)df\ d\theta \tag{5.2}$$

with the significant wave height , mean direction at peak frequency and peak wave period defined as:

$$H_s = 4\sqrt{m_0} \tag{5.3}$$

$$Dpm = tan^{-1}\frac{\int_{-\pi}^{\pi} E(f_p,\theta)\ sin\theta\ d\theta}{\int_{-\pi}^{\pi} E(f_p,\theta)\ cos\theta\ d\theta} \tag{5.4}$$

$$T_p = \frac{1}{f_p} \tag{5.5}$$

where f_p is the peak wave frequency of the one-dimensional spectra and $E(f_p,\theta)$ is the energy contained in the peak wave frequency band.

Mean wave periods were defined from the first and second spectral moments as:

$$T_{m01} = \frac{m_1}{m_0}; \quad T_{m02} = \frac{m_2}{m_0} \tag{5.6}$$

and the spectral width parameter was calculated as:

$$S_{we} = \sqrt{\frac{1 - m_2^2}{m_0 m_4}} \tag{5.7}$$

5.2. Model validation

5.2.1. Measured data

The model wave hindcast was validated against time series of wave parameters calculated from measured wave spectra obtained at five different sites, shown in Table 5.2 and Figure 5.3. Bottom-mounted pressure sensors were used to measure waves at the four nearshore sites (W1-W4). The wave spectra measured and modelled at these sites were integrated over the 0.04–0.25 Hz range. Conversely the entire model frequency range was used at site WRB, where the Waverider buoy was deployed. The results from the validation are presented in Figure 5.4 to Figure 5.9.

5.2.2. Accuracy measures

Wave parameters calculated from the hindcast model output x_h and from the measured data x_m were co-located in time and compared using the following measures of accuracy:

Mean Absolute Error (MAE): $$|x_h - x_m| \tag{5.8}$$

RMS Error (RMSE): $$\sqrt{(x_h - x_m)^2} \tag{5.9}$$

Mean Absolute Relative Error (MAE): $$\left|\frac{x_h - x_m}{x_m}\right| \tag{5.10}$$

Bias: $$x_h - x_m \tag{5.11}$$

Scatter Index (SI): $$\frac{\sqrt{(x_h - x_m)^2}}{x_h} \tag{5.12}$$

The accuracy measures are presented in Table 5.3. Note that the validation was performed over a relatively short time period for the nearshore sites W1–W4 (Table 5.2) and only limited data points were available for the comparison.

Table 5.3 Accuracy measures of the hindcast significant wave height H_s and mean absolute period from the second spectral moment T_{m02} for the five measurement sites.

		Bias	RMSE	MAE	MRAE	SI
WRB	Hs	-0.07 m	0.21 m	0.15 m	0.20	0.25
	Tm02	-0.71 s	1.27 s	0.97 s	0.19	0.25
W1	Hs	0.04 m	0.15 m	0.11 m	0.41	0.57
	Tm02	-1.75 s	2.34 s	1.98 s	0.22	0.26
W2	Hs	0.04 m	0.13 m	0.10 m	0.36	0.43
	Tm02	-1.05 s	1.78 s	1.49 s	0.19	0.22
W3	Hs	-0.07 m	0.15 m	0.11 m	0.34	0.44
	Tm02	-1.93 s	2.56 s	2.08 s	0.22	0.27
W4	Hs	0.05 m	0.09 m	0.06 m	0.60	0.80
	Tm02	-0.17 s	1.70 s	1.35 s	0.16	0.21

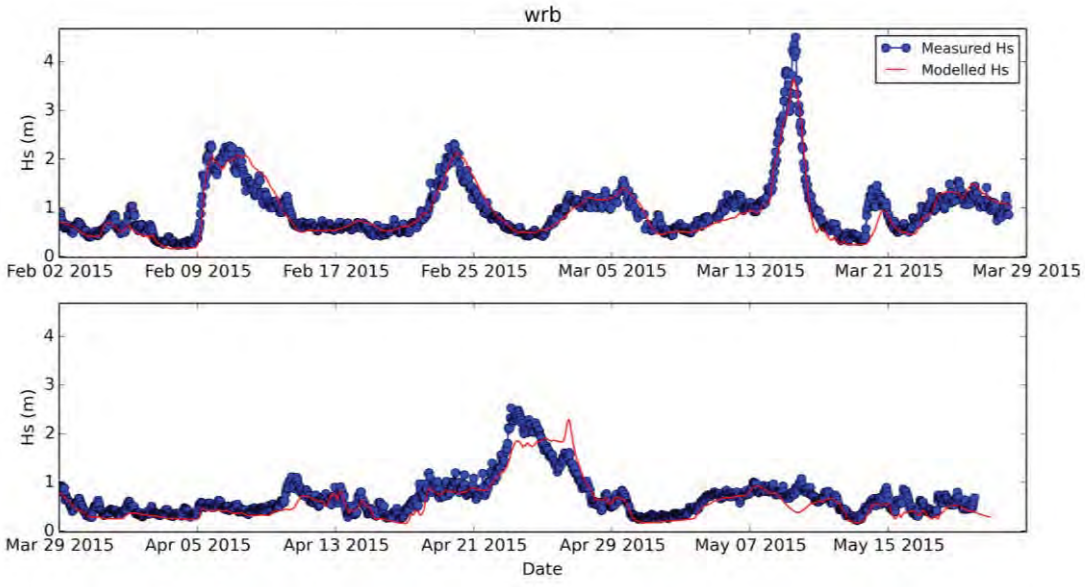

Figure 5.4 Time series of measured (blue) and modelled (red) significant wave height H_s at the WRB site.

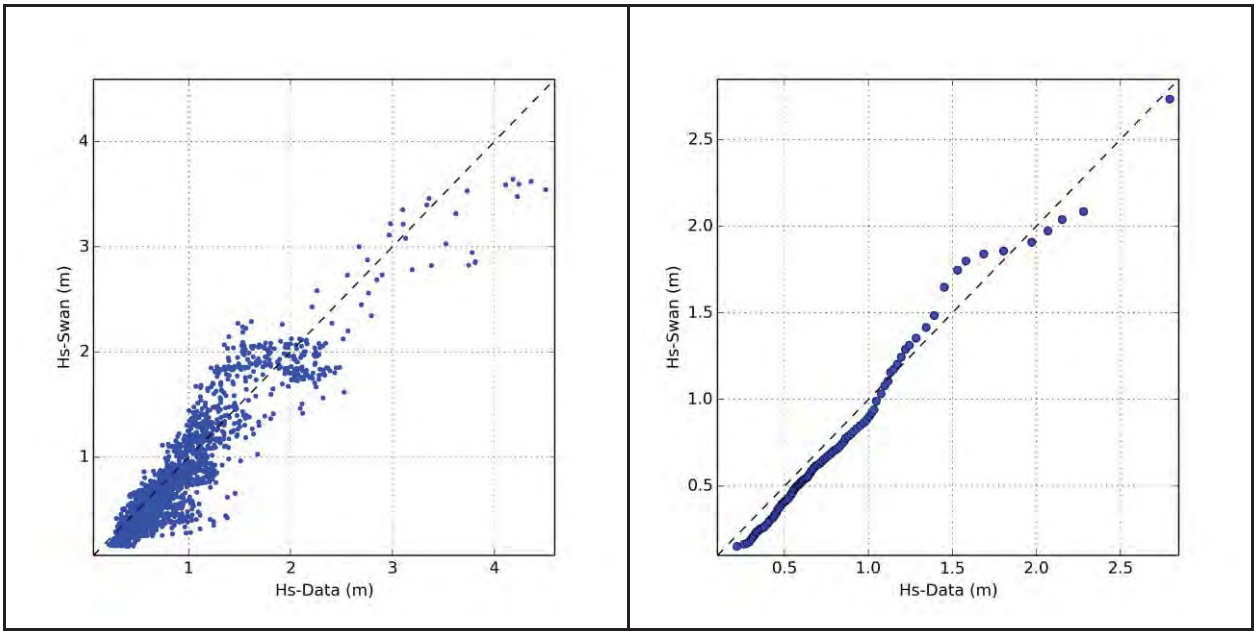

Figure 5.5 Scatter diagram (left) and quantile-quantile plot (right) of measured and modelled significant wave height H_s at WRB site.

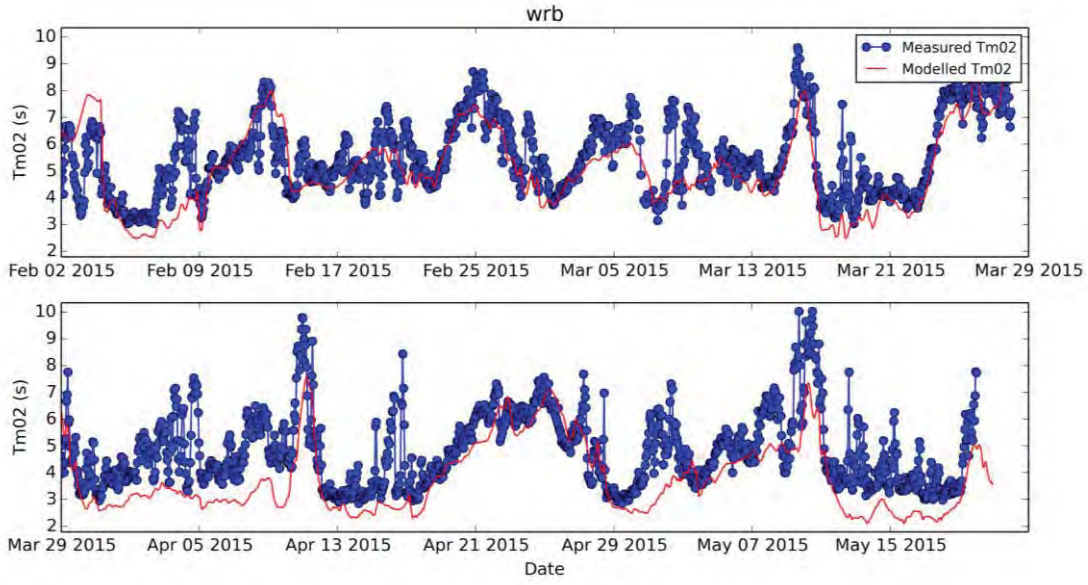

Figure 5.6 Time series of measured (blue) and modelled (red) mean absolute period from the second spectral moment T_{m02} at the WRB site.

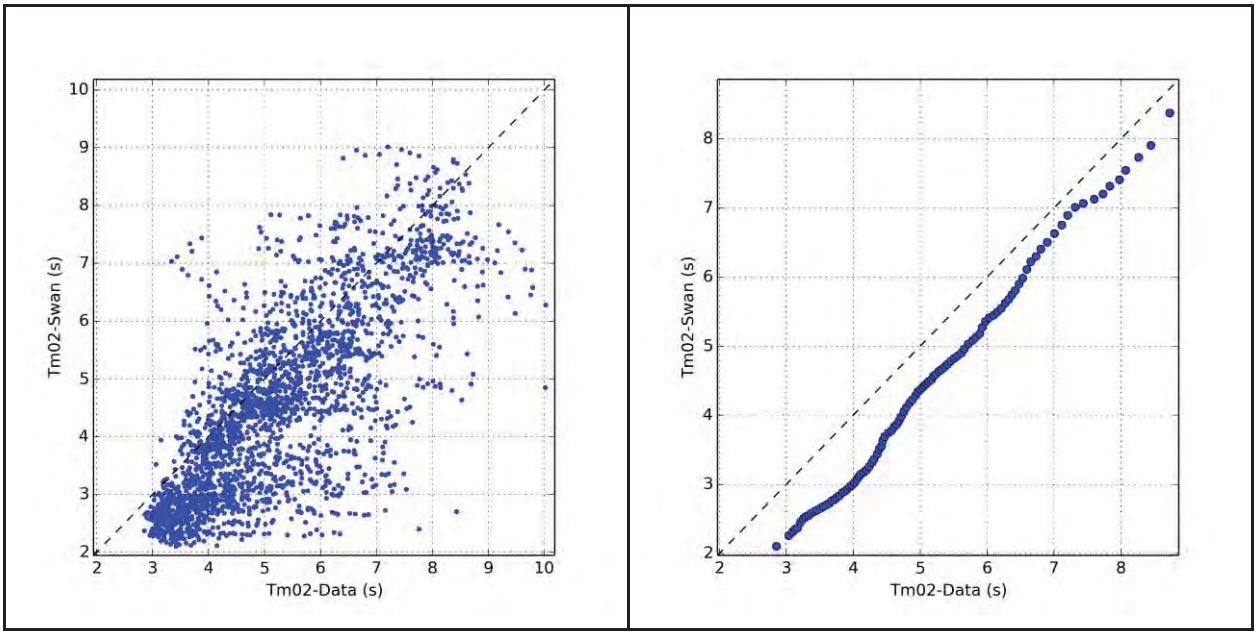

Figure 5.7 Scatter diagram (left) and quantile-quantile plot (right) of measured and modelled mean absolute period from the second spectral moment T_{m02} at WRB site.

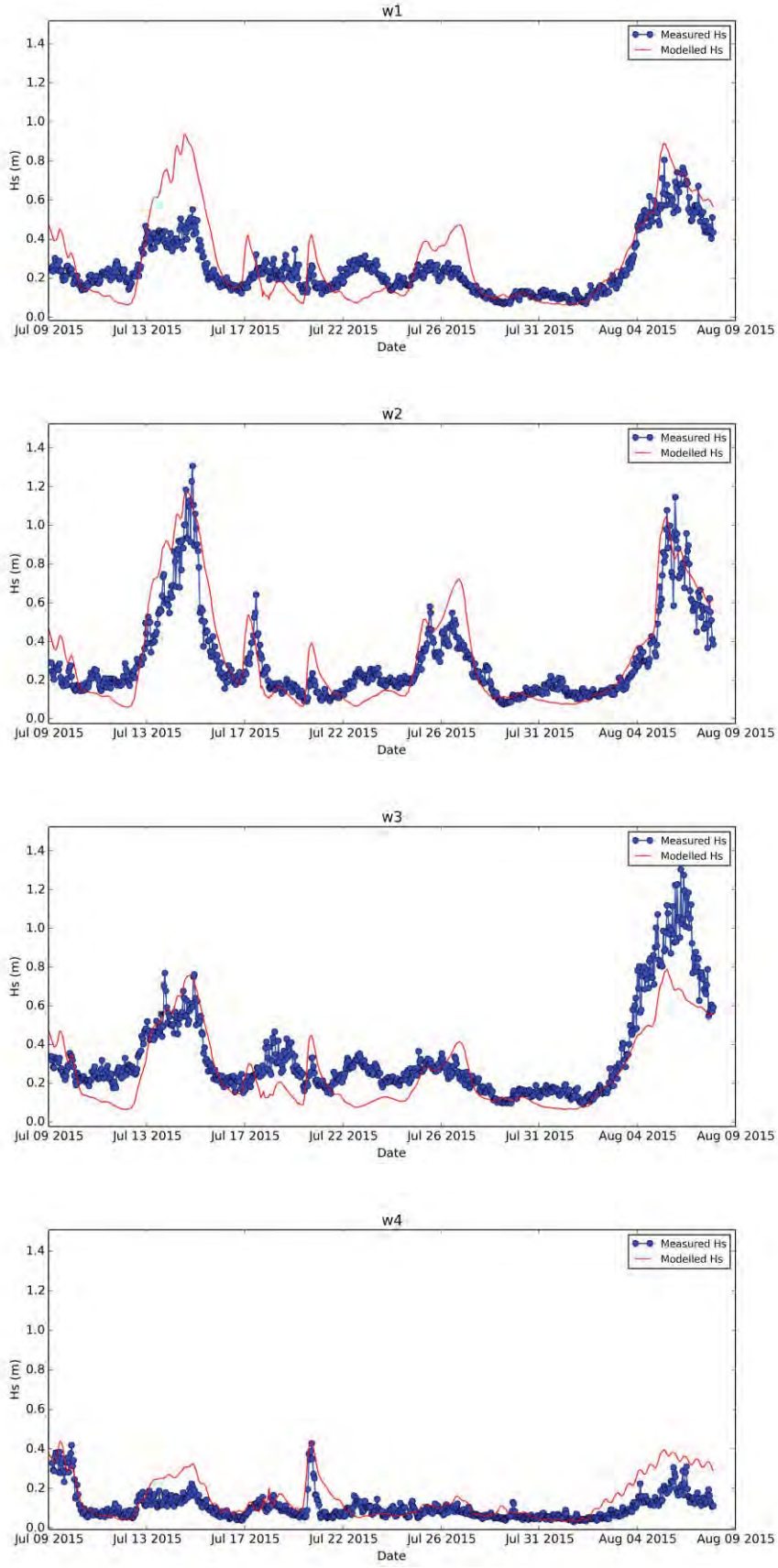

Figure 5.8 Time series of measured (blue) and modelled (red) significant wave height H_s at the four nearshore sites W1–W4.

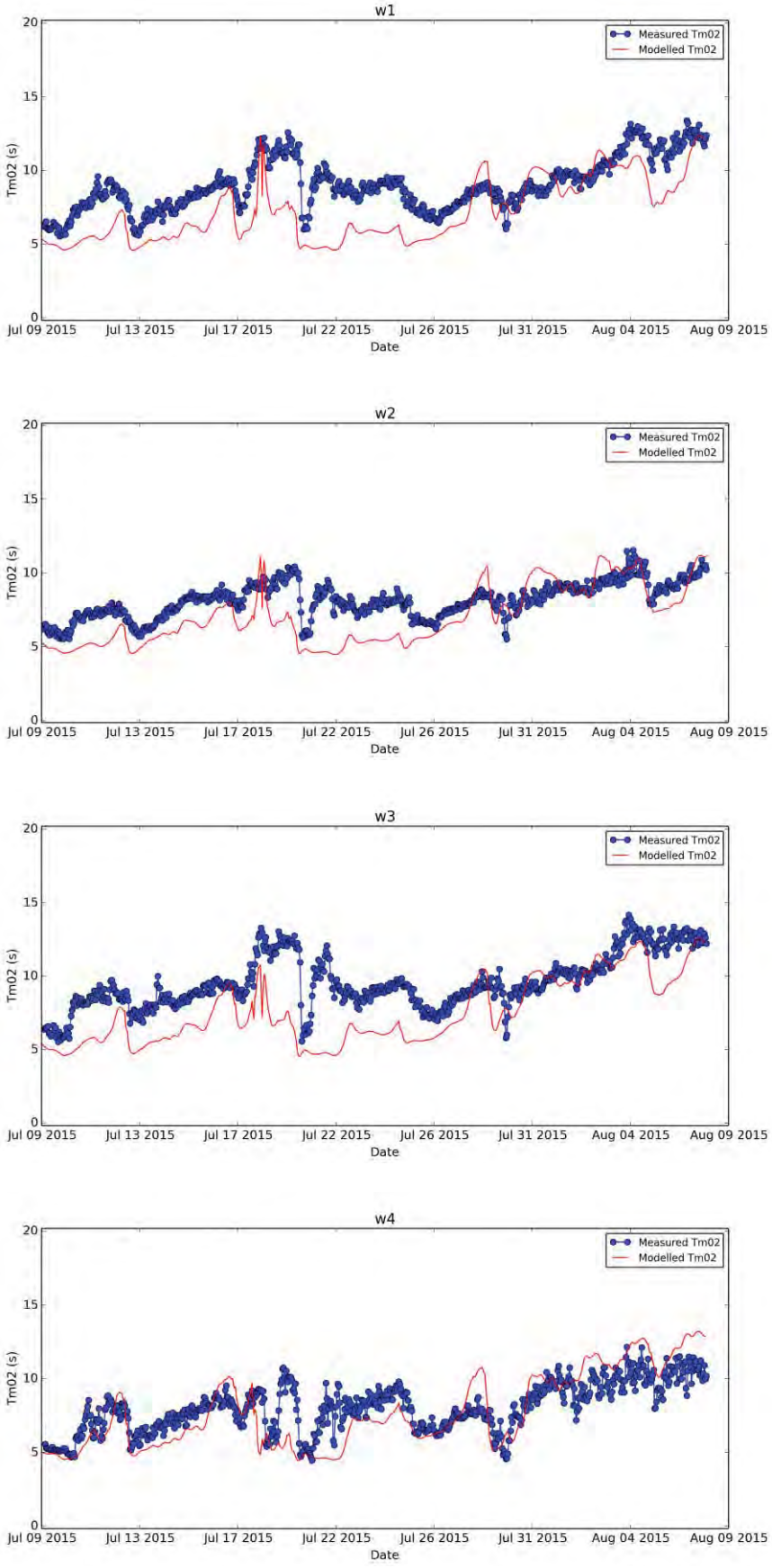

Figure 5.9 Time series of measured (blue) and modelled (red) mean absolute period from the second spectral moment T_{m02} at the four nearshore sites W1–W4.

5.3. Wave climate

A summary of the significant wave height statistics at WRB site (WGS84: 174.548294 E, 35.883099 S) is provided in Table 5.4. The largest significant wave height over the hindcast period was 5.86 m, while the mean annual significant wave height was 0.80 m. The annual 99th percentile non-exceedance level (P99) was 2.85 m (i.e. on an annual basis, for 99% of the time the total significant wave height is less than 2.85 m). Summary significant wave height statistics for swell and windsea components are provided in

Table 5.5 and Table 5.6, respectively.

The monthly and annual significant wave height exceedance probabilities are presented in Table 5.7. The annual joint probability distribution of total significant wave height and mean wave direction at peak energy is presented in Table 5.8. The annual joint probability distribution of total significant wave height and peak spectral wave period is provided in Table 5.9. The annual persistence non-exceedance probabilities for total significant wave height are provided in Table 5.10. For example, on average the total significant wave heights are less than 1.0 m for durations of 36 hours and greater for 72.93 % of the time.

Annual and monthly wave roses for the total significant wave height are presented in Figure 5.10 and Figure 5.11, showing the predominance of waves incoming from the E sector for all months. Density plots of total significant wave height versus peak wave period, wave direction versus peak wave period, and swell direction versus windsea direction are provided in Figure 5.12 - Figure 5.14.

Table 5.4 Annual and monthly total significant wave height statistics at WRB.

H_s (m)	Parameter					
	Mean (m)	**Median (m)**	**P90 (m)**	**P95 (m)**	**P99 (m)**	**Max (m)**
Jan	0.82	0.68	1.48	1.89	2.82	3.85
Feb	0.92	0.79	1.63	1.98	2.85	4.51
Mar	0.90	0.75	1.62	1.94	2.74	5.86
Apr	0.86	0.73	1.59	1.93	2.68	4.63
May	0.80	0.67	1.46	1.82	2.64	5.09
Jun	0.81	0.64	1.59	1.98	2.87	4.89
Jul	0.90	0.66	1.88	2.45	3.68	5.35
Aug	0.78	0.61	1.51	2.01	3.08	4.97
Sep	0.74	0.58	1.41	1.80	2.80	4.51
Oct	0.66	0.55	1.22	1.52	2.16	4.29
Nov	0.69	0.54	1.30	1.62	2.56	5.00
Dec	0.75	0.63	1.33	1.62	2.35	3.59
1979	0.81	0.67	1.44	1.84	2.69	3.69
1980	0.73	0.58	1.31	1.72	3.01	4.15
1981	0.88	0.73	1.63	1.97	2.73	4.16
1982	0.75	0.58	1.39	1.91	3.01	4.33
1983	0.76	0.61	1.43	1.83	2.91	4.54
1984	0.88	0.70	1.71	2.00	3.06	5.09
1985	0.94	0.75	1.75	2.09	3.01	3.88
1986	0.71	0.59	1.33	1.62	2.35	3.37
1987	0.73	0.61	1.24	1.66	2.92	3.50
1988	0.84	0.65	1.59	2.05	3.52	5.86
1989	0.99	0.82	1.89	2.28	3.44	4.97
1990	0.68	0.59	1.23	1.46	1.88	2.34
1991	0.70	0.60	1.26	1.56	2.16	2.89
1992	0.70	0.56	1.26	1.65	2.73	4.63
1993	0.71	0.54	1.42	1.81	2.48	4.22
1994	0.75	0.60	1.39	1.79	2.30	3.31
1995	0.78	0.65	1.38	1.64	2.36	3.15
1996	0.78	0.62	1.48	1.93	2.89	4.89
1997	0.77	0.62	1.37	1.85	2.96	4.51
1998	0.95	0.81	1.64	2.10	2.92	5.00
1999	0.88	0.76	1.53	1.87	2.51	2.91
2000	0.85	0.62	1.71	2.14	3.58	4.40
2001	0.90	0.75	1.67	1.97	3.13	4.05
2002	0.73	0.61	1.33	1.71	2.73	4.21
2003	0.86	0.72	1.58	2.09	2.99	4.51
2004	0.72	0.62	1.26	1.51	2.25	2.92
2005	0.79	0.63	1.58	1.91	2.57	3.14
2006	0.71	0.58	1.31	1.82	2.72	3.38
2007	0.83	0.65	1.59	1.93	3.04	5.02
2008	0.87	0.71	1.57	1.98	2.85	4.12
2009	0.79	0.59	1.54	1.91	2.63	5.35
2010	0.80	0.68	1.47	1.77	2.49	4.29
2011	0.87	0.73	1.62	2.07	2.77	3.88
2012	0.85	0.68	1.61	1.91	2.80	4.63
2013	0.83	0.70	1.59	1.92	2.64	3.41
2014	0.80	0.62	1.51	2.08	3.50	4.84
Annual	0.80	0.65	1.50	1.89	2.85	5.86

Table 5.5 Annual and monthly significant swell wave statistics at WRB.

H_s (m)	Parameter					
	Mean (m)	**Median (m)**	**P90 (m)**	**P95 (m)**	**P99 (m)**	**Max (m)**
Jan	0.50	0.39	1.00	1.39	2.09	3.22
Feb	0.57	0.45	1.17	1.42	2.04	3.24
Mar	0.55	0.41	1.13	1.39	2.00	4.85
Apr	0.53	0.40	1.15	1.44	2.03	3.83
May	0.45	0.31	1.00	1.32	2.10	4.03
Jun	0.43	0.26	1.04	1.40	2.13	4.08
Jul	0.52	0.28	1.36	1.85	2.78	4.28
Aug	0.44	0.28	0.98	1.42	2.39	3.99
Sep	0.40	0.25	0.91	1.25	2.01	3.33
Oct	0.33	0.21	0.77	1.06	1.70	2.96
Nov	0.38	0.25	0.84	1.13	1.95	4.05
Dec	0.46	0.35	0.91	1.14	1.76	3.16
1979	0.46	0.35	0.96	1.23	1.91	2.73
1980	0.37	0.23	0.83	1.15	1.96	3.11
1981	0.51	0.40	1.12	1.41	1.80	3.01
1982	0.42	0.28	0.85	1.35	2.31	3.34
1983	0.44	0.31	0.97	1.28	2.12	3.55
1984	0.55	0.38	1.24	1.50	2.55	4.03
1985	0.55	0.39	1.21	1.50	2.26	3.07
1986	0.40	0.29	0.86	1.13	1.72	2.30
1987	0.40	0.29	0.88	1.21	2.12	2.71
1988	0.50	0.31	1.11	1.43	2.88	4.85
1989	0.60	0.43	1.39	1.76	2.63	3.99
1990	0.36	0.28	0.76	0.97	1.33	1.67
1991	0.37	0.25	0.85	1.08	1.54	2.00
1992	0.34	0.22	0.66	1.02	1.96	3.50
1993	0.39	0.23	0.92	1.19	1.78	2.92
1994	0.40	0.25	0.99	1.29	1.94	2.43
1995	0.43	0.30	0.95	1.19	1.94	2.69
1996	0.43	0.29	0.91	1.27	2.38	4.08
1997	0.43	0.30	0.88	1.24	2.32	3.63
1998	0.60	0.47	1.10	1.47	2.21	4.05
1999	0.53	0.40	1.13	1.31	1.73	2.12
2000	0.52	0.30	1.27	1.69	2.74	3.49
2001	0.54	0.40	1.16	1.49	2.34	3.11
2002	0.36	0.20	0.86	1.17	2.20	3.23
2003	0.52	0.36	1.16	1.55	2.32	3.55
2004	0.39	0.27	0.82	1.14	1.80	2.37
2005	0.47	0.31	1.17	1.43	2.04	2.89
2006	0.40	0.27	0.86	1.24	2.23	2.95
2007	0.48	0.34	1.04	1.34	2.08	4.12
2008	0.48	0.34	1.09	1.39	1.98	2.92
2009	0.47	0.32	1.05	1.33	1.88	4.28
2010	0.47	0.33	1.03	1.27	1.65	2.96
2011	0.54	0.40	1.16	1.45	2.18	2.92
2012	0.52	0.39	1.19	1.46	2.11	3.83
2013	0.55	0.41	1.21	1.55	2.00	2.58
2014	0.49	0.35	1.05	1.56	2.59	3.85
Annual	0.46	0.32	1.03	1.36	2.13	4.85

Table 5.6 Annual and monthly significant windsea wave statistics at WRB.

H_s (m)	Parameter					
	Mean (m)	**Median (m)**	**P90 (m)**	**P95 (m)**	**P99 (m)**	**Max (m)**
Jan	0.62	0.52	1.13	1.39	2.03	2.76
Feb	0.69	0.60	1.21	1.46	2.10	3.17
Mar	0.68	0.59	1.19	1.45	2.06	3.37
Apr	0.64	0.55	1.14	1.38	1.97	2.68
May	0.62	0.53	1.10	1.35	1.97	3.11
Jun	0.64	0.53	1.19	1.49	2.17	3.03
Jul	0.68	0.53	1.35	1.78	2.54	3.31
Aug	0.60	0.48	1.15	1.51	2.12	3.11
Sep	0.58	0.48	1.06	1.31	2.09	3.05
Oct	0.53	0.46	0.96	1.15	1.65	3.11
Nov	0.55	0.45	1.00	1.21	1.87	2.99
Dec	0.57	0.48	1.03	1.23	1.76	2.73
1979	0.63	0.52	1.12	1.40	2.07	2.74
1980	0.59	0.49	1.09	1.37	2.31	2.88
1981	0.68	0.58	1.19	1.50	2.12	2.97
1982	0.58	0.46	1.07	1.35	2.22	2.88
1983	0.59	0.49	1.08	1.31	2.15	2.85
1984	0.64	0.53	1.17	1.48	2.00	3.11
1985	0.72	0.61	1.34	1.59	2.12	2.61
1986	0.55	0.47	0.97	1.20	1.87	2.76
1987	0.57	0.49	1.00	1.25	2.02	2.53
1988	0.64	0.52	1.23	1.53	2.26	3.37
1989	0.74	0.63	1.28	1.68	2.32	3.11
1990	0.54	0.48	0.96	1.20	1.62	1.85
1991	0.55	0.46	0.99	1.17	1.77	2.51
1992	0.58	0.48	1.05	1.26	2.10	3.31
1993	0.55	0.43	1.11	1.33	2.13	3.05
1994	0.59	0.52	1.03	1.27	1.61	2.45
1995	0.61	0.52	1.05	1.23	1.60	2.38
1996	0.62	0.51	1.17	1.45	2.09	2.84
1997	0.60	0.49	1.09	1.43	2.14	3.04
1998	0.70	0.59	1.26	1.55	2.29	3.04
1999	0.67	0.59	1.18	1.44	1.93	2.55
2000	0.64	0.50	1.18	1.59	2.29	3.07
2001	0.68	0.59	1.18	1.46	2.27	2.65
2002	0.59	0.50	1.04	1.27	1.77	2.94
2003	0.64	0.55	1.12	1.43	2.06	3.17
2004	0.56	0.49	0.96	1.15	1.61	2.32
2005	0.60	0.51	1.10	1.31	1.77	2.17
2006	0.54	0.46	0.96	1.21	1.83	2.62
2007	0.64	0.51	1.21	1.52	2.36	3.05
2008	0.68	0.58	1.23	1.47	2.18	2.94
2009	0.60	0.47	1.10	1.48	2.08	3.21
2010	0.62	0.53	1.09	1.38	2.09	3.12
2011	0.64	0.54	1.23	1.50	2.09	2.65
2012	0.63	0.53	1.21	1.43	2.04	2.77
2013	0.58	0.50	1.04	1.26	1.86	2.65
2014	0.59	0.45	1.11	1.56	2.39	3.06
Annual	0.62	0.51	1.12	1.39	2.09	3.37

Table 5.7 Monthly and annual total significant wave height exceedance probabilities at WRB.

H_s (m)	Exceedence (%)												
	January	**February**	**March**	**April**	**May**	**June**	**July**	**August**	**September**	**October**	**November**	**December**	**Year**
>0.5	71.68	79.24	76.61	72.69	69.06	63.54	66.11	62.24	60.01	56.10	55.23	65.57	66.45
>1	24.35	33.68	31.82	30.45	25.18	26.96	29.41	22.61	20.66	16.32	18.52	22.66	25.17
>1.5	9.72	13.21	13.03	11.54	9.33	11.54	15.99	10.09	8.52	5.14	6.27	6.68	10.07
>2	4.22	4.84	4.41	4.24	3.72	4.80	8.40	5.05	3.13	1.69	2.48	2.13	4.09
>2.5	1.95	1.68	1.46	1.56	1.38	1.92	4.82	2.45	1.40	0.35	1.16	0.80	1.75
>3	0.53	0.71	0.73	0.51	0.48	0.83	2.64	1.24	0.72	0.11	0.30	0.36	0.77
>3.5	0.08	0.20	0.40	0.16	0.20	0.42	1.38	0.34	0.31	0.03	0.20	0.02	0.31
>4	0.00	0.02	0.21	0.07	0.08	0.20	0.57	0.13	0.05	0.01	0.14	0.00	0.12
>4.5	0.00	0.01	0.10	0.02	0.03	0.05	0.19	0.02	0.01	0.00	0.08	0.00	0.04
>5	0.00	0.00	0.08	0.00	0.01	0.00	0.03	0.00	0.00	0.00	0.00	0.00	0.01
>5.5	0.00	0.00	0.02	0.00	0.00	0.00	0.00	0.00	0.00	0.00	0.00	0.00	0.00

Table 5.8 Annual joint probability distribution (parts per thousand) of the total significant wave height and mean wave direction at peak energy at WRB.

H_s (m)	Wave direction (degT)								
	337.5 -22.5	**22.5 -67.5**	**67.5 -112.5**	**112.5 -157.5**	**157.5 -202.5**	**202.5 -247.5**	**247.5 -292.5**	**292.5 -337.5**	**Total**
0 - 0.5	0.2	6.5	269.3	11.9	10.8	17.2	12.5	8.4	336.8
0.5 - 1	0.1	6.8	337.8	15.6	17.0	23.9	6.8	4.0	412.0
1 - 1.5	0.0	0.3	143.6	3.8	1.5	1.4	0.1	0.0	150.7
1.5 - 2	0.0	0.0	58.5	1.1	0.0	0.0	0.0	0.0	59.6
2 - 2.5	0.0	0.0	22.9	0.5	0.0	0.0	0.0	0.0	23.4
2.5 - 3	0.0	0.0	9.8	0.0	0.0	0.0	0.0	0.0	9.8
3 - 3.5	0.0	0.0	4.5	0.0	0.0	0.0	0.0	0.0	4.5
3.5 - 4	0.0	0.0	1.8	0.0	0.0	0.0	0.0	0.0	1.8
4 - 4.5	0.0	0.0	0.8	0.0	0.0	0.0	0.0	0.0	0.8
4.5 - 5	0.0	0.0	0.3	0.0	0.0	0.0	0.0	0.0	0.3
5 - 5.5	0.0	0.0	0.1	0.0	0.0	0.0	0.0	0.0	0.1
Total	0.3	13.6	849.4	32.9	29.3	42.5	19.4	12.4	1000.0

Table 5.9 Annual joint probability distribution (parts per thousand) of the total significant wave height and peak wave period at WRB.

H_s (m)	Peak wave period T_p (s)									
	2-4	**4-6**	**6-8**	**8-10**	**10-12**	**12-14**	**14-16**	**16-18**	**18-20**	**Total**
0 - 0.5	60.0	13.5	27.9	138.2	63.9	19.6	5.7	1.5	0.1	330.4
0.5 - 1	62.8	42.8	61.1	159.2	62.4	19.7	3.5	0.5	0.1	412.1
1 - 1.5	2.1	11.3	37.2	62.7	29.1	7.4	0.7	0.1	0.0	150.6
1.5 - 2	0.0	1.1	11.0	27.6	16.2	3.7	0.2	0.0	0.0	59.8
2 - 2.5	0.0	0.1	4.2	9.9	7.1	2.1	0.0	0.0	0.0	23.4
2.5 - 3	0.0	0.0	0.9	4.7	3.2	0.9	0.0	0.0	0.0	9.7
3 - 3.5	0.0	0.0	0.2	1.8	2.0	0.4	0.1	0.0	0.0	4.5
3.5 - 4	0.0	0.0	0.0	0.7	0.9	0.3	0.0	0.0	0.0	1.9
4 - 4.5	0.0	0.0	0.0	0.3	0.4	0.1	0.0	0.0	0.0	0.8
4.5 - 5	0.0	0.0	0.0	0.1	0.2	0.0	0.0	0.0	0.0	0.3
5 - 5.5	0.0	0.0	0.0	0.0	0.1	0.0	0.0	0.0	0.0	0.1
Total	124.9	68.8	142.5	405.2	185.5	54.2	10.2	2.1	0.2	1000.0

Table 5.10 Annual persistence non-exceedance (%) for total significant wave height at WRB.

Hs (m)	Duration (hours)											
	> 6	**> 12**	**> 18**	**> 24**	**> 30**	**> 36**	**> 42**	**> 48**	**> 54**	**> 60**	**> 66**	**> 72**
<= 0.5	33.06	32.11	31	29.63	28.29	26.66	25.27	23.51	21.73	20.21	18.71	17.16
<= 1	74.75	74.54	74.2	73.87	73.42	72.93	72.4	71.73	71.18	70.59	69.99	69.37
<= 1.5	89.89	89.83	89.71	89.56	89.32	89.13	88.99	88.86	88.71	88.53	88.33	88.17
<= 2	95.88	95.83	95.8	95.77	95.75	95.69	95.63	95.55	95.5	95.41	95.33	95.28
<= 2.5	98.24	98.22	98.21	98.19	98.19	98.18	98.17	98.12	98.11	98.11	98.11	98.06
<= 3	99.23	99.22	99.21	99.19	99.19	99.18	99.18	99.18	99.18	99.18	99.18	99.18
<= 3.5	99.68	99.68	99.68	99.68	99.67	99.67	99.67	99.67	99.67	99.67	99.67	99.67
<= 4	99.87	99.87	99.87	99.87	99.87	99.87	99.87	99.87	99.87	99.87	99.85	99.85

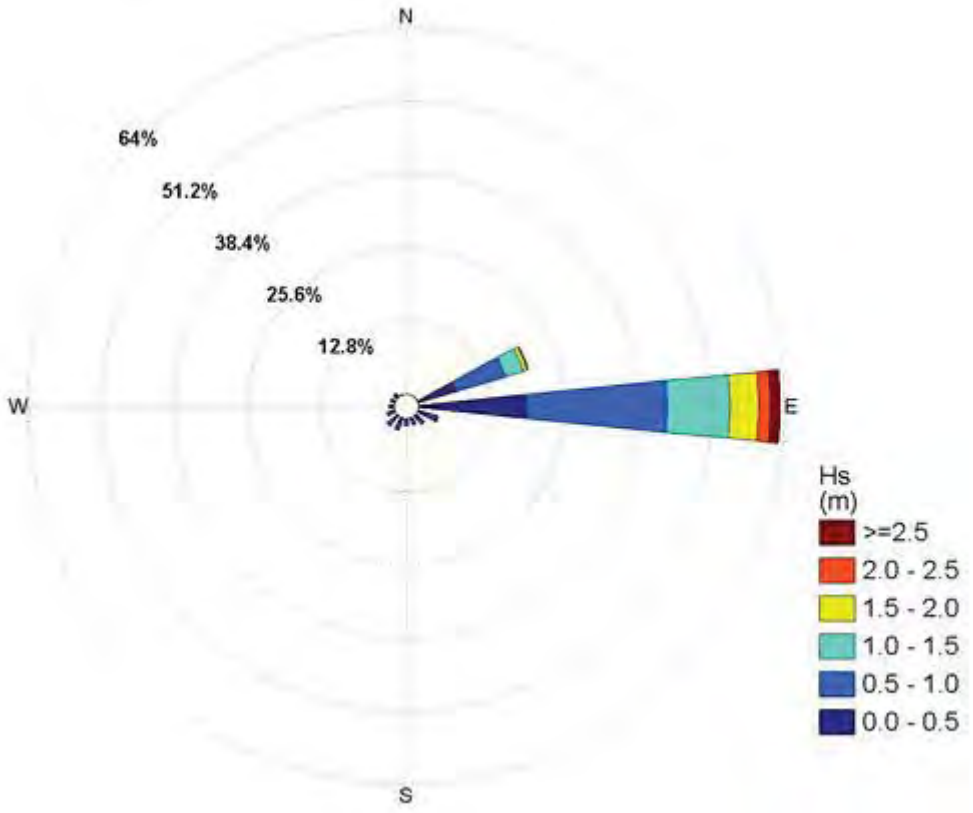

Figure 5.10 Annual wave rose plot for the total significant wave height at WRB. Sectors indicate the direction from which waves approach.

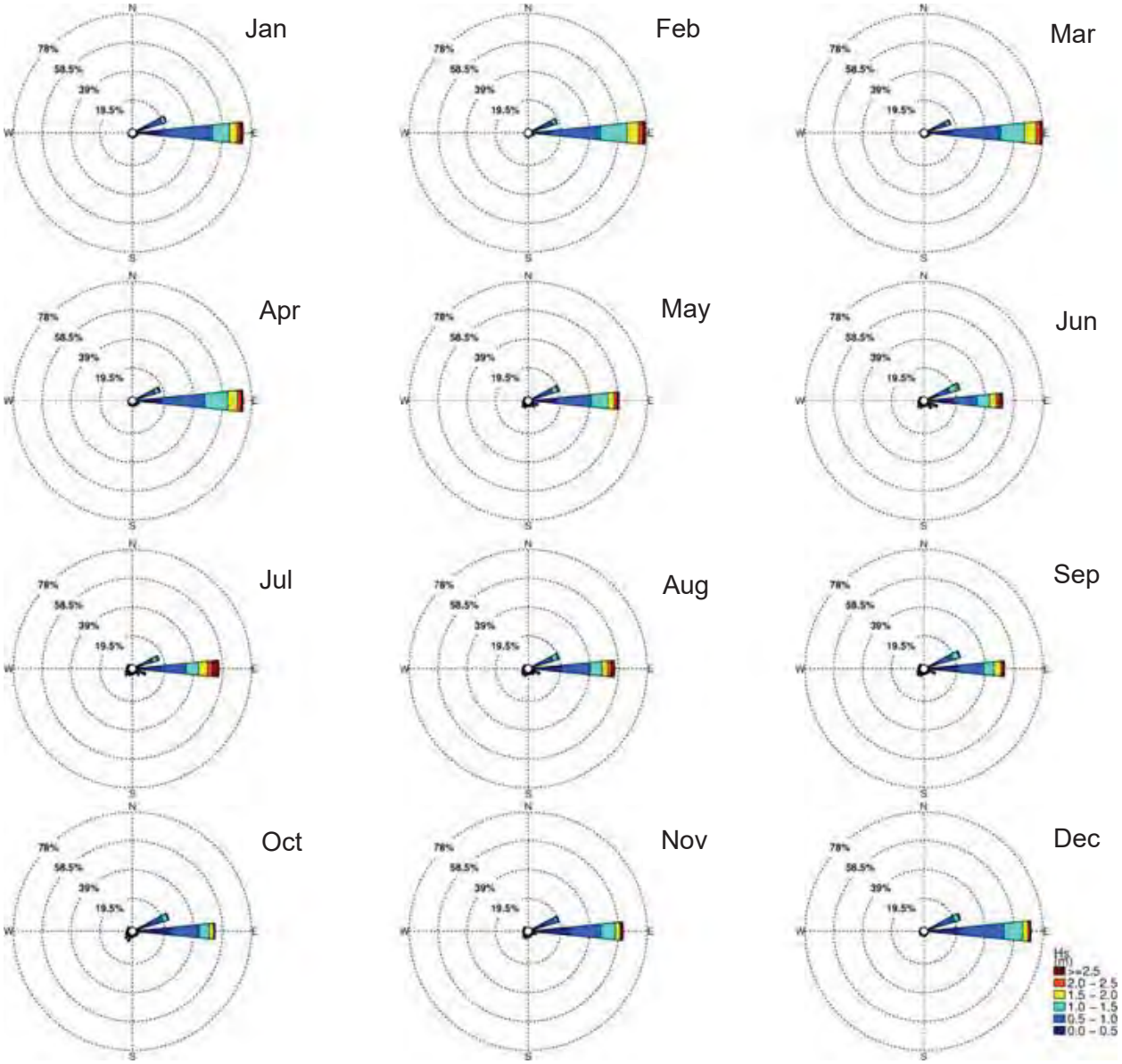

Figure 5.11 Monthly wave rose plots for the total significant wave height at WRB. Sectors indicate the direction from which waves approach.

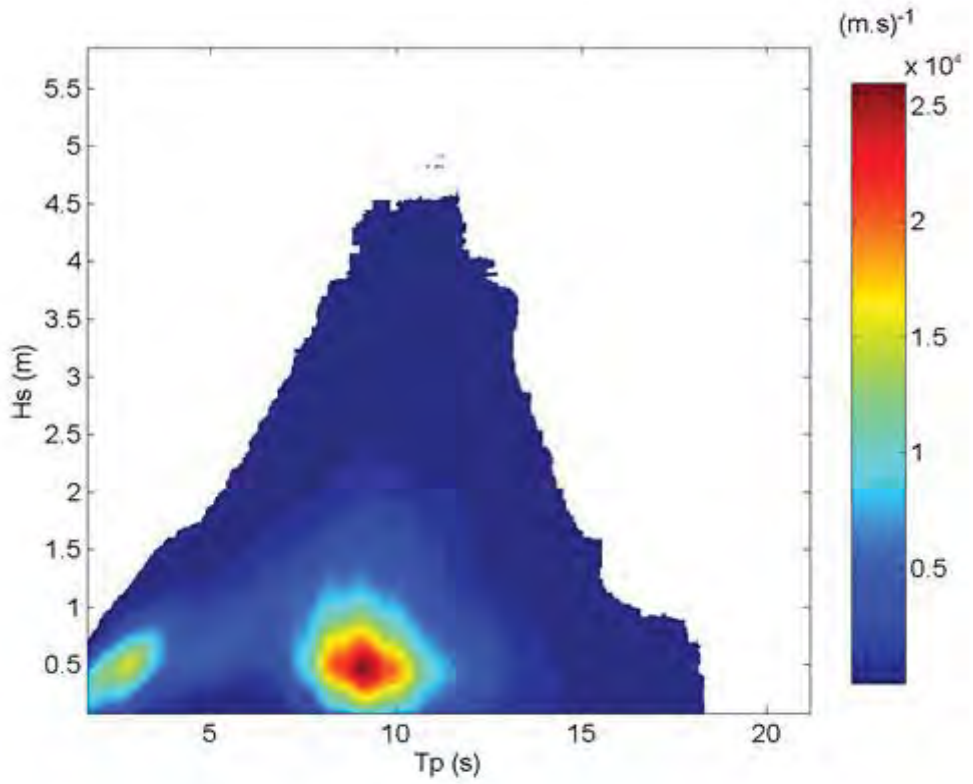

Figure 5.12 Density plot of the total significant wave height vs. the peak wave period at WRB for the period 1979-2014.

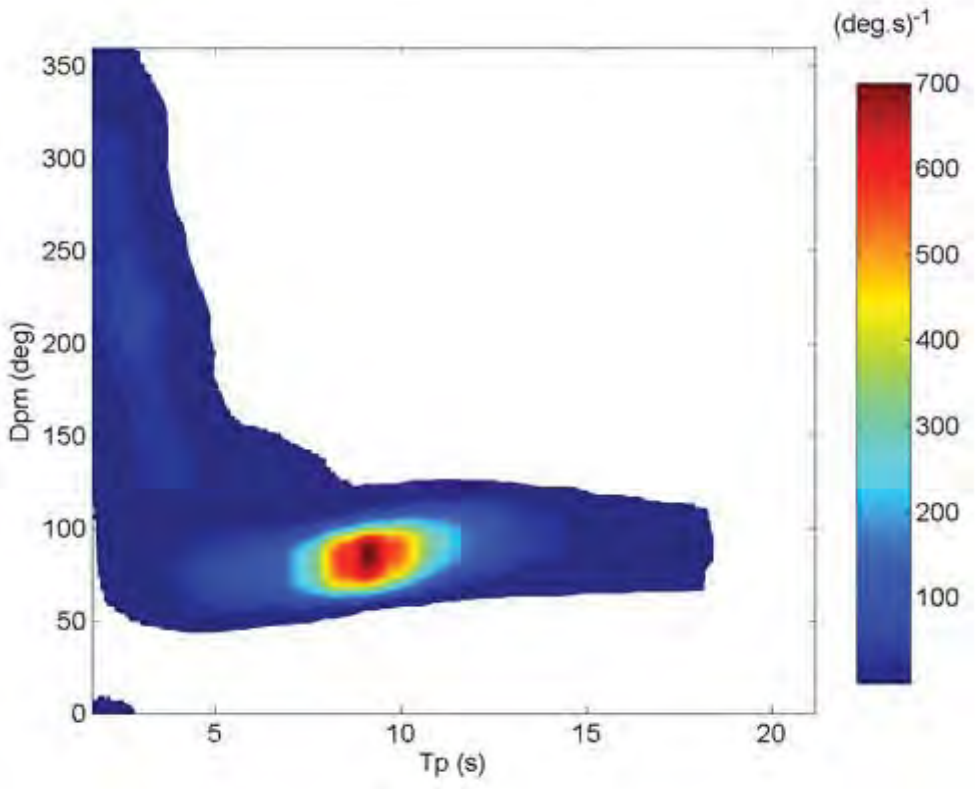

Figure 5.13 Density plot of the mean wave direction at peak energy vs. peak wave period at WRB for the period 1979-2014.

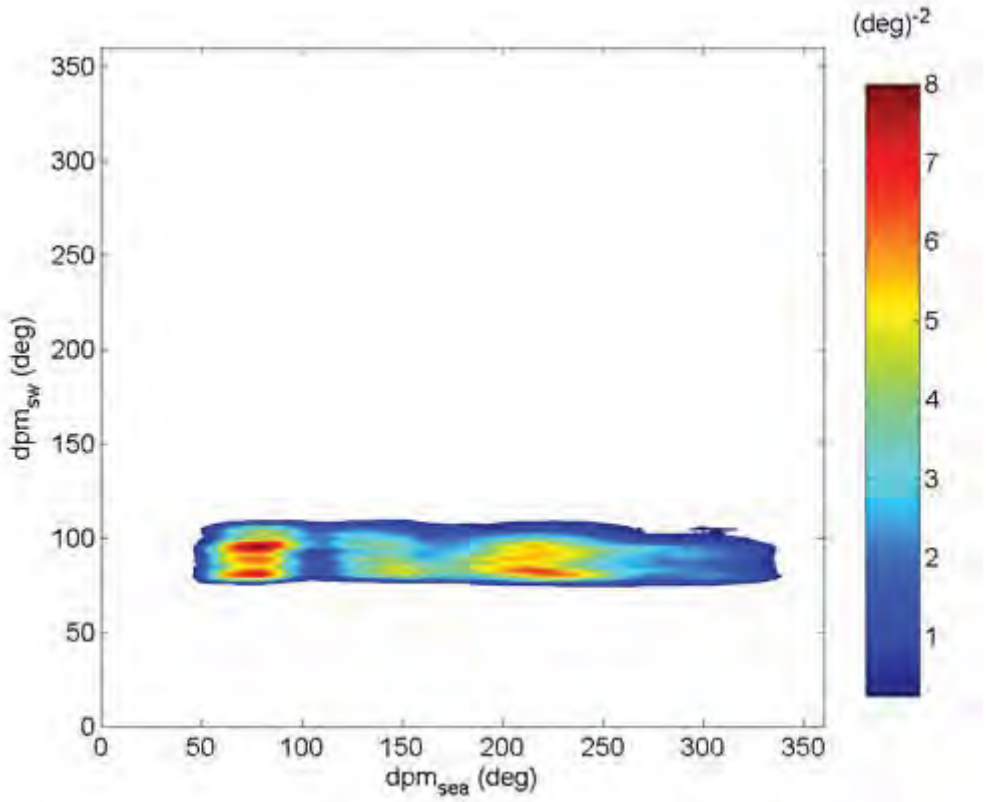

Figure 5.14 Density plot of the co-temporal swell wave direction vs the windsea wave direction at WRB for the period 1979-2014.

6. REGIONAL HYDRODYNAMIC CLIMATE

The characterisation of the circulation in the continental shelf waters adjacent to the Whangarei Harbour is of importance when considering the local scale hydrodynamic and sediment transport processes, as they prescribe the boundary conditions for the nearshore and harbour entrance numerical modelling. The presence of strong along-shelf winds and offshore oceanic boundary currents year round can all play a role in forcing the circulation near the coast. A careful modelling strategy is required to reproduce the different spatial and temporal scales and circulation phenomena at the shelf and deep ocean environments and adequately feed the local scale models. This section describes the modelling studies that were undertaken to characterise regional hydrodynamics.

6.1. Model description

A 10-year hindcast was performed using the ROMS hydrodynamic model version 3.7 (Regional Ocean Modelling System, described in Haidvogel et al., 2008) to characterise the tidal and residual shelf scale circulation regime. This modelling tool has been used widely in the scientific and commercial consultancy communities for a wide range of ocean basin, regional and coastal scales and other specific phenomena. ROMS has a curvilinear horizontal coordinate system and solves the hydrostatic, primitive equations subject to a free-surface condition. It is a state-of-the-art model widely used for regional and coastal dynamics assessment. Its terrain-following vertical coordinate system results in accurate modelling of shelf seas with variable bathymetry, allowing the vertical resolution to be inversely proportional to the local depth. Besides tidal and wind-driven currents, ROMS resolves frontal structures and baroclinic pressure gradients quite well. Vertical mixing may be resolved by different separate turbulent closure schemes, that are flexible to shallow and deep water dynamics.

6.2. Modelling strategy and domain setup

The hindcast setup was configured with a three-level nesting approach to adequately transfer the energy gradually from larger to smaller coastal scales, and to properly resolve the flow associated with local and remote forcing, both essential for the resultant currents in the area of interest. The open boundary conditions that were imposed to the highest level nest (NZ) consisted of tri-dimensional velocity, temperature, salinity and sea surface height fields derived from the 6-hourly Climate Forecast System Reanalysis product (Saha et al., 2010) from the National Centers for Environmental Prediction (NCEP), which consisted of a 0.5 degree global reanalysis with comprehensive data assimilation.

The larger scale ROMS nest encompassed the area shown in the left panel of Figure 6.1 with 7 km horizontal resolution, the goal of which was to absorb the basin scale circulation estimated by the CFSR global reanalysis, thus avoiding a large parent-to-child resolution step. This domain, called NZ hereinafter, was able to more adequately capture the oceanic circulation and its variability. The second domain (HRKI) covered the entire Hauraki Gulf and continental shelf surrounding the area of interest with a horizontal resolution of 1.7 km. With this grid spacing, the local bathymetry was more accurately captured resulting in fine scale representation of the local coastal currents. The third domain (WHANG) covers the continental shelf near the area of interest with a much higher resolution (350 m), and resolved the detailed local wind-driven and tidal circulation, producing accurate

currents and thermohaline fields to support the subsequent local scale hydrodynamic and sediment models.

The 3D flow and thermohaline fields were transferred from the top level domains to the refined ones by the offline one-way nesting technique, the stable one available at ROMS to the present date. CFSR 3D fields were fed to NZ in a 6-hourly interval and NZ-HRKI and HRKI-WHANG ROMS in a 3-hourly interval.

All ROMS domains were submitted to spin-up phases prior to the 10-year hindcast period to allow the adjustment of the coarser initial conditions to higher resolution and its better represented bathymetry. The spin-up times were hierarchically established according to the main scales that each one was required to resolve. This information and all other relevant information for each of the hydrodynamic model domains considered for this study are summarised in Table 6.1. The bathymetry for the ROMS grids was derived from electronic navigation charts and field data whenever available (i.e. Section 3.2).

Table 6.1 ROMS model nests configurations.

Model Settings	**NZ**	**HRKI**	**WHANG**
Horiz Resolution	8 km	1.7 km	350 m
Vertical layers	30	19	15
Tidal forcing	No	No	Yes
Meteo forcing	MSL WRF NZRA	MSL WRF NZRA	MSL WRF NZRA

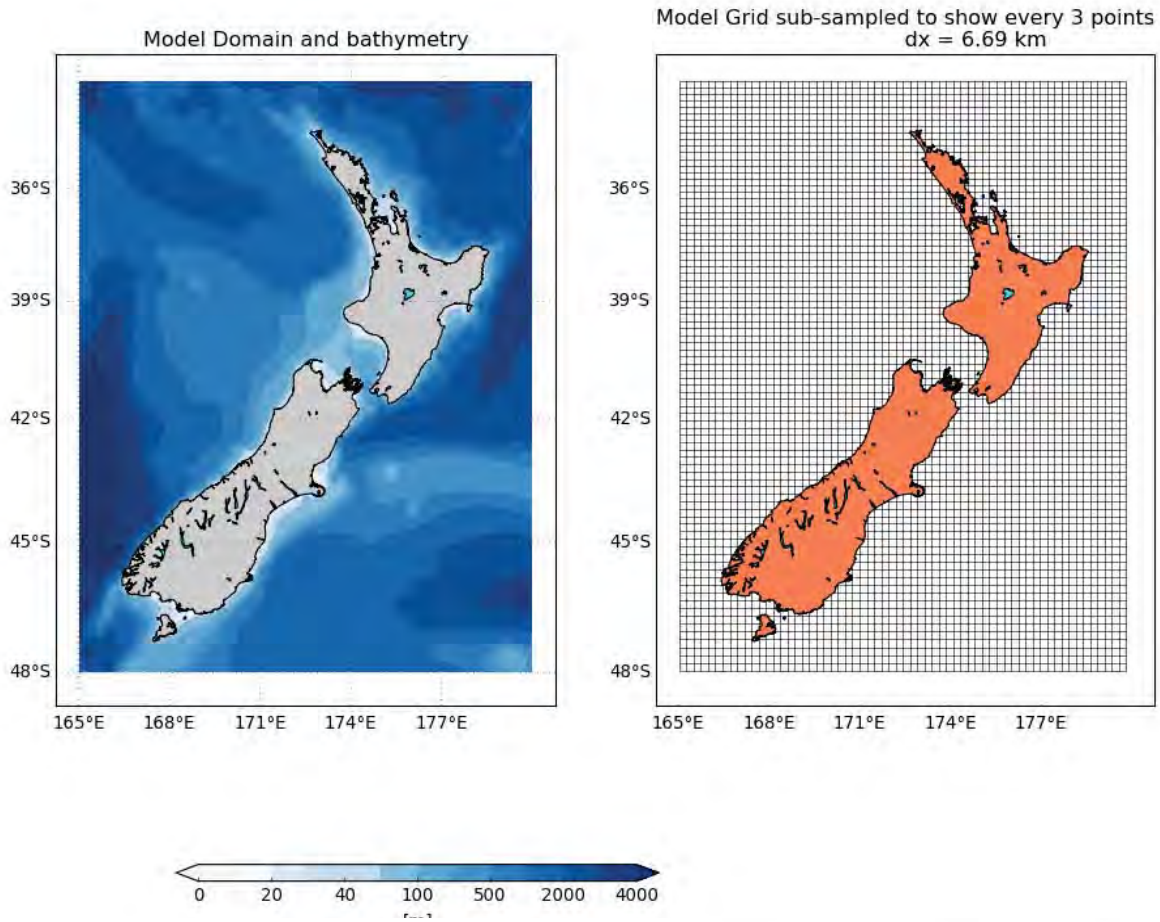
Model Domain and bathymetry
Model Grid sub-sampled to show every 3 points
dx = 6.69 km
36°S
39°S
42°S
45°S
48°S
165°E
168°E
171°E
174°E
177°E
0
20
40
100
500
2000
4000

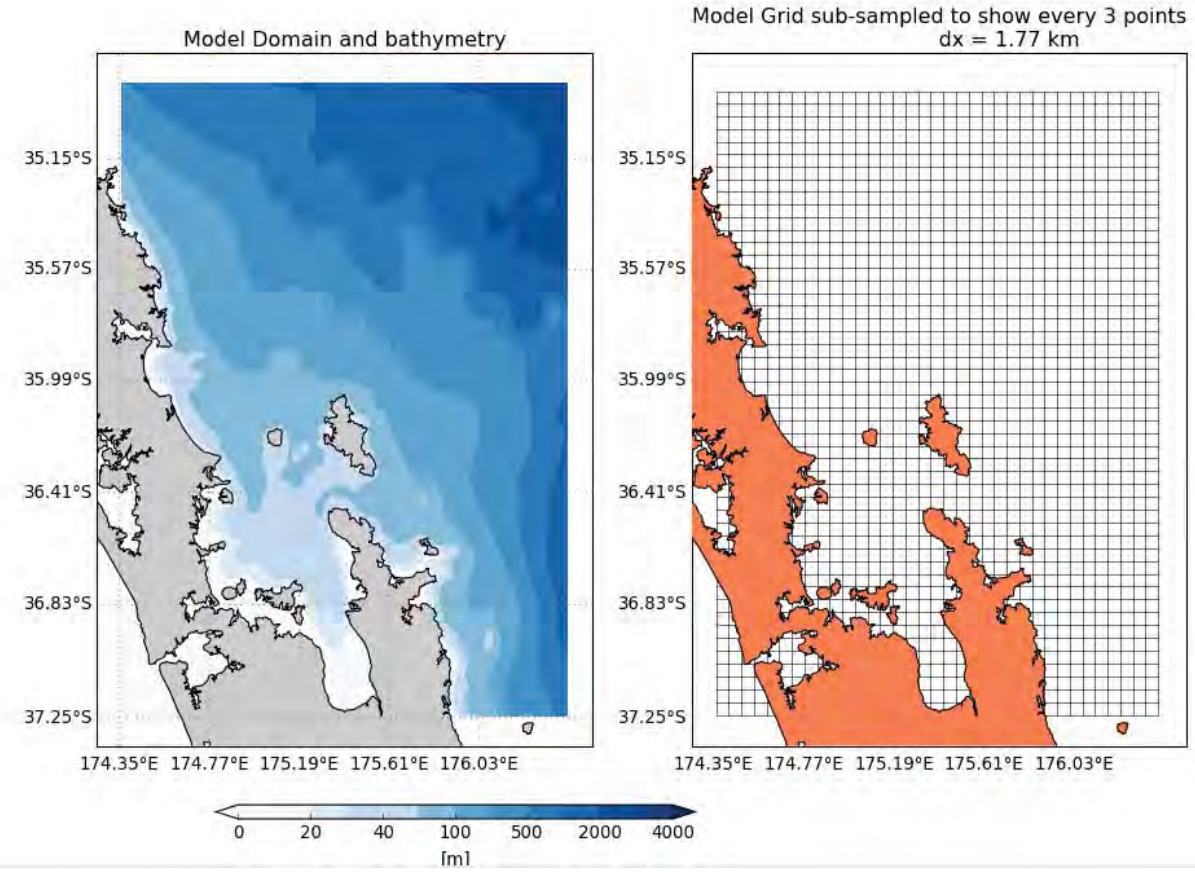
Model Domain and bathymetry
Model Grid sub-sampled to show every 3 points
dx = 1.77 km
35.15°S
35.57°S
35.99°S
36.41°S
36.83°S
37.25°S
174.35°E
174.77°E
175.19°E
175.61°E
176.03°E
0
20
40
100
500
2000
4000
[m]

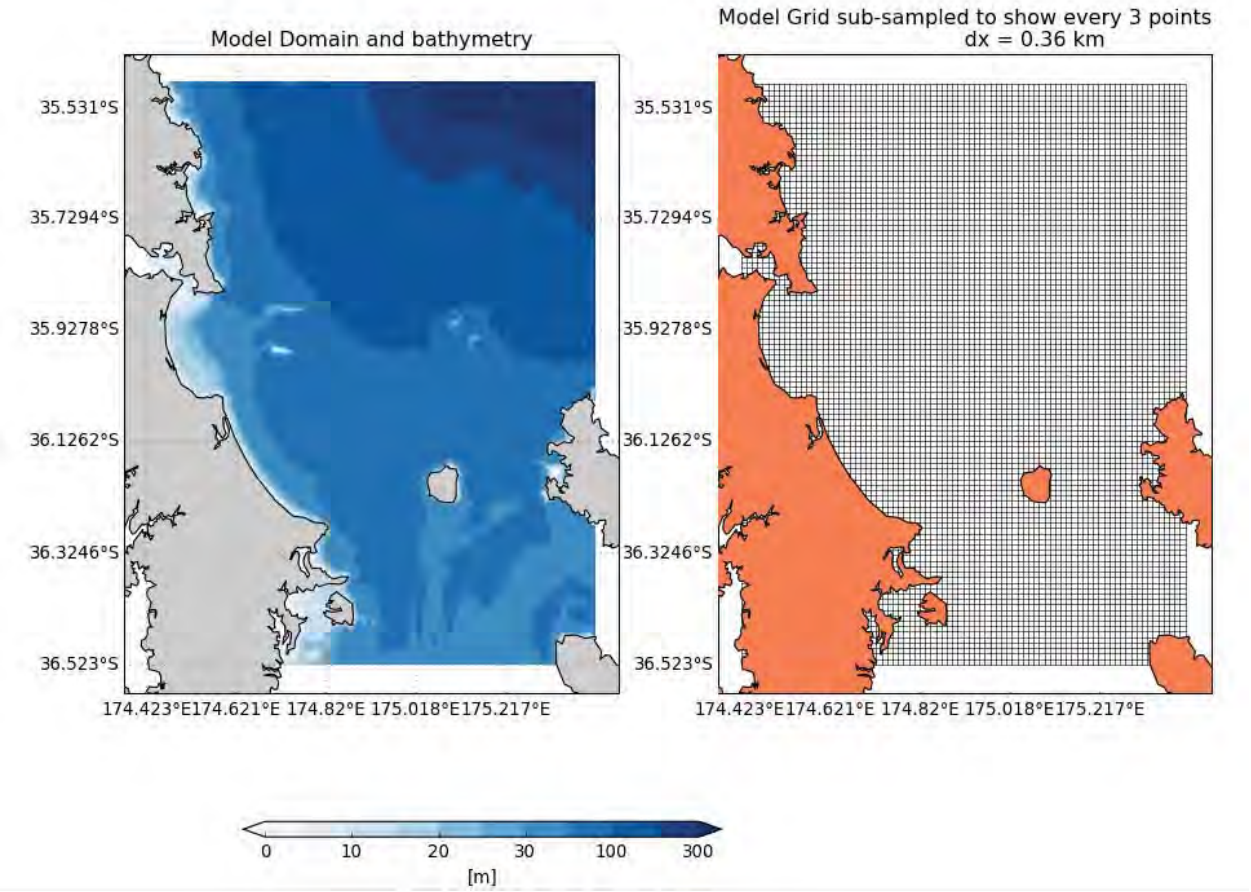

Figure 6.1 Hydrodynamic hindcast downscaling approach with ROMS. Upper panel shows the NZ domain, mid panel shows the HRKI domain and lower panel shows the WHANG domain. The grids are showing every other 3 grid points, to allow easier graphical visualisation.

6.2.1. Atmospheric forcing

MSL maintains an atmospheric reanalysis with variable nests and resolutions for New Zealand using the WRF model and the atmospheric forcing for ROMS was derived from this data. Horizontal resolution varied from 16 to 4 km in the ROMS modelling area. Atmospheric fields consisted of winds, atmospheric pressure, relative humidity, surface temperature, long and short wave radiation and precipitation rate, imposed at hourly intervals to provide air-sea fluxes to drive ROMS in all domains, using a *bulk flux* parameterisation (Fairall et al., 2003).

6.2.2. Open boundary conditions

High frequency (6-hourly for CFSR-NZ and 3-hourly for NZ-HRKI and HRKI-WHANG) open boundary 3D thermohaline, velocity and sea surface height fields were included for all domains. Passive/active prescriptions were applied for all 3D variables at the open boundaries, where a radiation scheme was applied when outflows were estimated by ROMS algorithms. Where inflow was detected, a nudging condition was applied, allowing the penetration of 3D transports and T-S from the external sources, a key setting to guarantee the deep ocean circulation contributions to the smaller scales. To account for the fast propagating tidal oscillations, 2D velocities and surface elevations were treated with *Flather* and *Chapman* schemes, respectively.

6.2.3. Tidal forcing

ROMS WHANG was forced at the open boundaries by tidal elevations and currents, harmonic constituents derived from a MetOcean Solutions' New Zealand 2D hydrodynamic model consisting of a 5 km resolution grid, which was in turn forced at its open boundaries by the renowned OTIS Atlantic Ocean solution (Oregon State University Tidal Inverse Solution (Egbert and Erofeeva, 2002).

6.2.4. Model calibration

Through comprehensive testing of model parameters such as sub-grid scale parameterisations, forcing sources and grid settings including open boundary locations, spatial resolution and downscaling rate between parent and child grids, the model was calibrated with respect to available published literature and representation of the main identified forcing mechanisms. Numerical diagnosis such as checking kinetic energy equilibrium and trends in the 3D fields were successfully conducted.

6.3. Model verification

A qualitative analysis of the hydrodynamic patterns obtained from the 10-year ROMS hindcast was conducted, while in Section 6.4 a more qualitative approach was adopted to validate the model results against recently obtained *in situ* measurements.

The results depicted by the HRKI nest specifically show that mean flow patterns at the Hauraki Gulf were preferably oriented in the along-shore direction, due to open ocean currents and the predominant wind forcing (Figure 6.2). Offshore Whangarei harbour, channelling effects between the coast and the islands intensify and steer the flow to a quasi-meridional orientation (Figure 6.2, Figure 6.3, Figure 6.4 and Figure 6.6).

The long term 10-year net flow was oriented from north to south, and most of the strength and variability of the currents were in the along-shore direction (Figure 6.3 and Figure 6.5). The high order hydrodynamics at the inner shelf and vicinities of Whangarei harbour were mainly controlled by the tides and the interaction between the offshore flows along the 50 m isobath and local bathymetry (Figure 6.6). The residual circulation at Bream Bay is complex, has a light and variable regime, and normally responds to the shelf flow to the east of the bay (Figure 6.6).

The analysis of ROMS results motivated the choice of an optimal location for an ADCP measurement campaign to further validate the model (Section 6.4). The suggested location for the measurement campaign lay in the axis of this offshore climatological jet (Figure 6.2 and Figure 6.3). This was an appealing area to test the model ability to replicate the hydrodynamics, as it involved a wider spectrum of scales of forcing. If the model was proven to be accurate in this particular location, considering the high quality bathymetry used in the coastal area, it will be accurate for the areas that are under high order influence of it.

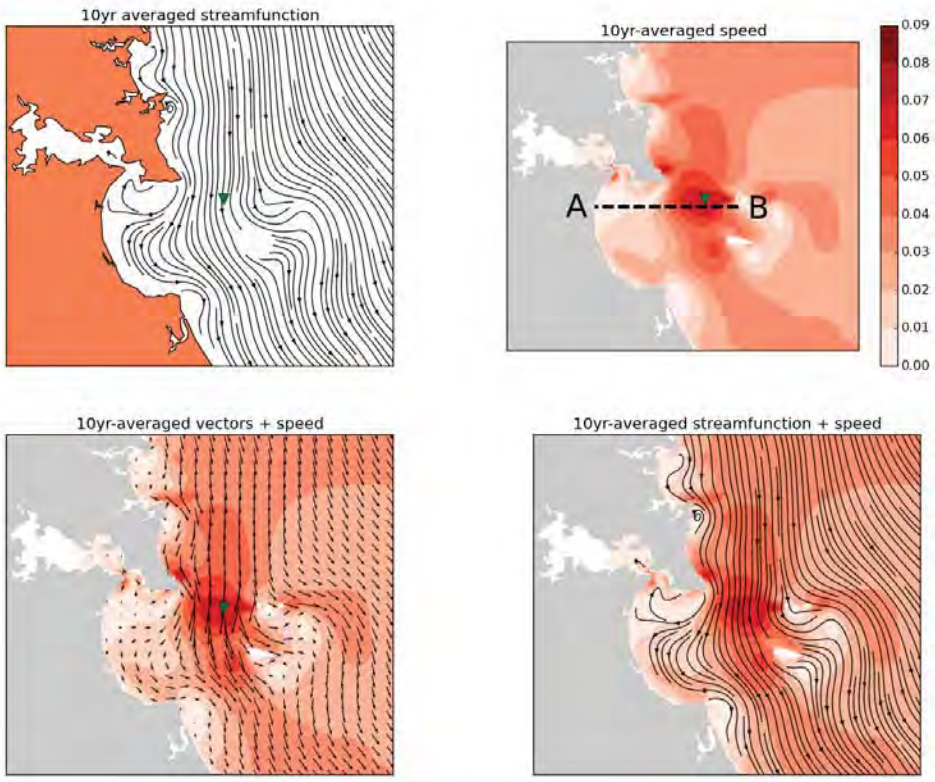

Figure 6.2 Climatological flow patterns offshore Whangarei Harbour based on mean current speeds computed off a 10 year (2000-2010) ROMS hindcast. Current speeds in red shades (m s^{-1}). The green mark denotes the suggested location for a 2 month current measurement campaign. Note the intensification and channelling effect between Bream Bay and the offshore islands.

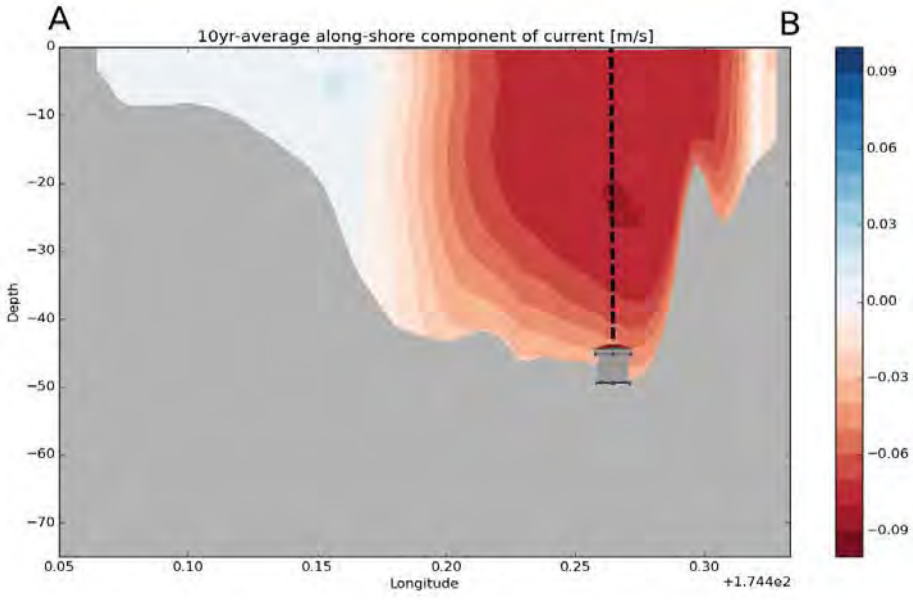

Figure 6.3 10-year averaged “AB” cross-shore distribution of alongshore current (red denotes southward flow and blue denotes northward flow) across the proposed current meter location. Note the climatological jet-like along-shore flow.

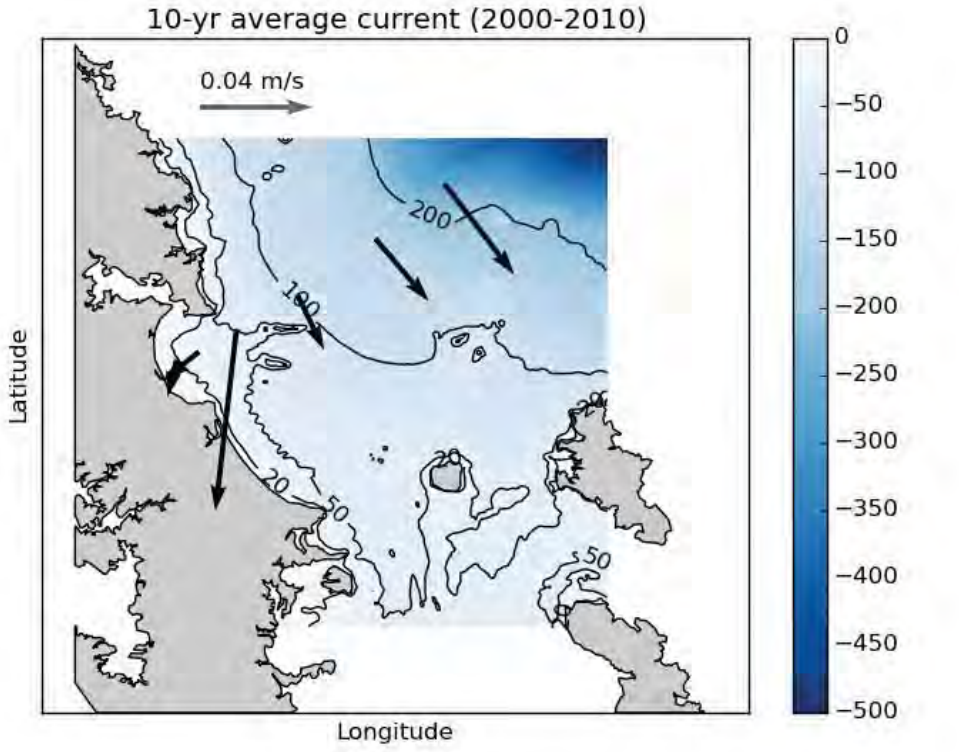

Figure 6.4 An examination of the central Hauraki Gulf cross-shelf variability of the long term averaged flow based on the 10 year ROMS hindcast. Note the south-eastward preference of the flow orientation. Note also the intensification of the flow between Bream Bay and the offshore islands.

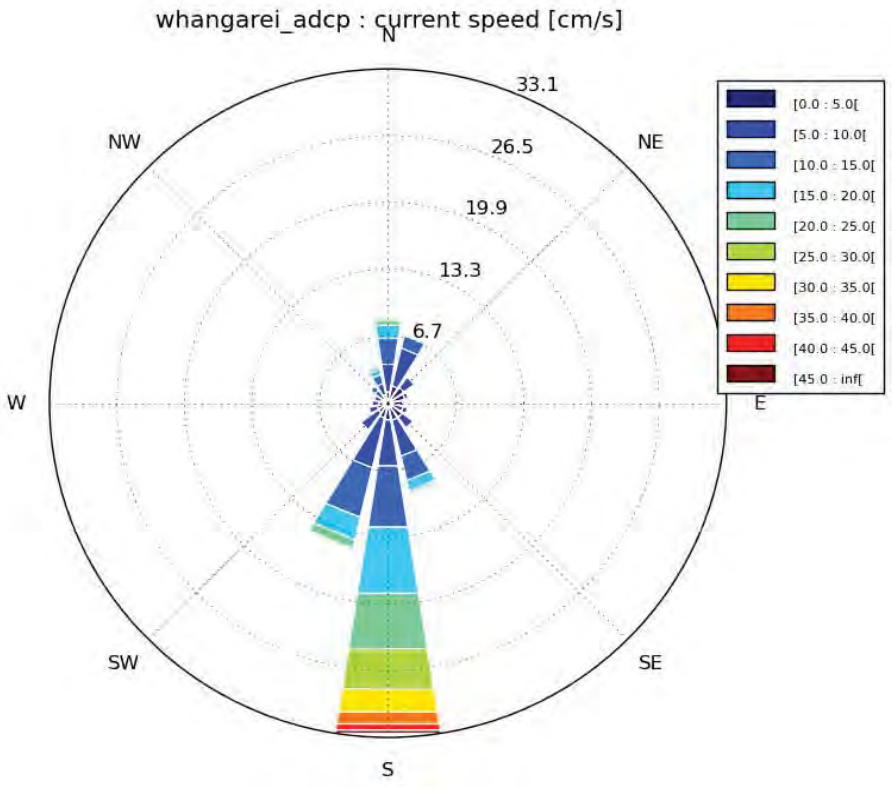

Figure 6.5 Current rose at the suggested current meter location (current direction are represented as “going to”). Note the currents show much more strength and variability in the along-shore direction and have a significant preferable flow direction from North to South year round, specifically the stronger events.

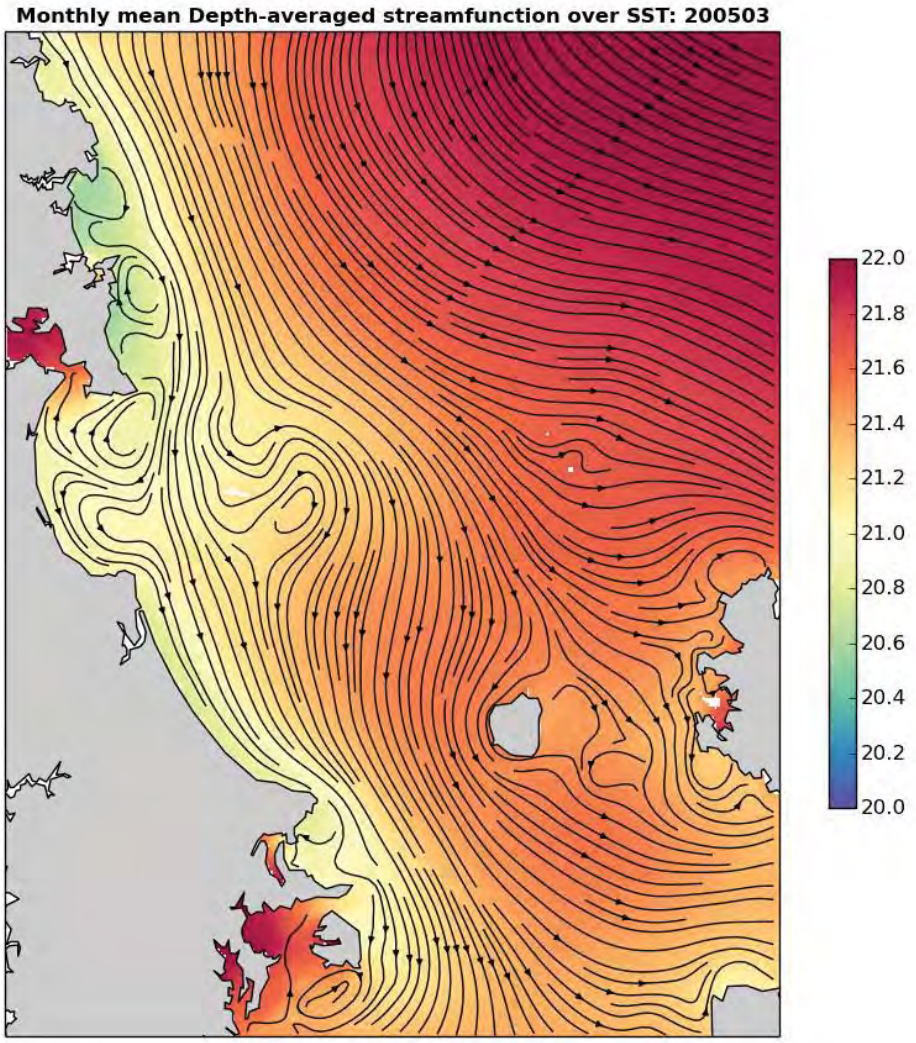

Figure 6.6 Monthly averaged flow for March 2005 as an example of the regional circulation. Note the interaction of the southward flow and the coastline geometry between Bream Bay and the offshore islands, generating coastal eddies and bifurcations.

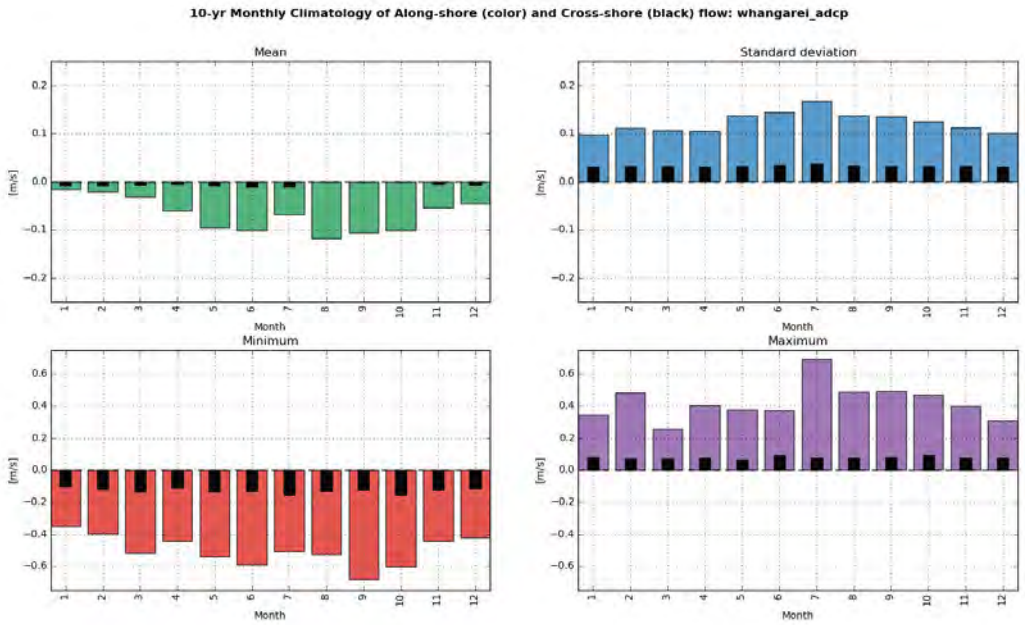

Figure 6.7 Monthly climatology of alongshore current at the suggested location for the current meter campaign. Note that the late winter and early spring months show stronger currents, although the difference between seasons/months is not too substantial. The currents show much more strength and variability in the along-shore direction and have a significant preferable flow direction from North to South year round. Note that the months of November and December are overall within the typical regime observed year round.

6.4. Model validation

A current profiler (ADCP) was deployed in the Parry Channel at 35° 54.795' S, 174° 35.385 E (WGS84) in approximately 54 m water depth from 15 January 2016 to 5 March 2016. The ADCP was deployed on the seabed facing upwards and recording data in 5-minute bursts and 4 m vertical bins sampled at 1 Hz, every 30 minutes. The data were interpolated to 5, 15 and 30 m below sea surface (bss) for direct comparison with the ROMS data at these same levels. Because the measured and hindcast dataset are not co-temporal, the comparison is qualitative.

6.4.1. Validation results

The comparisons between the 2000-2010 ROMS hindcast data and the 2016 deployment are presented as current roses in Figure 6.8 to Figure 6.11 for the current at 5 m bss, 15 m bss and 30 m bss, respectively. There is a general good agreement between the modelled and measured current directions, but in general the measured currents were stronger than the hindcast for the upper half of the water column (Figure 6.10 and Figure 6.11). These stronger measured currents are likely to be caused by stronger wind events from the NE quadrant during the deployment period (Figure 6.12); an assertion supported by the wind/current correlations (presented in Figure 6.13 and Figure 6.14).

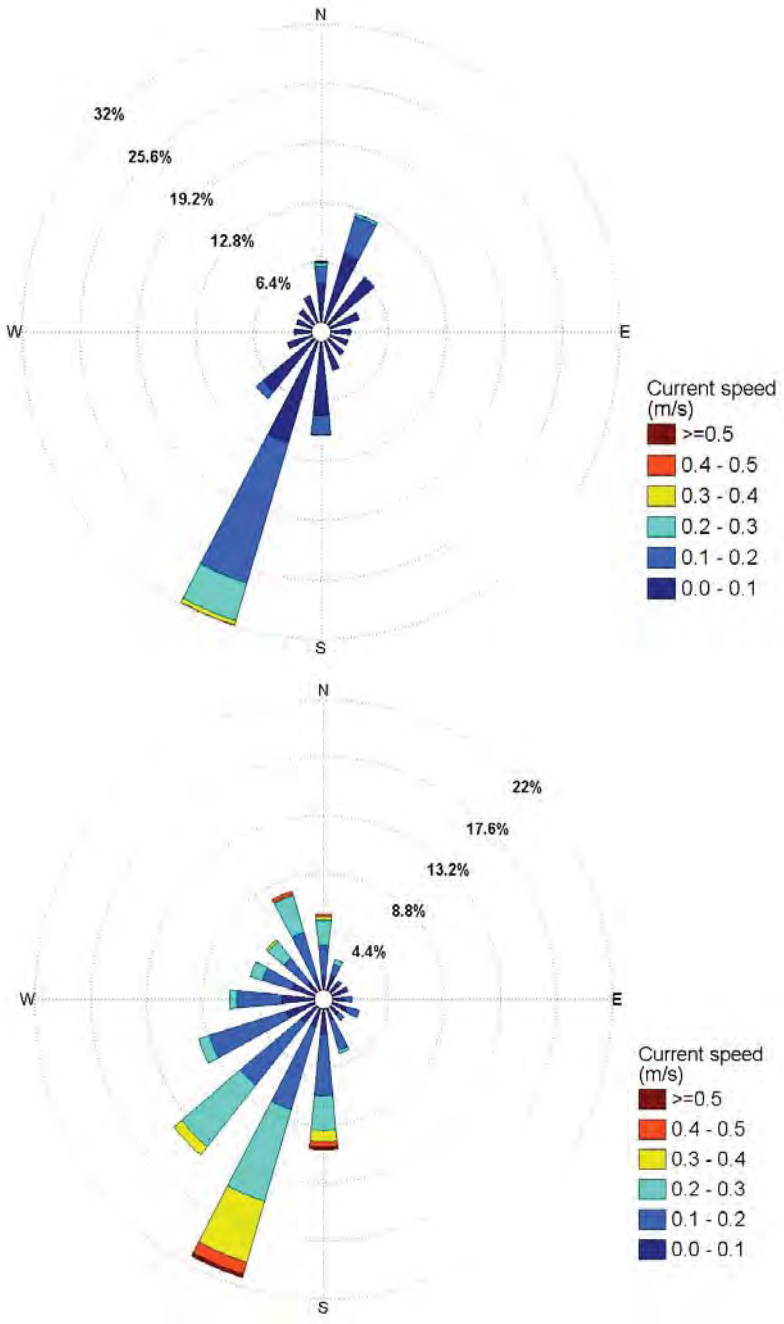

Figure 6.8 Current roses showing depth averaged total current speed from (top) ROMS hindcast data for the period 2000-2010 and (bottom) measured ADCP data from 16 January 2016 to 4 March 2016. Current directions are in the “going to” convention.

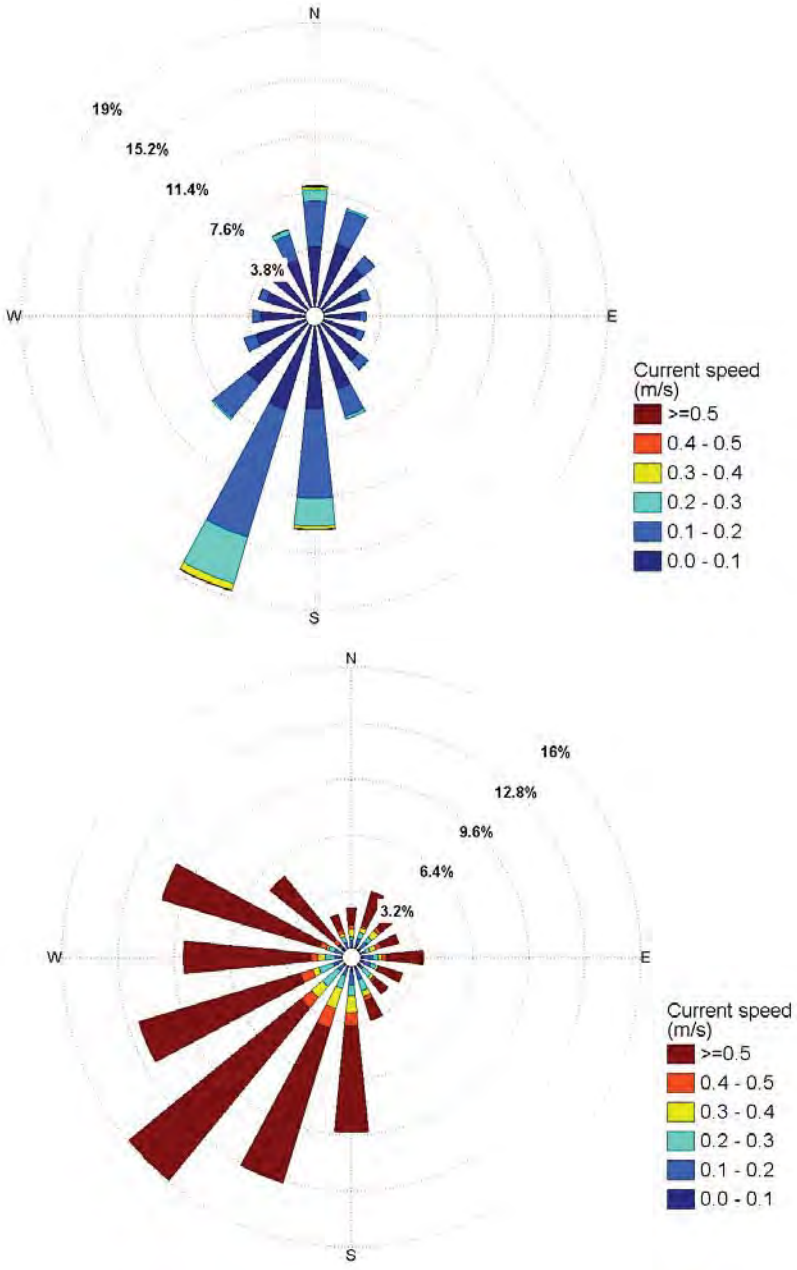

Figure 6.9 Current roses showing total current speed at 5 m bss from (top) ROMS hindcast data for the period 2000-2010 and (bottom) measured ADCP data from 16 January 2016 to 4 March 2016. Current directions are in the “going to” convention.

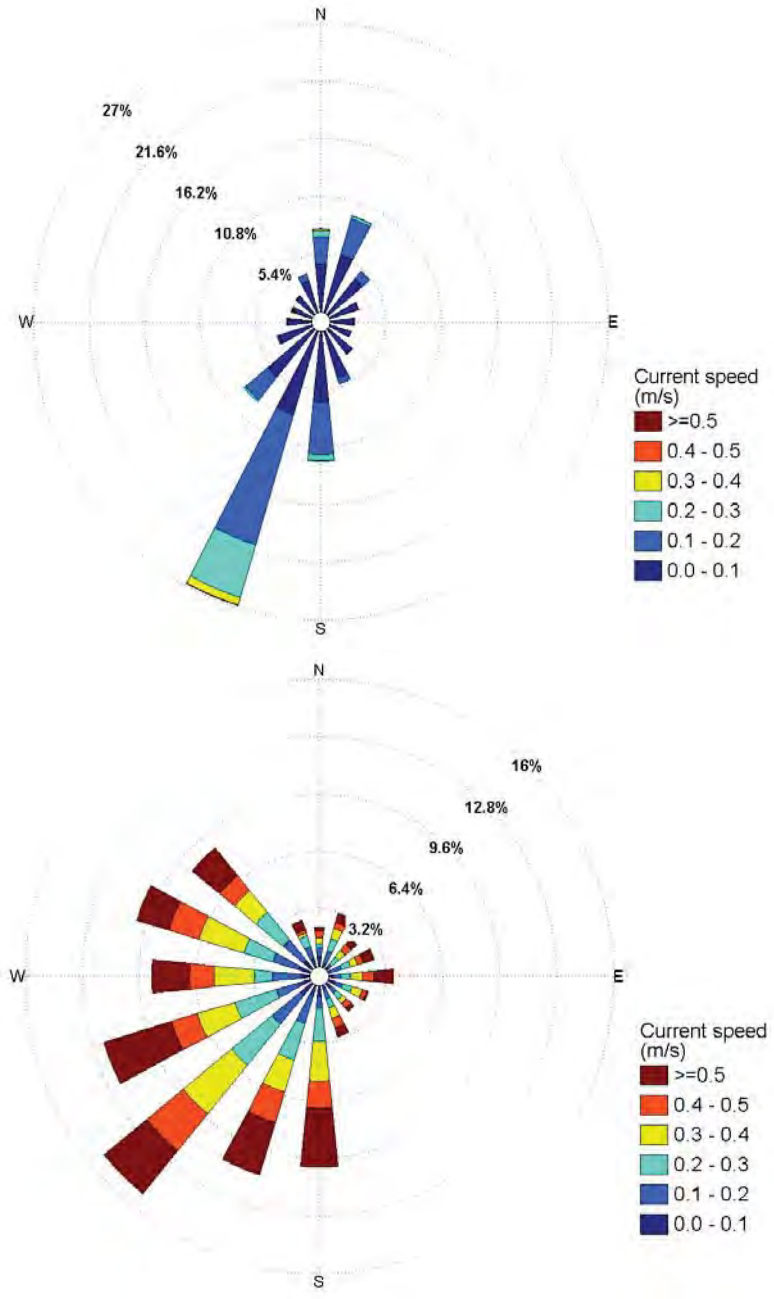

Figure 6.10 Current roses showing total current speed at 15 m bss from (top) ROMS hindcast data for the period 2000-2010 and (bottom) measured ADCP data from 16 January 2016 to 4 March 2016. Current directions are in the “going to” convention.

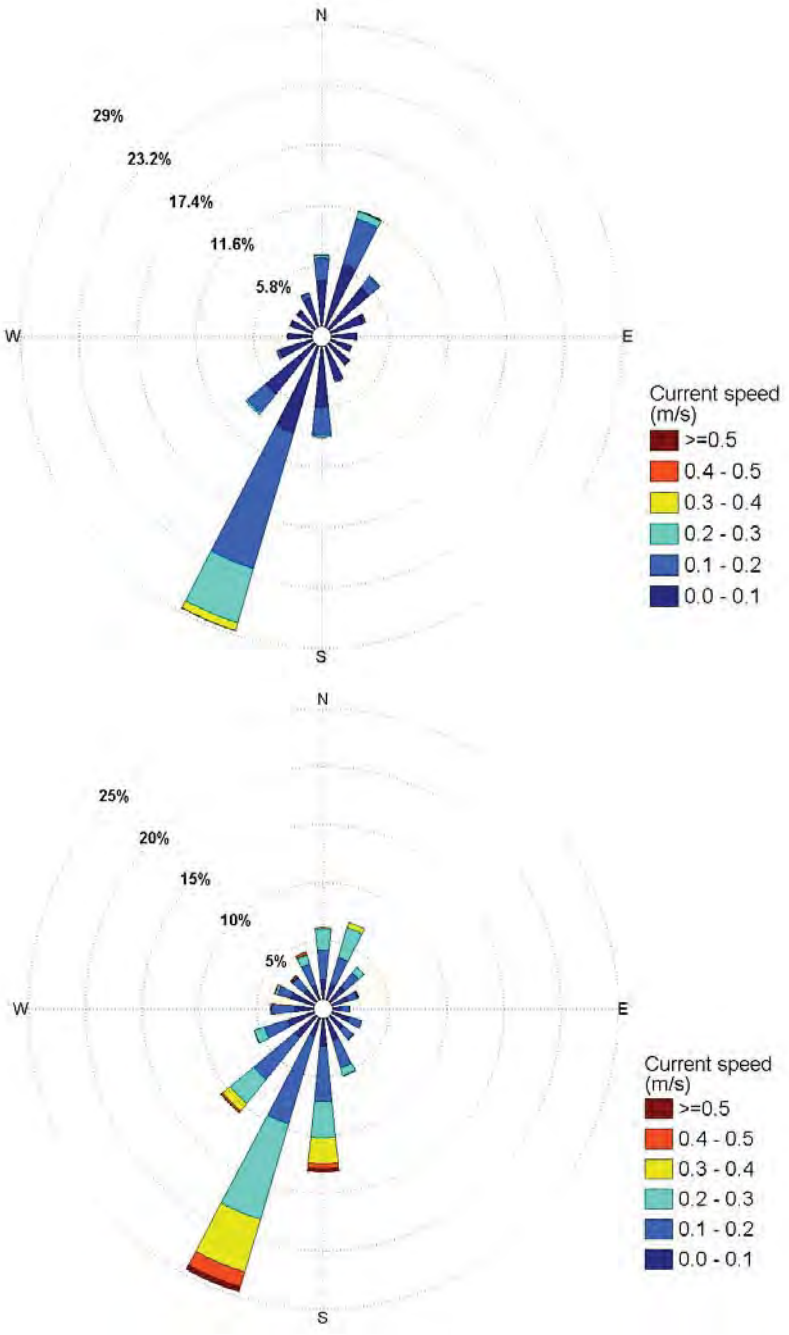

Figure 6.11 Current roses showing total current speed at 30 m bss from (top) ROMS hindcast data for the period 2000-2010 and (bottom) measured ADCP data from 16 January 2016 to 4 March 2016. Current directions are in the “going to” convention.

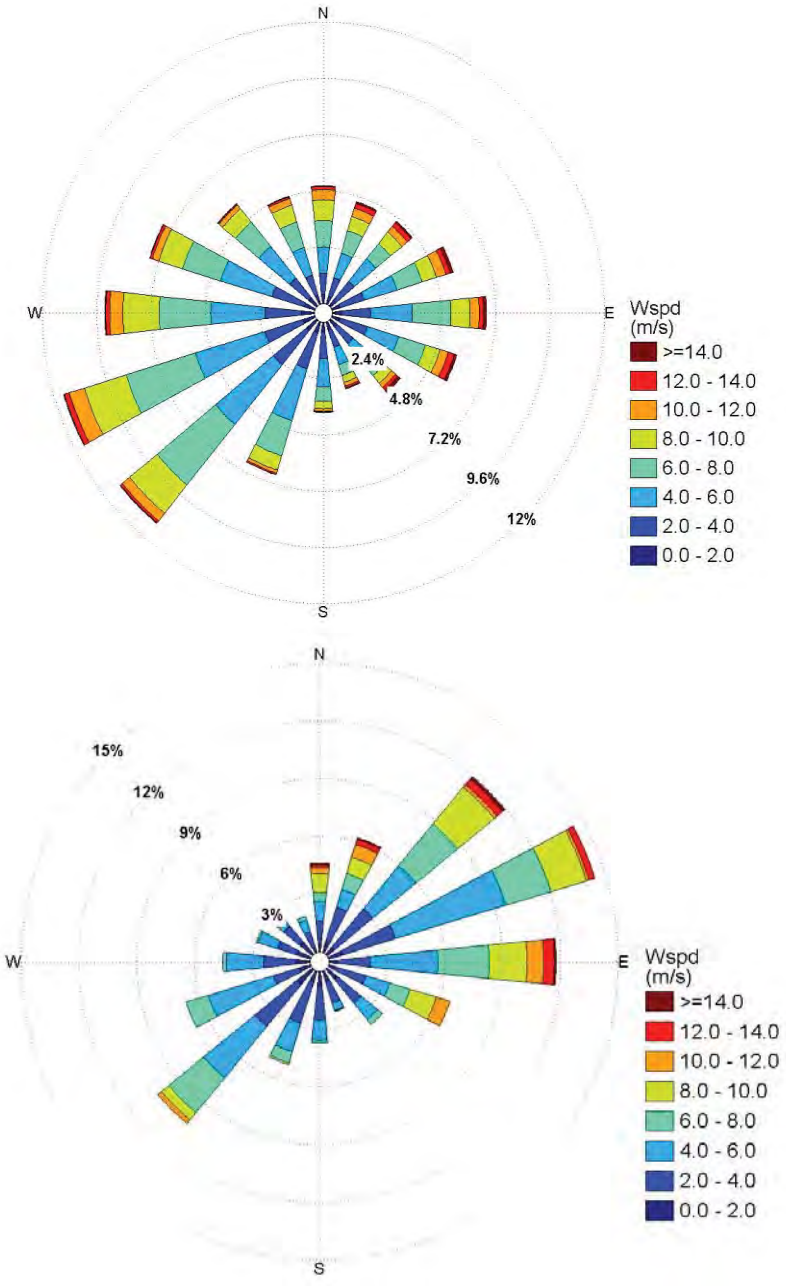

Figure 6.12 Wind roses from (top) WRF hindcast data for the period 2000-2010 and (bottom) nowcast data from 16 January 2016 to 4 March 2016 at location 35.917° S 174.519° E in the vicinity of the ADCP deployment, showing the predominance of winds coming from the NE quadrant during the deployment. Wind directions are in the “coming from” convention.

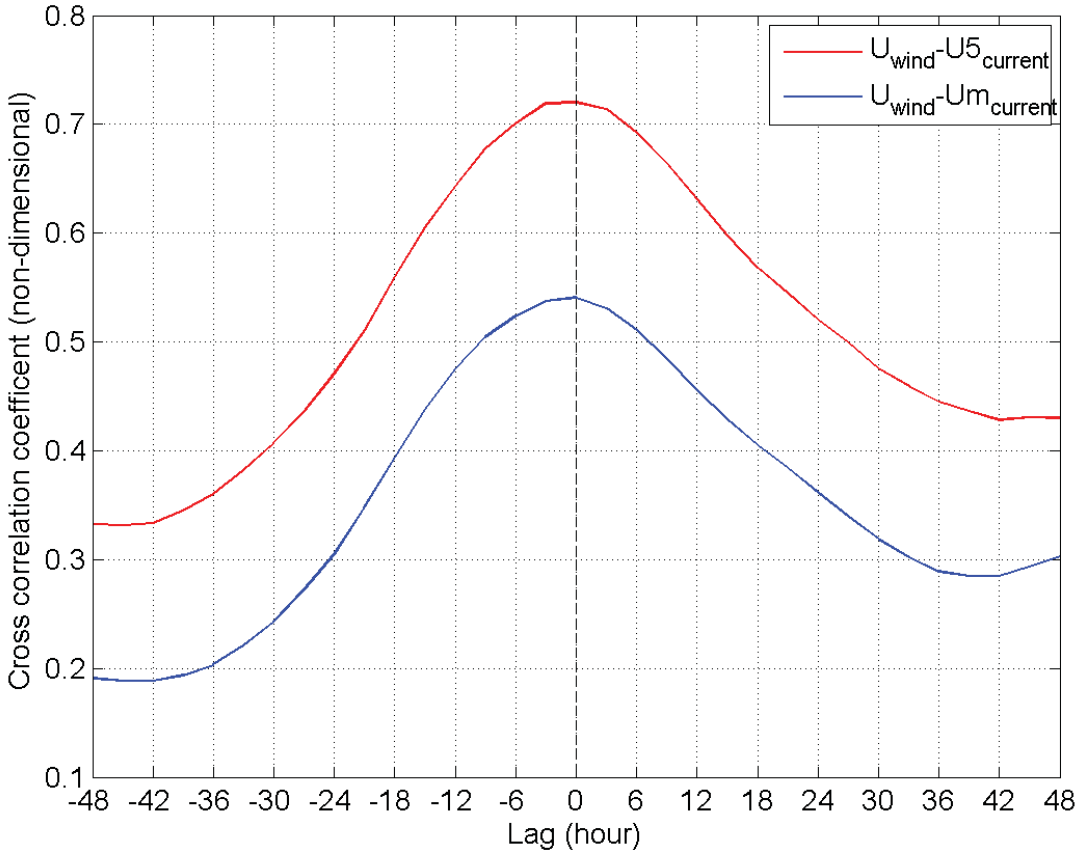

Figure 6.13 Cross-correlation coefficients of the pairs [east component of wind speed, east component of total current at 5 m bss (red) and [east component of wind speed, east component of total depth averaged current] (blue) as a function of the lag between the two parameters of each pair. Note a negative lag indicates the correlation of the first parameter with the second parameter delayed by this lag. This figure shows that the east component of wind and current are correlated, with no significant lag. The data used to create this figure were the nowcast wind data and the measured current data for the period 16 Jan – 4 Mar 2016.

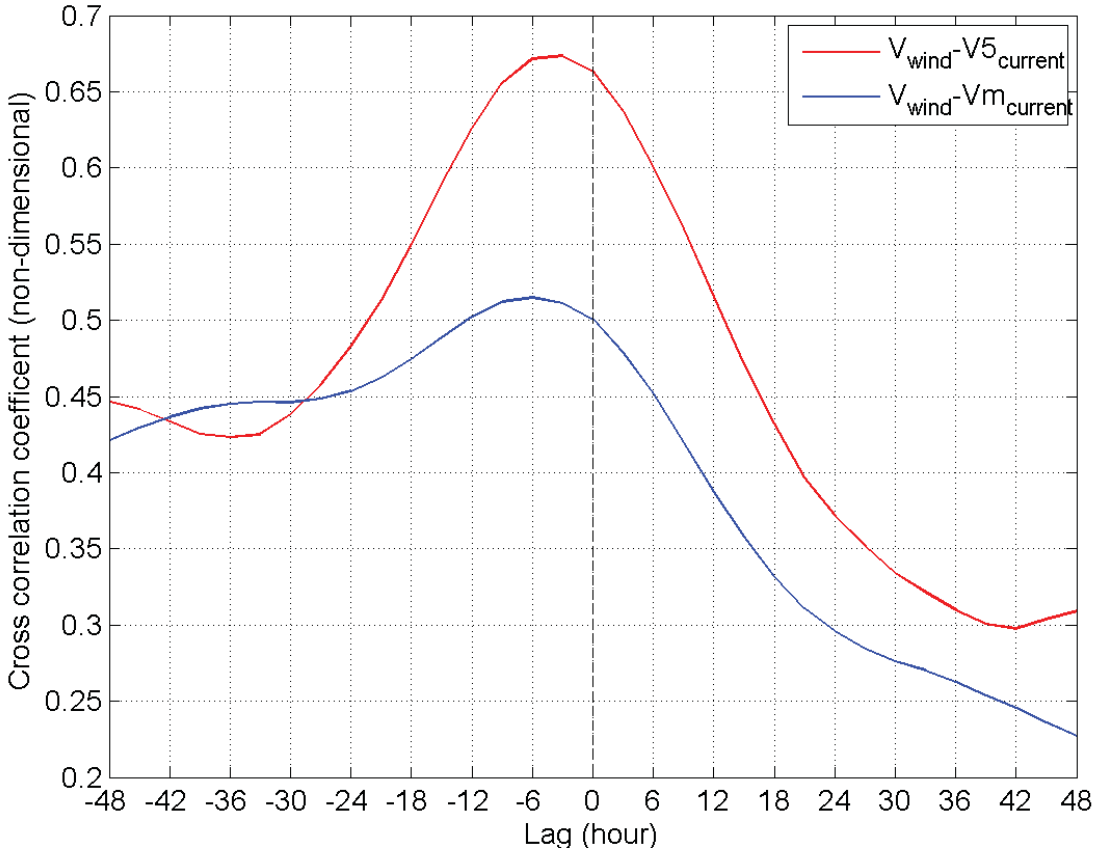

Figure 6.14 Cross-correlation coefficients of the pairs [north component of wind speed, north component of total current at 5 m bss] (red) and [north component of wind speed, north component of total depth averaged current] (blue) as a function of the lag between the two parameters of each pair. Note a negative lag indicates the correlation of the first parameter with the second parameter delayed by this lag. This figure shows a typical 3-6 hour lag for currents at 5 m bss to be affected by northerly winds and a 6 hour lag for depth averaged current to be generated. The data used to create this figure were the nowcast wind data and the measured current data for the period 16 Jan – 4 Mar 2016.

7. NEARSHORE TIDAL HYDRODYNAMICS

The SELFE model was used to explore the tidal hydrodynamics of Whangarei Harbour. This section details the set up and validation of the model, the outputs of which was used to drive the sediment dispersal modelling described in Section 8.

SELFE is a prognostic finite-element unstructured-grid model designed to simulate 3D baroclinic, 3D barotropic or 2D barotropic circulation. The barotropic mode equations employ a semi-implicit finite-element Eulerian-Lagrangian algorithm to solve the shallow-water equations, forced by relevant physical processes (atmospheric, oceanic and fluvial forcing). SELFE uses either pure terrain-following sigma, or S-layer coordinates in the vertical, or a hybrid system using both S and Z-layers as required and uses sophisticated vertical turbulent closure models. A detailed description of the SELFE model formulation, governing equations and numerics can be found in Zhang and Baptista (2008).

The SELFE model is physically realistic, in that well understood laws of motion and mass conservation are implemented. Therefore water mass is generally conserved within the model although it can be added or removed at open boundaries (e.g. through tidal motion at the ocean boundaries, or river discharges) and water is redistributed by incorporating aspects of the real-world systems (e.g. bathymetric information, forcing by tides and wind). The model transports water and other constituents (e.g. salt, temperature, turbulence) through the use of triangular volumes (connected 3-D polyhedrons) of varying size and is described as an unstructured finite element model.

7.1. Model mesh bathymetry

Model bathymetries were derived from a combination of relevant ENC (Electronic Navigation Charts), LIDAR, and survey data (single beam and offshore multibeam surveys) (Section 3.2). All data were converted to a common horizontal projection (NZTM), and reduced to a common vertical datum.

The model domain extents are shown in Figure 7.1. It was chosen to be sufficiently large to ensure the appropriate tidal boundaries (elevations and velocities) can be applied. The mesh resolution varies from approximately 300 m in the offshore, to ~5 m nearshore and around salient features. Model bathymetry is given in Figure 7.2.

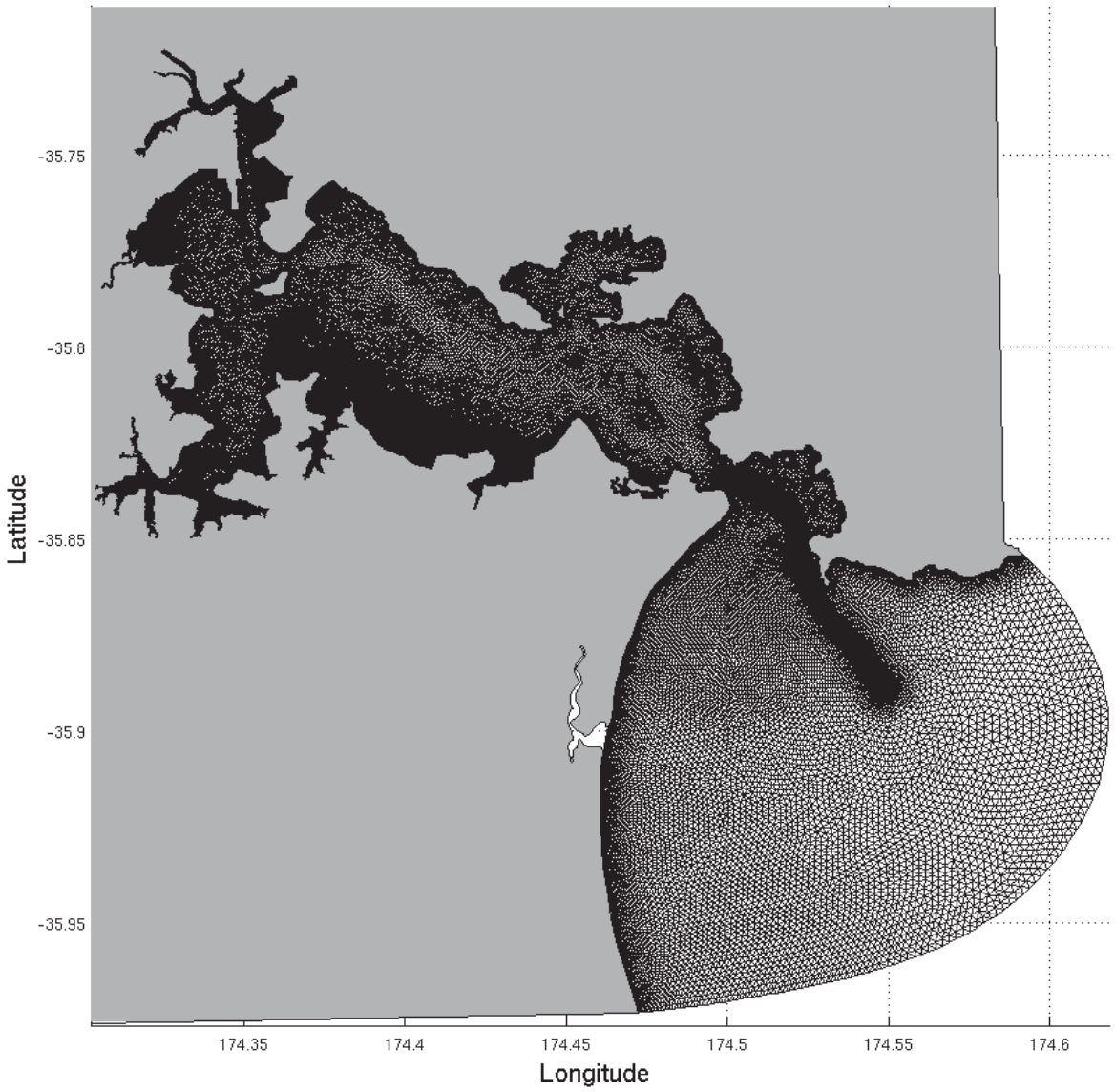

Figure 7.1 Model mesh of the Whangarei Harbour and environs. The mesh covers the offshore region, including the ebb tidal delta, while salient bathymetric features are represented inside the harbour.

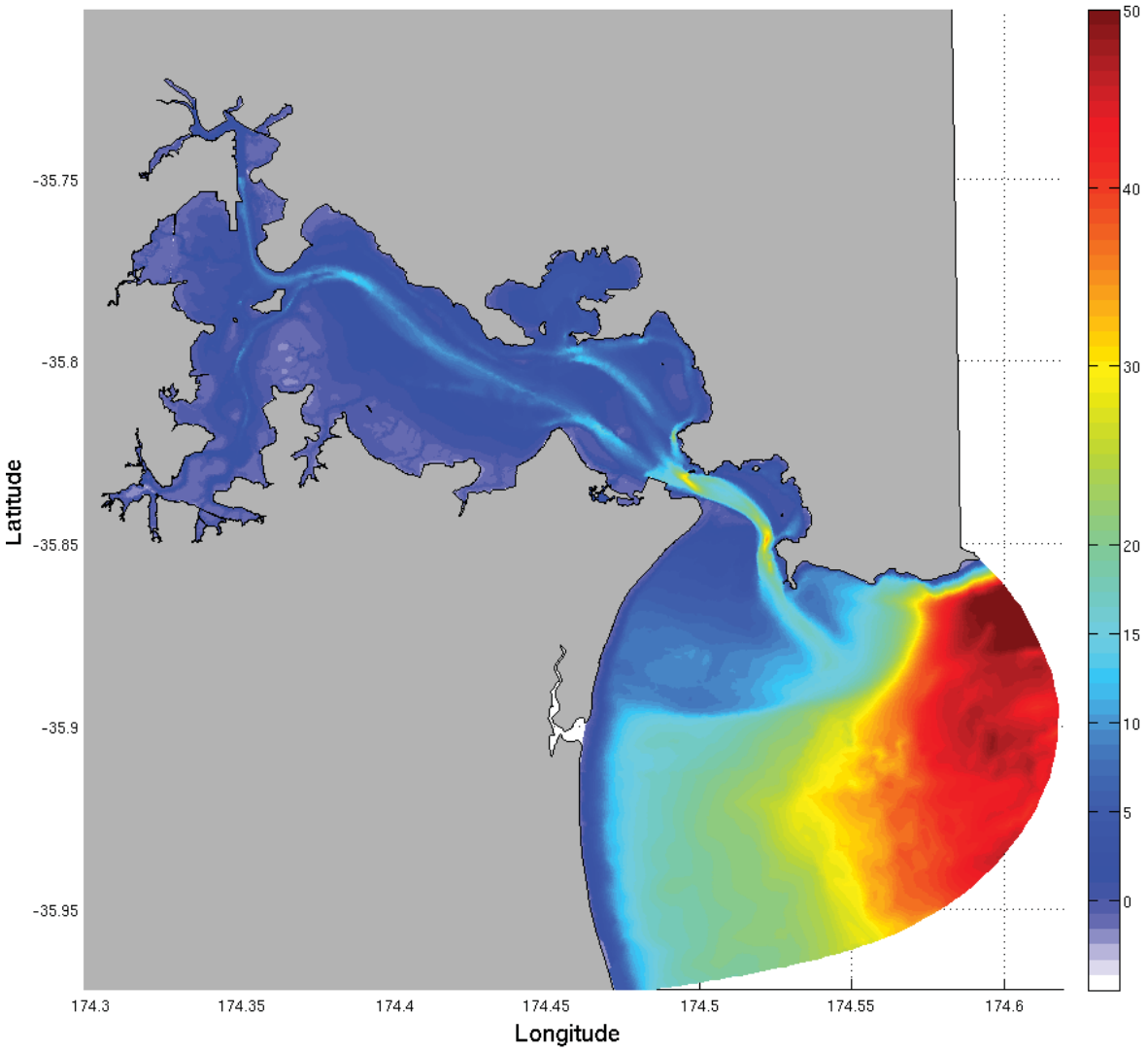

Figure 7.2 Model bathymetry/topography showing the ebb tidal delta and the inner harbour topography. Depths are given in metres below Mean Sea Level (MSL)

7.2. Tidal elevations and currents

A national New Zealand tidal solution derived from an implementation of the Princeton Ocean Model (POM) nested within the TPXO7.2 Pacific inverse tidal dataset (Egbert and Erofeeva, 2002) was used to prescribe the tidal elevation and current velocity at the boundaries of the grid. Depth dependent velocities along the offshore boundaries were defined using a standard logarithmic velocity profile. Equation 2.2.13 in Van Rijn (1993) was used, shown in the following equation for the *u* component:

$$\tilde{u}(x,y,z,t) = \left[\frac{\bar{u}(x,y,t)}{z_0/h - 1 + \ln(h/z_0)}\right]\ln\left(\frac{z}{z_0}\right) \quad (7.1)$$

where z is the particle elevation above the seabed, z_0 is the zero-velocity elevation (set here at 1 mm), h is the water-column height boundary node location (x,y), and u is the depth-averaged horizontal current velocity at the boundary node.

7.3. Model validation

Model calibration was undertaken by adjusting key parameters within the model to ensure model predicted velocities and elevations agreed with measured data (both site specific data and Acoustic Doppler Current Profiler (ADCP) data collected from a vessel transiting across the channel during different tidal flow conditions. Locations of the spot instruments and the three zones (Zone A, B and C) over which the vessel transit ADCP data was collected are provided in Figure 7.3. Comparisons between the measured and model predicted water levels at sites k17, p10, Parua and W2 are given in Figure 7.4 to Figure 7.7, while Figure 7.8 to Figure 7.10 compare the measured and model predicted current velocities within Zone A, B and C respectively. The model is shown to faithfully reproduce both the site specific water level data and the direction and magnitude of the current velocities within the three zones surveyed (A, B and C, Figure 7.3)

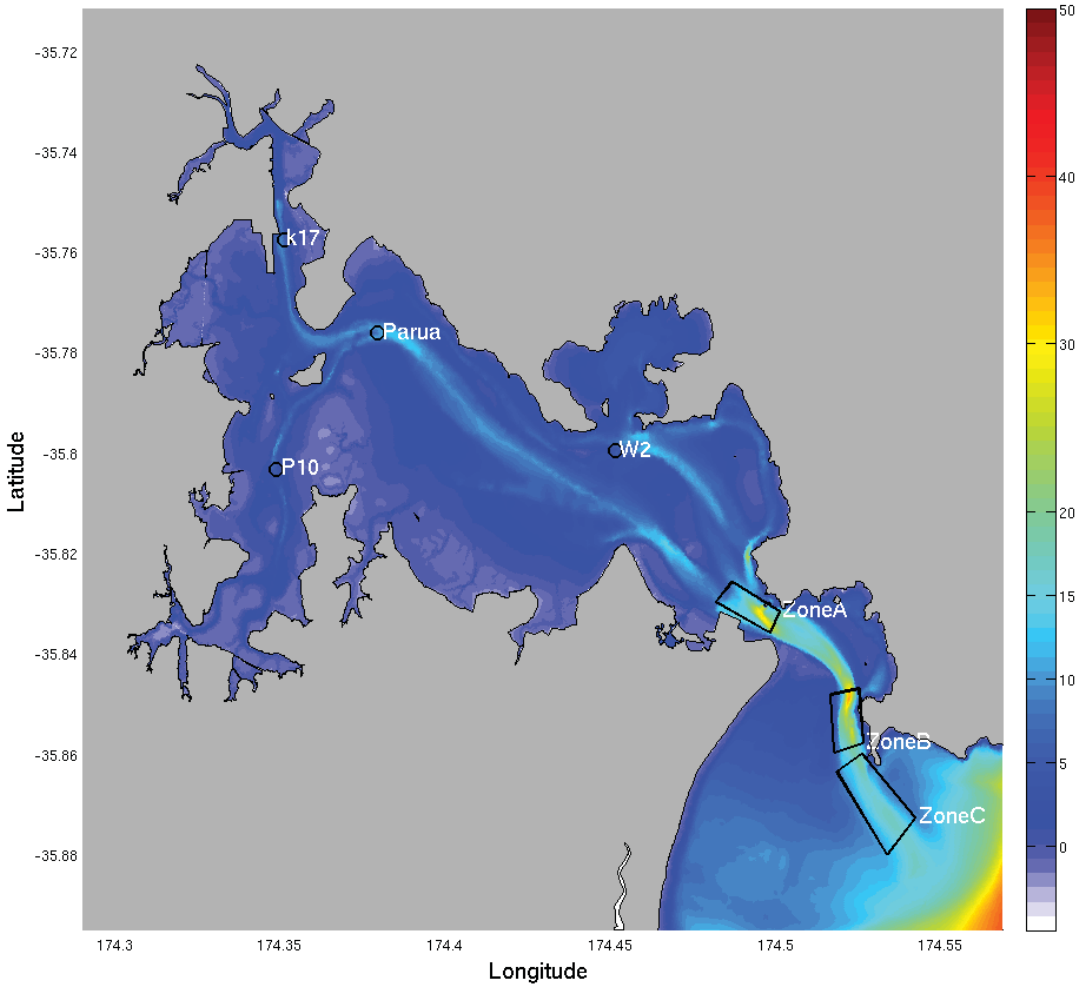

Figure 7.3 Measurement locations for the current velocities and water levels used to calibrate and validate the SELFE tidal model.

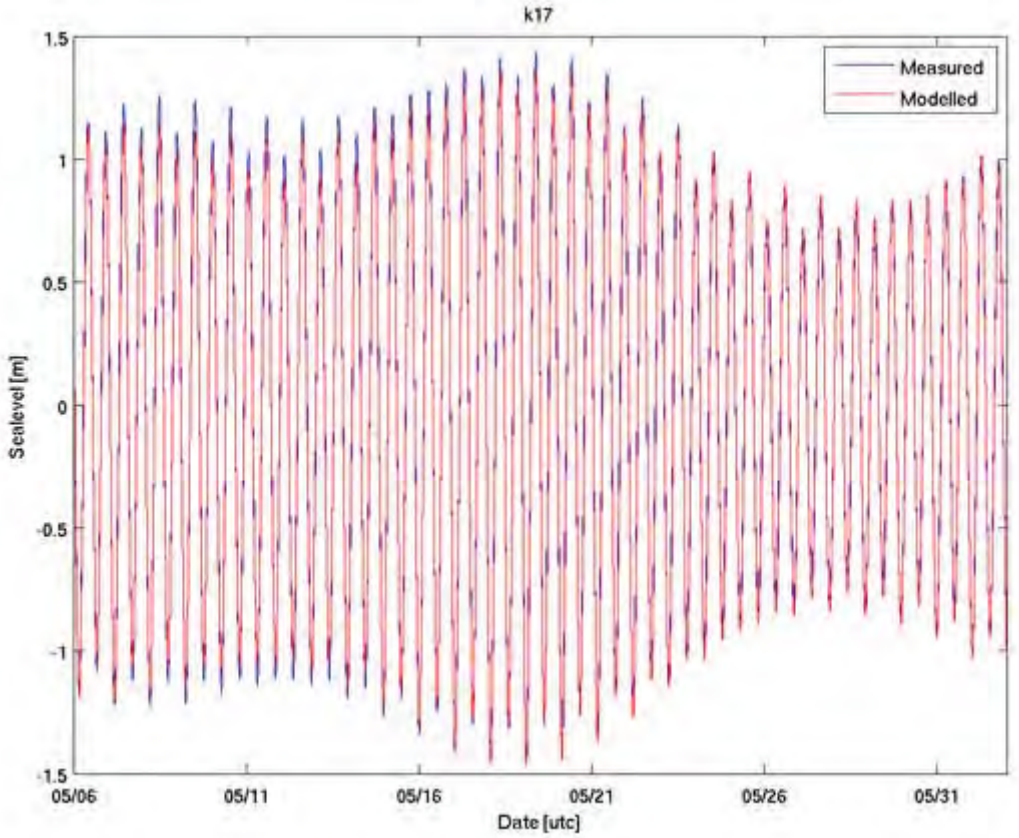

Figure 7.4 Measured and modelled water level comparisons at site k17.

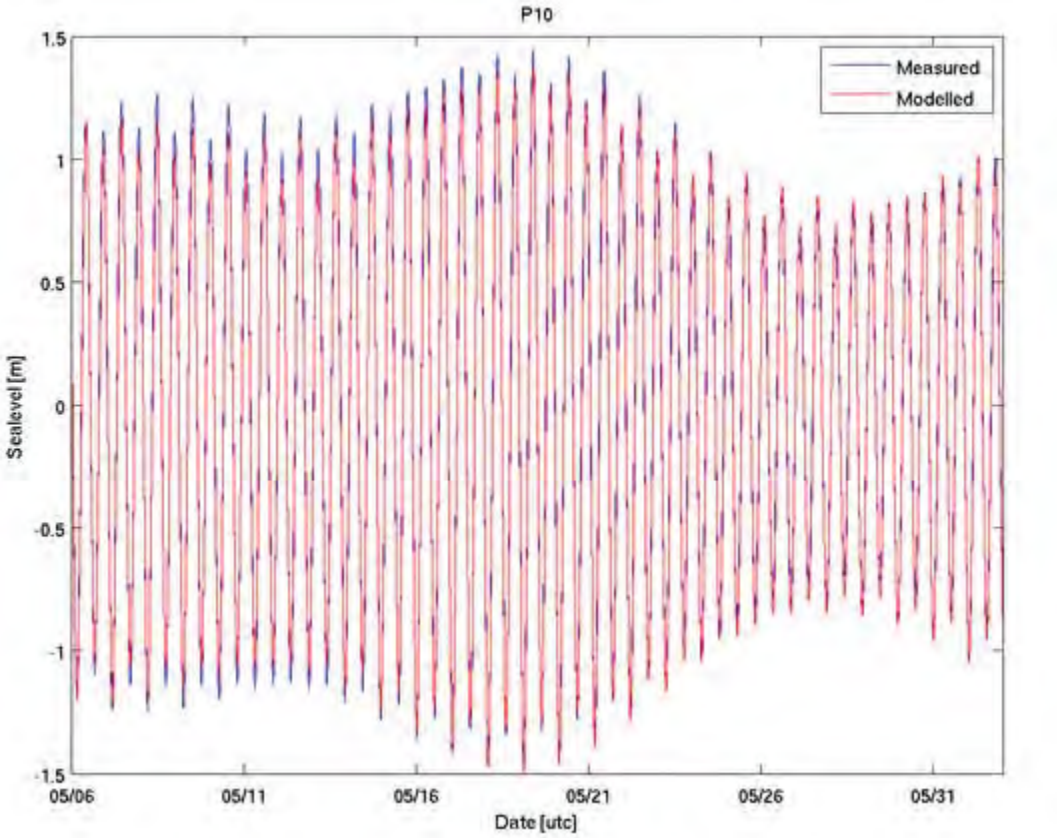

Figure 7.5 Measured and modelled water level comparisons at site p10.

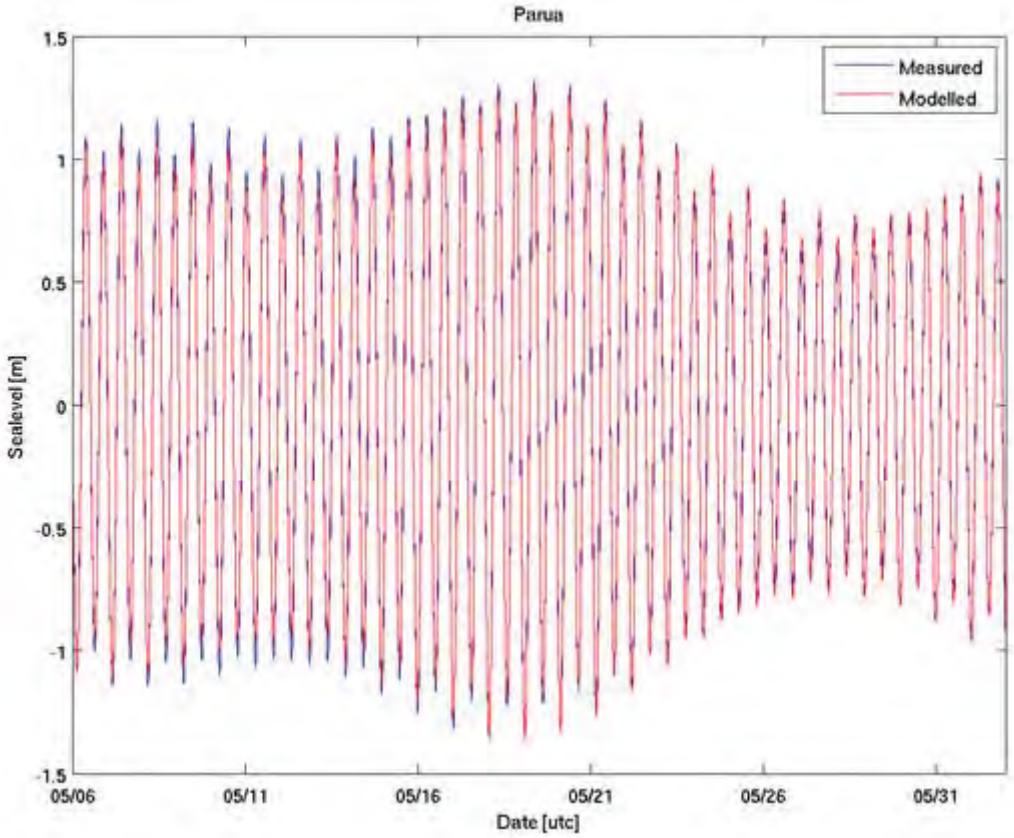

Figure 7.6 Measured and modelled water level comparisons at site Parua.

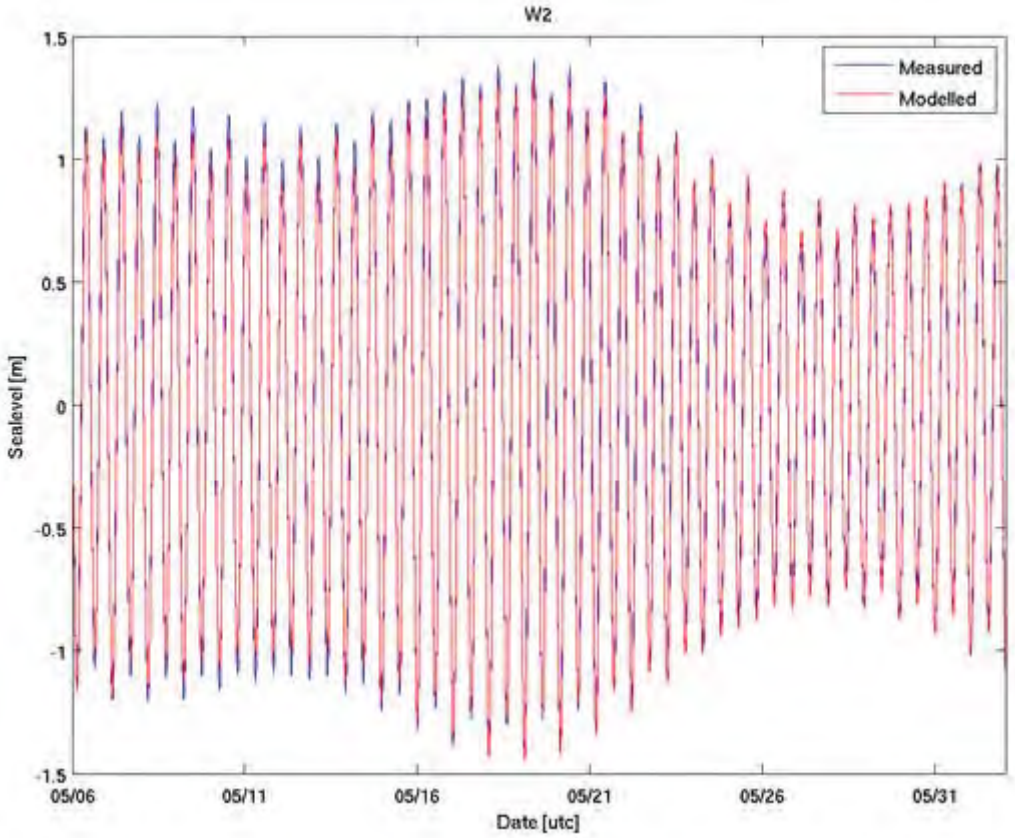

Figure 7.7 Measured and modelled water level comparisons at site W2.

Figure 7.8 Model and measured velocity comparisons for the M2 tidal constituent, within Zone A (Figure 7.3).

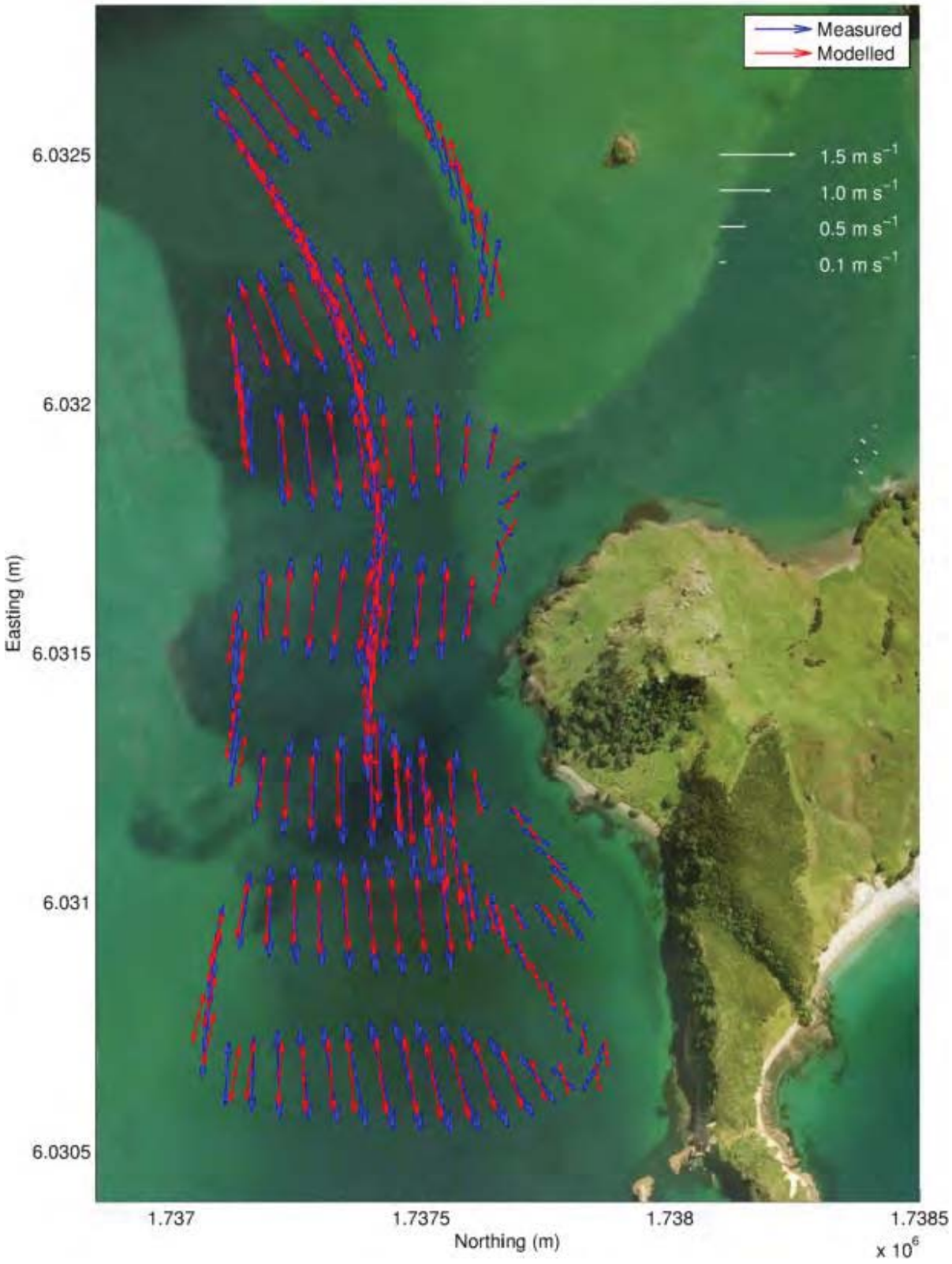

Figure 7.9 Model and measured velocity comparisons for the M2 tidal constituent, within Zone B (Figure 7.3).

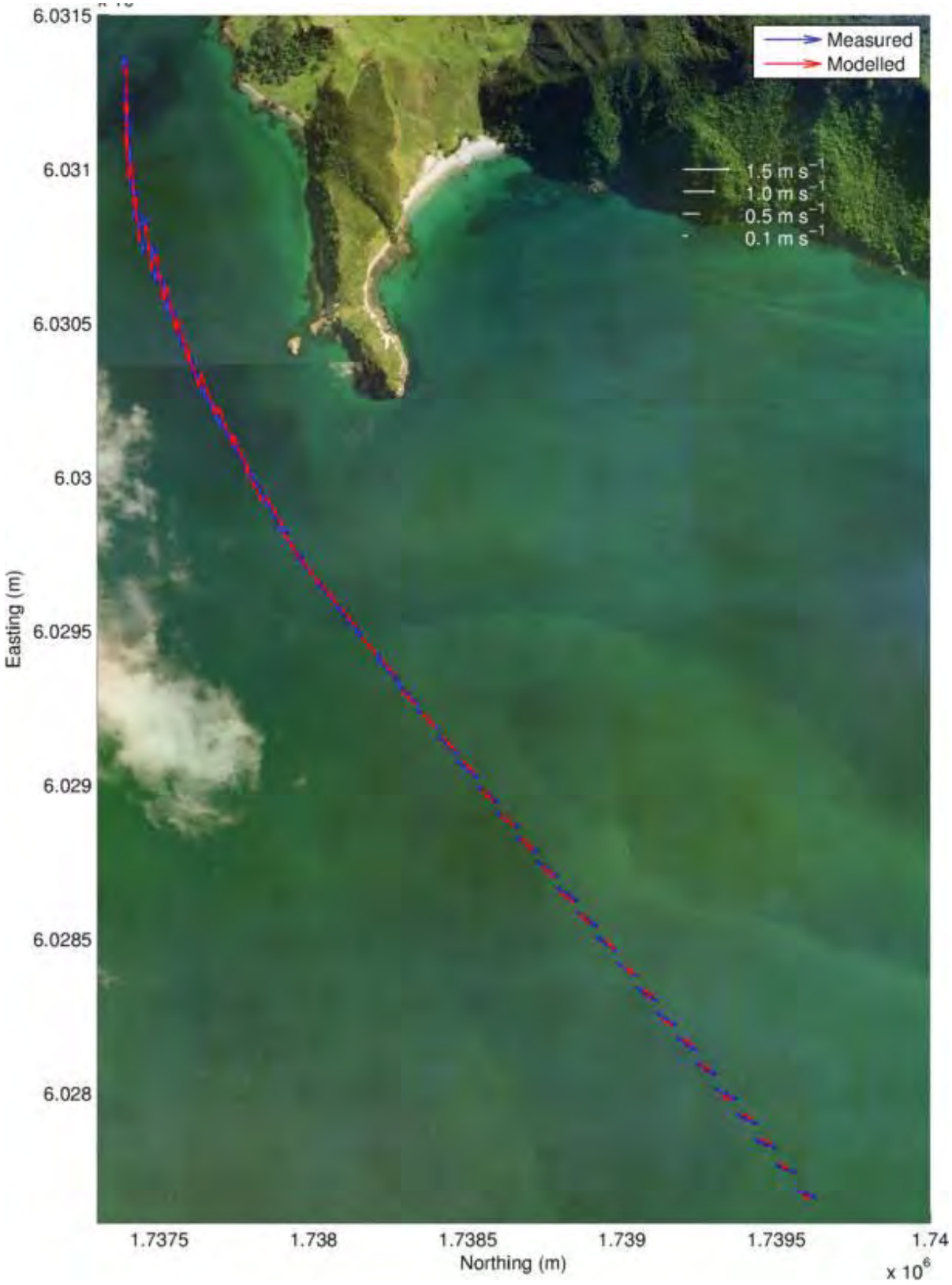

Figure 7.10 Model and measured velocity comparisons for the M2 tidal constituent, within Zone C (Figure 7.3).

8. SEDIMENT DYNAMICS

The process-based numerical model, Delft3D, was implemented here to simulate the morphodynamics driven by the relevant hydrodynamic and wave components at Whangarei Harbour entrance. This section provides an overview of the model as well as the different approaches and settings used to undertake the sediment transport modelling in this complex region. A description of the validation process applied to qualitatively assess the model performances is also presented.

8.1. Modelling system

The modelling system Delft3D (Lesser et al., 2004) was used to set up and run high-resolution process-based morphodynamic models. The software is based on interlinking three separate components that together simulate flow, waves and sediment transport. The three components are fully coupled to simulate morphodynamic feedbacks. An overview of the main parameters and components is given in this section.

8.1.1. Delft3D-WAVE

The third-generation SWAN model (Simulating WAves Nearshore) was used as the wave module (Booij et al., 1999; Ris et al., 1999). SWAN computes the evolution of random, short-crested waves in coastal regions with deep, intermediate and shallow water depths. The SWAN model accounts for (refractive) propagation due to depth and current and can represent the processes of wave generation by wind, dissipation due to white-capping, bottom friction and depth-induced wave breaking, and non-linear wave-wave interactions explicitly with state-of-the-art formulations (Delft3D-WAVE User Manual).

For the present work, the local wave model boundary conditions were nested 2D spectral boundaries obtained from a regional scale grid forced either by representative wave events (i.e. accelerated morphological simulations) or real hindcast conditions (i.e. real-time simulations). The nesting allows the retention of spatial variability in the incident wave field due to large scale regional refraction and sheltering effects. Bottom friction was modelled using the formulation of Collins (1972) and the default coefficient value was 0.016. Dissipation by friction and wave breaking was applied in the model. The formulation of Van der Westhuysen (2007) was used to reproduce the wave dissipation due to whitecapping.

Real hindcast conditions available at intervals of 60 min were applied as offshore boundary conditions. This coincides with the interval of the sequential two-way coupling between SWAN and the hydrodynamic module (Delft3D – FLOW) that allows the exchange of relevant parameters on curvilinear model grids via a communication file. Wave parameters and the forcing terms associated with the wave radiation stresses computed by SWAN were read by the FLOW module to model the hydrodynamic conditions. At the end of each assigned 60 minute runtime, bottom elevation, water level and current fields were used as input to the computation in SWAN. The model loops through these sequential module applications until the end of the complete simulation. Morphodynamic modelling is thus performed through the implementation of a fully coupled wave – hydrodynamic system based on wave and current interactions.

In the scientific community, there is an ongoing debate about the vertical distribution of wave-induced radiation stresses that generally split up into a surface component, a bottom component and a body force and their implementation within

3-D momentum equations (Ardhuin and Roland, 2013; Ardhuin et al., 2008; Bennis et al., 2011). The debate indicates that important wave-induced processes interacting with the flow circulation may still be inadequately implemented in Delft3D. These limitations are accepted in the present study considering that they do not significantly impact the sedimentology and morphology in the area of interest.

8.1.2. Delft3D-FLOW

The basis hydrodynamics were computed in the Delft3D – FLOW module, which can be used in a full 3D or 2DH (depth averaged) mode. The hydrodynamic module Delft3D-FLOW solves the Navier-Stokes equations for an uncompressible fluid under the shallow water and Boussinesq assumptions. The system solves the horizontal equations of motion, the continuity equation, the transport equations for conservative constituents, and a turbulence closure scheme. The details of equations and associated sub-models are fully described in Lesser (2004) and in Deltares (2010).

In a tidal inlet environment, the 3D mode is more appropriate than the 2DH mode as the cross-shore velocity profile in neashore areas where breaking waves cause return flow can exhibit a strong vertical shear (Ranasinghe et al., 1999), which can significantly affect bed dynamics of deltas. A calibration process based on a comparison between 2D and 3D modes of Delft3D highlighted important wave effects in the 3D simulation, as wave-induced mass flux adjusted for the vertical non-uniform Stokes drift, additional turbulence and vertical mixing processes and streaming as an additional wave-induced shear stress in the wave boundary layer (Walstra et al., 2001). The model consisted of 10 *sigma* layers in the vertical direction focused on the surface and on the bottom levels of the water column to better reproduce wave – current interactions and sediment transport processes. Model domains implemented in the present study are presented in Section 8.2.

Bed shear stresses were computed using a quadratic friction law. The non-linear enhancement of the bed shear stress in the presence of waves was taken into account by means of the wave-current interaction model of Fredsøe (1984). Turbulence effects were modelled using constant background horizontal and vertical eddy viscosity and eddy diffusivity coefficients. Horizontal background eddy viscosity was set 1 $m^2 s^{-1}$ while diffusivity was equal to 1 $m^2 s^{-1}$. A value of 10e-6 was used for the vertical background viscosity and diffusivity. The bottom roughness distribution used in this study was based on Manning formulation (depth dependency) with a coefficient of 0.02, which is commonly used in Delft3D (Deltares, 2010).

Current and water elevation conditions at open boundaries were prescribed based on tidal constituents generated from a high resolution tidal model (see Section 7). Hydrodynamic conditions were provided at intervals of 15 min to the Delft3D – FLOW module. The set value for the numerical time step was 3 seconds based on a stability criterion defined for a Courant Number lower than 10 in Delft3D-FLOW (Deltares, 2010).

8.1.3. Delft3D-MOR

The module Delft3D-MOR combines the information provided by the flow and wave modules to compute the sediment transport fluxes at each computational time step. The seabed level can then be updated as a result of the sediment sink and sources terms and computed transport gradients.

Data on bed composition and sediment properties are essential to adequately predict morphodynamics in nearshore regions, particularly in tidal inlet environments where the seabed composition is usually divided into several fractions of sediments from silty cohesive material to non-cohesive fine gravel.

In the present study, based on the sediment sampling (Tonkin and Taylor, 2016), model simulations were restricted to non-cohesive sand fractions with a grain size of 200 μm for the potential sediment fluxes approach, and from 100 to 10000 μm for the sediment transport pathways approach. For such an approach, a set of four layers was implemented, including the active layer and the base well mixed layer. Details on the methodology used to generate the bed composition with a multi-layer seabed scheme are discussed in Section 8.3.2.

Note that the biomass of pipi over Mair Bank has been mimicked adding a fraction (80%) of coarse gravel in the uppermost layer of the bed layer model, the so-called active layer. Although this approach is still very simplistic, it allows us to reduce the potential rates of transport maintaining the overall stability of Mair Bank as has been observed in Morgan et al. (2011). The “erodibility” of Mair Bank decreases purportedly because the pipi population causes an increase in the shear stress resistance as described in (Black, 1983).

For non-cohesive sediments, the total sediment transport is defined as the sum of the suspended load and bedload transport (Van Rijn et al., 2004). The sediment transport predictor TRANSPOR 2004 of Van Rijn (2004) was used in the present study rather than the default one (Van Rijn et al., 1993) due to the recalibration against new data and the extension of the model to incorporate the wave zone. The approach first computed the magnitude and direction of the bed-load sand transport used by Van Rijn. The computed sediment transport vectors were then relocated from water level points to velocity points using an upwind computational scheme to ensure numerical stability.

The slope of the banks and of the channel is an important factor to consider in a tidal inlet environment. The non-cohesive bedload transport in the model is affected in the longitudinal and transverse direction by bedslope effect definitions, particularly in tidal inlet environments. These definitions represent a gradient in the initial direction of sediment transport. The longitudinal transport was defined according to Bagnold (1966) by default and Van Rijn (1993) was used for the transverse direction. Bedslope effects can be modified by factors AlfaBs and AlfaBn in the longitudinal and transverse directions, respectively. While it has been shown that the longitudinal bed slope factor AlfaBs was not of high importance, in the calibration of the model a too high transverse bedslope factor induced an unrealistic incision of the main tidal channel (Van der Wegen and Roelvink, 2008; Dastgheib, 2012; Dissanayake et al., 2012). Indeed, the default value (AlfaBn 1.5) defined in Delft3D commonly leads to unrealistic channel slope with gradients larger than the angle of repose. However, calibration processes showed that decreasing the default values as suggested in Dissanayake (2012) led to significant erosion of the edges of the channel, as a result infilling the channel, particularly to the east and northeast of Mair Bank. In reality, long-term bathymetry surveys between 2000 and 2015 have demonstrated that the channel is morphologically stable (Section 3). The steep channel slope suggests some degree of cohesiveness and armouring induced by hundreds of years of morphodynamics which cannot be fully reproduced by the model. Consequently, the channel stability was modelled within Delft3D - MOR using the non-restrictive upper range of values for the longitudinal and transverse bed slope factors (1.0 AlfaBs and 1.5 AlfaBn).

The erosion of dry cells in Delft3D was controlled by the drycell erosion factor (DCE, thetSd keyword in Delft3D) to simulate bank erosion. The DCE default value was set to zero in Delft3D. However, calibration processes showed that as suggested in Dissanayake (2012) large cell erosion factors produced better representations of the ebb-delta than did low values. Unrealistic seaward extensions of the delta in long term simulations were observed, which is contrary to the evolution of Mair Bank described in Morgan et al. (2011) and Williams and Hume (2014).The use of larger values, 0.5 (50% of erosion in neighbouring dry cell) as defined in the present study, is predicted to improve the model's capability to reproduce the channel morphological variability.

In Delft3D, a commonly used approach for the bed composition modelling is based on 2DH computations as a well-mixed single layer including one or several grain sizes of sediments However, another approach described in Dastgheib (2012) incorporates the concept of layered bed stratigraphy. The bathymetry is subdivided into cells with a specific thickness and a specific fraction of different sediment grain size. The uppermost sediment layer corresponding to the transport layer (or active layer) imports sediments when sedimentation happens and export sediments when erosion happens. In case of deposition, sediment is imported to the transport layer by settling from the water column where it is mixed and redistributed to the underlayer, thereby maintaining its defined constant thickness. In case of erosion, the transport layer imports sediment from the underlayer directly beneath it to replenish and thereby retains its defined constant thickness. The underlayer is indirectly eroded. Conceptually, a layered bed stratigraphy permits specifications of bed composition and sediment characteristics corresponding to the hydrodynamic conditions and the bathymetry.

Both approaches described above have been used in the present study to simulate the potential sediment fluxes and the evolution of the sea bed. Configurations of the underlayers and sediment grain size distribution are described in Section 8.1.2.

More information on numerical aspects can be found in the Delft3D user manual.

8.2. Model domains

The Delft3D - FLOW model grid covers the northern region of Bream Bay from the Ruakaka river mouth to Bream Head, and Whangarei Harbour entrance from Mair Bank to One Tree Point, with grid resolutions of approximately 12 m over Mair Bank and within the inlet channel, and 150 m close to Ruakaka and Bream Head (Figure 8.1). Note that the model domain embeds the entire channel including the offshore section to capture the jet flow extension during ebb tide.

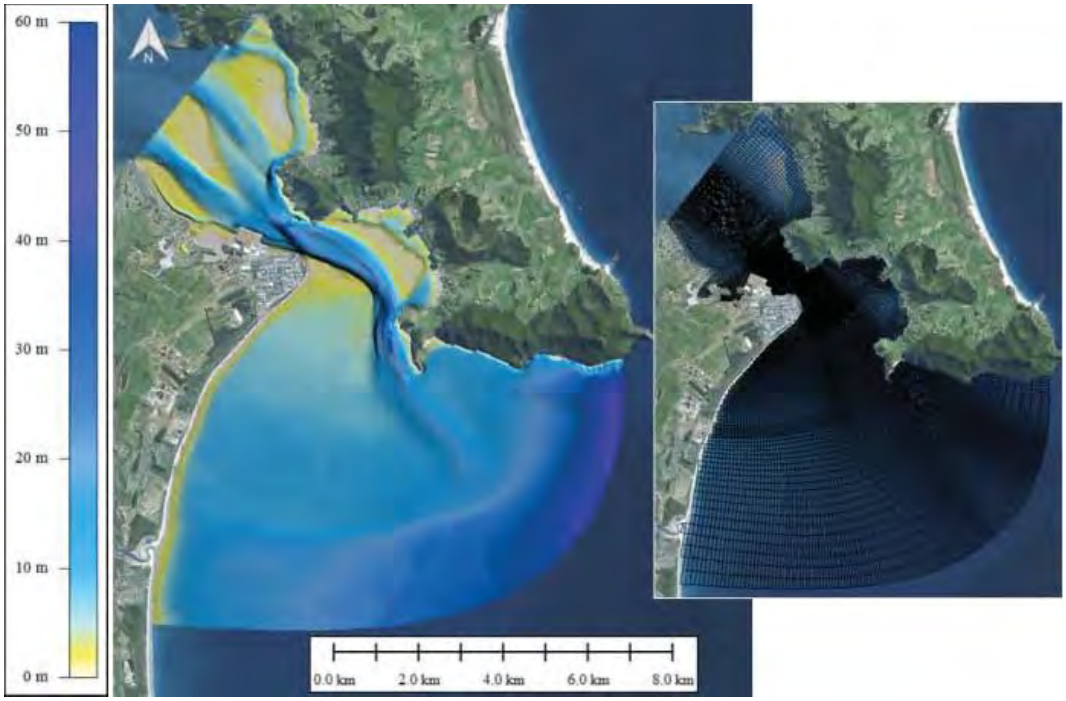

Figure 8.1 Delft3D – FLOW model grid (right) and depths (left). The bathymetry interpolated on the Delft3D - FLOW grid is defined by patch colours following a positive downward convention.

A one-way online nesting technique was used for the wave modelling based on the implementation of multiple model grids with different grid resolutions. The nesting allows the retention of spatial variability in the incident wave field due to large scale regional refraction and sheltering effects.

The coarse grid defined within Delft3D – WAVE covers the northern region of Hauraki Gulf, including Mokohinau Islands and Great Barrier Island, with resolutions ranging from 500 m to 3 km (see Figure 8.2). Boundary conditions were nested offline within a coarser regional SWAN domain described in Section 5.

The fine grid used in the wave model is almost the same as defined in Delft3D – FLOW and described previously. Note, however, that a small offshore extension was added to prevent the hydrodynamic model from discontinuities along the seaward boundary.

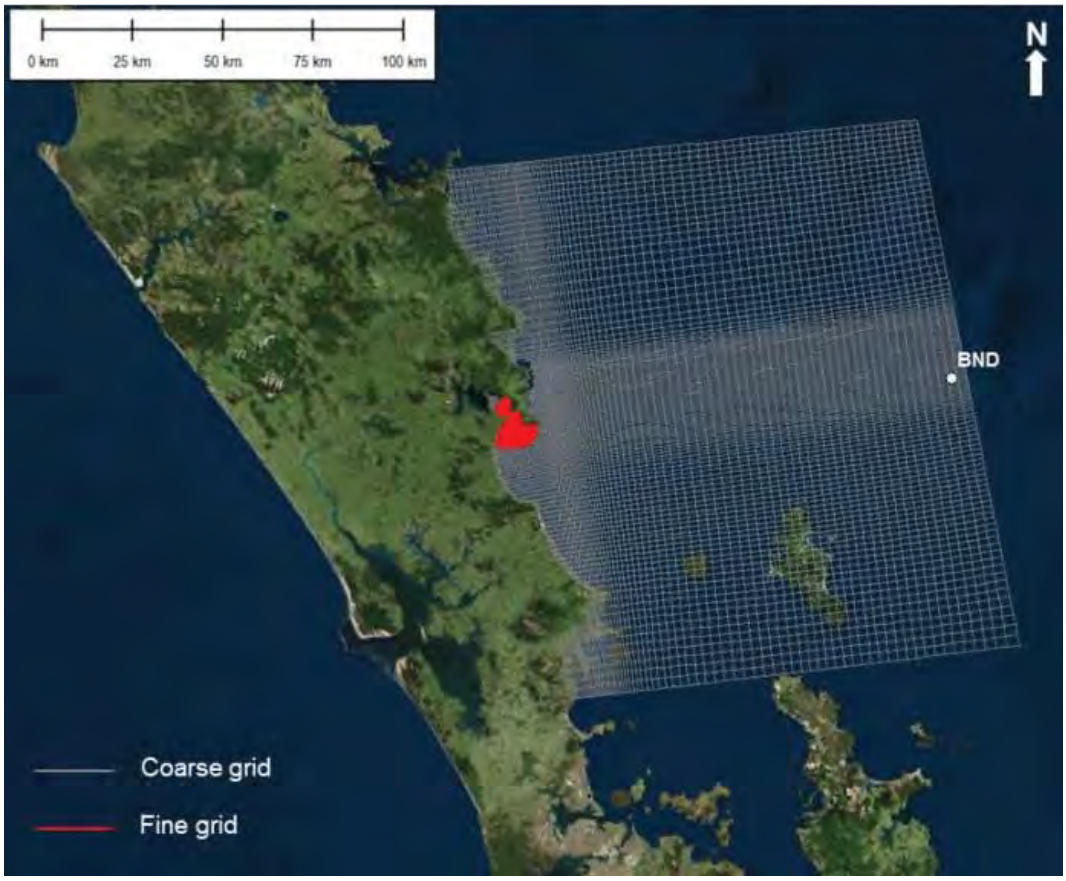

Figure 8.2 Delft3D – WAVE model grids for the modelling of the wave spectral transformation from the offshore region to the coast. The bathymetry interpolated on the Delft3D - WAVE grids is defined by patch colours following a positive downward convention. The BND position indicates the site used to extract the wave climate shown in Section 8.3.1.

8.3. Modelling approaches

The main challenge with applying process-based models to predict morphological evolution is that the morphological behaviour of coastal systems generally develops over time scales several orders of magnitude larger than the time scale of the hydrodynamic fluctuations driving the sediment transport (i.e. hours to days versus years to decades and more).

This means that while a model system is able to predict the time series of instantaneous hydrodynamics and sediment transport it will require an unfeasibly long period of time to compute a multi-year real time simulation. Instead, several strategies are commonly used to understand and reproduce morphological dynamics.

The approach employed here combines the reduction of the input forcing (waves and tides) with the use of realistic simulations for both fair-weather and storm conditions. Input reduction essentially means selecting a limited number of representative forcing conditions (i.e. waves and tides) that will reproduce the medium-term residual sediment transport patterns and associated morphological evolution (De Vriend et al., 1993).

The application of these techniques to the present study is explained in the following sections.

8.3.1. Hydrodynamic and wave forcing

a) Discrete wave scenarios

- Tidal input reduction

Astronomical tides are deterministic and can therefore be accurately predicted for any period of time. However tidal oscillations exhibit significant long-term modulations (e.g. spring/neap, yearly and nodal cycles), which make chronological simulations of such cycles computationally demanding.

The basis for tidal input reduction is to find a representative tide that most closely reproduce the net and gross sediment transport as the naturally varying tides over the region of interest and for the time period considered, here one year. In the present study, the representative tide was determined following the approach of Latteux (1995), which is commonly applied (e.g. Brown and Davies, 2009; Dastgheib et al., 2012; Grunnet et al., 2004).

Tidal signals at a reference point located at the harbour entrance were generated from a high resolution tidal constituents grid, and time series of sediment transport were estimated using a simple power law Q=A.u b (Q is the transport flux, A is a constant factor, u is current velocity, b=5 following Engelund and Hansen (1967)). The single tide best reproducing the net and gross transport magnitude was identified and used in the representative scenarios (Figure 8.3).

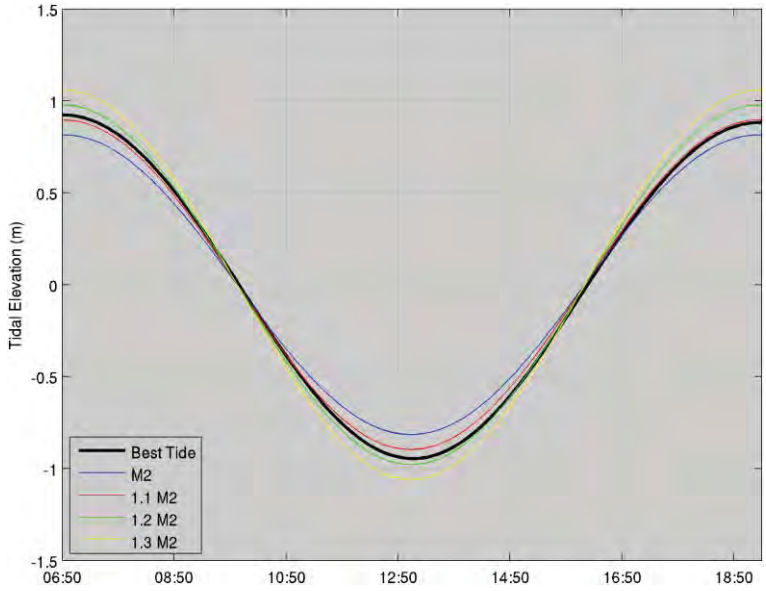

Figure 8.3 Comparison of the best tide, pure M2 tide, 1.1 M2, 1.2 M2 and 1.3 M2 tide curves at the harbour entrance.

- Wave climate reduction

The objective of wave input reduction is to define a set of offshore wave boundary conditions which reproduce the same residual sediment transport patterns and morphological evolution as the real time forcing over a given time period. The

approach employed here follows the input reduction framework provided in Lesser (2009) and Walstra et al. (2013).

The first step is the selection of a reduction period, which is the length of the real time wave time series that is used to define the representative conditions. This is typically governed by the time scale of the morphological evolution of interest (e.g. monthly, seasonal or annual behaviour). In the present study, the reduction was undertaken based on a 10 year hindcast wave climate obtained from SWAN simulations to define an average annual wave climate (Section 5). The wave condition timeseries was extracted at the middle of the southern boundary of the wave model domain. In a second step, a set of representative wave classes was defined by distributing the discrete wave data points into a finite number of height and direction bins, and computing a representative value for each bin.

The basic method to determine a representative value within a bin is to use a weighted average of the data points by their frequency of occurrence. To account for the non-linear dependence of sediment transport on wave height, an additional weighting was applied for the computation of the representative height. The initial wave data binning is relatively arbitrary and can be equidistant or non-equidistant (i.e. exhibiting varying bin size). In the non-equidistant case, bins can be defined following either (subjective) scientific judgment or more objective approaches. In the current study, the height and direction bins were defined so that the relative “morphological impact of waves” was similar in each bin (Dastgheib, 2012; Lesser, 2009). The morphological impact of waves of a given wave class was estimated according to the “potential sediment transport” indicator used in Dastgheib (2012).

To automate the determination of bin limits, this indicator was initially computed for a joint probability of wave height and direction with very fine equidistant bins (ΔH=0.1 m, ΔDir=2 deg.). Based on the number of directional and wave height bins to be used for the classification, the directional bin limits were determined first, such that the sum of the morphological impact of waves, Mj, within each bin was (approximately) equal. The same principle was then used within each of these directional bins to define the wave height bin limits. This way, the “morphological impact of waves” was similar in each bin.

The wave climate classification (Figure 8.4 and Figure 8.5) used in the following morphological simulations was defined using four directional bins and four wave height bins. The general classification obtained for the wave climate at the reference site reproduced the different levels of wave energy coming in the northeast and southeast directions.

The wave height delimitations were relatively homogeneous regarding the directionality of the wave propagation:

- 1st class with wave heights of 1 – 2 m.
- 2nd class with wave heights of 2 – 2.8 m.
- 3rd class with wave heights of 2.8 – 3.5 m.
- 4th class with wave heights of 3.5 – 5.4 m.

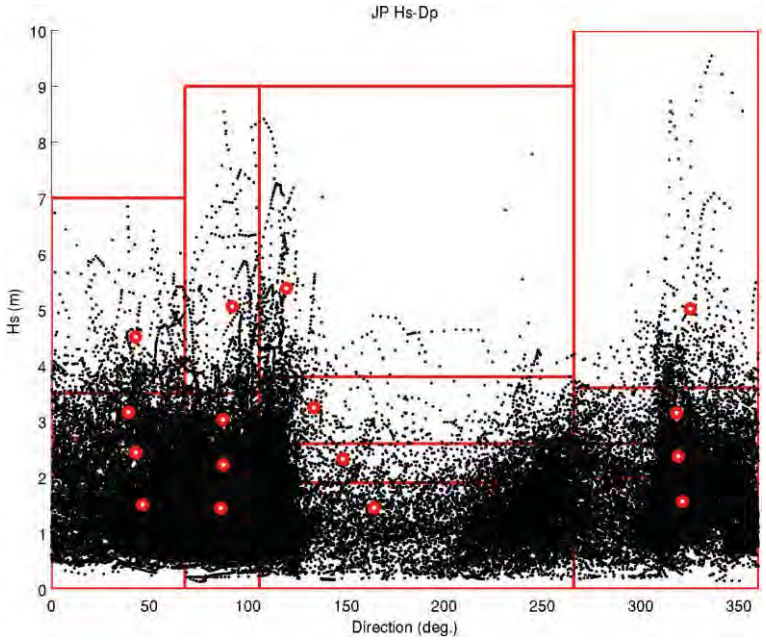

Figure 8.4 Scatter plot of wave heights as a function of wave directions for the 10-year time series, with delimitation of bins (red boxes). Red dots are the representative conditions of each bin.

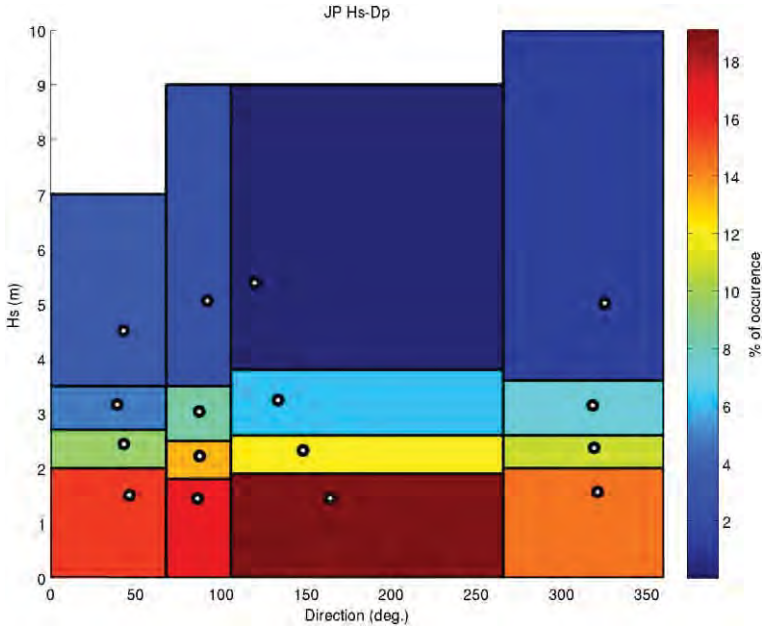

Figure 8.5 Reduced average annual wave climate based on the 10-year wave hindcast using four directional bins and four wave height bins (i.e. 16 wave classes). Colours indicate the probability of occurrence of a given class. The white dots are the representative wave condition of each wave class. Wave classes are summarised in

Table 8.1.

Table 8.1 Wave classification based on an average annual wave climate defined from a 10-year hindcast dataset.

Wave class	Representative Hs (m)	Representative Tp (sec)	Representative Dp (deg.)	Probability of occurrence (%)
1	1.5	8.6	46.4	17%
2	2.4	9.0	43.0	4%
3	3.2	9.7	39.1	2%
4	4.5	10.4	42.9	1%
5	1.5	9.1	86.2	18%
6	2.2	10.1	87.6	6%
7	3.0	10.2	87.3	3%
8	5.1	11.0	92.1	1%
9	1.5	7.5	164.3	19%
10	2.3	8.8	148.3	5%
11	3.2	9.2	133.6	2%
12	5.4	10.6	119.7	1%
13	1.6	7.2	321.1	15%
14	2.4	7.4	319.1	4%
15	3.2	8.3	318.3	3%
16	5.0	10.7	325.3	1%

b) *Tide-only* scenario

A tide only scenario was run with the best representative tide described in Section 8.3.1a to assess the impact of the tidal flows on the sediment transport dynamics. No wave forcing was considered for this simulation.

c) Real-time simulations

The tide-only and discrete wave scenarios were supplemented by real-world simulations for both fair-weather and storm conditions based on time series of significant wave height *Hs*, peak period Tp and peak direction Dp provided by SWAN hindcast (see Section 5).

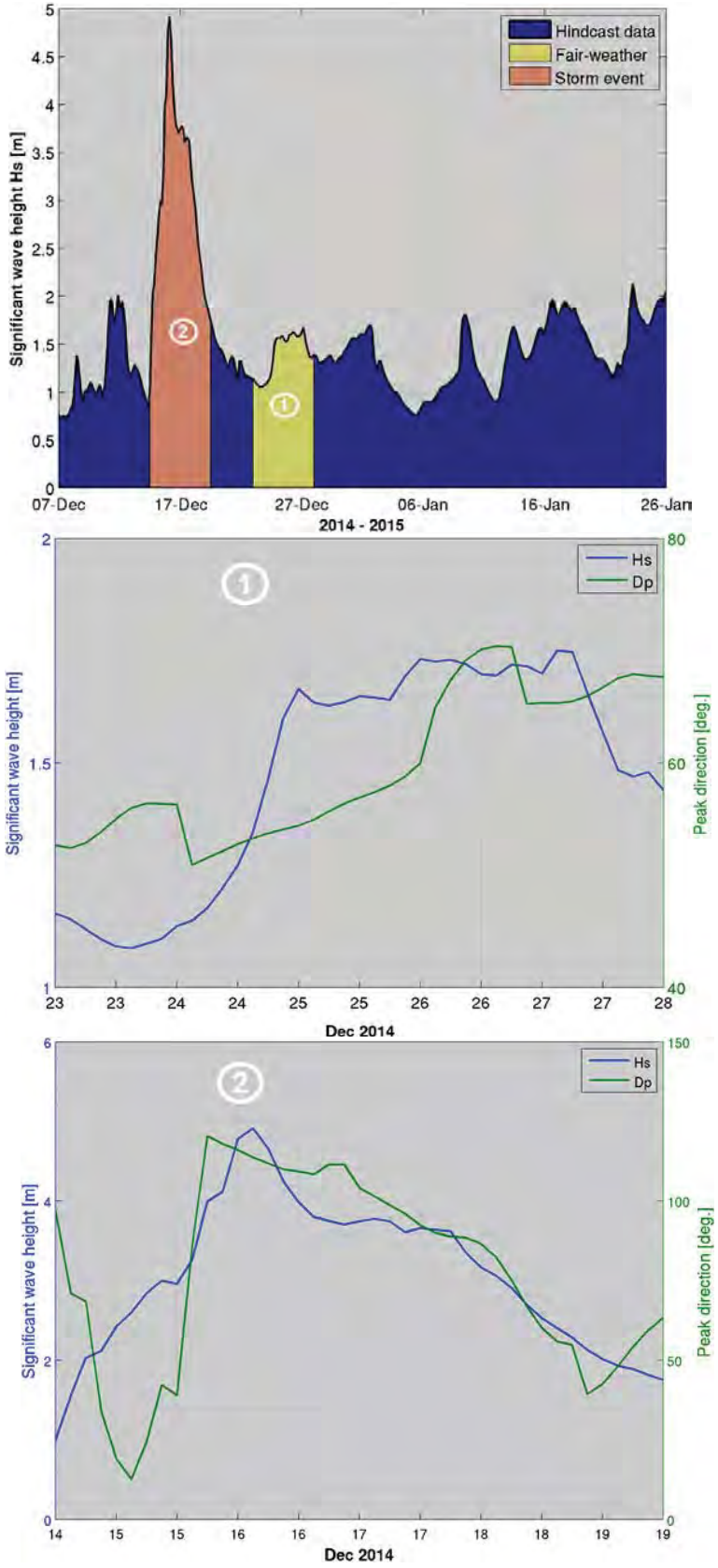

Figure 8.6 Time series of significant wave height and peak direction at location BND (see Figure 8.2) for December 2014 and January 2015. Wave conditions during periods 1) and 2) were used to simulate the sediment transport at Whangarei during fair-weather and storm conditions.

Firstly, a morphological acceleration factor (Section 8.1.3) of 45 was applied during a simulation of four days to predict the bed evolution that occur during approximately six months of fair-weather conditions keeping reasonably fast computations. The aim of this first run was to initialise the sediment grain size distribution over the domain. No bed level update was allowed. More details of the methodology are provided in Section 8.3.2.

In the second phase, the morphodynamic simulation during fair-weather conditions was followed by a 5-day storm simulation without any morphological acceleration (Morfac = 1) to avoid unrealistic changes in the bed evolution over a very short period of time due to high energy wave conditions. The distribution of sediment mass fractions characterised by a 6-month tidally dominated environment was directly fed into the subsequent storm event simulation. Note that the bed level update was turned on to reproduce the residual sediment transport, particularly around Mair Bank.

8.3.2. Initial bed configuration and composition

The adequate initialisation of spatially varying grain size distribution of bottom sediment in a process-based model is often constrained by a lack of appropriate field data for the entire model domain. As the sea bed composition is dependent on the bed shear stress imposed by the local flow and wave environments, using grain-size observations as initial conditions of simulations based on the author's judgement from the limited data available generally lead to unrealistic erosion or accretion patterns. Indeed, Camenen and Larroudé (2003) and Pinto et al. (2006) have shown that the physical parameter responsible for the greatest errors in the sediment characteristics is the spatial heterogeneity of grain size distributions of the surface sediment in the area of interest. In accordance, two complementary approaches were implemented to avoid this problem.

First, the conceptual models, including both the "tide-only" and the discrete wave scenarios, were set-up with a homogenous 200 µm grain size sediment layer and a fixed bathymetry to determine the sediment transport fluxes in the system. No modification of the sea bed during the simulation was allowed. Such a method is particularly helpful for giving an overview of the combined effect of the tidal and wave forcing on the seabed. It was assumed that the critical bed shear stress variability determined by the distribution of the sediment grain sizes would make a difference in the results.

The second method applied in the present study is described in van der Wegen et al. (2011) and based on a bed composition generation (BCG) run or "morphodynamic spin-up". A synthetic simulation was initiated with a uniform sediment type distribution over two bed layers (the active layer and the underlayer) as described in 8.1.3. This is depicted in Figure 8.7. Six sediment fractions (100, 150, 200, 300, 500 and 1000 µm) were available at 16.7 mass per cent each according to the general distribution obtained through the sediment sampling study (Tonkin and Taylor, 2016). The active layer had a thickness of 0.40 m and the underlayer thickness was 10 m. Note that small active layers result in a rapid coarsening of the system which tend to reduce the spin-up for a gain of computational time. Both layers were set-up with the same fractions of sediment grain size. A spatially limited active layer including 80 % of coarse gravel (>10000 µm grain size) and 20% of medium sand was defined to mimic the biomass of pipi over Mair Bank.

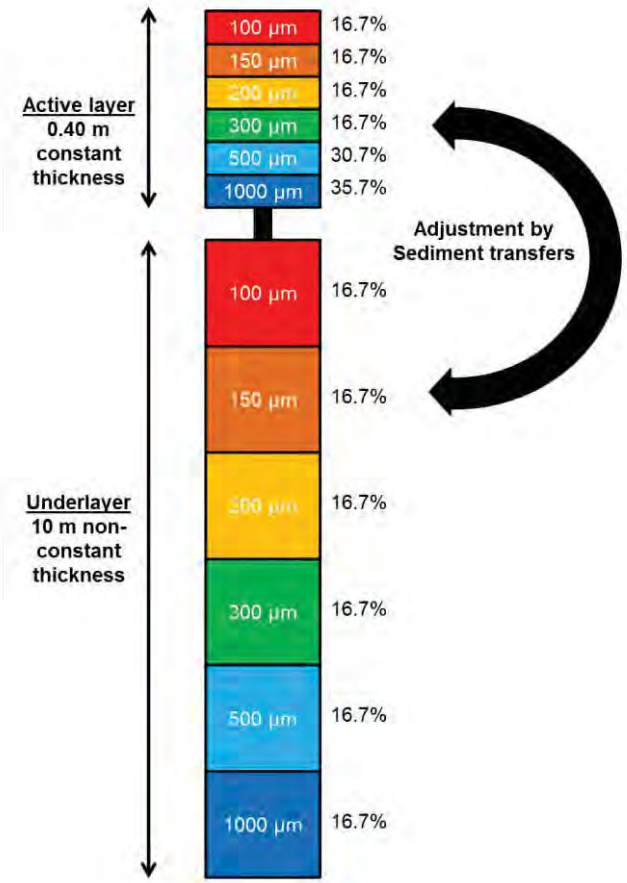

Figure 8.7 Bed stratigraphy approach implemented in Delft3D to initialise the bed composition over the domain.

During the simulation, sediment grain size fractions were redistributed vertically between layers and spatially over the domain in response to the combination of tide-induced currents and low energy wave conditions. At the end of the simulation, the bed composition converged to a more realistic sedimentological setting corresponding to the initial bathymetry, removing errors due to the initial model set-up. The BCG process rendered the model ready to investigate further morphodynamic developments.

8.4. Model validation

The validation of a morphodynamic model by field observations is generally very difficult. The complexity of the morphodynamic evolution in a tidal inlet environment driven by both short-term and long-term processes requires appropriate measured data of bathymetry and sediment distribution, which should ideally be available at different time scales and for relatively large areas.

Thus, the validation stage can be undertaken on a storm-induced bed evolution or on a long-term bed evolution to verify the level of agreement between the model and the measured data. Both methods provide useful information regarding the capability of the model to predict a range of morphodynamic mechanisms which control the overall tidal inlet dynamics. Analysing storm-induced bed evolution provides both calibration and a quantitative validation of the model configuration, while a long-term bed evolution study is useful in that it qualitatively characterises the overall relevance of the model.

In the present work, more than 15 years of annual bathymetric surveys over Mair Bank and within the tidal inlet channel was available (Section 3). Such data is particularly valuable for the validation of the model as it describes the relative stability of the system very well. Note, however, that no validation of a short-term high energy event was possible in the present study as no pre- and post-storm data were available. Moreover, the poor understanding of the interactions between the shell fragment layers, the biomass of *pipi* and the existing environment (both hydrodynamic and morphodynamic) made a strictly quantitative validation of the morphodynamic model difficult. Therefore, efforts were made to qualitatively compare the sandbar migrations around Mair Bank and the sediment grain size distribution obtained from both the BCG run and the sequence of real-world simulations. Available historical bed level data and recent sediment sampling inside the tidal inlet channel (Tonkin and Taylor, 2016; Williams and Hume, 2014) were used for this purpose.

8.5. Results

8.5.1. Conceptual modelling – tide only scenario

Model simulations showing the peak flood and ebb flows are shown in Figure 8.8, and corresponding bed shear stress and net transport flux fields are presented in Figure 8.9 to Figure 8.11. The Whangarei Harbour entrance is characterised by high energy tidal flows strong enough to mobilise fine and medium sand. The eastern edge and the southern areas of Mair Bank are particularly exposed to strong tidal flows during flood tide, with cross-bank velocities up to 1.3 m s^{-1} over very shallow waters. In the channel, tidal flows reach 1.4 m s^{-1} with higher water depths. During ebb tide, the hydrodynamic component adjacent to the eastern edge of Mair Bank is high, albeit to a lesser extent. Notice the medium to high current velocities up to 0.8 m s^{-1} over the northern intertidal area of Mair Bank which results in heterogeneous bed shear stress fields that may favour local erosion and accretion outcomes.

The resulting mean net transport fluxes over one tidal cycle highlights the high potential for the tidal component to mobilise sediments around Mair Bank and within the tidal inlet channel. Note that this potential sediment transport scenario is set-up with grain sizes of 200 µm (fine to medium sand) without any consideration of the biological component (biomass of *pipi*, shell hash, etc.).

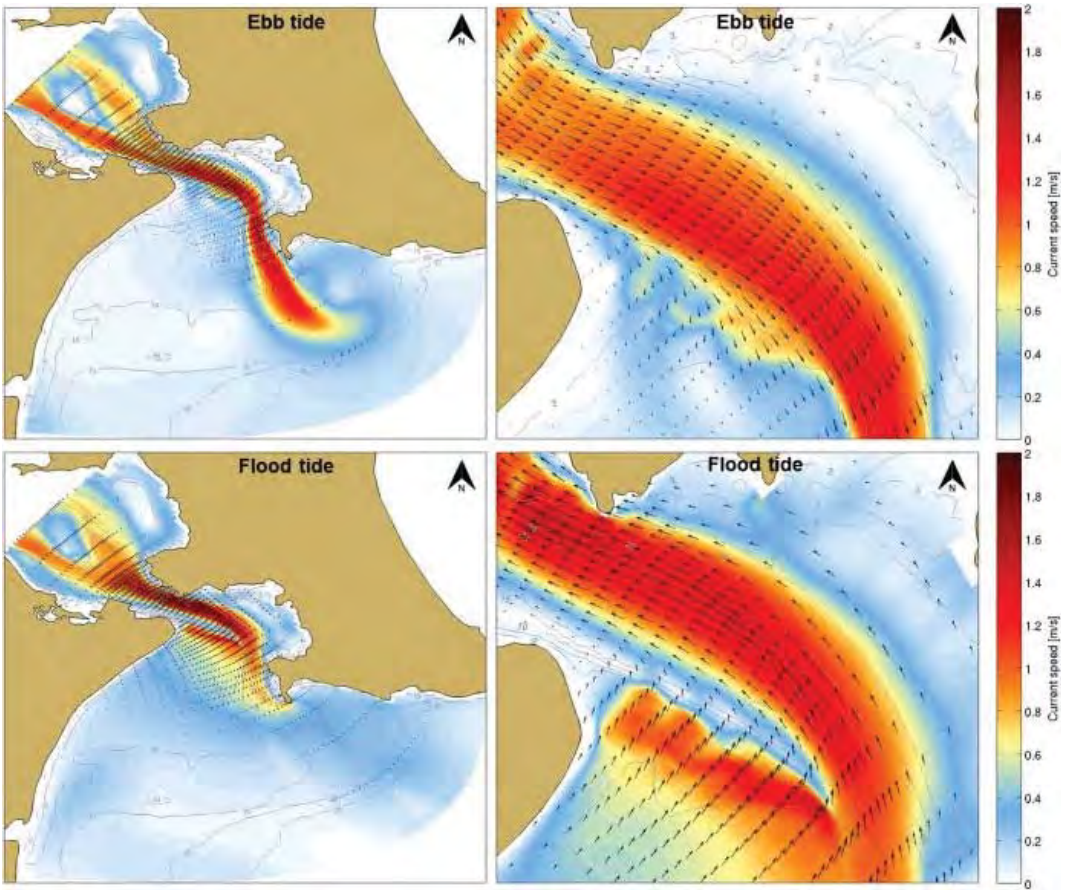

Figure 8.8 Modelled current speed fields over the whole domain (left) and over Mair Bank (right) for the tide-only scenario during ebb (top) and spring (bottom) tides.

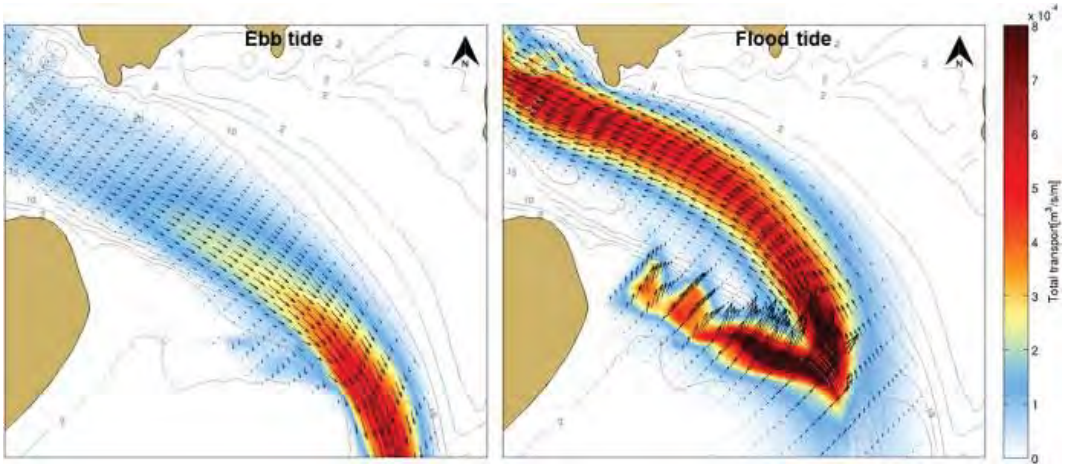

Figure 8.9 Modelled net transport fluxes over Mair Bank for the tide-only scenario during ebb (left) and spring (right) tides.

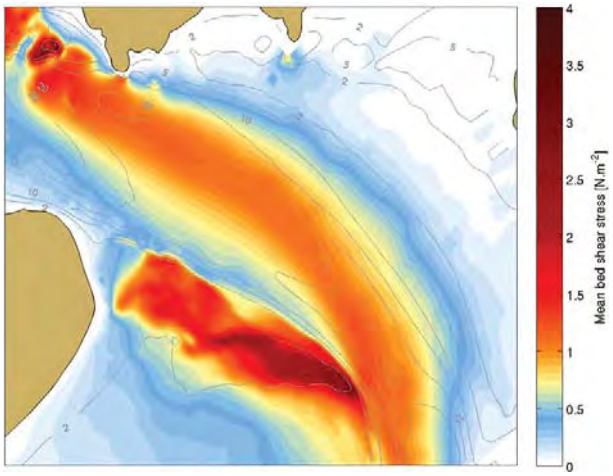

Figure 8.10 Modelled mean bed shear stress calculated over one tidal cycle for the tide-only scenario.

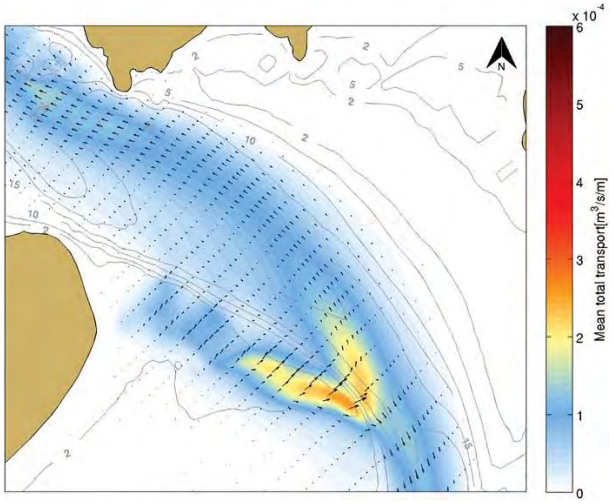

Figure 8.11 Modelled net transport fluxes calculated over one tidal cycle for the tide-only scenario.

8.5.2. Conceptual modelling – discrete wave scenarios

The Whangarei Harbour entrance is a tidally dominated environment. Busby Head reduces the exposure of the channel entrance and Mair Bank to the incident waves coming in the east-southeast quadrant (Figure 8.12) and the shoreline orientation shelters the entrance from northern storm wave events to a large extent (Figure 8.13). In spite of this degree of shelter afforded by the topography, adding wave forcing to the sediment modelling process significantly increases the net transport fluxes over Mair bank and along the edge of the channel (see Figure 8.14 and Figure 8.15). Strong northward residual net transport fluxes are observed over the southern margin of Mair Bank and along Ruakaka Beach. The south-western flank of Mair Bank displayed the strongest and most localised net transport fluxes due to wave refraction. High energy wave events showed a high erosive potential for sandy material over these areas.

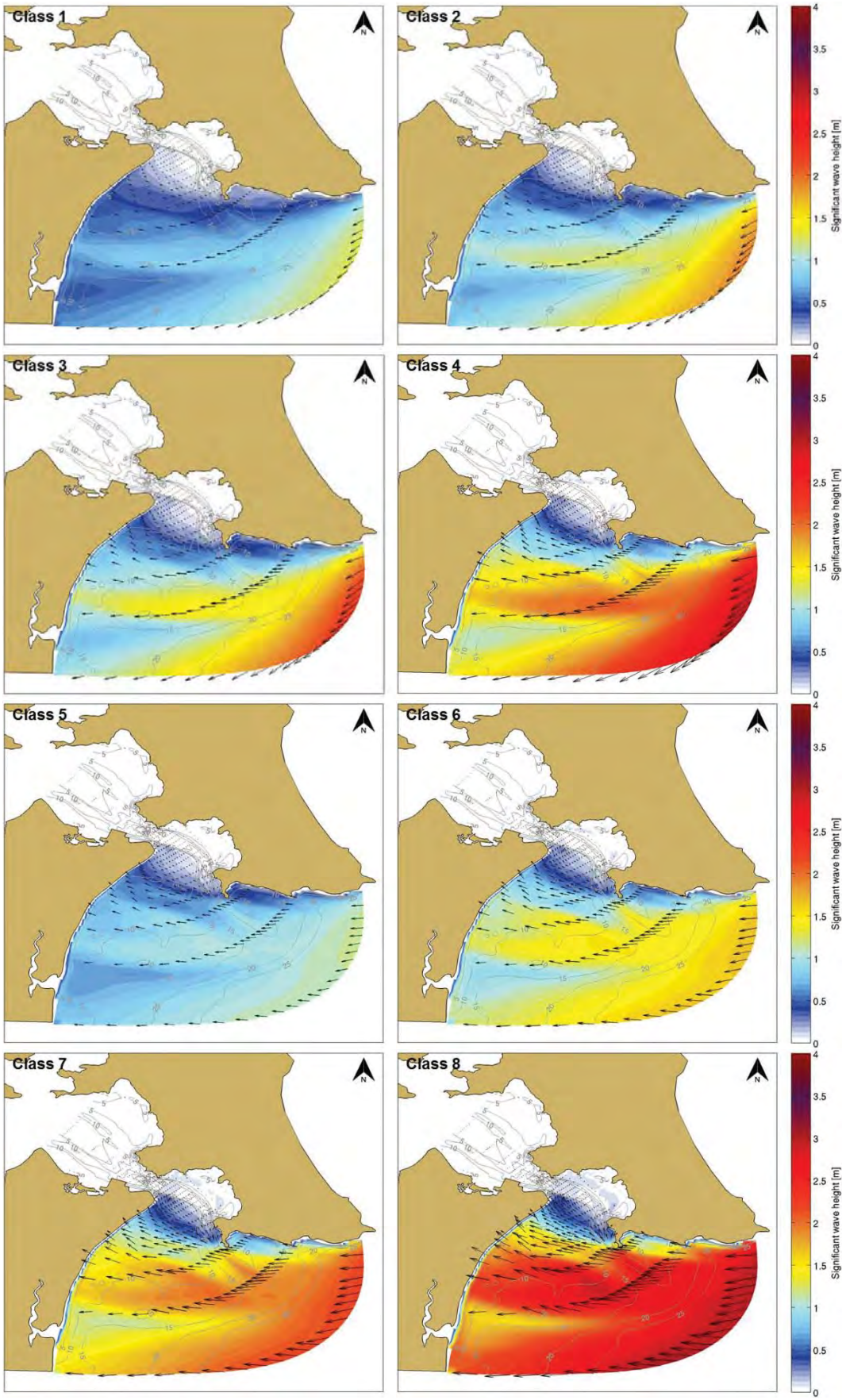

Figure 8.12 Wave height fields for Classes 1 to 8. Black arrows indicate the peak direction.

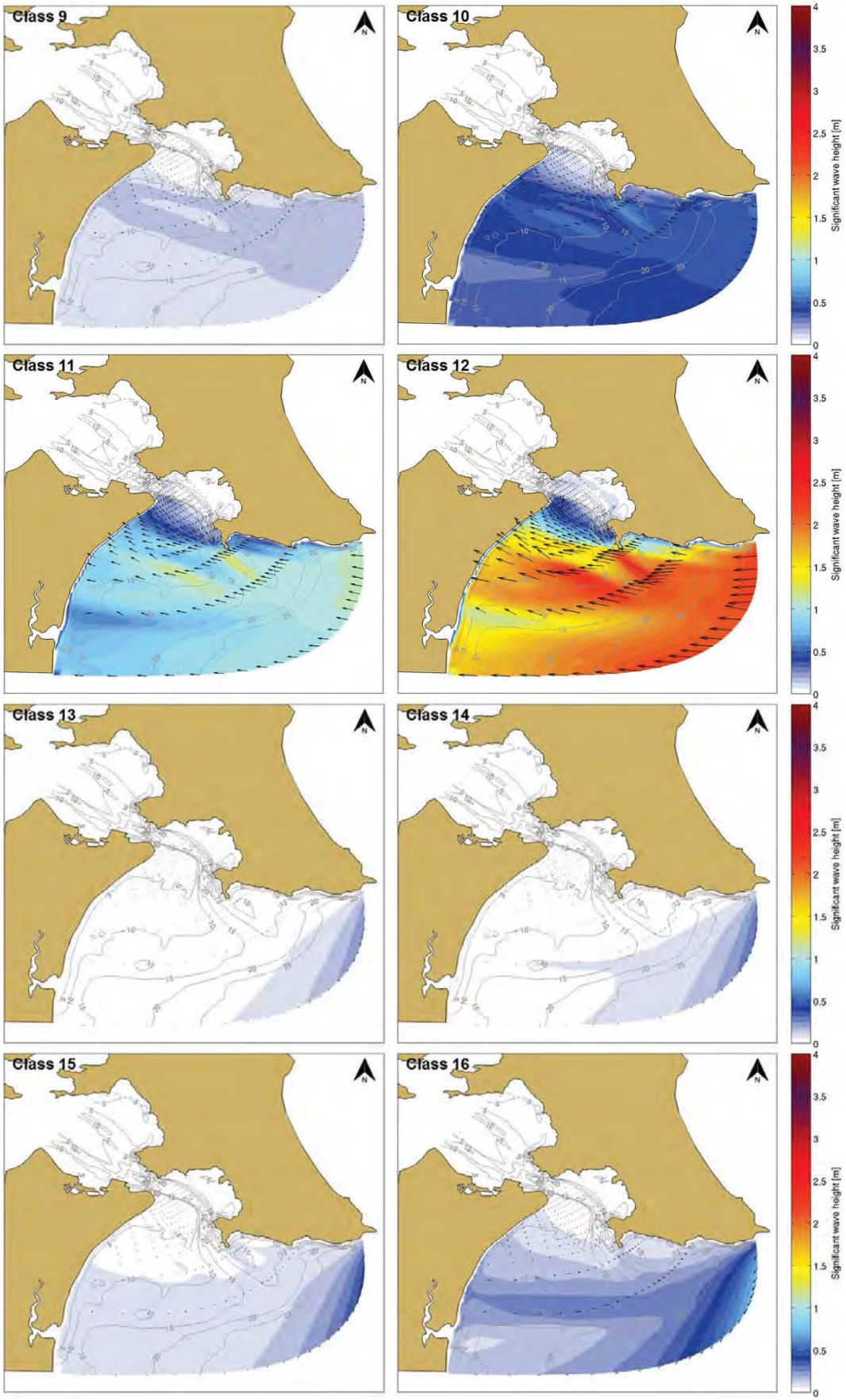

Figure 8.13 Wave height fields for Classes 9 to 16. Black arrows indicate the peak direction.

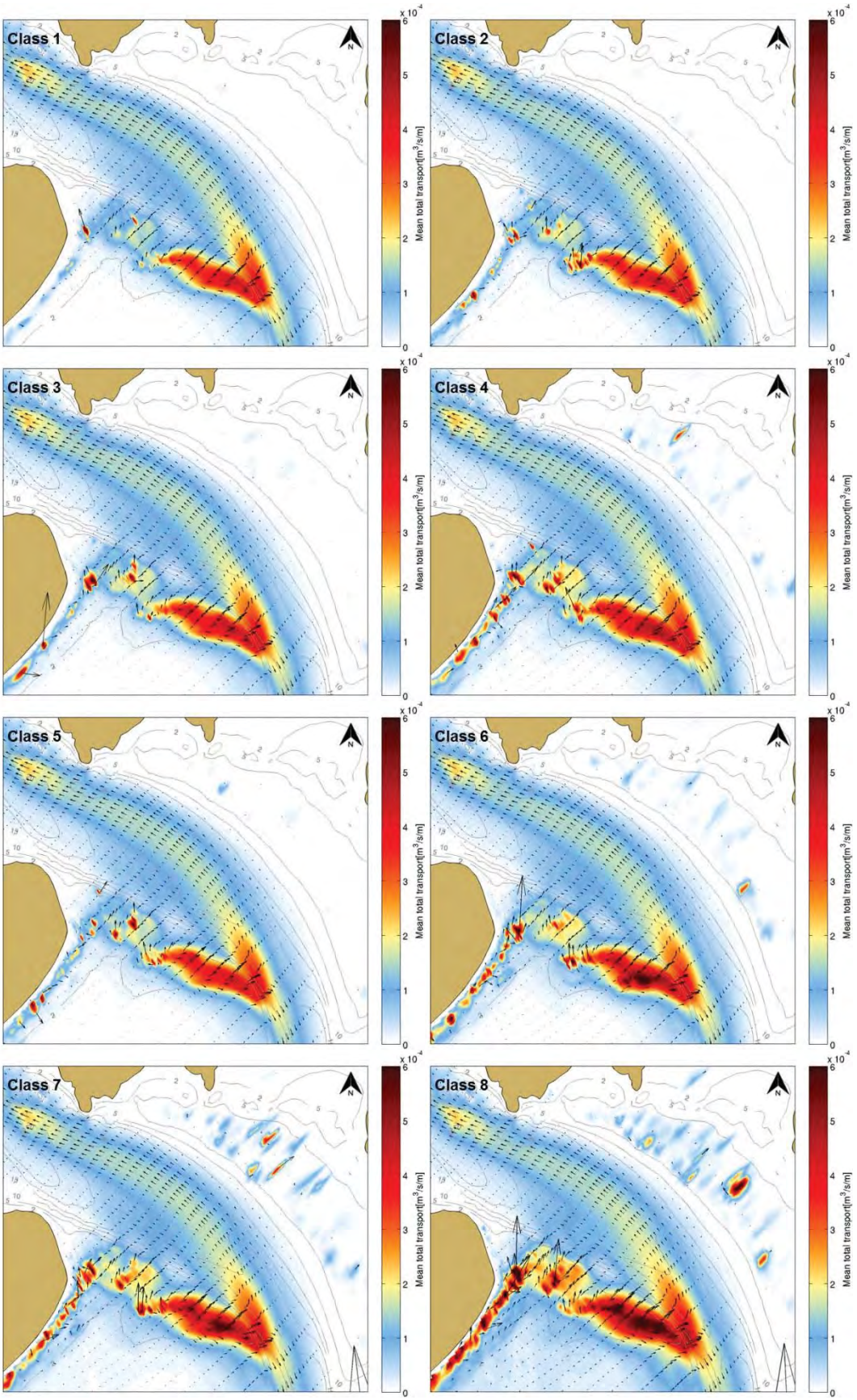

Figure 8.14 Mean net transport fluxes calculated over one tidal cycle for Classes 1 to 8.

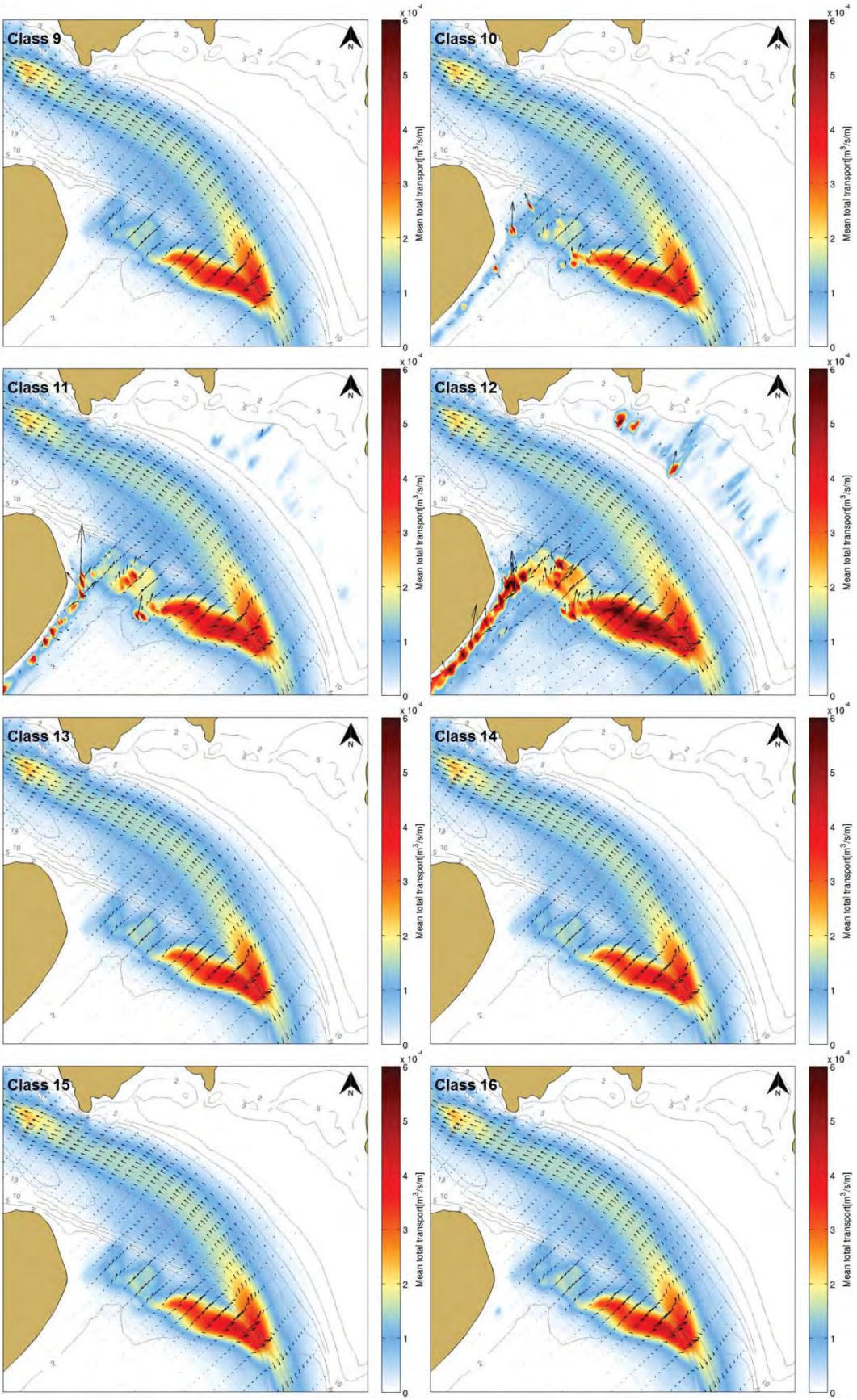

Figure 8.15 Mean net transport fluxes calculated over one tidal cycle for Classes 9 to 16.

8.5.3. Bed composition generation (BCG) run

Sediment distributions for each fraction generated by the BCG run are presented in Figure 8.16 to Figure 8.22.

The sediment distribution shows a significant coarsening of the mean surface sediment grain size within the channel. Most of the sandy material between 100 and 500 μm is washed away from the channel. Fine sand is deposited at the outermost ebb-tidal delta lobe where ebb-directed current velocities decreased due to increasing water depths. This is supported by the sediment sampling results where the fine sand fraction reached 17% in the offshore section of the channel.

The modelled channel bed was composed of medium and coarse sand particles. Field data showed the medium sandy sediment fraction to dominate the channel bed composition (~60%; Tonkin and Taylor, 2016) while modelled sediment distribution suggested a higher fraction of coarse sediments. This is probably related to the low rate of sampling of sediment grain sizes between 500 and 1000 μm in the bed composition initialisation. The presence of 500 μm grain size material in the channel indicates that the overall bed shear stress exerted by tidal flows in the throat is not much higher than the critical bed shear stress corresponding to medium to coarse sediment grain size. Adding fractions of grain size in the range of 500 – 800 μm may limit the overestimation of the coarse sediment fraction within the bed composition of the channel. However, the BCG run was limited to seven sediment fractions because of the computational expenses related to the implementation of the bed stratigraphy module and the 3D mode in the model. Note that the shell fragment layers found in the sediment samples (Tonkin and Taylor, 2016) were not considered in the present study. Shell fragments may shelter the grains lying underneath from the flow and thus reduce the erosion of medium grained sediments. The current understanding of interactions between the biological, morphological and hydrodynamic components in the model do not allow a full reproduction of the frictional forces acting on the surface transport layer. However, the model reproduces the relative stability of the fine sediment layer observed over the southern bottom edge of the channel section located north of Mair Bank well. Measured data indicated the presence of 16% fine sand in the bed composition, which agrees qualitatively with the modelled top layer composition shown in Figure 8.16.

The dredged area adjacent to NorthPort berths was shown by the model to be particularly favourable for the deposition of medium grain size sediments. In the vicinity of the berth, medium and coarse sediment fractions dominated the bed composition in the channels while fine sediments were largely present over the different shoals. The overall modelled sediment pattern was consistent with the configuration described in Longdill and Healy (2007) (Section 2), and shown in Figure 2.4.

The high bed shear stress fields over the intertidal and subtidal areas of Mair Bank, described in Section 8.5.1, leads to rapid redistribution of sediments in this type of simulation. Over subtidal areas, fine sediments entrained by tidal flows are transported offshore and through the harbour. Medium grain size sediments are washed away from the intertidal area deposited offshore. These results are not consistent with the sediment sampling reported in Williams and Hume (2014) which indicated a predominance of fine sand (~50%). Such discrepancies can be expected as the reduction of the bed shear stress provided by the shell hash layer and the biomass of *pipi* on the seabed cannot be reproduced in the present model. The discrepancies clearly show the stability that the biological component provides to Mair Bank. The model showed a substantial amount of fine and medium sand

sediments to be located along the harbour flank of the bank to the northeast controlled by the flood-tidal flows. The southern margin of Mair bank was predicted to show the largest range of sediment grain sizes from 100 to 1000 µm, with a predominance of coarse sand.

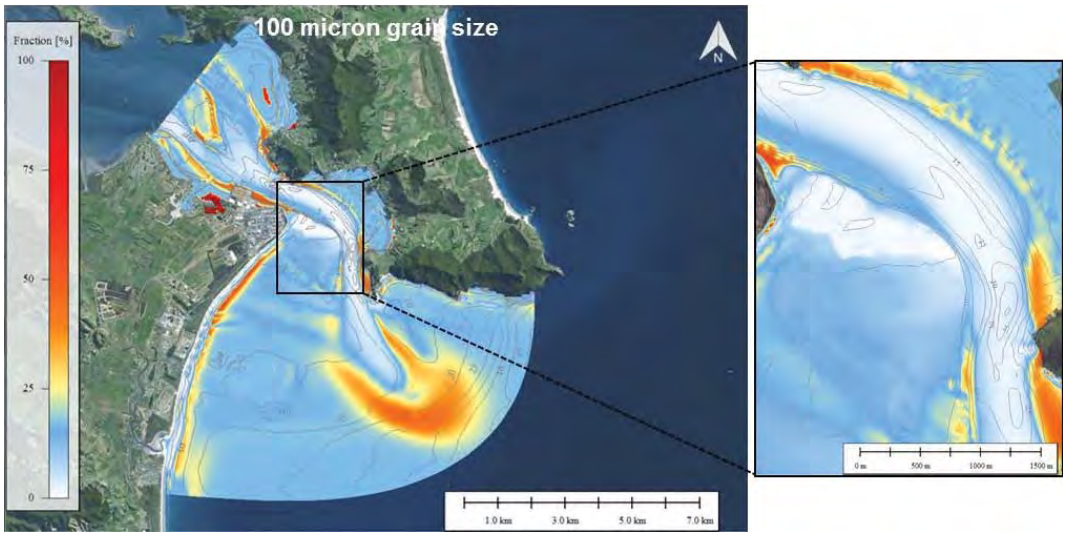

Figure 8.16 Distribution of 100 µm grain size sediments in the active layer generated by the BCG run for a 6-month fair-weather period.

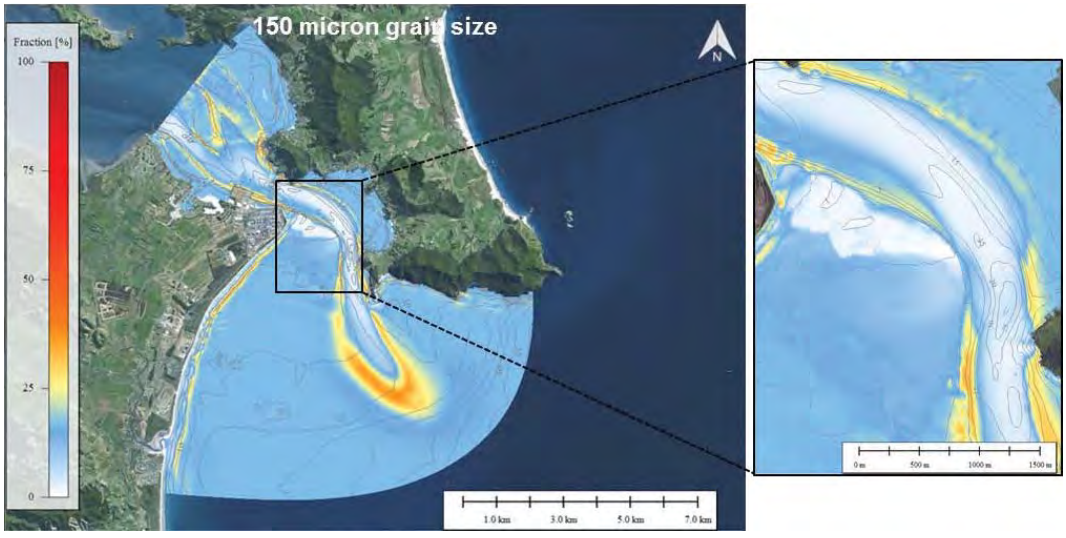

Figure 8.17 Distribution of 150 µm grain size sediments in the active layer generated by the BCG run for a 6-month fair-weather period.

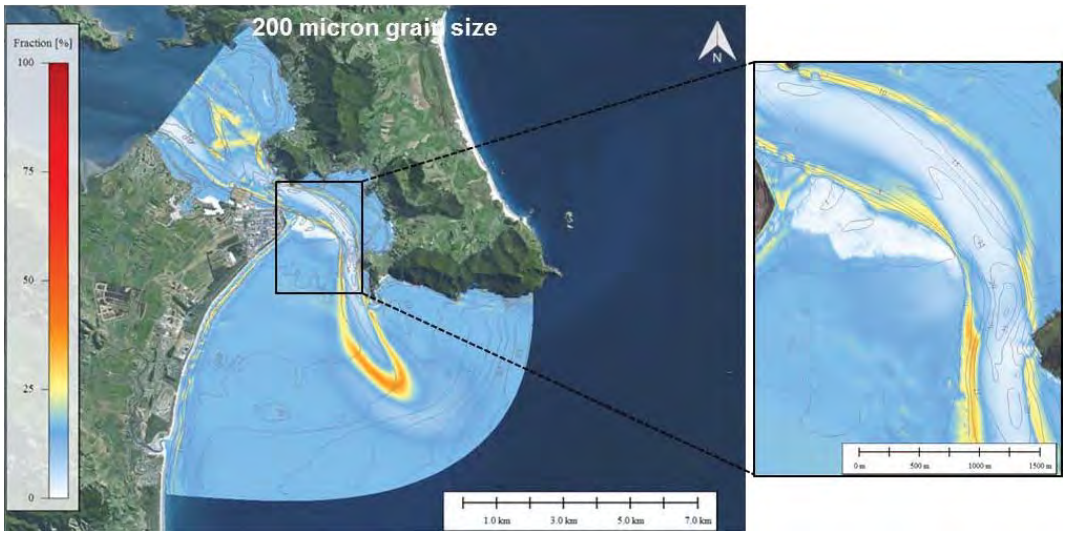

Figure 8.18 Distribution of 200 µm grain size sediments in the active layer generated by the BCG run for a 6-month fair-weather period.

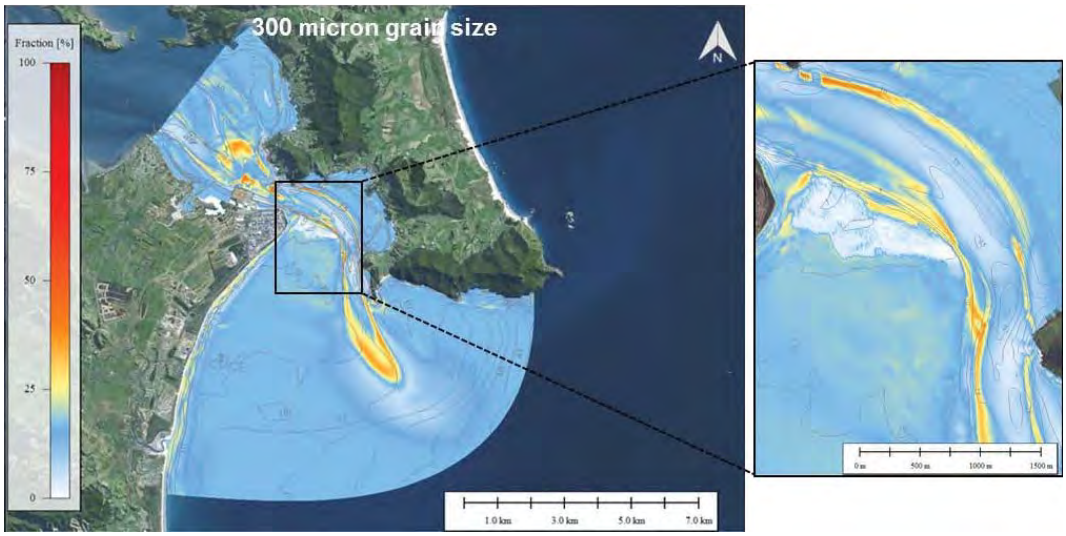

Figure 8.19 Distribution of 300 µm grain size sediments in the active layer generated by the BCG run for a 6-month fair-weather period.

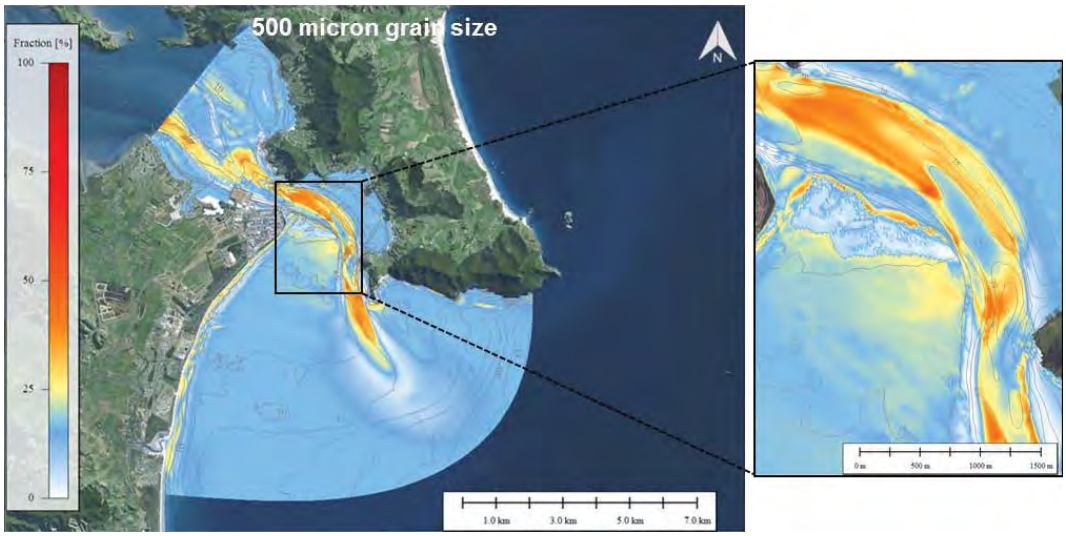

Figure 8.20 Distribution of 500 µm grain size sediments in the active layer generated by the BCG run for a 6-month fair-weather period.

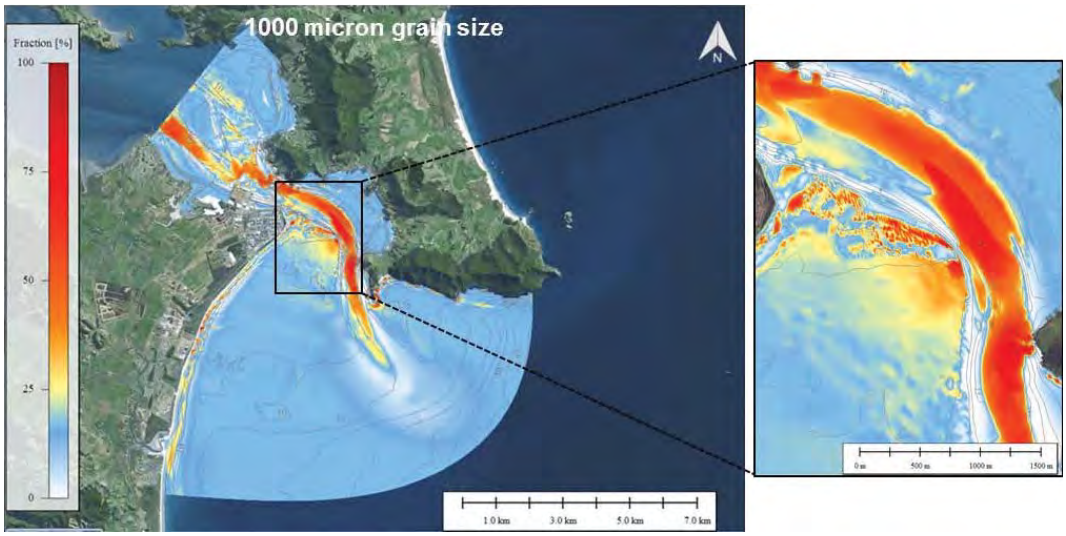

Figure 8.21 Distribution of 1 mm grain size sediments in the active layer generated by the BCG run for a 6-month fair-weather period.

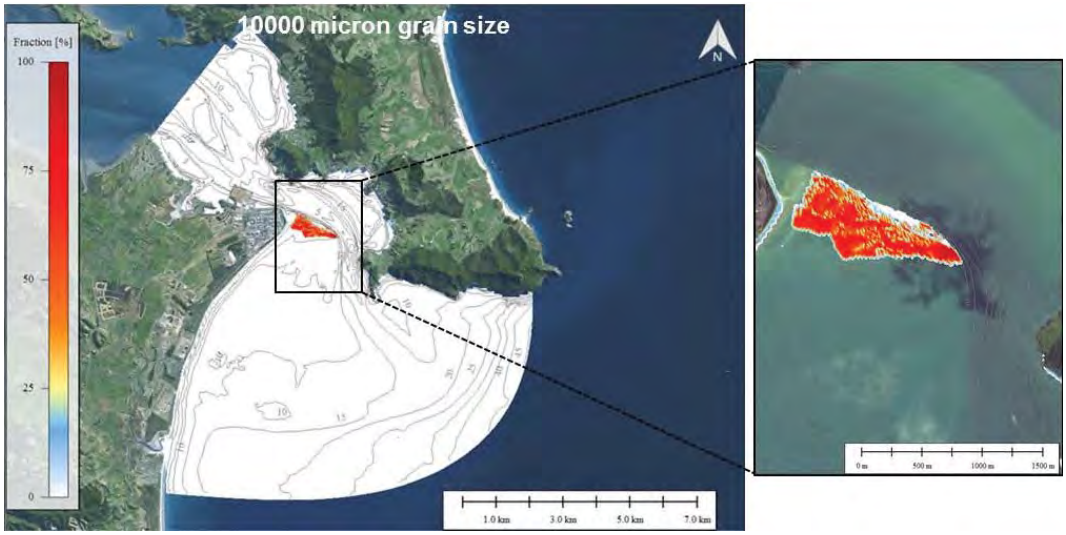

Figure 8.22 Distribution of 10 mm grain size sediments in the active layer generated by the BCG run for a 6-month fair-weather period.

8.5.4. 5-day storm period

During storm wave conditions (i.e. peak conditions shown on Figure 8.23), significant morphological and sedimentological adjustments occurred along Ruakaka Beach and Busby Head due to increasing sediment transport fluxes (Figure 8.24) generated by refracted waves (Figure 8.25). The residual bed load transport was south-southeastward-directed, which is particularly significant for fine sand sediments.

The short-term erosion/accretions patterns modelled over Mair Bank during storm conditions reflect the general consistency between the model and the observations provided in Section 3. Refracted and breaking waves over the southern margin of Mair Bank led to a slow landward net transport as described in Morgan et al. (2011). Notice the modelled low accretion of sand occurring between Madsen Bank and Mair Bank, which is in good agreement with the historical data. The model was reproducing the overall stability of the channel shape quite well, particularly along its edges. Note, however, the slight erosion of the sea bed over the channel section located to the North of Mair Bank. The extended accretion pattern over the intertidal area of Mair Bank is difficult to interpret as the morphodynamics in this region are highly related to the biological component. Indeed, the elevation of the ridges observed in Morgan et al. (2011) was interpreted as the migration of the shell swash bar. The gravel layer defined on the top of Mair Bank in the model to mimic the biological component seems to reproduce this behaviour leading to steeper lee slopes on the northern margin of the bank.

Inside the harbour where wave effect is negligible, no significant changes of the bathymetry occurred, reflecting the relative stability of the tidal inlet.

South of Busby Head, alternating erosion and deposition patterns indicate a migration of the fine to medium sand in the northwest direction, where they were initially deposited on the edges of the channel by ebb-tidal flows. The sediment grain size distributions obtained in the sediment sampling on both sides of the channel (Tonkin and Taylor, 2016) tend to support this behaviour with a clear coarser bed composition on the western edge of the offshore channel footprint.

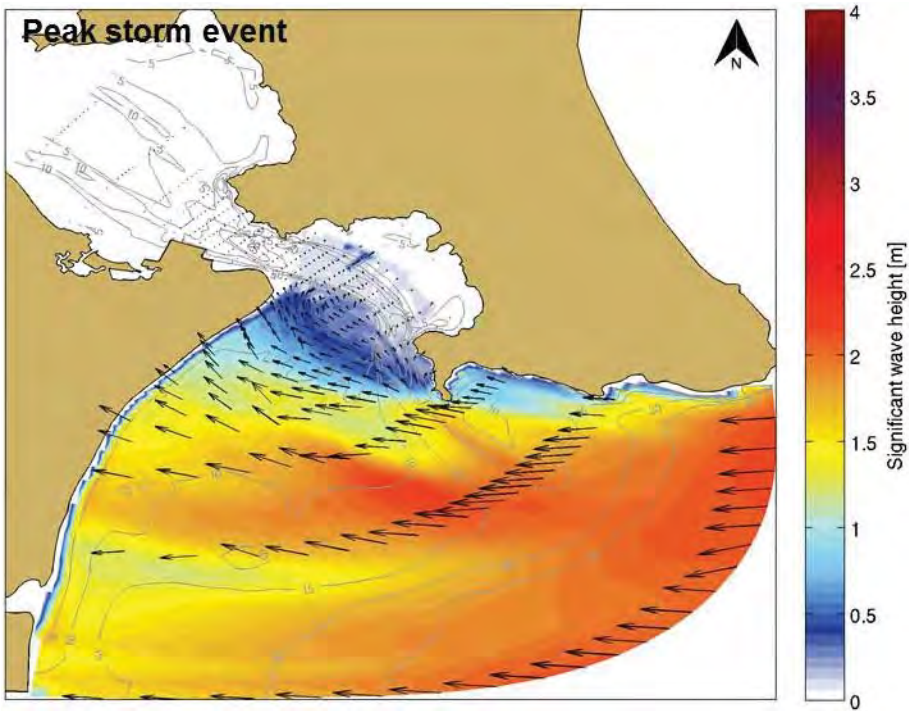

Figure 8.23 Wave height fields during storm event. Black arrows indicate the peak direction.

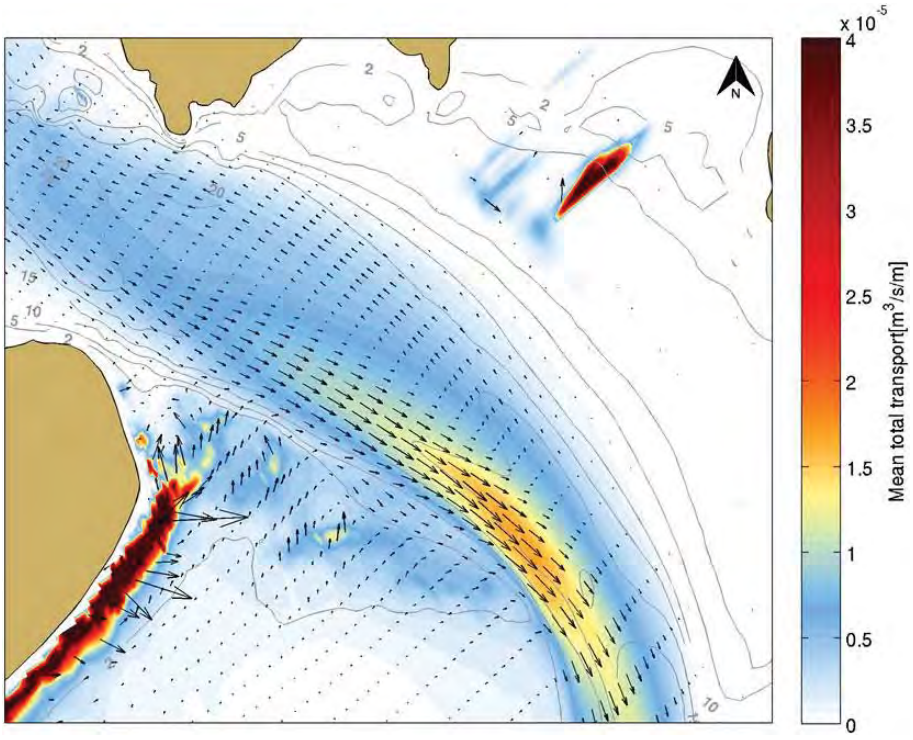

Figure 8.24 Mean total transport calculated during the 5-day storm period. Note that sediment transport was calculated over a complete number of tidal cycles (peak to peak).

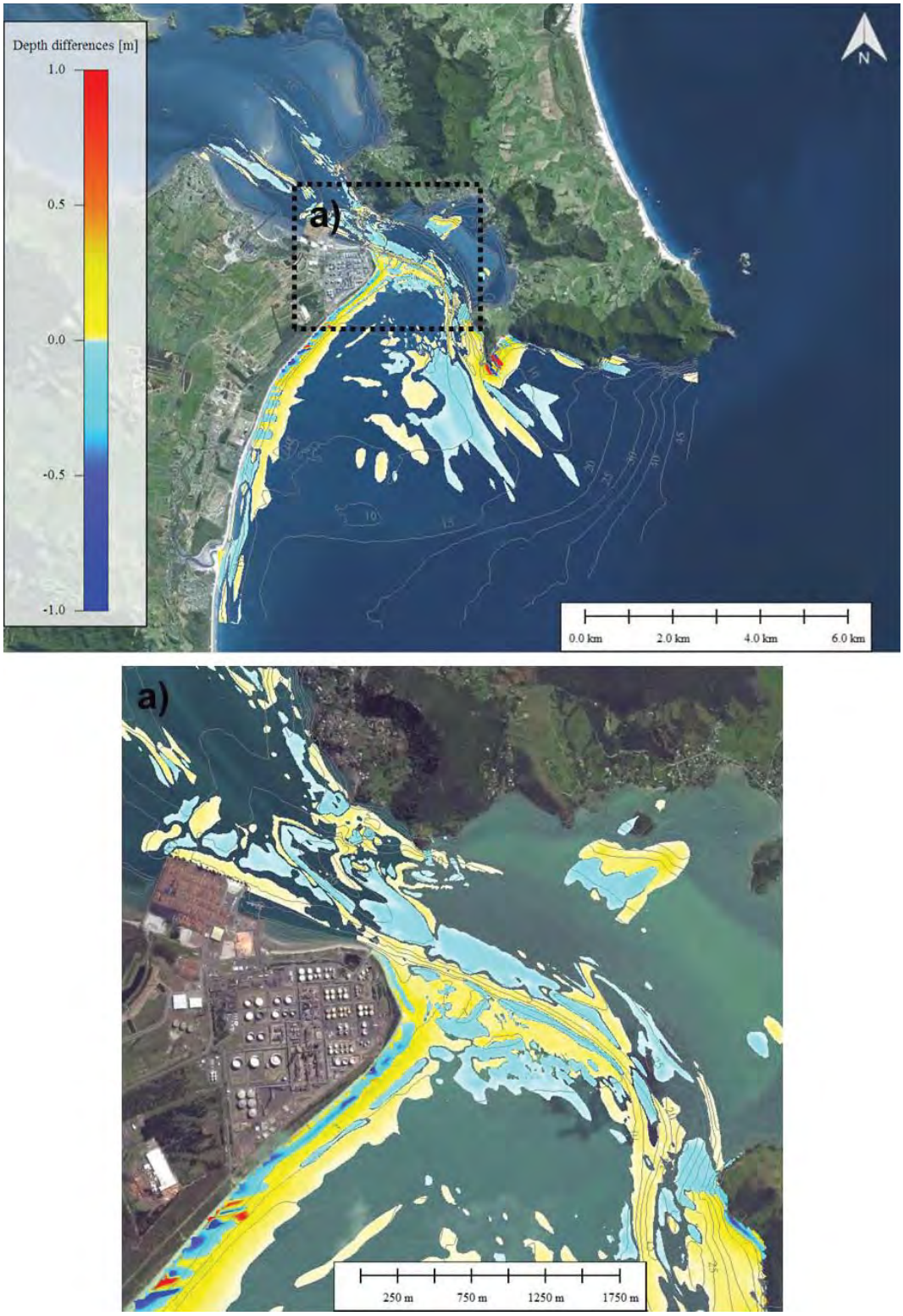

Figure 8.25 Simulated depth changes after 5 days of storm conditions with MORFAC 1 over the entire domain and over Mair Bank (a). Positive and negative magnitudes indicate sedimentation and erosion patterns, respectively.

8.6. Summary

A qualitative validation of the Delft3D model has been performed. The results suggest the model can be used to realistically reproduce a range of short- and medium-term morphodynamics at the Whangarei Harbour entrance. While the complexity and the limited understanding of the interactions between the biological, morphological and hydrodynamic components do not allow quantitative predictions to be made with confidence, it has confirmed the significance of the biomass of *pipi* on the enduring stability of Mair Bank. Inside the channel, the over coarsening of the sea bed during the initialisation of the bed composition indicated that the shell lag provides significant erosion sheltering to the sand sediments from the shear stress induced by strong tidal flows. In spite of these features, the model appears to satisfactorily reproduce the dominant mechanisms in the harbour entrance.

REFERENCES

Ardhuin, F., Rascle, N., Belibassakis, K.A., 2008. Explicit wave-averaged primitive equations using a generalized Lagrangian mean. Ocean Model. 20, 35–60. doi:10.1016/j.ocemod.2007.07.001

Ardhuin, F., Roland, A., 2013. The development of spectral wave models: coastal and coupled aspects, in: Proceedings of Coastal Dynamics. p. 7th.

Bagnold, R.A., 1966. An approach to the sediment transport problem. Gen. Phys. Geol. Surv. Prof Pap.

Bell, R.G., Goring, D.G., 1998. Seasonal Variability of Sea Level and Sea-surface Temperature on the North-east Coast of New Zealand. Estuar. Coast. Shelf Sci. 46, 307–318.

Bennis, A.-C., Ardhuin, F., Dumas, F., 2011. On the coupling of wave and three-dimensional circulation models: Choice of theoretical framework, practical implementation and adiabatic tests. Ocean Model. 40, 260–272. doi:10.1016/j.ocemod.2011.09.003

Black, K.P., 1983. Sediment Transport and Tidal Inlet Hydraulics. Hamilton, New Zealand: University of Waikato. Ph. D. thesis, 331p.

Black, K.P., Bell, R.G., Oldman, J.W., Carter, G.S., Hume, T.M., 2000. Features of 3-dimensional barotropic and baroclinic circulation in the Hauraki Gulf, New Zealand. J. Mar. Freshw. Res. 34, 1–28.

Black, K.P., Healy, T.R., Hunter, M.G., 1989. Sediment dynamics in the lower section of a mixed sand and shell-lagged tidal estuary, New Zealand. J. Coast. Res. 5, 503–521.

Booij, N., Ris, R.C., Holthuijsen, L.H., 1999. A third-generation wave model for coastal regions: 1. Model description and validation. J. Geophys. Res. Oceans 104, 7649–7666. doi:10.1029/98JC02622

Brown, J.M., Davies, A.G., 2009. Methods for medium-term prediction of the net sediment transport by waves and currents in complex coastal regions. Cont. Shelf Res. 29, 1502–1514.

Camenen, B., Larroudé, P., 2003. Comparison of sediment transport formulae for the coastal environment. Coast. Eng. 48, 111–132.

Collins, J., 1972. Prediction of Shallow Water Spectra. J. Geophys. Res. 77, 2693–2707.

Dastgheib, A., 2012. Long-term process-based morphological modeling of large tidal basins. UNESCO-IHE, Institute for Water Education.

Delft3D-WAVE_User_Manual.pdf, n.d.

Deltares, H.D., 2010. Delft3D-FLOW user manual. Version.

De Vriend, H.J., Capobianco, M., Chesher, T., De Swart, H. de, Latteux, B., Stive, M.J.F., 1993. Approaches to long-term modelling of coastal morphology: a review. Coast. Eng. 21, 225–269.

Dissanayake, D., Ranasinghe, R., Roelvink, J.A., 2012. The morphological response of large tidal inlet/basin systems to relative sea level rise. Clim. Change 113, 253–276.

Egbert, G.D., Erofeeva, S.Y., 2002. Efficient inverse modeling of barotropic ocean tides. J. Atmospheric Ocean. Technol. 19, 183–204.

Engelund, F., Hansen, E., 1967. A monograph on sediment transport in alluvial streams. TEKNISKFORLAG Skelbrekgade 4 Copenhagen V, Denmark.

Fairall, C.W., Bradley, E. F., Hare, J. E., Grachev, A. A., Edson, J. B., 2003. Bulk parameterization of air-sea fluxes: Updates and verification for the COARE algorithm. J. Clim. 16, 571–591.

Fredsøe, J., 1984. Turbulent boundary layer in wave-current motion. J. Hydraul. Eng. 110, 1103–1120.

Greig, M.J., 1990. Circulation in the Hauraki Gulf, New Zealand. N. Z. J. Mar. Freshw. Res. 24, 141–150.

Greig, M.J., Proctor, R., 1988. A numerical model of the Hauraki Gulf, New Zealand. N. Z. J. Mar. Freshw. Res. 22, 379–390.

Grunnet, N.M., Walstra, D.-J.R., Ruessink, B.G., 2004. Process-based modelling of a shoreface nourishment. Coast. Eng. 51, 581–607.

Holthuijsen, L.H., Booij, N., Ris, R.C., Haagsma, I.J., Kieftenburg, A.T.M.M., Kriezi, E.E., Zijlema, M., van der Westhuysen, A.J., 2007. SWAN cycle III version 40.51, Technical Documentation. Delft, 2600 GA Delft The Netherlands.

Inglis, G., Gust, N., Fitridge, I., Floerl, O., Woods, C., Hayden, B., Fenwick, G., 2006. Whangarei Harbour (Whangarei Port and Marsden Point) - Baseline survey for non-indigenous marine species (Research Project ZBS 2000/04). (No. Biosecurity New Zealand Technical Paper No: 2005/16.).

Kerr, V.C., 2016. Mair Bank channel edge additional characterisation: Crude Freight shipping project, Bream Bay, Whangarei (For Chancery Green on behalf of Refining NZ). Kerr and Associates.

Latteux, B., 1995. Techniques for long-term morphological simulation under tidal action. Mar. Geol. 126, 129–141.

Lesser, G.R., 2009. An approach to medium-term coastal morphological modelling. UNESCO-IHE, Institute for Water Education.

Lesser, G.R., Roelvink, J.A., van Kester, J.A.T.M., Stelling, G.S., 2004. Development and validation of a three-dimensional morphological model. Coast. Eng., Coastal Morphodynamic Modeling 51, 883–915. doi:10.1016/j.coastaleng.2004.07.014

Longdill, P.C., Healy, T.R., 2007. Sediment dynamics surrounding a flood tidal delta adjacent to reclamation and a dredged turning basin. J. Coast. Res. 1097–1105.

Lundquist, C.J., Oldman, J.W., Lewis, M.J., 2009. Predicting suitability of cockle Austrovenus stutchburyi restoration sites using hydrodynamic models of larval dispersal. N. Z. J. Mar. Freshw. Res. 43, 735–748.

Morgan, K.M., 2008. Biogenic sediment controls on ebb-tidal delta stability (MSc). Auckland, Auckland.

Morgan, K.M., Kench, P., Ford, R., 2011. Geomorphic change of an ebb-tidal delta: Mair Bank, Whangarei Harbour, New Zealand. N. Z. J. Mar. Freshw. Res. 45, 15–28. doi:10.1080/00288330.2010.533376

Morgan, K.M., Kench, P.S., Ford, R.B., 2011. Geomorphic change of an ebb-tidal delta: Mair Bank, Whangarei Harbour, New Zealand. N. Z. J. Mar. Freshw. Res. 45, 15–28.

Nichol, S., 2002. Morphology, Stratigraphy and origin of Last Interglacial Beach Ridges at Bream Bay, New Zealand. J. Coast. Res. 18, 149-159.

Pawley, M.D.M., 2014. Population and biomass survey of pipi (Paphies australis) on Mair Bank, Whangarei Harbour, Report prepared for Northland Regional Council.

Pinto, L., Fortunato, A.B., Freire, P., 2006. Sensitivity analysis of non-cohesive sediment transport formulae. Cont. Shelf Res. 26, 1826–1839.

Prediction of shallow-water spectra - Collins - 1972 - Journal of Geophysical Research - Wiley Online Library [WWW Document], n.d. URL http://onlinelibrary.wiley.com/doi/10.1029/JC077i015p02693/full (accessed 4.25.16).

Proctor, R., Greig, M.J., 1989. A numerical model investigation of the residual circulation in Hauraki Gulf. New Zealand. J. Mar. Freshw. Res. 23, 421–442.

Ranasinghe, R., Pattiaratchi, C., Masselink, G., 1999. A morphodynamic model to simulate the seasonal closure of tidal inlets. Coast. Eng. 37, 1–36. doi:10.1016/S0378-3839(99)00008-3

Ris, R.C., Holthuijsen, L.H., Booij, N., 1999. A third-generation wave model for coastal regions: 2. Verification. J. Geophys. Res. Oceans 104, 7667–7681. doi:10.1029/1998JC900123

Saha, S., Moorthi, S., Pan, H.-L., Wu, X., Wang, J., Nadiga, S., Tripp, P., Kistler, R., Woollen, J., Behringer, D., Liu, H., Stokes, D., Grumbine, R., Gayno, G., Wang, J., Hou, Y.-T., Chuang, H.-Y., Juang, H.-M.H., Sela, J., Iredell, M., Treadon, R., Kleist, D., Van Delst, P., Keyser, D., Derber, J., Ek, M., Meng, J., Wei, H., Yang, R., Lord, S., Van Den Dool, H., Kumar, A., Wang, W., Long, C., Chelliah, M., Xue, Y., Huang, B., Schemm, J.-K., Ebisuzaki, W., Lin, R., Xie, P., Chen, M., Zhou, S., Higgins, W., Zou, C.-Z., Liu, Q., Chen, Y., Han, Y., Cucurull, L., Reynolds, R.W., Rutledge, G.,

Goldberg, M., 2010. The NCEP Climate Forecast System Reanalysis. Bull. Am. Meteorol. Soc. 91, 1015–1057. doi:10.1175/2010BAMS3001.1

Sharples, J., Greig, M.J., 1998. Tidal currents, mean flows, and upwelling on the north-east shelf of New Zealand. N. Z. J. Mar. Freshw. Res. 32, 215–231.

Stanton, B.R., Sutton, P.J.H., Chiswell, S.M., 1997. The East Auckland Current, 1994–95. N. Z. J. Mar. Freshw. Res. 31, 537–549. doi:http://dx.doi.org/10.1080/00288330.1997.9516787

Swales, A., Gibbs, M., Pritchard, M., Budd, R., Olsen, G., Ovenden, R., Costley, K., Hemanspahn, N., Griffiths, R., 2013. Whangarei Harbour sedimentation - Sediment accumulation rates and present-day sediment sources. (No. NIWA client report: HAM2013-143). Prepared for Northland Regional Council. NIWA Project: NRC12204.

Tolman, H.L., 1991. A Third-Generation Model for Wind Waves on Slowly Varying, Unsteady and Inhomogeneous Depths and Currents. J. Phys. Oceanogr. 21, 782–797.

Tolman, H.L., Chalikov, D., 1996. Source terms in a third-generation wind wave model. J. Phys. Oceanogr. 26, 2497–2518.

Tomczak, M., Godfrey, J.S., 1994. Regional Oceanography: An Introduction. Pergamon, Oxford.

Tonkin and Taylor, 2016. Marsden point Refinery - Crude Freight Project, Vibrocore report (No. 30488.1000). Tonkin and Taylor.

Tonkin and Taylor, 2010. Coastal Erosion Hazard Zone Review. Report prepared for Whangarei District Council by Tonkin & Taylor.

van der Wegen, M., Dastgheib, A., Jaffe, B.E., Roelvink, D., 2011. Bed composition generation for morphodynamic modeling: case study of San Pablo Bay in California, USA. Ocean Dyn. 61, 173–186.

Van der Wegen, M., Roelvink, J.A., 2008. Long-term morphodynamic evolution of a tidal embayment using a two-dimensional, process-based model. J. Geophys. Res. Oceans 113.

van der Westhuysen, A.J., Zijlema, M., Battjes, J.A., 2007. Nonlinear saturation-based whitecapping dissipation in SWAN for deep and shallow water. Coast. Eng. 54, 151–170. doi:10.1016/j.coastaleng.2006.08.006

Van Rijn, L.C., van Rijn, L.C., van Rijn, L.C., 1993. Principles of sediment transport in rivers, estuaries and coastal seas. Aqua publications Amsterdam.

Van Rijn, L.C., Walstra, D.J.R., Ormondt, M. van, 2004. Description of TRANSPOR2004 and implementation in DELFT3D-ONLINE: final report. Deltares (WL).

Walstra, D.J.R., Hoekstra, R., Tonnon, P.K., Ruessink, B.G., 2013. Input reduction for long-term morphodynamic simulations in wave-dominated coastal settings. Coast. Eng. 77, 57–70.

Walstra, D.J.R., Roelvink, J.A., Groeneweg, J., 2001. Calculation of wave-driven currents in a 3D mean flow model, in: Coastal Engineering Conference. ASCE AMERICAN SOCIETY OF CIVIL ENGINEERS, pp. 1050–1063.

Williams, J.R., Hume, T.M., 2014. Investigation into the decline of pipi at Mair Bank, Whangarei Harbour. Prepared for Northland Regional Council (No. AKL2014-022). NIWA.

Zeldis, J.R., Walters, R.A., Greig, M.J., Image, K., 2004. Circulation over the northeastern New Zealand continental slope, shelf and adjacent Hauraki Gulf, during spring and summer. Cont. Shelf Res. 24, 543–561.

Zhang, Y.L., Baptista, A.M., 2008. A semi-implicit Eulerian-Lagrangian finite element model for cross-scale ocean circulation. Ocean Model. 21, 71–96.

MetOcean Solutions

CRUDE SHIPPING PROJECT, WHANGAREI HARBOUR

Establishment of numerical models of wind, wave, current and sediment dynamics

Report prepared for
Chancery Green for Refining NZ

Specialists in Oceanography and Meteorology

MetOcean Solutions Ltd: Report P0297-01

June 2016

Report status

Version	Date	Status	Approved by
RevA	15/06/2016	Draft for internal review	Monetti
RevB	17/06/2016	Draft for internal review	McComb
RevC	22/06/2016	Draft for client review	Gardiner
RevD	02/08/2016	Updated draft for internal review	Monetti
RevE	12/08/2016	Updated draft for client review	Gardiner
RevF	12/10/2016	Updated for client review	Monetti
RevG	19/01/2017	Updated for client review	Monetti

It is the responsibility of the reader to verify the currency of the version number of this report.

Acknowledgements
Thanks to Ross Sneddon from the Cawthron Institute for ADCP deployment and data collection.

Thanks to Ricky Eyre from Northland Regional Council for supplying LIDAR and single-beam data for Whangarei Harbour, Stuart Caie from LINZ for supplying offshore multi-beam data and historic survey data of Mair Bank and Jae Staite from Northport Ltd for supplying multi-beam survey data for main channel and multiple historic surveys of Mair Bank.

EXECUTIVE SUMMARY

Refining NZ is investigating options for the deepening and the realignment of the shipping channel leading to the Marsden Point Refinery at the entrance to Whangarei Harbour. MetOcean Solutions Ltd (MSL) participation in the effects assessment for the project has involved an evaluation of the effects of the channel deepening on the wave, current and sediment dynamics of the harbour entrance, the effects of dredging and disposal on water quality, and the effects of sediment disposal on the receiving environment. This has been undertaken through the use of a suite of numerical model investigations supported by empirical data, observations and historical and contemporary oceanographic measurements.

The study investigations are presented in technical reference documents. The present report (MSL Report P0297-01) provides details on the establishment of numerical models for wind, wave, current and sediment dynamics, and the data collection program that was undertaken to support the model establishment and to validate the numerical schemes. The second report MSL Report P0297-02 (MSL, 2016) summarises the existing physical environment and outlining the likely effects of the Crude Shipping Project on the waves, hydrodynamics and short- and long-term sediment dynamics. These reports should be read together.

The dominant physical processes at regional and local scales were replicated through the application of industry-standard numerical models based on published scientific methodologies and the background knowledge acquired from previous numerical modelling studies. Several models were investigated and the most appropriates ones chosen for the domain of application. Wherever possible, models were validated using historical and contemporary oceanographic data sets.

Wave modelling

The open-source SWAN model has been used in numerous studies around the world to simulate the coastal spectral wave transformation processes. Here, the model was used to hindcast the wave climate and further examine the wave transformation across the ebb tide delta and the nearshore environment in the vicinity of the ebb tide delta and the offshore disposal areas. The model was successfully validated with measurements from 5 locations, and was shown to replicate the wave climate at the entrance of Whangarei Harbour and along Ruakaka Beach. Based on the physical processes involved and the good validation of the model, it is considered an appropriate tool to predict the effect of the channel deepening on the wave climate.

Current modelling

Ocean currents were simulated with two different models to investigate regional and local scales. The open-source ROMS model was used to perform 3D hydrodynamic downscaling of the oceanic and tidal flows over the Hauraki Gulf and Bream Bay and to provide information for the site selection and detailed simulations of the proposed offshore disposal grounds. Validation of ROMS with measured current profile data showed that the model adequately represented the non-tidal flow regime while tidal flows were somewhat under-predicted by the model at Disposal 3.2. In the context of sediment transport, it has been concluded that such biases in the current speed were insufficient to result in significant changes to the seabed over a 40 m deep area. On the other hand, the impact of such bias on the plume modelling was investigated by forcing the model with the ADCP measured current profiles. Results did not highlight any increase of the

predicted plume extension associated to the release of sediments compared to the scenarios using the ROMS forcing. At local scale, the open-source SELFE model was used to simulate the 2D tidal flows in the vicinity of the ebb tide shoal, entrance and through the entire Whangarei Harbour. SELFE applies a finite-element mesh to allow resolution over complex bathymetries such as Whangarei Harbour. The model was validated against water levels measured at four locations and current profiles measured over regions of the outer channel where dredging is proposed. The validation showed the model to replicate the governing hydrodynamics of the harbour well, including the phase and amplitude of the tidal elevations and the spatially complex flows along the main shipping channel.

Morphodynamic modelling of the harbour entrance

The open-source Delft3D system was used to run high-resolution process-based morphodynamic simulations based on fully-coupled wave, current and seabed interactions. The morphodynamic system at the Whangarei Harbour entrance is influenced by the shellfish biomass on Mair Bank. Dealing with this unique environment within the numerical framework required the application of a range of published methodology approaches.

Climatic conditions were modelled to consider potential sediment transport and morphology evolution under conceptual and realistic scenarios. Morphological Acceleration Factors (MORFACs) for morphodynamic upscaling were applied to represent the likely short-term and long-term evolution of the seabed. For these scenarios, the sediment grain size distributions of the seabed were initialised from a 6-month fair-weather Bed Composition Generator (BCG) run. The resulting sedimentology was then qualitatively validated against contemporary sediment grain size observations.

Sediment plumes created during dredging

A Lagrangian particle model (ERcore) developed by MSL was used to simulate the likely extent and concentration of sediment plumes created during the dredging operation. This was achieved by simulating a plume continuously over a 28-day period at the various locations along the channel, and performing a subsequent statistical analysis of the predicted plume concentrations and extents. The plume dispersion associated with two different trailing suction hopper dredgers (TSHD), one cutter suction dredger (CSD) and one backhoe dredger (BHD) was simulated in the present study. The depth-averaged SELFE tidal currents were used as the environmental driver.

Sediment plumes created during disposal

The same Lagrangian particle model (ERcore) was also used to simulate the likely extent and concentration of sediment plumes created during the disposal operation. The 3D ROMS model and the measured current profile data were used as the environmental drivers to the plume modelling. Using measured data at the disposal site addresses the identified underestimation of tidal current speed in the ROMS model. Plumes were simulated over a 6-month period at 5 sites within the proposed offshore disposal ground 3.2, applying the same probabilistic approach to determine plume extent and concentration as for the dredging process. The modelling included three phases of convective descent, dynamic collapse and passive plume dispersion, using release depths according to the type of vessel involved.

Morphodynamic modelling of the disposal grounds

The Delft-3D modelling system was used to simulate the evolution of the proposed disposal grounds. A sequence of 16 representative wave and tide scenarios were run combined with weighted morphological acceleration factors to predict the long-term movement of material from the ground.

After an iterative process involving consideration of various alternatives and refinement of the preferred disposal areas, MetOcean modelled two offshore disposal sites. The first of these offshore disposal sites is referenced as Disposal Site 3.2, and is modelled for the placement of up to 97.5% of the capital dredge volume and up to 100% of the maintenance dredge volume. The capital dredge volume for this area is estimated at 3.7 million m^3, and the maintenance dredge volumes are estimated as 125,000 m3 per annum (Tonkin and Taylor, 2016a). Therefore, as a conservative estimate that 97.5% of the capital dredge volume, and the full amount of the maintenance dredge volume will be placed in Area 3.2, a 4 m high disposal mound was modelled over a proposed 2 km^2 area – equivalent to a total volume of 8 million m^3. The effect of the disposal mound on the wave climate within Bream Bay was assessed based on the wave modelling of the 16 representative scenarios including both the pre-disposal and the post-disposal bathymetries in the model.

Additionally, the Disposal Site 1.2 was designed for the disposal of 2.5 – 5% of the capital dredge and up to 100% of the maintenance dredge volume. The assessment of the disposal dynamics for the maintenance volumes was undertaken based on the numerical modelling of a representative value for a low mound, which was taken to be a 0.6 m high disposal mound (1.5 million m^3) defined on the ebb tide delta and corresponding to 5% of the capital dredge volume and 100% of the maintenance dredge volume over 10 years. Such approach is particularly conservative as the disposal mound will be continuously eroded between each disposal due to the relative low water depth (less than 10 m) characterising the southern flank of the tidal delta.

As for the offshore disposal mound, the long-term evolution of the disposal ground was simulated using a sequence of 16 representative wave and tide scenarios combined with weighted morphological acceleration factors.

TABLE OF CONTENTS

LIST OF FIGURES

LIST OF TABLES

1. INTRODUCTION

Refining NZ (RNZ) is investigating options for the deepening and the realignment of the shipping channel leading to the Marsden Point Refinery at the entrance to Whangarei Harbour. Increasing the navigable depth is necessary to allow vessels with increased draft to safely transit to the refinery. MetOcean Solutions Ltd (MSL) has been contracted to provide coastal oceanographic expertise and investigate the potential effects of channel deepening on the physical environment. The scope of work includes i) an evaluation of the wave, hydrodynamic and sediment dynamic regime throughout the Whangarei Harbour entrance region, ii) consideration of the effects of capital dredging on this environment, iii) potential effects on the coastal sediment budgets, iv) the stability of the adjacent beaches and the sub-tidal delta, and v) the effects of dredging and disposal on water quality in the receiving environment. A flow chart of the study processes is shown on Figure 1.1, and a map of Whangarei Harbour with the different locations referred to in the study is presented in Figure 1.2. Figure 1.3 presents a map showing the location of the proposed deepening. The location of the proposed disposal grounds for the placement of capital and maintenance volumes is shown in Figure 1.4.

The study investigations are presented in two reports:

- The present report is a technical reference document that details the establishment of numerical models for wind, wave, current and sediment dynamics, and the data collection program that was undertaken to support the model establishment and to validate the numerical schemes.

- The second report (MSL Report P0297-02) first characterises the existing environment and then investigates the likely physical effects of the Crude Shipping Project.

We recommend that the two reports be read together, in order to gain a complete understanding of our assessment approach and findings.

1.1. Report structure

The numerical modelling approach applied to characterise the regional wind and wave climate in the study area, is described in Sections 2 and 3 respectively, including validation against contemporary wind and wave data. Sections 4 and 0 explain the regional and nearshore hydrodynamic modelling techniques and present validations of the models used. Section 6 outlines the nearshore and harbour channel sediment transport modelling methods. The plume modelling approach used to consider the effects of dredging and disposal is detailed in Sections 7 and 8, respectively. The methods used to estimate the sediment transport from the preferred offshore disposal ground is provided in Section 9. An executive summary is presented at the beginning of the report.

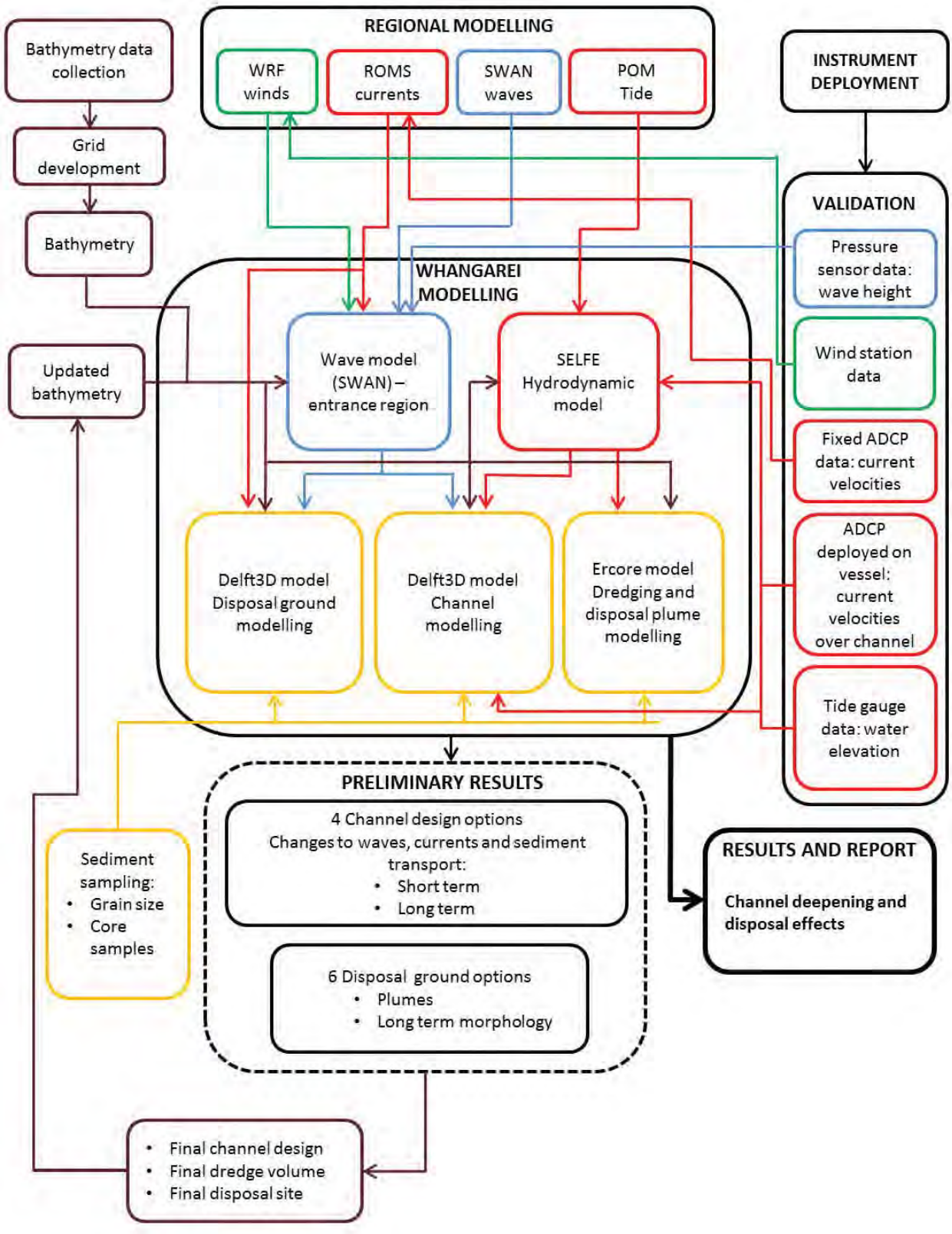

Figure 1.1 Flow chart showing the numerical modelling process for the study. Red lines indicate hydrodynamics; blue indicates waves; green indicate wind and yellow lines indicates bathymetry.

1.2. Study area

The different locations referred in the present report for the validation process and the description of the effect of the deepening channel on the coastal dynamics at Whangarei Harbour (MSL Report P0297-02) have been summarised in Figure 1.2.

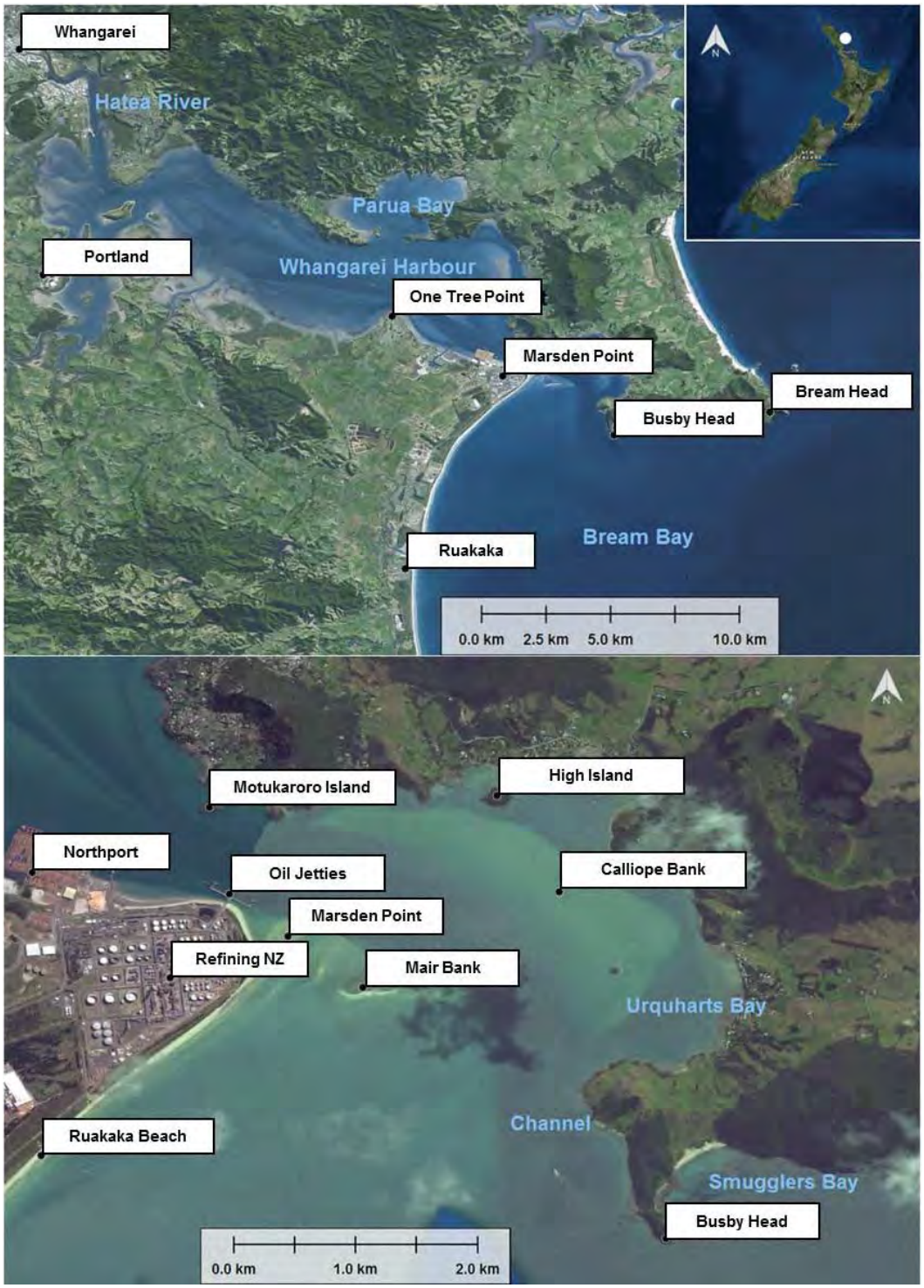

Figure 1.2 Maps of Whangarei Harbour (top) and its entrance (bottom) with the locations used in the present study for the establishment of the numerical models and the description of the effect of the channel deepening on the coastal dynamics.

1.3. Proposed channel deepening design

RNZ commissioned Royal Haskoning DHV (RHDHV) to define an optimal navigation channel design, including the associated dredging requirements, in order to provide high water access for vessels with increased draft to safely transit to the RNZ Crude Jetty.

Different options for the channel design (RHDHV Shipping Channel - Concept Design Report, Royal HaskoningDHV, 2016a) were provided and discussed with RNZ. An Under Keel Clearance study was completed by OMC in the OMC International (2016) - Mardsen Point Channel Optimisation report, based on the channel designs provided by RHDHV and the long period wave analysis performed by MSL. Further assessment of the channel was undertaken from a navigation perspective (RHDHV Report - Desktop Simulation Study, Royal HaskoningDHV, 2015). The Option 4.2 was the stated preferred option from a channel design perspective and was confirmed via the alternative assessment work presented in Tonkin and Taylor (2016a).

For the present study, Option 4.2 has been adopted as the design case for the numerical modelling. Details about the characteristics of the proposed channel and corresponding dredging requirements are described in Royal HaskoningDHV, 2016b, as part of the dredging methodology assessment provided by RHDHV to RNZ.

An overview of the proposed channel design (Option 4.2) and the resultant differences between existing and post-dredging bathymetries are shown on Figure 1.3 based on the depth datasets used by MSL to setup the model water depth.

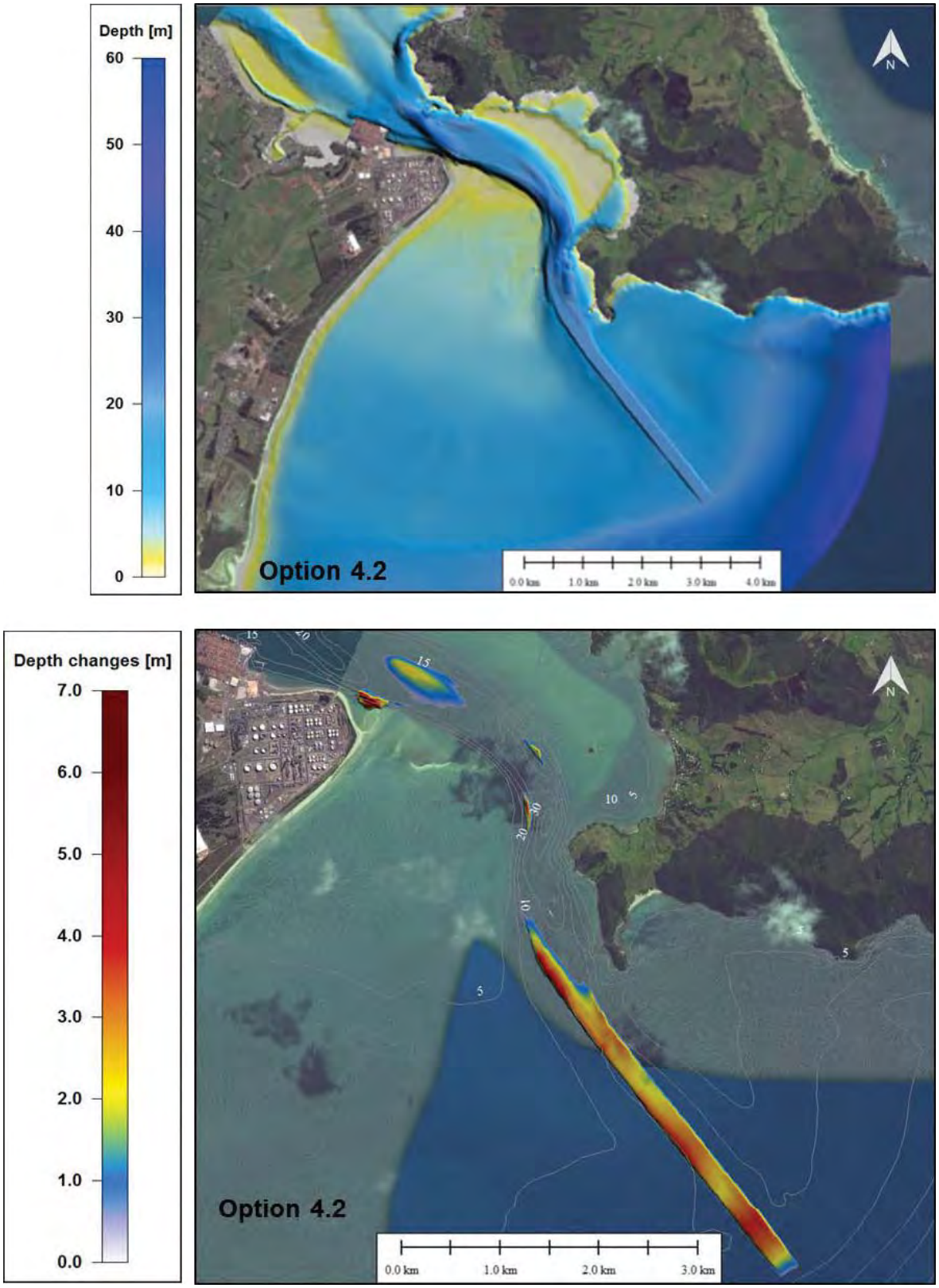

Figure 1.3 Depths (upper plot) and depth differences (lower plot) between the Option 4.2 channel design and the existing channel configuration. Positive amplitudes indicate a deepening of the channel.

1.4. Proposed offshore disposal ground designs

In consultation with Royal HaskoningDHV, Tonkin + Taylor, and MetOcean Solutions, as well as expert consultants from a range of other disciplines, the client went through a selection process which led to the identification of the preferred locations to dispose the capital and maintenance dredge volumes from the Crude Shipping Project. That process is described in the Tonkin and Taylor report (2016). In this context, two offshore disposal sites have been identified by RNZ as potential options for the disposal of capital and maintenance volumes (see Figure 1.4):

- Disposal Site 1.2 (yellow polygon) is located over the south-western flank of the tidal delta where depths range between 2 and 10 m. Its distance from Ruakaka Beach and Busby Head is approximately 2 km and 1.6 km, respectively. This disposal site is considered by RNZ as the preferred option for the placement of maintenance volume and up to 5% of the capital dredging volume, and the site has therefore been investigated in the present study.

- Disposal Site 3.2 (red polygon) is an area measuring approximately 2 km^2, which ranges in depth from 41 to 48 m. This option for the disposal of capital and maintenance volumes is located approximately 3.5 km to the South of Bream Head and 700 m to the east of 3 Mile Reef. Its distance from Busby Head and the inlet entrance is approximately 7 km. This disposal site is considered the preferred option for the placement of up to 95% of the capital volume and up to 100% of the maintenance volume by RNZ and the area was therefore investigated in the present study

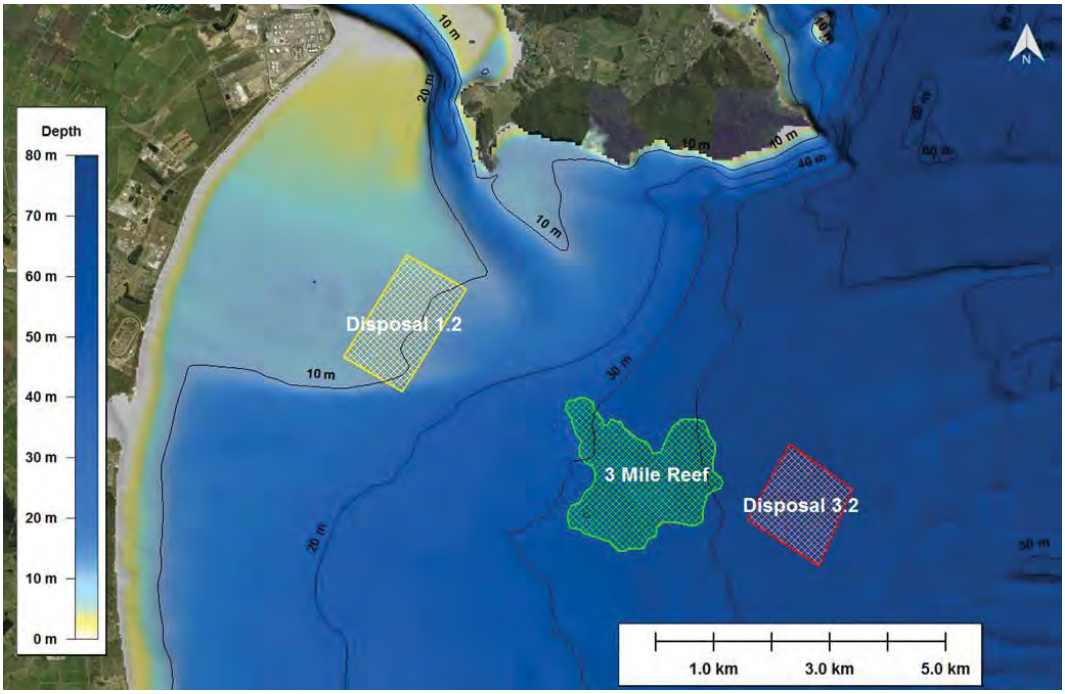

Figure 1.4 Location of Disposal grounds 1.2 and 3.2 (indicated by coloured diagonal cross-hatch polygons) for the disposal of capital and maintenance volumes. 3 Mile Reef indicated by a green polygon is a sensitive reef for its benthic encrusting communities.

1.5. Additional Northport berth

Additionally, the numerical modelling considered the existing Northport facilities, including Berths 1-3. It has also taken into account unimplemented resource consents held by NorthPort in respect of an additional proposed berth, known as Berth 4 (there are a series of consents issues by Northland Regional Council relating to the reclamation, construction, and use of Berth 4, primarily those consents numbered CON20030505523). As required pursuant to the RMA, the modelling included Berth 4 (see reclaim area in Figure 1.5) as if those resource consents had been given effect to as part of the "existing environment".

Figure 1.5 Satellite image showing the NorthPort Berth4 reclaim area included in the hydrodynamic model bathymetry.

2. WIND MODELLING

The numerical modelling of the atmospheric dynamics at Whangarei was undertaken by MSL to provide the wind conditions required to force the regional hydrodynamic and wave models presented in Sections 3 and 4.

2.1. Model approach

The near-surface wind field was prescribed by a 36-year (1979-2014) regional atmospheric hindcast carried out by MSL. The WRF (Weather Research and Forecasting) model was established over all of New Zealand at hourly intervals and at approximately 12 km resolution. The hindcast was specifically tuned to provide appropriate marine wind fields for metocean studies around the country. The WRF model boundaries were sourced from the CFSR (Climate Forecast System Reanalysis) dataset distributed by NOAA, which was available at hourly intervals and 0.31° spatial resolution. While the WRF hindcast produced atmospheric parameters at hourly intervals over the 36 years, only the near surface wind field (i.e. 10 minute mean at 10 m elevation) is used here.

2.2. Model validation

Validation of the WRF hindcast was undertaken at the Marsden Point wind station situated at 35.840 S, 174.487 E (WGS84) as shown in Figure 2.1. Wind data were recorded at approximately 10 m elevation above mean sea level between 1979 and 1990.

Figure 2.1 Location of the wind station (red circle) at Mardsen Point. Geographic coordinates are provided in Appendix A.

The quantitative validation shows the model to exhibit a reasonable correspondence with the measured data (Table 2.1). The hindcast wind speed was biased slightly high (0.59 ms^{-1}). The time series of measured and hindcast wind speed and direction are provided in Figure 2.2 and Figure 2.3 respectively, while the scatter and quantile-quantile (Q-Q) plots for the wind speed validation are

presented in Figure 2.4. These figures illustrate the good consistency between the measured and hindcast wind speed data.

The comparison between modelled and measured annual wind roses at Mardsen Point shown on Figure 2.5 indicates that the model realistically replicates the regional coastal wind climate, albeit with a relative low bias of approximately 0.7 $m.s^{-1}$ in speed and 11 degrees in direction, and illustrates that it does not include the influence of the local topography on the micro-scale wind regime. The topography of Mount Mania, Whangarei Heads, Bream Head and Ruakaka Forest creates wind corridors over some areas and provides sheltering for others; these are not fully replicated in the model given the resolution of the model grid is only 12 km. This spatial variability of the wind fields onshore is not expected to have a significant effect on the wave and current generation over the study area. On Figure 2.6, the distribution of wind directions are shown as histograms instead of Q-Q plots, which is more suitable for directional comparisons. The predominance of winds incoming from the SW sector is consistent between the measured and hindcast data, and the northeast and east sector winds are also relatively well replicated by the hindcast.

In summary, the model adequately replicates the regional wind dynamics, and it was therefore assessed that it is suitable for the forcing of the hydrodynamic and wave models.

Table 2.1 Accuracy measures for wind speed and direction at Marsden Point (1979-1990).

Parameter	Wind speed	Wind direction
MAE	1.92 ms^{-1}	31 deg.
RMSE	2.44 ms^{-1}	44 deg.
MRAE	0.59	0.31
BIAS	0.67 ms^{-1}	-11 deg.
Scatter Index	0.47	0.22

Mean absolute error (MAE):

$$\overline{|x_h - x_m|} \qquad (2.1)$$

Root Mean Square Error (RMSE):

$$\sqrt{\overline{(x_h - x_m)^2}} \qquad (2.2)$$

Mean relative absolute error (MRAE):

$$\left|\overline{\frac{x_h - x_m}{x_m}}\right| \qquad (2.3)$$

Bias:

$$\overline{x_h - x_m} \qquad (2.4)$$

Scatter Index (SI):

$$\frac{\sqrt{\overline{(x_h - x_m)^2}}}{\overline{x_h}} \qquad (2.5)$$

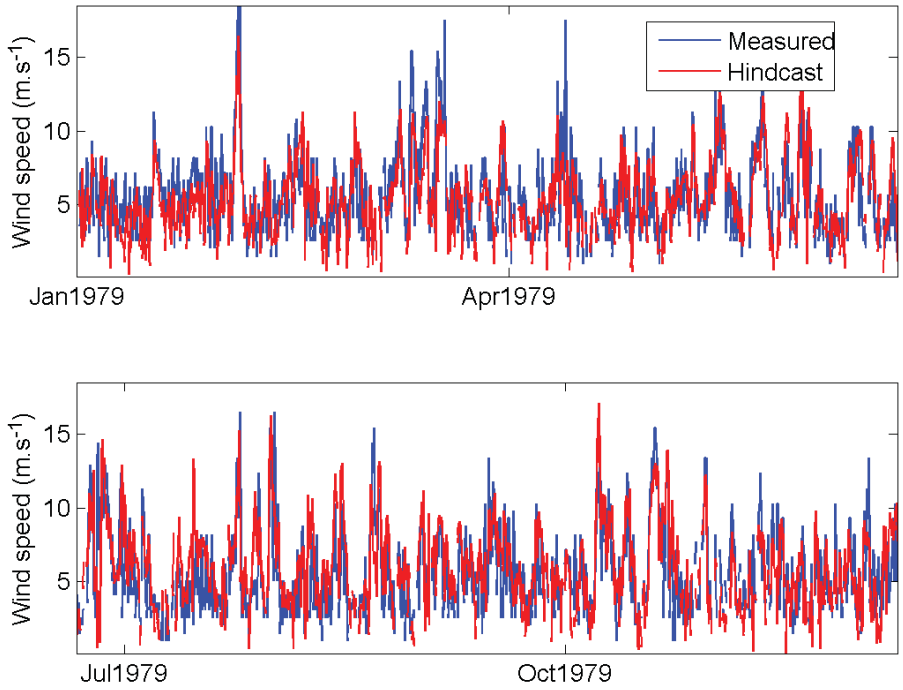

Figure 2.2 Time series plot of the measured and hindcast wind speed and wind direction at Marsden Point (year 1979). Note only a portion of the 12 years of data used for validation is shown here for better visualisation.

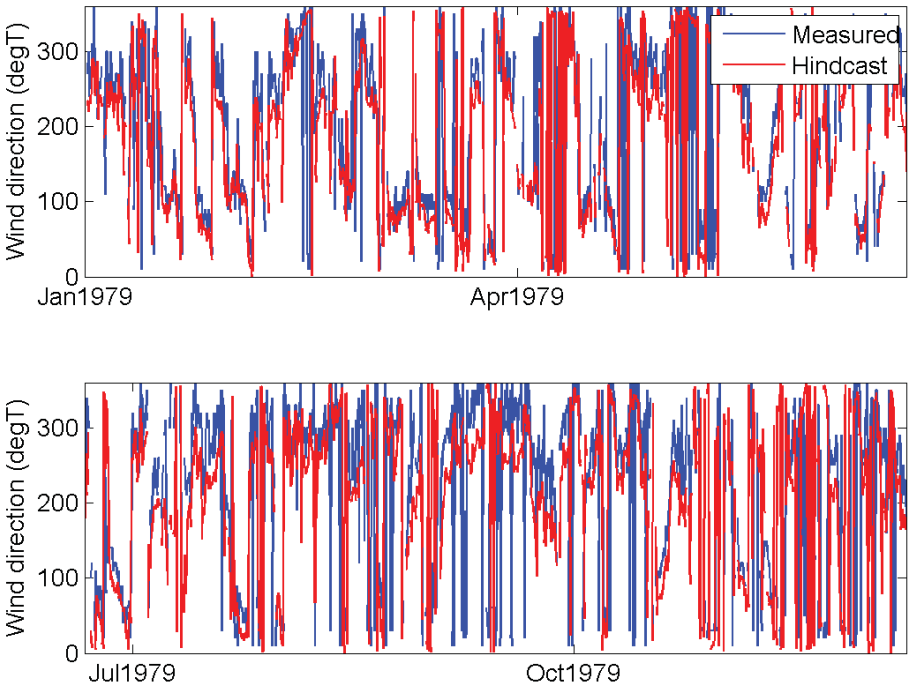

Figure 2.3 Time series plot of the measured and hindcast wind direction at Marsden Point (year 1979). Note only a portion of the 12 years of data used for validation is shown here for better visualisation.

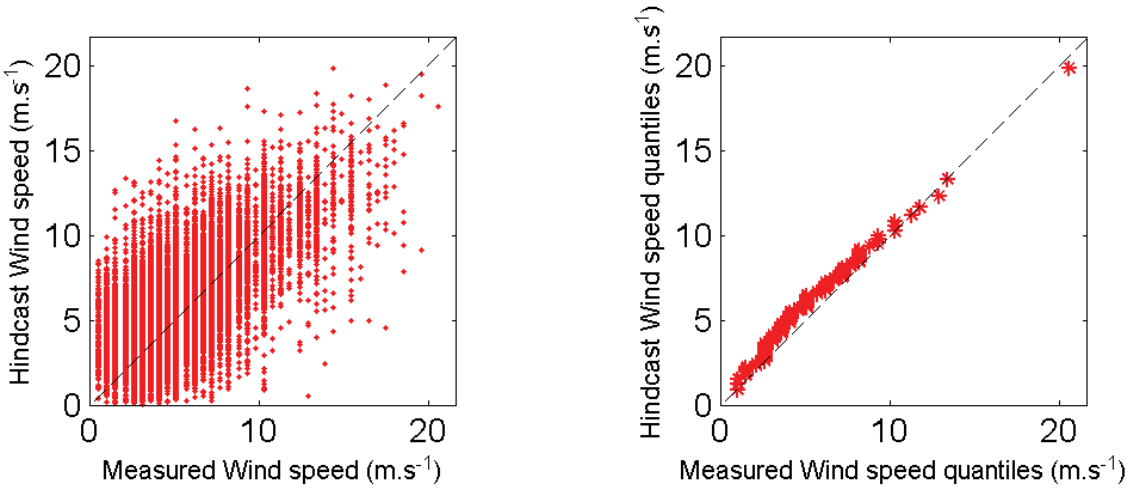

Figure 2.4 Scatter and Quantile-Quantile plots of the measured and hindcast wind speed at Marsden Point (1979-1990). Also shown are the lines of equivalence.

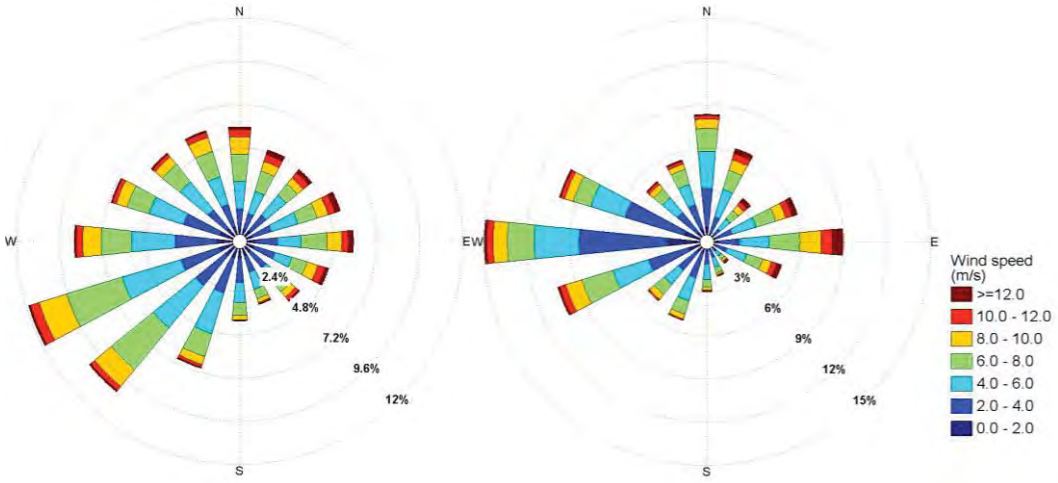

Figure 2.5 Modelled (left) and measured (right) annual wind rose at position WS shown on Figure 2.1. Geographic coordinates of this location are provided in Appendix A.

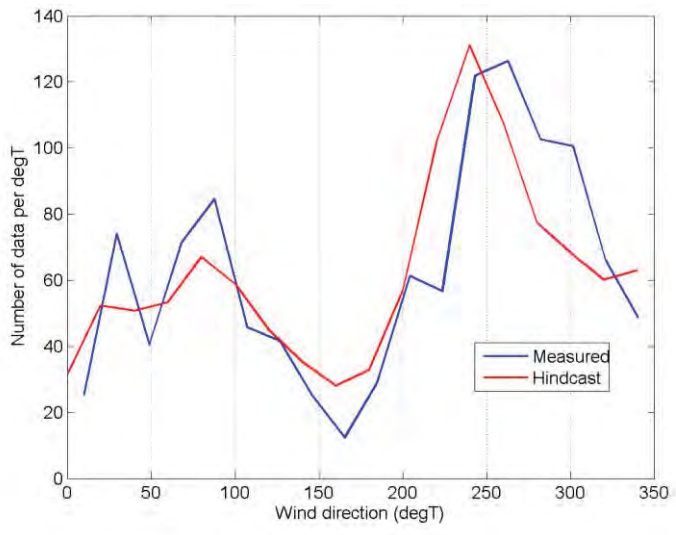

Figure 2.6 Histograms of measured and hindcast wind directions at Marsden Point (1979-1990).

3. WAVE MODELLING

This section details the numerical wave hindcast modelling used to characterise the regional wave climate as well as the nearshore wave transformations from offshore and into the harbour entrance.

3.1. Model approach

3.1.1. Model description

A modified version of SWAN[1] (Simulating Waves Nearshore) was used for the hindcast wave modelling for the project. The wave hindcast extended over a 36-year period between 1979 and 2015.

SWAN is a third generation ocean wave propagation model which solves the spectral action density balance equation for wavenumber-direction spectra. This means that the growth, refraction, and decay of each component of the complete sea state, each with a specific frequency and direction, is solved, giving a complete and realistic description of the wave field as it changes in time and space. A detailed description of the model equations, parameterisations and numerical schemes can be found in Holthuijsen (2007) or the SWAN documentation[2]. Physical processes that are simulated include the generation of waves by surface wind, dissipation by white-capping, resonant nonlinear interaction between the wave components, bottom friction and depth limited breaking. All 3rd generation physics are included. The BYDRZ physics package developed for WW3 model, which accounts for the effects of full air flow separation and therefore relative reduction of the input at strong wind forcing, was implemented in SWAN and used for the hindcast. The Collins (1972) friction scheme was used for wave dissipation by bottom friction.

The solution of the wave field is found for the non-stationary (time-stepping) mode. Boundary conditions, wind forcing and resulting solutions are all time dependent, allowing the model to capture the growth, development and decay of the wave field.

3.1.2. Pertinence of the model for the present study

The SWAN model was selected in the present study for its unconditionally stable numerical scheme and its ability to accurately reproduce the wave spectral transformations from deep to shallow water regions over complicated nearshore bathymetry. SWAN is considered the most suitable tool to compute the offshore-to-nearshore transformation of wave fields. Other types of models, notably non-hydrostatic or Boussinesq-type phase resolving time-domain models have a more complete description of the (nonlinear) wave transformation and resolve the wave shape, but are impractical to apply over large domains and/or over long-term periods.

SWAN has widely been applied all over the world in many coastal wave studies and successfully validated against measured data. Dodet (2013) investigated the wave-current interactions in a wave-dominated tidal inlet (Albufeira Lagoon) and showed that SWAN was able to faithfully represent the wave dynamics at the seaward entrance of the delta and within the inlet. The authors of that study used a three-level nested design structure within SWAN forced by WW3 spectra outputs

[1] Modified from SWAN version of the 40.91 release (publicly available code)
[2] http://swanmodel.sourceforge.net/online_doc/online_doc.htm

and coupled with a high-resolution hydrodynamic model. This corresponds to the same approach applied in the present study of the entrance to Whangarei Harbour.

3.1.3. Model domain and boundary conditions

The wave hindcast involved three-level SWAN downscaling to model the nearshore region at approximately 50 m resolution. Full spectral boundaries for the parent domain were prescribed from MSL implementation of WW3 global wave model (Tolman, 1991) with the Tolman and Chalikov (1996) physics.

The limits and resolutions for each SWAN nest are shown in Table 3.1 and Figure 3.1. The parent domain was forced with full spectral boundaries from WW3 and provided boundaries to run a first SWAN child at 0.0015 degree. A second child nest with about 50 m resolution was defined to resolve the complex bathymetric features near the shore. All nests were configured with 24 frequency bins (logarithmic scale from 0.04 to 0.66 Hz) and 36 directional bins. SWAN was run with wind fields specified from the MSL WRF New Zealand reanalysis.

Table 3.1 Boundary, resolution and limits defined for each SWAN nest.

Domain	Boundary	Longitude (degree)			Latitude (degree)		
		x1	x2	dx	y1	y2	Dy
Parent	WW3	174.45	176.15	0.009	-37.23	-35.23	0.009
Child 1	Parent	174.451	174.8	0.0015	-36.04	-35.8	0.0015
Child 2	Child 1	174.458	174.558	0.0005	-35.925	-35.825	0.0005

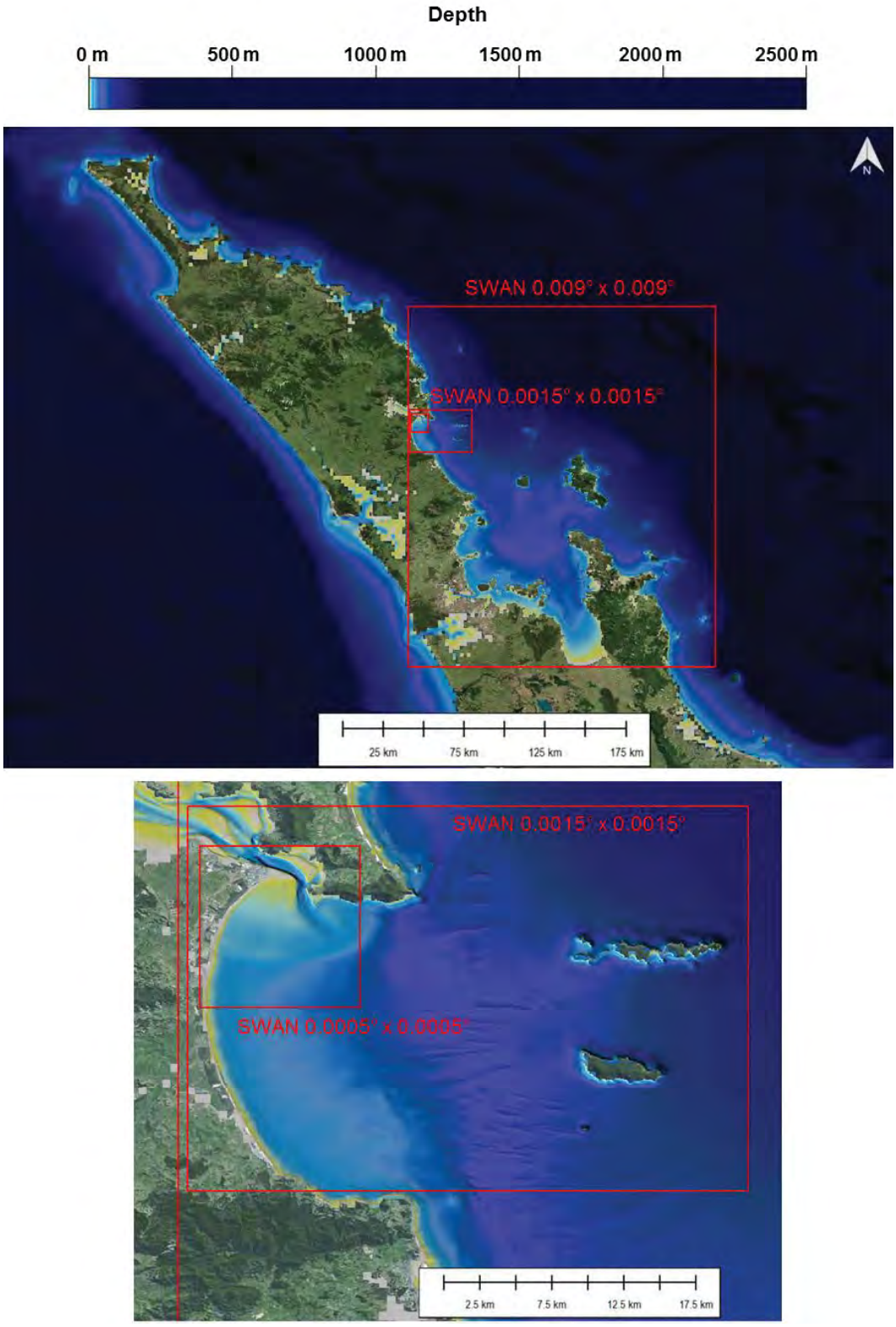

Figure 3.1 Water depth and model domains used to reproduce the spectral wave transformation from offshore to nearshore. The geographical extent of each domain is shown by the red rectangles.

3.1.4. Post-processing

Two-dimensional frequency-direction wave spectra were output at hourly intervals from the highest resolution SWAN domain at four nearshore. The spectra were post-processed to calculate wave statistics for the total wave field, as well as for sea and swell components. One – dimensional frequency spectra, spectral moments, significant wave height, mean direction at peak frequency and peak wave period were calculated based on the equations provided below:

- One-dimensional frequency spectra:

$$S_n(f) = \int_{-\pi}^{\pi} E_n(f,\theta) d\theta \tag{3.1}$$

- Spectral moments were calculated as:

$$m_x = \int \int f^x E(f,\theta) df \, d\theta \tag{3.2}$$

- Significant wave height , mean direction at peak frequency and peak wave period defined as:

$$H_s = 4\sqrt{m_0} \tag{3.3}$$

$$Dpm = tan^{-1} \frac{\int_{-\pi}^{\pi} E(f_p,\theta)\, sin\theta \, d\theta}{\int_{-\pi}^{\pi} E(f_p,\theta)\, cos\theta \, d\theta} \tag{3.4}$$

$$T_p = \frac{1}{f_p} \tag{3.5}$$

where f_p is the peak wave frequency of the one-dimensional spectra and $E(f_p,\theta)$ is the energy contained in the peak wave frequency band.

- Mean wave periods were defined from the first and second spectral moments as:

$$T_{m01} = \frac{m_1}{m_0}; \quad T_{m02} = \frac{m_2}{m_0} \tag{3.6}$$

- Spectral width parameter was calculated as:

$$S_{we} = \sqrt{\frac{1 - m_2^2}{m_0 m_4}} \tag{3.7}$$

3.2. Model validation

A program of wave measurements was undertaken to validate the nearshore wave transformation model. This involved the deployments of a waverider buoy and pressure sensors. The validation data locations are shown on Figure 3.2 and the observational durations are specified in Table 3.2.

The model wave hindcast was first validated against the offshore waverider buoy (WRB) data to ensure the sequence of hindcast model domains could reproduce the wave boundary conditions to the study area. The second step was to demonstrate the ability of the nearshore model to capture the governing wave dynamics across the ebb tide delta from the nearshore wave data sites (W1 – W4) along Ruakaka Beach (Figure 3.2). Note that the water depth at these nearshore sites ranged from 2.8 to 7 m (see Table 3.2).

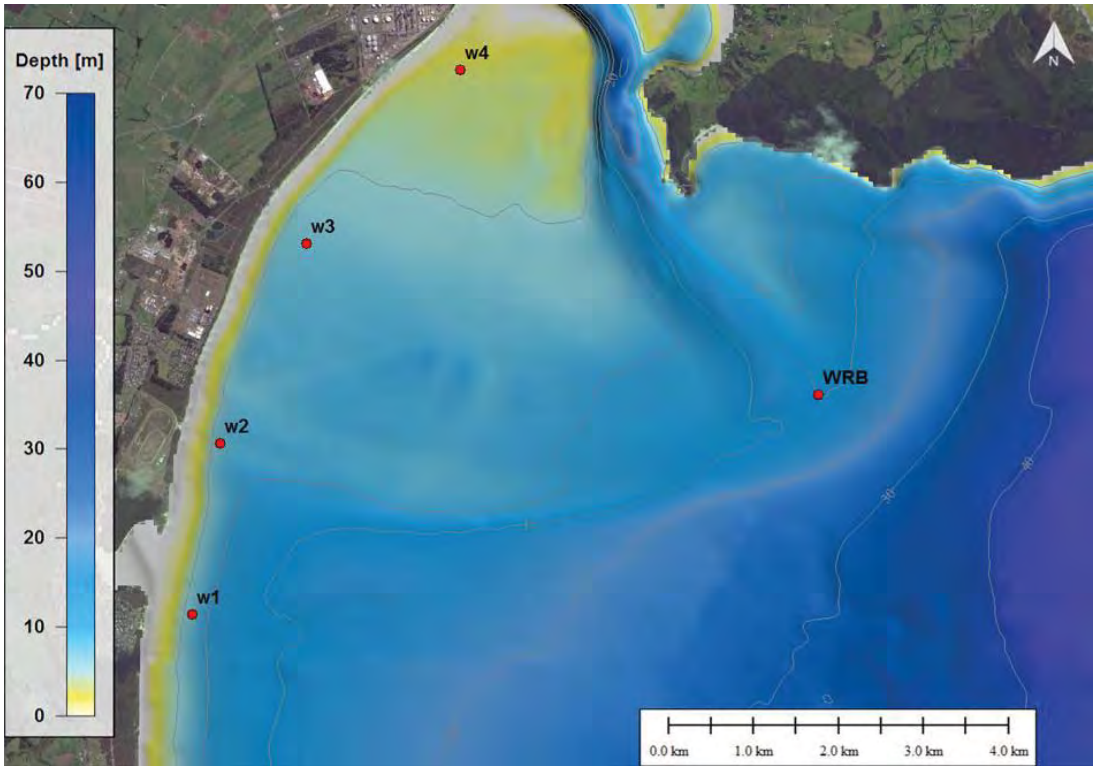

Figure 3.2 Locations of the instruments (red circles) deployed for measuring the wave conditions along Ruakaka Beach and offshore of the entrance.

Table 3.2 Measured wave data sources used for the hindcast validation.

Site name	Water depth (m)	Data coverage
WRB	15.0	continuous
W1	6.9	10/07 to 08/08 2015
W2	7.0	10/07 to 08/08 2015
W3	6.9	10/07 to 08/08 2015
W4	2.8	10/07 to 08/08 2015

3.2.1. Frequency range and accuracy measures

The wave spectra (measured and modelled) at the nearshore sites W1 – W4 were integrated over the 0.04 – 0.25 Hz range, while the entire frequency range was used at site WRB. Co-temporal, co-located wave parameters calculated from the hindcast model and from the measurements were compared directly.

3.2.2. Validation results

Comparisons between measured and modelled significant wave heights (Figure 3.3 and Figure 3.4) at location WRB outside the ebb-tidal delta indicate that the model adequately predicts the time-varying wave conditions. On average the hindcast wave heights were biased slightly high (0.07 m in absolute value) while the hindcast peak wave period was biased slightly low, by about 0.7 s (see Figure 3.5). The model tends to slightly under-predict the wave heights in the range low energy range (Figure 3.4) which could be due to a slight underestimation of the local wind wave growth. Moderate energy swell events (1-2 m in height) are slightly overestimated, which is due to the incident directional spectra from WW3 having a slightly high bias along the east coast of New Zealand.

The hindcast results for the nested inner wave domain, which includes the ebb tide delta and the harbour entrance region, are provided in Figure 3.5 to Figure 3.9. Here the time series of measured and predicted wave heights are co-plotted, showing a general agreement with the time varying conditions and also the gradient in wave energy that decreases with distance to the north along Ruakaka Beach. Site W1 exhibits some anomalous behaviour however, with the model over-predicting the wave height for one event, which is being well replicated at the other sites. Close examination of the model results indicates that strong wave refraction over the ebb tide delta causes zones of high and low wave energy to be distributed along the beach. The location of these zones depends on the incident wave period and wave direction. So, while the hindcast boundary spectra to the inner nest are a very good estimate, it is not a perfect replication of the 2D wave spectra and subtle differences in the incoming wave directionality will be readily expressed in the nearshore results. This is made particularly evident on the ebb tide delta because the waves travel for several km slightly oblique to the bathymetric contours, and therefore refraction effects on the nearshore wave conditions becomes highly evident. The measured and modelled data clearly shows that the shape of the ebb tide delta causes distinct redistribution of the wave energy along the shore, an important finding highlighting the influence of the offshore bathymetry on the nearshore wave conditions.

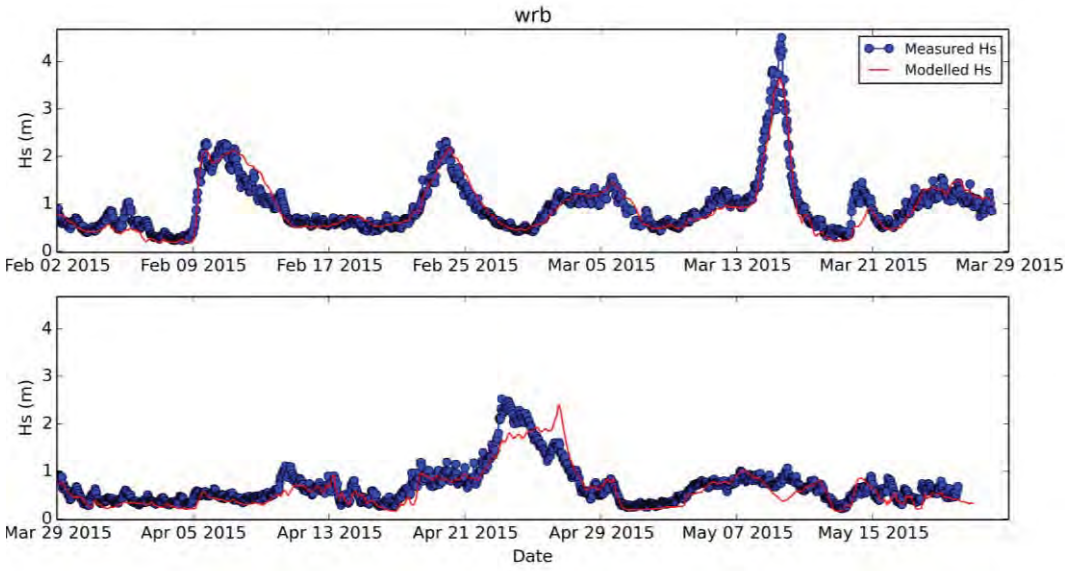

Figure 3.3 Time series of measured (blue) and modelled (red) significant wave height H_s at the WRB site.

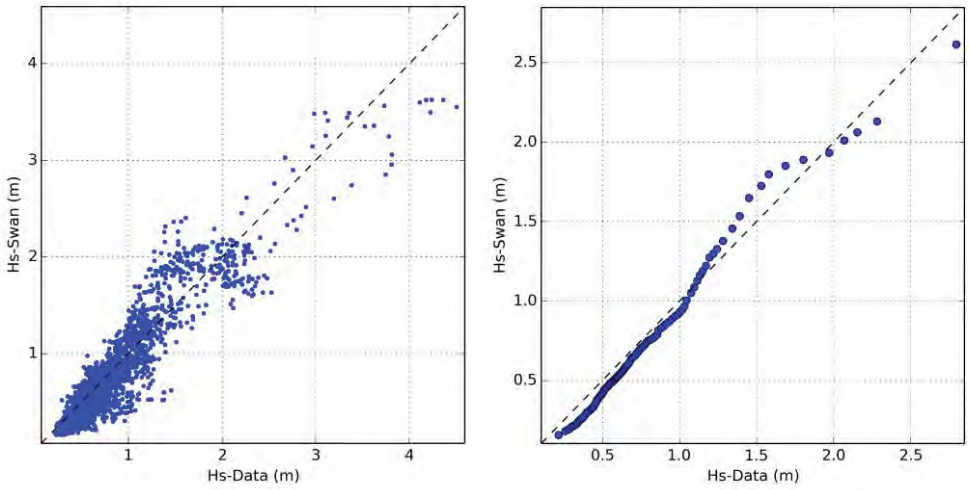

Figure 3.4 Scatter diagram (left) and quantile-quantile plot (right) of measured and modelled significant wave height H_s at WRB site.

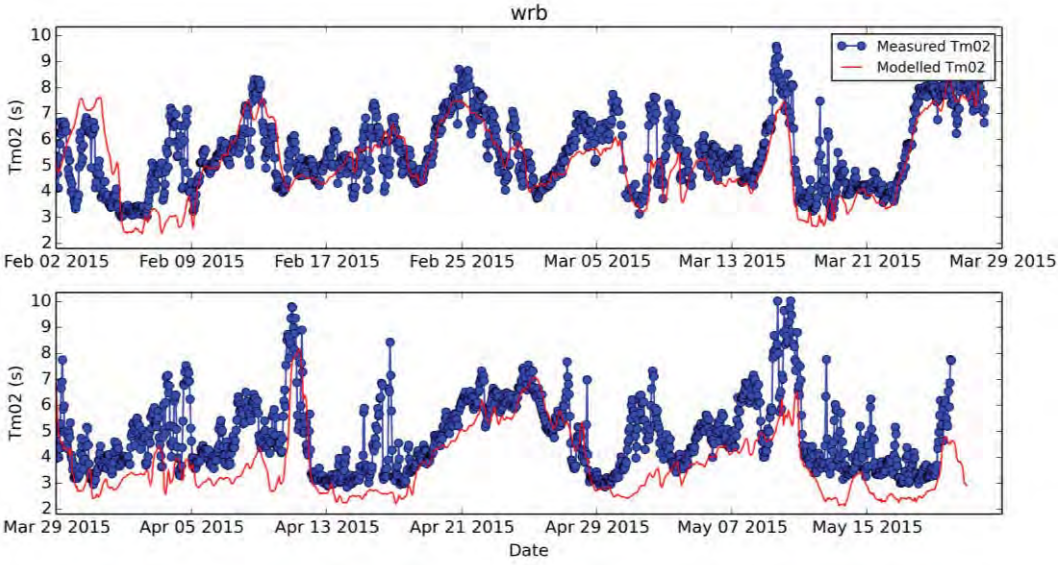

Figure 3.5 Time series of measured (blue) and modelled (red) mean absolute period from the second spectral moment T_{m02} at the WRB site.

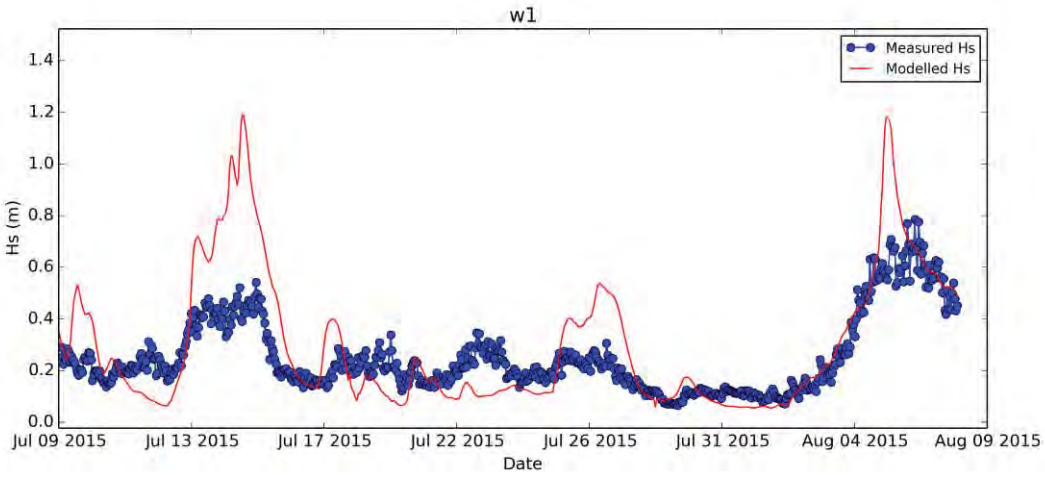

Figure 3.6 Time series of measured (blue) and hindcast (red) significant wave height H_s at site W1.

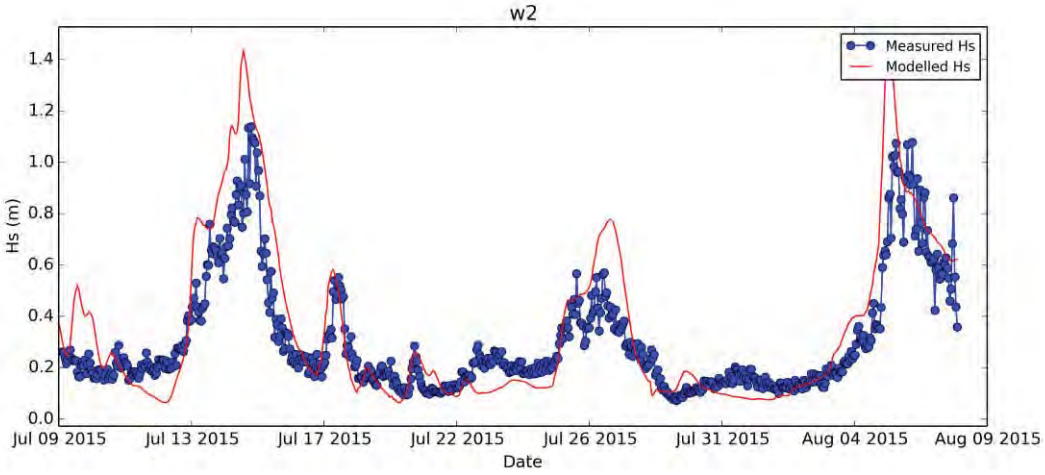

Figure 3.7 Time series of measured (blue) and hindcast (red) significant wave height H_s at site W2.

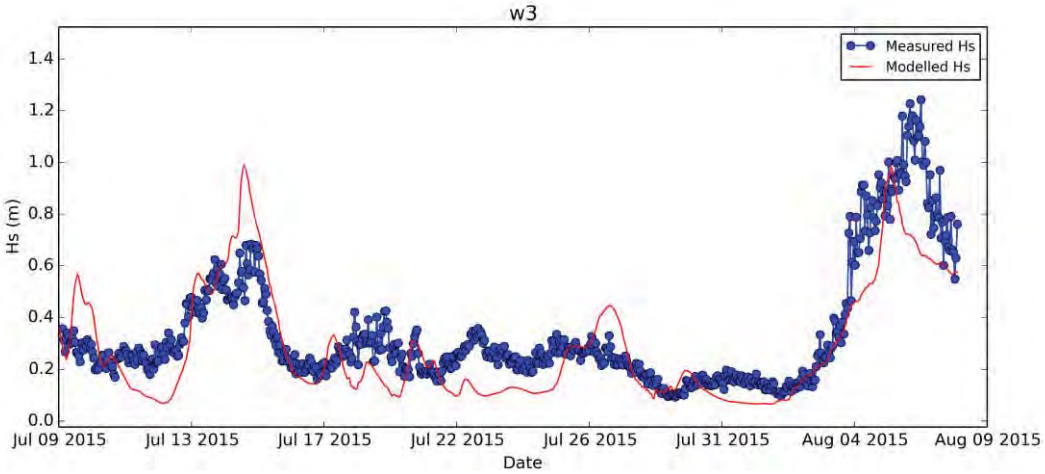

Figure 3.8 Time series of measured (blue) and hindcast (red) significant wave height H_s at site W3.

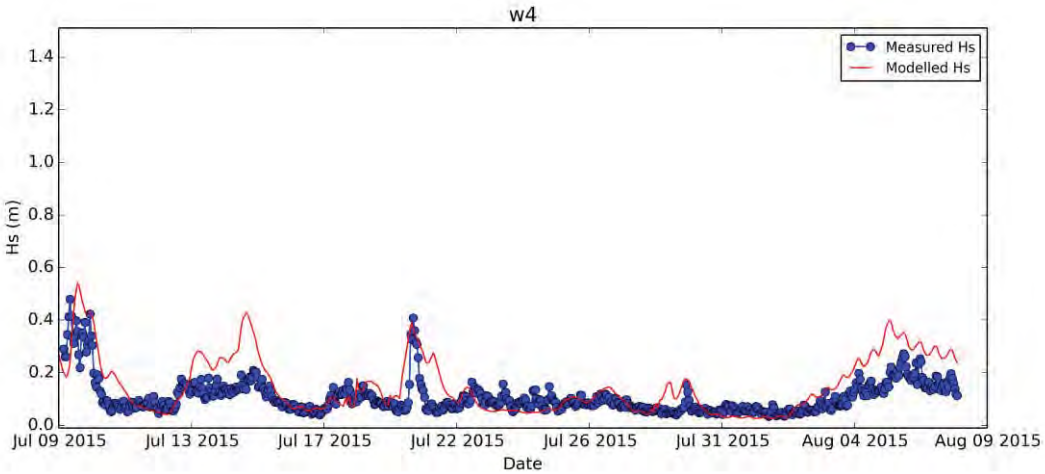

Figure 3.9 Time series of measured (blue) and hindcast (red) significant wave height H_s at site W4.

4. REGIONAL HYDRODYNAMIC MODELLING

Characterising the circulation in the continental shelf waters adjacent to Whangarei Harbour is important when considering the local scale hydrodynamic and sediment transport processes, as it prescribes the boundary conditions for the nearshore and harbour entrance numerical modelling. The presence of strong, along-shelf winds and offshore oceanic boundary currents year round can all play a role in forcing the circulation near the coast. A careful modelling strategy is required to reproduce the different spatial and temporal scales and circulation phenomena at the shelf and deep ocean environments and adequately feed the local scale models. This section describes the modelling studies that were undertaken to characterise regional hydrodynamics.

4.1. Model approach

4.1.1. Modelling description and pertinence of the model

A 10-year hindcast was performed using the ROMS hydrodynamic model version 3.7 (Regional Ocean Modelling System, described in Haidvogel (2008) to characterise the tidal and residual shelf scale circulation regime. The application of the ROMS model at regional scale fully captures the interaction of the wind and tidal circulation with the morphology of the Hauraki Gulf. This modelling tool has been used widely in the scientific and commercial consultancy communities for a wide range of ocean basin at regional and coastal scales.

ROMS has a curvilinear horizontal coordinate system and solves the hydrostatic, primitive equations subject to a free-surface condition. It is a state-of-the-art model widely used for regional and coastal dynamics assessment. Its terrain-following vertical coordinate system results in accurate modelling of shelf seas with variable bathymetry, allowing the vertical resolution to be inversely proportional to the local depth. Besides tidal and wind-driven currents, ROMS resolves frontal structures and baroclinic pressure gradients quite well. Vertical mixing may be resolved by different separate turbulent closure schemes, that are flexible to shallow and deep water dynamics. These features make ROMS particularly well-adapted for the modelling of regional hydrodynamic systems and ROMS is one of the hydrodynamic models most used for regional study applications. It is a modern code which captures sub-, meso- and macro-scale hydrodynamic mechanisms while maintaining robustness, accuracy and numerical stability.

4.1.2. Model domains

The hindcast setup was configured with a three-level nesting (Figure 4.1, top) approach to best transfer the energy gradually from larger to smaller coastal scales, and to properly resolve the flow associated with local and remote forcing, both essential for the resultant currents in the area of interest. The open boundary conditions that were imposed to the highest level nest (NZ) consisted of tri-dimensional velocity, temperature, salinity and sea surface height fields derived from the 6-hourly Climate Forecast System Reanalysis (CFSR) product (Saha et al., 2010) from the National Centers for Environmental Prediction (NCEP), which consisted of a 0.5 degree global reanalysis with comprehensive data assimilation.

The larger scale ROMS nest encompassed the area shown in the lower panel of Figure 4.1 with 7 km horizontal resolution, the goal of which was to absorb the basin scale circulation estimated by the CFSR global reanalysis, thus avoiding a large parent-to-child resolution step. This domain, called NZ hereinafter, was able

to more adequately capture the oceanic circulation and its variability. The second domain (HRKI) covered the entire Hauraki Gulf and continental shelf surrounding the area of interest with a horizontal resolution of 1.7 km. With this grid spacing, the local bathymetry was more accurately captured resulting in fine scale representation of the local coastal currents. The third domain (WHANG) covers the continental shelf near the area of interest with a much higher resolution (350 m), and resolved the detailed, local wind-driven and tidal circulation, producing accurate currents and thermohaline fields to support the subsequent local scale hydrodynamic and sediment models.

The 3D flow and thermohaline fields were transferred from the top level domains to the refined ones by the offline one-way nesting technique commonly used with ROMS.CFSR 3D fields were fed to NZ at 6-hourly intervals and NZ-HRKI and HRKI-WHANG ROMS at 3-hourly intervals.

All ROMS domains were submitted to spin-up phases prior to the 10-year hindcast period to allow the adjustment of the coarser initial conditions to higher resolution and its better represented bathymetry. The spin-up times were hierarchically established according to the main scales that each one was required to resolve. This information, along with all other relevant information for each of the hydrodynamic model domains considered for this study, is summarised in Table 4.1. The bathymetry for the ROMS grids was derived from electronic navigation charts and field data whenever available.

Table 4.1 ROMS model nests configurations.

Model Settings	NZ	HRKI	WHANG
Horiz Resolution	8 km (0.08° x 0.06°)	1.7 km (0.02° x 0.02°)	350 m (0.004° x 0.004°)
Vertical layers	30	19	15
Tidal forcing	No	No	Yes
Meteo forcing	MSL WRF NZRA	MSL WRF NZRA	MSL WRF NZRA

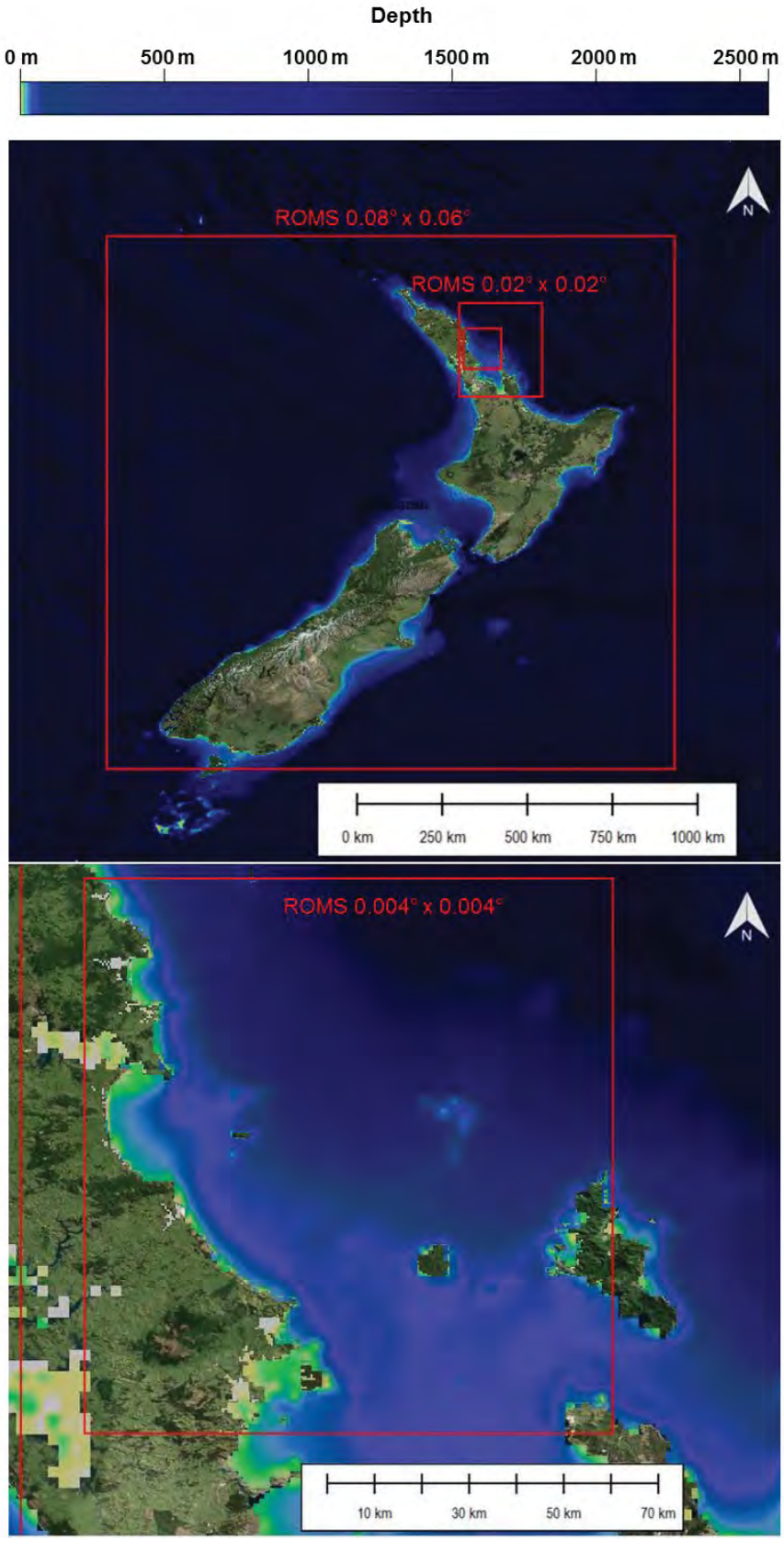

Figure 4.1 Hydrodynamic hindcast modelling approach with ROMS. Upper panel shows the NZ domain, and HRKI domain and lower panel shows the WHANG domain.

4.1.3. Atmospheric forcing

Atmospheric forcing for ROMS was derived from the WRF model outputs described in Section 2. Horizontal resolution varied from 16 to 4 km in the ROMS modelling area. Atmospheric fields consisted of winds, atmospheric pressure, relative humidity, surface temperature, long and short wave radiation and precipitation rate, imposed at hourly intervals to provide air-sea fluxes to drive ROMS in all domains, using a *bulk flux* parameterisation (Fairall et al., 2003).

4.1.4. Open boundary conditions

High frequency (6-hourly for CFSR-NZ and 3-hourly for NZ-HRKI and HRKI-WHANG) open boundary 3D thermohaline, velocity and sea surface height fields were included for all domains. Passive/active prescriptions were applied for all 3D variables at the open boundaries, where a radiation scheme was applied when outflows were estimated by ROMS algorithms. Where inflow was detected, a nudging condition was applied, allowing the penetration of 3D transports and T-S from the external sources, a key setting to guarantee the deep ocean circulation contributions to the smaller scales. To account for the fast propagating tidal oscillations, 2D velocities and surface elevations were treated with *Flather* and *Chapman* schemes, respectively.

4.1.5. Tidal forcing

ROMS WHANG was forced at the open boundaries by tidal elevations and currents, harmonic constituents derived from a MetOcean Solutions‟ New Zealand 2D hydrodynamic model consisting of a 5 km resolution grid, which was in turn forced at its open boundaries by the renowned OTIS Atlantic Ocean solution (Oregon State University Tidal Inverse Solution (Egbert and Erofeeva, 2002).

4.1.6. Model calibration

Through comprehensive testing of model parameters such as sub-grid scale parameterisations, forcing sources and grid settings including open boundary locations, spatial resolution and downscaling rate between parent and child grids, the model was calibrated with respect to available published literature and representation of the main identified forcing mechanisms. Numerical diagnosis such as checking kinetic energy equilibrium and trends in the 3D fields were successfully conducted.

4.2. Model validation

4.2.1. Current measurement program

Four ADCP measurement campaigns were undertaken between January and July 2016 at four different locations (see Figure 4.2). For each deployment, the ADCP was installed on the seabed facing upwards and recording data in 5-minute bursts every 30 minutes. The vertical bins ranged between 0.5 and 5 m depending on the water depth at the deployment location. The water depth and period of each deployment are summarised in Table 4.2 while the geographic coordinates of each deployment are provided in Appendix Aand time series plots of the depth-average data in Appendix B.

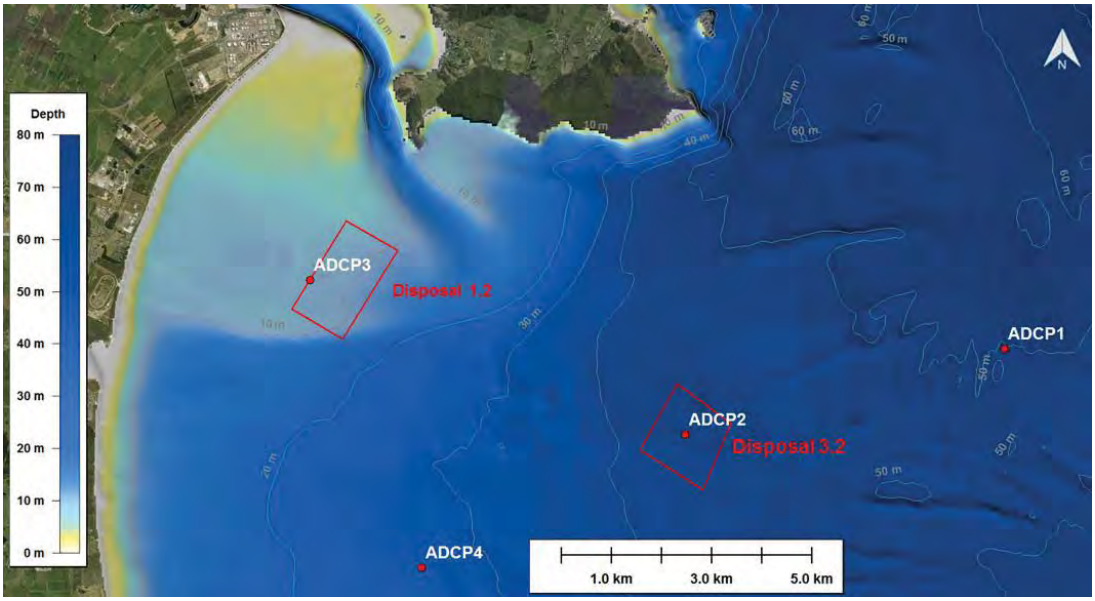

Figure 4.2 Location of the four ADCP deployments in Bream Bay between January and July 2016. The geographic coordinates of each position is presented in Table 4.2. Also shown are the proposed disposal grounds 3.2 and 1.2.

Table 4.2 Details of the current measurement program undertaken in Bream Bay from January to July 2016.

Position	Depth (m)	Measurement period (2016)
ADCP1	50	15 Jan - 5 Mar
ADCP2	44	5 Mar - 14 Apr
ADCP3	9	17 Apr - 3 Jun
ADCP4	25	12 Jun – 14 Jul

4.2.2. Validation

In addition to the 10-year ROMS hindcast used in the study, the ROMS model was run over a two-month period between March and May 2016 to allow the co-temporal validation of the model with measured data at position ADCP2, located at the centre of the proposed disposal ground 3.2 illustrated in Figure 4.2. The validation of the model at position ADCP2 allows a good assessment of the performance of the regional model, which was used to force both the disposal plume and the disposal ground models.

The model outputs were archived at 5-minute intervals to be consistent with the ADCP data, and the modelled and measured current speeds were vertically-averaged from 10 to 30 m depth for the time-domain comparison. Because the measured data duration was not long enough to resolve all tidal components by harmonic decomposition, a 25-hour filter was applied to separate the tidal and non-tidal flows for the validation.

The measured and modelled depth-averaged current velocities (Figure 4.3 - Figure 4.7) indicate that the model faithfully predicts the northeast-southwest bi-modal circulation at position ADCP2. The residual (non-tidal) component of the current is reasonably well replicated by the model, as shown on the Q-Q plot (Figure 4.7, top

plot). The correlation between the model and measured dominant V-component of the non-tidal velocity provides a good level of confidence in the model. Given that the U-component of the velocity is very low (rarely exceeding 0.05 $m.s^{-1}$), the relative low correlation between the measured and the modelled data for this component is assumed to have minor importance on the model performance assessment.

On the other hand, the tidal component is under-predicted by around 20%. This results in a total bias (tidal and non-tidal components) ranging between 5 – 20% of the existing current speed (i.e. between 0.005 – 0.03 m/s). The impact of such bias on the prediction of sediment transport has to be considered based on the local sedimentology, the ratio between currents and waves and the water depth. In this regard, it seemed preferable to discuss the consequences of such bias in the context of short-term and long-term sediment transports caused by the placement of material over the offshore disposal area. This bias in modelled data is therefore considered in the interpretation of the disposal plume and ground modelling results in MSL Report P0297-02 (MSL, 2016). Note that a scenario including the use of measured current profiles as forcing within the sediment transport model was performed to assess the impact of such bias on the model results. Conclusions are also presented in MSL Report P0297-02.

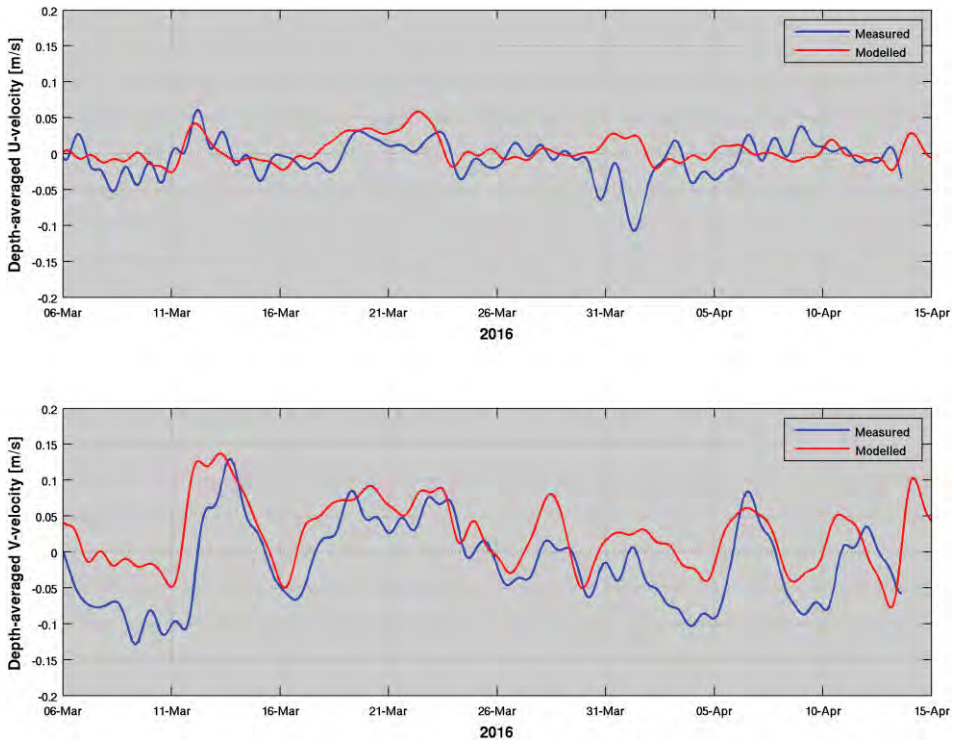

Figure 4.3 Time series of modelled and measured non-tidal depth-averaged current velocity at position ADCP2 from 5 March to 14 April 2016.

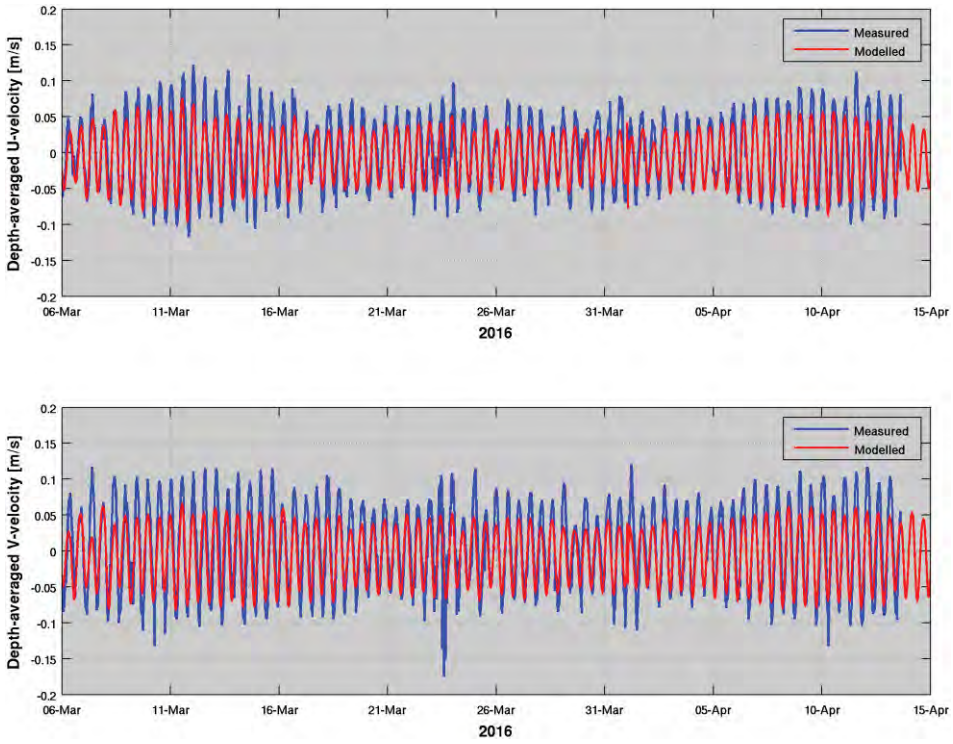

Figure 4.4 Time series of modelled and measured tidal depth-averaged current velocity at position ADCP2 from 5 March to 14 April 2016.

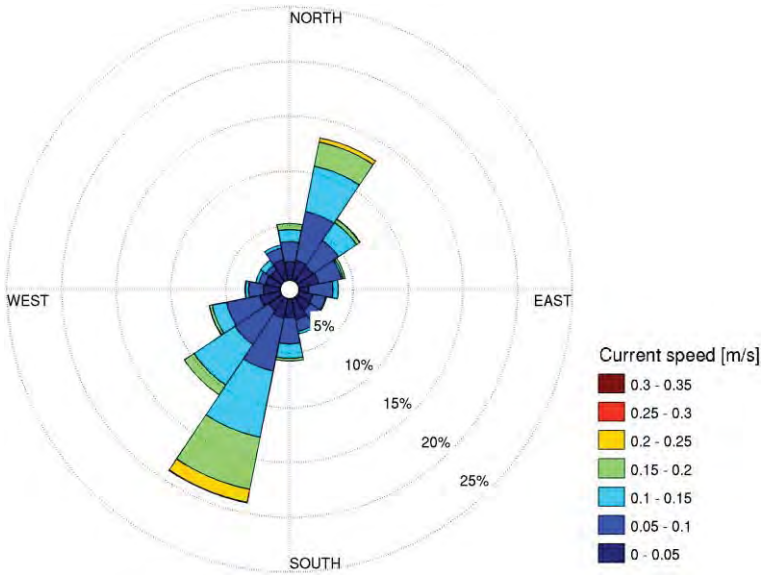

Figure 4.5 Measured depth-averaged current rose at position ADCP2 (5 March – 14 April 2016).

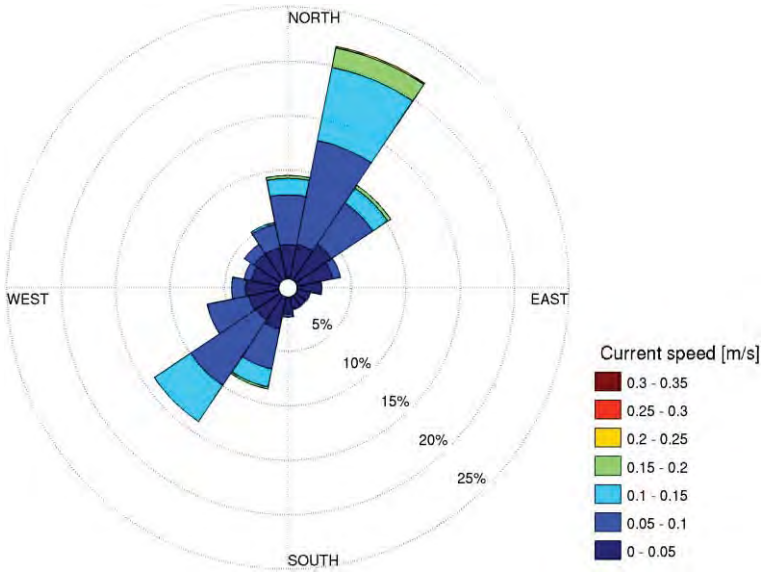

Figure 4.6 Modelled depth-averaged current rose at position ADCP2 (5 March – 14 April 2016).

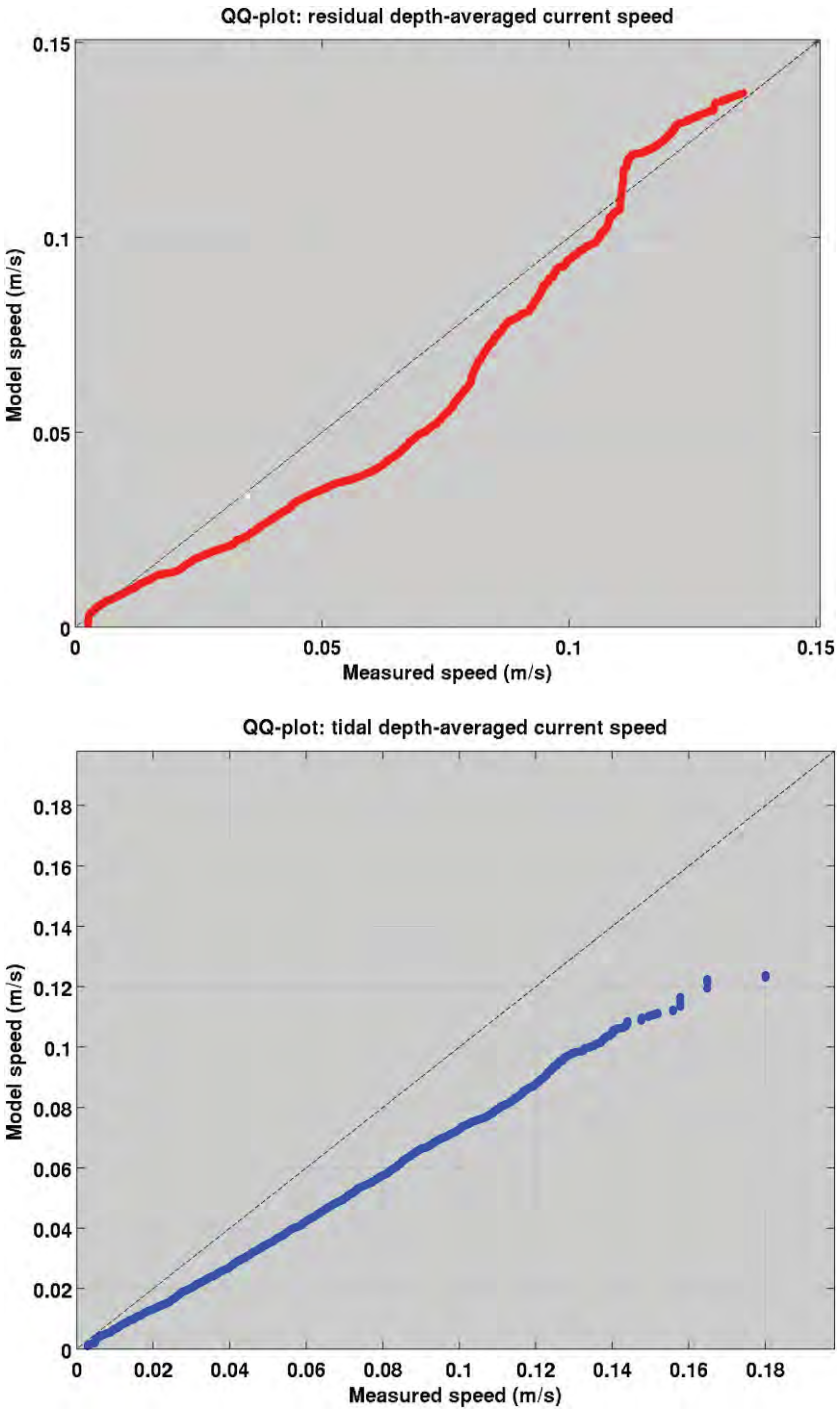

Figure 4.7 Quantile-Quantile plots of the measured and modelled non-tidal (top) and tidal (bottom) depth-averaged current speed at position ADCP2 (5 March – 14 April 2016).

5. HARBOUR TIDAL HYDRODYNAMIC MODELLING

Whangarei Harbour is characterised by a relative complex morphology with numerous channels, sand banks and small islands. In this context, a regional model such as ROMS is not the best option to accurately replicate the tidal flows over the study area and an alternate model, SELFE, was used that was better suited.

This section details the set-up of the high-resolution hydrodynamic modelling that was undertaken to simulate the tidal dynamics over Whangarei Harbour, given that the non-tidal component was of low importance. This nearshore hydrodynamic modelling stage aimed to provide the boundary conditions to the morphological model and assess the effect of the channel deepening on the local tidal dynamics.

The model water elevation and current velocities were validated at several positions within Whangarei Harbour and over the navigation channel using contemporary measured data. The key aim of the present numerical modelling was to capture both the temporal and spatial variability of the tidal dynamics to anticipate the changes in amplitude and phase caused by a different channel configuration.

5.1. Model approach

5.1.1. Model description

SELFE is a prognostic finite-element unstructured-grid model designed to simulate 3D baroclinic, 3D barotropic or 2D barotropic circulation. The barotropic mode equations employ a semi-implicit finite-element Eulerian-Lagrangian algorithm to solve the shallow-water equations, forced by relevant physical processes (atmospheric, oceanic and fluvial forcing). SELFE uses either pure terrain-following sigma, or S-layer coordinates in the vertical, or a hybrid system using both S and Z-layers as required and uses sophisticated vertical turbulent closure models. A detailed description of the SELFE model formulation, governing equations and numerics can be found in Zhang and Baptista (2008).

The SELFE model is physically realistic, in that well understood laws of motion and mass conservation are implemented. Therefore water mass is generally conserved within the model although it can be added or removed at open boundaries (e.g. through tidal motion at the ocean boundaries, or river discharges) and water is redistributed by incorporating aspects of the real-world systems (e.g. bathymetric information, forcing by tides and wind). The model transports water and other constituents (e.g. salt, temperature, turbulence) through the use of triangular volumes (connected 3-D polyhedrons) of varying size and is described as an unstructured finite element model.

5.1.2. Pertinence of the model for the present study

SELFE has been used for the present study as it provides robust capability to replicate the key hydrodynamic processes in shallow and intertidal environments. An important feature is its capability to simulate wetting and drying in shallow areas. The model sensitivity to bottom friction considered as a determinant mechanism in shallow waters has been demonstrated in the past. Moreover, the unstructured triangular grid approach implemented in SELFE allows for increase in model in the channel, along adjacent beaches and over sand banks without increasing dramatically the total computational runtime.

The SELFE model has been extensively applied to study circulation in coastal margins (bays, estuaries, tidal inlets and rivers) around the world (www.strccmop.org), including reported excellent representation of the hydrodynamic in a wave-dominated tidal inlet (Dodet, 2013).

5.1.3. High-resolution bathymetry and domain

Model bathymetries were derived from a combination of relevant ENC (Electronic Navigation Charts), LIDAR, and survey data (single-beam and multi-beam surveys). All data were converted to a common horizontal projection (NZTM), and reduced to a common vertical datum.

The model domain extents and bathymetry are shown in Figure 5.1. The domain was chosen to be sufficiently large to ensure the appropriate tidal boundaries (elevations and velocities) could be applied. The mesh resolution varies from approximately 300 m in the offshore, to ~5 m nearshore and around salient features.

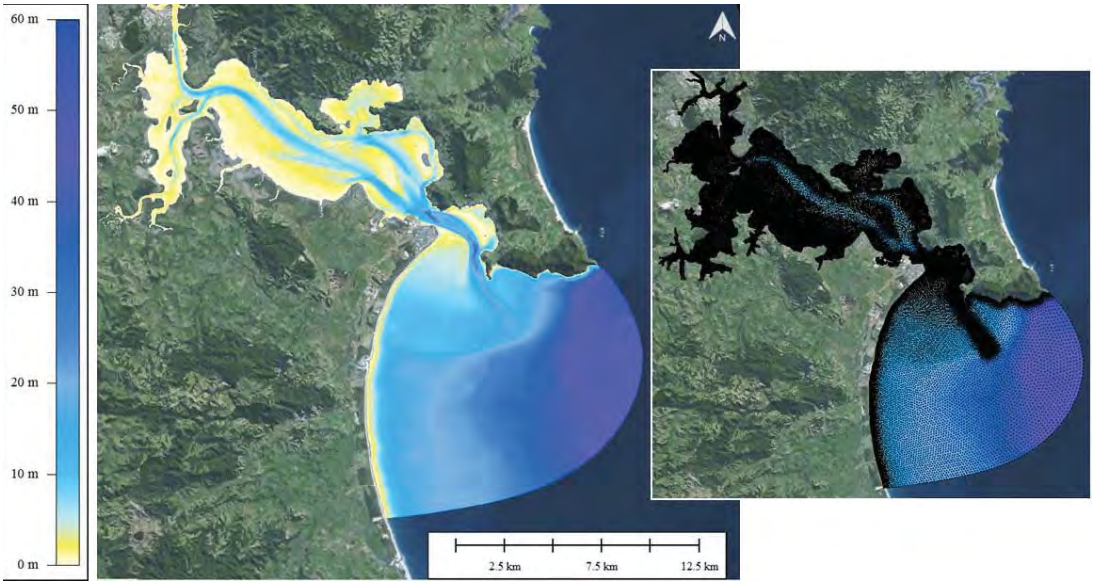

Figure 5.1 Model depth and mesh of the Whangarei Harbour and surrounds. Depths are given in metres below Mean Sea Level (MSL) The mesh covers the offshore region, including the ebb tidal delta, while salient bathymetric features are represented inside the harbour.

5.1.4. Open boundary conditions

A national New Zealand tidal solution derived from an implementation of the Princeton Ocean Model (POM) nested within the TPXO7.2 Pacific inverse tidal dataset (Egbert and Erofeeva, 2002) was used to prescribe the tidal elevation and current velocity at the boundaries of the grid. Depth dependent velocities along the offshore boundaries were defined using a standard logarithmic velocity profile (Van Rijn, 1993).

5.2. Model validation

5.2.1. Data collection program

A targeted measurement campaign was undertaken to provide data specifically for model validation. There were two components; water level measurements at four

locations in the harbour over one month and a moving vessel ADCP survey in the entrance region. ADCP moving vessel deployments have the benefit of providing 3-dimensional velocity data over different sections of the navigation channel thereby allowing a spatial time-dependent validation of the tidal models. Note however that velocity data provided by ADCP moving vessel deployments are slightly degraded by various factors such as Doppler noise, large sampling volume and beam divergence over rapidly changing bathymetry. Nonetheless, it was the preferred method to provide a spatial validation source in the complex tidal flows of the entrance.

In the present study, the ADCP moving vessel deployment was undertaken over three different zones A, B, C illustrated on Figure 5.2 from 19 May to 21 May 2015. Current velocities were measured during 13 hours through each area to capture the peak ebb and flood tidal stages.

5.2.2. Validation results

Comparisons between the measured and predicted water levels (Figure 5.3 to Figure 5.6) indicate that the model reproduces the tidal water elevation variability within Whangarei Harbour well. The magnitude and timing of the tidal propagation throughout the harbour confirms both the suitability of the tidal boundary conditions as well as the ability of the model to replicate the hydrodynamics, which include the prescription of the bathymetry and the frictional parameterisation.

The validation of the depth-averaged flows in the channel indicates an acceptable capability to replicate the complex tidal hydrodynamics at the Whangarei Harbour entrance. Snapshots of the measured and modelled flows are presented in Figure 5.7 to Figure 5.9 for the peak tidal ebb and flood situation. Here, the modelled depth-averaged currents are plotted with co-located measured values. The modelled speeds and directions show good correspondence with the measurements in most of the areas, including the zones of high flow and the recirculating eddy features on the channel margins. This relative good agreement between modelled and measured data is also outlined by the Q-Q plots calculated from the peak ebb and flood tidal velocities for all the measured locations. Note that no statistics are provided for Zone C due to insufficient measured data for a meaningful analysis.

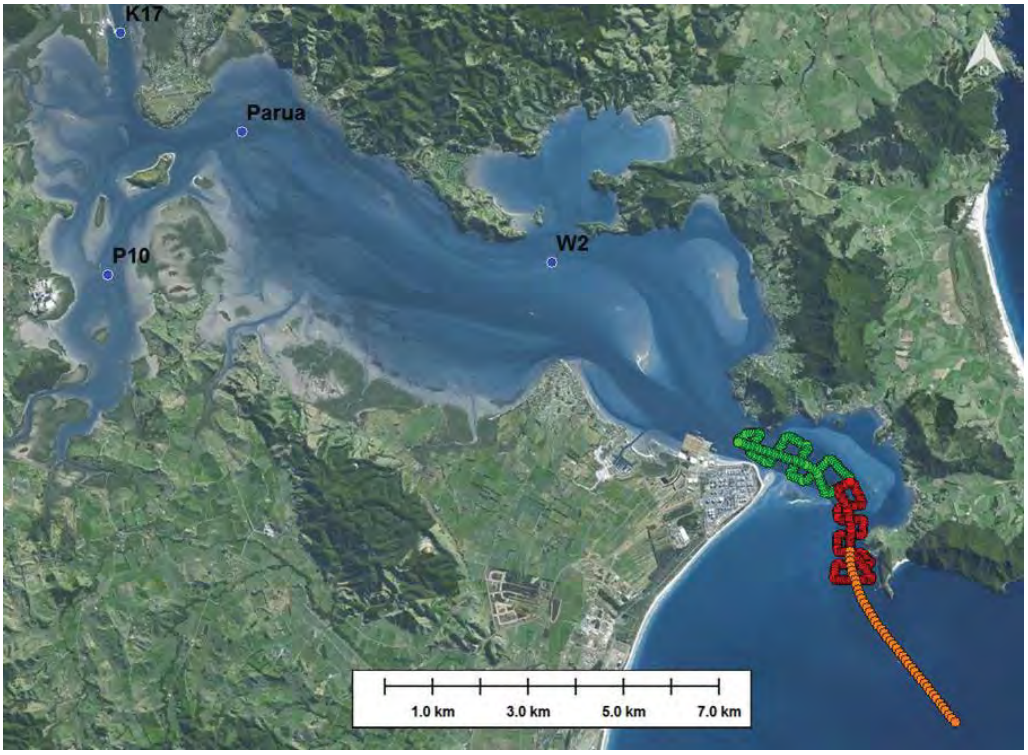

Figure 5.2 Locations of current velocity measurements (Zone A in green, B, in red and C in orange) and water level measurements (K17, P10, W2 and Parua)used to calibrate and validate the SELFE (and Delft3D) tidal model within Whangarei Harbour and Bream Bay.

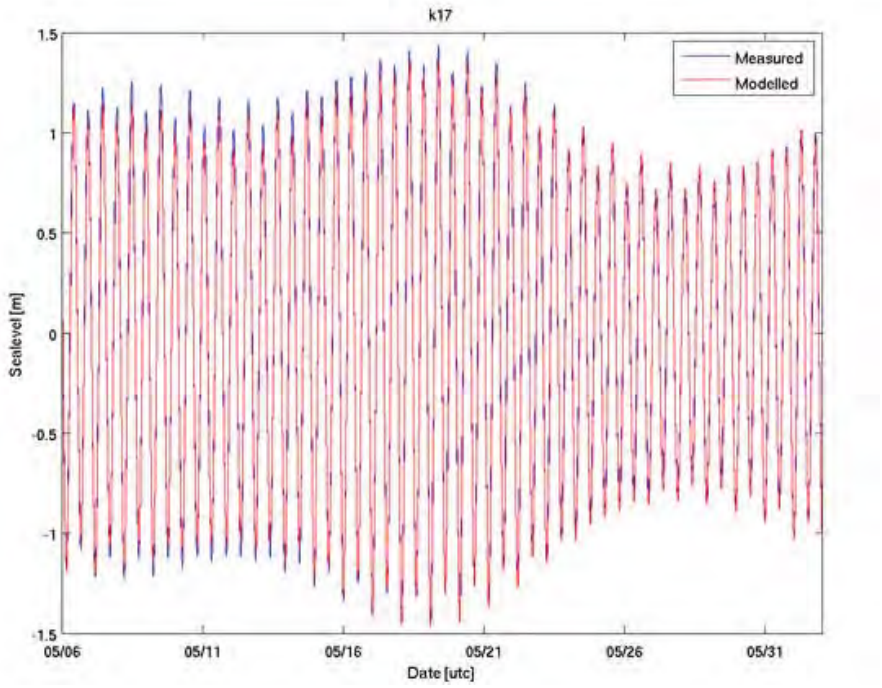

Figure 5.3 Measured and modelled water level comparisons at site k17.

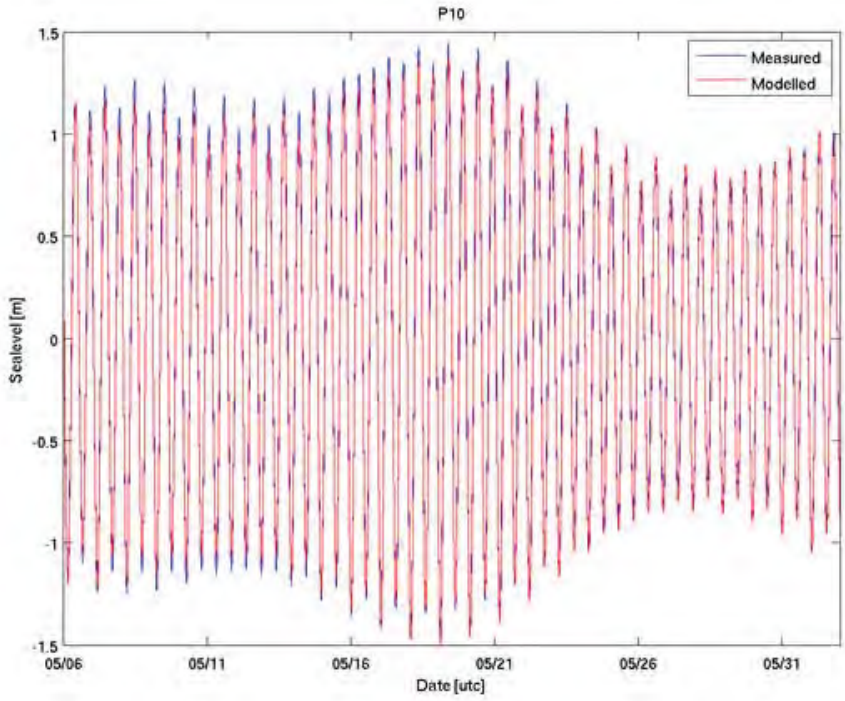

Figure 5.4 Measured and modelled water level comparisons at site p10.

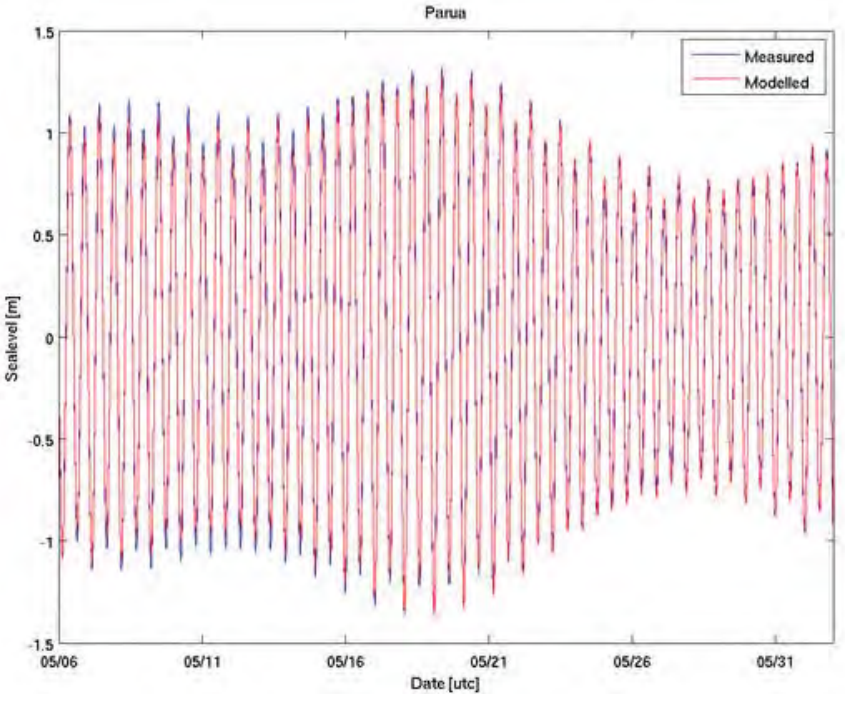

Figure 5.5 Measured and modelled water level comparisons at site Parua.

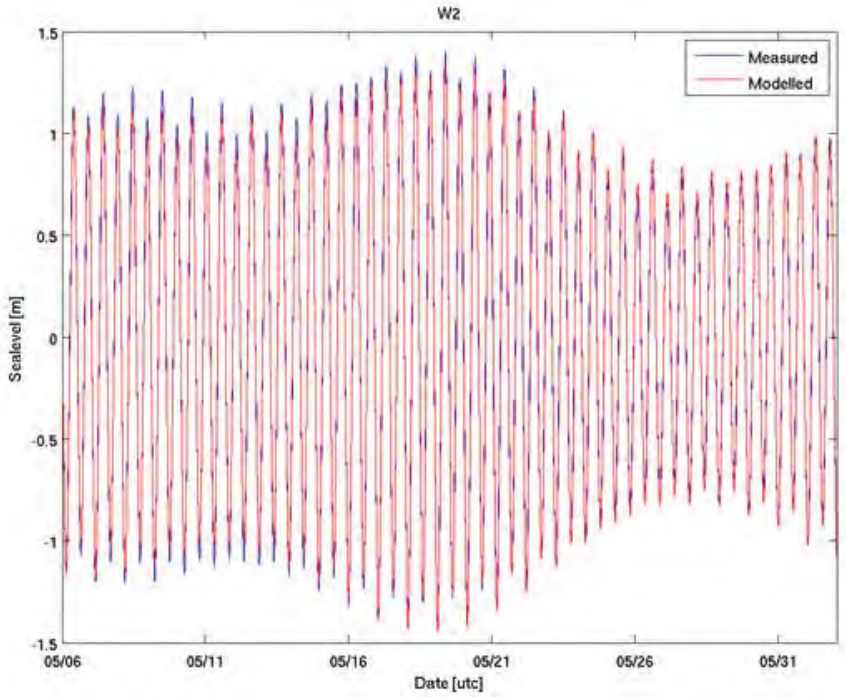

Figure 5.6 Measured and modelled water level comparisons at site W2.

Figure 5.7 Modelled (SELFE) and measured velocity comparisons within Zone A (Figure 5.2) for the peak ebb (upper) and flood (lower) tidal stages.

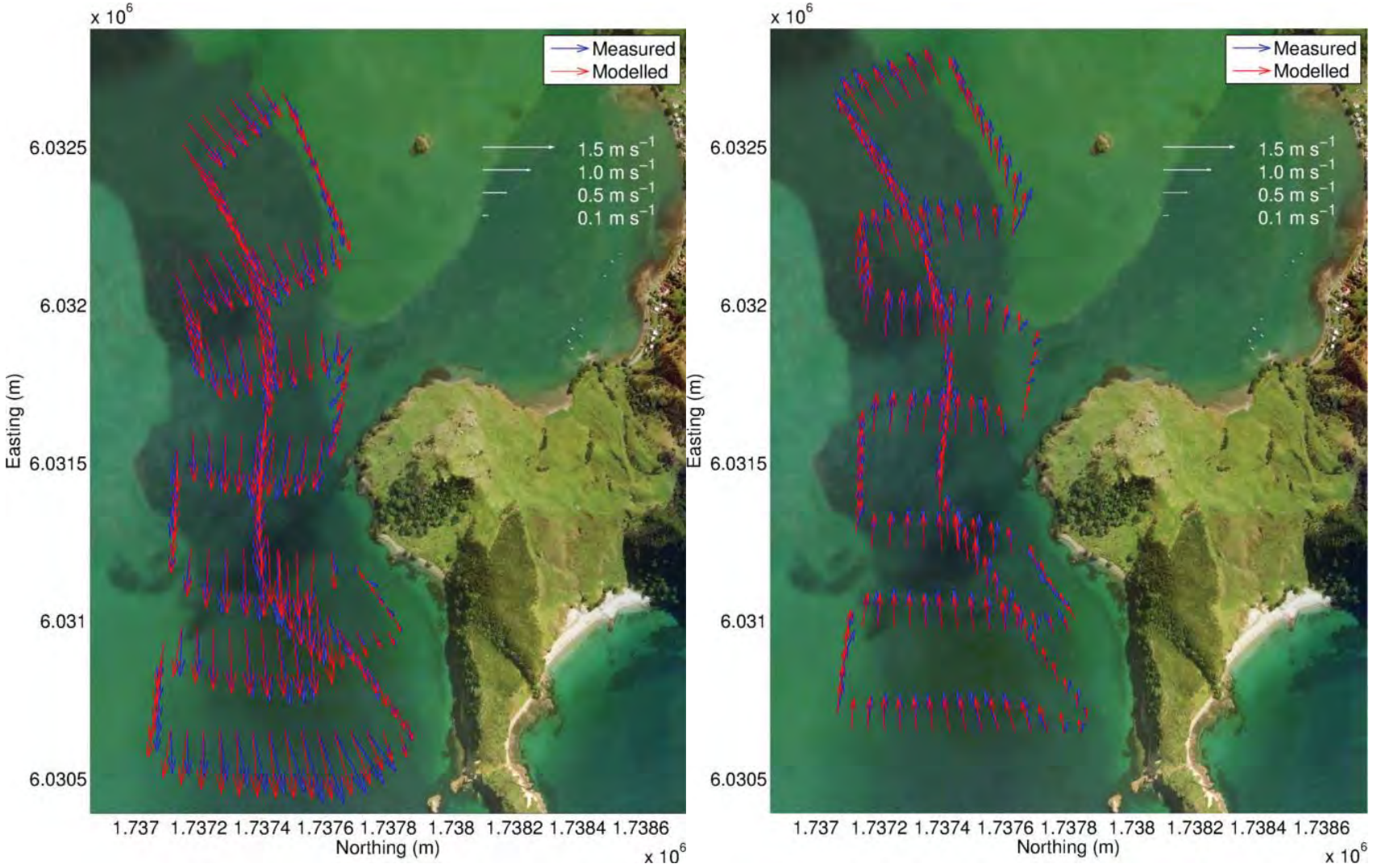

Figure 5.8 Modelled (SELFE) and measured velocity comparisons within Zone B (Figure 5.2) for the peak ebb (left) and flood (right) tidal stages.

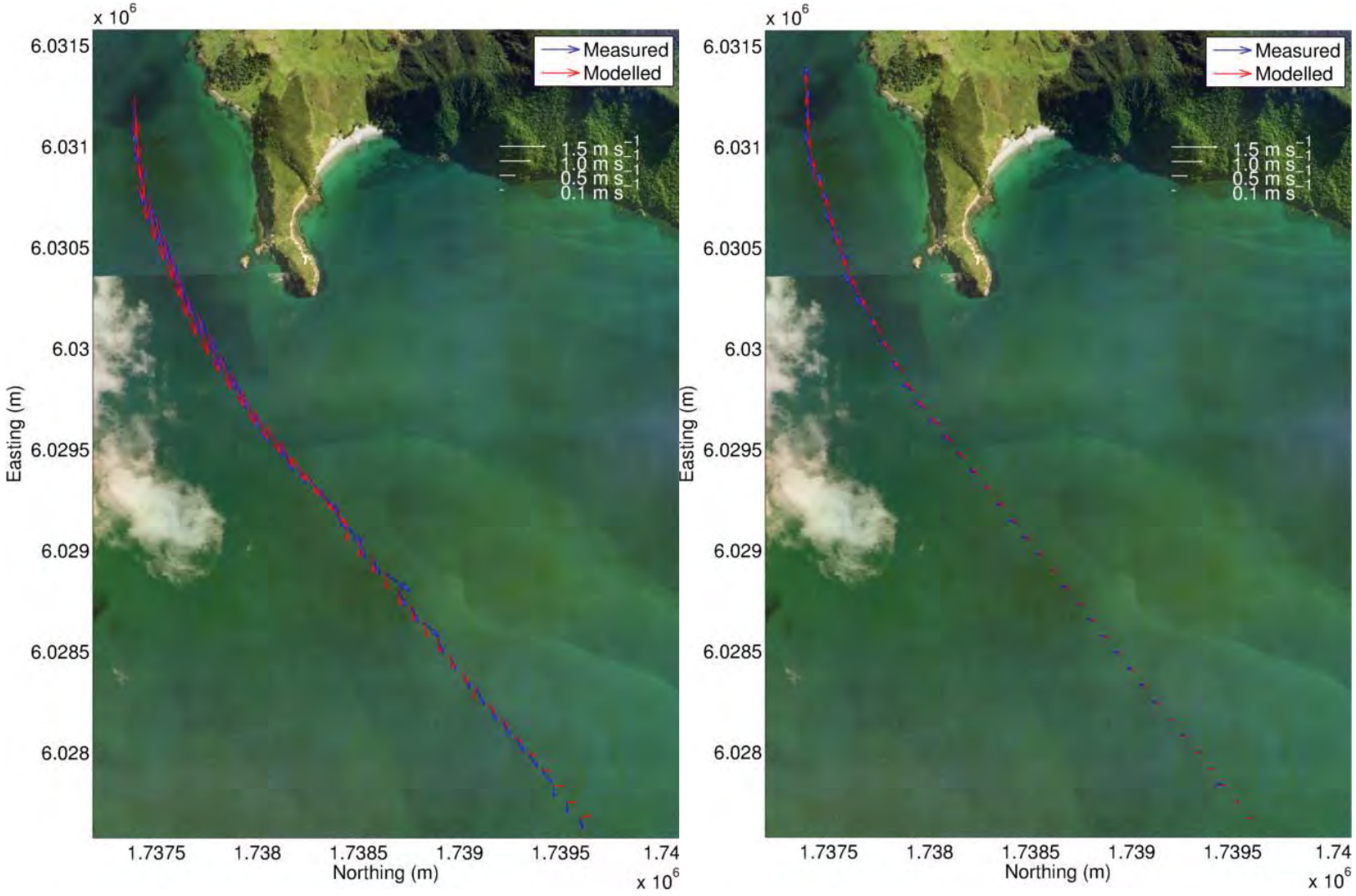

Figure 5.9 Modelled (SELFE) and measured velocity comparisons within Zone C (Figure 5.2) for the peak ebb (left) and flood (right) tidal stages.

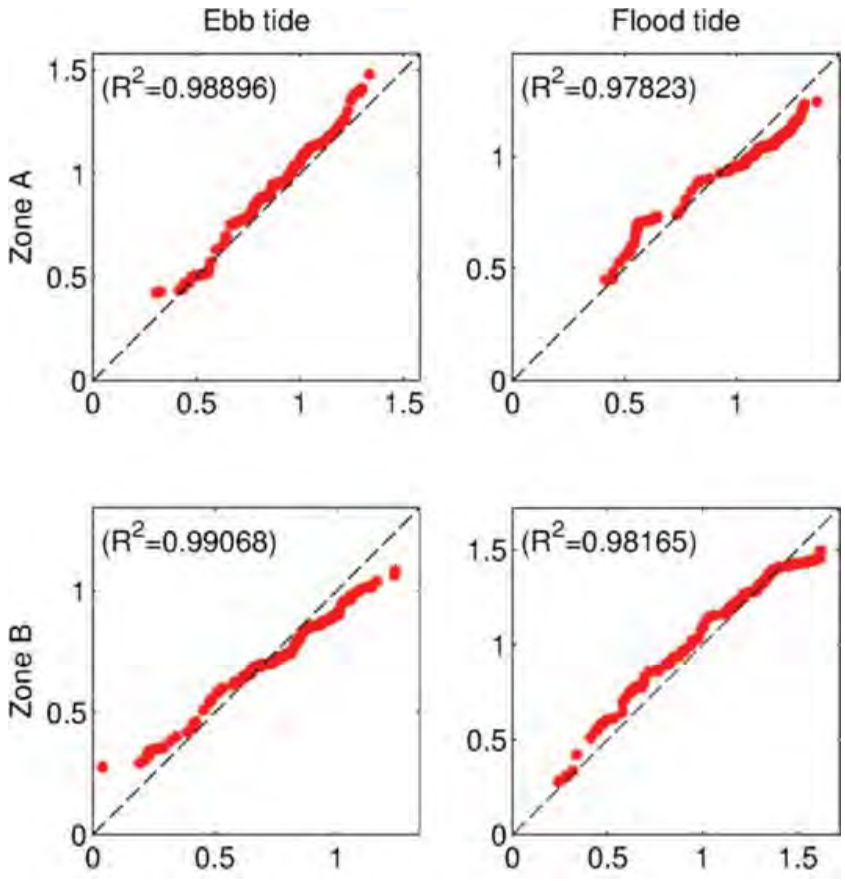

Figure 5.10 Quantile – Quantile plots of the measured and modelled (SELFE) peak tidal ebb and flood current speed (m/s) along the vessel tracks within zones A and B for both peak ebb and flood stages. The root mean squared errors corresponding to the different distributions are presented in the top-left corner of each plot.

6. SEDIMENT TRANSPORT MODELLING

Nearshore wave and tidal models were previously established at the entrance to Whangarei Harbour and the surroundings. One of the purposes of these models was to provide high-resolution data to force the morphological model. Indeed, the overall response of the coastal morphodynamic is largely controlled by the interactions between currents, waves and sediments. In this context, a fully coupled numerical model is required to capture the short-, medium- and long-term morphological processes that affect the study area in order that the effect of the channel deepening on the existing coastal dynamics can be anticipated. The fully coupled process-based numerical model, Delft3D, was thus implemented based on the wave and tidal conditions provided by SWAN and SELFE, respectively.

This section provides an overview of the model as well as the different approaches and settings used to undertake the sediment transport modelling in this highly complex region. The validation of the hydrodynamic component of the model applied to assess the model performance is also presented using the same methodology as previously applied for the SELFE model validation.

6.1. Modelling system

The modelling system Delft3D (Lesser et al., 2004) was used to set up and run high-resolution process-based morphodynamic models. The software is based on interlinking three separate components that together simulate flow, waves and sediment transport. The three components are fully coupled to simulate morphodynamic feedbacks. An overview of the main parameters and components is given in this section.

6.1.1. Delft3D-WAVE (SWAN)

The third-generation SWAN model (Simulating WAves Nearshore) was used as the wave module (Booij et al., 1999; Ris et al., 1999). SWAN computes the evolution of random, short-crested waves in coastal regions with deep, intermediate and shallow water depths. The SWAN model accounts for (refractive) propagation due to depth and current and can represent the processes of wave generation by wind, dissipation due to white-capping, bottom friction and depth-induced wave breaking, and non-linear wave-wave interactions explicitly with state-of-the-art formulations (Deltares, 2013a)).

For the present work, the local wave model boundary conditions were nested with 2D spectral boundaries obtained from a regional scale grid forced either by representative wave events (i.e. accelerated morphological simulations) or real hindcast conditions (i.e. real-time simulations). The nesting allows the retention of spatial variability in the incident wave field due to large scale regional refraction and sheltering effects. Bottom friction was modelled using the formulation of Collins (1972) and the default coefficient value was 0.016. Dissipation by friction and wave breaking was applied in the model. The formulation of Van der Westhuysen et al. (2007) was used to reproduce the wave dissipation due to whitecapping.

Hindcast conditions available at hourly intervals were applied as offshore boundary conditions. This coincides with the interval of the sequential two-way coupling between SWAN and the hydrodynamic module (Delft3D – FLOW) that allows the exchange of relevant parameters on curvilinear model grids via a communication file. Wave parameters and the forcing terms associated with the wave radiation stresses computed by SWAN were read by the FLOW module to model the

hydrodynamic conditions. At the end of each assigned 60 minute runtime, bottom elevation, water level and current fields were used as input to the computation in SWAN. The model loops through these sequential module applications until the end of the complete simulation. Morphodynamic modelling is thus performed through the implementation of a fully coupled wave – hydrodynamic system based on wave and current interactions.

In the scientific community, there is an on-going debate about the vertical distribution of wave-induced radiation stresses that generally split up into a surface component, a bottom component and a body force and their implementation within 3D momentum equations (Ardhuin and Roland, 2013; Ardhuin et al., 2008; Bennis et al., 2011). The debate indicates that important wave-induced processes interacting with the flow circulation may still be inadequately implemented in Delft3D. These limitations are accepted in the present study considering that they do not significantly impact the sedimentology and morphology in the area of interest.

6.1.2. Delft3D-FLOW

The base hydrodynamics were computed in the Delft3D – FLOW module, which can be used in a full 3D or 2DH (depth averaged) mode. The hydrodynamic module Delft3D-FLOW solves the Navier-Stokes equations for an incompressible fluid under the shallow water and Boussinesq assumptions. The system solves the horizontal equations of motion, the continuity equation, the transport equations for conservative constituents, and a turbulence closure scheme. The details of equations and associated sub-models are fully described in Lesser et al. (2004) and in (Deltares, 2013b).

In a tidal inlet environment, the 3D mode is more appropriate than 2D as the cross-shore velocity profile in nearshore areas where breaking waves cause return flow and exhibit a strong vertical shear (Ranasinghe et al., 1999), which can significantly affect bed dynamics of deltas. A calibration process based on a comparison between 2D and 3D modes of Delft3D highlighted important wave effects in the 3D simulation, as wave-induced mass flux adjusted for the vertical non-uniform Stokes drift, additional turbulence and vertical mixing processes and streaming as an additional wave-induced shear stress in the wave boundary layer (Walstra et al., 2001). The model consisted of 10 *sigma* layers in the vertical direction focused on the surface and on the bottom levels of the water column to better reproduce wave – current interactions and sediment transport processes. Model domains implemented in the present study are presented in Section 6.2.

Bed shear stresses were computed using a quadratic friction law. The non-linear enhancement of the bed shear stress in the presence of waves was taken into account by means of the wave-current interaction model of Fredsøe (1984). Turbulence effects were modelled using constant background horizontal and vertical eddy viscosity and eddy diffusivity coefficients. Horizontal background eddy viscosity was set 1 $m^2 s^{-1}$ while diffusivity was equal to 1 $m^2 s^{-1}$. A value of 10e-6 was used for the vertical background viscosity and diffusivity. The bottom roughness distribution used in this study was based on Manning formulation (depth dependency) with a coefficient of 0.02, which is commonly used in Delft3D (Deltares, 2013b).

Current and water elevation conditions at open boundaries were prescribed based on tidal constituents generated from the high resolution SELFE tidal model (see Section 5). Hydrodynamic conditions were provided at intervals of 15 min to the Delft3D – FLOW module. The set value for the numerical time step was 3 s based

on a stability criterion defined for a Courant Number lower than 10 in Delft3D-FLOW (Deltares, 2013b).

6.1.3. Delft3D-MOR

The module Delft3D-MOR combines the information provided by the flow and wave modules to compute the sediment transport fluxes at each computational time step. The seabed level can then be updated as a result of the sediment sink and sources terms and computed transport gradients.

Data on bed composition and sediment properties are essential to adequately predict morphodynamics in nearshore regions, particularly in tidal inlet environments where the seabed composition is usually divided into several fractions of sediments from silty cohesive material to non-cohesive fine gravel.

In the present study, based on vibrocoring results (Tonkin and Taylor, 2016c), model simulations were restricted to non-cohesive sand fractions with a grain size of 200 µm for the potential sediment fluxes approach, and from 100 to 10000 µm for the sediment transport pathways approach. For such an approach, a set of four layers was implemented, including the active layer and the base well mixed layer. Details on the methodology used to generate the bed composition with a multi-layer seabed scheme are discussed in Section 6.3.2.

The biomass of pipi over Mair Bank was mimicked by adding a fraction (80%) of coarse gravel in the uppermost layer of the bed layer model, the so-called active layer. This approach aims to decrease the sediment transport and thus reproduce the overall stability of Mair Bank as observed in Morgan et al. (2011). The potential erodibility of Mair Bank suggested by the shear stress values decreases because the Pipi population causes an increase in the shear stress resistance, as first described in (Black, 1983) and repeated in other studies completed since then.

For non-cohesive sediments, the total sediment transport is defined as the sum of the suspended load and bedload transport. The sediment transport predictor TRANSPOR 2004 of Van Rijn et al. (2004) was used in the present study rather than the default (Van Rijn, 1993) due to the recalibration against new data and the extension of the model to incorporate the wave zone. The approach first computed the magnitude and direction of the bed-load sand transport used by Van Rijn. The computed sediment transport vectors were then relocated from water level points to velocity points using an upwind computational scheme to ensure numerical stability.

The slope of the banks and of the channel is an important factor to consider in a tidal inlet environment. In tidal inlet environments, the non-cohesive bedload transport definitions in the model have a bed slope effect, which represents a gradient in the initial direction of sediment transport. The Bagnold (1966) equations were used for longitudinal transport (*AlfaBs*) and Van Rijn (1993) for the transverse direction (*AlfaBn*). It is reported that *AlfaBs* was of lesser importance in model calibration compared with *AlfaBn* which can cause „unrealistic incision of the main tidal channel" (Van der Wegen and Roelvink, 2008; Dastgheib, 2012; Dissanayake et al., 2012). The default value (AlfaBn 1.5) commonly leads to unrealistic channel slope with gradients larger than the angle of repose. However, calibration processes have shown that decreasing the default values (as suggested in Dissanayake et al. (2012)) leads to significant erosion of the edges of the channel, as a result infilling the channel, particularly to the east and northeast of Mair Bank. In reality, long-term bathymetry surveys between 2000 and 2015 have demonstrated that the channel is morphologically stable (MSL Report P0297-02).

The steep channel slope suggests some degree of cohesiveness and armouring induced by many decades of morphodynamics which cannot be fully reproduced by the model. Consequently, the channel stability was modelled within Delft3D - MOR using the non-restrictive upper range of values for the longitudinal and transverse bed slope factors (1.0 *AlfaBs* and 1.5 *AlfaBn*).

The erosion of dry cells in Delft3D was controlled by the drycell erosion factor (DCE, thetSd keyword in Delft3D) to simulate bank erosion. The DCE default value was originally set to zero in Delft3D. However, calibration processes showed that as suggested in Dissanayake et al (2012) large cell erosion factors produced better representations of the ebb-delta than did low values. Unrealistic seaward extensions of the delta in long term simulations were observed, which is contrary to the evolution of Mair Bank described in Morgan et al. (2011) and Williams and Hume (2014).The use of larger values, 0.5 (50% of erosion in neighbouring dry cell) as defined in the present study, is predicted to improve the model's capability to reproduce the channel morphological variability.

In Delft3D, a commonly used approach for the bed composition modelling is based on 2DH computations as a well-mixed single layer including one or several grain sizes of sediments However, another approach described in Dastgheib (2012) incorporates the concept of layered bed stratigraphy. The bathymetry is subdivided into cells with a specific thickness and a specific fraction of different sediment grain size. The uppermost sediment layer corresponding to the transport layer (or active layer) imports sediments when sedimentation happens and export sediments when erosion happens. In case of deposition, sediment is imported to the transport layer by settling from the water column where it is mixed and redistributed to the underlayer, thereby maintaining its defined constant thickness. In case of erosion, the transport layer imports sediment from the underlayer directly beneath it to replenish and thereby retains its defined constant thickness. The underlayer is indirectly eroded. Conceptually, a layered bed stratigraphy permits specifications of bed composition and sediment characteristics corresponding to the hydrodynamic conditions and the bathymetry.

Both approaches described above have been used in the present study to simulate the potential sediment fluxes and the evolution of the sea bed. Configurations of the underlayers and sediment grain size distribution are described in Section 6.1.2. More information on numerical aspects can be found in the Deltares (2013b).

6.1.4. Pertinence of the model

Interactions between morphological, tidal and wave components play a major role in the dynamics of coastal areas such as bays, estuaries and inlets. In this context, using a process-based model as Delft3D, which integrates a fully 2-way coupled system between these components, is particularly pertinent. Delft3D has been specifically developed to simulate the physics of such complex regions and it provides the necessary multi-disciplinary approach and numerical modelling. Moreover, the Delft3D model has been successfully applied worldwide for a large range of coastal studies over both short – term and long – term periods. In New Zealand, the model has been successfully used at Port Otago (Weppe et al., 2015) and Tauranga Harbour (Ramli et al., 2015).

6.2. Model domains

The Delft3D - FLOW model grid covers the northern region of Bream Bay from the Ruakaka river mouth to Bream Head, and Whangarei Harbour entrance from Mair

Bank to One Tree Point, with grid resolutions of approximately 12 m over Mair Bank and within the inlet channel, and 150 m close to Ruakaka and Bream Head (Figure 6.1).

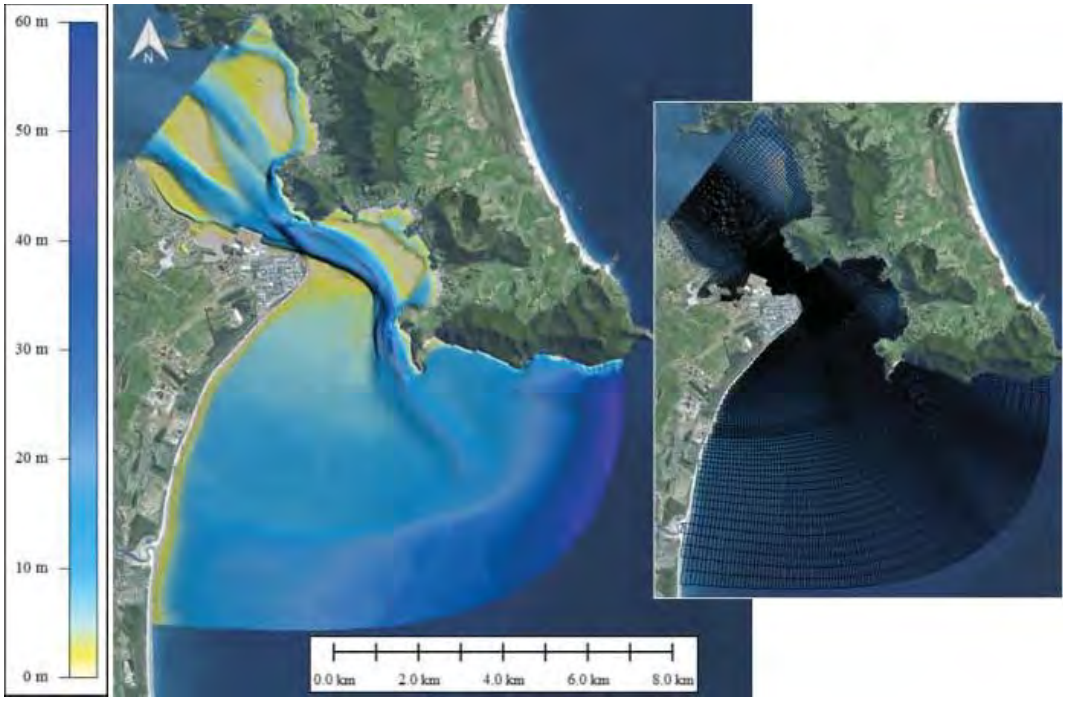

Figure 6.1 Delft3D – FLOW model grid (right) and depths (left).

A one-way online nesting technique was used for the wave modelling based on the implementation of multiple model grids with different grid resolutions. The coarse grid defined within Delft3D – WAVE covers the northern region of Hauraki Gulf, including Mokohinau Islands and Great Barrier Island, with resolutions ranging from 500 m to 3 km (see Figure 6.2). Boundary conditions were nested offline within a coarser regional SWAN domain described in Section 5. The fine grid used in the wave model is slightly more extended along the seaward boundary than the Delft3D – FLOW grid to more accurately force the hydrodynamic model.

The configuration of the model domains has been set-up to fully replicate important physical features in the study area such as:

- The retention of spatial variability in the incident wave field due to both large and high resolution scale regional refraction and sheltering effects.

- The inclusion of the ebb-jet flow extension at the delta entrance.

- The local hydrodynamic current patterns due to the presence of marginal channels sand banks within the harbour.

- The 3-dimensional wave – current interactions over Mair Bank and within the main channel.

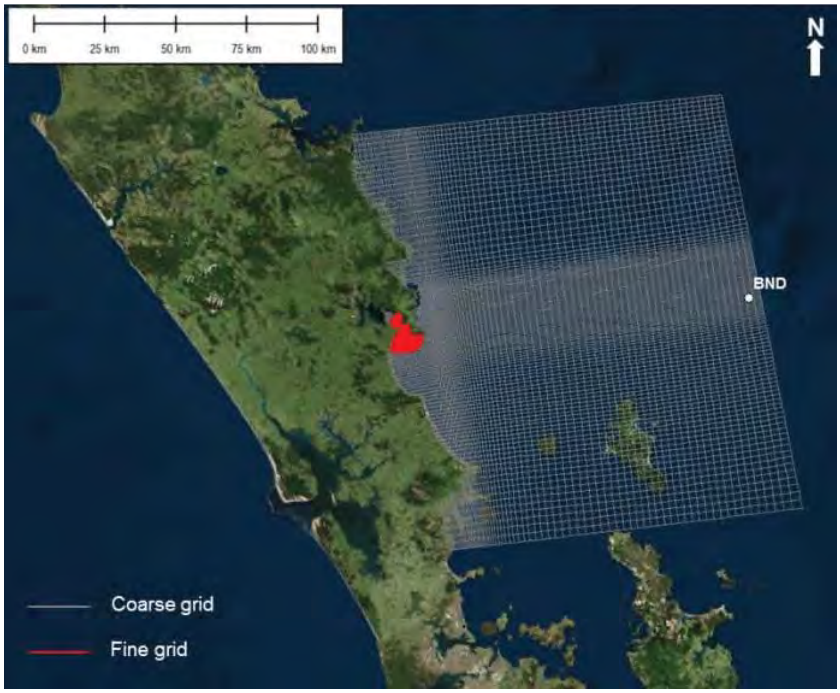

Figure 6.2 Delft3D – WAVE model grids for the modelling of the wave spectral transformation from the offshore region to the coast. The BND position indicates the site used to extract the wave climate described in Section 6.3.1.

6.3. Modelling approach

The main challenge with applying process-based models to predict morphological evolution is that the morphological behaviour of coastal systems generally develops over time scales several orders of magnitude larger than the time scale of the hydrodynamic fluctuations driving the sediment transport (i.e. hours to days versus years to decades and more). This means that while a model system is able to predict the time series of instantaneous hydrodynamics and sediment transport, it will require an unfeasibly long period of time to compute a multi-year real time simulation. Instead, several strategies are commonly used to understand and reproduce morphological dynamics.

The approach employed here combines the reduction of the input forcing (waves and tides) with the use of realistic simulations for both fair-weather and storm conditions. Input reduction essentially means selecting a limited number of representative forcing conditions (i.e. waves and tides) that will reproduce the medium-term residual sediment transport patterns and associated morphological evolution (De Vriend et al., 1993). The application of these techniques to the present study is explained in the following sections.

6.3.1. Hydrodynamic and wave forcing

a) Discrete wave scenarios

- Tidal input reduction

Astronomical tides are deterministic and can therefore be accurately predicted for any period of time. However, tidal oscillations exhibit significant long-term modulations (e.g. spring/neap, yearly and nodal cycles), which make chronological simulations of such cycles computationally demanding. The basis for tidal input

reduction is to find a representative tide that most closely reproduce the net and gross sediment transport as the naturally varying tides over the region of interest and for the time period considered, here one year. In the present study, the representative tide was determined following the approach of Latteux (1995), which is commonly applied (e.g. Brown and Davies, 2009; Dastgheib, 2012; Grunnet et al., 2004).

Tidal signals at a reference point located at the harbour entrance were generated from a high resolution tidal constituents grid, and time series of sediment transport were estimated using a simple power law Q=A.u b (Q is the transport flux, A is a constant factor, u is current velocity, b=5 following Engelund and Hansen (1967)). The single tide best reproducing the net and gross transport magnitude of a given cycle relative to the long term mean transport values was identified and used in the representative scenarios (Figure 6.3).

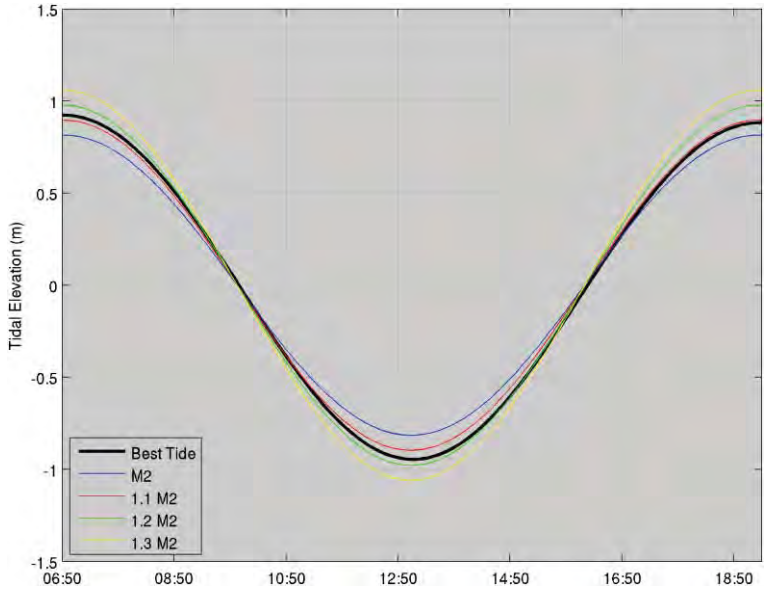

Figure 6.3 Comparison of the best tide, pure M2 tide, 1.1 M2, 1.2 M2 and 1.3 M2 tide curves at the harbour entrance.

- Wave climate reduction

The objective of wave input reduction is to define a set of offshore wave boundary conditions which reproduce the same residual sediment transport patterns and morphological evolution as the real time forcing over a given time period. The approach employed here follows the input reduction framework provided in Lesser (2009) and Walstra et al. (2013).

The first step is the selection of a reduction period, which is the length of the real time wave time series that is used to define the representative conditions. This is typically governed by the time scale of the morphological evolution of interest (e.g. monthly, seasonal or annual behaviour). In the present study, the reduction was undertaken based on a 10 year hindcast wave climate obtained from SWAN simulations to define an average annual wave climate (Section 3). The wave condition timeseries was extracted at the middle of the southern boundary of the wave model domain. In a second step, a set of representative wave classes was defined by distributing the discrete wave data points into a finite number of height and direction bins, and computing a representative value for each bin.

The basic method to determine a representative value within a bin is to use a weighted average of the data points by their frequency of occurrence. To account for the non-linear dependence of sediment transport on wave height, an additional weighting was applied for the computation of the representative height. The initial wave data binning is relatively arbitrary and can be equidistant or non-equidistant (i.e. exhibiting varying bin size). In the non-equidistant case, bins can be defined following either (subjective) scientific judgment or more objective approaches. In the current study, the height and direction bins were defined so that the relative "morphological impact of waves" was similar in each bin (Dastgheib, 2012; Lesser, 2009). The morphological impact of waves of a given wave class was estimated according to the "potential sediment transport" indicator used in Dastgheib (2012).

To automate the determination of bin limits, this indicator was initially computed for a joint probability of wave height and direction with very fine equidistant bins (ΔH=0.1 m, ΔDir=2 deg.). Based on the number of directional and wave height bins to be used for the classification, the directional bin limits were determined first, such that the sum of the morphological impact of waves, Mj, within each bin was (approximately) equal. The same principle was then used within each of these directional bins to define the wave height bin limits. This way, the "morphological impact of waves" was similar in each bin.

The wave climate classification (Figure 6.4 and Figure 6.5) used in the following morphological simulations was defined using four directional bins and four wave height bins. The general classification obtained for the wave climate at the reference site reproduced the different levels of wave energy coming in the northeast and southeast directions.

The wave height delimitations were relatively homogeneous regarding the directionality of the wave propagation:

- 1st class with wave heights of 1 – 2 m.
- 2nd class with wave heights of 2 – 2.8 m.
- 3rd class with wave heights of 2.8 – 3.5 m.
- 4th class with wave heights of 3.5 – 5.4 m.

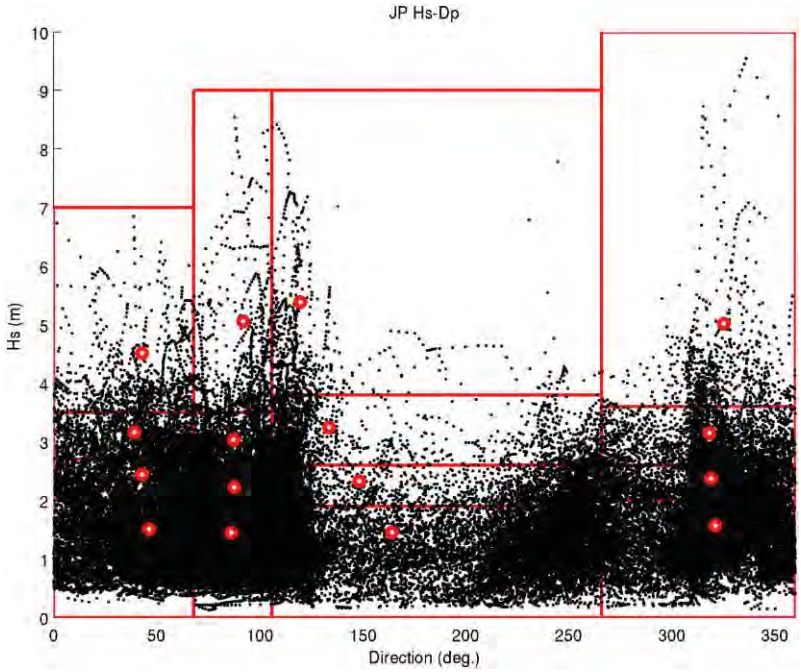

Figure 6.4 Scatter plot of wave heights as a function of wave directions for the 10-year time series, with delimitation of bins (red boxes). Red dots are the representative conditions of each bin.

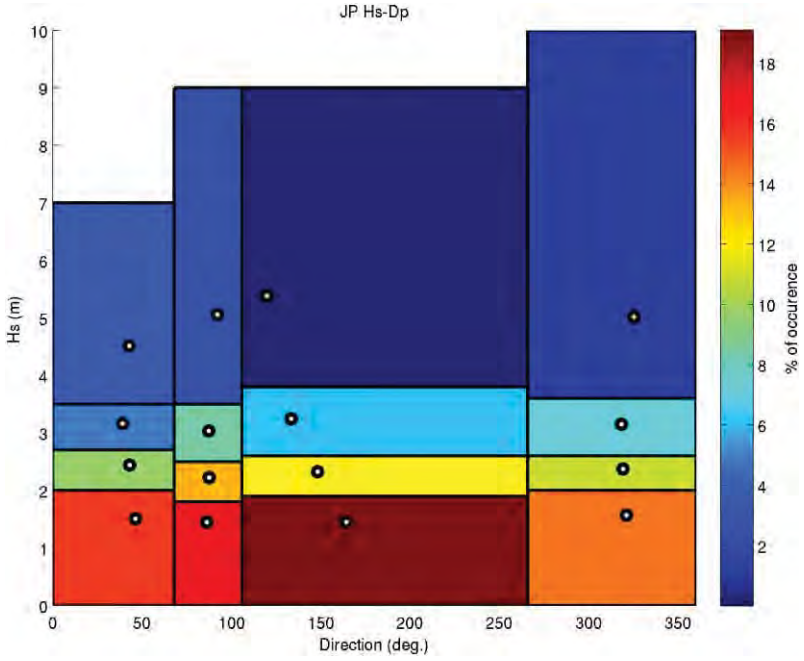

Figure 6.5 Reduced average annual wave climate based on the 10-year wave hindcast using four directional bins and four wave height bins (i.e. 16 wave classes). Colours indicate the probability of occurrence of a given class. The white dots are the representative wave condition of each wave class. Wave classes are summarised in Table 6.1.

Table 6.1 Wave classification based on an average annual wave climate defined from a 10-year hindcast.

Wave class	Representative Hs (m)	Representative Tp (sec)	Representative Dp (deg.)	Probability of occurrence
1	1.5	8.6	46.4	17%
2	2.4	9.0	43.0	4%
3	3.2	9.7	39.1	2%
4	4.5	10.4	42.9	1%
5	1.5	9.1	86.2	18%
6	2.2	10.1	87.6	6%
7	3.0	10.2	87.3	3%
8	5.1	11.0	92.1	1%
9	1.5	7.5	164.3	19%
10	2.3	8.8	148.3	5%
11	3.2	9.2	133.6	2%
12	5.4	10.6	119.7	1%
13	1.6	7.2	321.1	15%
14	2.4	7.4	319.1	4%
15	3.2	8.3	318.3	3%
16	5.0	10.7	325.3	1%

b) Tide-only scenario

A tide-only scenario was run with the best representative tide described in Section 6.3.1 to assess the impact of the tidal flows on the sediment transport dynamics. No wave forcing was considered for this simulation.

c) Historical simulations

The tide-only and discrete wave scenarios were supplemented by historical simulations for both fair-weather and storm conditions (Figure 6.6) based on time series of significant wave height *Hs*, peak period Tp and peak direction Dp provided by SWAN hindcast (see Section 3).

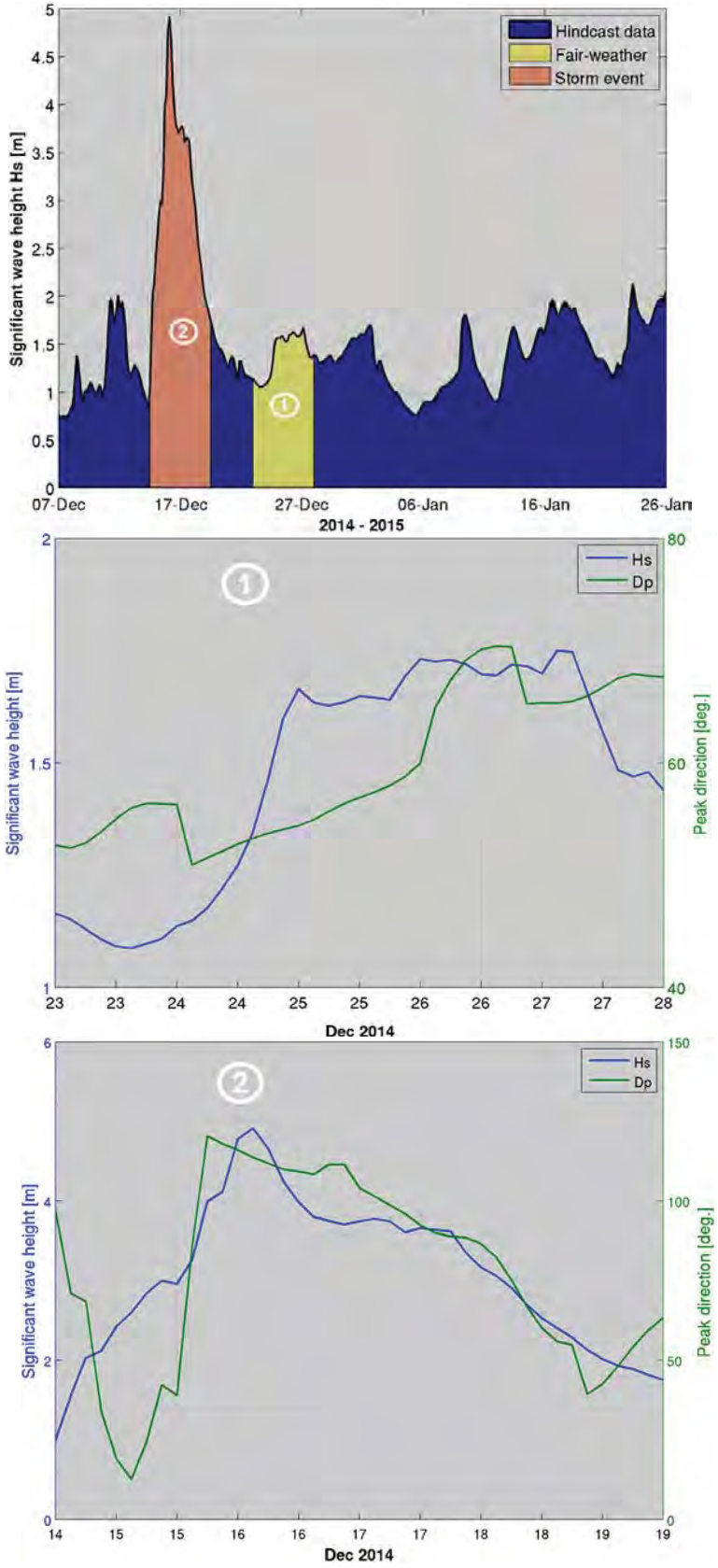

Figure 6.6 Time series of significant wave height and peak direction at location BND (see Figure 6.2) for December 2014 and January 2015. Wave conditions during periods 1) and 2) were used to simulate the sediment transport at Whangarei Harbour during fair-weather and storm conditions.

Firstly, a morphological acceleration factor (Section 6.1.3) of 45 was applied during a simulation of four days to predict the bed evolution that occurred during approximately six months of fair-weather conditions, keeping reasonably fast computations. The aim of this first run was to initialise the sediment grain size distribution over the domain. No bed level update was allowed. More details of the methodology are provided in Section 6.3.2.

In the second phase, the morphodynamic simulation during fair-weather conditions was followed by a 5-day storm simulation without any morphological acceleration (Morfac = 1) to avoid unrealistic changes in the bed evolution over a very short period of time due to high energy wave conditions. The distribution of sediment mass fractions characterised by a 6-month tidally dominated environment was directly fed into the subsequent storm event simulation. Note that the bed level update was turned on to reproduce the residual sediment transport, particularly around Mair Bank.

Finally, the 4-day fair weather simulation was rerun with a MORFAC 4 from the 5-day storm simulation outputs to assess the overall morphological response to a sequence of high/low wave energy events. This corresponds to the morphological evolution of 16 days.

6.3.2. Initial bed configuration and composition

The adequate initialisation of spatially varying grain size distribution of bottom sediment in a process-based model is often constrained by a lack of appropriate field data for the entire model domain. As the sea bed composition is partially dependent on the bed shear stress imposed by the local flow and wave environments, using grain-size observations as initial conditions of simulations based on the author"s judgement from the limited data available generally led to unrealistic erosion or accretion patterns. Indeed, Camenen and Larroudé (2003) and Pinto et al. (2006) have shown that the physical parameter responsible for the greatest errors in the sediment characteristics is the spatial heterogeneity of grain size distributions of the surface sediment in the area of interest. In accordance, two complementary approaches were implemented to avoid this problem.

First, the conceptual models, including both the “tide-only” and the discrete wave scenarios, were set-up with a homogenous 200 µm grain size sediment layer and a fixed bathymetry to determine the sediment transport fluxes in the system. No modification of the sea bed during the simulation was allowed. Such a method is particularly helpful for giving an overview of the combined effect of the tidal and wave forcing on the seabed. It was assumed that the critical bed shear stress variability determined by the distribution of the sediment grain sizes would make a difference in the results.

The second method applied in the present study is described in Van der Wegen et al. (2011) and based on a bed composition generation (BCG) run or “morphodynamic spin-up”. A synthetic simulation was initiated with a uniform sediment type distribution over two bed layers (the active layer and the underlayer) as described in 0. This is depicted in Figure 6.7. Six sediment fractions (100, 150, 200, 300, 500 and 1000 µm) were available at 16.7% mass each according to the general distribution obtained through the sediment sampling study (Tonkin and Taylor, 2016c). The active layer had a thickness of 0.40 m and the underlayer thickness was 10 m. Note that small active layers result in a rapid coarsening of the system which tend to reduce the spin-up for a gain of computational time. Both layers were set-up with the same fractions of sediment grain size. A spatially

limited active layer including 80% of coarse gravel (>10000 µm grain size) and 20% of medium sand was defined to mimic the biomass of pipi over Mair Bank.

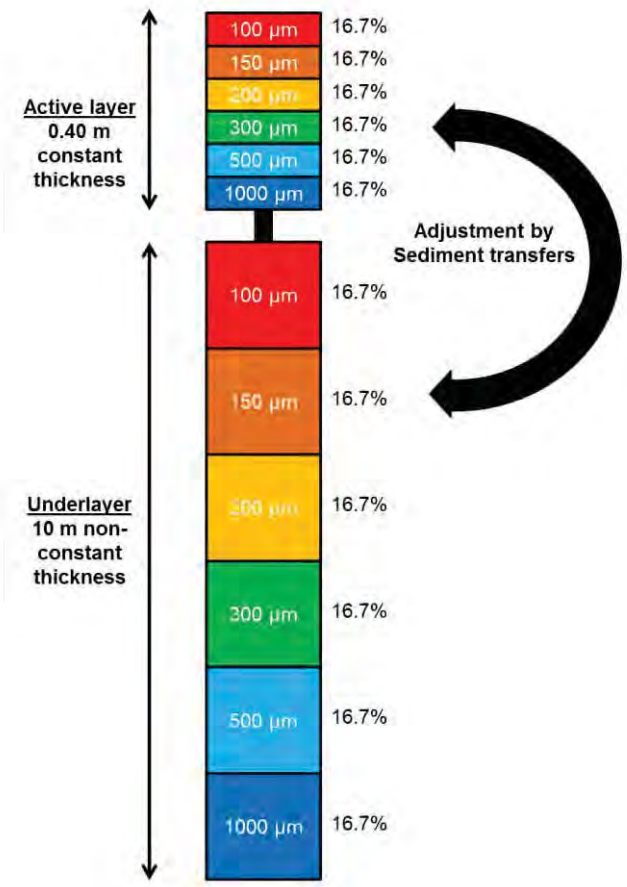

Figure 6.7 Bed stratigraphy approach implemented in Delft3D to initialise the bed composition over the domain.

During the simulation, sediment grain size fractions were redistributed vertically between layers and spatially over the domain in response to the combination of tide-induced currents and low energy wave conditions. At the end of the simulation, the bed composition converged to a more realistic sedimentological setting corresponding to the initial bathymetry, removing errors due to the initial model set-up. The BCG process rendered the model ready to investigate further morphodynamic developments.

6.4. Delft3D – FLOW hydrodynamic validation

The Delft3D – FLOW model was validated based on the measured data provided by the ADCP moving vessel deployment described in Section 5.2.1. Snapshots of measured and modelled peak ebb and flood tidal flows within zones A, B and C over the channel are provided on Figure 6.8, Figure 6.9 and

Figure 6.10. Q-Q plots calculated from the measured and modelled peak ebb and flood tidal flows over these areas are presented on Figure 6.11. Note that these values are not co-temporal; the maximums were extracted from the measured and modelled period from that tidal cycle.

The validation of the depth-averaged flows indicates the model adequately replicates the complex tidal hydrodynamics at the Whangarei Harbour entrance. In Zone A, the model represents the strong tidal flows in the channel between Marsden Point and Mair Bank. Within Zone B, the modelled current fields exhibit good overall agreement with the measured current fields between Mair Bank and the southern margin of Calliope Bank. Both peak tidal ebb and flood current speeds and directions are reasonably well replicated by the model. At Zone C, the peak ebb flows were slightly overestimated.

Figure 6.8 Modelled (Delft3D) and measured velocity comparisons within Zone A (Figure 5.2) for the ebb (upper) and flood (lower) tidal stages.

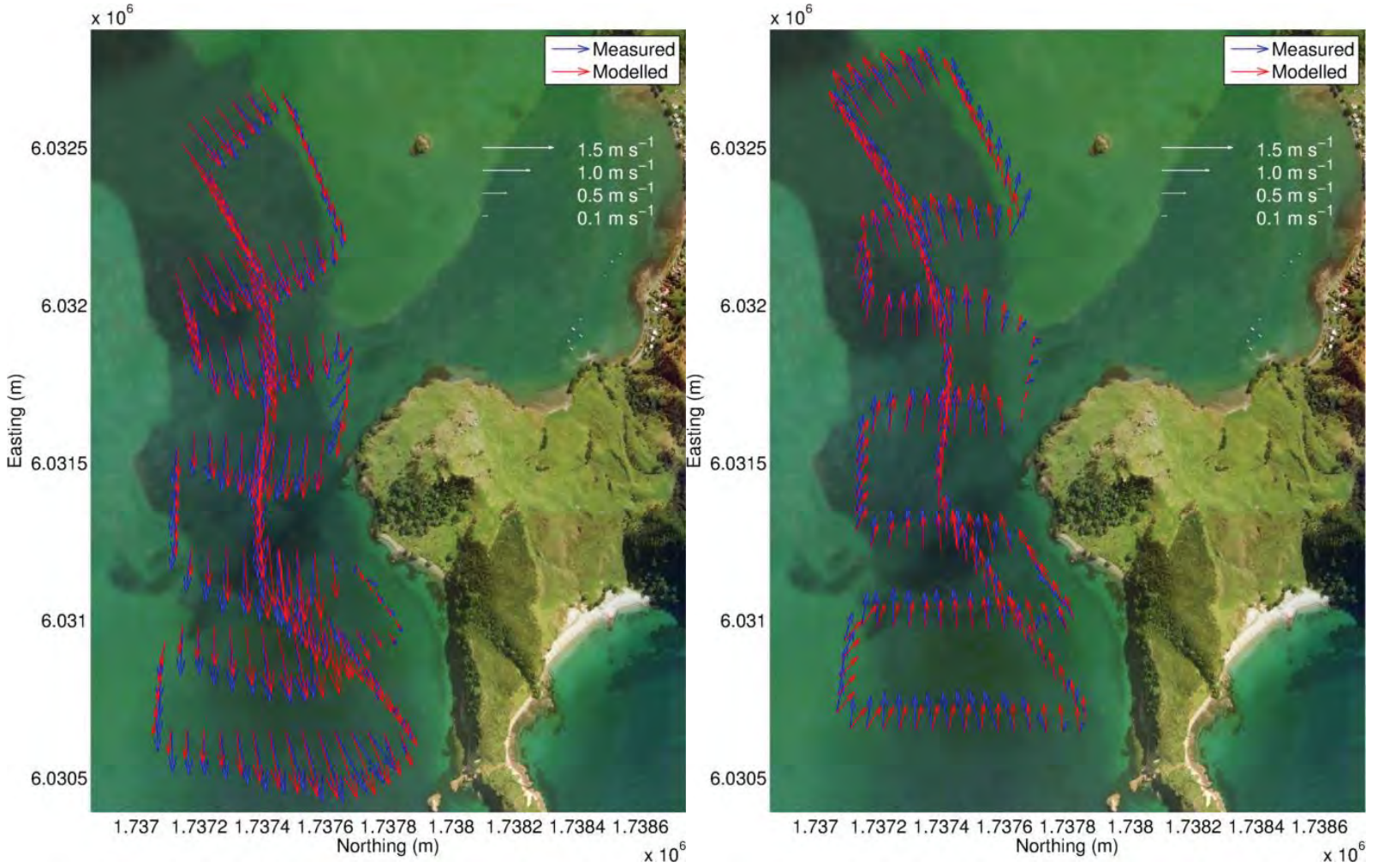

Figure 6.9 Modelled (Delft3D) and measured velocity comparisons within Zone B (Figure 5.2) for the ebb (left) and flood (right) tidal stages.

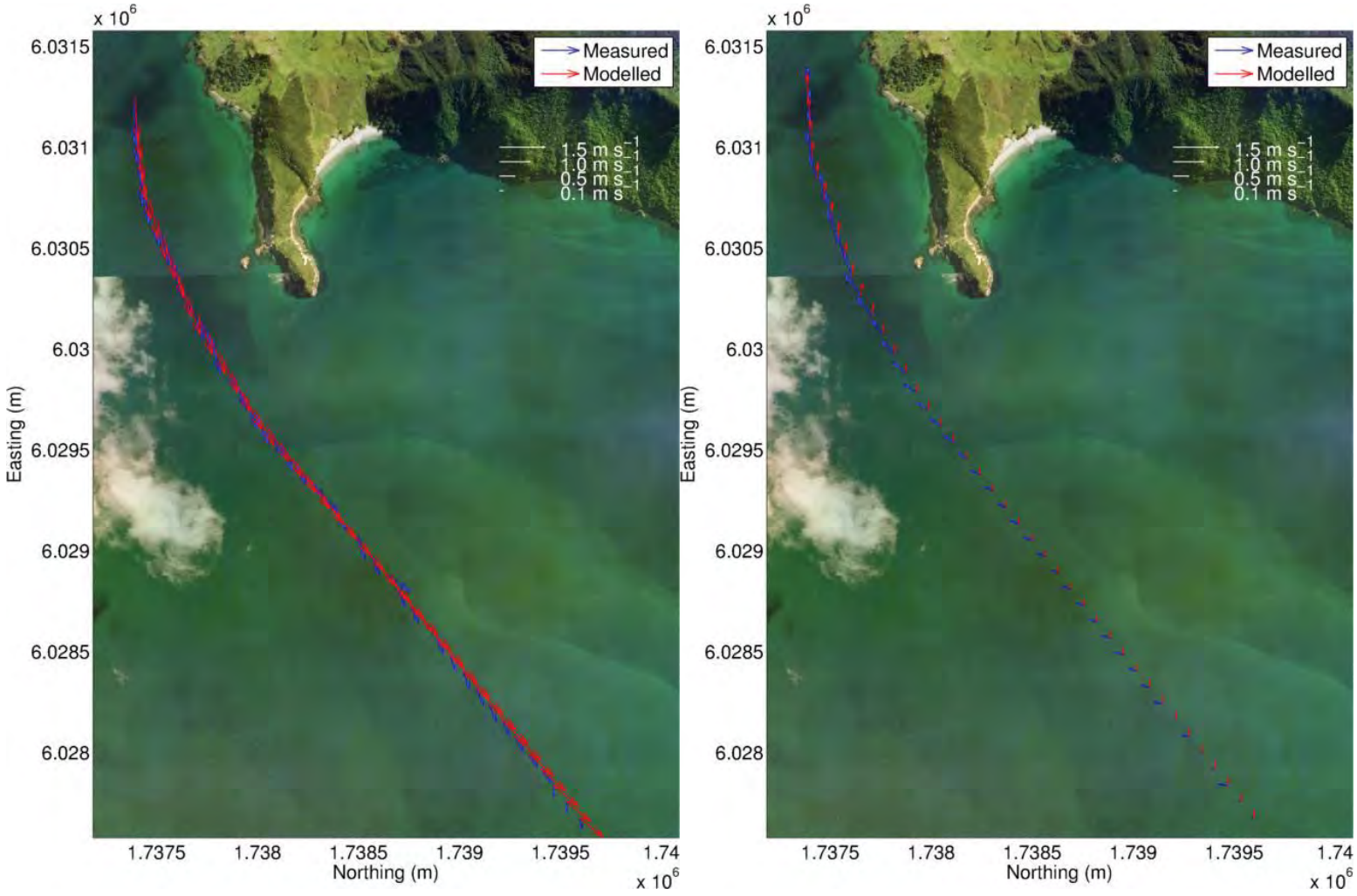

Figure 6.10 Modelled (Delft3D) and measured velocity comparisons within Zone C (Figure 5.2) for the ebb (left) and flood (right) tidal stages.

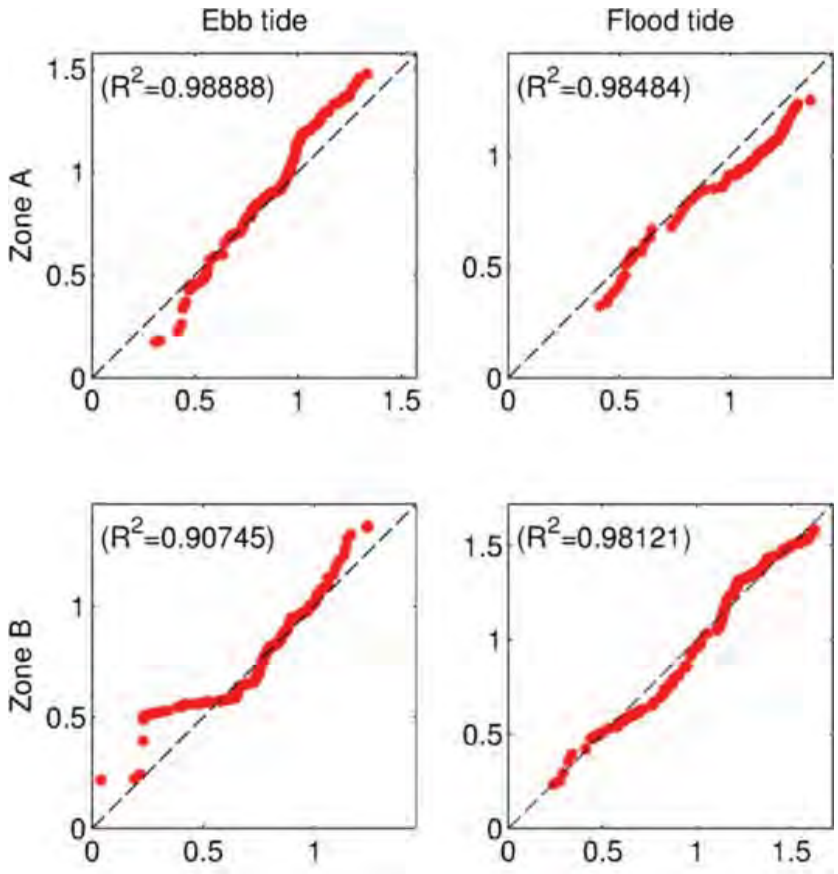

Figure 6.11 Quantile – Quantile plots of the measured and modelled (Delft3D) peak tidal ebb and flood current speed (m/s) along the vessel tracks within Zones A and B for both peak ebb and flood stages. The root mean squared errors corresponding to the different distributions are presented in the top-left corner of each plot.

6.5. Morphodynamic validation

The validation of a morphodynamic model by field observations is generally very difficult to achieve. The complexity of the morphodynamic evolution in a tidal inlet environment driven by both short-term and long-term processes requires appropriate measured data of bathymetry and sediment distribution, which should ideally be available at different time scales and for relatively large areas. Thus, the validation stage can be undertaken on a storm-induced bed evolution or on a long-term bed evolution to verify the level of agreement between the model and the measured data. Both methods provide useful information regarding the capability of the model to predict a range of morphodynamic mechanisms which control the overall tidal inlet dynamics. Analysing storm-induced bed evolution provides both calibration and a quantitative validation of the model configuration, while a long-term bed evolution study is useful in that it qualitatively characterises the overall relevance of the model.

In the present work, more than 15 years of annual bathymetric surveys over Mair Bank and within the tidal inlet channel were available. Such data is particularly valuable for the validation of the model as it describes the relative stability of the system very well. Note however that no validation of a short-term high energy event was possible as detailed pre- and post-storm data are not available. Moreover, the complex interactions between the shell fragment layers, the biomass of Pipi and the existing environment (both hydrodynamic and morphodynamic) made a strictly

quantitative validation of the model difficult. Therefore, the sandbar migrations and the sediment grain size distribution obtained from the BCG run were compared qualitatively to the sediment sampling (MSL Report P0297-02). Available historical bed level data and recent sediment sampling inside the tidal inlet channel (Tonkin and Taylor, 2016c; Williams and Hume, 2014) were used for this purpose.

7. DREDGE PLUME MODELLING

The action of dredging the shipping channel will produce a plume of suspended sediments while the dredger is in operation. This section describes the modelling that was undertaken to simulate the extent and duration of such a plume.

An actual release of sediment in the oceanic environment is a process that is finite in time (i.e. occurring at a specific time, over a finite period) and inherently non-deterministic (i.e. controlled by a range of random and unpredictable variables such as currents and turbulences). However, unlike the offshore sediment disposal for which a range of forcing may be significant (i.e. wind, wave, residual currents), tidal forcing dominates the navigation channel from the delta entrance to Mardsen Point, the dredging activities within which are the focus of the present section.

The cyclic nature of tides, as well as the ability to confidently predict tidal hydrodynamics with numerical modelling, simplifies the approach to obtain robust estimations of the sediment dispersion patterns. To ensure the expected variability in plume dispersions is captured; simulations are usually undertaken over two complete spring-neap tidal cycles (~ 28 days).

Patterns of the dredging plume dispersion are initially investigated at key tidal stages including peak flows during ebb and flood phases of neap and spring tides. The full spring-neap tidal cycle simulations capture the entire range of hydrodynamic forcing encountered during a cycle; model outputs were combined and further post-processed into probabilistic suspended sediment concentration (*SSC*) fields which provide valuable guidance on the extents and magnitudes of dredging-related plumes.

7.1. Trajectory modelling

ERcore, a Lagrangian model, developed by MSL, was used to simulate the trajectories of particles released at the various dredging sites within the channel and turning basin. The model consists of trajectory scheme applied to the existing 2D Eulerian current field $(\tilde{u}, \tilde{v})$ (Section 0), solving for the motion of discrete particles.

$$\frac{dx_p}{dt} = \tilde{u}(x, y, z, t) + u_t$$
$$\frac{dy_p}{dt} = \tilde{v}(x, y, z, t) + v_t \qquad (7.1\text{ a,b,c})$$
$$\frac{dz_p}{dt} = -w_s + w_g + w_t$$

where (x_p,y_p,z_p) are the particle coordinates,. (u_t,v_t,w_t) are the diffusion components representing turbulent motions, w_s is the particle settling velocity and w_g is a vertical velocity component accounting for bathymetric gradients.

In the horizontal plane, the model uses an Ordinary Differential Equations (ODE) solver, including a 4th order Runge-Kutta method, to calculate the trajectory of a given particle (x_p,y_p) in the time-varying derivative field.

$$\int_t^{t+\Delta t} u_t . dt = \sqrt{6 . k_{u,v} . \Delta t} \; . \theta(-1,1) \qquad (7.2)$$

where $\theta(-1,1)$ is a random number from a uniform distribution between -1 and 1, Δt is the time-step of the model in seconds and $k_{u,v}$ is the horizontal eddy diffusivity coefficient in $m^2.s^{-1}$.

In absence of specific field data on diffusive processes, the determination of the diffusion coefficient $k_{u,v}$ is generally based on guidance from empirical relationships. Several relationships are summarized in Fischer et al., 1979 including that of Elder, J.W., 1956 for simple unidirectional shear flows that estimates the longitudinal diffusion coefficient as a function of the water depth and current velocity of the form,

$$k_{u,v} = 5.93 .H .u^* \tag{7.3}$$

where *H* and *u** are the water depth and friction velocity respectively.

Transverse mixing can be estimated using a relationship of the same form but with reduced proportionality factor (with 50 % error bound).

$$k_{transverse} \sim 0.6 .H .u^* \tag{7.4}$$

The vertical diffusion is generally expected to be at least one order or magnitude smaller. Elder"s formula suggests a vertically averaged value of :

$$k_{vertical} \sim 0.067 .H .u^* \tag{7.5}$$

Here, both depth and mean current velocities vary along the channel but these equations can still be used to provide a bracketing of reasonable diffusion coefficient values for the present application.

Assuming a generic water depth of 16 metres in the channel and a mean current velocity of 0.8 $m.s^{-1}$, the above equations yields coefficient of ~[3-5] $m^2.s^{-1}$, [0.3-0.5] $m^2.s^{-1}$, and ~[0.03-0.05] $m^2.s^{-1}$ for the longitudinal, transverse and vertical diffusivities respectively.

Furthermore, in numerical models, the role of the horizontal diffusion coefficient is also to implicitly account for sub-grid scale turbulent processes such as eddies that are not explicitly resolved in the model due to the limited resolution. This means that horizontal diffusion must generally increase as grid size increases since eddies of increasing scale are unrepresented. Conversely, the reduction of grid size allows explicit resolution of flow patterns and eddies at finer scales which thereby reduce the required amount of added diffusion.

For dispersion at oceanic scales, (Okubo, A., 1971) notably showed that $k_{u,v}$ varies approximately (with wide scatter) as :

$$k_{u,v} = \alpha .L^{4/3} \tag{7.6}$$

where L is the horizontal scale of the mixing phenomena and α is an empirical proportionality factor. The hydrodynamic model resolution in Whangarei Harbour is generally less than 100 m which yields diffusion coefficient of order 0.1 $m^2.s^{-1}$. Here, the average of the longitudinal and lateral diffusivities obtained with the Elder formula yields coefficients of order ~0.1-0.2 $m^2.s^{-1}$. Given results provided by the Okubo Equations, a generic diffusion coefficient of 0.1 $m^2.s^{-1}$ was eventually selected. Vertical diffusion is not expected to be the dominant process during the

descent of the disposed sediment and a small generic value of 0.0005 $m^2.s^{-1}$ was used.

The trajectory of particles in the vertical plane is controlled by the particle's settling velocity w_s, the vertical diffusion component w_t as defined in equation 7.1c, and a component w_g related to the bathymetric gradients to ensure that the trajectory of a particle close to the sea-floor is parallel to it (before settling and diffusion components are applied):

$$w_g = \frac{(h - z)}{h}\left(\tilde{u}(x, y, z, t) \times \frac{dh}{dx} + \tilde{v}(x, y, z, t) \times \frac{dh}{dy} \right) \quad (7.7)$$

where *z* is the particle elevation above the seabed, *h* is the water-column height at the particles' horizontal location (*x*,*y*), $(\tilde{u}, \tilde{v})$ is the current field from equation 7.1 and $\left(\frac{dh}{dx}, \frac{dh}{dy} \right)$ are the bathymetry gradients in the *x* and *y* directions, respectively. Note a logarithmic profile was used to extrapolate the 2D depth-averaged current magnitudes to any water column level (Smart et al., 2002).

In the present model implementation, any particle reaching the shoreline, the seabed or the outside domain boundaries remained at the position of intersection (*i.e.* 'sticky' boundaries), thus allowing no sediment re-suspension.

7.2. Particle size distribution and settling velocity

Representative particle sizes were determined from the observed sediment distribution (Tonkin and Taylor, 2016c). The particle size distribution used for the dredging and disposal plume modelling includes:

- 5% of silt (D50 = 60 µm)
- 26% of fine sand (D50 = 130 µm)
- 59% of medium sand (D50 = 400 µm)

Note that the coarse sand and gravel sediment fractions identified in sampling program were not included in the plume modelling analysis as they settle directly to the bottom and therefore do not contribute to a plume. The very low fraction of clays detected in the sampling results (approx. 0.3%) was considered below the tolerance threshold and was thus not included in the numerical modelling.

Although general equations are available to compute the settling velocity of individual particles of given sizes (e.g. Stokes Law), it is unrealistic to assume that the sediment consists of single particles in the fine silt range (~60 µm or smaller) because of the cohesive nature of material and associated flocculation effects (e.g. Van Rijn, 2007). A representative settling rate of 1 $mm.s^{-1}$ for the flocculated sediment is applied, consistent with the findings of Whitehouse et al (2000) and Smith and Friedrichs (2011). Particle settling velocities were determined using the standard equation of Van Rijn, (1984) for non-cohesive sediment. Dry densities for the silt and sand material were set to 500 $kg.m^{-3}$ and 1650 $kg.m^{-3}$, respectively. The characteristics of the 3 representative classes and relative proportion of the total volumes are summarized in Table 7.1

Table 7.1 Representative median grain sizes, settling velocities, and proportions of total volume released for the 3 discrete sediment classes considered.

	Representative D50 [microns]	Settling velocity [m/s]	Percentage of total volume [%]
Class 1	60	0.0010	5
Class 2	130	0.0080	26
Class 3	400	0.0365	59

Appropriate simulation time steps were chosen to correctly capture the horizontal trajectories due to the ambient tidal and residual flows. A time step of 60 seconds was applied to ensure sufficient resolution of the vertical settling. The total number of particles released per time-step varied for each of the different size classes according to the different settling rates. This ensured a sufficient number of particles remained in suspension, taking into account the diffusion processes and allowing statistically representative concentrations to be derived. For example, a larger number of medium sand particles were released per discharge event compared to the fine sand since a greater proportion of the medium sand would settle over a given time period due to the higher settling velocities. Each sediment fraction is simulated separately and all results are combined afterwards to produce total suspended sediment concentration (*SSC*) fields.

7.3. Dredging scenarios

The processes by which sediment is released and suspended in the water column during dredging operations are briefly outlined in the context of the choice of the source term magnitudes and release depths for the particle tracking simulations undertaken in this study.

The dredging method likely to be used in the present case involves the use of two different types of trailing suction hopper dredgers (TSHD) (one large and one smaller), a cutter suction dredger (CSD) and a backhoe dredger (BHD).

7.3.1. TSHD

TSHD are vessel classes operating in two modes: dredging and overflow modes.

During the dredging phase, sediment is sucked into the hopper using a drag head; a fraction of the sediment disturbed by the drag head is not pumped into the hopper and remains suspended in the water column. Sediment suspension is also expected due to the action of propeller wash (Source 1 and 3 respectively in Figure 7.1). These two sources of sediment suspension form a passive plume that is expected to be contained in the bottom part of the water column. In the present study, the drag head source was defined over the water column at 2 m above seabed, while the propeller source was set to 4 m from the seabed.

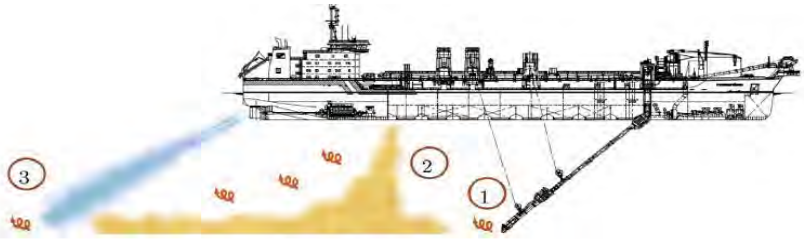

Figure 7.1 Sources of a dredge plume for a Trailing Suction Hopper Dredger: 1-Drag Head, 2-Overflow, 3-Propeller wash (after Becker J. et al., 2015).

The large and small TSHD considered for the present project are characterized by an average dredge work rate of 5400 m^3/hour and 1050 m^3/hour, respectively. Release rates of 6.15 $kg.s^{-1}$ (1.5% production rate) and 12.3 $kg.s^{-1}$ (3% production rate) were used for the drag head source term in the case of the small TSHD. For the large TSHD, values of 31.15 $kg.s^{-1}$ and 62.3 $kg.s^{-1}$ were applied.

The propeller wash component depends on many factors that are likely to vary in time and space (i.e. grain size, draft between prop and seabed, horsepower of dredger, angle of dredger relative to the ambient current etc) and is often included in the term related to overflow (Becker J. et al., 2015). For the purposes of this study, the propeller wash source term is considered separate to the overflow, and defined with rates of 25 and 80 $kg.s^{-1}$ for the small and the large TSHD, respectively, which is considered conservative but not unrealistic for these environs. This initial "dredging phase" will continue until the hopper is full and is expected to last up to 25 minutes in the present application.

After the initial hopper infilling, the actual content of the hopper is a sediment/water mixture which is expected to contain ~20% solids by volume (Spearman, J. et al., 2007). To maximize the amount of sediment in the hopper, the vessel can continue to pump sediment and water into the hopper, which will result in "overflowing" and thereby releasing some sediment into the water column. This phase is referred to as the "overflow phase", and is shown as the source "2" in Figure 7.1. Depending on how the dredge is operated, the overflow rates can create highly-evident sediment plumes.

The overflow load consists of a highly concentrated mixture of sediment and water and the bulk behavior of that sediment mixture becomes dominant over the individual particle settling processes (Winterwerp, 2002). As a result, it is expected that the overflow release will be followed by a dynamic plume phase where the sediment mixture descends to the bottom as a jet-like feature, and impacts the seabed, suspending sediment and forming an initial density driven near-field plume. A fraction of the sediment load will also be de-entrained from the dynamic plume during descent and become suspended in the water column. This is comparable to processes involved during the offshore disposal presented in Section 8 (see Figure 8.1).

The general length scales expected for the overflow process are an order of magnitude smaller than the discharge of sediment at the offshore disposal ground. Additionally, the overflow sediment mixture is less concentrated than in an offshore sediment disposal context. In the present study, this overflow phase was modelled considering two sources of sediment to the passive plume:

- Suspension of sediment de-entrained from the dynamic plume descent uniform released within the entire water column, and
- Passive plume generated following the dynamic plume impact: release within a cylinder of 2 m height and 60 m radius on the seabed (representing the boundary between the dynamic plume collapse and the passive plume).

The release rate of the initial total raw overflow was taken as 63 $kg.s^{-1}$ and 20 $kg.s^{-1}$ for the large and the small TSHD, respectively.

In the present application, a fraction of 25% was considered appropriate for the sediment source term released within the entire column (i.e. sediment suspension due to dynamic plume descent). A similar proportion of 25% was used for the amount of the overflow load found in the bottom source release, i.e. resulting from the density current following the dynamic plume impact (see Figure 7.2). The impact of that overflow phase was tested considering overflow period times of 10, 20, and 50 minutes for both the small and the large TSHD. Maximum overflow period of 79 and 95 minutes were additionally tested for the large and the small TSHD respectively.

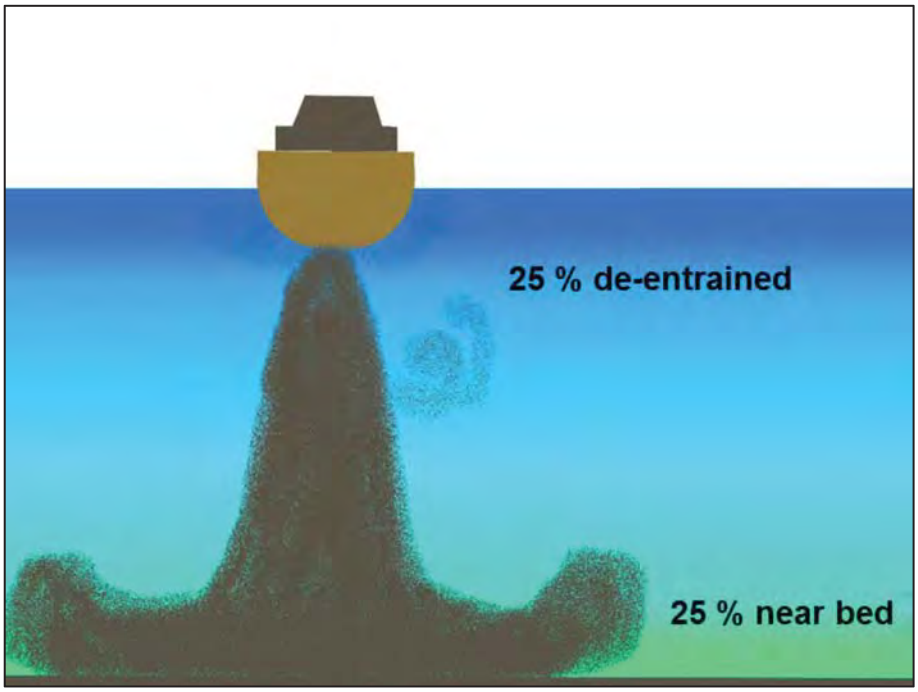

Figure 7.2 Percentages of sediment transferred from the near-field density driven plume to the far-field plume during overflowing

7.3.2. BHD

A BHD (Figure 7.3) is a stationary mechanical equipment, anchored by spuds and usually used for the dredging of small volumes in confined areas. The release mechanisms from a BHD include three main components:

- impact and excavation
- hoisting
- slewing to the barge

The release of sediments associated with a BHD varies with operator expertise and the use of open or closed buckets. A realistic discharge rate corresponding to the bucket source term was defined in Becker et al. (2015) as between 0 – 4 % of the production rate. For dredging at the jetty pocket area three BHD are considered, with production rates ranging between 270 – 475 $m^3.h^{-1}$. At a realistic, but conservative production rate (i.e. 500 $m^3.h^{-1}$), this corresponds to a discharge rate 8 $kg.s^{-1}$ released through the entire water column

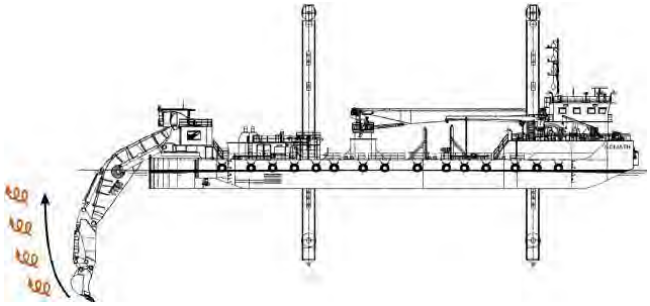

Figure 7.3 Source of a dredge plume for a Backhoe Dredger (after Becker et al., 2015).

7.3.3. CSD

The dredging operations associated with a CSD (Figure 7.4) include two simultaneous phases:

- The (hard) sediments are cut and fragmented by a rotating cutter head using different rotation and swing speeds.

- Sediment is sucked up by dredge pumps, and typically discharged through floating pipeline and pipes to a deposit area.

The sediment release mechanisms are thus largely associated with the rotating cutter head action and are located near the seabed. A fraction of the fragments are expelled during the fragmentation while the turbulence induced by the centrifugal force result in the suspension of sediments around the cutter head.

Although the corresponding sediment source term depends on specific parameters including the cut height and step length, the cutter head rotation and swing speeds, and the suction velocity, discharge rates are typically in the order 1 – 5% of the production rate (Becker et al., 2015). For this project, the CSD was characterised as having an average dredge work rate of 1600 $m^3.h^{-1}$. The resultant sediment discharge associated with the cutter head source term in the plume model was thus taken as 31 $kg.s^{-1}$ near the seabed, based on a 5% conservative discharge rate. Note that CSDs are usually fitted with spuds which increase their precision and avoid any suspension of sediments associated with the propeller wash (e.g. Figure 7.4).

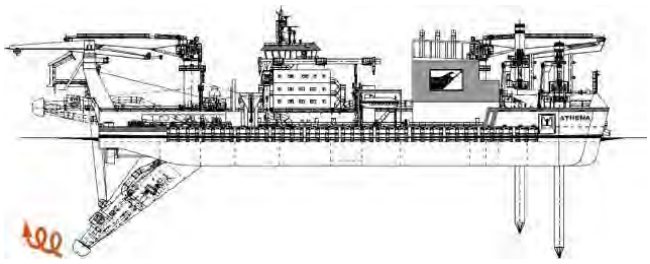

Figure 7.4 Source of a dredge plume for a Cutter Suction Dredger (after Becker et al., 2015).

The use of a CSD for the dredging operations at the jetty pocket and within the inner section of the channel is not the preferred option of RNZ, this dredger has been tested in the present study for completeness in case it"s required as an option.

7.4. Post-processing

The results of the 28-day particle tracking simulations were post-processed to produce maps of the instantaneous and probabilistic suspended sediment concentration fields. The probabilistic approach aimed to provide sufficient statistical power (capturing the effect of the monthly tide variability) to investigate the 3D plume dispersion associated with the sediments released by the dredging operations. This process, which is statistically more robust than a case by case approach, nevertheless requires a significant computational runtime. In the model, sediments are released continuously for 28 days, allowing consideration of two complete spring / neap tidal cycles.

The general methods employed to reconstruct concentration fields from the particle tracking model outputs are outlined below.

7.4.1. Concentration and depositional thickness computation

To reconstruct concentrations from the particle tracking simulations at chosen receptors, a kernel method with variable bandwidth was used. The use of a variable bandwidth (kernel size) attempts to represent true variability of spatial concentration, while minimizing statistical variability that inevitably occurs away from the source due to a necessarily finite number of particles. A small kernel is used in regions gathering a high number of particles, where it is statistically appropriate to infer relatively small scale changes in concentration. Conversely, a larger kernel is used in regions presenting a low number of particles, so as to prevent unrealistically high concentrations around the precise (but partially random) locations of a few isolated particles.

In practice, the concentration C at a given receptor location (x,y) is computed as:

$$C(x,y) = \sum_{i=1}^{n} \frac{m_i}{\lambda_x(x,y)\lambda_y(x,y)} K\left(\left|\frac{x_i - x}{\lambda_x}\right|\right) K\left(\left|\frac{y_i - y}{\lambda_y}\right|\right) \tag{7.8}$$

where (x_i,y_i) is the location of each particle i, n is the total number of particles, m_i is the loading for each particle, λ_x and λ_y are the kernel bandwidth in the x and y directions for location (x,y) and K is the kernel function.

Following Vitali et al. (2006), an Epanechnikov kernel function was used:

$$K(q) = \begin{cases} 0.75\left(1 - q^2\right), & |q| \le 1 \\ 0, & |q| > 1 \end{cases} \tag{7.9}$$

where q is the ratio of the particle distance from receptor to bandwidth ($q_x = d_x / \lambda_x$, or $q_y = d_y / \lambda_y$).

A receptor-based method derived from the RL3 method in Vitali et al. (2006) was used to define the bandwidths λ_x and λ_y.

For each receptor location, a neighborhood was defined as the region enclosing the 1/20th closest particles. Then, for each direction x and y, the bandwidths λ_x and λ_y were defined as the minimum value between the maximum projected distance of the particles within the neighborhood and twice the standard deviation of the projected distances within the neighborhood. Finally, in order to prevent

unrealistically elongated kernels, the aspect ratio λ_x / λ_y was limited to be no greater than 5:1, with the smaller value increased.

The loading of each particle directly depends on the quantity being modelled. Here, each discrete particle was attributed a certain sediment mass which was determined as the ratio from the total true sediment volume of a given class released per step, to the total number of particles of that class introduced in the model at each release.

7.4.2. Application to the present study

Sediment concentration fields were determined following the methods outlined above for the suspended particle cloud associate with each sediment class. The individual sediment concentration fields were then combined to produce total SSC magnitudes considering all sediment classes. The particle load governs the concentration magnitudes and is a function of the amount of sediment released into the environment and the number of particles modelled. The predicted suspended sediment concentrations should be interpreted as dredging-related SSC only, and would add to any ambient SSC from other sources, such as river inputs or catchment run-offs.

7.5. Sites for dredge plume modelling

Nine sites along the navigation channel were used to simulate the dredge plume dispersion. The maps of peak ebb and flood tide flows over the channel (presented in MSL Report P0297-02) shows limited spatial variability in current velocities within each proposed dredged area. Using a limited number of points over the channel to perform the dredge plume modelling was thus justified in the present study. Locations and water depths associated with the different sites are presented in Table 7.2 and Figure 7.5.

The plume modelling at positions R0 to R8 was undertaken using the existing hydrodynamic fields from the SELFE model. Note however that hydrodynamic conditions at positions R2, R3 and R8 were derived from both the existing and the post-dredging configurations to assess the impact of changes in the hydrodynamic field on the plume dispersion.

Table 7.2 Depths and depth changes of release sites along the dredged channel.

Positions	Existing depth [m]	Depth $_{\text{post-dredging}}$ – depth $_{\text{existing}}$ [m]
R0	12.4	5.3
R1	16.3	2.1
R2	15.0	3.7
R3	15.2	4.4
R4	16.5	3.5
R5	16.7	3.8
R6	16.2	2.7
R7	17.2	1.1
R8	17.8	0.5

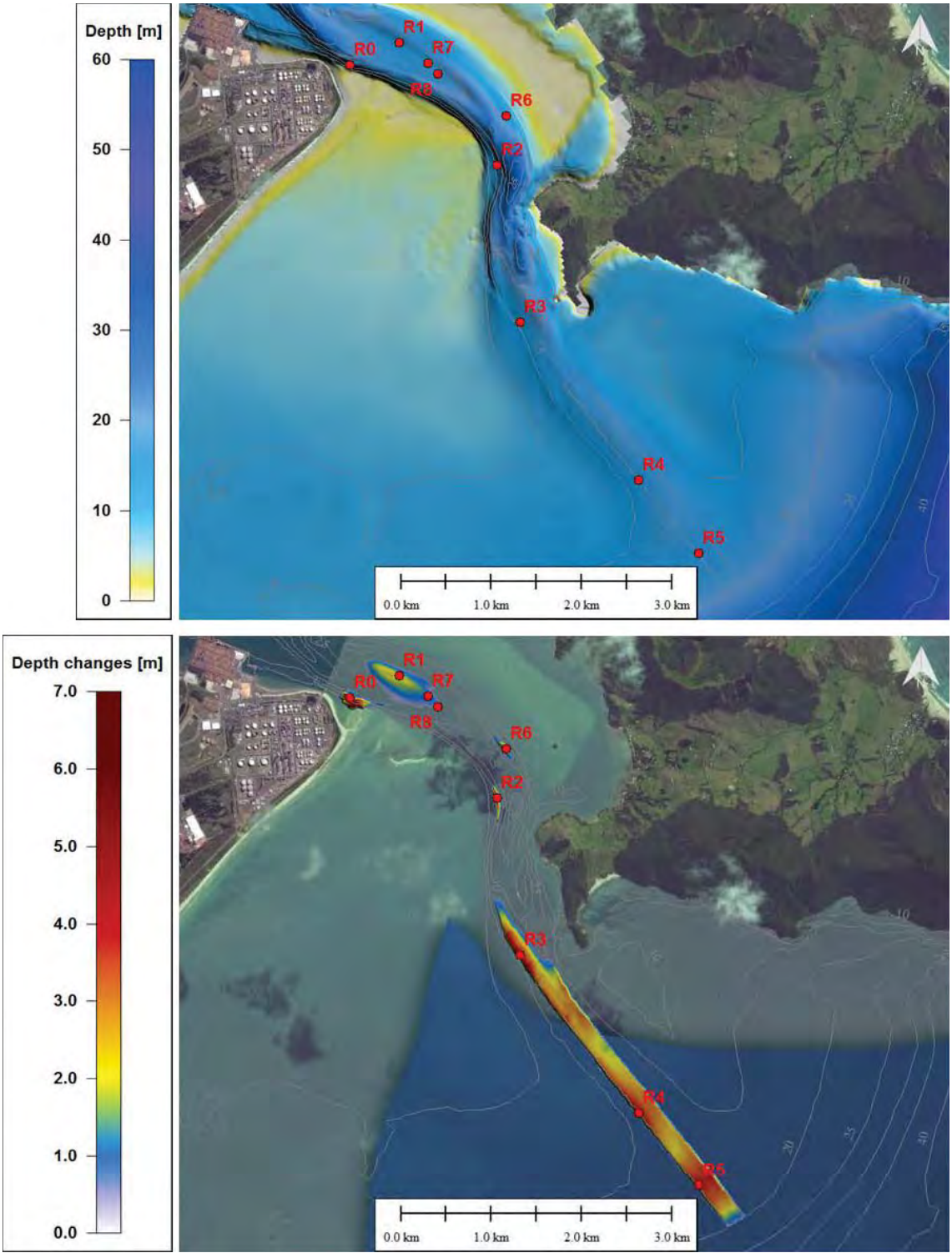

Figure 7.5 Simulated release sites along the dredged channel. Existing depth and depth changes are provided in Table 7.2. Geographic coordinates are presented in Appendix B.

8. DISPOSAL PLUME MODELLING

The placement of the dredged material over the proposed disposal areas is expected to produce a temporary plume of sediments in the water. The behaviour of this plume is driven by both the sediment grain-size distribution and the local hydrodynamics which control both the vertical and horizontal transport. In this context, a probabilistic approach was used to anticipate the plume dispersion under several hydrodynamic conditions.

This section presents the methodology applied, and the different scenarios considered, to assess the disposal plume dispersion.

8.1. Trajectory modelling

ERcore, the Lagrangian model used for the dredge plume modelling (Section 7) was applied to simulate the disposal plume in Bream Bay. The existing 2D Eulerian current field for the trajectory modelling was derived from the 10-year ROMS hindcast (Section 4) to ensure both residual and tidal current velocities were considered. This was chosen based on the importance of the non-tidal component of the current in the eastern region of Bream Bay characterised by increasing depths. In contrast, the hydrodynamic conditions used for the dredge plume modelling (Section 7) included only the tidal component which dominates the entrance region. A different vertical diffusivity was used for the disposal plume modelling, with a value of 0.0001 m^2s^{-1} chosen due to increasing water depths and decreasing current velocities compared to the navigation channel. The parameters for the trajectory modelling described in Section 7.1 were conserved, except those previously cited above.

8.2. Simulated scenarios

8.2.1. Sources terms

The processes by which sediment is released and suspended in the water column during disposal operations are briefly outlined here in the context of the choice of the source term magnitudes and release depths for the particle tracking simulations.

In the case of silt to fine sand, the content of a loaded dredge consists of a highly concentrated mixture of sediment and water and the bulk behaviour of that sediment mixture becomes dominant over the individual particle settling processes. When the dredge opens its bottom door for release, the contents will typically be released as a jet-like sediment flux quickly descending to the seabed. The behaviour of the released sediment can be separated in the three main phases illustrated on Figure 8.1.

During the convective descent, the dense sediment material quickly descends to the bottom. Ambient water can become entrained around the perimeter of the jet which can strip, or de-entrain some sediment, which becomes suspended in the water column. The proportion lost is expected to be small, commonly cited as 1-5% of the disposed load (Bokuniewicz et al., 1978; Bokuniewicz and Gordon, 1980; Gordon, 1974; Truitt, 1988).

Following its descent, the dredge material collapses on impact with the seabed; this phase is known as the dynamic collapse phase. The collapse results in a large fraction of the disposed sediment depositing on the seabed and is often coupled to

the generation of the density current generated by the excess energy available following collapsing, whereby a fraction of the disposed sediment is suspended and propagates radially from the point of impact. The density current is expected to be contained within the bottom 15-20% of the water column, with excursion length scales of order 100-500 m (e.g. Aarninkhof and Luijendijk, 2010).

These two initial phases relating to the dissipation of the initial plume momentum are also referred to as dynamic plume stage (e.g. Spearman et al., 2007). The passive dispersion phase relates to the subsequent dispersion of the sediment that became suspended in the water column during the dynamic phase, i.e. de-entrained during descent, sediment entrained during the collapse of the dynamic plume, and sediment suspension by the density current developing near the seabed.

In the present study, the focus is on characterising the extents and concentrations of the plume resulting from this passive dispersion phase, as these plumes have the potential to effect order of magnitude greater spatial extents than the dynamic plume (which settles quickly). In that respect, the particle tracking simulations considered two main source terms:

A. De-entrained sediment during descent – release at the bottom of the vessel used for disposal as a point source.

B. Entrained sediment resulting from the collapse of the dynamic plume - release within a cylinder near the seabed of given height and radius.

C. Surface sediment losses - release within the top layer of the water column (from the sea surface to bottom of vessel hull)

Note a degree of conservatism is introduced by releasing the sediment de-entrained from the descending plume at the vessel bottom rather than distributed within the water column, as these sediments have further to fall. The present application also considered an additional sediment source released at near-surface, representative of sediment which, in the unlikely event, is entrained vertically around the hull of the dredger due to turbulence associated with the discharge of sediment.

Entrained sediment resulting from the collapse of the dynamic plume (B above) was simulated assuming 20% of the discharged sediment enters the passive plume phase. This entrained sediment was distributed within a circular volume of 100 m radius and a 2 m height centred on the discharge location. This was combined with the mid-water and near surface release source terms (i.e. de-entrained and surface loss) which were assumed to consist of 5% and 0.5% of the disposed load respectively (see Figure 8.2).

The use of ratios for the proportion of sediment involved transferred in the passive plumes due to de-entrainment during descent and other losses near the surface (i.e. 5 and 0.5% respectively), is a relatively simplistic approach. Sensitivity testing of the ratio suggests it does not significantly alter the predicted *SSC* magnitudes, particularly in the surface.

The release depths for the source terms and total discharged volumes were varied according to the dredge being simulated (i.e. for the large and small dredge). Details of the dredging vessels are summarized in Table 8.1 and associated source terms are given in Table 8.2.

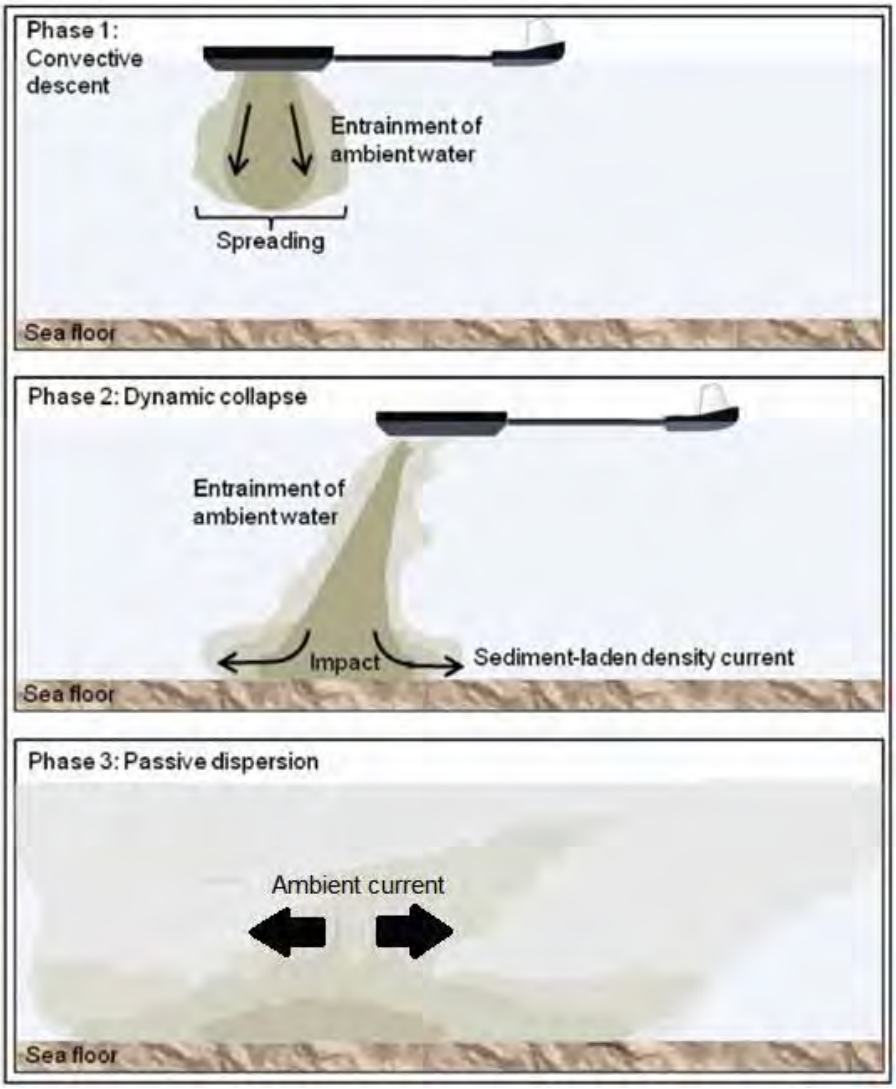

Figure 8.1 Three main phases occurring during the disposal of dredged material: 1) convective descent, 2) dynamic collapse, and 3) passive plume dispersion.

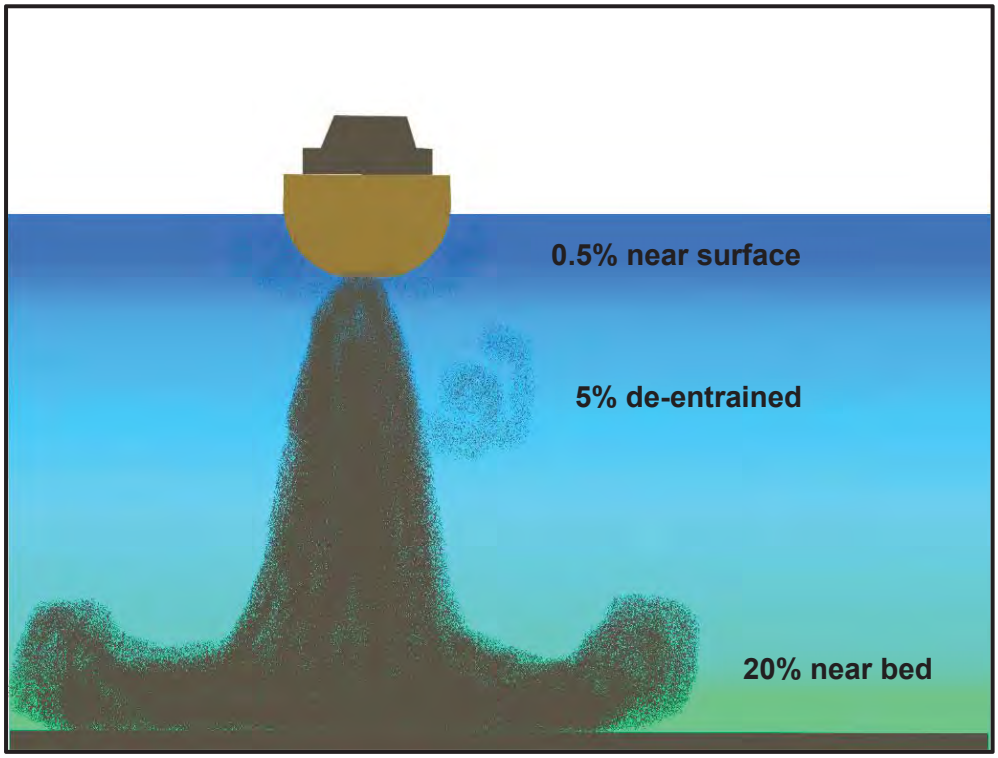

Figure 8.2 Percentages of sediment transferred from the near-field density driven plume to the far-field plume.

Table 8.1 Details of the dredging vessels likely to be used for dredging and disposal works.

Vessel	Hopper load [m3]	Draft [m]	Disposal load [min]
Large	10,830	-9.5	10
Small	2,130	-5.6	10

Table 8.2 Source terms and release depths.

Sources Terms	Percent of hopper volume	Release depth	Release type
Surface losses	1%	sea-surface to vessel draft	point source
De-entrained during descent	5%	vessel draft	point source
Density current	21%	2 m layer above seabed	100 m radius circle

8.2.2. Sediment distribution and settling velocity

The particle size distribution of the sediment to be disposed was conserved from the sediment distribution used for the dredge plume modelling. It includes three sediment fractions of silt (60 µm), fine sand (130 µm) and medium sand (400 µm). The coarse sand and gravel sediment fractions identified in the sampling results were not included within the disposal plume modelling as they directly settle to the bottom.

The particle size distribution and associated fall velocity of the sediment discharged at the proposed disposal site was identical to that of the distribution simulated during the dredging operations (see Table 7.1). The coarse sand and gravel sediment fractions identified in the sampling results were not included within the disposal plume modelling as they are expected to directly settle to the bottom.

8.2.3. Release sites and events

Five sites were considered for the discharge of dredge material (see Figure 8.3, Appendix C and Appendix B); one at each corner of the disposal and one in the centre where measured current data was collected using an ADCP current profiler.

The dispersion model was run for two discrete periods during which the hydrodynamic conditions were representative of the expected range at the disposal site, including strong west-directed currents at surface and bottom levels, respectively. This last scenario is considered as “worst case scenario” due to the location of 3 Mile Reef from the disposal area 3.2.

These discrete short-term simulations were also supplemented by two 1-month periods during summer and winter months (i.e. January and August, 1995 see Table 8.3). For the historical simulations, discharges were simulated at 140 minutes and 185 minutes interval for the large and small TSHD, respectively. These intervals were estimated based on the periods of dredging, overflow, travel and disposal.

The long-term simulation of the plume dispersion over a 6-month period assumed continuous release of sediment throughout the period, allowing statistical analysis of the predicted plume concentrations and extents. The choice of the modelling period was motivated by the necessity to consider a large range of weather conditions without increasing dramatically the computational runtime. Simulating plumes from the near-bed, near-surface and de-entrained from the dynamic phase of the plume descent for each of the representative grain sizes, while computationally expensive, provides the necessary information to allow realistic climatic and representative statistical measures of the predicted plume extents.

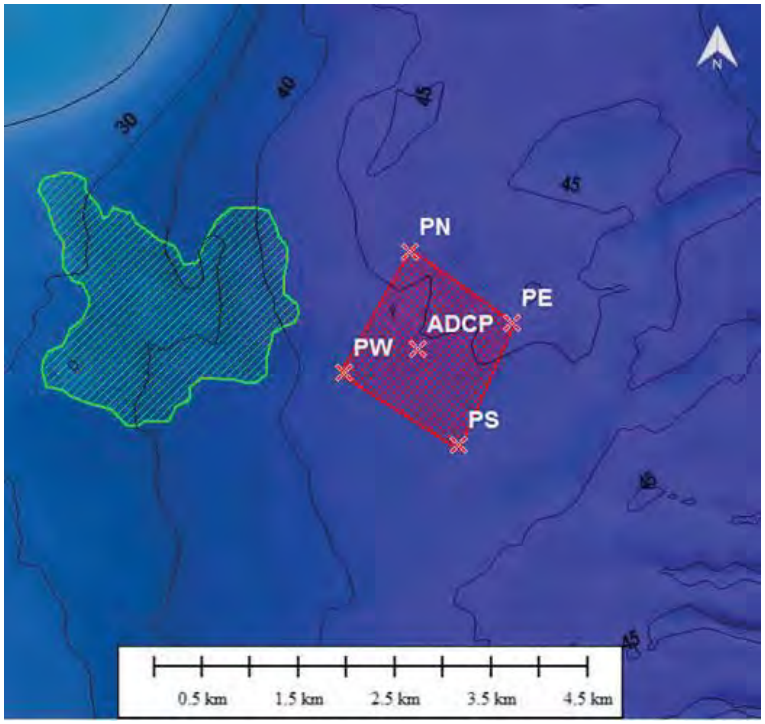

Figure 8.3 Location of the sites over the disposal ground used for the release of particles as part of the disposal plume modelling. The green polygon indicates the contour of a reef classified as sensitive.

Table 8.3 Summary of simulation periods.

Disposal simulations	Period
Strong west-directed current on surface	10/12/1995-12:00
Strong west-directed current near bottom	06/02/1995-12:00
Summer hydrodynamic conditions	January (1995)
Winter hydrodynamic conditions	August (1995)

9. DISPOSAL GROUND MODELLING

This section describes the numerical modelling that was adopted to estimate the long-term dynamics of the proposed disposal grounds 1.2 and 3.2 (see Figure 1.4) for the placement of maintenance and capital volumes, respectively. The present work aims to provide solid information regarding the predicted effect of the disposal mound on the physical and ecological components of the coastal system in Bream Bay. Main expected outcomes are listed below:

- Estimation of the degree of stability of the disposal mound under a range of wave and tidal forcing.
- Prediction of the magnitudes of the sediment transport over adjacent areas.
- Identification of potential ecological harm related to the transport of large amount of disposed sediments.
- Impact of the depth changes on the wave climate in Bream Bay and adjacent beaches associated to the disposal of material.

9.1. Modelling approach

The Delft3D model was implemented to predict the disposal ground dynamic using an input reduction approach. A limited number of representative forcing conditions (including tides, waves, residual currents and residual water elevations) was used to reproduce the long-term residual sediment transport patterns and associated morphological evolutions. This methodology was combined with the application of morphological acceleration factors (MORFAC) based on the occurrence of each scenario to improve computational efficiency by acceleration computed morphological evolution. Details about the input reduction approach and corresponding references are provided in Section 6.3.1.

Outcomes of the consultation process involving RNZ and the relevant experts resulted in the identification of two offshore disposal sites referenced as Disposal Sites 1.2 and 3.2. At Disposal Site 3.2 it is intended to place up to 97.5% of the capital dredge volume and up to 100% of the maintenance dredge volume. Although the capital dredge volume for this area is estimated at 3.7 million m^3, a 4 m high disposal mound was set-up over a proposed 2 km^2 area - equivalent to a total volume of 8 million m^3. This conservative approach aimed to consider both the total capital dredge volume and the maintenance dredge volumes accumulated over 35 years based on a stable disposal mound. The effect of the disposal mound on the wave climate within Bream Bay was assessed based on the wave modelling of the 16 representative scenarios presented in Section 6 (see Table 6.1) including both the pre-disposal and the post-disposal bathymetries in the model.

Disposal Site 1.2 is intended to receive 2.5 – 5% of the capital dredge and up to 100% of the maintenance dredge volume. The assessment of the nearshore disposal dynamics was undertaken based on the numerical modelling of a representative value for a low mound, which was taken to be a 0.6 m high disposal mound (1.5 million m^3) defined on the ebb tide delta.

This corresponds to a conservative approach considering 5% of the capital dredge volume and 100% of the maintenance dredge volume accumulated over 10 years. The relative low water depth (less than 10m) of the Disposal ground 1.2 is expected to make the mound morphologically unstable with a relative high rate of erosion per annum. In this context, considering 35 years of accumulation of sediments (as for the Disposal ground 3.2) for a total volume of 4.3 million m^3 would have been largely unrealistic. The 1-year disposal ground dynamics for disposal sites 1.2 and 3.2 were simulated using a sequence of 16 representative scenarios (Table 6.1). The modelled sediment thickness and depth changes obtained at the end of each scenario were used for the initialisation of the next one.

The distribution of sediments used to characterise the disposal mound composition included five classes according to the results of the vibrocoring (Tonkin and Taylor, 2016c):

- 5% of silt (D50 = 60 µm)
- 26% of fine sand (D50 = 130 µm)
- 59% of medium sand (D50 = 400 µm)
- 4% of coarse sand (D50 = 1300 µm)
- 6% of gravel (D50 = 2000 µm)

9.2. Model domains

The Delft3D – FLOW domain includes the whole of Bream Bay from Bream Head to Langs Beach. To the North, the grid extends to Busby Head excluding Mair Bank and the Whangarei Harbour entrance (Figure 9.1). The resolution of the hydrodynamic/morphologic model grid ranges between 35 and 180 m, with higher resolution focused over the proposed disposal grounds. Delft3D – WAVE model was implemented on the same high-resolution curvilinear grid than Delft3D – FLOW. However, a nesting approach was implemented, including a coarser grid (Figure 9.2) to correctly reproduce the spectral wave transformation during the propagation of wave energy from deep to shallow water.

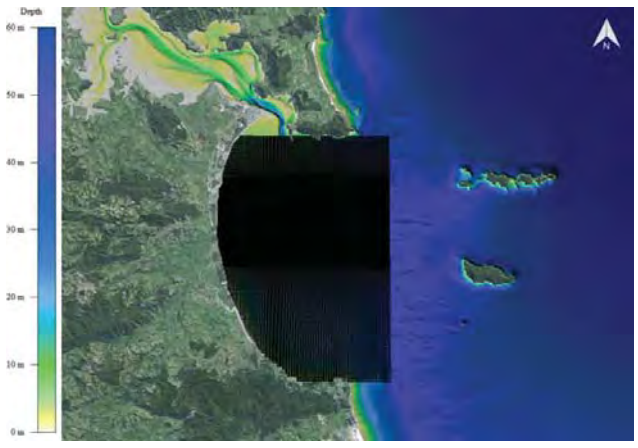

Figure 9.1 Bathymetry and Delft3D – FLOW model grid for the proposed disposal ground modelling.

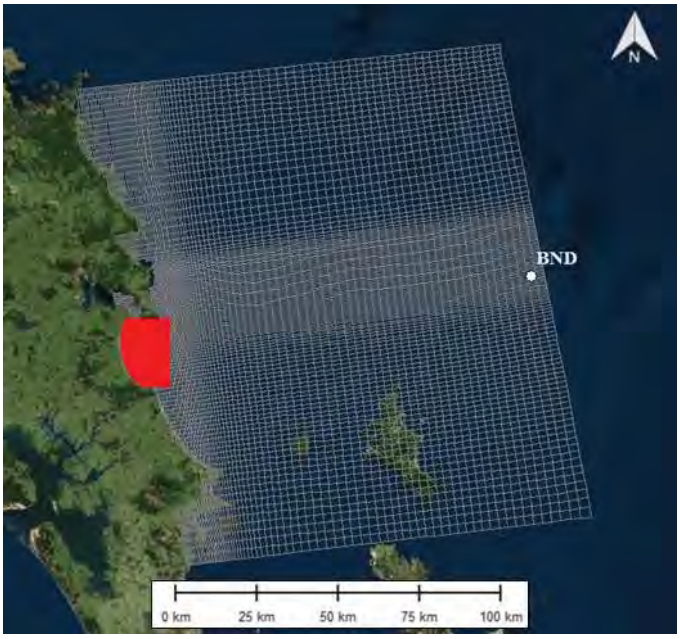

Figure 9.2 Delft3D –WAVE model grid for the proposed disposal ground modelling. Location (BND) for representative wave climate is shown at the centre of the eastern boundary.

REFERENCES

Aarninkhof, S., Luijendijk, A., 2010. Safe disposal of dredged material in an environmentally sensitive environment. Port Technol. Int. 47, 39–45.

Ardhuin, F., Rascle, N., Belibassakis, K.A., 2008. Explicit wave-averaged primitive equations using a generalized Lagrangian mean. Ocean Model. 20, 35–60. doi:10.1016/j.ocemod.2007.07.001

Ardhuin, F., Roland, A., 2013. The development of spectral wave models: coastal and coupled aspects, in: Proceedings of Coastal Dynamics. p. 7th.

Bagnold, R.A., 1966. An approach to the sediment transport problem. Gen. Phys. Geol. Surv. Prof Pap.

Becker J., van Eekelen E., van Wiechen J., de Lange W., Damsma T., Smolders T., van Koningsveld M., 2015. Estimating source terms for far field dredge plume modelling. J. Environ. Manage. 149, 282–293.

Bennis, A.-C., Ardhuin, F., Dumas, F., 2011. On the coupling of wave and three-dimensional circulation models: Choice of theoretical framework, practical implementation and adiabatic tests. Ocean Model. 40, 260–272. doi:10.1016/j.ocemod.2011.09.003

Black, K.P., 1983. Sediment Transport and Tidal Inlet Hydraulics. Hamilton, New Zealand: University of Waikato. Ph. D. thesis, 331p.

Bokuniewicz, H.J., Gebert, J., Gordon, R.B., Higgins, J.L., Kaminsky, P., 1978. Field Study of the Mechanics of the Placement of Dredged Material at Open-Water Disposal Sites. Volume I. Main Text and Appendices A-1. DTIC Document.

Bokuniewicz, H.J., Gordon, R.B., 1980. Sediment transport and deposition in Long Island Sound. Adv Geophys. States 21.

Booij, N., Ris, R.C., Holthuijsen, L.H., 1999. A third-generation wave model for coastal regions: 1. Model description and validation. J. Geophys. Res. Oceans 104, 7649–7666. doi:10.1029/98JC02622

Brown, J.M., Davies, A.G., 2009. Methods for medium-term prediction of the net sediment transport by waves and currents in complex coastal regions. Cont. Shelf Res. 29, 1502–1514.

Camenen, B., Larroudé, P., 2003. Comparison of sediment transport formulae for the coastal environment. Coast. Eng. 48, 111–132.

Collins, J., 1972. Prediction of Shallow Water Spectra. J. Geophys. Res. 77, 2693–2707.

Dastgheib, A., 2012. Long-term process-based morphological modeling of large tidal basins. UNESCO-IHE, Institute for Water Education.

De Vriend, H.J., Capobianco, M., Chesher, T., De Swart, H. de, Latteux, B., Stive, M.J.F., 1993. Approaches to long-term modelling of coastal morphology: a review. Coast. Eng. 21, 225–269.

Deltares, 2013. User Manual Delft3D-FLOW. version: 3.15.2789. Deltares.

Dissanayake, D., Ranasinghe, R., Roelvink, J.A., 2012. The morphological response of large tidal inlet/basin systems to relative sea level rise. Clim. Change 113, 253–276.

Dodet, G., 2013. Morphodynamic modelling of a wave-dominated tidal inlet: the Albufeira lagoon. La Rochelle.

Egbert, G.D., Erofeeva, S.Y., 2002. Efficient inverse modeling of barotropic ocean tides. J. Atmospheric Ocean. Technol. 19, 183–204.

Elder, J.W., 1956. The dispersion of marked fluid in turbulent shear flow. J. Fluid Mech. 5, 544–560.

Engelund, F., Hansen, E., 1967. A monograph on sediment transport in alluvial streams. TEKNISKFORLAG Skelbrekgade 4 Copenhagen V, Denmark.

Fairall, C.W., Bradley, E. F., Hare, J. E., Grachev, A. A., Edson, J. B., 2003. Bulk parameterization of air-sea fluxes: Updates and verification for the COARE algorithm. J. Clim. 16, 571–591.

Fischer, H.B., Koh, R.C.Y., Imberger, J., Brooks, N.H., 1979. Mixing in Inland and Coastal Waters. Academic Press, San Diego, Califonia USA.

Fredsøe, J., 1984. Turbulent boundary layer in wave-current motion. J. Hydraul. Eng. 110, 1103–1120.

Gordon, R.B., 1974. Dispersion of dredge spoil dumped in near-shore waters. Estuar. Coast. Mar. Sci. 2, 349–358.

Grunnet, N.M., Walstra, D.-J.R., Ruessink, B.G., 2004. Process-based modelling of a shoreface nourishment. Coast. Eng. 51, 581–607.

Haidvogel, D.B., Arango, H., Budgell, W.P., Cornuelle, B.D., Curchitser, E., Di Lorenzo, E., Fennel, K., Geyer, W.R., Hermann, A.J., Lanerolle, L., others, 2008. Ocean forecasting in terrain-following coordinates: Formulation and skill assessment of the Regional Ocean Modeling System. J. Comput. Phys. 227, 3595–3624.

Holthuijsen, L.H., Booij, N., Ris, R.C., Haagsma, I.J., Kieftenburg, A.T.M.M., Kriezi, E.E., Zijlema, M., van der Westhuysen, A.J., 2007. SWAN cycle III version 40.51, Technical Documentation. Delft, 2600 GA Delft The Netherlands.

Latteux, B., 1995. Techniques for long-term morphological simulation under tidal action. Mar. Geol. 126, 129–141.

Lesser, G.R., 2009. An approach to medium-term coastal morphological modelling. UNESCO-IHE, Institute for Water Education.

Lesser, G.R., Roelvink, J.A., van Kester, J.A.T.M., Stelling, G.S., 2004. Development and validation of a three-dimensional morphological model. Coast. Eng., Coastal Morphodynamic Modeling 51, 883–915. doi:10.1016/j.coastaleng.2004.07.014

Morgan, K.M., Kench, P.S., Ford, R.B., 2011. Geomorphic change of an ebb-tidal delta: Mair Bank, Whangarei Harbour, New Zealand. N. Z. J. Mar. Freshw. Res. 45, 15–28.

MSL, 2016. Crude Shipping Project, Whangarei Harbour - Predicted physical environmental effects from channel deepening and offshore disposal.

Okubo, A., 1971. Oceanic diffusion diagrams. Deep-Sea Res. 18, 789–802.

OMC International, 2016. Mardsen Point Channel Optimisation.

Pinto, L., Fortunato, A.B., Freire, P., 2006. Sensitivity analysis of non-cohesive sediment transport formulae. Cont. Shelf Res. 26, 1826–1839.

Prediction of shallow-water spectra - Collins - 1972 - Journal of Geophysical Research - Wiley Online Library [WWW Document], n.d. URL http://onlinelibrary.wiley.com/doi/10.1029/JC077i015p02693/full (accessed 4.25.16).

Ramli, A., de Lange, W.P., Bryan, K.R., Mullarney, J., 2015. Coupled flow-wave numerical model in assessing the impact of dredging on the morphology of Matakana Banks, in: Proceedings of the Australasian Coasts & Ports Conference.

Ranasinghe, R., Pattiaratchi, C., Masselink, G., 1999. A morphodynamic model to simulate the seasonal closure of tidal inlets. Coast. Eng. 37, 1–36. doi:10.1016/S0378-3839(99)00008-3

Ris, R.C., Holthuijsen, L.H., Booij, N., 1999. A third-generation wave model for coastal regions: 2. Verification. J. Geophys. Res. Oceans 104, 7667–7681. doi:10.1029/1998JC900123

Royal HaskoningDHV, 2016a. Shipping Channel - Concept Design Report, prepared for Refining NZ., Refining NZ Crude Freight Project.

Royal HaskoningDHV, 2016b. Dredging Methodology Assessment.Technical Memo, prepared for Refining NZ., Refining NZ Crude Freight Project.

Royal HaskoningDHV, 2015. Desktop Simulation Study, prepared for Refining NZ., Refining NZ Crude Freight Project.

Smart, G.M., Duncan, M.J., Walsh, J.M., 2002. Relatively rough flow resistance equations. J. Hydraul. Eng. 128, 568–578.

Smith, S.J., Friedrichs, C.T., 2011. Size and settling velocities of cohesive flocs and suspended sediment aggregates in a trailing suction hopper dredge plume. Cont. Shelf Res. 10.

Spearman, J., Bray, R.N., Land, J., Burt, T.N., Mead, C.T., Scott, D., 2007. Estuarine and Coastal Fin Sediments Dyanmics.

Tolman, H.L., Chalikov, D., 1996. Source terms in a third-generation wind wave model. J. Phys. Oceanogr. 26, 2497–2518.

Tolman, H.L., 1991. A Third-Generation Model for Wind Waves on Slowly Varying, Unsteady and Inhomogeneous Depths and Currents. J. Phys. Oceanogr. 21, 782–797.

Tonkin and Taylor, 2016a. Crude Freight Project, Whangarei Harbour - Dredging and disposal options - synthesis report. Tonkin and Taylor.

Tonkin and Taylor, 2016b. Crude Shipping project, Mid-point multi-criteria alternatives assessment. Prepared for ChanceryGreen for Refining NZ.

Tonkin and Taylor, 2016c. Marsden point Refinery - Crude Freight Project, Vibrocore report (No. 30488.1000). Tonkin and Taylor.

Truitt, C.L., 1988. Dredged material behavior during open-water disposal. J. Coast. Res. 489–497.

van der Wegen, M., Dastgheib, A., Jaffe, B.E., Roelvink, D., 2011. Bed composition generation for morphodynamic modeling: case study of San Pablo Bay in California, USA. Ocean Dyn. 61, 173–186.

Van der Wegen, M., Roelvink, J.A., 2008. Long-term morphodynamic evolution of a tidal embayment using a two-dimensional, process-based model. J. Geophys. Res. Oceans 113.

van der Westhuysen, A.J., Zijlema, M., Battjes, J.A., 2007. Nonlinear saturation-based whitecapping dissipation in SWAN for deep and shallow water. Coast. Eng. 54, 151–170. doi:10.1016/j.coastaleng.2006.08.006

Van Rijn, L.C., van Rijn, L.C., van Rijn, L.C., 1993. Principles of sediment transport in rivers, estuaries and coastal seas. Aqua publications Amsterdam.

Van Rijn, L.C., Walstra, D.J.R., Ormondt, M. van, 2004. Description of TRANSPOR2004 and implementation in DELFT3D-ONLINE: final report. Deltares (WL).

Van Rijn, L.C., 2007. A unified view of sediment transport by current and waves, Part II: Suspended transport. J. Hydraul. Eng. ASCE 22.

Van Rijn, L.C., 1984. Sediment Transport Part II: Suspended Load Transport. J. Hydraul. Eng. 110, 1613–1641.

Vitali, L., Monforti, F., Bellasio, R., Bianconi, R., Sachero, V., Mosca, S., Zanini, G., 2006. Validation of a Lagrangian dispersion model implementing different kernel methods for density reconstruction. Atmos. Environ. 40, 8020–8033.

Walstra, D.J.R., Hoekstra, R., Tonnon, P.K., Ruessink, B.G., 2013. Input reduction for long-term morphodynamic simulations in wave-dominated coastal settings. Coast. Eng. 77, 57–70.

Walstra, D.J.R., Roelvink, J.A., Groeneweg, J., 2001. Calculation of wave-driven currents in a 3D mean flow model, in: Coastal Engineering Conference. ASCE AMERICAN SOCIETY OF CIVIL ENGINEERS, pp. 1050–1063.

WEPPE, S., MCCOMB, P., COE, L., 2015. NUMERICAL MODEL STUDIES TO SUPPORT THE SUSTAINABLE MANAGEMENT OF DREDGE SPOIL DEPOSITION IN A COMPLEX NEARSHORE ENVIRONMENT, in: The Proceedings of the Coastal Sediments 2015. World Scientific.

Whitehouse R., et al, 2000. Dynamics of estuarine muds, Thomas Telford, London. ed.

Williams, J.R., Hume, T.M., 2014. Investigation into the decline of pipi at Mair Bank, Whangarei Harbour. Prepared for Northland Regional Council (No. AKL2014-022). NIWA.

Winterwerp, J.C., 2002. Near-field behavior of dredging spill in shallow water. J. Waterw. Port Coast. Ocean Eng. 128, 96–98.

Zhang, Y.L., Baptista, A.M., 2008. A semi-implicit Eulerian-Lagrangian finite element model for cross-scale ocean circulation. Ocean Model. 21, 71–96.

APPENDIX A – LOCATION OF INSTRUMENTS

Geographic coordinates of instruments used to collect data and validate the different models implemented in the present study.

Positions	Description	Geographic coordinates (WGS 84 datum)	
		Longitude (East)	Latitude (North)
WS	Wind station location at Mardsen Point	174.48700	-35.84000
WRB	Wave measurement at tidal delta entrance	174.54830	-35.88310
w1	Wave measurement along Ruakaka Beach	174.46720	-35.90740
w2	Wave measurement along Ruakaka Beach	174.47050	-35.88930
w3	Wave measurement along Ruakaka Beach	174.48140	-35.86800
w4	Wave measurement along Ruakaka Beach	174.50110	-35.84930
ADCP1	Current profiler position in the Parry Channel	174.66077	-35.89648
ADCP2	Current profiler position at Disposal site 3.2	174.59075	-35.912833
ADCP3	Current profiler position at Disposal site 1.2	174.50742	-35.886233
ADCP4	Current profiler position at Disposal site 2.2	174.53307	-35.937559
K17	Water elevation measurement at Port Whangarei (near Hatea river)	174.35120	-35.75750
P10	Water elevation measurement near Portland	174.34890	-35.80330
Parua	Water elevation measurement at the Parua Bay entrance	174.37950	-35.77600
W2	Water elevation measurement between Tamaterau and Rat Island	174.45160	-35.79970

APPENDIX B – MEASURED CURRENTS

Time series and rose plots of the depth-averaged measured currents at sites ADCP1-4.

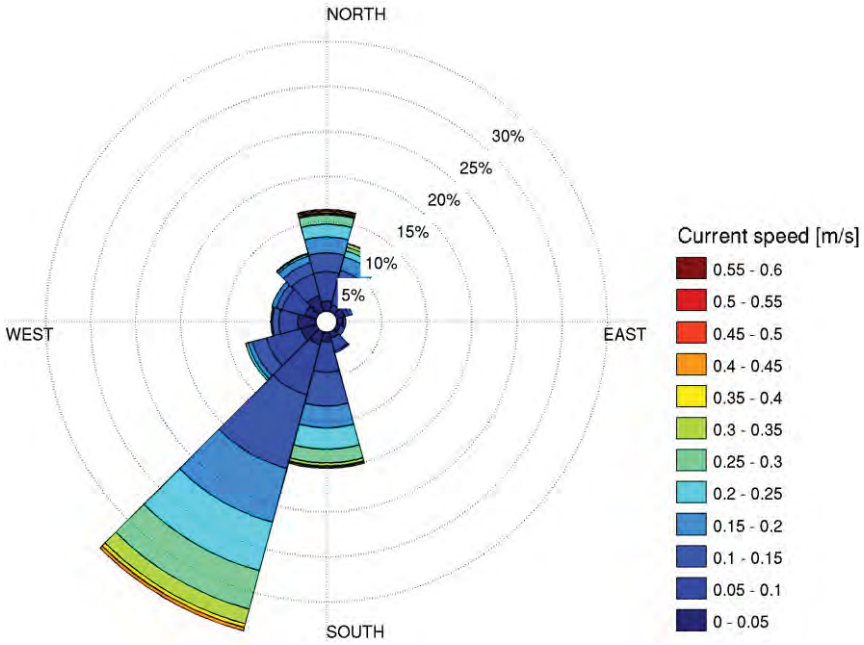

ADCP1

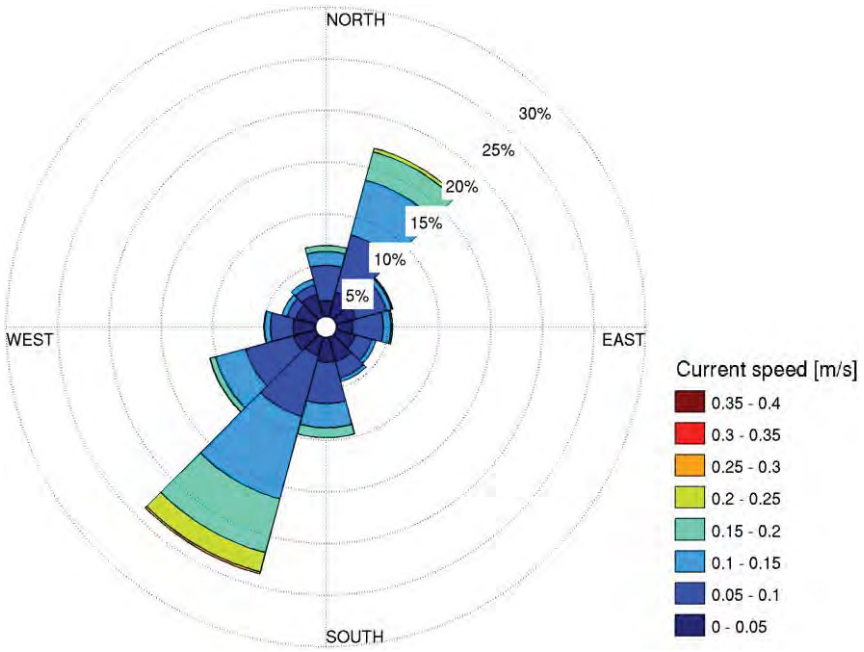

ADCP2

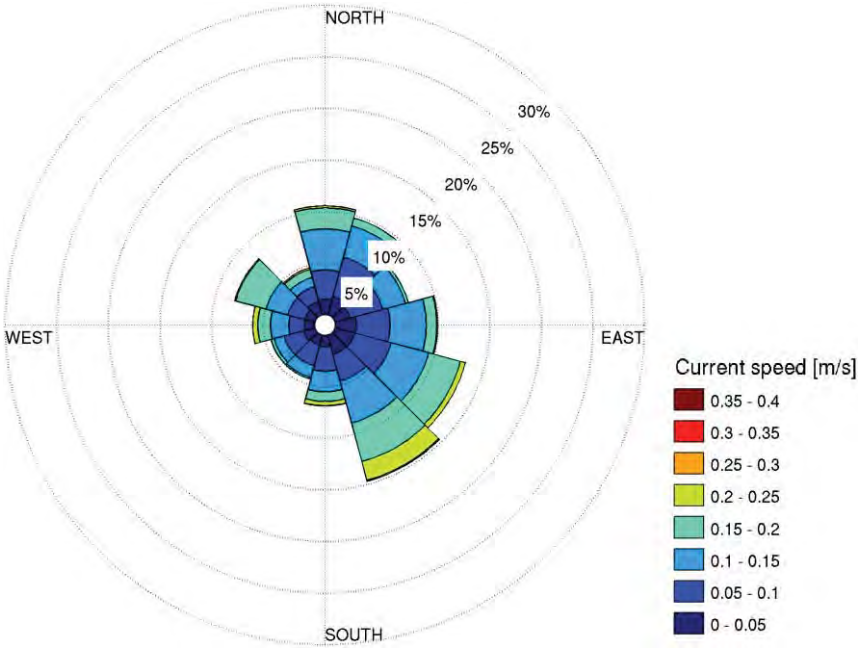
NORTH
30%
25%
20%
15%
10%
5%
WEST
EAST
SOUTH
Current speed [m/s]
0.35 - 0.4
0.3 - 0.35
0.25 - 0.3
0.2 - 0.25
0.15 - 0.2
0.1 - 0.15
0.05 - 0.1
0 - 0.05

ADCP3

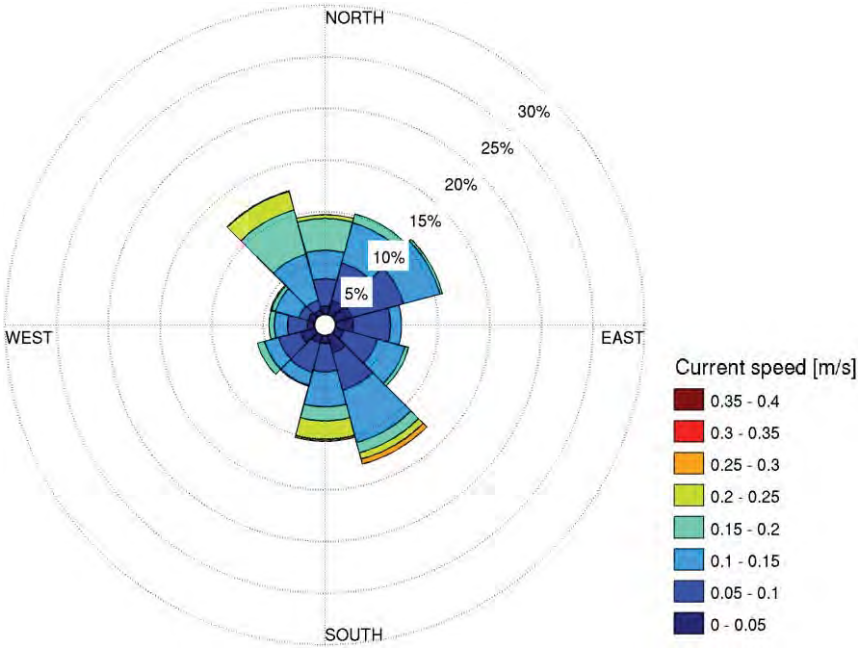
NORTH
30%
25%
20%
15%
10%
5%
WEST
EAST
SOUTH
Current speed [m/s]
0.35 - 0.4
0.3 - 0.35
0.25 - 0.3
0.2 - 0.25
0.15 - 0.2
0.1 - 0.15
0.05 - 0.1
0 - 0.05

ADCP4

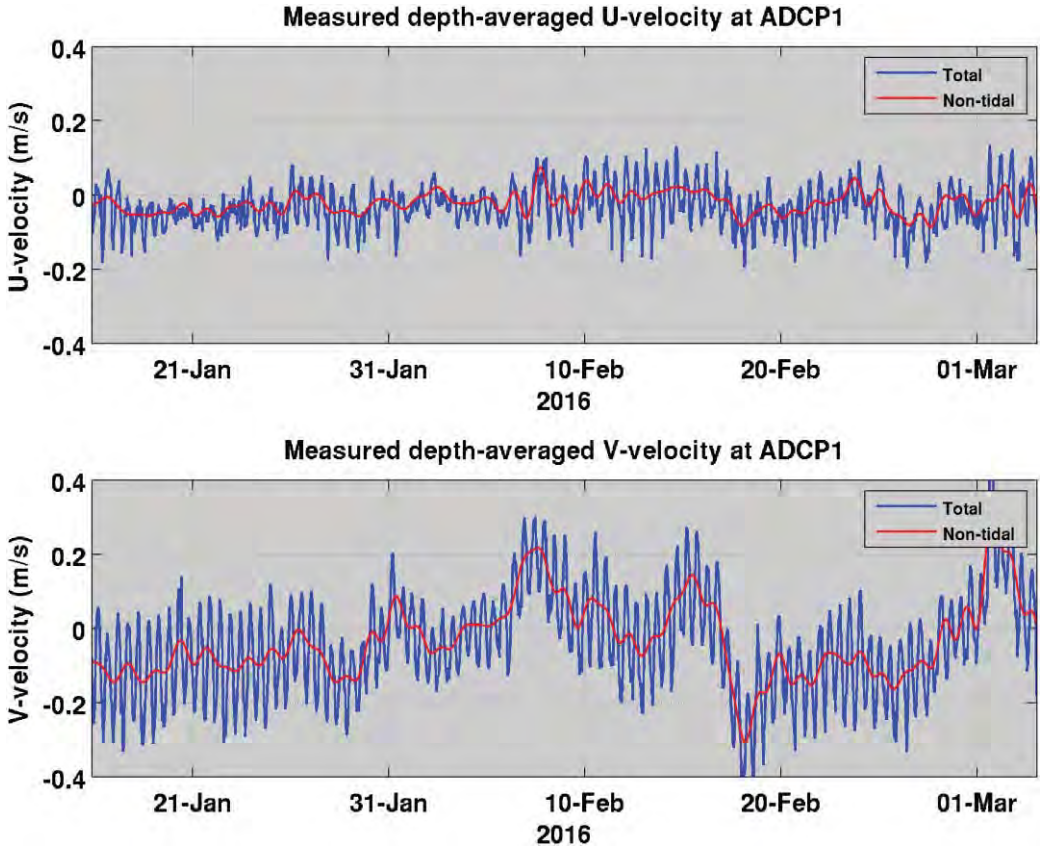
Measured depth-averaged U-velocity at ADCP1
U-velocity (m/s)
0.4
0.2
0
-0.2
-0.4
Total
Non-tidal
21-Jan
31-Jan
10-Feb
20-Feb
01-Mar
2016
Measured depth-averaged V-velocity at ADCP1
V-velocity (m/s)
0.4
0.2
0
-0.2
-0.4
Total
Non-tidal
21-Jan
31-Jan
10-Feb
20-Feb
01-Mar
2016

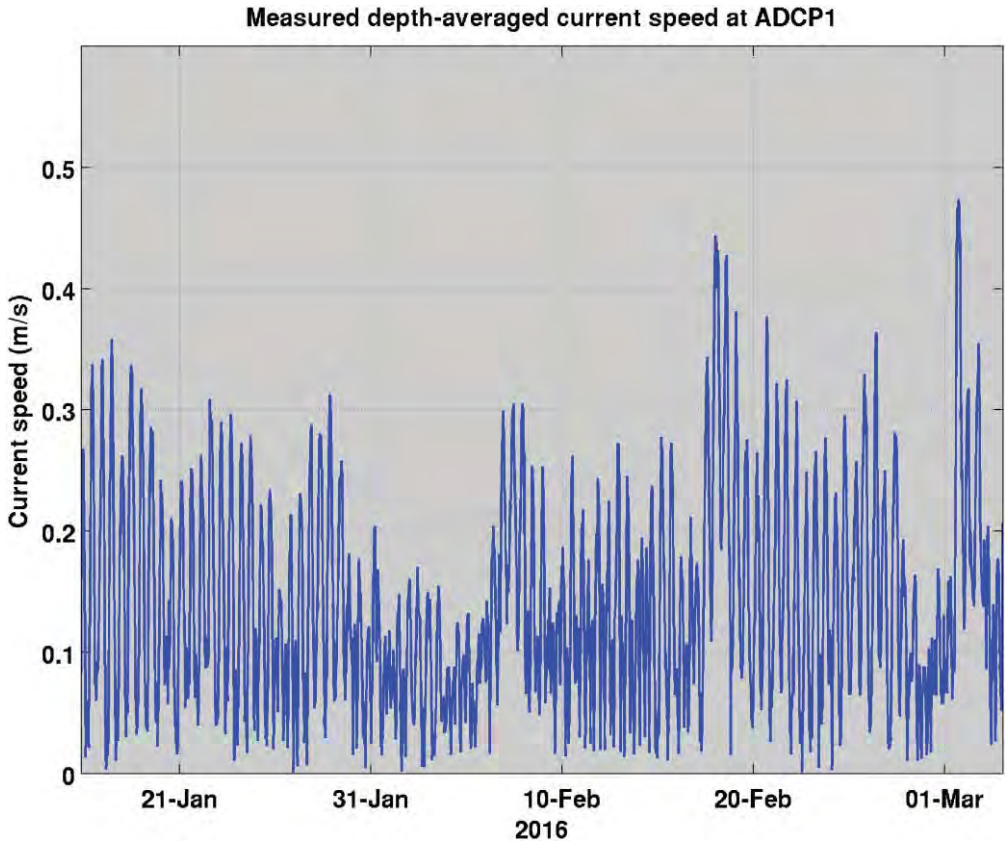
Measured depth-averaged current speed at ADCP1
Current speed (m/s)
0.5
0.4
0.3
0.2
0.1
0
21-Jan
31-Jan
10-Feb
20-Feb
01-Mar
2016

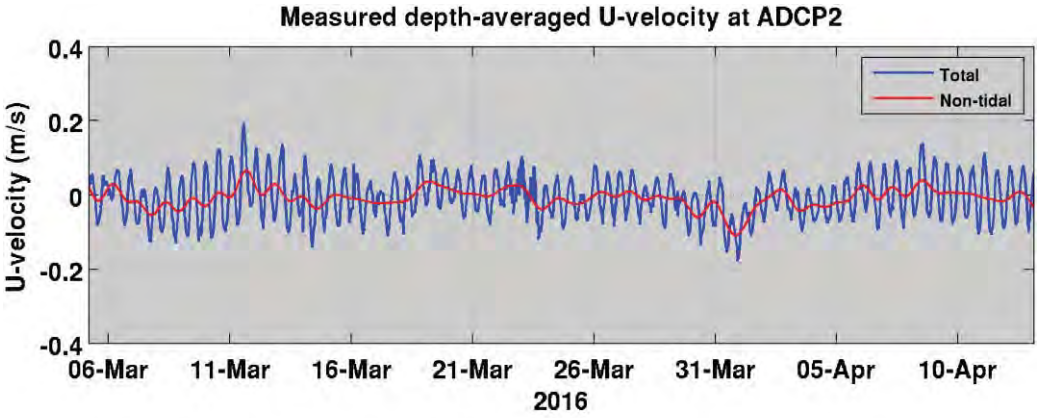
Measured depth-averaged U-velocity at ADCP2
U-velocity (m/s)
0.4
0.2
0
-0.2
-0.4
Total
Non-tidal
06-Mar
11-Mar
16-Mar
21-Mar
26-Mar
31-Mar
05-Apr
10-Apr
2016

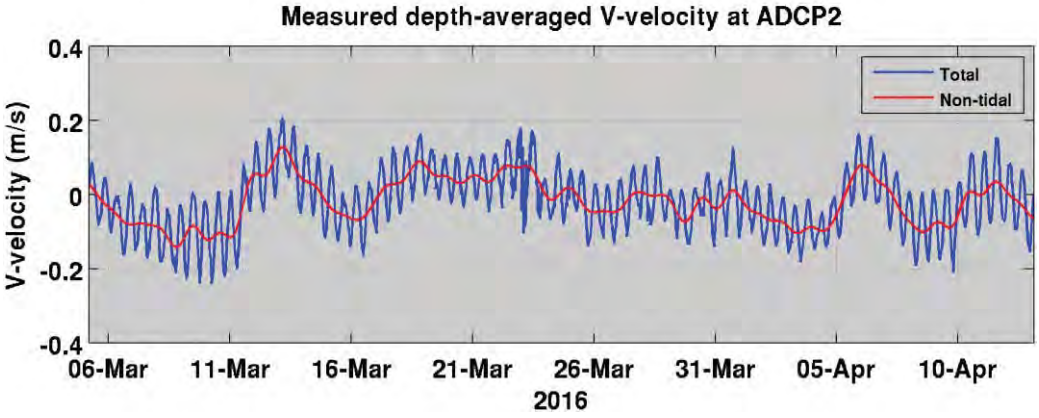
Measured depth-averaged V-velocity at ADCP2
V-velocity (m/s)
0.4
0.2
0
-0.2
-0.4
Total
Non-tidal
06-Mar
11-Mar
16-Mar
21-Mar
26-Mar
31-Mar
05-Apr
10-Apr
2016

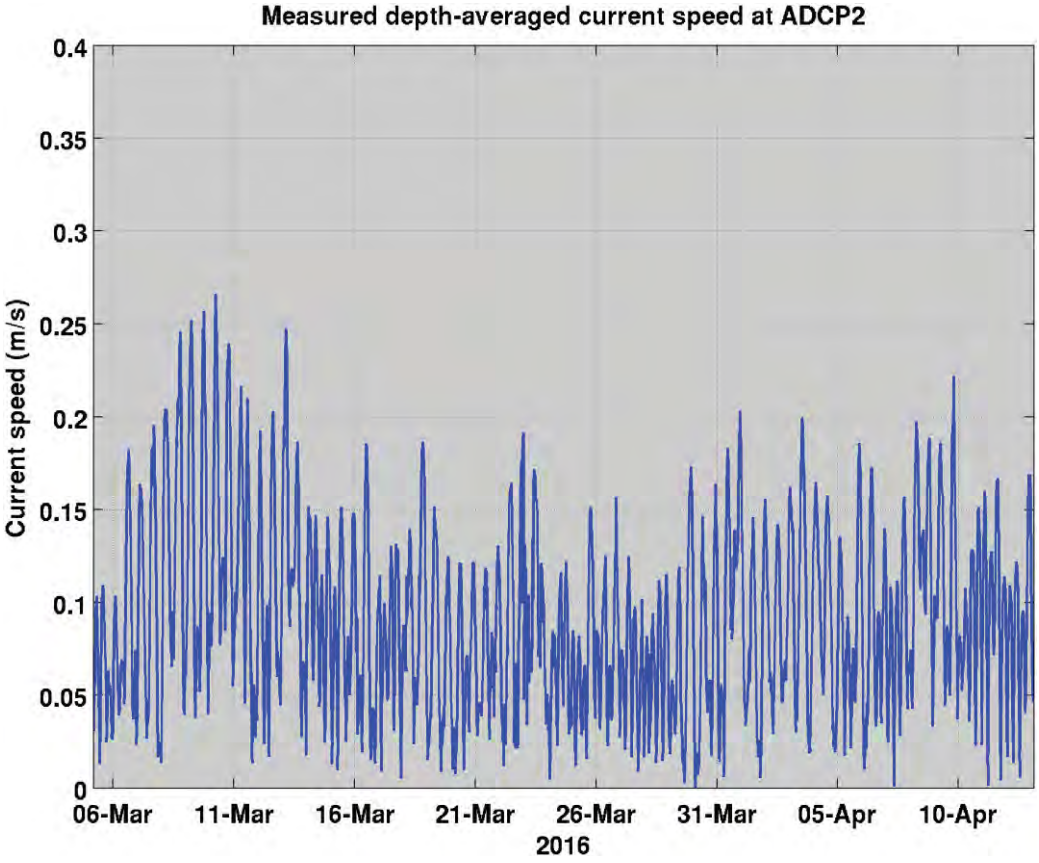
Measured depth-averaged current speed at ADCP2
Current speed (m/s)
0.4
0.35
0.3
0.25
0.2
0.15
0.1
0.05
0
06-Mar
11-Mar
16-Mar
21-Mar
26-Mar
31-Mar
05-Apr
10-Apr
2016

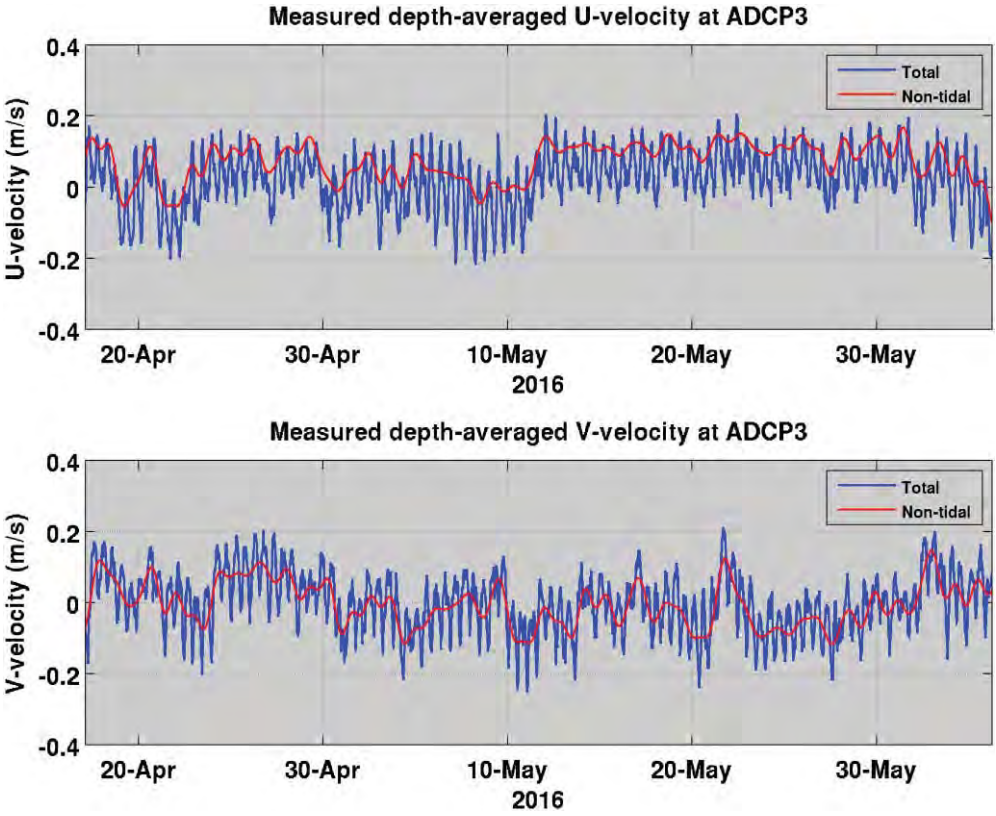
Measured depth-averaged U-velocity at ADCP3
U-velocity (m/s)
0.4
0.2
0
-0.2
-0.4
Total
Non-tidal
20-Apr
30-Apr
10-May
20-May
30-May
2016
Measured depth-averaged V-velocity at ADCP3
V-velocity (m/s)
0.4
0.2
0
-0.2
-0.4
Total
Non-tidal
20-Apr
30-Apr
10-May
20-May
30-May
2016

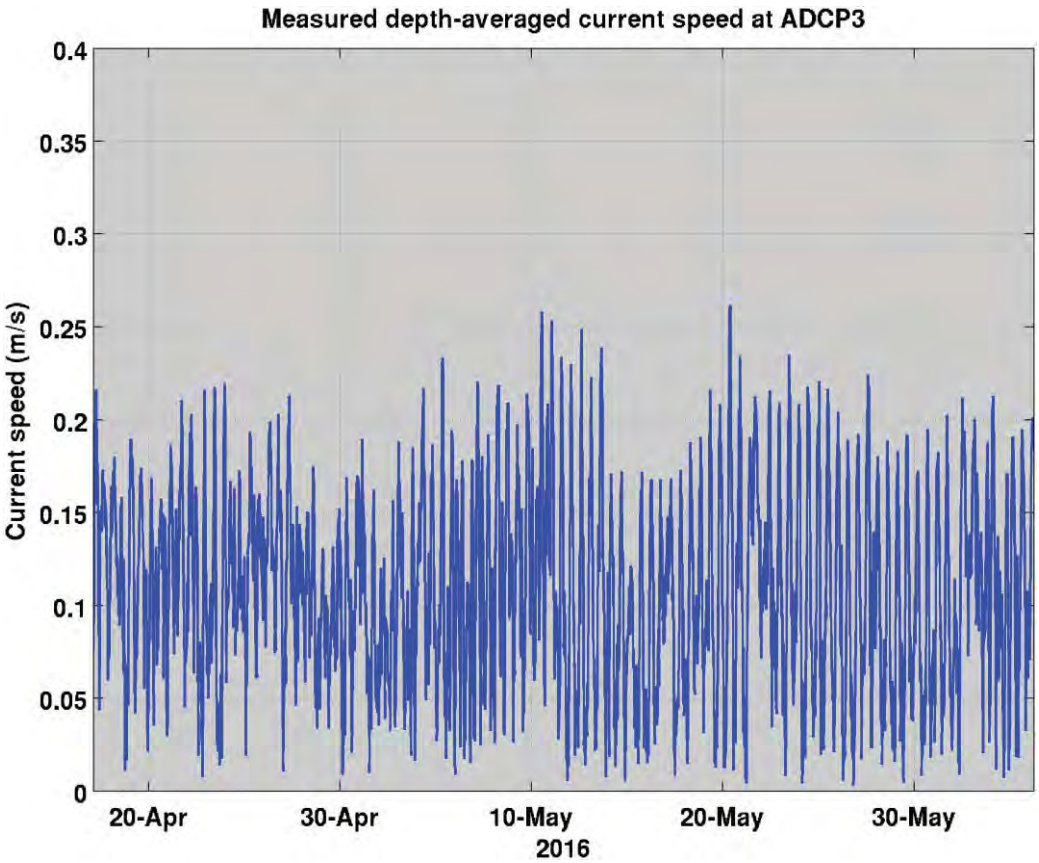
Measured depth-averaged current speed at ADCP3
Current speed (m/s)
0.4
0.35
0.3
0.25
0.2
0.15
0.1
0.05
0
20-Apr
30-Apr
10-May
20-May
30-May
2016

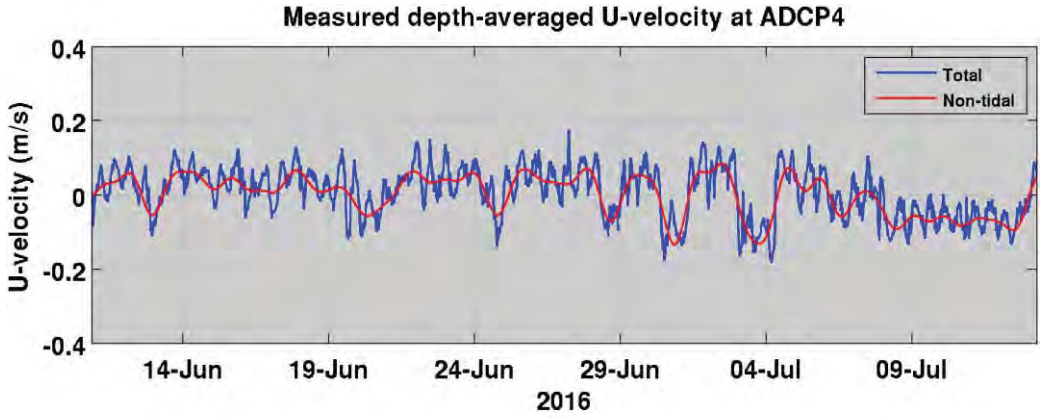
Measured depth-averaged U-velocity at ADCP4
U-velocity (m/s)
0.4
0.2
0
-0.2
-0.4
Total
Non-tidal
14-Jun
19-Jun
24-Jun
29-Jun
04-Jul
09-Jul
2016

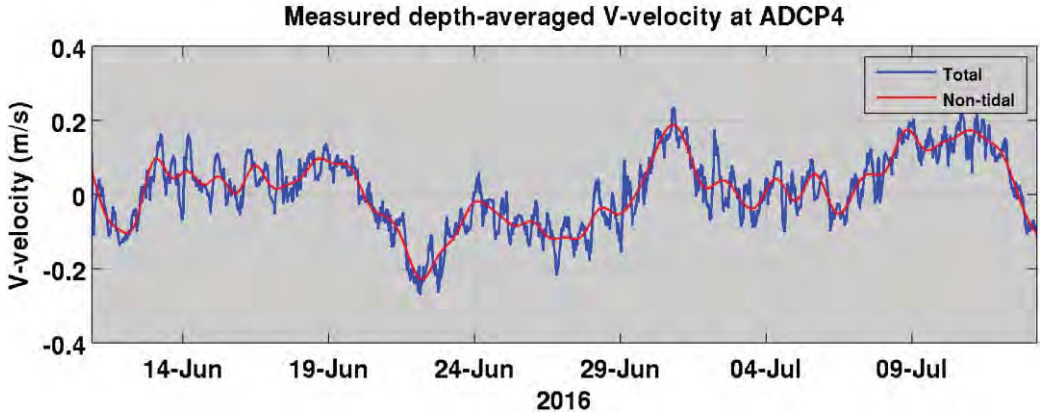
Measured depth-averaged V-velocity at ADCP4
V-velocity (m/s)
0.4
0.2
0
-0.2
-0.4
Total
Non-tidal
14-Jun
19-Jun
24-Jun
29-Jun
04-Jul
09-Jul
2016

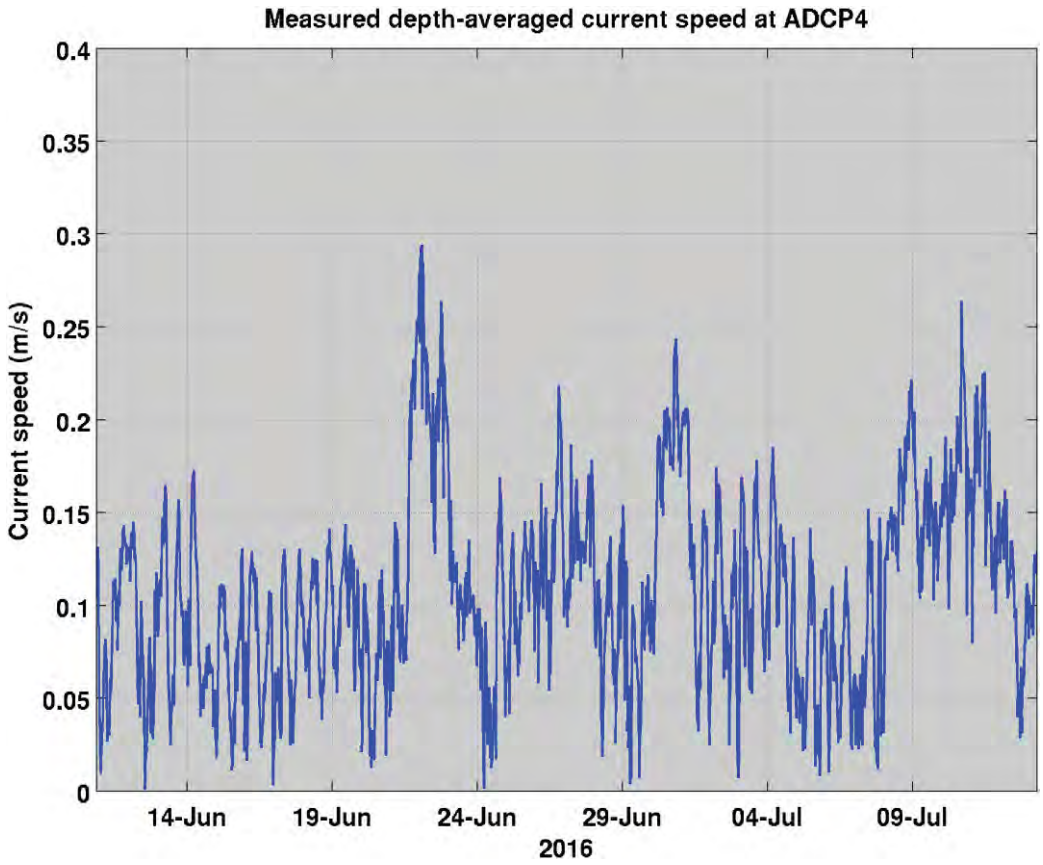
Measured depth-averaged current speed at ADCP4
Current speed (m/s)
0.4
0.35
0.3
0.25
0.2
0.15
0.1
0.05
0
14-Jun
19-Jun
24-Jun
29-Jun
04-Jul
09-Jul
2016

APPENDIX C – LOCATION OF RELEASE SITES

Geographic coordinates of release sites used for the dredging and the disposal plume modelling.

Positions	Geographic coordinates (WGS 84 datum)	
	Longitude (East)	Latitude (North)
R0	174.501963	-35.837500
R1	174.507890	-35.835210
R2	174.520148	-35.847333
R3	174.523247	-35.862960
R4	174.538100	-35.878500
R5	174.545600	-35.885700
R6	174.521125	-35.842327
PW	174.581275	-35.915609
PN	174.588669	-35.904212
PE	174.600443	-35.910711
PS	174.594556	-35.922250
ADCP	174.590750	-35.912833